NUREG/ CP-0034
Vol. 2

Proceedings of the Topical Meeting on Advances in Reactor Physics and Core Thermal Hydraulics

Held at Kiamesha Lake, NY
September 22-24, 1982

Sponsored by
Northeastern New York Section of the American Nuclear Society

Reactor Physics Division of the American Nuclear Society

Thermal Hydraulics Division of the American Nuclear Society

Proceedings printed by
U.S. Nuclear Regulatory
Commission

Available from

GPO Sales Program
Division of Technical Information and Document Control
U.S. Nuclear Regulatory Commission
Washington, DC 20555

Printed copy price: $13.00

and

National Technical Information Service
Springfield, VA 22161

NUREG/CP-0034
Vol. 2

Proceedings of the Topical Meeting on Advances in Reactor Physics and Core Thermal Hydraulics

Held at Kiamesha Lake, NY
September 22-24, 1982

Manuscript Completed: July 1982
Date Published: August 1982

Sponsored by
Northeastern New York Section of the American Nuclear Society

Reactor Physics Division of the American Nuclear Society

Thermal Hydraulics Division of the American Nuclear Society

Proceedings printed by
U.S. Nuclear Regulatory Commission
Washington, D.C. 20555

ABSTRACT

Technical papers presented at the ANS Topical Meeting on Advances in Reactor Physics and Core Thermal Hydraulics, September 22-24, 1982, at Kiamesha Lake, N.Y. are included in these Proceedings. Reactor physics, core thermal hydraulics, and the interactions between core physics and thermal hydraulics are covered both for thermal reactors and for fast breeders. There are sessions on current challenges in these areas, on measurement and analysis of fast reactor physics parameters, on coupled core physics and thermal-hydraulics analysis, on in-core fuel management, on nodal and homogenization methods in reactor physics, on core thermal hydraulic and nuclear instrumentation, and on validation of fast reactor thermal hydraulic methods. In addition there are sessions on reactor theory, on measurement and analysis of thermal reactor physics parameters, on validation of thermal reactor thermal hydraulics methods, and on development and utilization of differential and integral nuclear data.

The conference brings together experts from many countries to present papers and exchange ideas on these closely related core physics and thermal hydraulics aspects of fission reactors.

PLANNING COMMITTEE MEMBERS

General Chairman: R.C. Block

Program Chairman: M.R. Mendelson

Program Committee:

P.B. Abramson
R.C. Block
R.L. Crowther
H.B. Currin
D.J. Diamond
A.M. Erdman
F. Feiner
N.C. Francis
O.C. Jones
D.R. Harris
L.E. Hochreiter
S.W. Kitchen
M.J. Ohanian
S.N. Purohit
R.R. Rippel
P.J. Turinsky
C.R. Weisbin
M. Podowski
R.T. Lahey, Jr.

Registration Chairman: T.F. Ruane

Publications Chairman: D.R. Harris

Public Information Chairman: E.R. Wagner

Finance Chairman: J. L. Bear

Hotel and Transportation Arrangements: R.C. Rohr

Best Paper Award: D.R. Harris and N. Todreas

Guest Activities: Rita Block

Student Liaison: B. Malaviya

TABLE OF CONTENTS

TABLE OF CONTENTS CONTINUED

TABLE OF CONTENTS CONTINUED

TABLE OF CONTENTS CONTINUED

FOREWORD

The 1982 topical meeting on Advances in Reactor Physics and Core Thermal Hydraulics is the first topical meeting to be jointly sponsored by the Reactor Physics and Thermal Hydraulics divisions. A major purpose of this joint venture, aside from airing the technical issues within each area of expertise, is to stimulate and encourage better communication between these two fundamental but intimately related disciplines. Too often, the working Reactor Physicist or Thermal Hydraulicist is concerned only with the immediate problems within his own field, and does not (or is not able to) step back and view his work in the context of the requirements and limitations of the other discipline. Thus, in a joint meeting of this type, it is hoped that new insights will be gained, and better focused development programs will result.

When the program committee first considered the idea of a Reactor Physics/Thermal Hydraulics Cosponsorship, an immediate concern was that the number of papers would be so overwhelming, and that they would cover such a broad range of topics, that it might not be possible to provide a meaningful focus for the meeting. Using the 1980 Saratoga topical meeting on thermal hydraulics as a guide, it became apparent that the developmental aspects of both disciplines could not possibly be covered in one meeting. For this reason the thermal hydraulics sessions were limited to validation of methods, whereas the reactor physics sessions included both development and validation of methods. Even with this limitation, a large number of papers were accepted for this meeting (about 85), forcing the program committee to arrange triple concurrent sessions.

The papers are split about 60% on reactor physics and 40% on thermal hydraulics. A significant percentage of the papers (about 22%) originated outside of the United States. Among the approximately 45 papers dealing strictly with reactor physics, there is strong representation in four fields of specialization: measurement and analysis of physics parameters (13 papers), reactor theory and methods development (13 papers) reactor physics aspects of fuel management (11 papers), and the development, use, and testing of nuclear data (8 papers). About one-third of these papers deal with fast reactors. There are about 16 papers dealing with validation of thermal hydraulic methods; these are split nearly equally between fast reactor methods (7 papers), and thermal reactor methods (9 papers). Two sessions (11 papers) are devoted to the interaction of neutronic and thermal hydraulic effects in reactor analysis codes and models. Finally, a session on new developments in core instrumentation features about 6 papers dealing with thermal hydraulic phenomena, and two papers dealing with monitoring of power distributions and subcriticality.

The papers span such a broad spectrum of activities that it does not appear to be possible to characterize trends. Suffice it to say that progress appears to be ongoing in all of the areas mentioned, despite what are sometimes severe handicaps due to cutbacks in funding and dwindling supply of fresh young talent. Although today's scene is still one of vigorous technical development, it is with some trepidation that we anticipate the results of a similar assessment in ten years time.

The program for this meeting was planned by the members of the Technical Program Committee (listed elsewhere), with input from a number of sources - members of the New York Northeastern Section of the ANS, members of the Reactor Physics and Thermal Hydraulics Division of the ANS, Colleagues of the General and Technical Program Chairman at RPI and KAPL, paper reviewers, and session chairman. The latter carried the lead responsibility of arranging for invited speakers. We are indebted to all of these participants for their cheerful cooperation and expert guidance.

MR Mendelson
Program Chairman

ACKNOWLEDGEMENTS

The efforts of the speakers and their colleagues are gratefully acknowledged. Also acknowledged are the many persons who provided expert reviews for the papers contributed to the meeting. We are grateful to the U.S. Nuclear Regulatory Commission for publishing these Proceedings.

DEDICATION

It is the traditional task of the General Chairman to review the technical content of the program and to thank all of the people who have made the meeting successful. I have read Dick Mendelson's review and I can not express myself any better, so I wholeheartedly support and agree with all of Dick's comments and will not repeat them here. I would like, along with Dick, to thank all of the people who have worked long and hard in preparing for this meeting and, in addition, I also thank all who came to Kiamesha Lake to participate in the program and discussions.

I will take the Chairman's privilege to dedicate this meeting to one man who could not attend and participate in the discussions but whose presence is felt by many of us. We dedicate this ANS Topical Meeting on Advances in Reactor Physics and Core Thermal Hydraulics to Dr. Robert A. Dannels, a very special person who passed away last year. Bob Dannels, a Fellow of the American Nuclear Society, had served our Society in many capacities. He was Chairman and a member of the Executive Committee of both the Reactor Physics Division and of the Mathematics and Computations Division. In addition, Bob chaired the ANS committee which produced the ANSI standard for nuclear data. I first met Bob when he served both as a member of the Cross Section Evaluation Working Group and later as Acting Director of the National Nuclear Data Center at Brookhaven National Laboratory; I learned to appreciate and respect his technical competence and his ability to inspire colleagues to work hard towards achieving the goals he set forth. From his colleagues at Westinghouse I heard only glowing descriptions about Bob's abilities both technically and administratively; he was one of the best liked managers there.

Far and above Bob's technical credits were his marvelous personality, his keen wit and the fact that he was a most feeling and warm human being. We missed you at this meeting, Bob, but your presence was felt throughout.

Robert C. Block
General Chairman

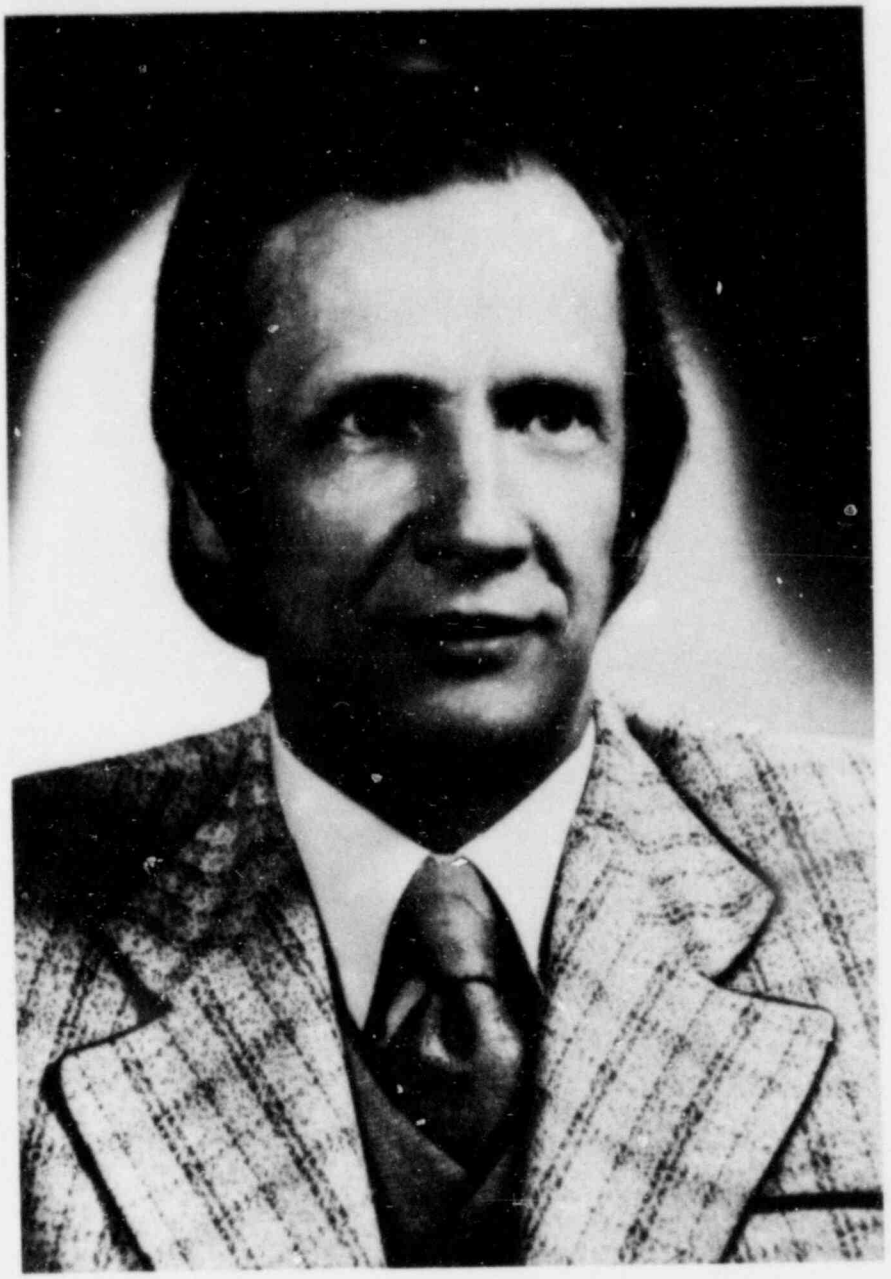

Robert A. Dannels

A VALIDATION STUDY OF THE COBRA-WC COMPUTER PROGRAM FOR LMFBR CORE THERMAL-HYDRAULIC ANALYSIS

E. U. Khan, J. M. Bates

May 1981

Prepared for
the U.S. Department of Energy
under Contract DE-AC06-76RLO 1830

Pacific Northwest Laboratory
Richland, Washington 99352

ACKNOWLEDGEMENT

The authors would like to thank Dr. R. J. Neuhold of the Department of Energy for supporting this research.

A VALIDATION STUDY OF THE COBRA-WC COMPUTER PROGRAM FOR LMFBR CORE THERMAL-HYDRAULIC ANALYSIS

E. U. Khan, J. M. Bates

Battelle, Pacific Northwest Laboratory
Richland, Washington 99352

ABSTRACT

The COBRA-WC (Whole Core) computer program has been developed as a benchmark code to predict flow and temperature fields in LMFBR rod bundles. Consequently, an extensive validation study has been conducted to reinforce its credibility. A set of generalized parameters predicts data well for a wide range of geometries and operating conditions which include conventional (current generation LMFBRs) fuel and blanket assembly geometry in the forced, mixed, and natural convection regimes. The data base used for validating COBRA-WC was obtained from out-of-pile and in-pile tests. Most of the data was obtained in fully heated bundles with bundle power skew across flats up to 3:1 (max:min), Reynolds number between 500 and 80,000, and coolant mixed-mean temperature rise ($\Delta\bar{T}$) in the range, $78^{\circ}F \leq \Delta\bar{T} \leq 340^{\circ}F$. Within the bundle, 95% of the predicted coolant temperature data points fall within $\pm 25^{\circ}F$ for $150^{\circ}F \leq \Delta\bar{T} \leq 340^{\circ}F$ and within $\pm 17^{\circ}F$ for $78^{\circ}F \leq \Delta\bar{T} \leq 150^{\circ}F$.

A VALIDATION STUDY OF THE COBRA-WC COMPUTER PROGRAM FOR LMFBR CORE THERMAL-HYDRAULIC ANALYSIS

INTRODUCTION

Investigators have developed a number of analytical methods for predicting Liquid Metal Fast Breeder Reactor (LMFBR) core thermal hydraulics. Because of core geometrical complexities, various physical approximations are required to develop tractable analytical models that can be readily solved on high-speed computers. These approximations reduce model complexity and computational resource needs, but they also reduce model generality. As the model generality diminishes, the degree of empiricism increases, and because of this the range of application of an analytical method for different geometric and operating conditions requires validation.

The COBRA-WC (Whole Core) computer program [1,2], based on the COBRA-IV-I code [3] is a compromise between the free-field prediction methods and the more empirical methods [4,5]. COBRA-WC can predict either subassembly temperatures on a subchannel basis or core-wide temperatures on a 'lumped-channel' basis.

COBRA-WC is being used by industry, universities, and the national laboratories to predict flow and temperature fields in the rod assemblies of an LMFBR. Because of its wide use and its intended use for core licensing, this validation document was required to support the credibility of the code. Most of the data base used for validating COBRA-WC was obtained from out-of-pile and in-pile tests in wire-wrapped pin bundles in which the pins are arranged in a triangular array.

A set of generalized input parameters are presented for COBRA-WC that accurately predict both hydrodynamic and thermal data for a wide range of geometries, including conventional-size LMFBR blanket and fuel assembly geometry, and operating conditions extending from laminar to turbulent flows and from forced to natural convection.

The following terms used in the paper are defined for clarification. Data Assessment refers to evaluation of data for application to the validation study. A code is said to be "verified" if the numerical techniques and the computer program give "correct" solution to the mathematical model. Code validation requires that the mathematical model represent, at least to the intended degree of approximation, the true physical situation being analyzed. The code validation procedure that has been followed involved: 1) validation of the code with analytical solutions, standard problems sets, and other codes; and 2) "separate" and "combined" model testing by comparing the code predictions with a large data base. To economize on space, only the combined model testing of the code will be presented here. The scope of the validation

study is limited to nominal (undistorted) rod bundles operating in forced, mixed, or natural convection between Reynolds numbers of 500 to 80,000. The code has been validated with out-of-pile and in-pile data.

DESCRIPTION OF COBRA-WC (WHOLE CORE) COMPUTER PROGRAM

The COBRA-WC code is an extension of the COBRA-IV-I code for multiassembly thermal-hydraulic analysis of LMFBR cores. It was specifically developed to analyze core flow coastdown to natural circulation cooling. In this transient, single-assembly analysis is not sufficient since heat transfer between adjacent assemblies and interassembly flow redistribution can be significant, particularly for heterogeneous cores. The COBRA-WC code was designed to model many assemblies simultaneously and can account for these interassembly effects.

For application to single-phase cooling of isolated assemblies, COBRA-WC has the same thermal-hydraulic models and governing equations as COBRA-IV-I (Table 1). The code contains thermal-hydraulic models for pressure drop, turbulent mixing, diversion crossflow, wire-wrap sweep flow, thermal conduction, inlet flow split, buoyancy-induced flow redistribution, and fuel rod and structure thermal models. The method of solution of the COBRA-WC equations is an improvement over those in COBRA-IV-I because it led to reduction in COBRA-WC computation times. However, because the models and equations are identical in COBRA-IV and COBRA-WC, the converged solutions have been found to be identical. Consequently, any COBRA-IV-I validation study performed using data obtained from a single-phase/single-assembly system also validates COBRA-WC.

The various COBRA-WC thermal-hydraulic models (Table 1) are used to develop the governing equations for mass, momentum, and energy transport in a rod bundle or a portion of the core. The presence of rods and spacers makes it necessary to make approximations and assumptions for terms in the governing equations. As a result, the following input code parameters are needed [1,2]:

- subchannel friction factor, f
- wire-wrap sweep flow coefficient, DUR
- turbulent mixing coefficient, β
- crossflow resistance coefficient, k_{ij}
- transverse momentum control volume width-to-length ratio, s/ℓ (or transverse momentum length, ℓ)
- conduction shape factor, G
- bundle tolerance factor, RPF.

The channel friction factor and its dependence on Reynolds number is a required input to the code. The friction factor is used in the axial momentum equation. The flow distribution between the various channels is sensitive to friction factor.

TABLE 1. COBRA-WC Thermal-Hydraulic Models

Intra-Assembly

- pressure drop (channel friction factor)
- turbulent mixing
- diversion crossflow
- wire-wrap sweep flow (swirl flow)
- thermal conduction
- inlet flow (velocity) distribution
- buoyancy-induced flow redistribution
- flow recirculation
- fuel rod model

Interassembly

- interassembly heat transfer
- interassembly flow redistribution

COMPARISON OF COBRA-WC PREDICTIONS WITH MEASURED DATA

The input parameters to the COBRA-WC code are listed below with the standard values used for subchannel analysis. The parameters are limited for use in wire-wrap rod bundles contained in a hexagonal duct. The rods are arranged in a triangular array, and the wire starts on each rod at the same axial and circumferential location.

- modified subchannel smooth tube friction factor (Equation [1] below)
- DUR = 1.0
- β = 0.01
- k_{ij} = 0.05
- ℓ = 2.0 * S (gap width between interior rods)
- G = 0.5
- RPF = bundle tolerance factor adjusted to provide 97% of the bundle porosity within the bundle

The smooth tube friction factor is modified based on flow split measurements [6,7] as follows:

$$f = \frac{f_{smooth}}{X_1^2} \frac{d_{interior}}{\overline{d}_{bundle}} \quad \text{(interior channels)} \tag{1a}$$

$$f = \frac{f_{smooth}}{X_2^2} \frac{d_{wall}}{\overline{d}_{bundle}} \quad \text{(wall channels)} \tag{1b}$$

where X is the flow split ($U/\bar{U}$) for the channel under investigation, f_{smooth} is the smooth tube friction factor, $\bar{d}_{bundle}$ is the bundle average hydraulic diameter, and $d_{channel}$ is the channel hydraulic diameter. Typical measured flow split parameters [6,7,8] X_1 and X_2 for interior and wall channels, respectively, are shown in Figure 1 for turbulent flow. In transition and laminar flow the flow split parameters were obtained from Wang and Todreas [9]. When the friction factor of Equation (1) is multiplied by Novendstern's multiplier (M) for wire-wrapped bundles [10], the product gives the friction factor used for interior and wall channels. Figures 2 and 3 show the flow split as a function of Reynolds number for a wire-wrapped rod bundle with $h/d = 8$ and $p/d = 1.063$.

Table 2 shows the geometry and regime of operation of the experiments used for validating COBRA[a]. The ANL salt trace experiment [11], the ANL dye trace experiment [12], the MIT tests [7], the PNL laser-Doppler experiments [13,14], and the French hydrodynamic tests [15] are used for testing the individual COBRA models separately. The ORNL THORS 19- and 61-pin data [16,17], the WARD data [18], the HEDL data [19], the EBR-II data [20], and the FFTF data [21] are used for testing the combined thermal-hydraulic models in COBRA.

VALIDATION OF COMBINED COBRA MODELS

The Oak Ridge National Laboratory THORS-IIA data [16] was taken in the 19-pin bundle shown in Figure 4. Liquid sodium was used to cool the electrically heated pins. The heated length of the rods is 21 in. The coolant enters the bundle approximately 6 in. below the plane where the rods are heated to provide a fully developed flow field at the entrance to the heated section. Thermocouples are located in the rod walls and also in the wire wraps. An exit rake is located 3 in. above the exit of the heated bundle and is instrumented with thermocouples which directly measure coolant temperatures at the center of various subchannels. The axial power profile is uniform. The hexagonal duct is surrounded by guard heaters to minimize heat losses. The data reported covers a wide range of skews, power-to-flow ratios, and Reynolds numbers. Figure 5 shows a typical comparison of the COBRA predictions with data in the forced-convection regime of bundle operation. Figure 6 shows a typical comparison in the mixed-convection regime of operation. As expected, the transverse temperature gradients are significantly reduced at low Reynolds number, primarily because of significant increase in transverse energy redistribution by conduction and buoyancy-induced crossflow.

The geometry of the THORS 61-pin test bundle [17] (Table 2) is similar to the THORS 19-pin test bundle except for the total number of pins and an axially varying power profile. The bundle was modeled axially by a 9-in. cold entrance length and a 36-in.-long heated length that was followed by a

(a) COBRA is used in the text to mean COBRA-WC. For analysis of single assemblies, COBRA-WC and COBRA-IV-I models and governing equations are very similar, as discussed in the preceding section.

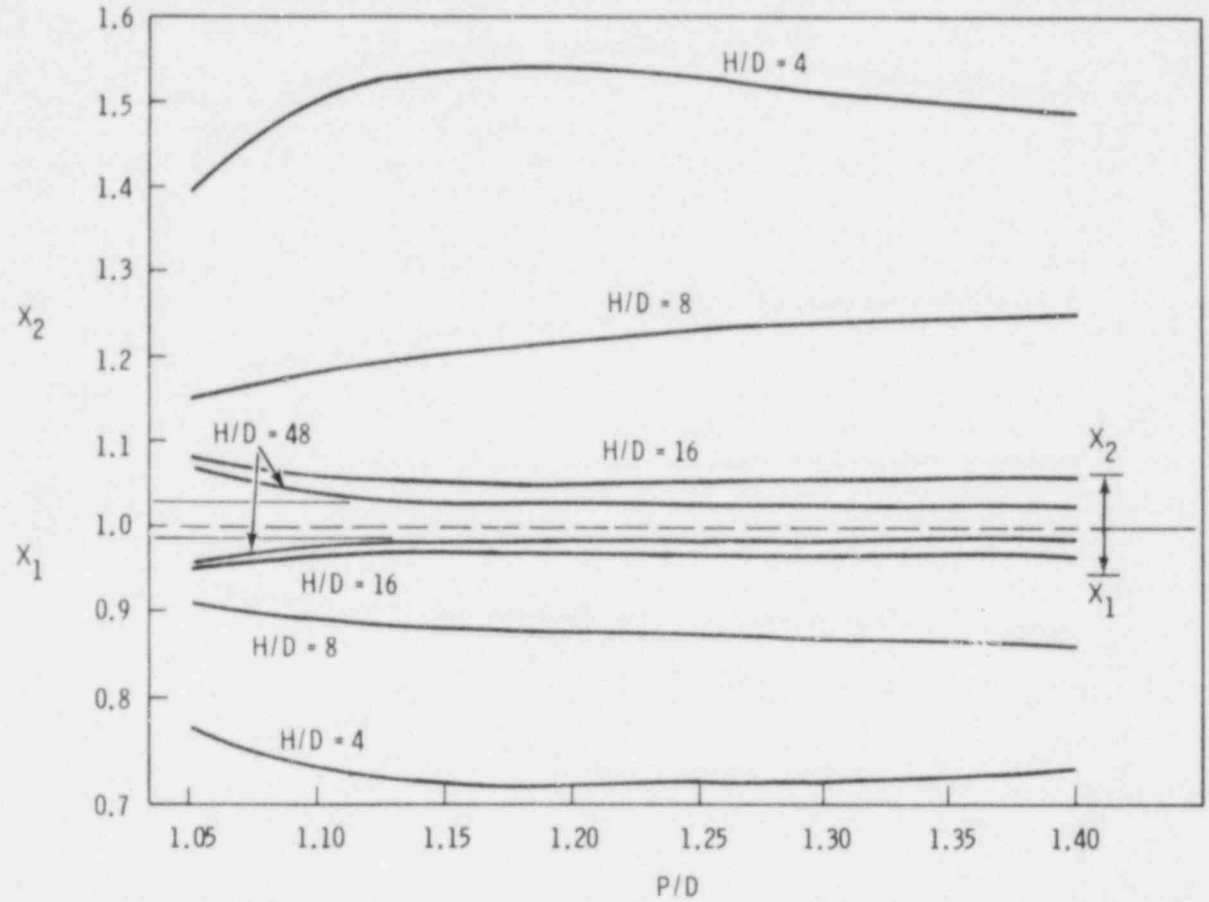

FIGURE 1. Turbulent Flow Split Plot in Interior and Wall Channels for Varicus Geometries in a 61-Pin Bundle [6,9]

1-in.-long unheated length. Figures 7 and 8 show a typical comparison of the COBRA-WC predictions with forced-convection data for a uniform and 3:1 (max:min) power skew using the standard COBRA parameters and estimated channel friction factors from Chiu's [6] correlations. The smooth tube friction factor correlations without Novendstern's multiplier (M) for the interior and wall channels are $f = 0.32/Re^{0.25}$ and $f = 0.31/Re^{0.25}$ in the turbulent flow regime. The prediction of the peak coolant temperature improved when β and DUR were set to zero, but the prediction of the temperature distribution across the bundle was worse. For all ORNL 61-pin data analyzed, $\beta = 0.01$ and DUR = 1 appeared to give the best agreement with data both in the interiors of the bundle as well as in the wall region. At low Reynolds number, the combined effect of thermal conduction and buoyancy-induced cross-flow mixing cause flattening of the transverse temperature profile as seen in Figure 9.

Figure 10 shows the axial location of the thermocouples for the Westinghouse Advanced Reactor Division (WARD) 61-pin simulated blanket assembly tests [18]. Thermocouples are located at three axial elevations in the

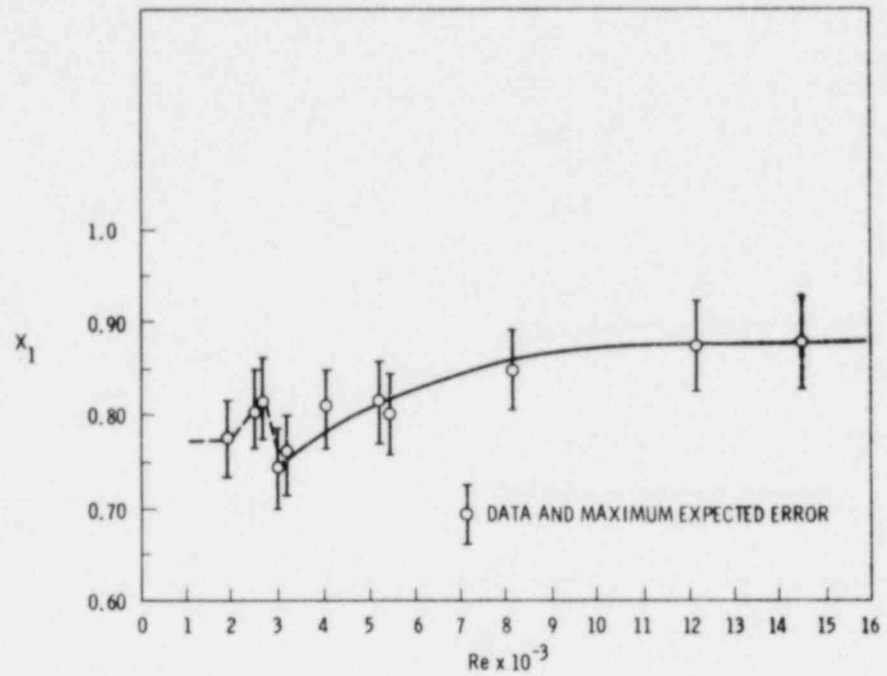

FIGURE 2. Interior Subchannel Flow Split Parameter X_1 Versus Re for the Section of H/D = 8.0, P/D = 1.063 [6,8,9]

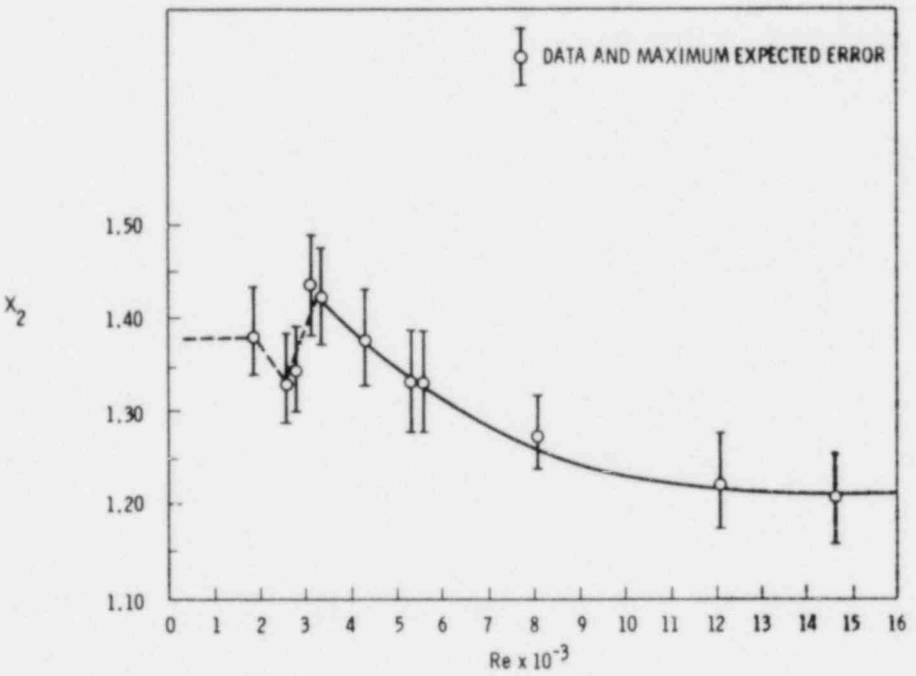

FIGURE 3. Edge Subchannel Flow Split Parameter X_2 Versus Re for the Test Section of H/D = 8.0 and P/D = 1.063 [6,8.9]

TABLE 2. Geometrical and Operating Conditions for Validation Study

Data	Reference	Geometrical Characteristics p/d	h/d	Number of Pins	Experiment Type[a]	Operating Conditions[a] Forced	Mixed	Natural Convection
1. Separate Thermal-Hydraulic Model Testing								
a. ANL Salt Trace Expt.	Lorenz, Ginsberg and Morris 1974	1.24	48	91	SI[a]	X		
b. ANL Dye Trace Expt.	Lorenz, Pedersen and Pierce 1973	1.20	48	91	D/HW[a]	X		
c. MIT LDA Expt.	Chen, Ip and Todreas 1974	1.25	24	61	LDV[a]	X		
d. PNL LDV 2x6 Expt.	Bates and Khan 1980	1.21	--	12	HP[a] LDV[a]		X	X
e. French Hydrodynamic Experiment	Lafay, Menant and Barrois 1975	1.18	19	19		X		
2. Combined Model Testing								
Out-of-Pile								
a. ORNL THORS Tests	Fontana 1973, Morris 1980	1.24	52	(19, 61)	HP[a]	X[b]	X	
b. WARD Blanket 61-Pin Test	Engel, Markley and Minushkin 1978	1.08	7.7	61	HP[a]	X[b]	X[b]	X[b]
c. HEDL Fuel 217-Pin Test	Milburg, Hassberger and Boasso 1977	1.24	52	217	HP[a]		X	
In-Pile								
d. EBR-II XX08 Test	Gillette et al. 1979	1.28	34.5	61	HP[a]	X[b]		
e. FFTF FOTA Data	Hoth 1981	1.24	52	217	HP[a]	X[b]	X[b]	X[b]

(a) Type of experiment: HP=heated pin, LDV=Laser Doppler Velocimeter, D/HWI=dye or hot water injection, SI=salt injection

(b) Indicates steady state and transients

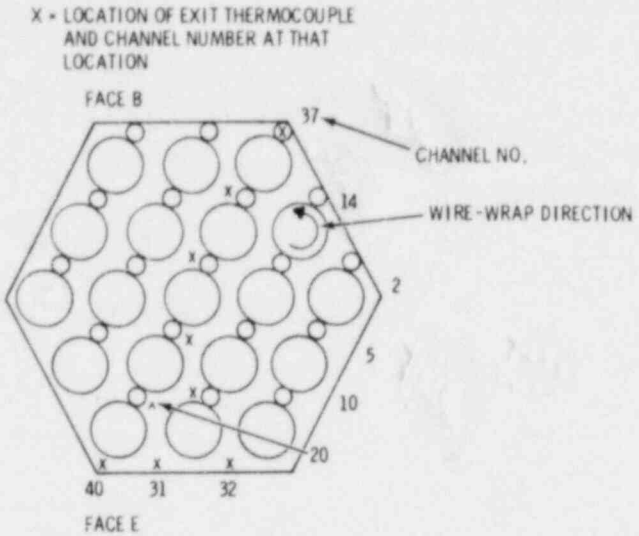

TEST PARAMETERS: REF. 13

1. FLUID - LIQUID Na
2. FLOW RATE - UP TO 56 GPM (Re - 1,000 to 70,000)
3. POWER SKEW
   a. ALL RODS UNIFORMLY HEATED
   b. EACH ROD HEATED INDIVIDUALLY
   c. B 20% HIGHER THAN E
   d. E 20% HIGHER THAN B
   e. B 300% HIGHER THAN E
   f. E 300% HIGHER THAN B
4. d = 0.23 IN.
   h/d = 52
   p/d = 1.24

FIGURE 4. Oak Ridge THORS-IIA 19-Pin Bundle Geometrical and Test Parameters

heated zone and at three axial elevations above the heated zone. The flow housing around the pins has two auxiliary ducts on opposite faces. Each duct contains five simulator rods. The auxiliary ducts can have their own independent power generation and flow rates and provide data on cross-duct heat transfer effects. The pins are spaced by helically wound wire-wrap of 4-in. lead. Within the pin there is a resistance coil of nichrome wire wound in a manner so as to provide a chopped cosine axial heat flux profile over a 45-in. length. Sodium is used to cool the pins. Each row of pins can operate at different power levels.

Table 3 shows the typical range of test parameters for the WARD 61-pin experiments. A large range of power skews, Reynolds numbers, and thermal regimes are covered by the data. COBRA predictions use the standard parameters described at the beginning of this section. The friction factor correlations in the turbulent flow regime are $0.389/Re^{0.25}$ and $0.24/Re^{0.25}$ for interior and wall channels, respectively, determined by using Equation (1) and flow split from Figures 2 and 3. The friction factors correlations should be multiplied by Novendstern's friction factor multiplier for wire-wrapped bundles. The standard parameters used for the blanket assembly, except for

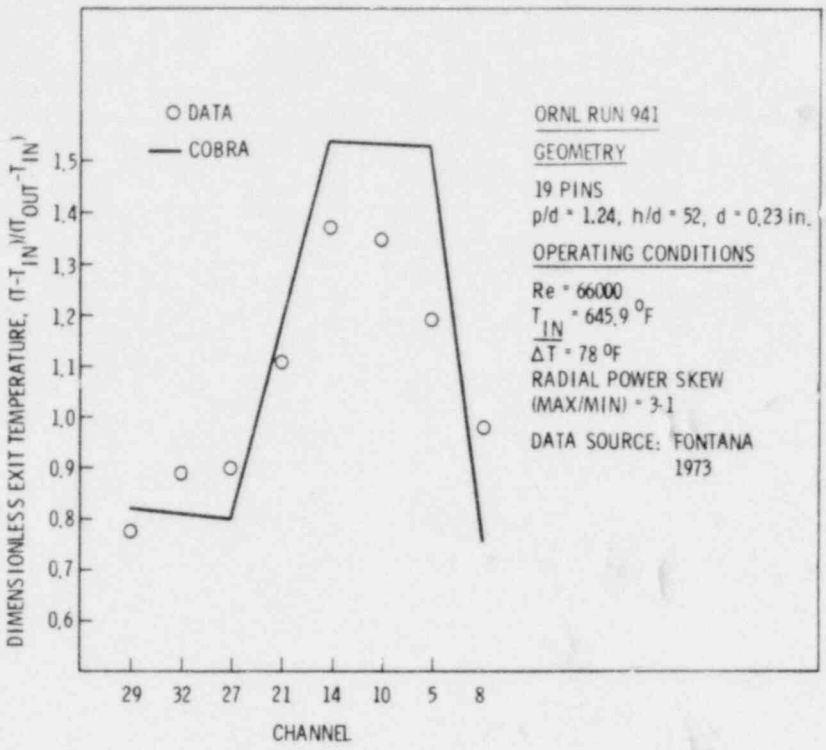

FIGURE 5. Comparison of COBRA-WC Predictions with ORNL 19-Pin Data

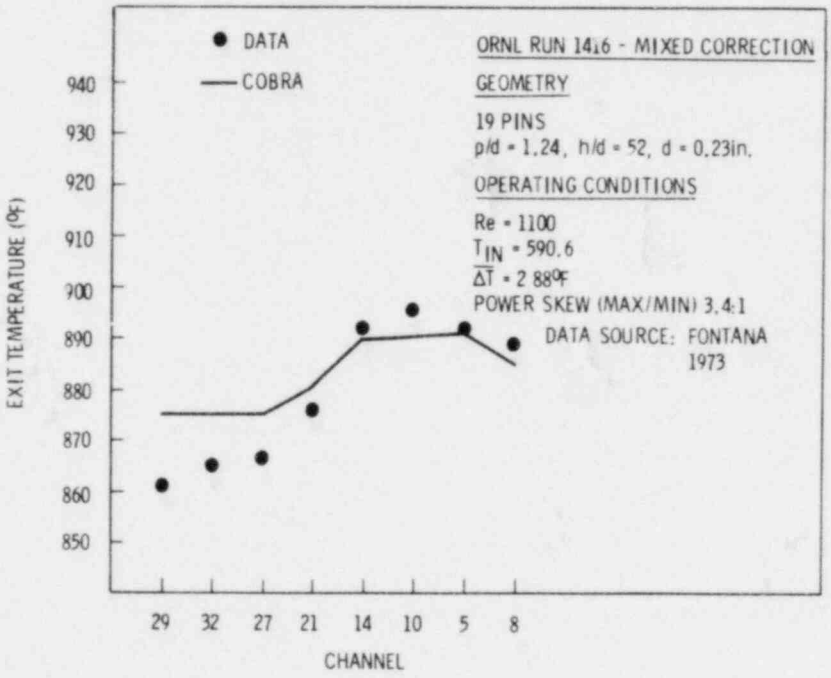

FIGURE 6. Comparison of COBRA-WC Predictions with ORNL THORS-IIA 19-Pin Data

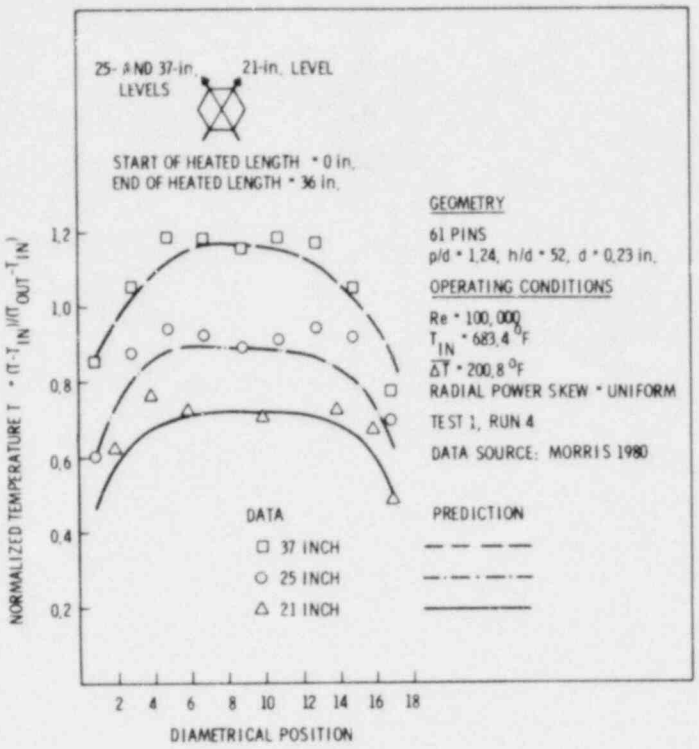

FIGURE 7. Comparison of COBRA-WC Predictions and THORS 61-Pin Data

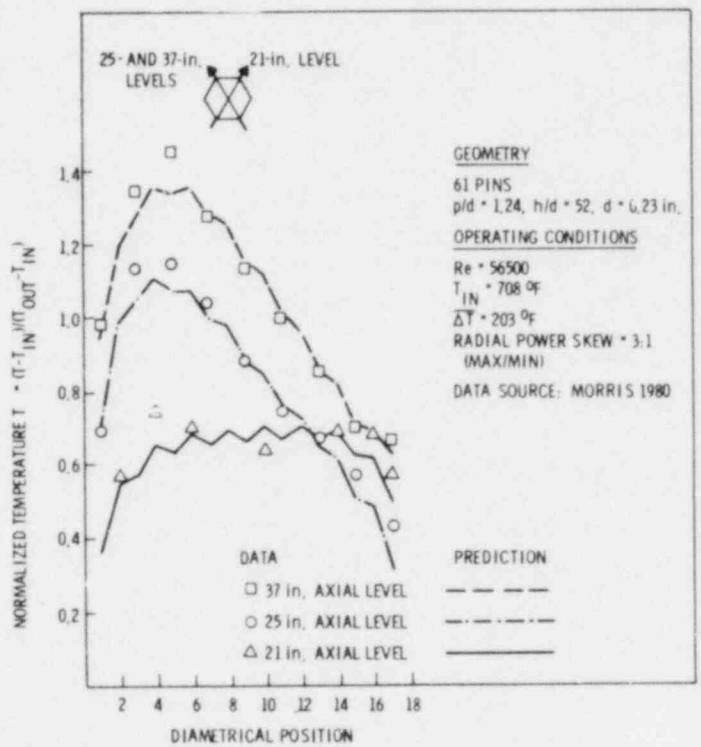

FIGURE 8. Comparison of COBRA-WC Predictions and THORS 61-Pin Data

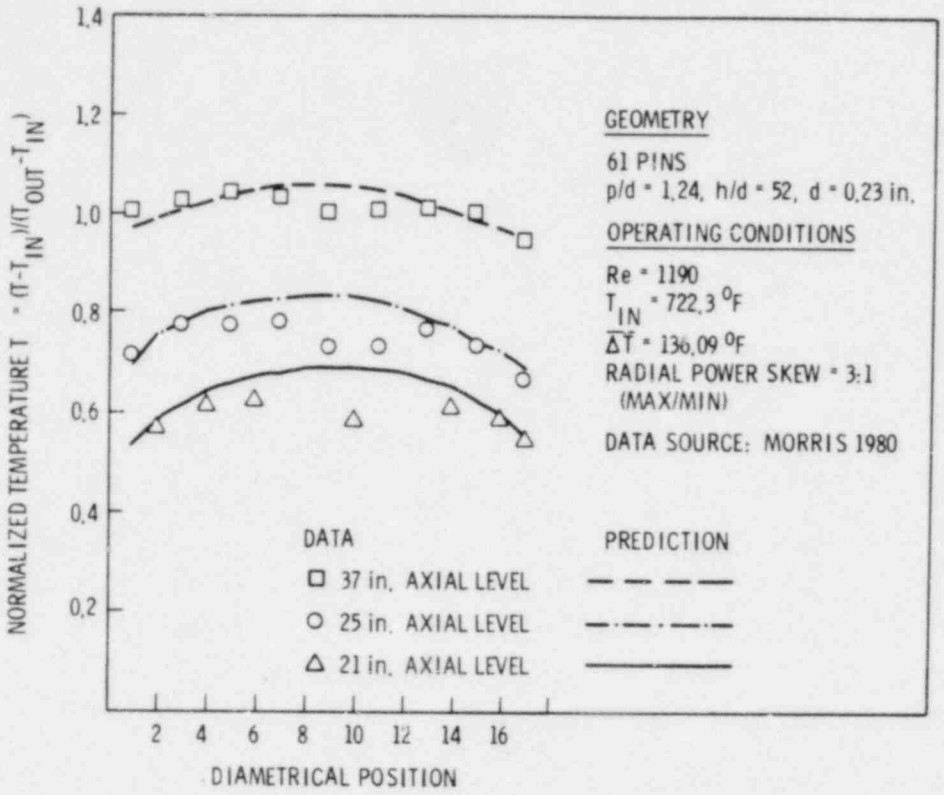

FIGURE 9. Comparison of COBRA-WC Predictions and THORS 61-Pin Data

channel friction factors, were also used for predicting the ORNL 61-pin fuel assembly data. As can be seen in Figures 11 through 13, the COBRA predictions match data well. Figure 11 shows a typical comparison of predictions and data near the exit of the heated length for run 220. The corresponding plot for run 229, shown in Figure 12, shows a significant flattening of the transverse temperature profile at a Reynolds number of about 1025. The flattening of the temperature profile at the low flow rates is attributed to a combined effect of thermal conduction and buoyancy-induced flow redistribution within the assembly. The thermal conduction shape factor (G) was found to be 0.5 by varying G over a range to determine the value that best matched the data. The WARD data was used to validate the buoyancy-induced flow redistribution model in COBRA and the intra-assembly heat transfer model. Radial heat transfer from the test section to the auxiliary ducts was accurately predicted by COBRA. This was determined by a comparison of COBRA temperature predictions and temperatures measured in the auxiliary duct. Figure 13 shows the transverse temperature distribution for run 220 at a plane about 10 in. above the end of the heated zone. The COBRA predictions match data well except in the channel next to the wall. For most data sets reported in Table 3 the temperature was significantly overpredicted at this location. The probable cause of this is not clear but is attributed to a faulty thermocouple, a radial heat loss effect, or both.

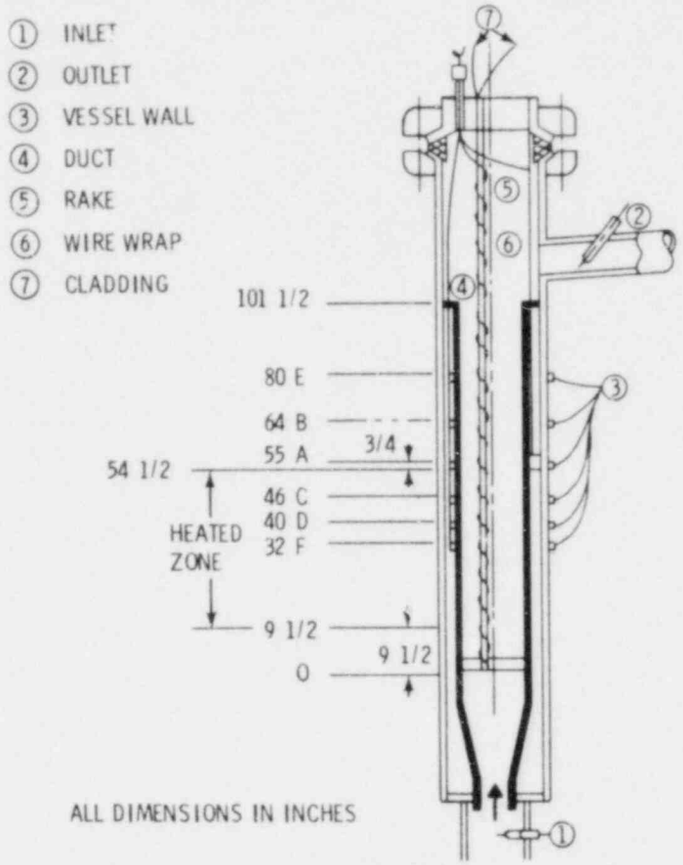

FIGURE 10. Thermocouple Locations in the WARD 61-Pin Bundle Tests

Steady-state and natural-convection transient predictions for the Fast Flux Test Facility (FFTF) core-wide temperature distribution were made using the COBRA-WC code. Subsequently, pretest predictions were compared with data from the instrumented Fuel Open Test Assemblies (FOTA). Figure 14 shows a schematic of the FFTF reactor vessel modeled. Figure 15 shows a one-sixth sector of the core modeled by COBRA-WC. The sector contains both the instrumented FOTA assemblies. Figure 16 shows a comparison of the COBRA-WC subchannel temperature predictions and data at the top of the heated length for the 100% power and flow steady-state conditions. In this calculation the mixed-mean temperature rise was adjusted to be the same as that measured. The predictions were made using standard COBRA-WC parameters and friction factors obtained from Figure 1 and Equation (1). Since the power profile across the row 2 FOTA is almost uniform, it is not clear why the data near the center of the bundle shows a significant dip. A number of such comparisons were made for steady-state and transients both for the row 2 and row 6 FOTAs. The COBRA-WC predictions compare favorably with data. Figure 17 shows a typical comparison of predicted and measured coolant temperature history.

TABLE 3. Test Parameters for WARD 61 Pin Experiment (Engel, Markley and Minushkin 1978)

Run Number	Flow Regime	Power Gradient	Power Input (kW)	Test Section Flow (gpm) and Reynolds Number[b]	Auxiliary Heater 1 Flow[a] (gpm)	T_{INLET} (°F)
220	mixed convection	2.8/1	131.4	19.0/4085	2	599.4
221	mixed convection	2.8/1	129.7	18.1/3890	---	602.8
223	forced convection	2.8/1	257.8	36.8/7905	---	605.2
224	forced convection	uniform	259.2	36.9/7910	---	596.4
225	forced convection	uniform	257.7	36.8/7895	2.8	598.0
227	mixed convection	uniform	33.3	5.0/1050	---	601.9
228	mixed convection	uniform	32.3	4.9/1030	0.7	603.4
229	mixed convection	2.8/1	31.4	4.8/1025	---	598.5
230	mixed convection	2.8/1	32.1	4.8/1010	0.7	600.1
724	natural convection	2.8/1	61.1	4.3/910	---	590.0

(a) Auxiliary heater 2 on cold side of bundle not operating
(b) Inlet Reynolds number

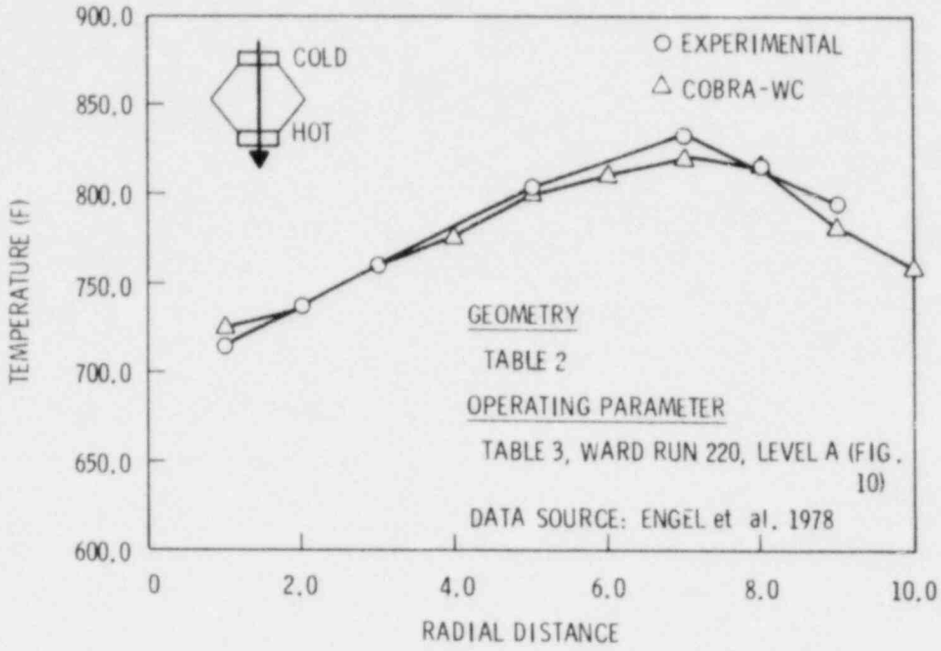

FIGURE 11. Comparison of COBRA-WC Predictions with WARD Data (Run 220)

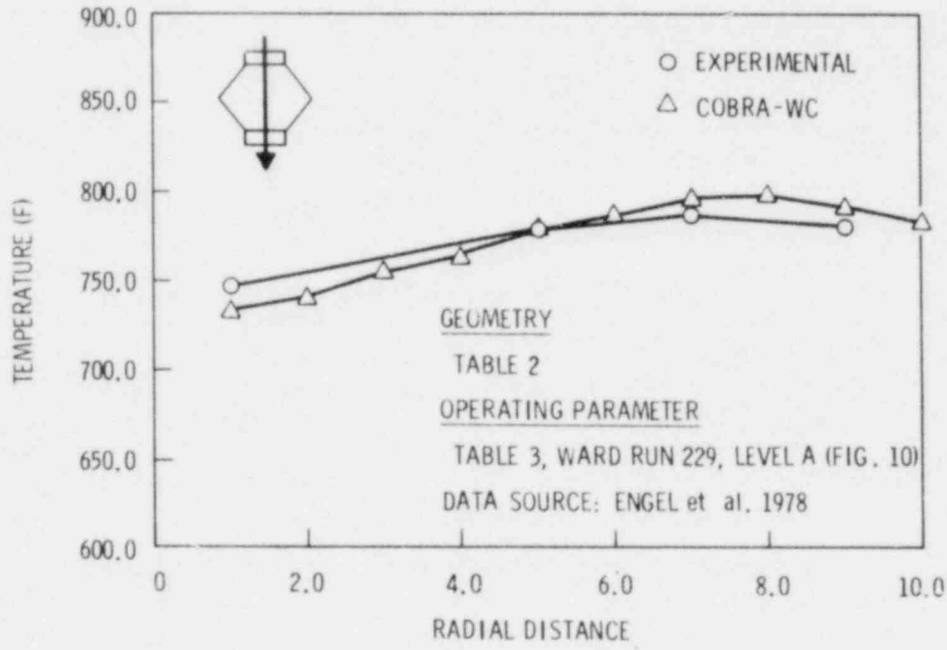

FIGURE 12. Comparison of COBRA-WC Predictions with WARD Data (Run 229)

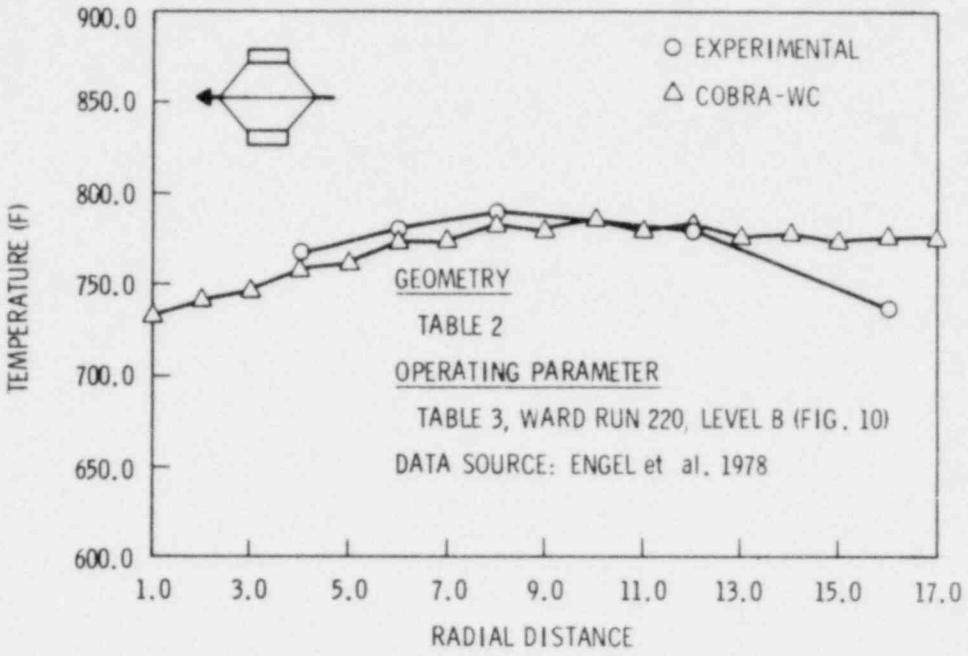

FIGURE 13. Comparison of COBRA-WC Predictions with WARD Data (Run 220)

ASSESSMENT OF CODE PREDICTION ACCURACY

Statistical analysis of all data showed that the code predicts coolant temperature to within ±25°F of measured temperature at a 95% confidence level. This includes temperature measured in the interior of the bundle as well as in the wall channels at all axial levels. No direct correlation was observed between accuracy of coolant temperature prediction with $\Delta\bar{T}$, the coolant mixed-mean temperature rise. However, it was estimated that 95% of the predicted coolant temperature data points fall within ±25°F for $150 \leq \Delta\bar{T} \leq 340$°F and within about ±17°F for $70 \leq \Delta\bar{T} \leq 150$°F. Figure 13 shows a typical plot of the predicted versus measured data for the WARD tests.

One of the major uncertainties in analysis of LMFBR bundle thermal-hydraulic data is how the bundle tolerance is accommodated within the bundle. The manner in which the bundle tolerance is accommodated can significantly affect flow distribution and thus temperature distribution. Another factor that affects flow and temperature and is not accurately known is the subchannel friction factor. Although bundle average friction factor is estimated with reasonable accuracy from a knowledge of bundle pressure drop and bundle flow rate, subchannel friction factor is a derived quantity associated with larger error bars than the bundle average friction factor. Subchannel friction factor is affected by the manner in which tolerance is accommodated within the bundle. For all bundles analyzed, the best match between temperature predictions and data was obtained when the bundle tolerance was accommodated in the interior of the bundle.

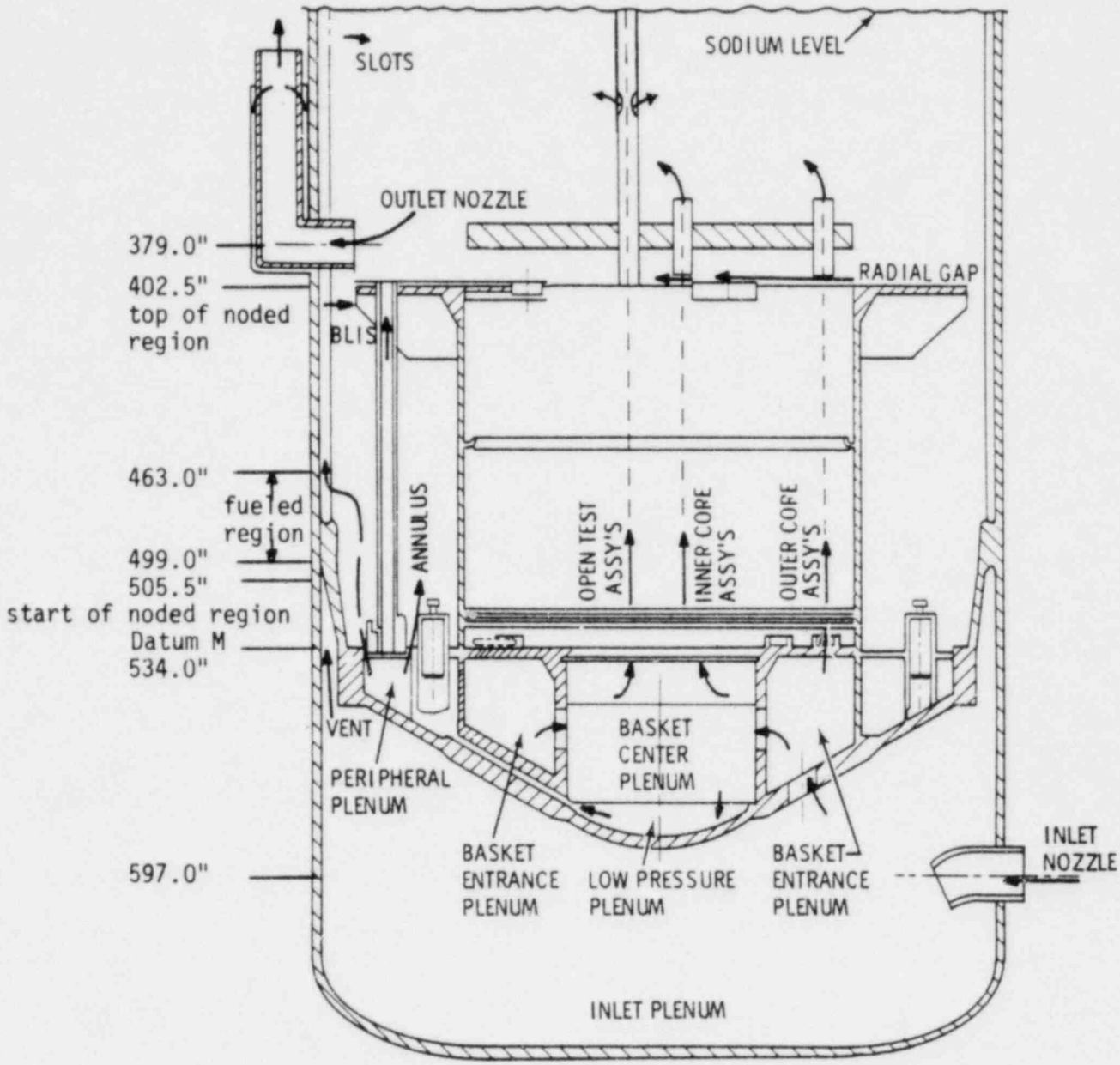

FIGURE 14. Schematic of FFTF Cross Section

Other factors that can lead to differences between code predictions and data are pin bundle distortion and radial heat loss. Pin bundle distortion can affect flow distribution and swirl flow at the duct wall, and thus can affect temperature distribution. Distortion of the pin bundle can also cause movement of the thermocouples located in the wire wrap and of the heater pins from their

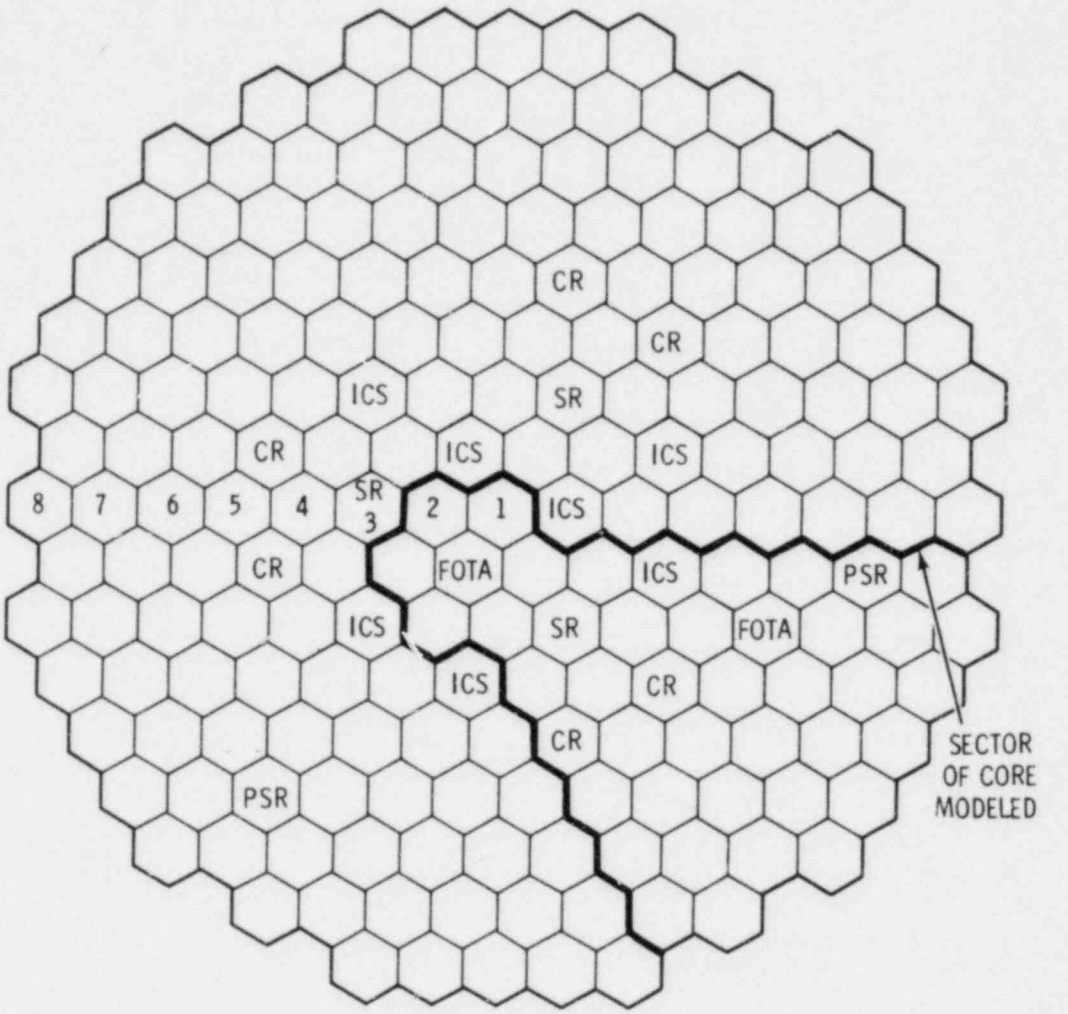

FIGURE 15. Sector of Core Modeled for Predicting Core-Wide Temperature Distribution Using COBRA-WC

normal positions. This uncertainty about the thermocouple location within the pin bundle could increase the difference between the measured temperatures and the temperatures predicted by the code.

In the analysis of heated bundle data at low flows (Re < 1500), it was found that radial heat loss at the duct wall affects bundle temperature distribution not only in the duct wall region but also in the interior of the

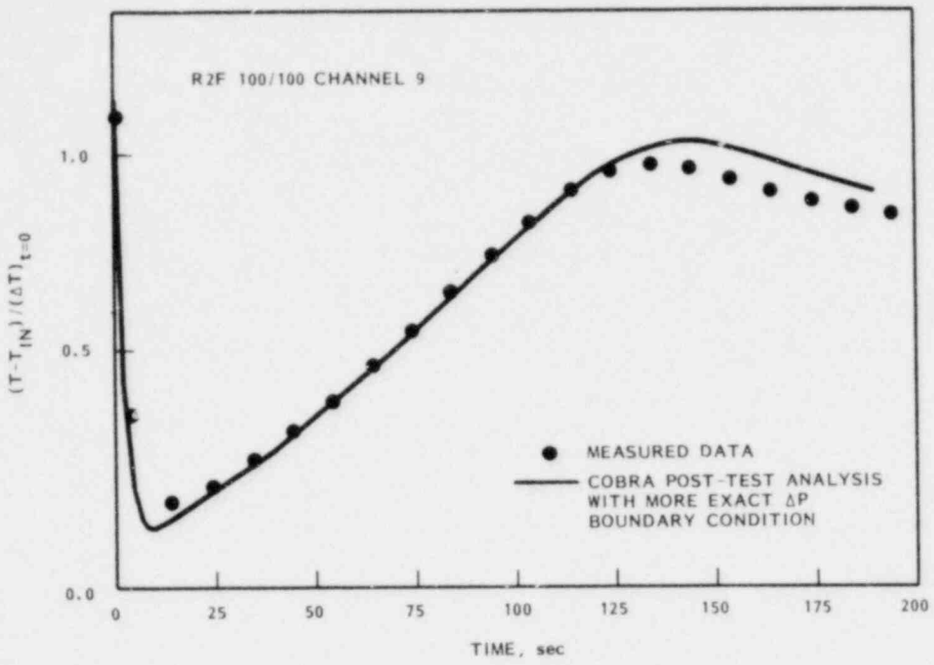

FIGURE 16. Comparison of COBRA-WC Predictions and Row 2 FOTA Data at Top of Heated Length (100% power and flow conditions)

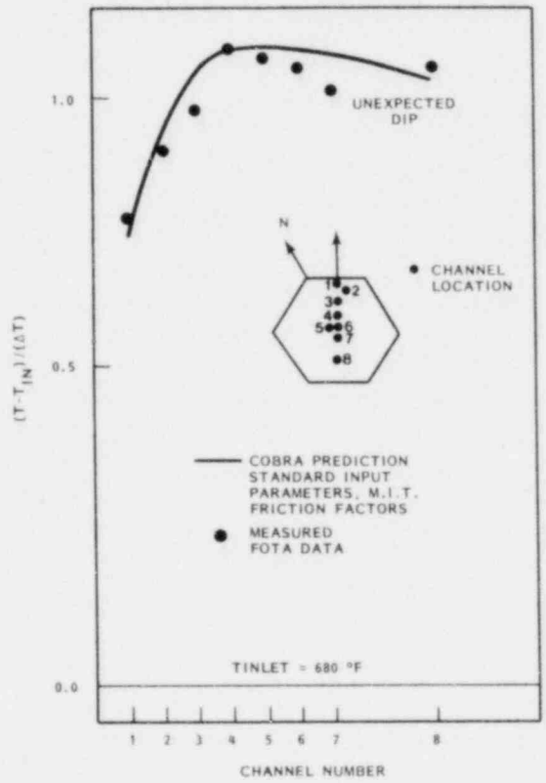

FIGURE 17. Comparison of COBRA Predicted and FOTA Measured Temperature History

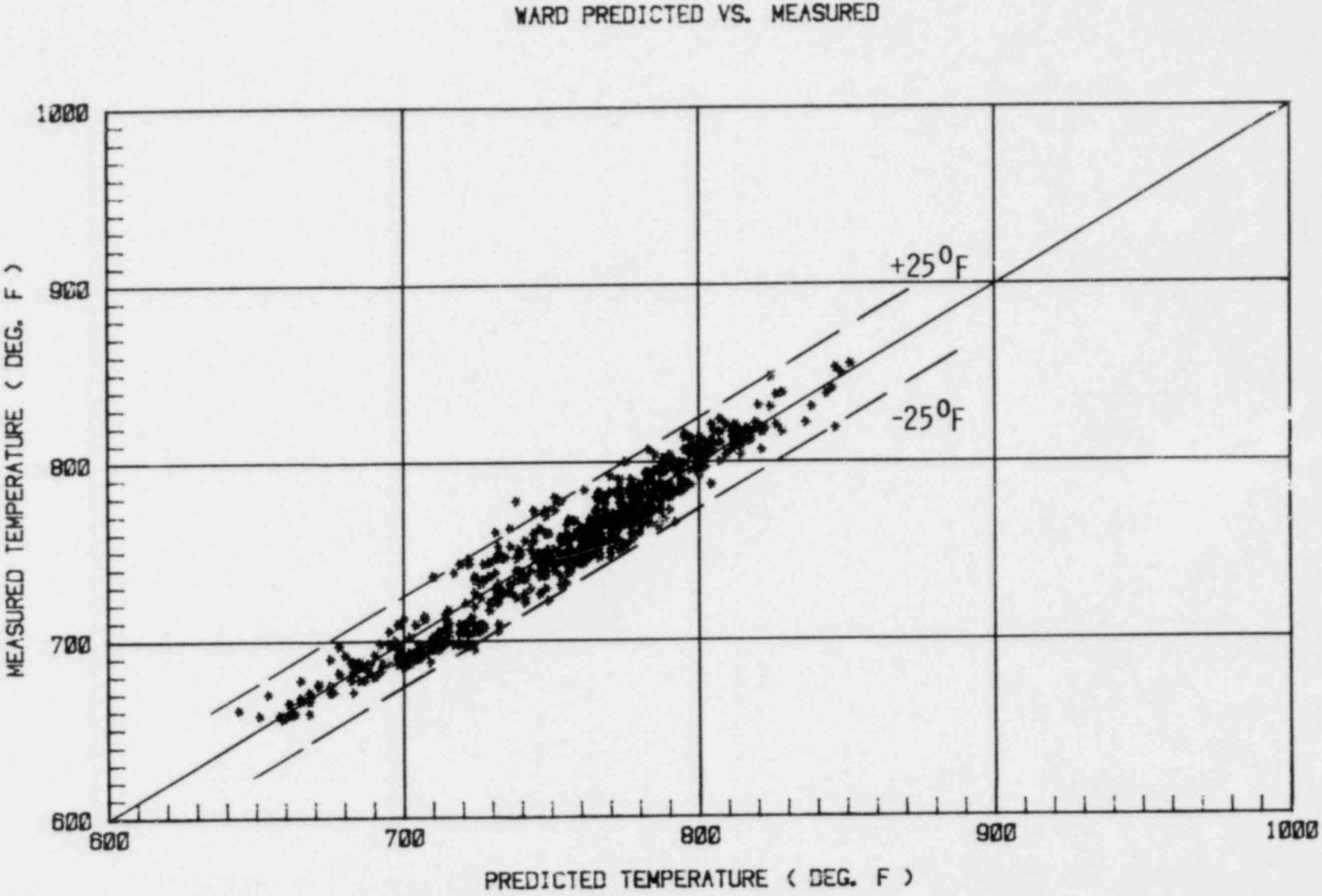

FIGURE 18. Comparison of COBRA-WC Predicted Temperatures and Ward Test Data

bundle. The effect of the wall heat loss on temperature distribution becomes increasingly important as the Reynolds number decreases below 1500. A heat loss at the duct wall causes buoyancy-induced flow redistribution from the wall to the interior channels, thereby flattening (in some cases significantly) the bundle temperature distribution. None of the experiments performed at low flow conditions included an assessment of the radial heat loss from the bundle. Consequently, the COBRA calculations did not include the effect of heat loss on temperature distribution. This is partially responsible for differences between measured and code-predicted data at low flows.

Differences between the code predictions and measured data can occur because of a lack of knowledge of the exact thermocouple position in the cladding wall. Another reason for the differences is that local temperatures measured in regions of high temperature gradients can be quite different than the subchannel average temperatures predicted by the code.

CONCLUSIONS

The COBRA-WC thermal-hydraulic models have been validated by analysis of existing thermal-hydraulic data in (nominal) rod bundles. One set of COBRA-WC input parameters were found to predict data well for the wide range of assembly geometrical and operating conditions listed in Table 2. The wire-wrap-induced swirl flow model was validated by data sets 1a and 1b in Table 2. Data set 1c was used to test the axial velocity development and flow split models; data set 1d confirmed the buoyancy-induced crossflow model; and data set 1e validated the combined wire-wrap-induced and diversion crossflow model. Data set 2 (Table 2) validated the combined COBRA thermal-hydraulic models for assembly geometries ranging from typical fuel assembly geometries to blanket assembly geometries and operating conditions ranging from laminar to turbulent flows ($500 \leq Re \leq 100{,}000$) and forced, mixed, and natural convection. Power skews across the assemblies ranged from uniform to 3.4:1 (max:min).

Accommodation of looseness within the bundle has a significant effect on the flow and temperature fields, especially in forced convection. At high Reynolds numbers of operation of assemblies in forced convection, subchannel friction factor and wire-wrap-induced crossflow mixing are also important and govern the flow and thermal fields. In mixed and natural convection regimes of assembly operation, thermal conduction and buoyancy-induced crossflow become as important, and in many cases significantly more important than wire-wrap mixing in determining flow and temperature fields. The COBRA input parameters of interest at low flow conditions are the conduction shape factor (G), subchannel friction factor, and heat losses at the duct wall.

Table 5 gives the COBRA generalized input parameters that were used to predict assembly peak coolant temperature data and coolant temperature distribution data from in-pile and out-of-pile experiments. Most of the data was taken in wire-wrapped fuel and blanket rod assemblies. The coolant temperature was predicted within ±25°F at a 95% confidence level for an assembly

mixed-mean temperature rise in the range $150^{\circ}F \leq \Delta\bar{T} \leq 340^{\circ}F$. In those tests for which $70^{\circ}F \leq \Delta\bar{T} \leq 150^{\circ}F$, the number of data points were not large enough to allow a formal statistical analysis required to determine the accuracy of prediction within a σ or 2σ confidence level. However, almost all measured coolant temperatures were predicted by COBRA within $\pm 17^{\circ}F$ for $70^{\circ}F \leq \Delta\bar{T} \leq 150^{\circ}F$.

TABLE 5. COBRA Input Parameters

Parameter	Blanket	Fuel
wire-wrap sweep flow coefficient, DUR	1.0	1.0
crossflow resistance, K_{IJ}	0.5	0.5
S/ℓ parameter	0.5	0.5
conduction shape factor, G	0.5	0.5
fraction of bundle flat-to flat tolerance accommodated at the wall	0.0	0.0
turbulent mixing parameter, β	0.01	0.01(a) 0.00(b)
subchannel friction factors, f	$f = \frac{Mf_{smooth}}{X_i^2} \frac{d_i}{d_{bundle}}$	

where i = 1 for interior channels
i = 2 for wall channels
M = Novendstern's friction factor multiplier for wire-wrapped rod bundles
f_{smooth} = smooth tube friction factor
X_i = flow split from [6,8,9]

(a) For prediction of coolant temperature distribution across the assembly.
(b) For prediction of peak coolant temperature within the assembly.

The COBRA code will predict coolant temperature distribution for nominal conventional reactor wire-wrapped fuel and blanket assemblies with an accuracy of about $\pm 25^{\circ}F$ under steady-state (normal) operating conditions. After extensive analysis of available data it was concluded that this limit was generally set by differences in predicted and measured temperatures in the channels near the duct wall (2 to 3 rows) and by the peak channel within the assembly.

RECOMMENDATIONS

1) A standard procedure needs to be established to assess the applicability, reliability, and uncertainties associated with a set of data for code validation purposes.

2) In the ORNL 61-pin bundle tests, in the FFTF FOTA tests, and in the EBR-II XX08 experiments unexpected peaks and valleys in the flat-to-flat coolant temperature distribution were found. It is not clear if these were due to pin-bundle distortion or faulty thermocouples. When the bundle is disassembled, the relevant thermocouples should be checked to ascertain the cause of the anomalous thermocouple reading.

3) In order to improve models for prediction of duct wall and coolant temperature distribution in channels adjacent to the duct wall, a data base is needed where the number of thermocouples in the vicinity of the wall region of the bundle are increased from that generally used in existing experiments. For low-flow, mixed- and/or natural convection experiments, radial heat loss measurements at the duct wall are needed at several axial levels.

4) A need exists for reassessment of the wire-wrap model in the turbulent flow regime and its extension to the laminar regime.

5) The interassembly flow redistribution and transient heat transfer models in COBRA need to be further validated with data from the WARD natural convection transient tests, ORNL single and planned multi-assembly tests, and the planned EBR-II experiments involving XX09 and XX10 assemblies.

6) In analyzing data obtained in heated-pin bundles cooled with sodium with $p/d < 1$, circumferential conduction along the duct wall and transverse conduction through the heater pins should be taken into account.

REFERENCES

1. George, T. L., K. L. Basehore, C. L. Wheeler, W. A. Prather and R. E. Masterson. 1980. COBRA-WC: A Version of COBRA for Single-Phase Multiassembly Thermal-Hydraulic Transient Analysis. PNL-3259, Pacific Northwest Laboratory, Richland, Washington. Also see AIChE Symposium Series, No. 199, Vol. 76, pp. 205-214.

2. Coomes, E. P., E. U. Khan, T. L. George, R. L. Cheatham and D. R. Rector. 1982. User Manual for COBRA-WC: A Version of COBRA for Single-Phase, Single and Multi-Assembly Thermal-Hydraulic Transient Analysis. PNL-4303, Pacific Northwest Laboratory, Richland, Washington.

3. Wheeler, C. L., C. W. Stewart, R. J. Cena, D. S. Rowe and A. M. Sutey. 1976. COBRA-IV-I: An Interim Versions of COBRA for Thermal-Hydraulic Analysis of Rod Bundle Nuclear Fuel Elements and Cores. BNWL-1962, March 1976, Pacific Northwest Laboratory, Richland, Washington.

15. Lafay, J., B. Menant and J. Barrois. 1975. "Influence of Helical Wire-Wrap Spacer System in a 19-Rod Bundle." Presented to the 1975 Heat Transfer Conference, April 1975, San Francisco, California.

16. Fontana, M. H. 1973. Temperature Distribution in the Duct Wall and at the Exit of a 19-Rod Simulated LMFBR Fuel Assembly (FFM Bundle 2A). ORNL-4852, Oak Ridge National Laboratory, Oak Ridge, Tennessee.

17. Morris, R. H., et al. 1980. Single-Phase Sodium Tests in 61-Pin Full-Length Simulated LMFBR Fuel Assembly-Record of Phase 1 Experimental Data for THORS Bundle 9. ORNL/TM-7313, Oak Ridge National Laboratory, Oak Ridge, Tennessee.

18. Engel, F. C., R. A. Markley, and B. Minushkin. 1978. "Buoyancy Effects on Sodium Coolant Temperature Profiles Measured in an Electrically Heated Mockup of a 61-Rod Breeder Reactor Blanket Assembly." ASME paper 78-WA/HT-25, American Society of Mechanical Engineers, New York, New York.

19. Milburg, M. L., J. A. Hassberger and C. J. Boasso. 1977. Natural Circulation Heat Transfer Testing with a Simulated Full-Scale LMFBR 217-Pin Electrically Heated Fuel Assembly. HEDL-TME77-3, Hanford Engineering Development Laboratory, Richland, Washington.

20. Gillette, J. L., R. M. Singer, J. V. Tokar and J. W. Sullivan. 1979. "Experimental Study of the Transition from Forced to Natural Circulation in EBR-II at Low Power and Flow." Paper No. 79-HT-10, American Society of Mechanical Engineers, New York, New York.

21. Personal Communication between E. U. Khan (PNL) and C. W. Hoth (HEDL), May, 1981.

22. Khan, E. U., W. A. Prather, T. L. George and J. M. Bates. 1981. A Validation Study of COBRA-WC for LMFBR Steady-State and Transient Analysis. Presented at the National Heat Transfer Conference, Milwaukee, Wisconsin.

ANALYSIS OF IN-CORE COOLANT TEMPERATURE DISTRIBUTIONS WITHIN FFTF INSTRUMENTED FUEL ASSEMBLIES

C. W. Hoth
Westinghouse Hanford Company
Richland, Washington 99352

ABSTRACT

Instrumented fuel assembly tests are installed in the Fast Flux Test Facility and are monitoring in-core coolant temperatures. Comparison of measured temperature data to calculated temperatures from a thermal-hydraulic code confirms the validity of the thermal-hydraulic models.

TEST DESCRIPTION AND RESULTS

In support of the LMFBR Fuels Development Program, Westinghouse Hanford Company (WHC) designed the Fuels Open Test Assembly (FOTA) for fuels testing at the Fast Flux Test Facility (FFTF). The FOTA is a test vehicle designed to contain instrumented fuel experiments. Two FOTA tests were installed in the FFTF in December of 1979 in Row 2 and Row 6 core positions. The initial two FOTA tests provide temperature measurements within contact instrumented driver fuel assemblies that were designed specifically to match the thermal-hydraulic behavior of standard non-instrumented driver assemblies. Each test includes 217 standard driver fuel pins and uses wire-wrap thermocouples on selected fuel pins to replace the spacer wire wrap. The thermocouple data from the tests are used for evaluating the in-reactor coolant temperature distribution during reactor operation. The objectives of these initial FOTA tests are to characterize the FFTF driver fuel assembly performance and to provide experimental data to evaluate thermal-hydraulic models used to predict assembly performance.

The placement of the FOTA thermocouple measuring junctions are distributed at various radial and axial locations within each fuel pin bundle. The pattern of radial placement of the thermocouples allows measurement of temperature profiles parallel to and perpendicular to the flux gradient. The four axial planes selected for thermocouple placement in each test are; bottom of fuel, fuel midplane, top of fuel and top of pin. The pattern for thermocouple placement for the Row 6 FOTA is shown in Figure 1.

The two FOTA tests have operated at full power level during five major reactor testing periods completed through December 1981 and have accumulated 32 equivalent full power days (EFPD) of exposure, and 150 days at full flow. The power history of the FFTF through December 1981 is shown in Figure 2.

An objective of the FOTA tests is to provide data for calibration and verification of thermal-hydraulic codes used to predict fuel assembly temperatures. The SUPERENERGY-II[1] computer code was used for comparison to the FOTA in-core coolant temperature measurements. SUPERENERGY provides calculated subchannel temperatures by solving the steady-state heat transfer equations. The code requires the assembly geometry, coolant flowrate and fuel pin powers as input and calculates the corresponding coolant temperatures within the fuel assembly.

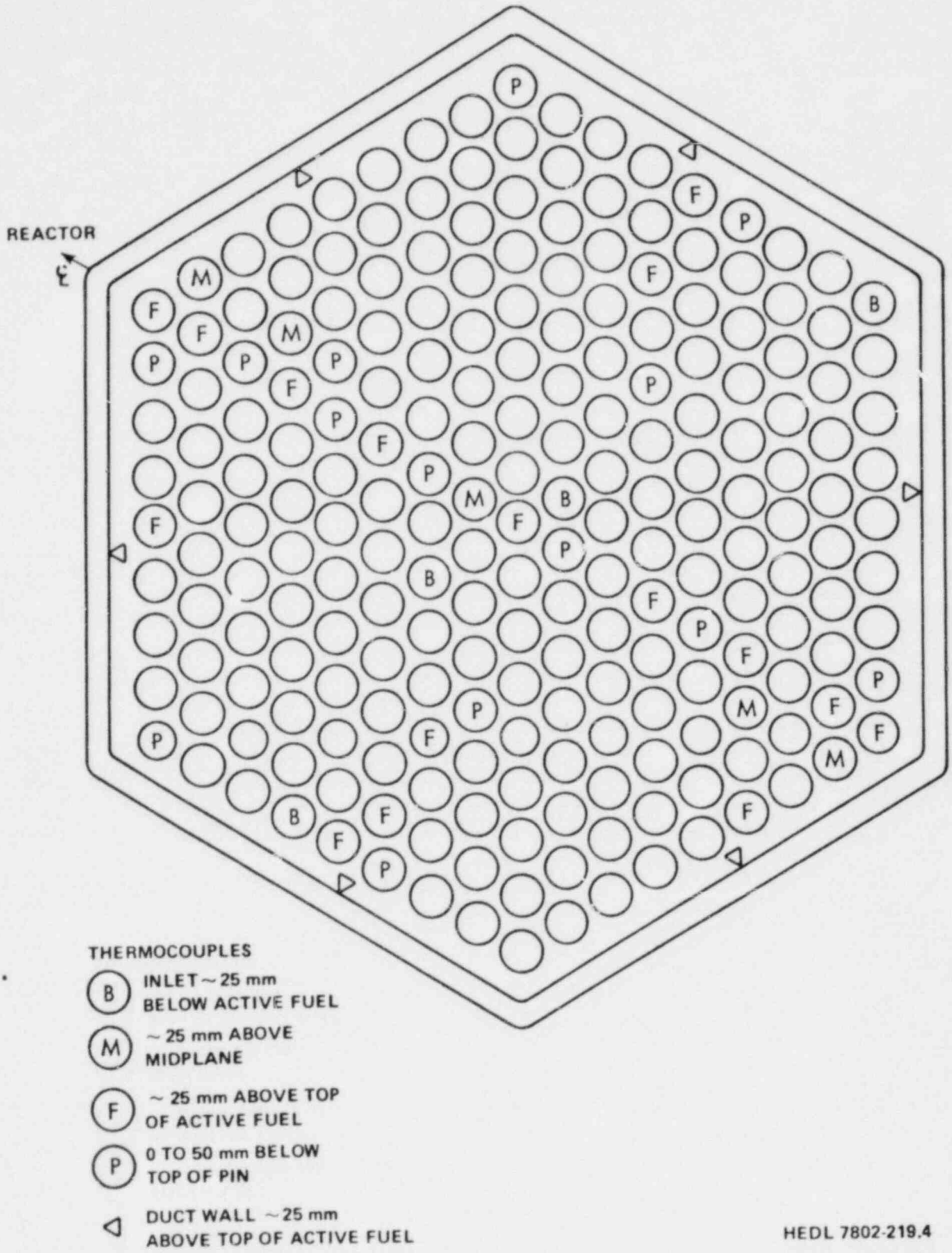

FIGURE 1. Placement of Wire-Wrapped Thermocouple Instrumented Fuel Pins in the Row 6 FOTA Test.

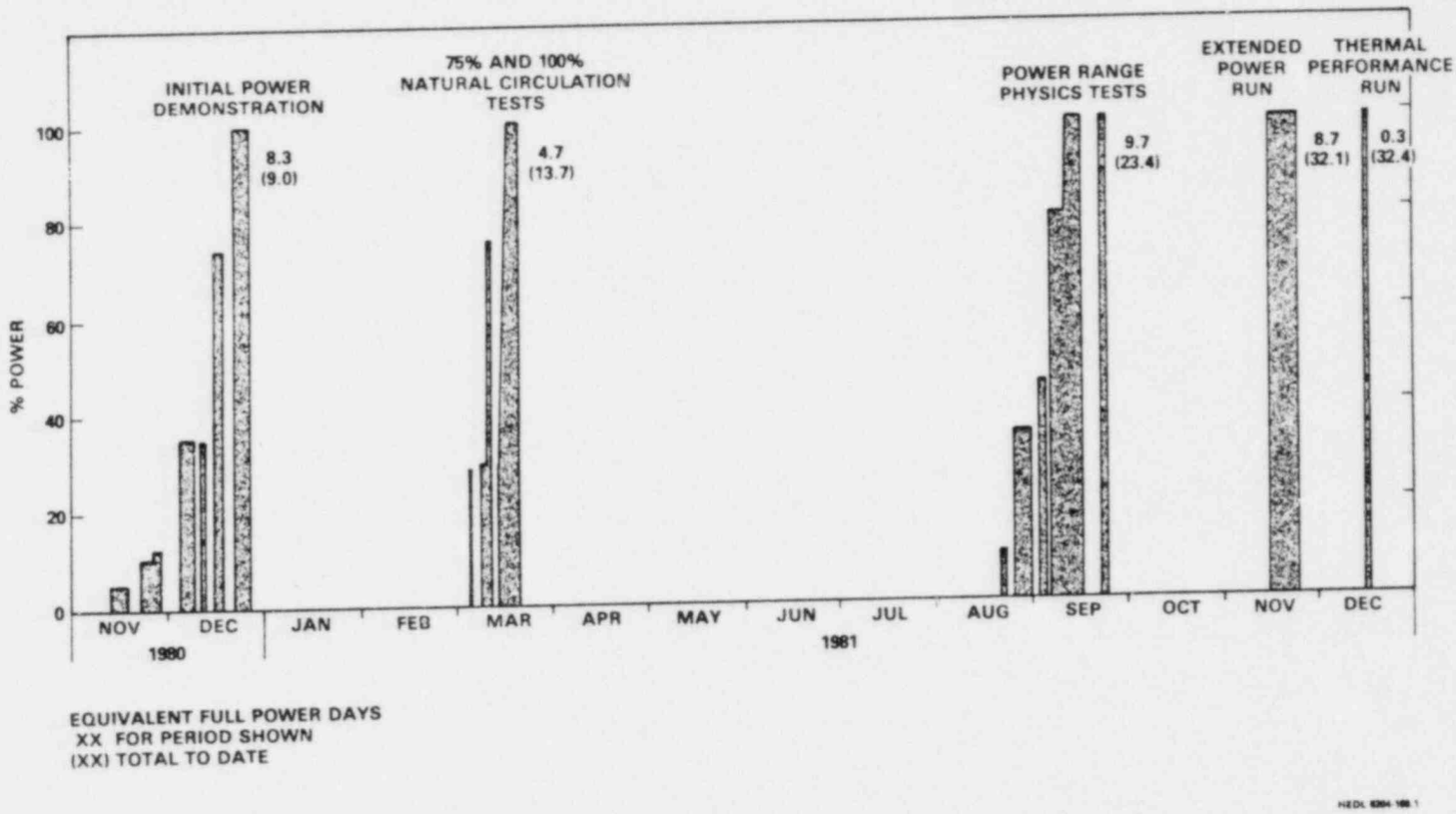

FIGURE 2. Power History for the FFTF Through December 1981.

The code uses empirical constants to account for the coolant mixing effects (e.g., diversion cross flow, wall channel flows). Previous out-of-reactor experiments provided the data to establish the empirical constants used in the computer code.

The input to the SUPERENERGY-II calculation was specified to correspond with the measured inlet and outlet temperatures of the FOTA tests. The comparison of the calculated temperature to the measured temperatures therefore does not contain any bias due to flow or power measurement uncertainties or variations in the coolant inlet temperature.

A comparison of the measured and calculated temperatures for the Row 2 FOTA test is shown in Figure 3 for the top of fuel elevation. The measured data displays good agreement with the SUPERENERGY calculation although the data does indicate that the central coolant channels are slightly cooler than predicted. A comparison of the measured data and calculated temperatures of the top of fuel pin elevation (1.1 m above the top of fuel elevation) is shown in Figure 4. The data confirm the predicted flattening of the radial temperature profile due to coolant mixing. At the top of fuel pin elevation, the data also indicates the central coolant channels are cooler than predicted.

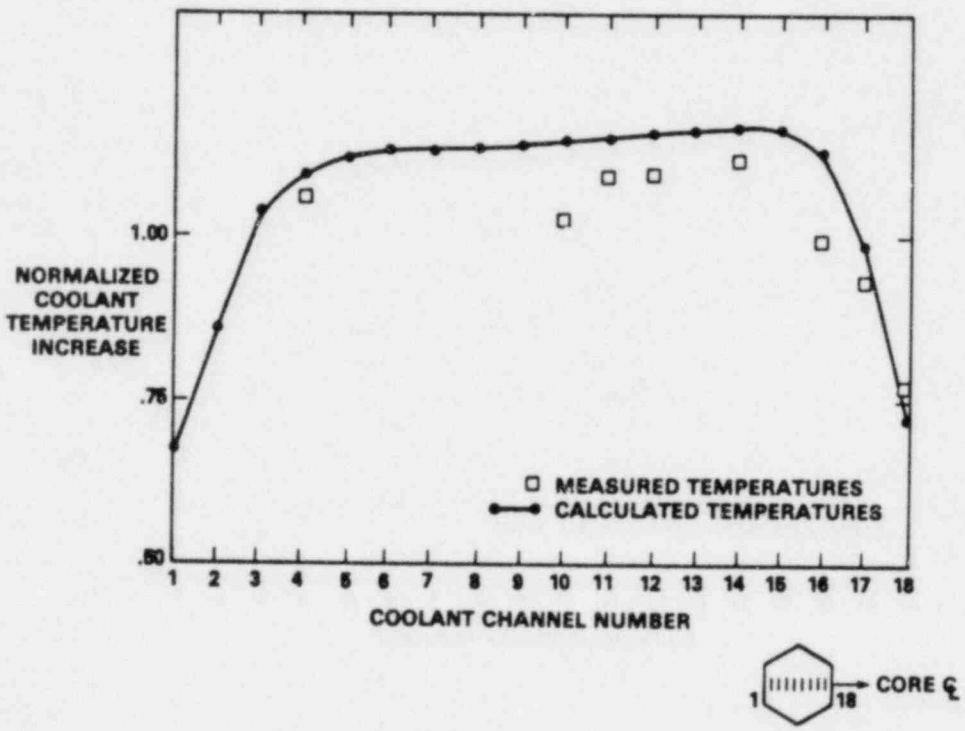

FIGURE 3. Comparison of Measured and Calculated Temperatures for the Row 2 FOTA at the Top of Fuel Elevation.

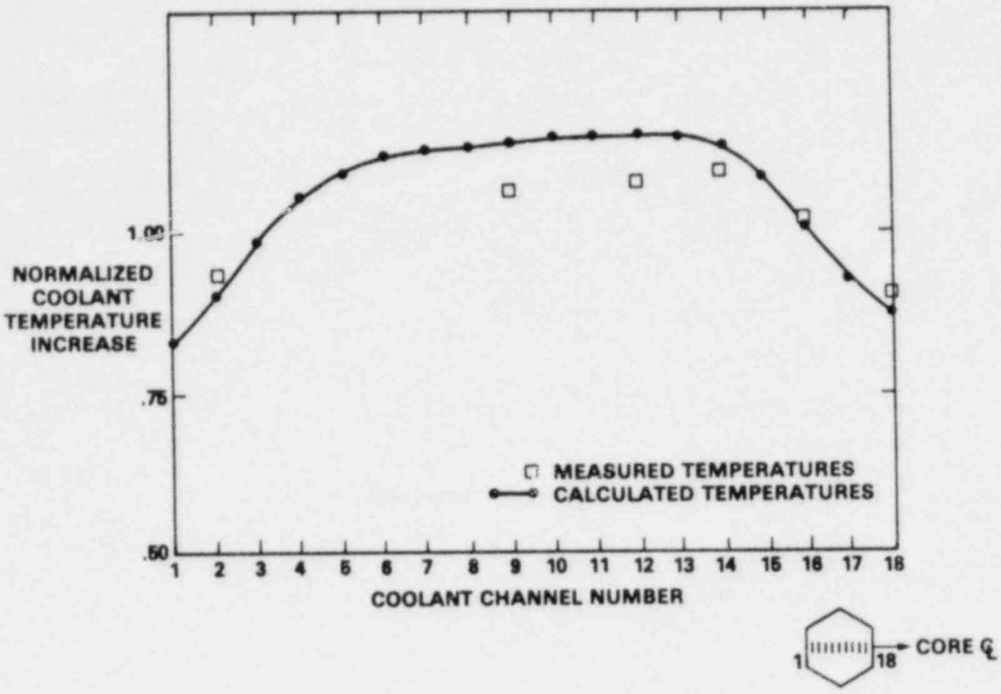

FIGURE 4. Comparison of Measured and Calculated Temperatures for the Row 2 FOTA at the Top of Pin Elevation.

The Row 6 FOTA provides temperature data for an assembly in a steep power gradient. Comparision of measured data and calculated temperatures for the Row 6 FOTA at the top of fuel elevation and top of fuel pin elevation are shown in Figures 5 and 6, respectively. The Row 6 FOTA temperature data provide excellent confirmation of the calculated temperatures at both the top of fuel and top-of-pin elevations. These data confirm both the accuracy of the thermal-hydraulic code calculation of coolant temperature redistribution and the accuracy of the predicted power skew of the fuel assembly as determined from core physics calculations.

The reduced temperatures in the central coolant channels in the Row 2 FOTA could be caused by slight increases in the area of the central coolant channels due to redistribution of the fuel pins within the assembly. The SUPERENERGY calculation was based on a uniformly distributed fuel pin bundle with the same flow area for all interior fuel pins. Coolant channel sizes are expected to change during operation as the fuel pins shift due to thermal stresses imposed on cladding due to the thermal gradient that exists across the assembly. As these thermal stresses relax due to creep the fuel pins will shift and resultingly alter the coolant channel size and the temperature profiles. Also, the distribution of deposited power within the assembly will vary during irradiation due to: 1) fissile depletion, 2) radial and axial neutron flux profile changes due to control rod withdrawal, and 3) global power variations due to changes in the core loading. Some changes in the fuel assembly coolant temperature distribution are, therefore, expected during steady-state operation due to these factors.

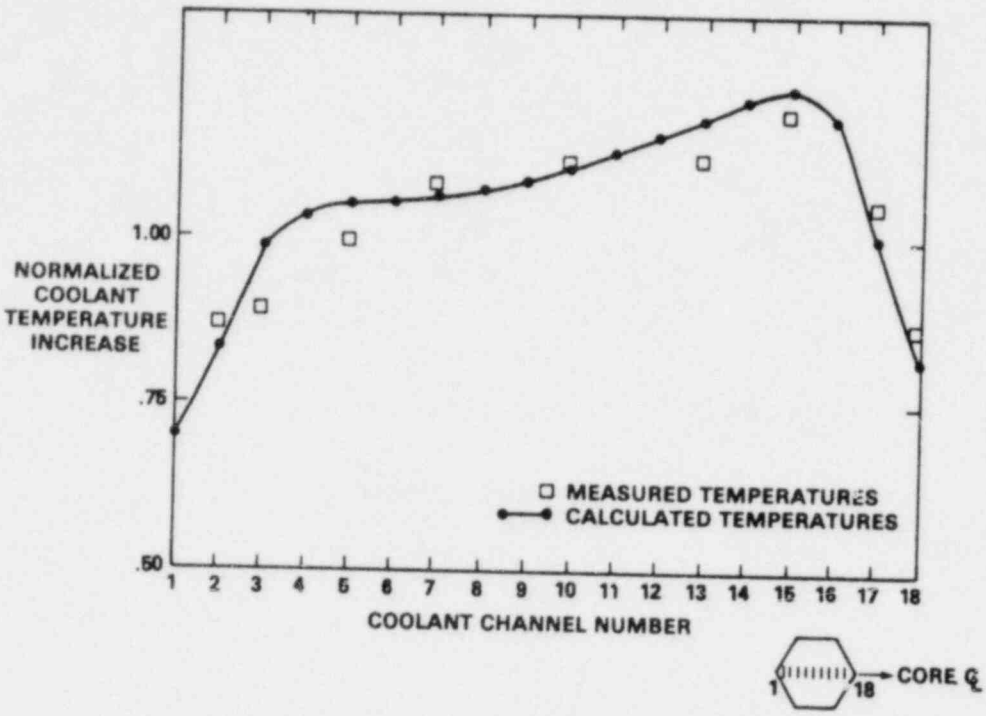

FIGURE 5. Comparison of Measured and Calculated Temperatures for the Row 6 FOTA at the Top of Fuel Elevation.

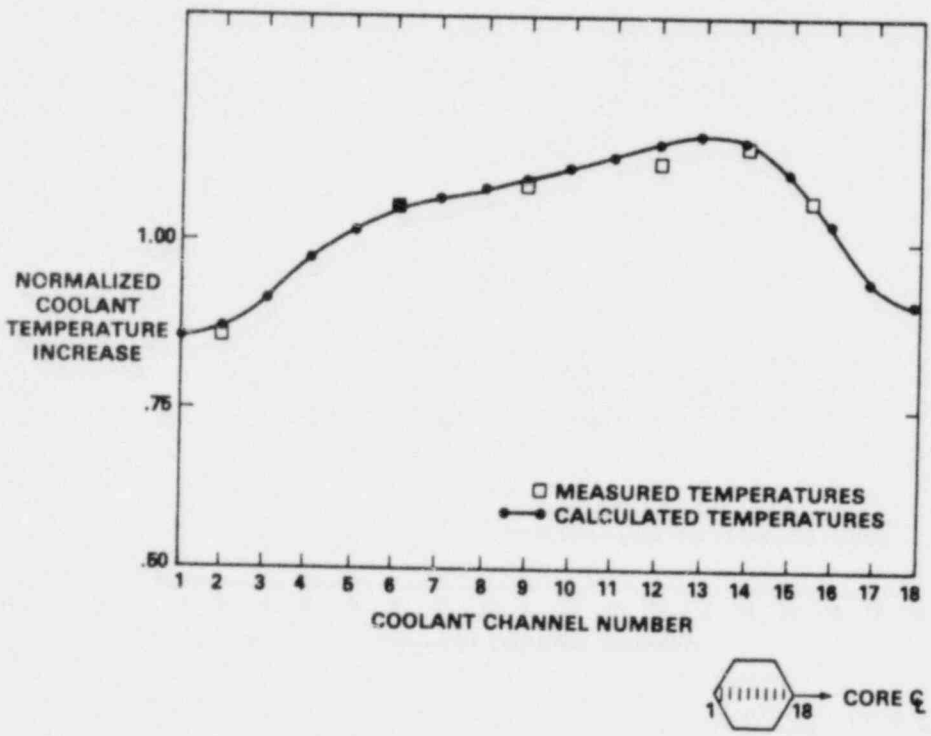

FIGURE 6. Comparison of Measured and Calculated Temperatures for the Row 6 FOTA at the Top of Pin Elevation.

The FOTA tests use reactor grade Type K thermocouples. The accuracy of these thermocouples is nominally given as 3/8% of reading, but due to a metallurgical instability of the thermoelement material, the expected accuracy of measurement of absolute temperature is 2% or ∿10 C°.[2] Measurement of relative temperatures on a given axial plane is expected to be closer to the 3/8% of reading or ∿2 C°. Thermocouple accuracy is also affected by the fact that thermocouples placed on the edge fuel pins inherently have their measuring junctions located in a steep thermal gradient. Any movement of the wire wrap would cause a shift of the measuring junction in the thermal gradient and indicate a temperature different than expected. Discrepancies between the measured and calculated coolant temperatures may be partially due to uncertainties in the precise in-reactor location of the thermocouple measuring junction.

The comparison of measured temperature data to SUPERENERGY calculated temperature confirms the validity of the thermal-hydraulic code models. Agreement between the measured and calculated temperatures is, in general, excellent and the minor deviations in agreement can be accounted for with allowances for instrument accuracy and the generalized nature of the thermal-hydraulic code input.

The FOTA experiments are scheduled to remain in the FFTF to full driver exposure (i.e., 300 EFPD for Row 2 and 400 EFPD for Row 6). Data obtained later in the test lifetime will reveal the effects of prolonged exposure on bundle geometry and the resulting coolant temperature distribution. The modeling of relatively minor shifts of the temperature profiles is not within the scope of existing thermal-hydraulic code calculations but the FOTA data will provide detailed characterization of such thermal behavior of driver assemblies throughout their lifetime.

REFERENCES

1. K. L. Basehore and N. E. Todreas, "SUPERENERGY-II: A Multiassembly Steady-State Computer Code for LMFBR Core Thermal-Hydraulic Analysis," COO-2245-57TR (August 1980).

2. T. G. Kollie et al., "Temperature Measurement Errors with Type K (Chromel vs Alumel) Thermocouples Due to Short Range Ordering in Chromel," Rev. Sci. Instrum., Vol. 46, No. 11, November 1975.

THE EFFECTS OF RADIAL HEAT FLUX GRADIENTS AND FLOW REGIMES ON THE PEAK SODIUM TEMPERATURE RISE IN WIRE WRAPPED ROD BUNDLES

F. C. Engel and R. A. Markley
Westinghouse Advanced Reactors Division
Madison, Pennsylvania, U.S.A.

A. A. Bishop
University of Pittsburgh
Pittsburgh, Pennsylvania, U.S.A.

ABSTRACT

The peak sodium temperature rise in a wire wrapped rod bundle was determined experimentally over a range of radial heat flux gradients under forced, mixed and natural circulation conditions. The bundle tested was a full size blanket assembly typical of the type to be used in current liquid metal breeder reactors (LMFBR). The range of experimental parameters tested was:

1)	Radial heat flux gradient (maximum/minimum)	1.0 to 4.6
2)	Axial sodium temperature rise (°C)	50 to 150
3)	Reynolds number	500 to 26000
4)	Inlet sodium temperature (°C)	260 to 360
5)	Rod bundle power (kw)	10 to 880
6)	Flow rate (l/sec.)	0.1 to 7.7

At a given radial heat flux gradient, the peak sodium temperature rise was constant in the fully turbulent flow regime; however, in the mixed and natural circulation regimes, the peak sodium temperature was decreased significantly by buoyancy. A study was made of the dimensionless parameters which influence the peak temperature rise for the given geometry tested. The results were correlated using a dimensionless normalized peak temperature rise $(T-T_{in})/(\Delta T_{avg})$ and the ratio of rod bundle Grashof to Reynolds numbers. The peak temperature parameter ranged from 1.65 to 1.05. The forced, mixed and natural convection thermal-hydraulic regimes were identified. Sodium temperature rise peaking behavior presented the main difference between these flow regimes. Confirmation of the general behavior observed and of the correlation parameters used was obtained by examining other out-of-pile experimental data.

1. INTRODUCTION

The Reynolds numbers of coolant flow through the assemblies of a liquid metal breeder reactor (LMFBR) range from 16,000 in the radial blanket to 80,000 in the core during full power steady state operation. Following a reactor scram, pump coastdown and loss of site power, the hydraulic regime changes from forced to natural circulation and the Reynolds number in the blanket region can become as low as 500. The associated heat transfer modes change from forced or mixed to natural convection.

Radial power skews exist across both blanket and fuel assemblies. They cause coolant temperature peaking and high local cladding temperatures. A significant increase in fuel burnup and reduction in the margin to boiling can be achieved if the uncertainty in predicting the coolant temperature peak is reduced. However, the determination of the reduction in coolant temperature peaking requires an assessment of the effect of buoyancy on the coolant radial temperature profile under all flow conditions. Moreover, there is a need to know how different magnitudes of input power, power flux skew and Reynolds numbers influence the initiation of buoyant effects. An analytical solution to these questions is complicated by the rod bundle geometry (wire wraps which space fuel rods in both blanket and fuel assemblies) and the usual difficulties encountered in analyzing turbulent flows. To obtain the desired information, an electrically-heated full-size radial blanket assembly model was constructed and tested. Results and conclusions are presented in this paper.

The effect of buoyancy on flow stability, velocity profiles, heat transfer, turbulent-to-laminar flow transition and pressure drop has been studied for simple geometries. Until recently, all experimental studies and most analyses were limited to single circular tubes (References 1, 2, 3). Using these and other data, charts were constructed to show boundaries between the forced, mixed and free convection heat transfer regimes (References 4, 5, 6). The use of these charts for LMFBR rod bundle analyses is questionable because they are mainly for non-metal liquids, single tubes and uniform power (no power skew). Experimental work by Buhr, et al. (References 7, 8) demonstrated that the influence of buoyancy on the flow velocity profile in a tube extended to Reynolds numbers as high as 30,000 when a liquid metal such as mercury was used.

Borishanskii (Reference 9), Tsai (Reference 10), Ramm (Reference 11) and Yang (Reference 12), presented analyses for laminar flow through bare rod bundles. The analyses of Ramm included effects of a radial power skew. Dutton determined heat transfer rates under natural circulation conditions in a bundle of uniformly heated rods (Reference 13). Using water as the test fluid, the effect of buoyancy in rod bundles was studied by Quigley (Reference 14) and Namekawa (Reference 15). Khan proposed a criterion to predict when buoyancy becomes effective in wire wrapped rod bundles (Reference 16). In summary, with the exception of a parallel study at ORNL which employs a typical LMFBR fuel assembly (Reference 17), there have been no experimental data to determine the magnitude of coolant temperature peaking behavior and its response to buoyancy in liquid metal cooled wire wrapped rod bundles across which high radial power skews exist.

2. TEST SECTION

The heat transfer test section was required to be an accurate dimensional mock-up of an LMFBR blanket assembly. Additionally, the test section was required to reproduce as closely as practical the inlet flow conditions, power level and power distribution of blanket fuel rods and assemblies at various stages of its life in a reactor. These were discussed in more detail in Reference 18 together with test section and blanket assembly design parameters.

A full scale, vertical, electrical-resistance heated model rod bundle (Figure 1) was constructed. Figure 2 presents a horizontal section through the test

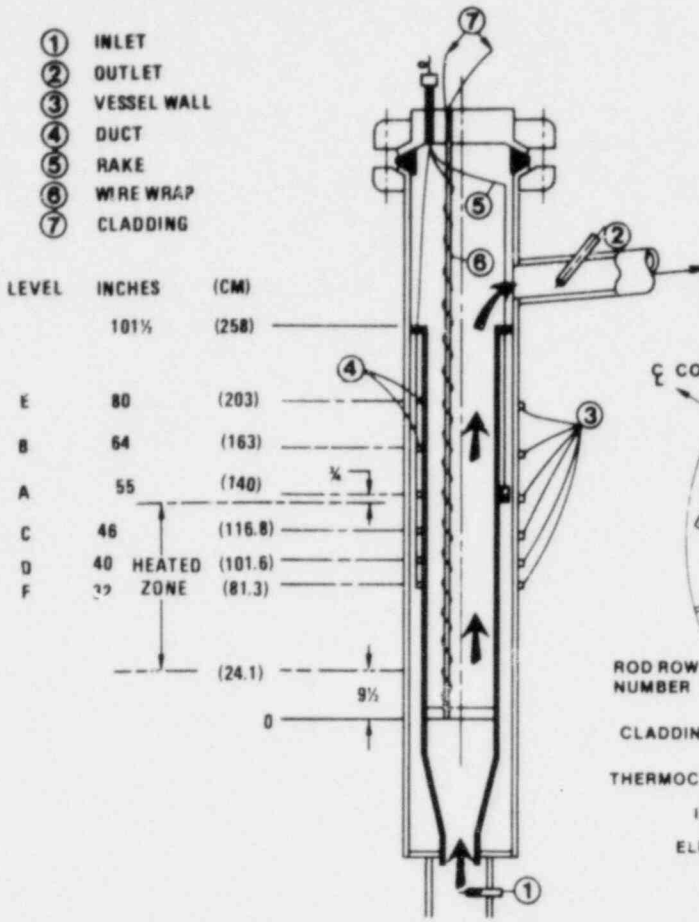

FIGURE 1: DIAGRAM OF THERMOCOUPLE LOCATIONS IN 61-ROD BLANKET TEST ASSEMBLY - ELEVATION VIEW

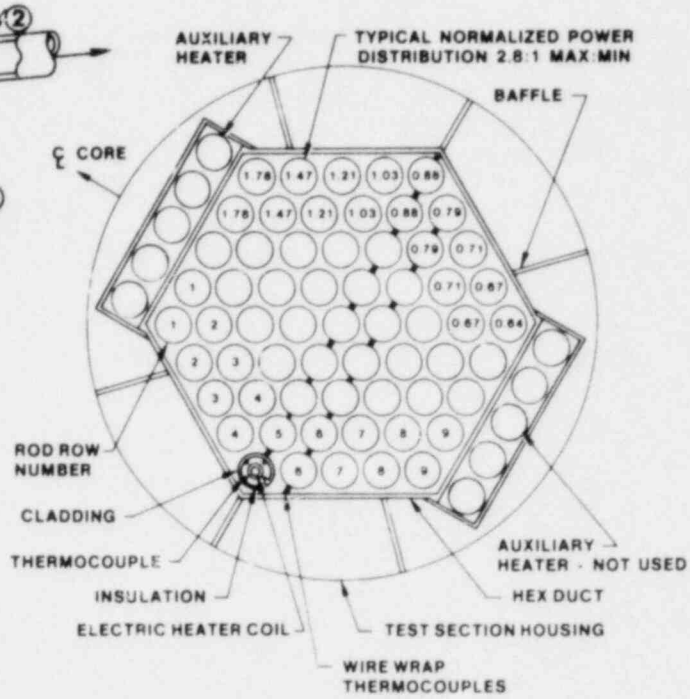

FIGURE 2: CONCEPTUAL TEST SECTION CROSS SECTION

assembly showing the 61 rods contained in the hexagonal duct and the 10 rods in the auxiliary ducts. The rods are spaced and separated from each other and the duct wall by helically wound wires of 4-inch (10.16 cm) lead. The spacer wires contain chromel-alumel thermocouple junctions at the six levels of measurements (A through F) shown in Figure 1. Each simulator rod contains a resistance heating element of nichrome wire. The heating element is a helically wound coil of varying lead to generate an axial heat output approximating a chopped cosine distribution with a 1.4 maximum-to-average ratio over a 45-inch (114.3 cm) length. The heat input pattern shown in Figure 2 is that of a radial blanket with a 2.8 gradient across flats. The power is supplied separately to each of the nine parallel rows or rods by saturable core reactors. Other power input patterns were obtained by connecting different groups of rods to each of the transformers. Sodium is pumped through the test section from a large volume test loop equipped with control valves, electromagnetic pump and flow meters, and an air-blast heater-cooler to maintain constant sodium supply temperature. Details of heater rod design and of wire wrap thermocouple construction and attachment were discussed in Reference 19, as were the data acquisition system, test method and calibration procedures for the test. The principal dimensions are listed in Table 1.

TABLE 1

BLANKET TEST SECTION DIMENSIONS

Number of Simulator Rods in Bundle	61
Number of Simulator Rods in Auxiliary Duct	10
Rod Diameter, mm/in.	13.18/0.519
Triangular Pitch-to-Diameter Ratio	1.082
Wire Wrap Diameter, mm/in.	0.94/0.037
Wire Wrap Lead, mm/in.	101.6/4.0
Total Rod Length, mm/in.	∿2670/∿105
Heated Length, mm/in.	1143/45.0
Inside Dimension of Hexagonal Duct Across Flats, mm/in.	114/4.49

Since the test results were to be compared with predictions of subchannel analysis codes of the marching type (e.g., CØBRA, Reference 20), the temperature sensors were grouped into distinct horizontal planes at selected elevations as shown in Figure 1. Numerous thermocouples are located at the test section inlet and outlet, and at the six discrete axial planes within the bundle assembly. Thermocouples were located at the vessel and duct walls, in the wire wraps and inside the heater rods, attached to the inner surface of the cladding (Figure 2). Resistance thermometers at the inlet, outlet and the duct wall at the six elevations were used for calibration. Flow, temperature and power input measurements were recorded on tape and discs by a computerized Data Acquisition System (DAS). Details of the data acquisition system and the calibration procedure were given in Reference 19. Power input to each row of rods was measured by a Hall-effect power computer. The sodium flow rate was determined by an electromagnetic flow meter.

3. TEST PROCEDURES

a) Pumped Circulation

The general test procedure with forced circulation was to adjust sodium flow and inlet temperature, then increase bundle power gradually to the value required to produce the desired test section power gradient and temperature rise. The approach to steady state power conditions was monitored by printing out selected temperatures, flow, power and pressure drop. Criteria for steady state were constancy of power, flow, inlet temperature ($\pm$5°F/2.8°C) and ΔT ($\pm$5°F/2.8°C) as indicated by the absence of trend lines for at least 30 minutes. When nominal steady state conditions were achieved, a file of 550 readings of each of 524 data channels was acquired by the DAS and logged on magnetic tape over a period of approximately 10 minutes. This data acquisition procedure was selected to provide a statistically valid sample, which would be quickly available and useful for testing consistency and steady state criteria.

b) Natural Circulation

For natural circulation tests, the test section and the bypass containing an air-blast cooler were isolated from the loop (Figure 3). Power was then applied to the heater rods until the desired flow rate was established. The system established its steady state when a balance between the heat input and the removal by the air-blast cooler was reached (as indicated by steady inlet and outlet temperatures). The approach to steady state conditions was monitored by printing out selected temperatures, flow, power and pressure drop. Data were taken at steady state as described for pumped circulation. The test data were then processed to yield averaged results in engineering units. The temperatures were normalized by dividing the measured local temperature rise at all elevations by the mixed mean temperature rise to level "A":

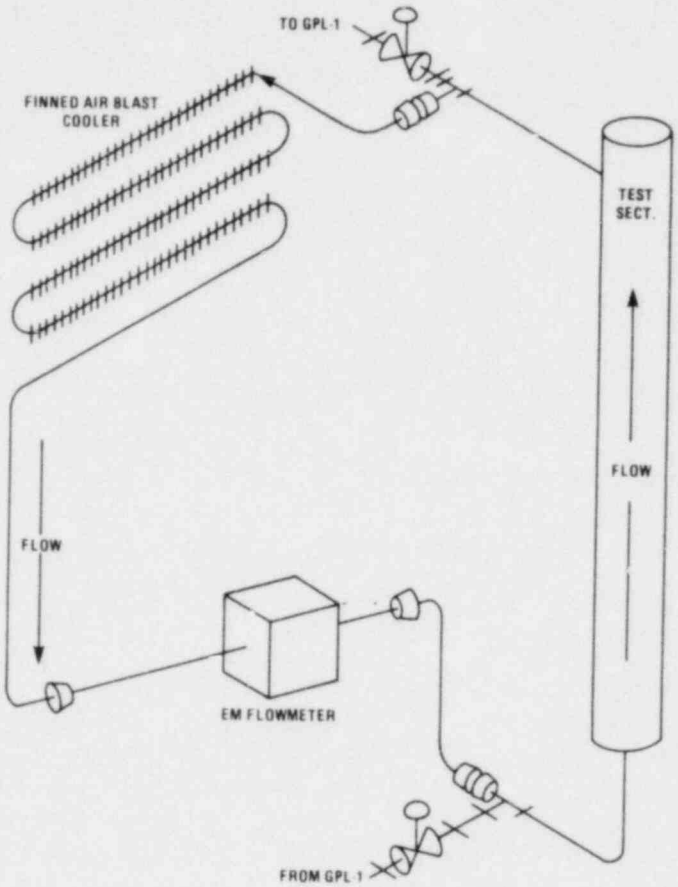

FIGURE 3: BLANKET HEAT TRANSFER TEST - NATURAL CIRCULATION LOOP

$$\Delta T_N = (T - T_{in})/(T_{AV} - T_{in}); \quad (1)$$

or

$$\Delta T_N = (T - T_{in})/(Q/Wc_p) \quad (2)$$

4. TEST RESULTS

Of principal interest to the thermal design of blanket assemblies is the highest (peak) temperature rise occurring in a subchannel of the rod bundle which usually occurs at the outlet of the heated zone. Most tests were performed with a heat input gradient (1:1 to 4.6:1) oriented row-by-row across flats (Figure 2). Tests were made with forced (pumped) circulation and with natural circulation around a loop containing an air-blast cooler. Temperature distributions were mapped from recorded data at selected horizontal planes (levels), and transverse temperature rise profiles were plotted as, e.g., on Figure 4 for a number of pumped circulation rates and 2.8:1 heat input

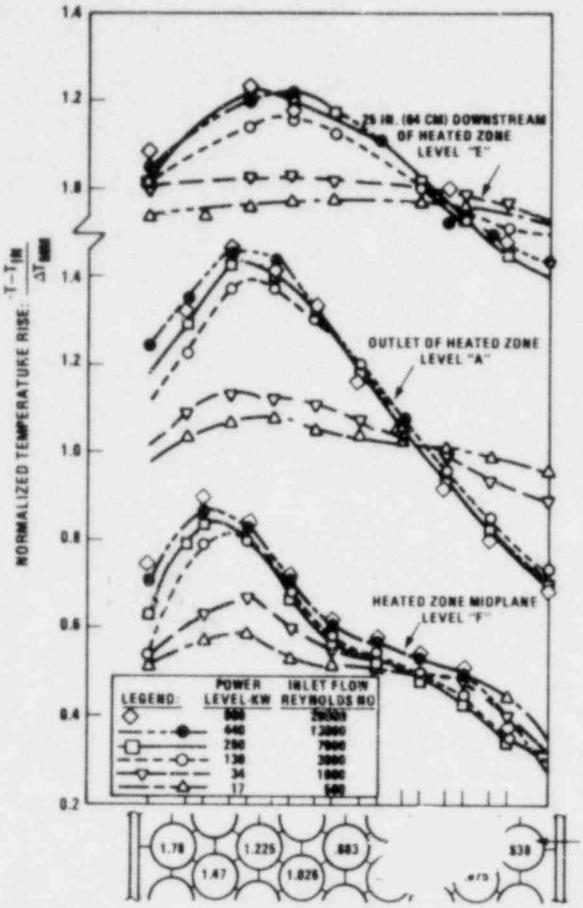

FIGURE 4: CHANGE IN TEMPERATURE PROFILE WITH POWER LEVEL - POWER INPUT GRADIENT 2.8:1 MAXIMUM/MINIMUM

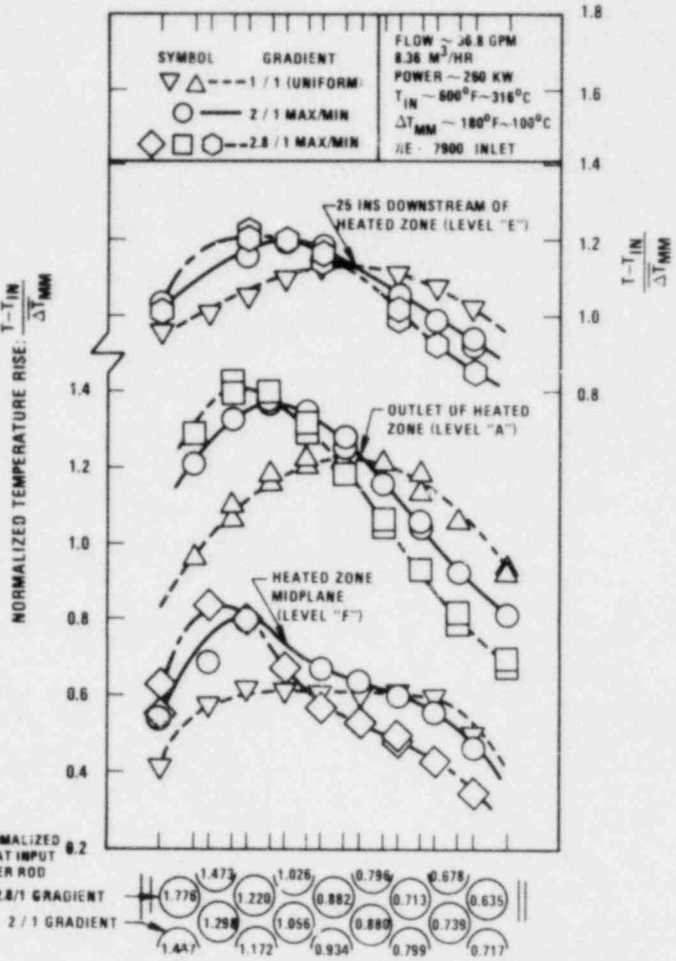

FIGURE 5: EFFECT OF HEAT INPUT GRADIENT ON TEMPERATURE PROFILES

gradient. The peak temperature rise values and their location in the bundle were determined. Figure 5 shows the effect of heat input gradient on the temperature profiles at constant total power input and flow. The peak temperature rise values were cross-plotted against Reynolds number (Figure 6) and heat input gradient (Figure 7) for forced circulation. The effect of buoyancy in the low flow regions is evident. In turbulent flow operation, peaking approaches a maximum value for each heat input gradient. In the transition flow region buoyancy effects a flattening of the temperature profiles and reduces the peak temperature obtained with the same heat input gradient and power-to-flow ratio. At fully laminar flow (Re < 500, see Figure 8* which was taken from Reference 21) the profile becomes quite flat. The same flattening of the circumferential temperature distribution was observed around the peripheral subchannels (Figure 9).

*Figure 8 shows the region of frictional transition from laminar to turbulent flow. For LMFBR blanket assemblies, this region had been found to extend over a Reynolds number range from about 500 to about 5000 (Ref. 21); for fuel assemblies from 800 to about 7000 (Ref. 22).

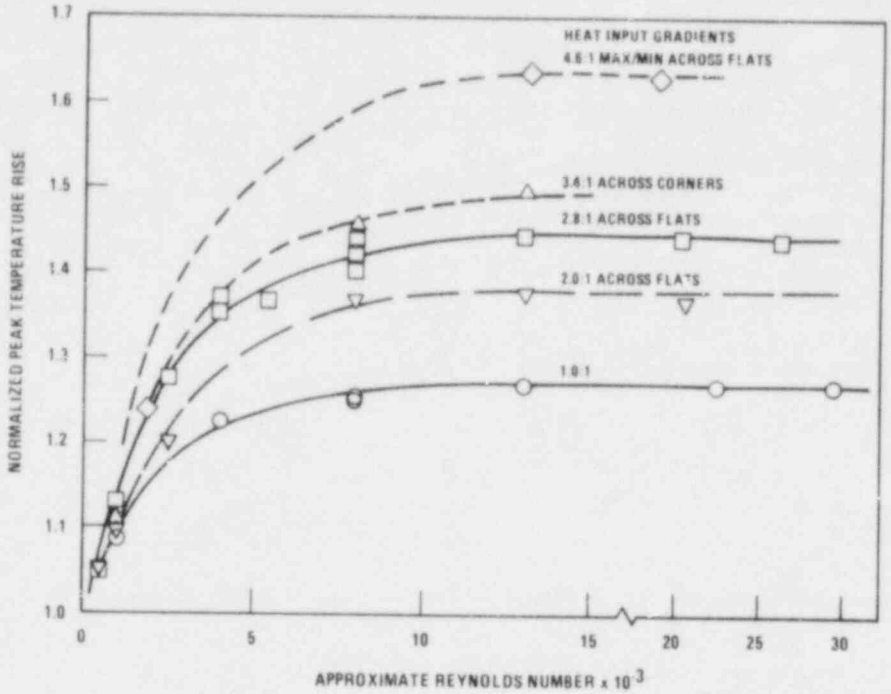

FIGURE 6: NORMALIZED TEMPERATURE PEAKING VS. FLOW RATE AT CONSTANT POWER TO FLOW RATIO (ΔT_{MM} = 100°C = 180°F)

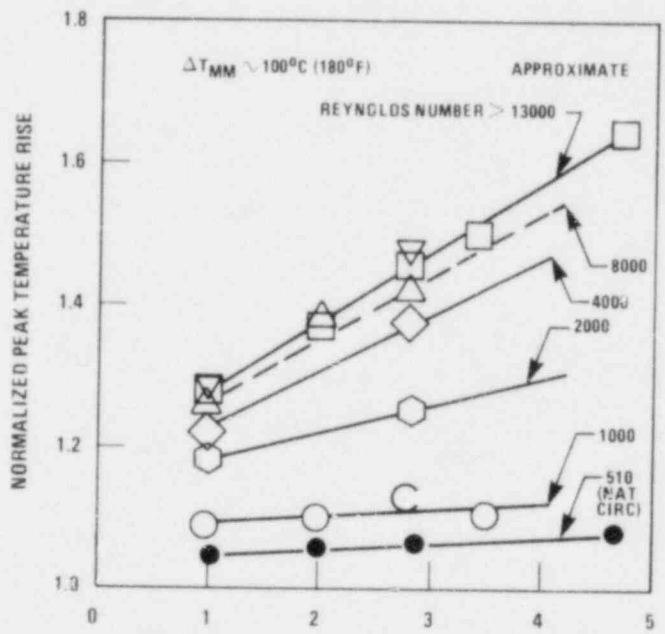

FIGURE 7: PEAKING VS. HEAT INPUT GRADIENT FORCED CIRCULATION

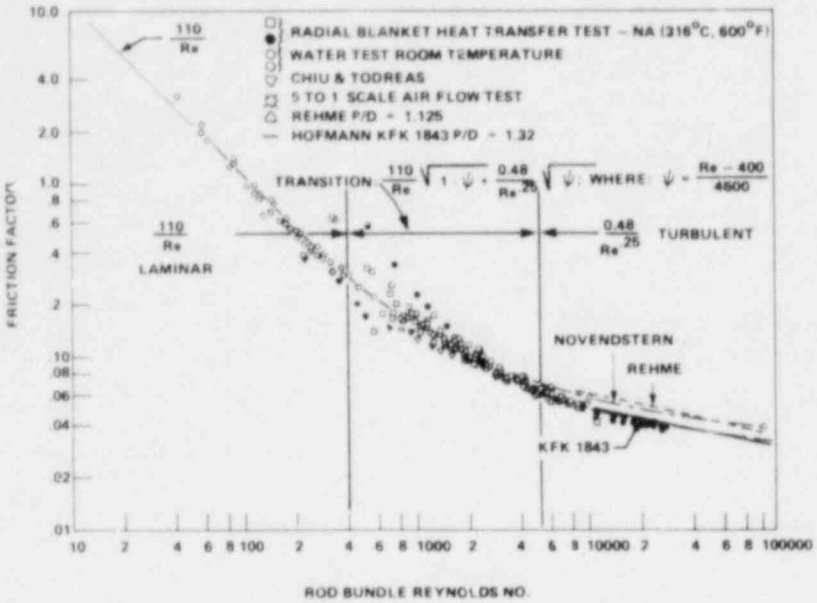

FIGURE 8: FRICTION FACTOR TEST DATA FOR TIGHT PITCH TO DIAMETER ROD BUNDLES WITH 4 INCH WIRE WRAP SPACER LEAD

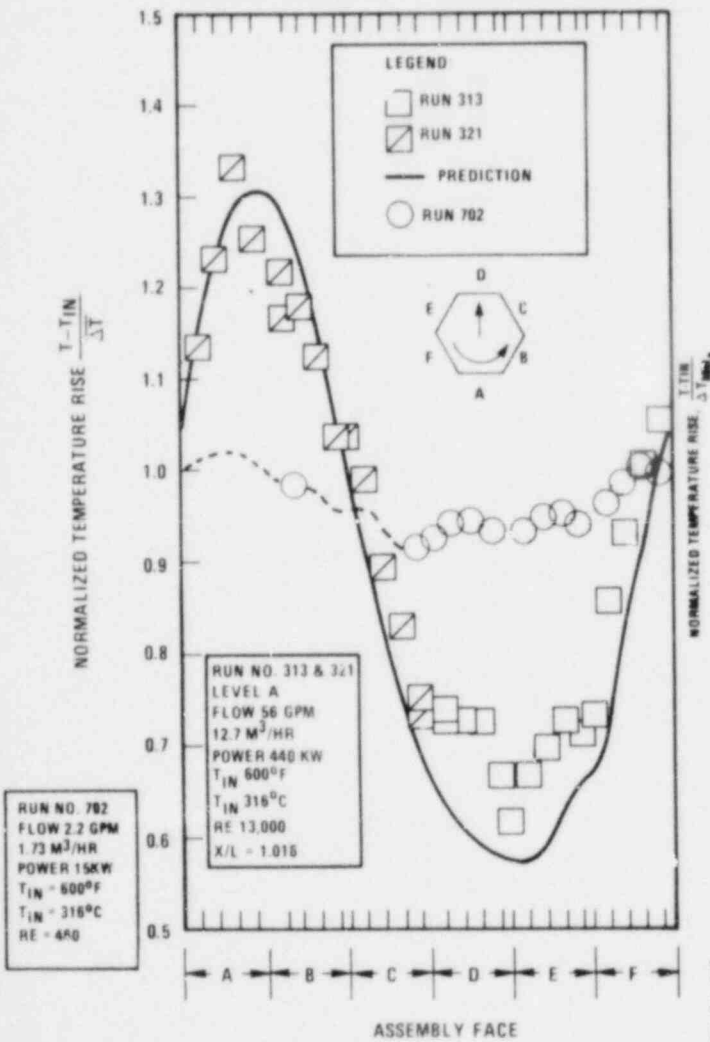

FIGURE 9: TEMPERATURE RISE DISTRIBUTION IN PERIPHERAL SUBCHANNELS 2.8:1 AND 1:1 GRADIENTS LEVEL "A", OUTLET OF HEATED ZONE

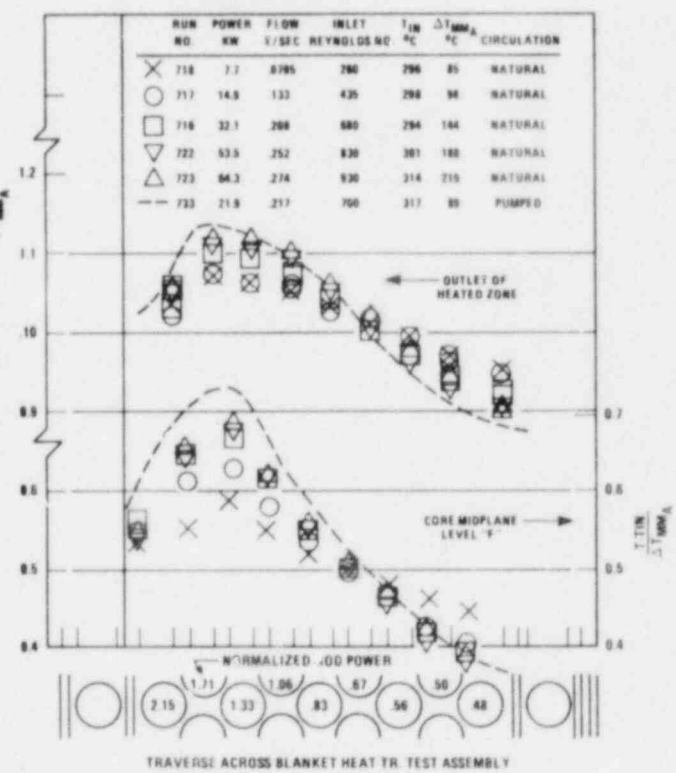

FIGURE 10: NORMALIZED TEMPERATURE RISE PROFILES FOR NATURAL CIRCULATION 4.6:1 HEAT INPUT GRADIENT

Similar plots were prepared for operation of the test section with natural circulation (Figures 10 and 11) where higher temperature rises were required to induce the desired flow rates. These flow rates were found to be a single valued function of test section heat input, independent of heat input gradient (Figure 13). Typical temperature profiles obtained with natural circulation induced by different heat input power levels at a fixed heat input gradient are shown in Figure 10. The peak temperatures, cross-plotted against the input gradients in Figure 11, also show a Reynolds number dependence. The peaks in natural circulation are slightly lower than those obtained with pumped circulation at the same Reynolds number and power gradient since the higher temperature required to induce the flow causes increased lateral heat conduction to the cooler peripheral subchannels (Figure 12).

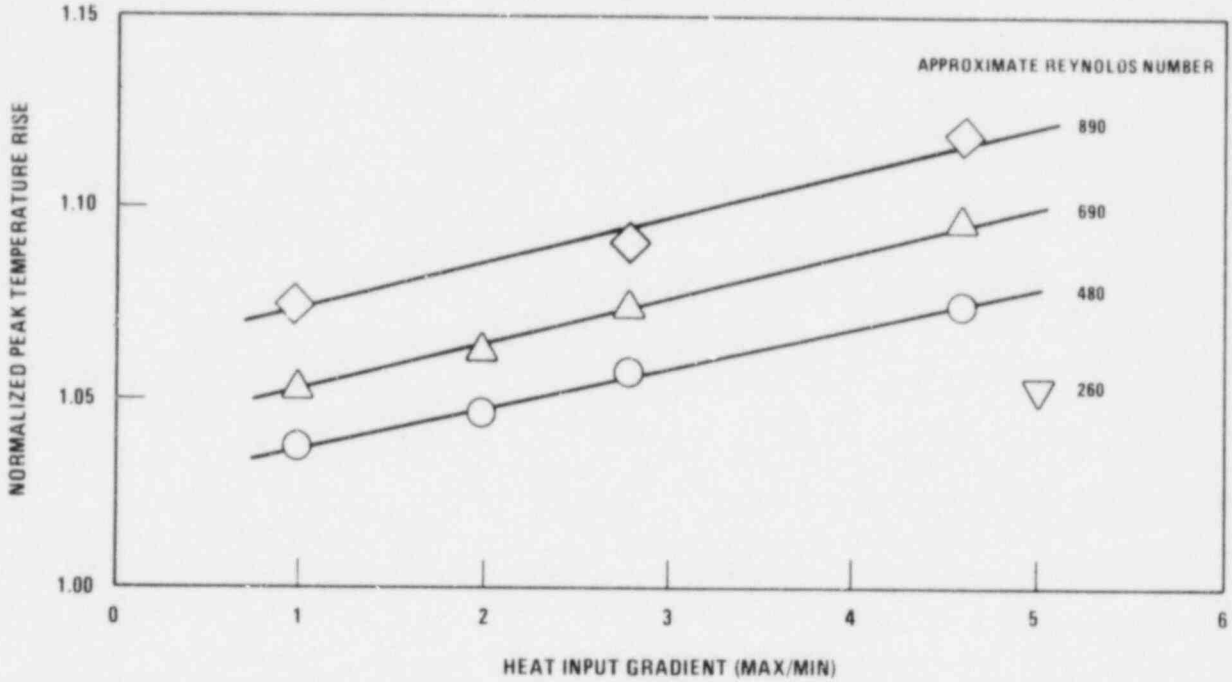

FIGURE 11: PEAKING VS. HEAT INPUT GRADIENT - NATURAL CIRCULATION

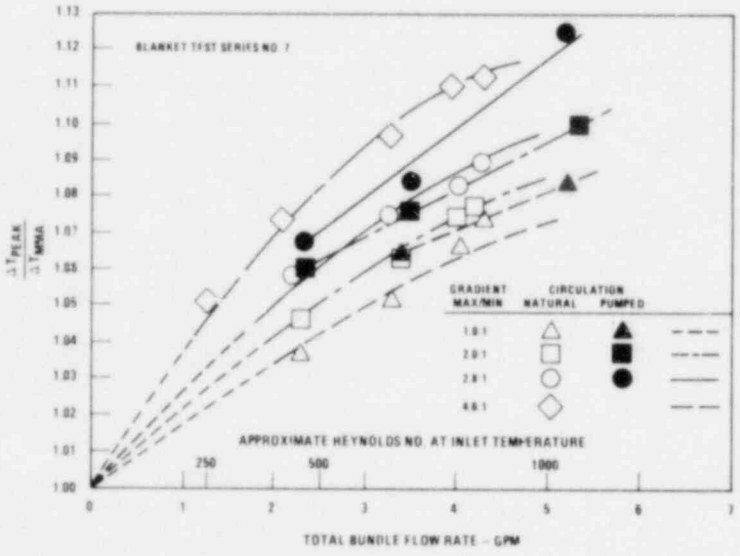

FIGURE 12: NORMALIZED PEAK TEMPERATURE RISE AT LEVEL "A" VS. CIRCULATING FLOW RATE

5. DISCUSSION

In this study, the mixed convection regime is defined as the region in which buoyancy reduces the normalized peak coolant temperature rise. The initiation of the mixed convection regime when the flow rate was reduced in the tested wire wrapped rod bundle was found to be a unique function of Gr_T/Re and was independent of the power gradient. This is shown in Figure 14. Although this result was not expected, it indicates that above a Reynolds number of approximately 15000 there are no more buoyancy effects. The transition boundary between turbulent forced convection and mixed convection can therefore be defined by:

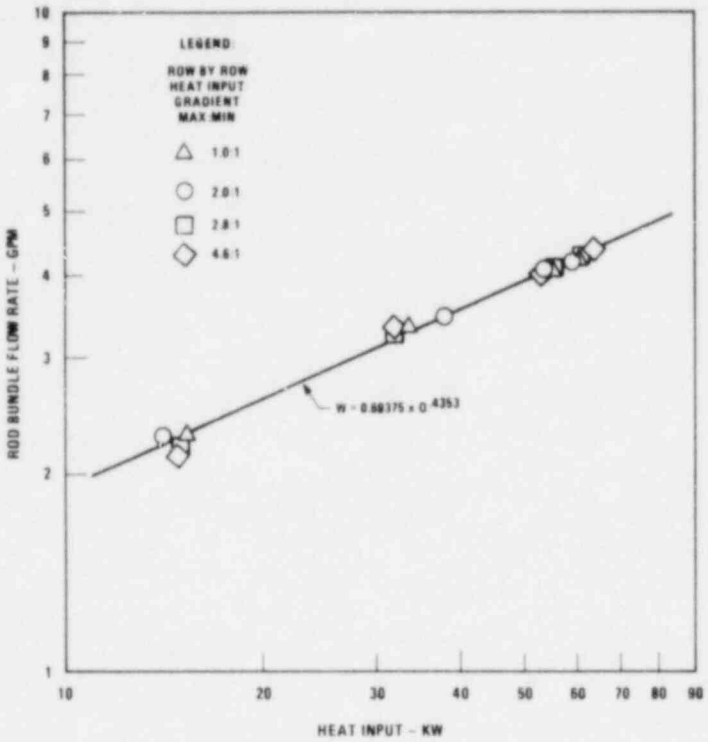

FIGURE 13: SODIUM CIRCULATION RATE INDUCED BY HEAT INPUT TO TEST SECTION IN NATURAL CIRCULATION

$$\left(\frac{Gr_T}{Re}\right)_I = 0.04 \tag{3}$$

Here, $(Gr_T/Re)_I$ is the value of Gr_T/Re where forced convection ends and mixed convection begins. (Observe that the Grashof number Gr_T is based on the overall axial average coolant temperature gradient. Several other Grashof-Reynolds number ratios were used to correlate the peak temperature increase including Gr_T/fRe^2; however, Gr_T/Re was judged to represent the data best). When the Gr_T/Re ratio is smaller than 0.04, the normalized peak coolant temperature rise is a function of the heat input gradient only:

$$\frac{\Delta T_{peak}}{\Delta T_{avg.}} = 1.27 + 0.11\ (\dot{Q}_{M-N} - 1) \tag{4}$$

When Gr_T/Re is larger than 0.04, buoyancy reduces the magnitude of the peak temperature rise by a lagorithmic function of the buoyancy parameter Gr_T/Re:

$$\frac{\Delta T_{peak}}{\Delta T_{avg.}} = \left(\frac{Gr_T}{Re}\right)_I - \phi\ [Q_{M-N},\ \log Gr_T/Re] \tag{5}$$

or

$$\frac{\Delta T_{peak}}{\Delta T_{avg.}} \approx 1.27 + 0.11\ (\dot{Q}_{M-N}^{-1}) - 0.169\ (\dot{Q}_{M-N})^{0.667} (\log 0.04 - \log \frac{Gr_T}{Re}) \tag{6}$$

For forced circulation tests the ratio $\Delta T_{peak}/\Delta T_{avg.}$ converges to a value equal to approximately 1.05, independent of the value of the maximum-to-minimum input gradient, $\dot{Q}_{M-N}$.

The difference in temperature peaking at the same forced or natural circulation flows is small. This difference is believed to be solely due to higher temperature gradient between the hot inboard and the cooler side channels in natural convection; i.e., at a given Reynolds number, the difference in coolant temperature rise peaking between forced and natural circulation is caused entirely by the higher mean temperature rise required in natural circulation to obtain the same flow rate. The hydraulic characteristics of the natural circulation test loop are similar to those of a LMFBR primary loop and the test assembly is a full size model. Therefore, it is judged that test results adequately represent natural circulation behavior in the prototype reactor. Figure 13 shows that natural circulation flow rates in the test loop are independent of the radial power gradient.

In general, it might be expected that for a wire wrapped rod bundle $(Gr_T/Re)_I$ is a function of the rod pitch-to-diameter ratio (P/D), the wire wrap lead ratio H/D, the peripheral rod pitch-to-diameter ratio PP/D and the heat loss Q_L, or

$$(\frac{Gr_T}{Re})_I = \phi\ (\frac{P-D}{D}, \frac{H}{D}, \frac{PP}{D}, Q_L) \tag{7}$$

Heat losses through the bundle enclosure and the peripheral rod pitch-to-diameter ratio are included in the relationship because temperature peaking reduction due to buoyancy occurs even when there is a uniform radial power input. The radial coolant temperature profile is accentuated by heat loss and particularly by transfer to the cooler peripheral flow subchannels. Use of the Rayleigh number instead of the Grashof number might permit other fluids to be included in a general correlation.

Buoyancy influences the peak coolant temperature rise even for Reynolds numbers as high as 10000 - 13000. Friction factor data obtained under isothermal conditions showed that the transition flow Reynolds number regime between laminar and turbulent flow also covered a wide range, $500 < Re < 5000$ as was seen in Figure 8.

Using the Gr_T/Re boundaries from Figure 14, boundaries of the forced, mixed and natural convection regions were constructed (as shown in Figure 15). Here Gr_T was converted to Gr_D for better comparison with previous similar Re - Gr flow regime maps which had been constructed using data obtained for non-metals flowing through circular tubes under uniform heating or temperature conditions (Reference 5). For tubes, initiation of a local inflection in the velocity profile is used to determine the onset of the mixed convection regime. Thus, it is questionable whether a comparison with tubes is meaningful, because criteria and conditions are vastly different.

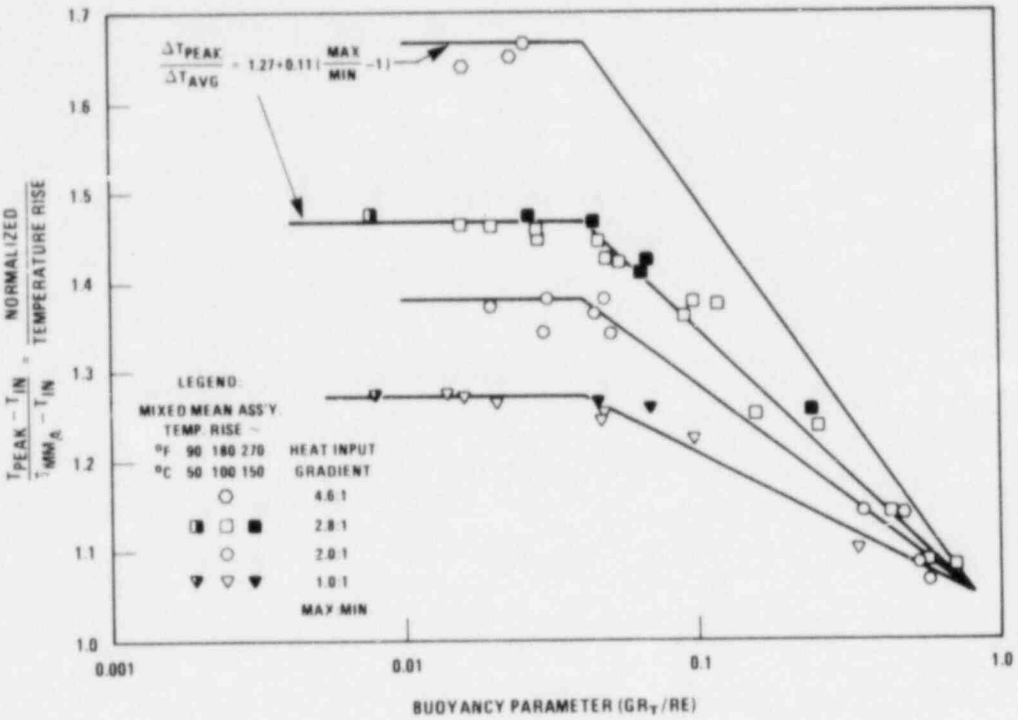

FIGURE 14: PEAKING VS. BUOYANCY IN TRANSITION REGION FORCED-CIRCULATION BLANKET HEAT TRANSFER TESTS

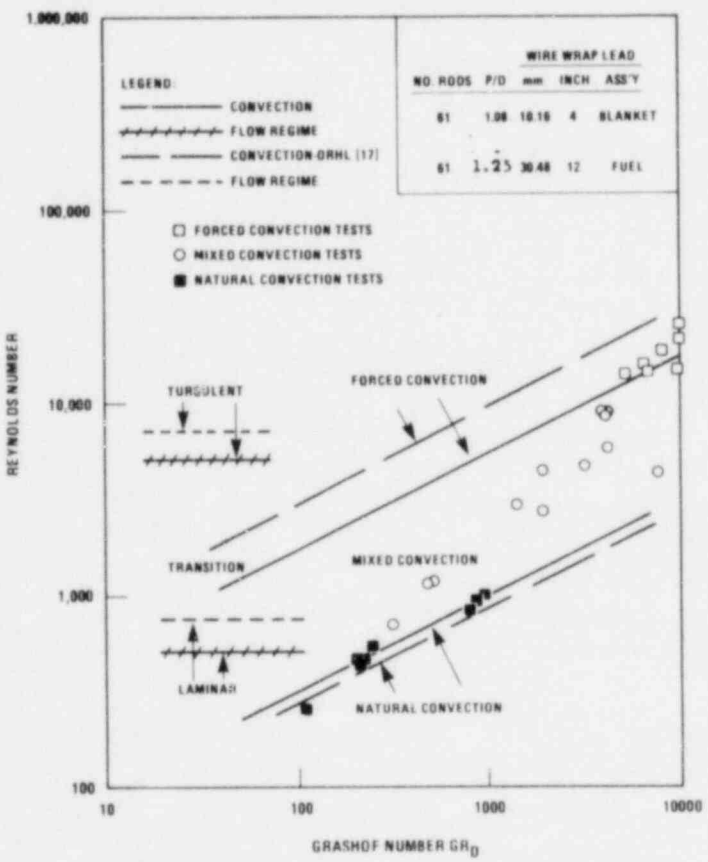

FIGURE 15: MODES OF HEAT TRANSFER 61-ROD BUNDLES

Recently, a 61-rod assembly having P/D = 1.25 and a wire wrap lead equal to 30.48 mm (12 inches) was tested in sodium under various power skews at ORNL. When some of the results were reduced in the same manner as done for the blanket test results, a similar relation and behavior was obtained. Here, the mixed convection regime is initiated at a lower value of $(Gr_T/Re)_I$ and extends to higher values of Gr_T/Re thereby delaying the onset of natural convection (Figure 15). This difference in convection boundaries may be caused solely by the differences in geometry. In the blanket model tests the increased mixing produced by a smaller wire wrap lead counteracts buoyant effects.

The boundaries of modes of convection and friction for round tubes are shown in Figure 16. In this figure, a reduction of the data of Buhr, et al. (Reference 7)(for mercury flowing through a tube) and of Wendling, et al. (Reference 23) are shown together with a modified equation of Polykov (Reference 24) for the mixed-convection turbulent free convection range. The Subbotin version of the Metais curve shows that even in round tubes, mixed convection effects extend to considerably higher Reynolds numbers than friction effects for liquid metal flows.

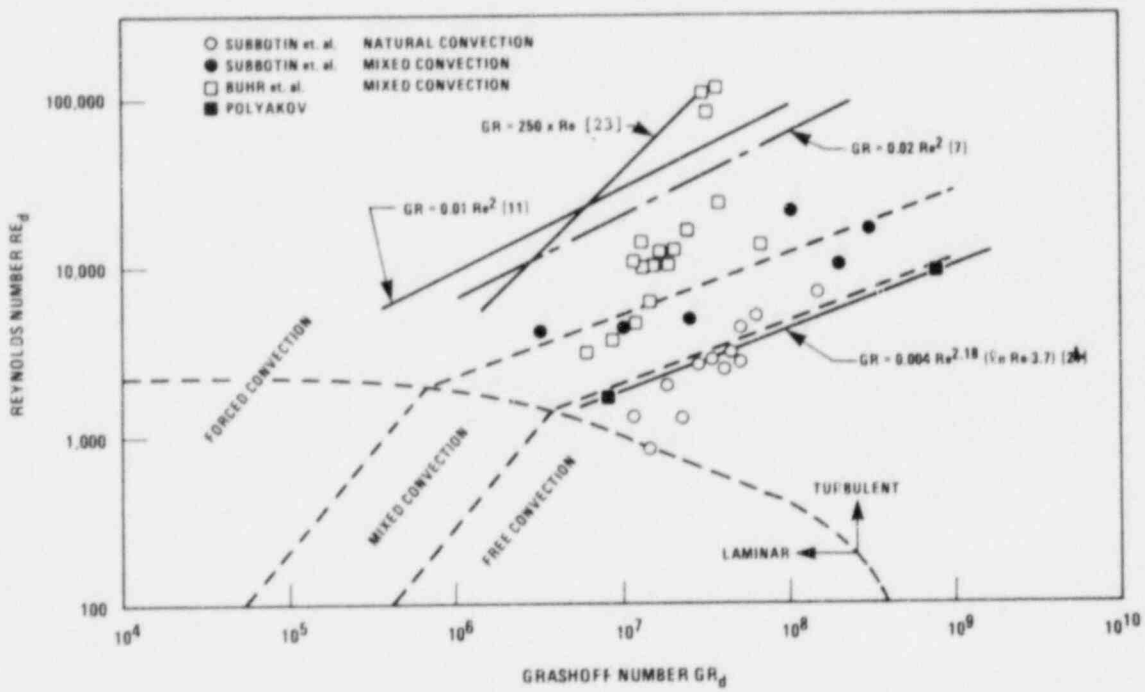

FIGURE 16: MODES OF CONVECTIVE HEAT TRANSFER (REF. 6) - ROUND PIPE

Figure 17 compares the analysis of Ramm and Johannsen (Reference 11) for coolant temperature peaking in a bare rod bundle under laminar mixed-convection and power skew conditions with blanket assembly data for different Rayleigh numbers.

Though there is agreement in the predicted and experimental shape of the curves, there is a difference of 2 units in the magnitude dimensionless parameter $T_i - T_{avg.}$ which is equivalent to 16°C in the peak coolant temperature.

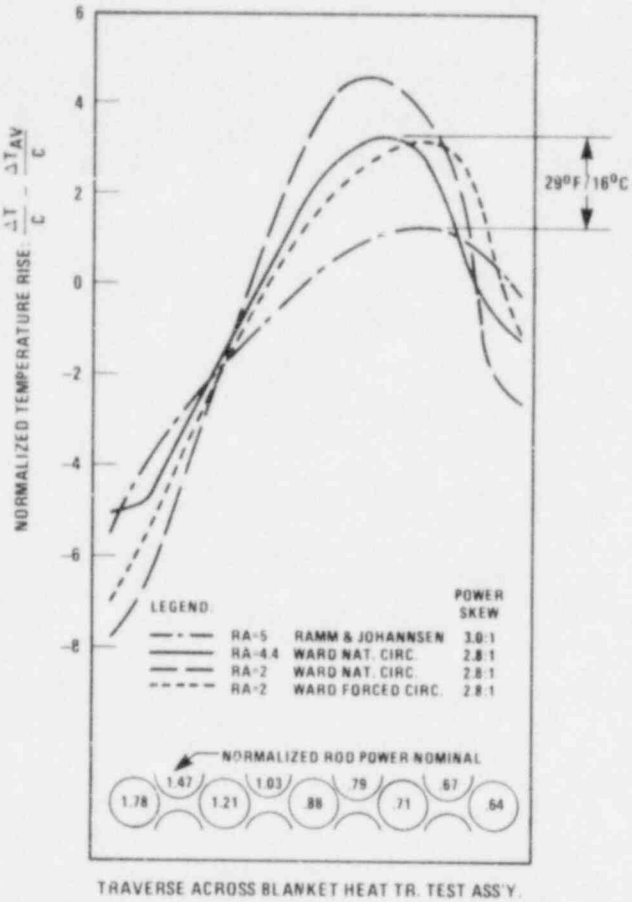

This difference in peak coolant temperature is in the direction expected, since mixing induced by the wire wrap delays and reduces buoyant effects.

No difference in the magnitude of the pressure drop was observed during mixed convection or natural circulation. No temperature fluctuations or flow recirculation zones were observed.

FIGURE 17: RADIAL SUBCHANNEL TEMPERATURE DISTRIBUTIONS AS A FUNCTION OF RAYLEIGH NUMBER FOR A 61-ROD ASSEMBLY WITH P/D = 1.08 (LAMINAR FLOW)

6. CONCLUSIONS

In wire wrapped rod bundles, the boundary between forced convection and mixed convection can be expressed as a constant value of Gr_T/Re and is independent of the power skew magnitude.

Buoyancy effects in rod bundles are experimentally observed at significantly lower values of the Grashof number and higher values of Reynolds number than for simple geometries and non-liquid metal applications.

Buoyancy effects significantly reduce coolant peak temperatures both at natural circulation and forced circulation flow rates.

The same type of convection regions can be mapped for tubes and for rod bundles.

For similar geometries, the mixed convection-forced convection boundary extends to higher Reynolds numbers in rod bundles of higher P/D ratio (Figure 15) and longer wire wrap lead.

REFERENCES

1. T.M. Hallman, "Experimental Study of Combined Forced and Free Convection in a Vertical Tube", NASA Technical Note D-1104, December 1961.

2. G.F. Sheele and J.J. Hanratty, "Effect of Natural Convection Instabilities on Rates of Heat Transfer at Low Reynolds Numbers", AIChE J., 9, pp. 183-185 (1963).

3. G.A. Kemeny and E.V. Somers, "Combined Free and Forced Convective Flow in Vertical Tubes - Experiments with Water and Oil", Trans. ASME, J. Heat Transfer, 84, pp. 339-346 (1962).

4. E. Eckert and P. Diaguila, "Convective Heat Transfer to Mixed, Free and Forced Flow through Tubes", ASME, 76, p. 497 (1954).

5. B. Metais and E.G.R. Eckert, "Forced, Mixed and Free Convection Regimes", Trans. ASME, J. of Heat Transfer, 86, pp. 295-296, May 1964.

6. V.I. Subbotin, F.A. Koslov and N.N. Ivanovskii, "Heat Transfer to Sodium Under Conditions of Free and Forced Convection and When Oxides are Deposited on the Transfer Surface", High Temperature, 1, No. 3, pp. 368-372, November 1963.

7. H.O. Buhr, A.D. Carr and R.E. Balzhiser, "Temperature Profiles in Liquid Metals and the Effect of Superimposed Free Convection in Turbulent Flow", Int. J. Heat and Mass Transfer, 11, pp. 641-654 (1968).

8. H.O. Buhr, E.A. Marsten, A.D. Carr, "The Distortion of Turbulent Velocity and Temperature Profiles on Heating, for Mercury in a Vertical Pipe", Trans. ASME, 96, pp. 152-171, May 1974.

9. V.M. Borishanskii, et al., "Analytical and Experimental Study of Mixed Convection in Tube Bundles with a Longitudinal Flow", J. of Engineering Physics (USSR), 24, pp. 7-11 (1973).

10. C. Tsai, R.A. Markley and A.A. Bishop, "Effect of Buoyancy Force on the Velocity and Temperature Distributions in an LMFBR Radial Blanket Fuel Rod Assembly", ASME Paper 73/HT-58, Atlanta, Georgia, August 5-8, 1973.

11. H. Ramm and K. Johannsen, "Combined Forced and Free Laminar Convection in Vertical Rod Bundles with Longitudinal Flow", ASME Paper 77/HT-44, August 15-17, 1977.

12. J.W. Yang, C. Scaccia, J. Goodman, "Laminar Natural Convection About Vertical Plates with Oscillatory Surface Temperature", Trans. Am. Soc. Mech. Engrs., 96, Series C, pp. 9-14 (1974).

13. J.C. Dutton and J.R. Welty, "An Experimental Study of Low Prandtl Number Natural Convection in an Array of Uniformly Heated Vertical Cylinders", Trans. ASME, J. of Heat Transfer, Series C, 97, pp. 372-377, August 1975.

14. M.S. Quigley and J.M. Bates, "Investigation of Buoyancy Dominated Flows in a 2x6 Rod Bundle", Fluid Flow and Heat Transfer Over Rod or Tube Bundles, ASME, p. 209 (1979).

15. F. Namekawa, et al., "Out-of-Pile Experiments for Natural Circulation Decay Heat Removal in LMFBR Fuel Assembly", Decay Heat Removal and Natural Convection in Fast Breeder Reactors, A.K. Agrawal and J.G. Guppy, Hemisphere Publications (1981).

16. E.U. Khan, W.M. Rohsenow, A.A. Souin and N.E. Todreas, "A Porous Body Model for Predicting Temperature Distribution in Wire Wrapped Rod Assemblies Operating in Forced and Free Convection", Nuclear Engineering and Design, 35, pp. 199-211 (1975).

17. S.D. Rose, et al., "Experimental and Numerical Thermal-Hydraulic Results from a 61-Pin Simulated LMFBR Subassembly", Trans. Am. Nucl. Soc., 34, pp. 800-882, June 1980.

18. F.C. Engel, B. Minushkin, R.J. Atkins and R.A. Markley, "Characterization of Heat Transfer and Temperature Distributions in an Electrically Heated Model of an LMFBR Blanket Assembly", Nucl. Eng. Des., 62, pp. 335-347 (1980).

19. B. Minushkin, F.C. Engel, R.J. Atkins and R.A. Markley, "Heat Transfer Tests of an Electrically Heated 7-Rod Mockup of an LMFBR Radial Blanket Assembly", ASME Paper 75-WA/HT-80 (1980).

20. C.L. Wheeler, et al., "CØBRA-IV-I: An Interim Version of CØBRA for Thermal-Hydraulic Analysis of Rod Bundle Nuclear Fuel Elements and Cores", BNWL-1962, March 1976.

21. F.C. Engel R.A. Markley and A.A. Bishop, "Laminar, Transition and Turbulent Parallel Flow Pressure Drop Across Wire Wrap Spaced Rod Bundles", Nucl. Science and Engrr., 69, pp. 290-296 (1979), and 74, p. 226 (1980).

22. D.R. Spencer and R.A. Markley, "Friction Factor Correlation for 217-Pin Wire Wrap Spaced LMFBR Fuel Assemblies", Trans. Am. Nucl. Soc., 39, pp. 1014-1015 (1981).

23. M. Wendling, R. Rique and R. Martin, "Mixed Convection with Sodium", Prog. in Heat and Mass Transfer, 7, pp. 81-92, Heat Transfer to Liquid Metals, O.E. Dwyer, Pergamon Press (1973).

24. A.F. Polyakov, "Transient Effects Due to Thermogravity in Turbulence and Heat Transfer", High Temperature, 11, pp. 90-98 (1973).

ACKNOWLEDGEMENT

The work described in this presentation was sponsored by the US/DOE Contract No. DE-AM02-76CH94000 under the guidance of Dr. R.J. Neuhold. The Heat Transfer Testing was performed under the supervision and guidance of Mr. B. Minushkin at Westinghouse Electric Corporation, Advanced Reactors Division.

NOMENCLATURE

β - Compressibility

C - Normalizing Constant: $k/(\rho\ cp\ \Delta T/\Delta Z\ V_{AV} D_H^2)$ (Reference 13)

cp - Specific heat

D_H - Rod bundle average hydraulic diameter

g - Acceleration of gravity

Gr_D - Grashof number based on film drop = $g\beta\Delta t\ D_H^3/\nu^2$

Gr_T - Grashof number based on temperature rise = $g\beta \frac{\Delta T}{\Delta Z} D_H^4/\nu^2$

k - Thermal conductivity

H - Wire wrap lead

P - Triangular rod pitch

Q - Total heat input into rod bundle

Re - Bundle average Reynolds number $D_H\ V/\nu$

Q_{M-N} - Heat input gradient, maximum-to-minimum

f - Friction factor

T - Temperature

V - Rod bundle average velocity

W - Weight flow rate

Δt - Average film temperature drops

ΔT - Temperature rise

ΔZ - Axial distance

ν - Kinematic viscosity

PP - Rod to wall spacing

ρ - Density

SUBSCRIPTS

AV - Average

MM - Mixed mean

MMA - Mixed mean at measurement level "A" (Figure 1)

IN - At inlet to rod bundle

N - Normalized

NAV - Normalized average

Peak - Maximum coolant temperature in rod bundle

I - Initiation

EFFECTS OF PIN BUNDLE DISTORTIONS ON LMFBR FUEL ASSEMBLY COOLANT TEMPERATURE DISTRIBUTIONS

K. H. Chen, S. Kaplan, T. L. Kurtz, J. D. Stephen
Advanced Reactor Systems Department
General Electric Company
Sunnyvale, California

INTRODUCTION AND SUMMARY

A liquid metal fast breeder reactor (LMFBR) fuel assembly operating under conditions of high temperature and high neutron irradiation during its lifetime will experience a phenomenon known as bundle-to-duct interaction (BDI) which is manifested by the differential swelling and creep between the fuel pin bundle and the hexagonal duct. Bundle-to-duct interaction may result in significant interference between the pin bundle and the duct, which in turn causes significant bundle geometry deformation in the latter part of the assembly life. This may cause a decrease in the local coolant flow channel area, and possible direct pin-to-pin and pin-to-duct contact, all resulting in increased clad temperature. Currently, an interference equivalent to one wire spacer diameter is used as a fuel assembly design allowable. This paper presents an evaluation of increasing the allowable BDI by analytically determining the limiting thermal-hydraulic design condition. Previous fuel bundle thermal-hydraulic models could only handle the uniform, beginning of life bundle geometry. As the use of these uniform geometry models to predict distorted bundle thermal hydraulics may lead to erroneous results, a predictive method of evaluating the complex interaction between the thermal-hydraulics and structural mechanics has been developed based on test data. Analyses have been conducted to determine the manner in which the distorted bundle temperature distribution differs from that predicted from beginning of life geometry. The results indicate that increasing the allowable interference to 1½-2 wire spacer diameters may be acceptable.

METHOD

The analytic procedure consists of implementing three basic models. The first model predicts the bundle-to-duct interference by determining the differential growth of the fuel pins, wires and duct due to swelling and creep during irradiation. The second model predicts the position of each pin at each axial location in conjunction with the bundle and duct growths derived from the first model, and determines the local flow areas and related hydraulic parameters throughout the distorted bundle. The model is based on out-of-pile bundle compression test data [1], which closely simulate the in-reactor fuel pin movement in the presence of BDI. The third model predicts the thermal hydraulics of the distorted assembly whose geometry is defined by the second model. The COBRA-WC code [2] developed by Pacific Northwest Laboratory has been adopted for the thermal-hydraulic model. The code solves the momentum, mass and energy equations on a subchannel basis and can accept non-uniform subchannel areas and gaps. These three models are organized and computerized such that the structural variations during reactor operation are continuously analyzed. Thus, the effects of BDI on the assembly thermal-hydraulic behavior can be evaluated throughout lifetime.

ANALYSIS OF BUNDLE-TO-DUCT INTERFERENCE

Bundle-to-duct interference occurs when the lateral growth of the pin bundle exceeds the clearance between the pin bundle and the duct. In estimating the BDI hex flat-to-hex flat interaction, an effective flat-to-flat growth across the duct is used. The "effective duct" is a regular hexagon that has the same area as the true duct cross-section that bulges at mid-flats due to the coolant pressure. Such an effective duct has been

shown, in bundle compression testing to produce similar bundle mechanical performance with respect to pin-pin displacements as does the bulged duct [1]. Also, the net coolant flow area is conserved.

The bundle-to-duct interference is defined as

$$BDI = \Delta Bundle - \Delta Duct - Porosity$$

where ΔBundle and ΔDuct are the total bundle and duct linear growths, respectively, and porosity is the clearance between a theoretically close-packed bundle and the duct. Bundle-to-duct interference occurs when the BDI is positive. Total bundle growth consists of the growth of all the wire spacers and the cladding. The growth common to both the wires and cladding is due to thermal expansion and swelling. Irradiation creep growth and elastic growth are additional major growth contributors for the cladding. Total duct growth consists of thermal expansion, swelling, and mechanical strain (elastic and creep) resulting from coolant pressure.

For the discussion here, the BDI can be functionally expressed as

$$BDI = f(P_d, P_p, T_c, T_w, T_d, \phi, t) \quad (1)$$

where P_d is the duct internal pressure due to coolant flow, P_p, the pressure within the pin, T_c, the cladding midwall temperature, T_w, the wire spacer temperature, T_D, the duct temperature, ϕ, the flux, t, the time, L_i, geometries of the i components (e.g., pin, wire or duct) and X_i, materials and thermal-physical properties of the i components. The distorted bundle due to the BDI affects the duct pressure P_d by changing the flow resistance gradually. The pin internal pressure, P_p, is assumed to be linear with time

between beginning of life (BOL) and end of life (EOL) conditions. The average values of T_c, T_w and T_D at each axial node are used.

The effect of the BDI is to distort the assembly geometry; the distorted geometry will redistribute the flow field throughout the assembly which, in turn, will create a temperature field different from that based on nominal geometry.

The primary concern now is the level of a local hot spot created due to the BDI. Specifically, it is necessary to be assured that for a given amount of BDI, the maximum local hot spot created will not degrade the intended design performance of the assembly. A realistic description of a distorted assembly geometry due to BDI is necessary for a proper thermal-hydraulic analysis.

THE PREDICTION OF A DISTORTED ASSEMBLY

A full analytical description of a distorted assembly due to BDI is complex and difficult. Assumptions made in the formulation may involve simplification and rationalization of a complex phenomenon not yet well understood. For the thermal-hydraulic design of a fuel assembly over its lifetime, a semi-empirical approach can be a viable alternative that will provide a reasonable estimate of the effect of BDI based on test data. Furthermore, the modeling effort can be greatly reduced. The semi-empirical approach is described below.

The positions of all pins at an in-pile bundle cross-section subjected to BDI are approximated by a linear superposition of two sets of displacements; that due to the free or unconstrained growth of the bundle and the duct, and that due to the mechanical interaction at the duct inner surface

as it compresses the bundle outer periphery. When compressing the bundle outer periphery, the duct to bundle loading is applied helically about the bundle periphery, following the wire spacer pattern, as shown in Figure 1. Mechanical compression tests [1] performed on 217-pin and 91-pin bundles to simulate BDI have shown distinct bundle distortion characteristics that appear not to be influenced by the bundle size. That observation provides a basis for extrapolating the test data for estimating the distortion of a 271-pin bundle, which is the pin bundle size to be used in large commercial plants.

The pin bundle, when compressed by a helical loading, produces pin lateral displacement data as shown by the vector representation of Figure 2. The data in Figure 2 is for a bundle axial location at which one of the helical line loads is applied to the "10 o'clock" hex flat. A near facsimile of the data, but appropriately rotated in orientation, repeats at each elevation at which a line load acts on a bundle face. The data shows that, at a given cross-section, the pins generally move toward a bundle cross-sectional location where no pin movement is observed. This location, or bundle "deformation centroid" is at the far side of the compressed bundle, and is conceptualized in Figure 3.

A statistical analysis was performed on the two sets of compression test data for the 217-pin assembly and the two sets of compression data for the 91-pin assembly. The analysis demonstrated the existence of a distorted bundle pattern common to the test data and amenable to further analysis. Figures 4 and 5 show characteristic results obtained from the 217-pin bundle test data. Figure 4 indicates lines of constant angle of the displacement vectors. Figure 5 shows contours of constant pin radial displacement which are directed toward a common origin, the deformation centroid. Using the distorted bundle pattern obtained from the statistical

data analysis, a procedure was established to locate the pin centroids as a function of BDI. With the pin centroids located, the resulting flow channel geometry and hydraulic parameters can be calculated.

An alternative to using the pattern method is the direct implementation of the compression test data, or extrapolation of the direct data to bundle sizes of interest. True distortions may differ from that of the calculated pattern geometry, but are believed to be a random occurrence from location to location, and result in only a small perturbation of the temperature distribution from the more global effect responding to the distortion pattern.

In subsequent discussions, BDI is frequently referred to in units of "wire diameters." This unit is convenient in that it provides a direct visualization of the edge region subchannel geometry when BDI occurs, including the effect of the mechanical instability of the compressed bundle as observed in the bundle compression tests of Reference 1. Referring to Figure 1, when BDI is zero (i.e., porosity no longer exists because of differential bundle and duct growths) an idealized bundle and duct geometry would provide a one wire diameter clearance between the bundle cladding and the duct. For BDI > 0, that same clearance occurs at the helical pattern of wire spacer to duct contact. Away from that contact, the cladding approaches the duct as the pin bends, and is expected to be closest to the duct midway between contacts at any hex face, i.e., at one-half the wire spacer lead. From the tests of Reference 1, it has been demonstrated that at approximately two wire diameters of BDI, the cladding will contact the duct at the location midway between wire-to-duct contact locations. If at a given cross-section, all pins exhibited the same lateral displacement, i.e., retained a uniform triangular pitch and undistorted interior flow subchannels, a BDI of one wire diameter would result in cladding to duct contact. However, due to an apparent mechanical instability, referred to as the dispersion mechanism, the pins shift laterally such that approximately

half the BDI is accommodated by changes in pin-to-pin spacing, and half the BDI is accommodated by a change in edge pin to duct spacing. The effect of that mechanism is apparent in Figure 2.

THERMAL HYDRAULIC ANALYSIS

The COBRA subchannel model was adopted for the thermal-hydraulic analysis. The COBRA-WC [2] code has detailed mechanistic models and has been the most widely used thermal-hydraulic analytical tool for LMFBR designs. It is also the U.S. national in-core thermal-hydraulic code. It is the best assembly thermal-hydraulic code available for analyzing distorted bundles.

However, some important points regarding distorted bundle thermal-hydraulic analysis should be noted: currently available subchannel codes, including COBRA, require some basic thermal-hydraulic parameters derived from experiments. At present, these parameters are based on nominal bundle geometries, the adequacy of these parameters for distorted geometries has not yet been determined. An example is the mixing coefficient which is used for calculating lateral heat transfer between channels and is dependent upon geometry and thermal boundary conditions.

Subchannel codes do not predict the temperatures well in regions of large temperature gradients such as in the vicinity of the duct wall. Significant uncertainties in temperature prediction could be expected along the outer region of a distorted bundle where the bundle and the duct wall would interfere. The lumped approach of subchannel analysis must be superseded on a local level with a more detailed local thermal-hydraulic analysis. Furthermore, for an assembly design with expected large BDI (beyond bundle and duct just touching), finite contact areas between "soft" fuel pins and

"hard" duct wall will develop. An accurate estimate of the local hot spot temperatures will require a different physical modeling approach such as thermal analysis of contacting bodies.

On the positive side, within the framework of thermal-hydraulic analysis for distorted bundles, a major concern has been the feasibility of performing an integrated analysis involving the coupling of thermal-hydraulic and mechanical feedback with sufficient details. The present computer simulation of a large 271-pin assembly has been successful in including a detailed subchannel analysis model and a systematic procedure to follow the evolution of the bundle distortion. An analysis of a typical large fuel assembly operating in the reactor environment for a period of two years is given below.

INTEGRATED THERMAL-HYDRAULIC AND MECHANICAL ANALYSIS OF A LARGE FUEL ASSEMBLY

A 271-pin fuel assembly of stainless steel alloy D9 material construction (i.e., alloy D9 for the duct, the cladding, and the wire spacers) was chosen to investigate the acceptability of increasing the allowable BDI.

The performance of the alloy D9 fuel assembly at large plant conditions is affected by the BDI behavior of the assembly. The BDI behavior is, in turn, influenced by the effect of uncertainties in the material swelling and creep, temperature distribution (i.e., sensitivity to difference in temperature between bundle and duct), temperature range (i.e., increase or decrease in assembly temperature reflecting uncertainty in power or flow),

as-built dimensions, flux, and assembly pressure drop. For the analyses discussed in this section, only swelling and creep uncertainties are considered.

Application of the swelling and creep uncertainties to alloy D9 was performed consistent with the demonstrated sensitivity of creep and swelling to small variations in the alloy composition, variations small enough so as to be a potential heat-to-heat variant during the production of commercial quantities of the alloy. Figure 6 shows the effects of adverse stack-ups of creep and swelling between the bundle and the duct on the fuel assembly BDI history at the axial mid-core location for an assembly lifetime of two years. The 271-pin assembly uses 0.275-inch diameter pins with 0.048-inch diameter spacer wires.

At BOL an initial looseness occurs due to the as-built clearance, slightly diminished by differential thermal expansion between the bundle and the duct. Early in life the looseness increases due to the creep induced duct dilation. During the mid-life range, the rate of increased looseness diminishes as the pin plenum pressure buildup results in increased cladding creep. Until this time swelling of the stainless steel components has not occurred; an incubation period is required before swelling commences. Toward the end of life the looseness diminishes and eventually the bundle is compressed as the swelling incubation fluence is exceeded. The bundle swelling rate considerably exceeds the duct swelling rate in accordance with the swelling temperature dependency. It can be seen that a large amount of bundle tightness can develop at the end of life with unfavorable stack-ups of swelling and creep uncertainties. The tightness can be several wire spacer diameters.

The predicted coolant temperature distribution under different amounts of BDI during an assembly lifetime is shown in Figures 7 and 8. Important

results to be noted are: the edge channel coolant temperatures increase and the interior channel coolant temperature decrease with the increase in bundle-to-duct interference.

It is also predicted that the increase in the edge channel coolant temperatures is higher along the edge of the bundle where the wires contact the duct wall than that of the edge channels opposite the non-wire contact region. At the channel region that includes the wires contacting the duct, even though the edge channel flow areas have not been diminished by the BDI, the interior channels have been considerably distorted, producing a significant decrease in flow areas and in coolant flow. At the opposite side, although the edge channels are considerably reduced in area as the cladding approaches the duct wall, very little distortion occurs to the pin array in that general region, and the interior flow channels in that general region remain relatively undistorted.

The increase in the maximum edge channel temperature is much faster than the decrease in the maximum interior temperature (Figure 8). Extrapolation of the two curves indicates that the maximum edge channel temperature would become equal to the maximum interior channel temperature at about a 2.75 wire spacer diameter interference. However, quantitative extrapolation beyond two wire diameters is not recommended because the structural response of the bundle changes at approximately a 2-wire space diameter interference as the cladding contacts the duct. For a 2-wire spacer diameter interference, the maximum edge channel temperature is about 65°F below the maximum interior channel temperature for the assembly analyzed.

CONCLUSIONS AND DISCUSSION

A thermal-hydraulic analysis including the effect of bundle distortion was performed for a 271-pin fuel assembly operating for two years lifetime. The results indicate that the assembly coolant temperatures will be skewed towards higher edge channel and lower interior channel temperatures relative to those of an assembly with nominal geometry. Edge channel coolant temperatures at the wire contact edge increase more than other edge channel temperatures. The rate of increase of the edge channel coolant temperature is faster than the rate of decrease of the interior channel coolant temperature. Extrapolation of the result indicates that the maximum edge channel coolant temperature will not reach the level of the maximum interior channel coolant temperature until well beyond 2-wire spacer diameter interference for the fuel assembly analyzed. For a 2-wire spacer diameter interference, the maximum edge channel coolant temperature was about 1195°F, which was about 65°F below the maximum interior coolant channel temperature, and the latter was lower than that obtained from the nominal geometry subchannel analysis.

In general, with the presence of BDI of up to two-wire spacer diameters, interior channel temperature changes appear to be acceptable. These preliminary results will be confirmed by further work, including ex-pile bundle mechanics and thermal-hydraulics tests to generate statistically significant data on distortion and flow parameters, theoretical modeling for analysis of local conditions which are beyond the capability of subchannel analysis, core-wide analyses to establish if core flow redistribution is significant, and in-pile data from tests in the FFTF FOTA (Fuel Open Test Assembly) instrumented positions.

The integrated approach to thermal-hydraulic analysis of a distorted bundle has made significant contributions to the understanding of the effect

of the BDI phenomenon on the coolant temperature distribution. It has been shown that the one wire spacer diameter BDI guideline is conservative. It has also been shown that the traditional assembly thermal-hydraulic design approach based upon the maximum interior channel temperature may not be adequate for designing fuel assemblies with high BDI in which high edge channel temperatures can be the controlling parameter in design. A methodology for the evaluation of high BDI assembly designs has been successfully achieved.

REFERENCES

1. S. Kaplan and P. Hirschberg, "Advances in Wire-Wrap Assembly Technology through Bundle Compression Testing," ANS Transactions, Vol. 23, 1976

2. T. L. George, et al., "COBRA-WC: A Version of COBRA for Single-phase Multiassembly Thermal Hydraulic Transient Analysis," PNL-3259 Pacific Northwest Laboratory, Richland, Washington, July 1980

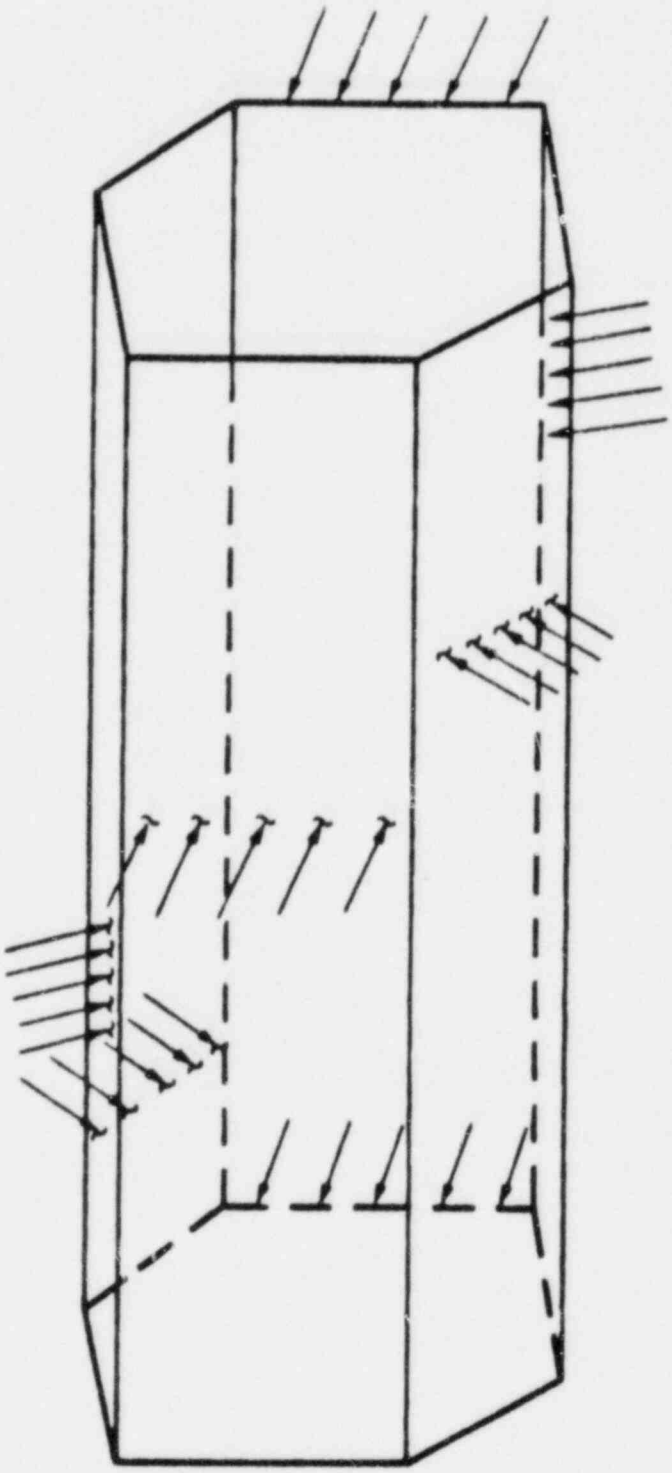

FIGURE 1.

HELICAL LOAD DISTRIBUTION APPLIED TO FUEL-PIN BUNDLE

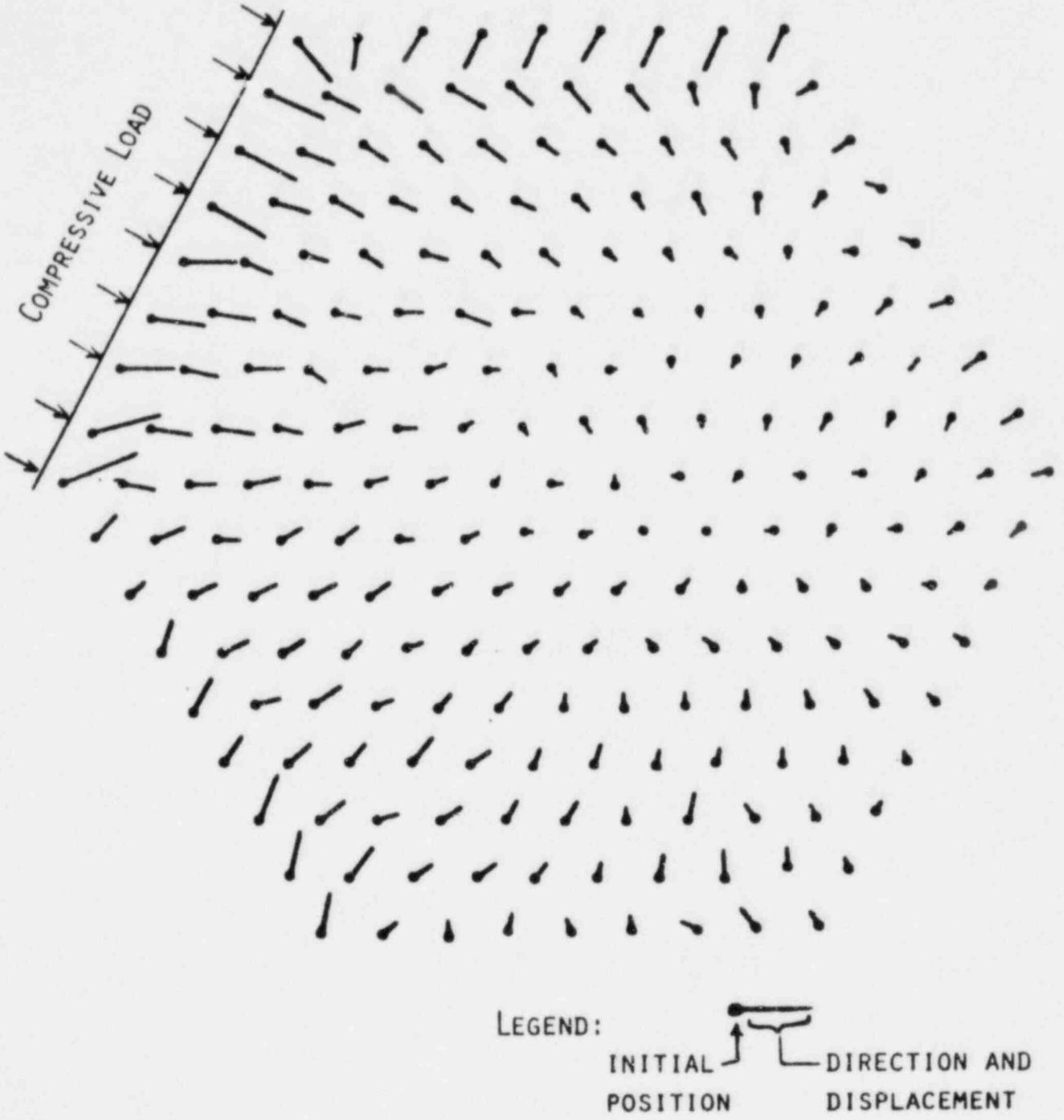

FIGURE 2.

PIN DISPLACEMENT MECHANICAL COMPONENT DATA FROM
217-PIN BUNDLE COMPRESSION TEST

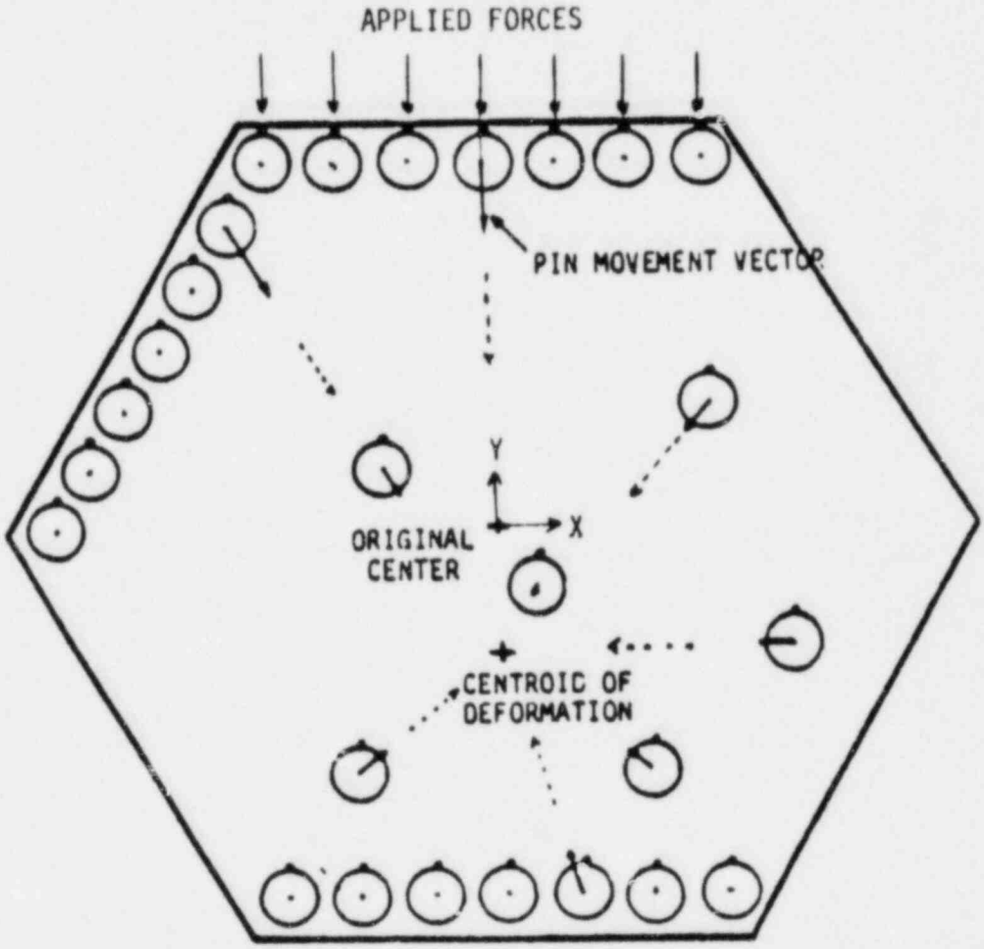

FIGURE 3.

CONCEPT OF PATTERN GEOMETRY FOR BUNDLE DEFORMATION

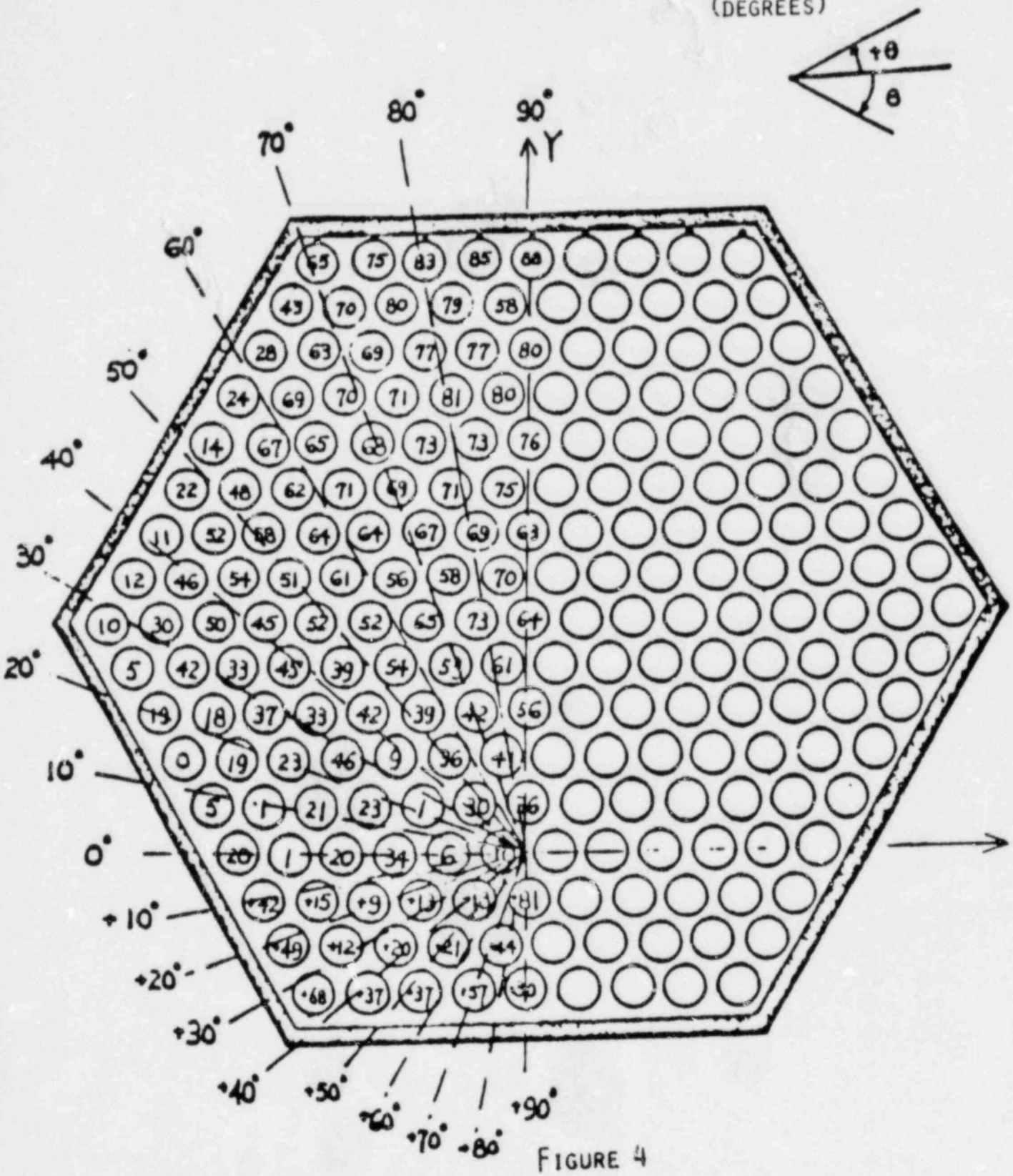

FIGURE 4

COMPRESSION TEST DATA ANALYSIS FOR ANGLE PATTERN

LEGEND: (X) , X = MAGNITUDE OF DISPLACEMENT (MILS)

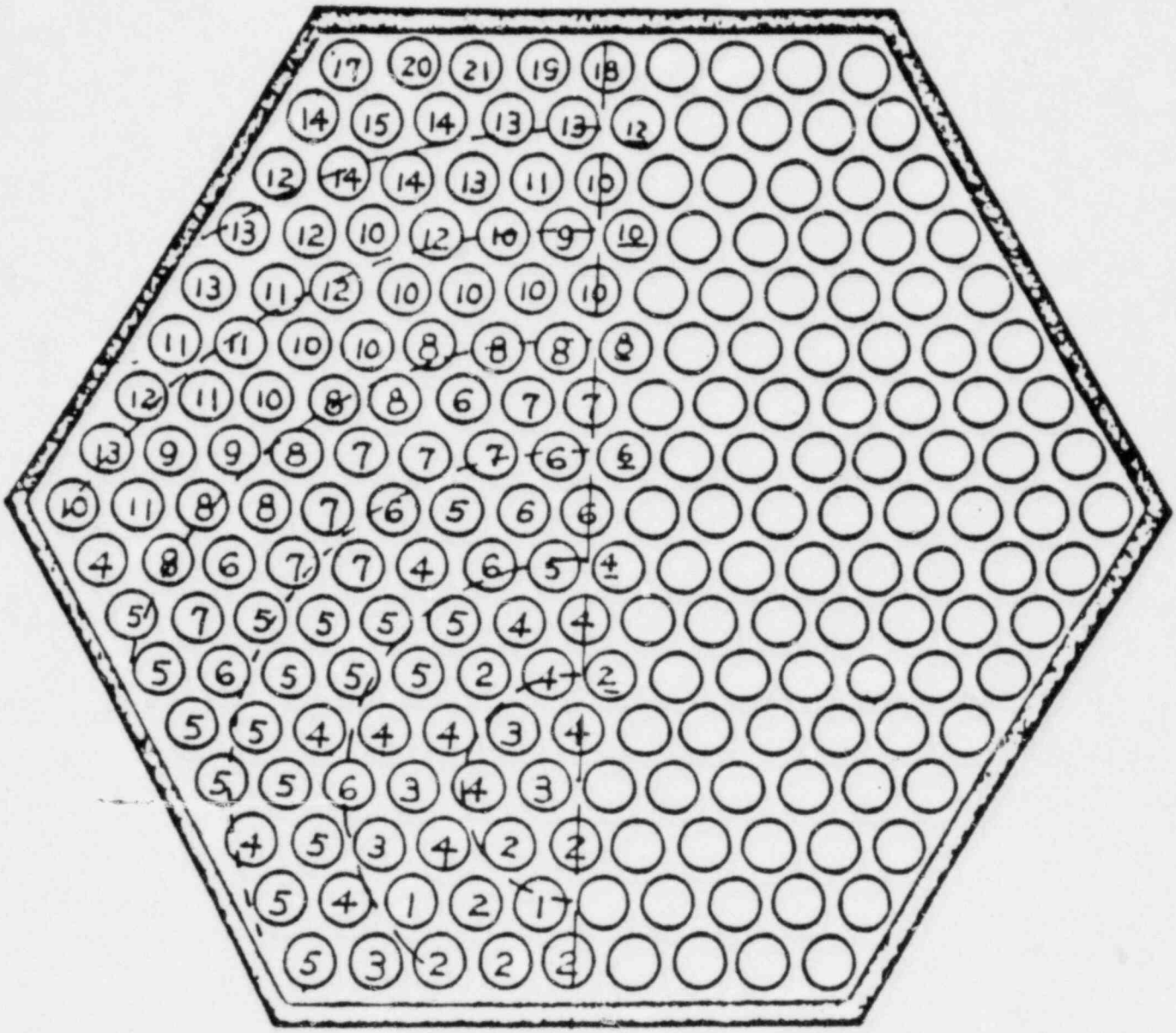

FIGURE 5.

COMPRESSION TEST DATA ANALYSIS FOR DISPLACEMENT PATTERN

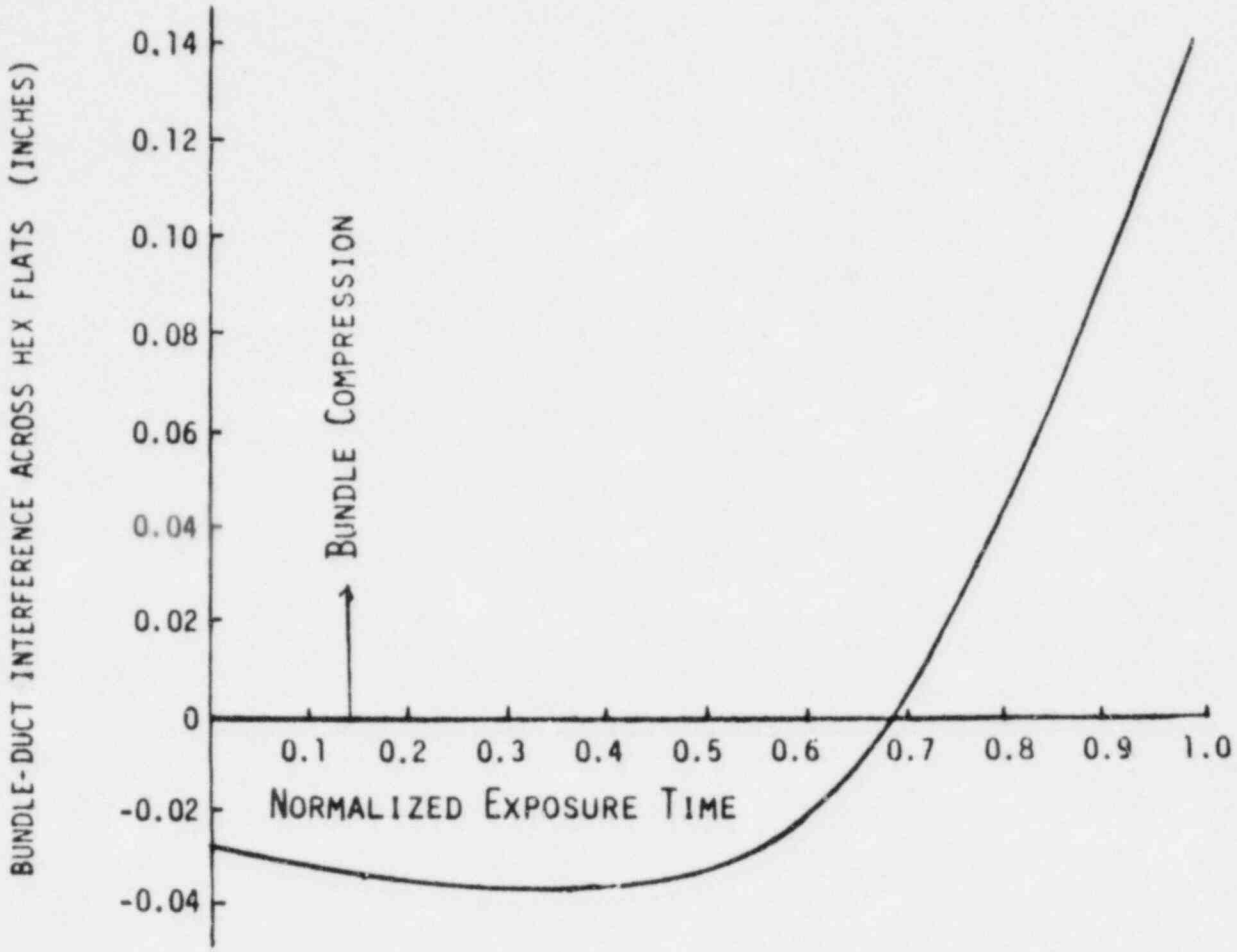

FIGURE 6.

BUNDLE-DUCT INTERFERENCE HISTORY AT
THE MID-CORE ELEVATION

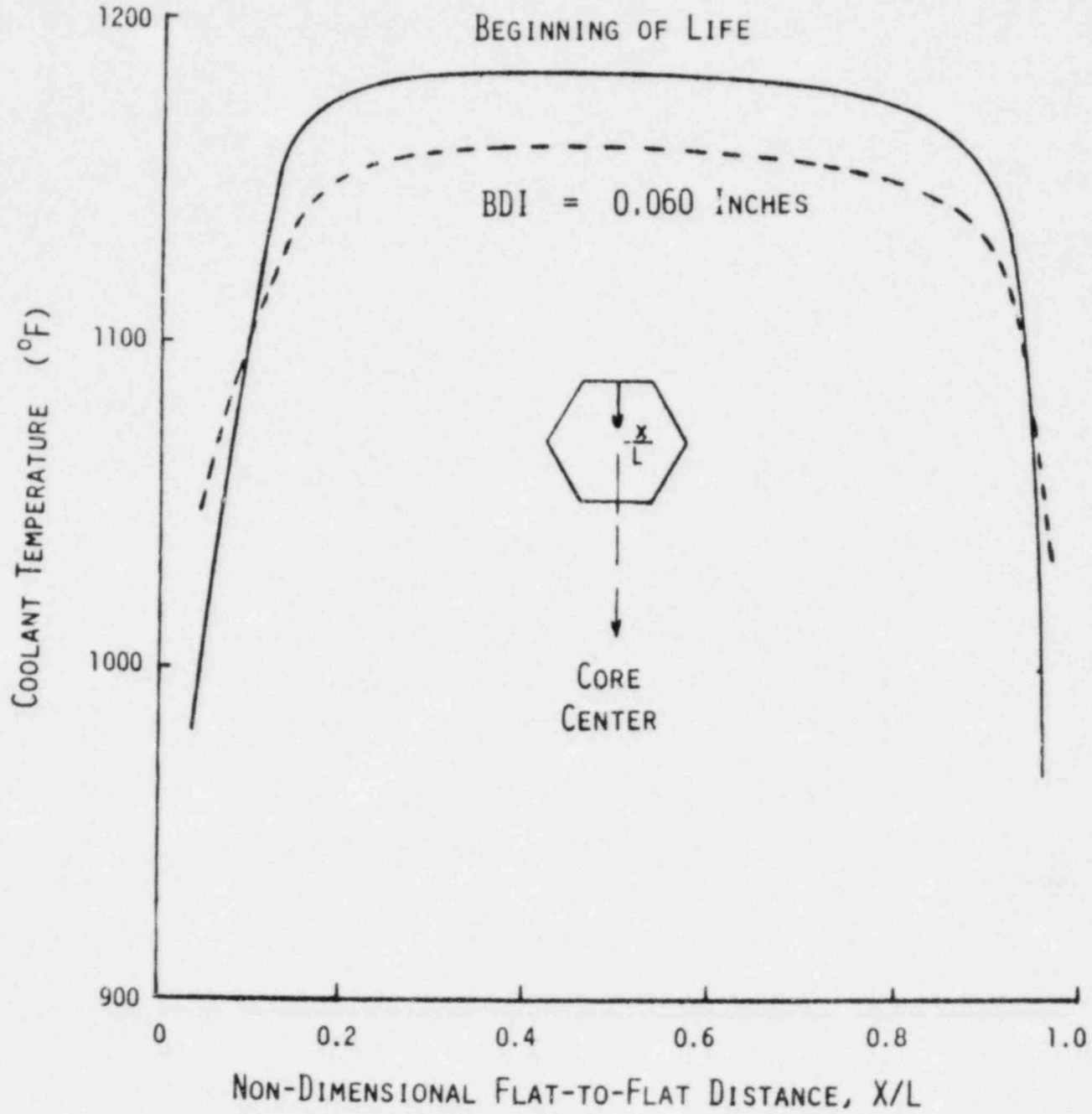

FIGURE 7.

COOLANT TEMPERATURE LATERAL DISTRIBUTION FOR DIFFERENT VALUES OF BDI

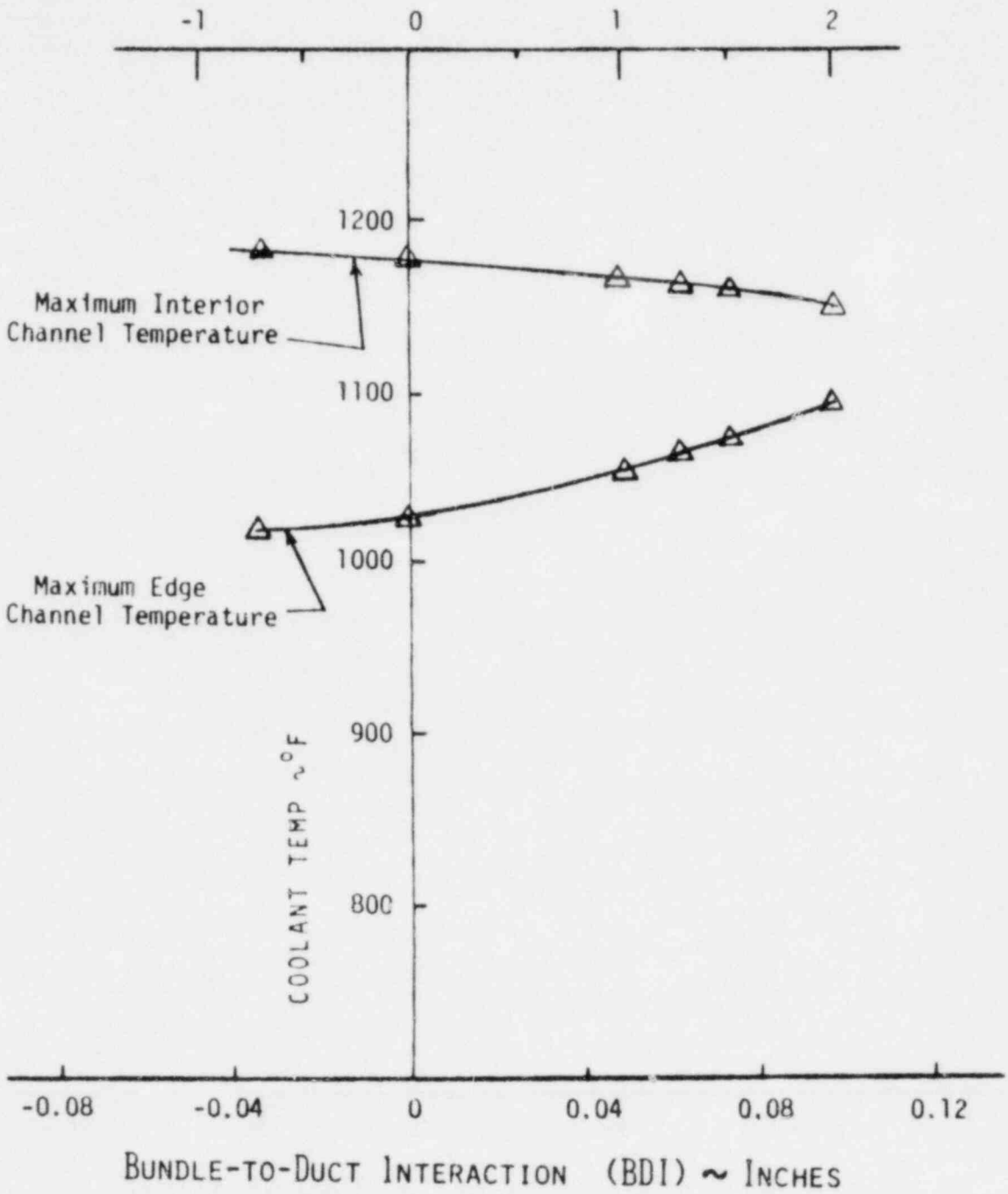

FIGURE 8.

XEBRA ANALYSIS OF 271-PIN ASSEMBLY ON
BDI EFFECT ON COOLANT TEMPERATURE

VALIDATION OF SSC USING THE FFTF NATURAL CIRCULATION TESTS

W.C. Horak, J.G. Guppy and R.J. Kennett

ABSTRACT

As part of the Super System Code (SSC) validation program, the 100% power FFTF natural circulation test has been simulated using SSC. A detailed 19 channel, 2 loop model was used in SSC. Comparisons showed SSC calculations to be in good agreement with the Fast Flux Test Facility (FFTF), test data. Simulation of the test was obtained in real time.

1. Introduction

The Super System Code (SSC)[1] was developed at the Brookhaven National Laboratory (BNL) for the thermohydraulic analysis of natural circulation transients, operational transients, and other system wide transients in nuclear power plants. SSC is a best estimate code that models the in-vessel components, heat transport loops, plant protection systems, and plant control systems. Recently, SSC has been coupled with the BNL developed code MINET,[2] which has extended its analysis capability to the balance of plant. SSC is also designed to be fast running, i.e., faster than real time on a CDC-7600. Thus, validation of SSC not only involves determination of the accuracy of the simulation, but determination of the computing time required to achieve that accuracy.

Previous SSC validation efforts have focused on two procedures; 1) comparison to numerically generated reference solutions,[3,4] and 2) comparisons to other computer codes.[5,6] Prior to system-wide evaluations, individual modules are tested on a stand-alone basis. Strict adherence to standard coding practices and naming conventions allows changes to be made to individual models and then incorporated into the main system code with minimal errors.[7]

Comparisons to numerically generated reference solutions are usually restricted to one specific module (i.e., the core, piping, etc.) to isolate the model and to minimize computer core storage requirements. The reference solution is generated by refining the nodalization and then extrapolating (if possible) to a fine mesh solution with an infinite number of nodes. In practice, however, the benchmark is a solution with a sufficiently large number of nodes such that further refinement of the mesh does not lead to significant changes in the calculated results. This procedure also provides information on the detail of nodalization necessary to analyze various transients in addition to checking the accuracy and consistency of the numerical algorithms. Even though SSC has been successfully tested using this method, the procedure is inadequate for determining deficiencies in the physical models used.

Comparisons between computer codes tend to be difficult and time consuming while providing minimal validation. To claim a code is valid simply because its analysis agrees with a reference code simply shifts the burden of validation to the reference code. However, useful information can be obtained especially the detection of Fortran coding errors.

The main difficulty in comparing any two codes is that their physical models are generally different. Thus differences in calculational results must be explained in terms of these modeling differences rather than induced by numerical or coding errors. In some cases, this means modification or relaxation of the code's model to conform to the reference code. For example, when comparisons were made between IANUS,[8] a proprietary code developed specifically for transient system analysis in the Fast Flux Test Facility (FFTF), and SSC,[6] it was necessary to suppress the transient core flow redistribution model in SSC since IANUS did not have this feature, even though core flow redistribution is an important effect in some of the transients analyzed in the comparison.

In summary, previous SSC system-wide validation studies were made with a numerically generated data base. Recently, a series of natural circulation transients at various powers and flows, including 100% power and flow, have been run at the FFTF as part of the facility's startup program. Since FFTF, which was designed for testing of materials for use in fast breeder reactors, is highly instrumented, an extensive experimental data base now exists which can be used in validating system codes for natural circulation transients. The SSC code

has been used to simulate the 100% power and flow natural circulation transient. Comparisons were made between the SSC predictions and the experimental data. These comparisons have demonstrated SSC's capability to simulate natural circulation transients, within the limits of the experimental data, while retaining its fast running capability.

2. Modeling of the FFTF Natural Circulation Transients Using SSC

2.1 Description of the Fast Flux Test Facility (FFTF)

The FFTF is a 400 MWt, sodium cooled, fast reactor having three independent heat transport trains.[9] Figure 1 is a schematic showing one of these trains, each consisting of a primary coolant loop, an intermediate heat exchanger (IHX), a secondary coolant loop, and a dump heat exchanger (DHX).

The FFTF heat transport trains are instrumented with electromagnetic flow meters located in the cold legs and temperature sensors located in the hot and cold legs of the primary and secondary loops. The inlet and outlet temperatures of the IHXs and DHXs are also monitored.

The FFTF core consists of 73 fuel assemblies, 3 safety rods, 6 control rods, and 9 unfueled assemblies. The flow rate and coolant exit temperature for each assembly are monitored by a flow meter and thermocouple located in an instrument tree above the core. A guide tube directs the assembly flow to the appropriate sensors (the sensors are physically located in the guide tubes.) Two of the fuel assemblies are referred to as Fueled Open Test Assemblies (FOTAs). Physically identical to the other fuel assemblies, they are located near the center of the core (Row 2 FOTA) and the outer edge of the core, adjacent to the reflector (Row 6 FOTA). A series of wire wrap thermocouples provide detailed temperature information along the axial length of each FOTA. The FOTAs also differ from the other fuel assemblies in that the guide tubes for the instrument tree are physically connected to the top of the assemblies. All the other fuel assemblies have a 1" to 2" gap between the top of the assembly and the guide tube. Therefore, at the low flow conditions typical of natural circulation events, the measured flow rates of the fuel assemblies (except the FOTAs) are unreliable. Moreover, the long response time of the thermocouples used in the instrument tree limits the usefulness of the transient assembly exit coolant temperature data.

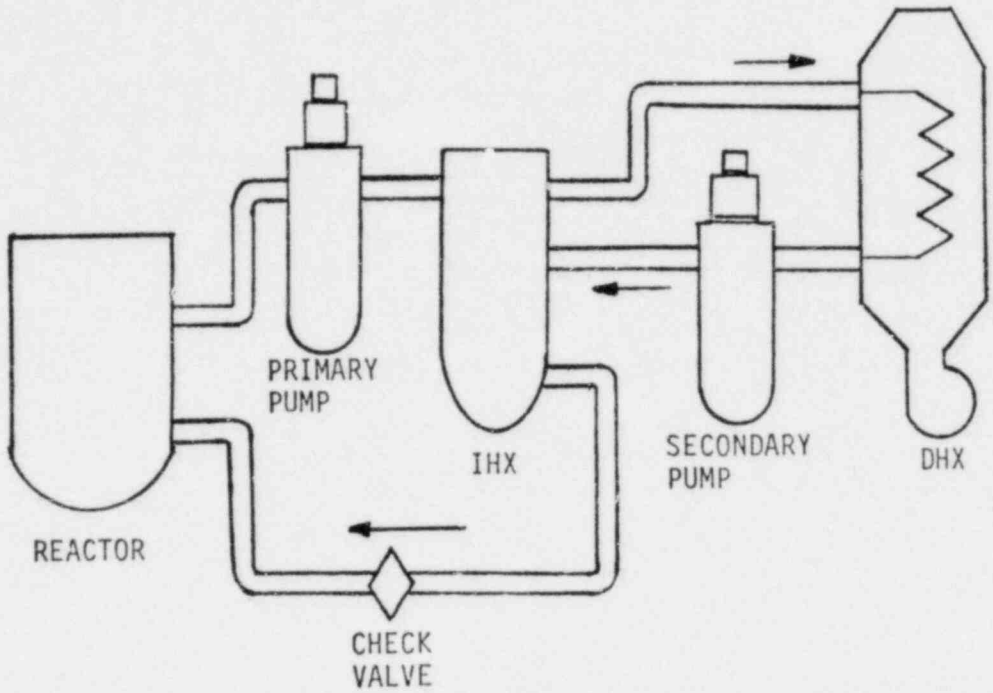

FIGURE 1: SCHEMATIC OF FFTF HEAT TRANSPORT TRAIN

2.2 SSC Modeling of FFTF

To model the FFTF, it was decided to use a 2 loop representation, with one loop representing two physical loops. Although no large asymmetries were observed in the 100% test simulated for this study, two loops were modeled for future studies where such asymmetries may occur.

Although a DHX module is part of the SSC program library, it was decided for this study that no validation of these modules would be done. This decision was made since the DHX modules are unique to FFTF and thus validation of these modules would be of limited value. Therefore, for this study the experimentally measured DHX outlet temperature was input as a forcing condition to SSC. The pressure drop across the DHX was simulated using a form loss coefficient and a buoyancy term.

The remainder of the secondary loop was modeled by five pipes, a pump with surge tank, and the tube side of the IHX. The nodalization was chosen on the basis of an earlier study for natural circulation transients (Table 1)[4].

Table 1 - SSC Nodalization of FFTF

Module	Number of Nodes
Secondary Loop:	
Pipe 1	38
Pipe 2	3
Pipe 3	3
Pipe 4	15
Pipe 5	19
IHX	21
Primary Loop:	
Pipe 1	29
Pipe 2	15
Pipe 3	10
Pipe 4	14
Reactor Core:	19 channels (including Row 2 and Row 6 FOTA explicitly modeled) 12 axial nodes per channel 3 radial fuel nodes per axial node 1 gap node per axial node 1 clad node per axial node 1 coolant node per axial node 1 structure node per axial node

The primary loop was modeled by 4 pipes, a pump, the shell side of the IHX, and a check valve in the cold leg. The nodalization is also shown in Table 1.

The in-vessel representation included: a one node, perfect mixing, lower plenum; core inlet module; a 19 channel core representation with bypass; core exit module; and a two region upper plenum. It is important to note that SSC dynamically calculates transient flow redistribution for all the core channels and the bypass. Each flow channel is hydrodynamically coupled to the others. Inter-assembly and intra-assembly heat transfer however, are not modeled. Each channel

is represented by an average rod with its associated coolant channel and structure. The channel is divided into 12 axial nodes; the fuel pin has 3 radial nodes in the fuel and one in the clad. An earlier numerical study showed this representation to be adequate for natural circulation type transients [3]. The steady state assembly powers and flow rates were determined from the experimental data and checked against pre-test numerical predictions.

The decay curve and initial decay power were obtained from the FFTF project office. The fission power was calculated using SSC's point kinetics package.

3. Results and Error Analysis

3.1 FOTA Coolant Temperatures

The average coolant temperatures at the top of the fuel axial level and at the top of the pin axial level for the Row 2 and Row 6 FOTA were obtained by averaging the thermocouple readings at these locations [13 at each level for the Row 2 FOTA; 14 at the top of fuel level and 16 at the top of pin level for the Row 6 FOTA.] The experimental data (shown with a $\pm 3^{o}K$ error bar at 10s intervals) are compared to the SSC calculations in Figs. 2-5. As can be seen, the SSC results are in good agreement with the FOTA test data. The lower test data temperature for the Row 6 FOTA top of pin location is probably caused by inter-assembly heat transfer (which is not modeled in SSC) to the adjacent reflector.

An error analysis was performed using the experimental data as the benchmark. The results are summarized in Table 2. Since SSC is a best estimate code, positive and negative maximum errors are shown. The maximum negative error in all cases occurs at 10(s), which is the time of the first transient test data point. Although the absolute temperature difference at this time is about $50^{o}K$ the relative error is still less than 9%. The maximum positive errors occur around 180(s) and are small with the exception of the Row 6 FOTA top of pin location; however, the relative errors are again small. The average absolute error of $3\text{-}4^{o}K$ is particularly good since the experimental data have an error band of $\pm 3^{o}K$.

3.2 Loop Temperatures and Flow Rates

The hot leg temperature, cold leg temperature, and loop flow for the pump loop are shown in Figs. 6-8. The corresponding parameters for the secondary loop are shown in Figs. 9-11. As can be seen, the SSC simulations are in good agreement with the experimental data. A detailed error analysis was not done for these data since the temperature profiles are relatively constant and the flow data have a wide error band (±16 kg/s).

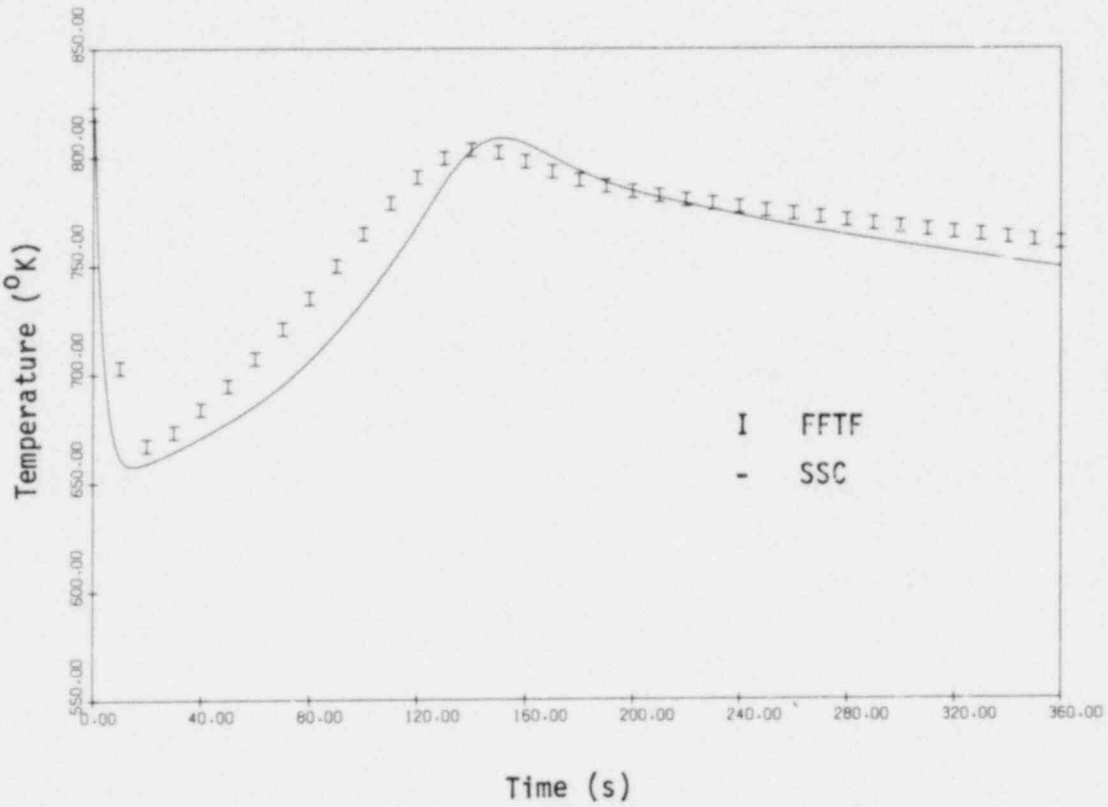

FIGURE 2: COMPARISON OF FFTF TEST DATA AND SSC CALCULATION FOR THE ROW 2 FOTA AVERAGE COOLANT TEMPERATURE AT THE TOP OF FUEL LOCATION

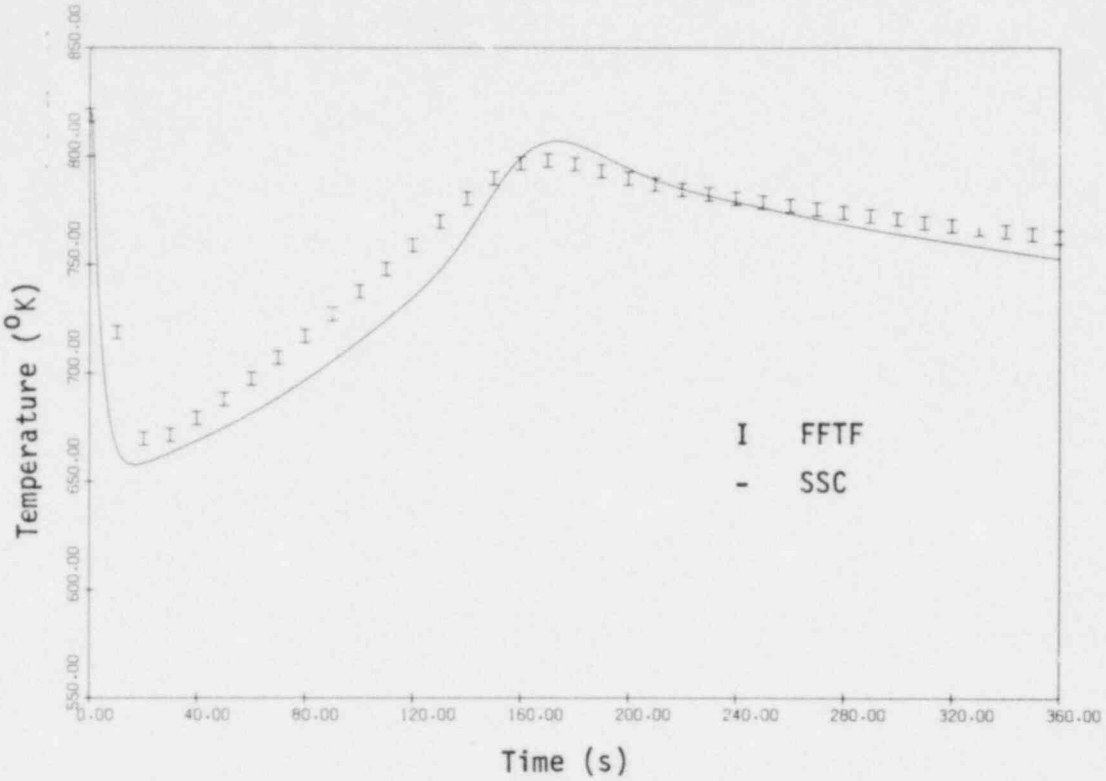

FIGURE 3: COMPARISON OF FFTF TEST DATA AND SSC CALCULATION FOR THE ROW 2 FOTA AVERAGE COOLANT TEMPERATURE AT THE TOP OF PIN LOCATION

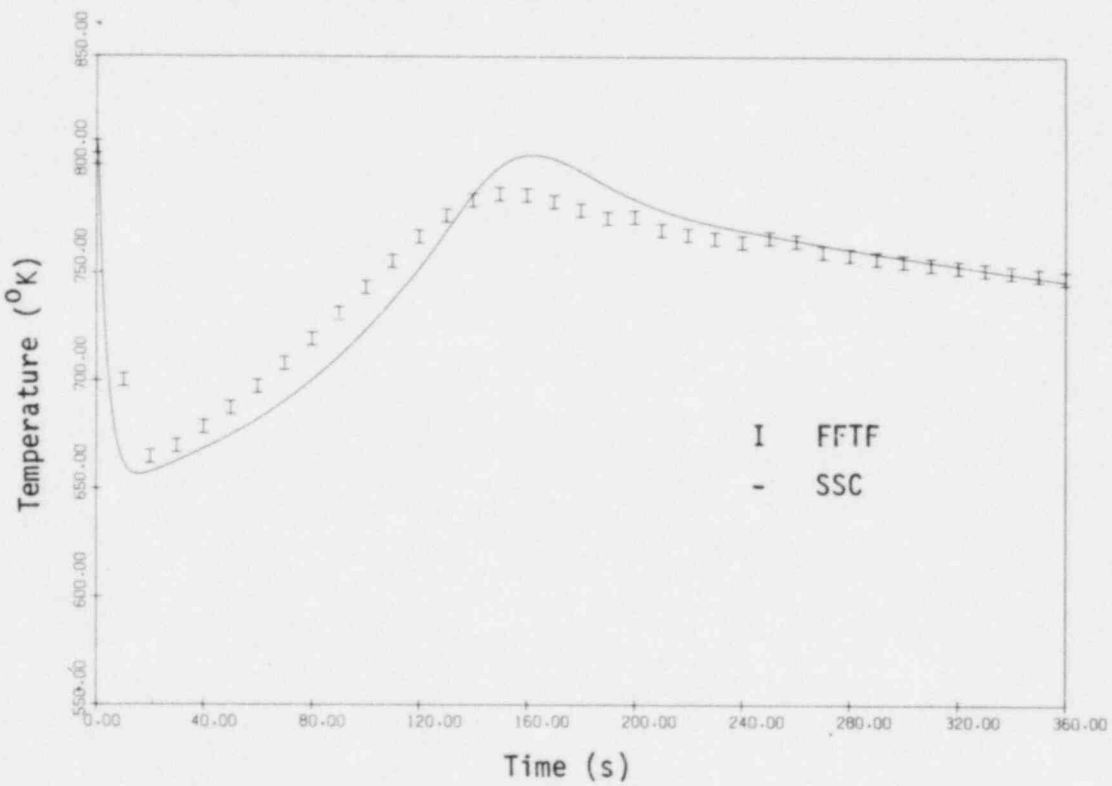

FIGURE 4: COMPARISON OF FFTF DATA AND SSC CALCULATION FOR THE ROW 6 FOTA AVERAGE COOLANT TEMPERATURE AT THE TOP OF FUEL LOCATION

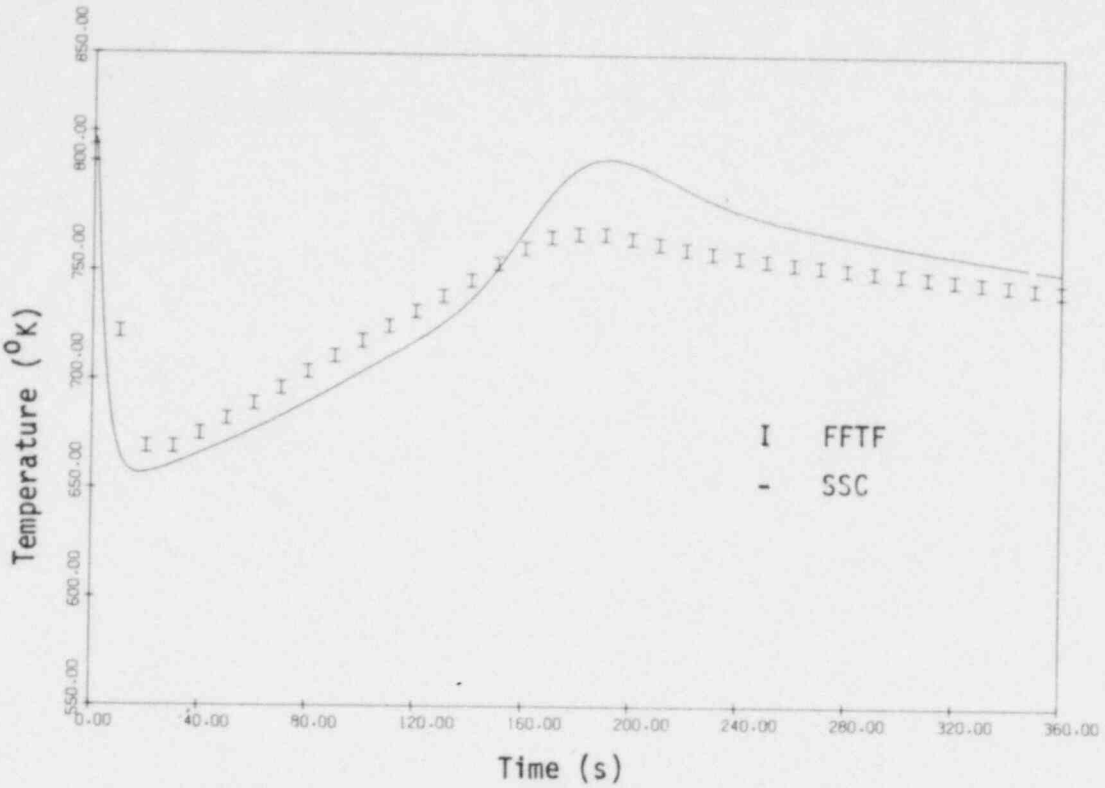

FIGURE 5: COMPARISON OF FFTF TEST DATA AND SSC CALCULATION FOR THE ROW 6 FOTA AVERAGE COOLANT TEMPERATURE AT THE TOP OF PIN LOCATION

Table 2 - FOTA Temperature Comparison Error Analysis

	Absolute (^{o}K)[a]	Relative (%)[b]	Time(s)
Maximum Negative Error			
Row 2 FOTA, top of fuel	41.	6.	10.
Row 2 FOTA, top of pin	54.	8.	10.
Row 6 FOTA, top of fuel	38.	6.	10.
Row 6 FOTA, top of pin	55.	8.	10.
Maximum Positive Error			
Row 2 FOTA, top of fuel	8.	1.	160.
Row 2 FOTA, top of pin	8.	1.	180.
Row 6 FOTA, top of fuel	20.	1.	170.
Row 6 FOTA, top of pin	34.	4.	190.
Average Error[c]			
Row 2 FOTA, top of fuel	3.	.4	-
Row 2 FOTA, top of pin	3.	.4	-
Row 6 FOTA, top of fuel	3.	.4	-
Row 6 FOTA, top of pin	4.	.6	-

a -- absolute error = $T^{FFTF}(^{o}K) - T^{o}K)$

b -- relative error = $[(T^{FFTF}(^{o}K)-T(^{o}K))/T^{FFTF}(^{o}K)] \times 100\%$

c -- averaged over the first 300 (s) of the transient

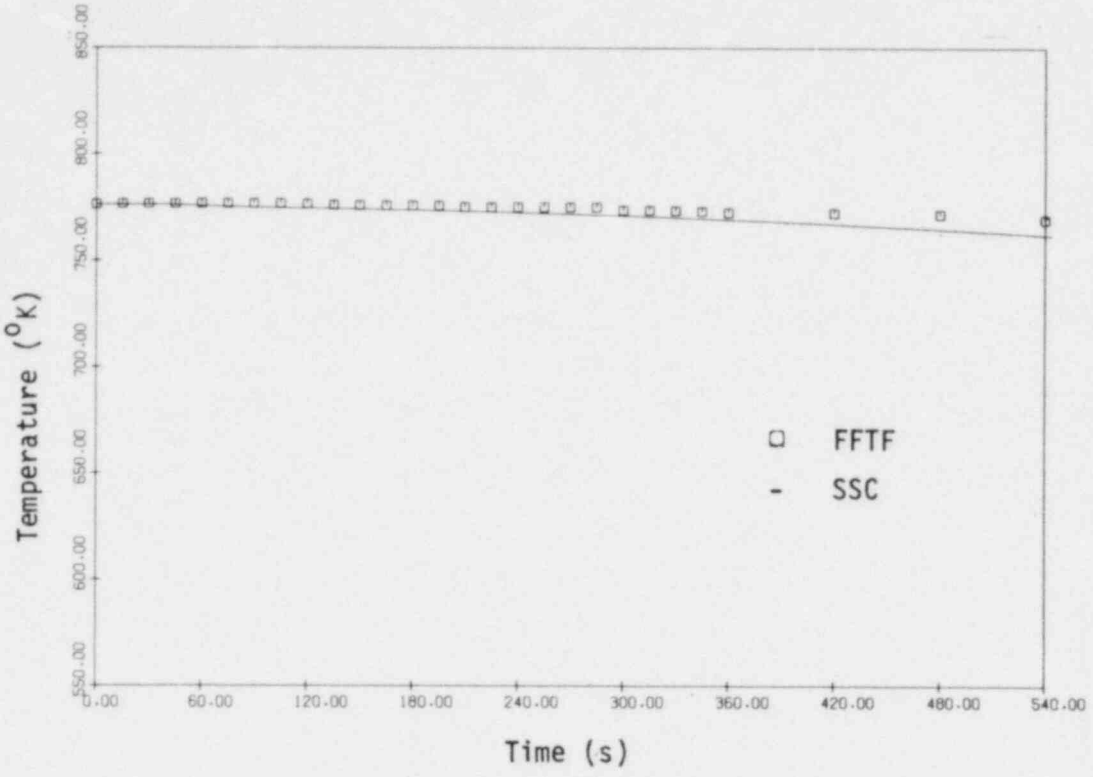

FIGURE 6: COMPARISON OF FFTF TEST DATA AND SSC CALCULATION FOR THE PRIMARY LOOP HOT LEG TEMPERATURE

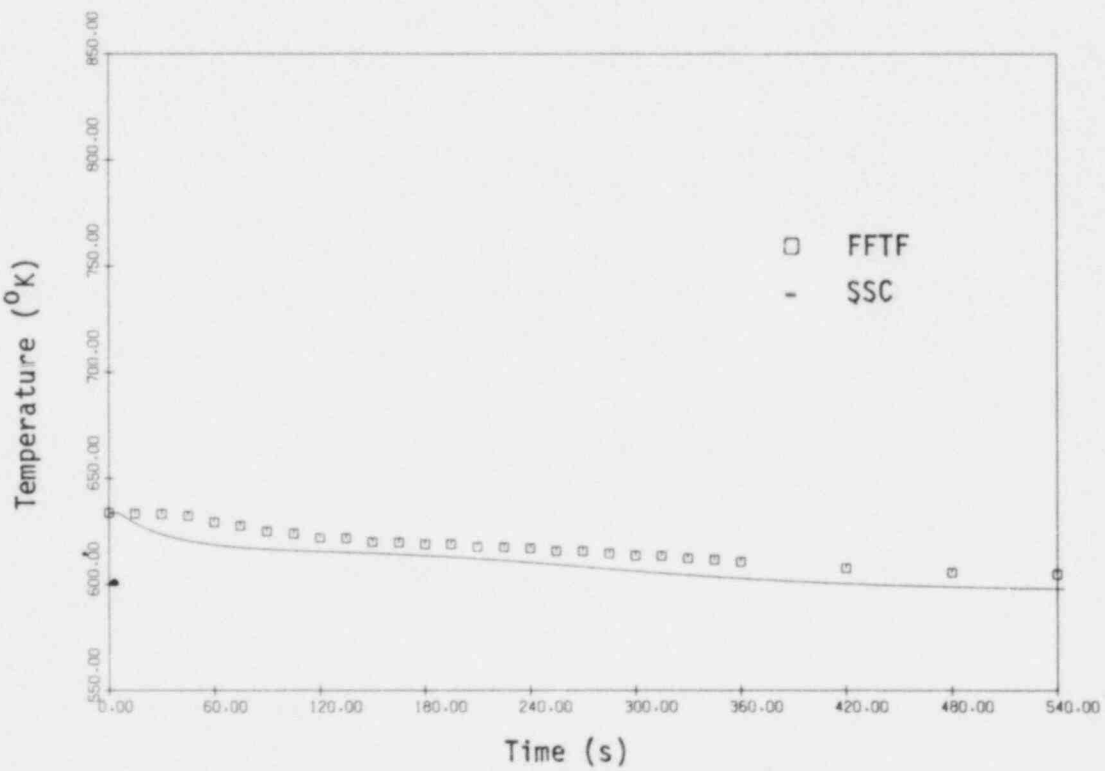

FIGURE 7: COMPARISON OF FFTF TEST DATA AND SSC CALCULATION FOR THE PRIMARY COLD LEG TEMPERATURE

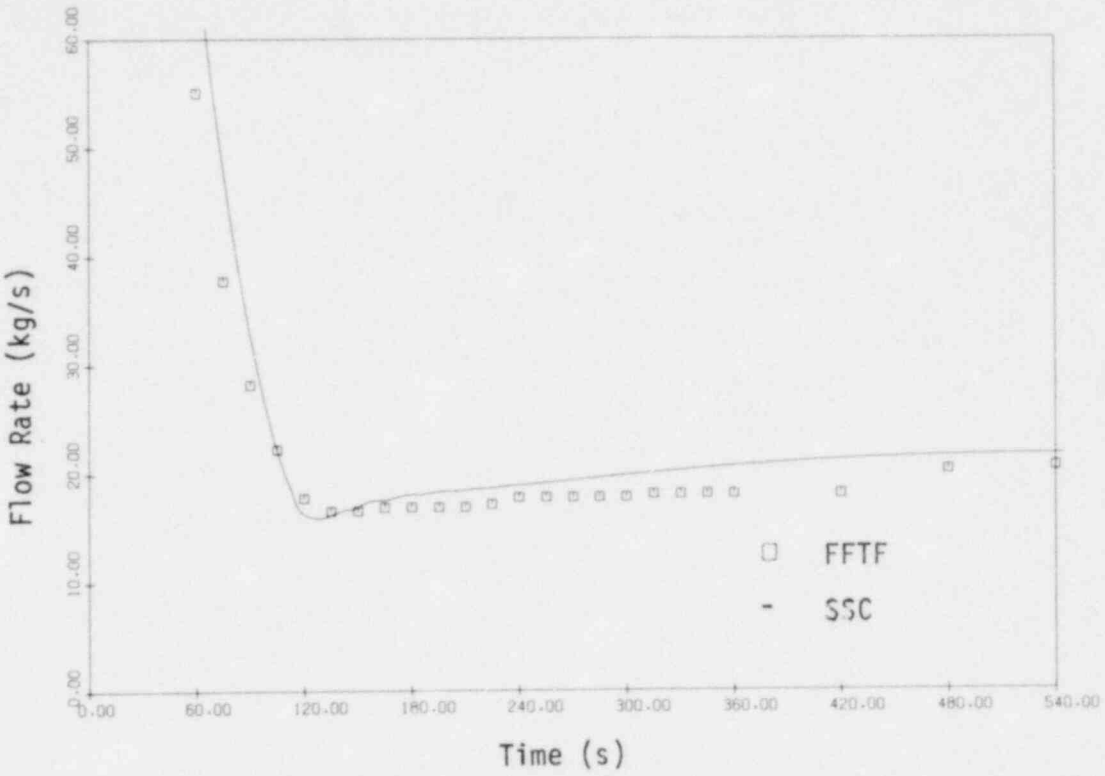

FIGURE 8: COMPARISON OF FFTF TEST DATA AND SSC CALCULATION FOR THE PRIMARY LOOP FLOW RATE

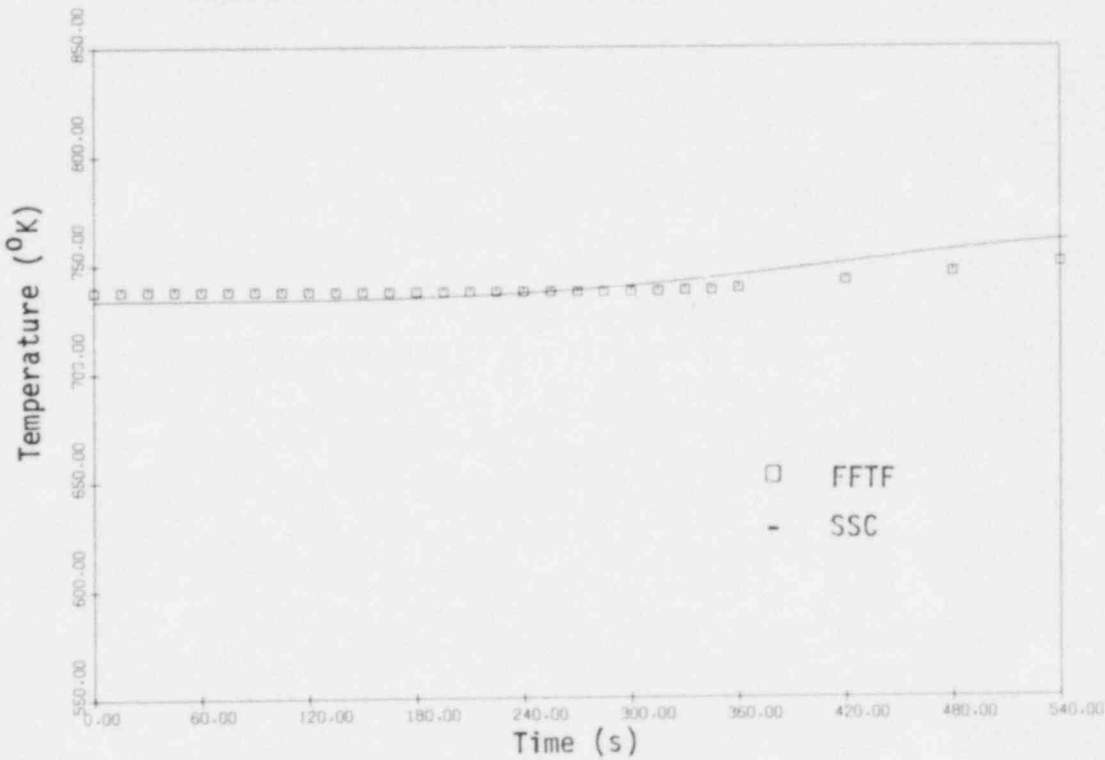

FIGURE 9: COMPARISON OF FFTF TEST DATA ANS SSC CALCULATION FOR SECONDARY LOOP HOT LEG TEMPERATURE

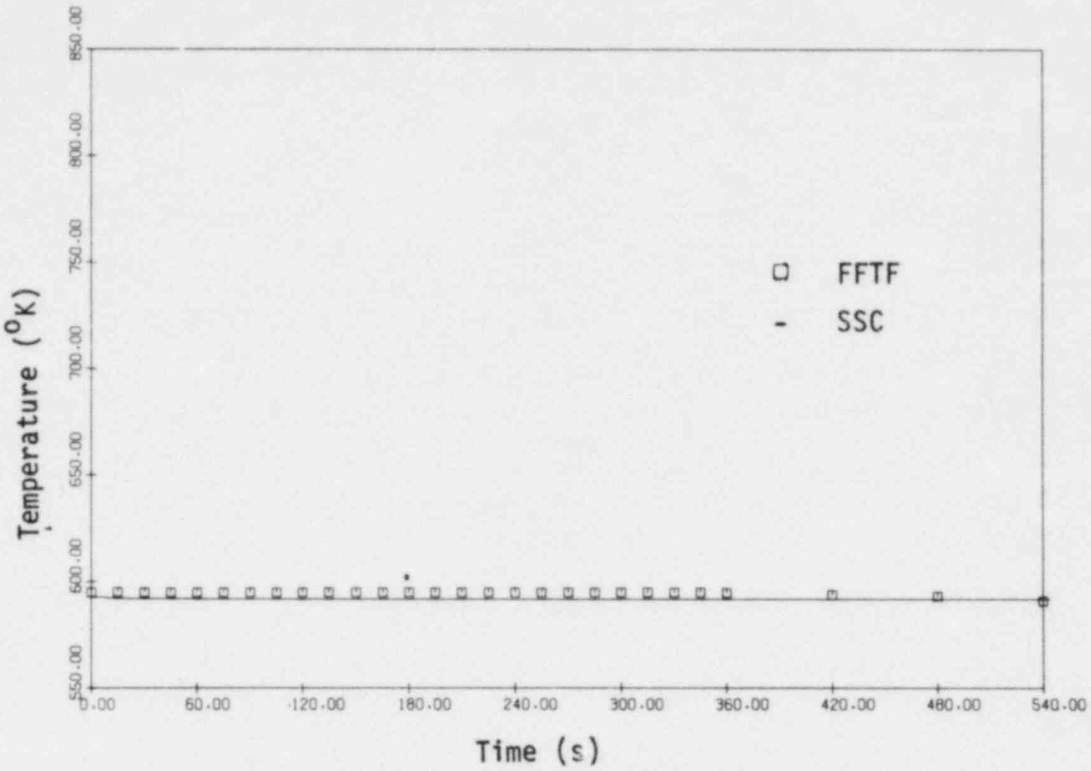

FIGURE 10: COMPARISON OF FFTF TEST DATA AND SSC CALCULATION FOR THE SECONDARY LOOP COLD LEG TEMPERATURE

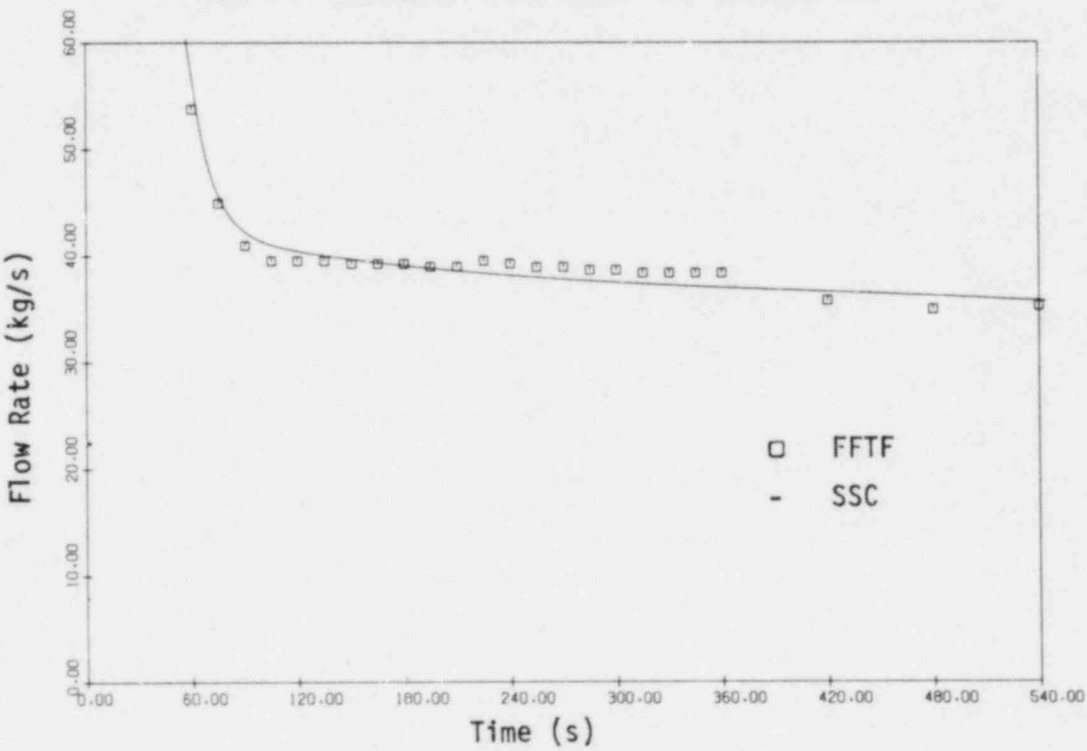

FIGURE 11: COMPARISON OF FFTF TEST DATA AND SSC CALCULATION FOR THE SECONDARY LOOP FLOW RATE

4. Conclusion

As part of the SSC validation program, the FFTF 100% power natural test was simulated using SSC. The FFTF test data and SSC calculations were found to be in good agreement. While the limited in-core instrumentation prevented a complete validation of the in-vessel energy transfer module of SSC, the FOTA data comparisons show that the flow redistribution model and heat transfer model are accurate in at least those two assemblies. The comparisons of loop parameters provide experimental validation of earlier numerical studies. It should be noted that even though a detailed 19 channel, 2 loop model was used in SSC, simulation in real time was achieved.

Further studies using FFTF experimental data include a long term ($\sim$1 hr) simulation of the 100% and 75% power tests. Aysmmetric heat transfer through the loops will also be studied.

References

1. J.G. Guppy, et al., "Super System Code (SSC-L, Rev. 2), An Advanced Thermohydraulic Simulation Code for Transients in LMFBRS", Brookhaven National Laboratory, (to be published, 1982).

2. G.J. Van Tuyle, "Analysis of CRBRP Station Blackout Using SSC/MINET", 2nd Joint ASME/ANS Nuclear Engineering Conference, Portland, OR., ASME Paper No. 82-NE-19. BNL-NUREG-31110. July 1982.

3. W.C. Horak, R.J. Kennett, J.G. Guppy, "A Numerical Procedure for Calculating Temperature Profiles in LMFBR Coolant Channels", Trans. ANS, V. 39, p. 495 (1981).

4. I.K. Madni, "Transient Analysis of Coolant Flow and Heat Transfer in LMFBR Piping System", Brookhaven National Laboratory Topical Report, BNL-NUREG-51179, (April 1980).

5. R. Pyare and J.G. Guppy, "Transient Analysis of LMFBR Plant with SSC-L and Comparison with DEMO Code", Brookhaven National Laboratory Report, BNL-NUREG-29313 (1981).

6. L.G. Epel and J.G. Guppy, "Comparisons of SSC-L with IANUS for FFTF Transients", BNL-NUREG-29912 (1981).

7. R.J. Kennett, "A Software Methodology Review of the Super System Code for the Simulation of Liquid Metal Fast Breeder Reactors", Brookhaven National Laboratory, (to be published, 1982).

8. S.L. Additon, T.B. McCall and C.F. Wolfe, "IANUS-Outline Description", Westinghouse Advanced Reactors Division, Waltz Mill, PA., FPC-939.

9. "FFTF Final Safety Analysis Report", HEDL-TI-75001, December 1975.

CRAB-II: A COMPUTER PROGRAM TO PREDICT HYDRAULICS AND SCRAM DYNAMICS OF LMFBR CONTROL ASSEMBLIES AND ITS VALIDATION

M. D. Carelli, L. A. Baker, J. M. Willis, F. C. Engel, and D. Y. Nee

Westinghouse Advanced Reactors Division
Madison, Pennsylvania, U.S.A.

ABSTRACT

This paper presents an analytical method, the computer code CRAB-II, which calculates the hydraulics and scram dynamics of LMFBR control assemblies of the rod bundle type and its validation against prototypic data obtained for the Clinch River Breeder Reactor (CRBR) primary control assemblies.

The physical-mathematical model of the code is presented, followed by a description of the testing of prototypic CRBR control assemblies in water and sodium to characterize, respectively, their hydraulic and scram dynamics behavior.

Comparison of code predictions against the experimental data are presented in detail; excellent agreement was found. In particular, the CRAB-II code was found to predict all the key design parameters: i.e., amount of flow cooling the absorber bundle, assembly pressure drop, flotation characteristics, and scram insertion response, well within the range of experimental uncertainties.

Also reported are experimental data and empirical correlations for the friction factor of the absorber bundle in the entire flow range (laminar to turbulent) which represent an extension of the state-of-the-art, since only fuel and blanket assemblies friction factor correlations were previously reported in the open literature.

1.0 INTRODUCTION

Control assemblies play a critical role in assuring the safe and reliable performance of nuclear reactors. The availability, therefore, of verified analytical methods to predict their behavior is of great importance to the core designer. These methods must satisfy the following basic design objectives:

- Provide an accurate prediction of the control assembly hydraulics, chiefly of the flow actually cooling the absorber bundle. Since the control assembly features a movable component (the "poison" bundle contained in an "inner" duct moving inside a fixed--or outer--duct), the coolant flow will divide into two main paths, one through the bundle and another (called bypass flow) between the movable inner duct and the fixed outer duct. Obviously, only the coolant actually flowing through the absorber rods must be considered in the thermal and structural design of the control assembly rod bundle.

- Provide an accurate prediction of the scram dynamics characteristics. One key design and safety requirement is to guarantee the insertion of the prescribed amount of reactivity (i.e., physical insertion of the control rods) within a specified time frame.

- Provide an accurate prediction of the flotation conditions of the control assembly. A design requirement is to assure that the control assembly will not float (with adequate margin) due to the force of the upward coolant flow when the driveline is disconnected.

While the three above objectives are a "must" for an analytical method to satisfy, it is also desired that this method have enough flexibility to be used in feasibility, optimization and parametric studies, in addition to detailed, specific design. Finally, this method must be adequately validated and verified against experimental data in order to be used with confidence in analyses and design.

To this end, since the early seventies, development of the analytical computer code CRAB (Control Rod Assembly Behavior) was pursued at Westinghouse ARD to predict the hydraulics, scram dynamics and flotation behavior of primary control assemblies (PCAs) of the rod bundle type. The code was used to predict the behavior of the Clinch River Breeder Reactor (CRBR) and Fast Flux Test Facility (FFTF) PCAs and was quite favorably compared against experimental data obtained in hydraulic and scram testing of prototypic models of the FFTF. A brief description of the CRAB model and a summary of the FFTF tests verification is reported in References 1 and 2.

In the past few years the physical and analytical models of the CRAB code have been vastly expanded and improved, leading to the development of the advanced version CRAB-II. The code predictions have been quite favorably compared against results of prototypic testing in water (assembly hydraulics) and sodium (scram dynamics) of the CRBR PCA. The purpose of this paper is to present the analytical model of the CRAB-II code and its validation against prototypic data for the CRBR primary control assemblies. Also reported are

experimental data and correlations for the absorber bundle friction factor in all three regimes, i.e., laminar (with Reynolds number as low as 300), transition and turbulent (Re up to 40,000). The wire wrapped bundle has a very tight pitch-to-diameter ratio (p/d = 1.05); the wire wrap lead is 12 in. (30.5 cm).

2.0 THE CRAB-II CODE

2.1 Code Features

The CRAB-II code analyzes the steady state hydraulics and scram dynamics behavior of control assemblies of the rod bundle type; a bundle of absorber rods (37 for CRBR, 61 for FFTF) housed in an hexagonal duct is free to move within a fixed hexagonal guide. Wear pads at the extremities of the movable assembly center and guide it through the fixed duct. A schematic representation of the control assembly is shown in Figure 1. The CRAB-II code has the following calculational capabilities:

A. Steady State Hydraulics

(1) Flow split between the pin bundle and the bypass. As mentioned in the introduction, knowledge of the fraction of assembly flow actually cooling the absorber rods is important to the designer.

(2) Flow distribution among the three different types of subchannels (inboard, edge and corner) in the absorber bundle.

(3) Detailed breakdown of the pressure drops across the bundle and bypass flow paths (e.g., rod bundle, inlet and exit, wear pads, bypass annulus, etc.).

B. Scram Dynamics

As a function of time during scram, the code calculates the following parameters: pin bundle position, velocity and acceleration; assembly flow rate; bundle/bypass flow split and flow distribution within the bundle; static pressure at various assembly locations (e.g., inlet and exit of the bundle).

C. Flotation Conditions

Minimum pressure drop across the assembly (and corresponding assembly flow rate) causing inception of upward movement of the absorber bundle when the driveline is disconnected.

D. Dashpot Parameters

The purpose of the dashpot is to decelerate the insertion of the control assembly once an amount of reactivity sufficient to scram the reactor has been inserted; this is to avoid damage to the assembly. CRAB-II calculates the dashpot hydraulics (ΔP and flow distribution in the dashpot) and the impact force/acceleration on the control assembly at the end of the scram.

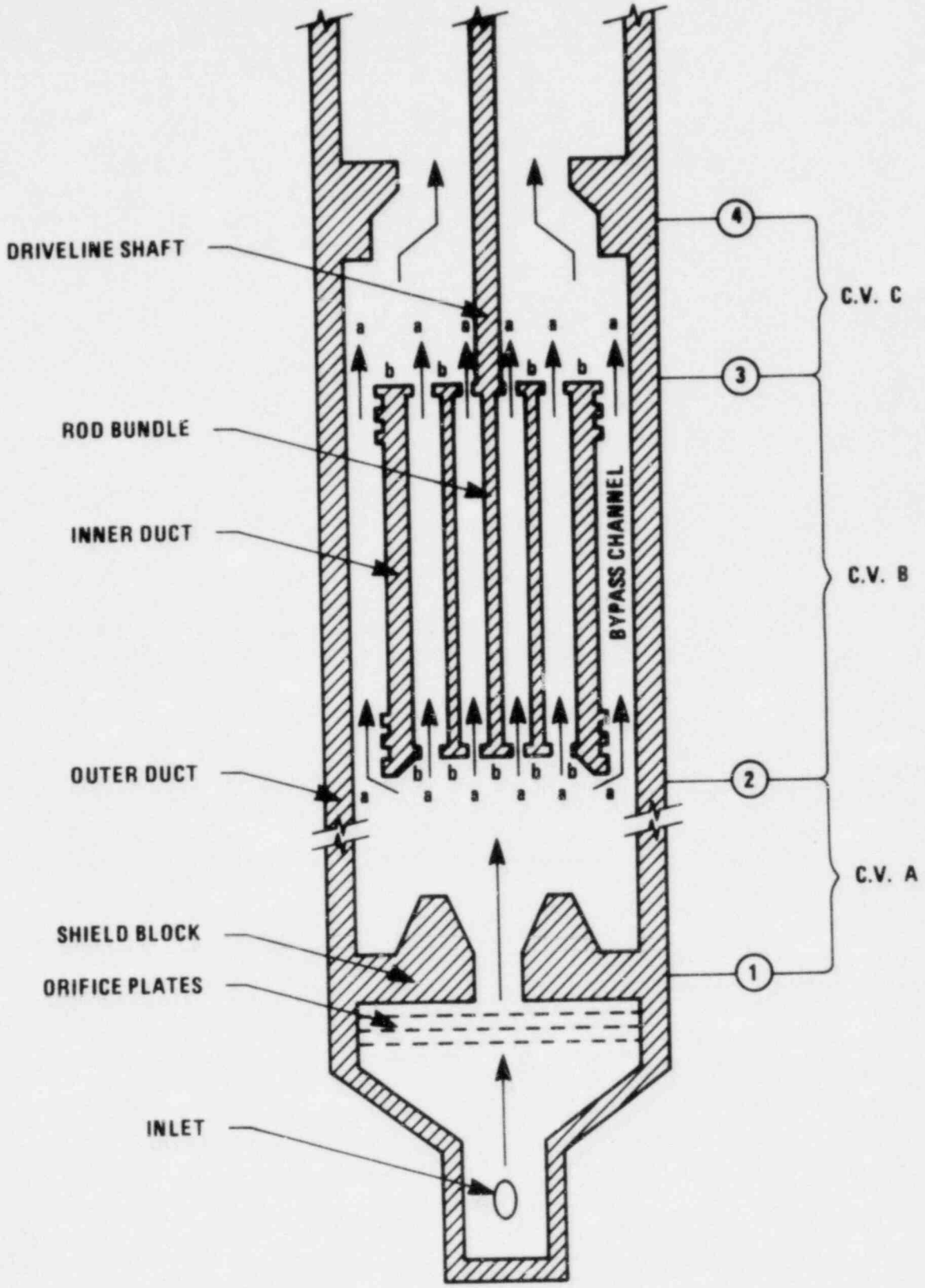

Figure 1. Control Assembly Schematic and CRAB-II Modeling

7197-1

E. Scram Affecting Forces

The code accounts for the effect of scram assisting forces such as springs and bellows as well as retarding forces such as friction and seismic loads, in addition, of course, to the effects of gravity, buoyancy and coolant drag/friction. Of particular interest is the capability of CRAB-II to properly account for the effect of seismic loads, since it is a design/safety requirement that the control rods be inserted during an earthquake. To accomplish this, the CRAB-II code has been given the capability to "read" the output of seismic codes which calculate the lateral loads on the assembly.

2.2 Physical-Mathematical Model

2.2.1 The Three-Control-Volume Model

This model which represents the core of the CRAB-II code is based on solving the three fundamental principles of conservation of mass, momentum and energy, together with Newton's second law of motion. As the name indicates, three control volumes are considered; the central one (control volume B in Figure 1), which encompasses the movable absorber bundle and the fluid flowing through and around the bundle, is situated between a lower control volume (A) which extends from the shield exit to the bundle inlet and an upper volume (C) describing the fluid between the movable bundle exit and the assembly exit. While the central volume does not change during scram, the two other volumes do; the upper volume increasing at the rate of decrease of the lower volume. The three volumes are tied together by the boundary condition of having a constant pressure drop across the entire control assembly, equal to the pressure drop across the core, since: 1) the flow allocated to the control assemblies is only a very minor fraction of the total core flow (approximately 1% in the CRBRP case); and 2) the scram insertion time (only a few seconds) is so brief that the effect on the overall core hydraulics is totally insignificant.

Unlike the overall core hydraulics, the hydraulics of the control assembly is drastically influenced by the scram. Since the relative velocity of the flowing sodium in respect to the absorber bundle increases due to the motion of the bundle, the overall control assembly flow rate must decrease in order to satisfy the boundary condition of constant pressure drop across the assembly.

Mathematically, the three-control-volume model translates in a system of twelve equations in twelve unknowns. The twelve unknowns are:

- the bundle insertion, z
- the time derivative of the assembly mass flow rate, $\ddot{m}$
- the mass flow rate in the 4 parallel flow paths in the bundle and bypass, $\dot{m}_i$, $\dot{m}_s$, $\dot{m}_c$, $\dot{m}_{by}$
- the static pressure at the inlet and outlet of the movable bundle, P_{2a}, P_{2b}, P_{3a}, P_{3b} (see Figure 1 for location)

- the static pressure at the inlet (P_1) and exit (P_4) of the control assembly (this corresponds to imposing a constant pressure drop across the assembly)

The twelve equations are:

- the Newton second law of motion applied to the rod bundle:
  $M\ddot{z} = \Sigma F_z$

  where ΣF_z = gravity + bellows + spring - dashpot - sliding friction - hydraulic forces (shear and pressure).

  The adopted sign convention is to have position forces acting concurrently with the bundle movement, i.e., downward.

- the continuity equation applied to control volume A

  $$\dot{m} + \rho S_2 \dot{z} = \dot{m}_i + \dot{m}_s + \dot{m}_c + \dot{m}_{by}$$

  where the term $S_2\dot{z}$ represents the additional flow entering control volume B during the scram.

- the conditions of equal pressure drops across the bypass, inboard, side and corner channels (3 equations)

  $$\Delta P_{by} = \Delta P_i = \Delta P_s = \Delta P_c$$

- the momentum equation applied to control volumes A and C (2 equations)

- the energy equation applied to control volumes A, B and C (3 equations)

- the boundary conditions at stations 1 and 4 (2 equations)

Since Newton's law is used for control volume B, either the momentum or the energy equation applied to control volume B are redundant. The energy equation is chosen as the explicit equation, since the momentum equation is used to calculate the shear force in the Newton's equation.

Formulation and elaboration of the conservation equations of momentum and energy, even though relatively straightforward, is quite involved; as an example, reported below are the momentum and energy equations for control volume A:

$$P_1 (A_1 + S_1) - F_{sh_A}(\dot{m},z) - P_{2a}A_2 - P_{2b}S_2 = \frac{\ddot{m}}{g}(L_z - z) + \frac{\dot{m}^2_{by}}{\rho g A_{2,by}}$$

$$+ \frac{\dot{m}^2_{rb}}{\rho g A_{2,rb}} + \frac{\rho \dot{z}^2}{g} S_2 - \frac{\dot{m}^2}{\rho g A_1}$$

and

$$K_A \left(\frac{\dot{m}^2}{2A_1^2 g}\right) = -\frac{\ddot{m}\,(L_A - z)}{gA_A} + \left(P_1 + \frac{\dot{m}^2}{2gA_1^2}\right) - \left(P_{2a} + \frac{\dot{m}C^2}{2\rho g A_2^2}\right)C$$

$$+ \left(P_{2b} - \frac{\rho \dot{z}^2}{2g}\right)\frac{\rho \dot{z} S_2}{\dot{m}}$$

with

$$C = 1 + \frac{\rho \dot{z} S_2}{\dot{m}}$$

The three-control-volume is the most significant difference between CRAB-II and its predecessor CRAB; the previous version of the code only modeled the central control volume and the boundary condition was a constant coolant flow rate instead of a constant pressure drop across the control assembly. The previous model was overconservative since it over-estimated the pressure drop during scram and therefore the fluid resistance to the bundle motion.

2.2.2 Hydraulic Models

The flow split between bundle and bypass and the flow distribution across the bundle is obtained by solving the system of equations imposing an equal pressure drop across the 4 different types of parallel flow paths and the continuity equation. The pressure drop in each component is calculated using analytical or experimental correlations obtained from prototypic testing (see following Section 3). One typical example of this experimental input is the friction factor in the absorber bundle (Section 3.1.3).

While the procedure is quite straightforward for steady state conditions (absorber bundle at rest), the same is not true during a scram, the key question being what characteristic fluid velocity should be used in the pressure drop equations. For pressure drops along the absorber bundle flow paths the characteristic velocity is obviously the relative velocity of the fluid and bundle, i.e., $U_i + \dot{z}$ (or $U_s + \dot{z}$, $U_c + \dot{z}$). The bypass flow path is however bounded by a "moving wall" (the inner duct) and a "fixed wall" (the outer duct). It was thus decided to divide the bypass pressure drops into two components: a moving wall part depending on the relative velocity $(U_{by} + \dot{z})$ and weighted by the factor β' and a fixed wall part depending on the bypass coolant velocity U_{by} and weighted by the factor β''.

The weighting factors β' and β'' were chosen as:

β' = ratio of moving wall wetted perimeter to the total channel wetted perimeter

and

$\beta'' = 1 - \beta'$ = ratio of stationary wall wetted perimeter to total channel wetted perimeter.

The form losses along the bypass flow path (inlet, exit, wear pads) were therefore expressed as:

$$\Delta P = a \frac{\rho}{2g} [\beta' (U_{by}A_r + \dot{z})^2 + \beta'' (U_{by}A_r)^2]$$

where a is an appropriate geometry coefficient, U_{by} is the fluid velocity in the bypass annulus and A_r is an area ratio yielding the proper local fluid velocity ($U_{by}A_r$) in the considered location. Of course, the values of β' and β'' are also locally dependent, since the channel wetted perimeter depends on the location considered, e.g., it is different at the bypass inlet/exit and at the wear pads.

In calculating the frictional pressure drop along the bypass, the thin annulus geometry effect must be considered in addition to the moving/fixed wall effect. A theoretical analysis based on solution of the velocity profile showed that the best representation of the pressure drop was given by the equation:

$$\Delta P = f_m \frac{L}{D} \frac{\rho U^2}{2g}$$

with

$$f_m = f_a [\beta'' + \beta' (1 + \dot{z}/U_{by})^{1.75}]$$

where f_a is an annular friction factor for a channel having stationary walls (hydraulic diameter D and velocity U_{by}), and can be approximated by the friction factor for a pipe at the same Reynolds number multiplied by an empirical constant, obtained from experimental testing (see Section 3.1).

Verification of the soundness of the adopted hydraulic modeling path under steady state and scram conditions was provided by a comparison of the CRAB-II predictions with prototypic data, as reported in Section 3.2.

2.2.3 Bellows Model

The bellows, which are located at the bottom of the Control Rod Drive Mechanism (CRDM) immediately above the reactor closure head, have the primary function of acting as a barrier to prevent the sodium vapor from reaching the cover gas. They operate in an inert Argon gas of pressure about double that of the cover gas, thus preventing sodium vapor diffusion into the working parts, if a bellows leak occurs.

The metal bellows also provide secondary scram-assist force, about one-tenth of that provided by the surrounding springs which are the primary scram assist force of the CRBRP and FFTF primary control assemblies.

A sketch of the bellows is shown in Figure 2. The bellows model incorporated in CRAB-II assumes:

- no hydraulic resistance to gas flow in the bellows support tube during scram;
- the entire bellows is adiabatic during scram.

The second assumption does preclude heat transfer between the bellows and its surroundings but not between the upper and lower volume of the bellows. It is conservative, since a little amount of heat transfer occurs following a slight reduction in the bellows temperature caused by the gas expansion. This compensates for the slight non-conservatism of the first assumption which overestimates the total work done by the gas expansion during scram. The scram assisting pressure exerted by the bellows during scram is expressed by the equation:

$$P_{bellows} = P_{in}[(V_o + x_{in}\Delta V^*)/(V_o + x\Delta V^*)]^k - P_{cg}$$

where ΔV^* represents the change in the bellows volume per unit length of driveline insertion, x is the insertion length during scram, and the indices in and o refer to the initial state of the bellows respectively, at start of scram and for fully withdrawn conditions. It should be noted that they are not necessarily the same since some primary control assemblies are partially inserted during reactor operation.

Figure 3 reports the good agreement between the bellows pressure predicted by CRAB-II and data obtained in prototypic scram tests during a full 36 inch scram. In addition to the scram-aiding pressure effect above, the bellows also have a spring-type effect on scram. This is considered in CRAB-II, in addition, of course, to the effect of the primary scram assisting spring.

2.2.4 Dashpot Model

As previously mentioned, the purpose of the dashpot is to decelerate the motion of the control assembly in the final part of its insertion once enough reactivity has been inserted to scram the reactor. A scheme of the dashpot is reported in Figure 4. The motion-retarding force of the fluid on the dashpot piston can be divided into two components: a pressure force on the piston surface and a vertical shear force on the piston lateral surface area. They depend on the annulus geometry determined by the relative position of the piston and dashpot. As the piston moves downwards, fluid is forced upwards through the clearance between the piston and the cylinder and downwards through the clearance between the driveline shaft and the dashpot cylinder lower guide. The flow split between the up and down flow paths depends on their relative hydraulic resistance, which changes during scram; as the control assembly (and piston) approaches full insertion, the reduction in the piston/cylinder clearance results in a preponderance of the downward flow. Modeling of the dashpot hydraulics is therefore similar to what was previously reported for the control assembly: a flow split between different flow paths and a time varying geometry during scram. Transient pressure drop equations are written for the considered flow paths (for example, as for the case of the control assembly bypass, the frictional loss in an annulus with one fixed wall--the cylinder--and one moving wall--the piston--must be considered), along with continuity, momentum and energy equations. The system of equations (six equations in six unknowns) was written for three control volumes describing the fluid behavior in, above and below the dashpot and was solved in a manner similar to the one used for the control assembly motion, thus obtaining the pressure field on the piston. The upward force on the piston is then simply obtained by integrating the pressure field over the surface of the piston.

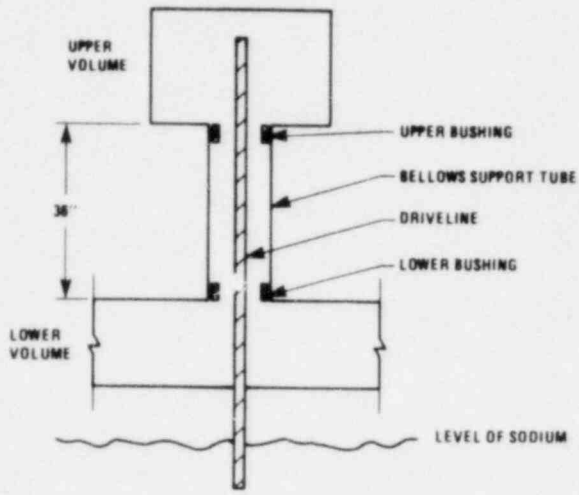

Figure 2. Sketch of Bellows Geometry

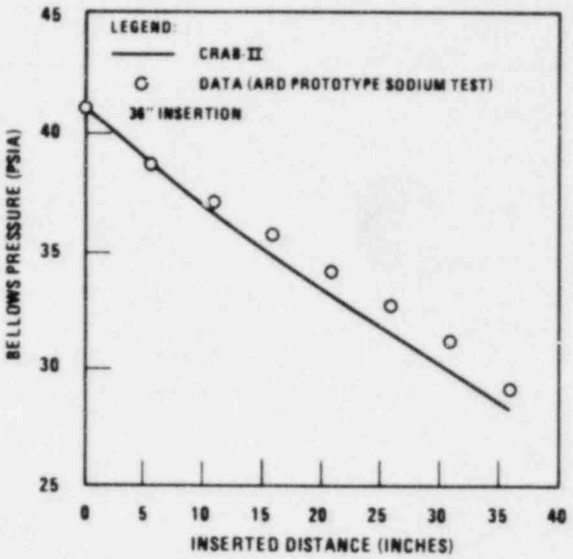

Figure 3. Comparison of CRAB-II Predicted and Observed Bellows Pressure

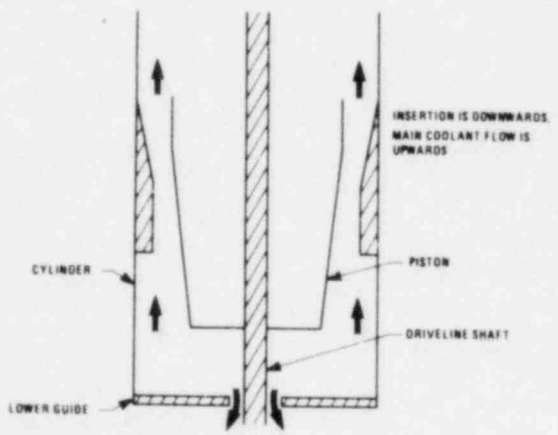

Figure 4. Dashpot Schematic

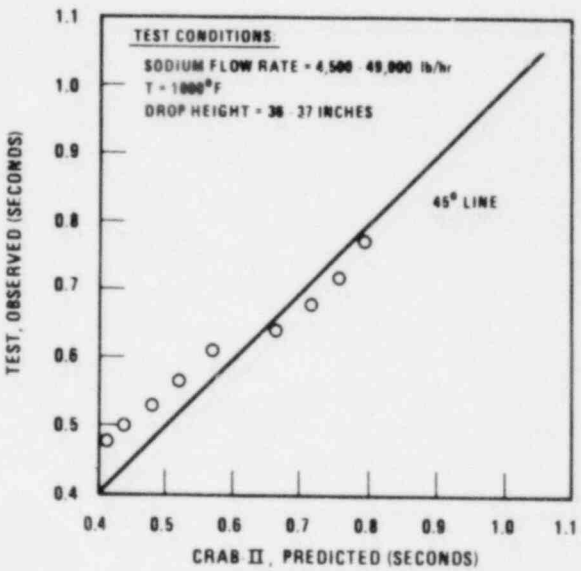

Figure 5. Comparison of CRAB-II Predicted and Observed Transit Time in Dashpot

7197-2

A comparison between the transient time in the dashpot predicted by CRAB-II during a full insertion scram and that observed in the prototypic tests is reported in Figure 5. The agreement is satisfactory with the code slightly underpredicting the short transient times and overpredicting the longer ones.

2.2.5 Determination of Flotation Conditions

As previously mentioned, a design requirement is that the control absorber bundle does not float when the control rod driveline is disconnected; this could conceivably happen if the pumps are inadvertently started up during refueling. Inception of flotation occurs when the upward hydraulic force is equal to the downward force; since the driveline is disconnected, the downward force is simply the wet weight of the absorber bundle, i.e., the dry weight minus the buoyancy force. The equation representing the balance of forces is solved by CRAB-II in terms of total assembly flowrate and pressure drop; these are the so-called "flotation characteristics."

2.3 Method of Solution

All the various equations discussed in the previous sections are eventually reduced to a system of differential equations of the type:

$$\ddot{z} = f\ (t,\ z,\ \dot{z},\ \dot{m})$$

and

$$\ddot{m} = g\ (t,\ z,\ \dot{z},\ \dot{m})$$

This system is then solved for z and $\dot{m}$, which are the key variables during scram, using a three-dimensional Runge-Kutta method. This solution method is sufficiently efficient under most circumstances, requiring only a few seconds of computer time for analyzing a scram from the fully withdrawn position. Only when seismic forces are considered, and they are severe enough to momentarily arrest the rod motion during the seismic acceleration peaks, does the CRAB-II running time tend to be moderately high (of the order of minutes). Consideration is being given to use a multistep predictor-corrector in lieu of the Runge-Kutta method when evaluating seismic scrams. The predictor-corrector method is inherently faster and also allows taking longer time steps when seismic accelerations remain fairly constant, without causing numerical instabilities as is the case when large time steps are used in the Runge-Kutta method.

The solution for steady state hydraulics is of course obtained in a similar, simplified manner with t, $\dot{z}$, $\ddot{z}$ and $\ddot{m}$ being set to zero.

3.0 EXPERIMENTAL PROGRAM AND VALIDATION OF CRAB-II

This section reports a description of the testing of full scale prototypes of the CRBR primary control assembly and a comparison of test results against CRAB-II predictions. Two different types of testing were performed: the first was an hydraulic testing in water of flow split, pressure drops and flotation conditions under Reynolds similitude; the second was testing of the

scram characteristics and associated forces (e.g., bellows, dashpot) in a sodium loop. In both loops (water and sodium) the assembly flow rate was varied to cover the entire range from laminar to turbulent. Particular attention was given to characterizing the assembly flow split at very low flow condition, since this is an important input to natural circulation transient analyses.

Similar tests had been performed by HEDL and ARD in the early seventies for the FFTF primary control assembly; the favorable comparison of the test results against the predictions by the previous version (CRAB) of the code was reported in References 1 and 2 and is not repeated here.

3.1 Hydraulic Tests

3.1.1 Test Facility

Hydraulic tests of the CRBRP PCA prototype were conducted at the WARD Thermal-Hydraulic Test Facility. The Control Assembly Hydraulic Test Loop is an open recirculation water loop with a 3,000 gallon (11.4 m^3) vertical holding tank; a 500 gpm (31.5 l/sec), 310 psig (21 atm) head centrifugal pump; 0.5 inch, 1.5 inch and 4 inch (1.3, 3.8, and 10.2 cm) orifice flowmeter sections; a full flow filter; and associated piping, valving and instrumentation to provide flow, pressure and temperature control for the test section. The water temperature ranges from room temperature to 180°F (82°C); the heat sources are the pump power and steam coils in the storage tank and the temperature is controlled by varying the flow rate to a secondary water-to-water heat exchanger.

Testing was conducted over a two-year period in 4 phases:

- Phase I: orifice pressure drop and cavitation characterization. Results of these tests are not reported here since they are only of marginal interest to the development and validation of the CRAB-II code.

- Phase II: characterization of the bypass channel pressure drops. These tests were run with the bundle blocked off at the top by means of a special sealing collar attached to the adaptor plate and hydrostatically leak tested at 6.0 psi (0.4 atm) to assure that no leakage occurred.

- Phase III: characterization of the minimum flotation conditions (pressure drop and flow rate).

- Phase IV: characterization of the total assembly pressure drops. By proper comparison of the results obtained in Phase II (bypass only) and Phase IV (bundle and bypass) the bundle-to-bypass flow split was determined as discussed in Section 3.1.4.

The loop flow rate was varied in the range of 2 to 150 gpm (0.13 to 9.5 l/sec); this provided simulation of CRBR conditions between natural circulation and 150% of the PCA design flow. Seventeen pressure taps were used to monitor the pressure drop across various portions of the test section;

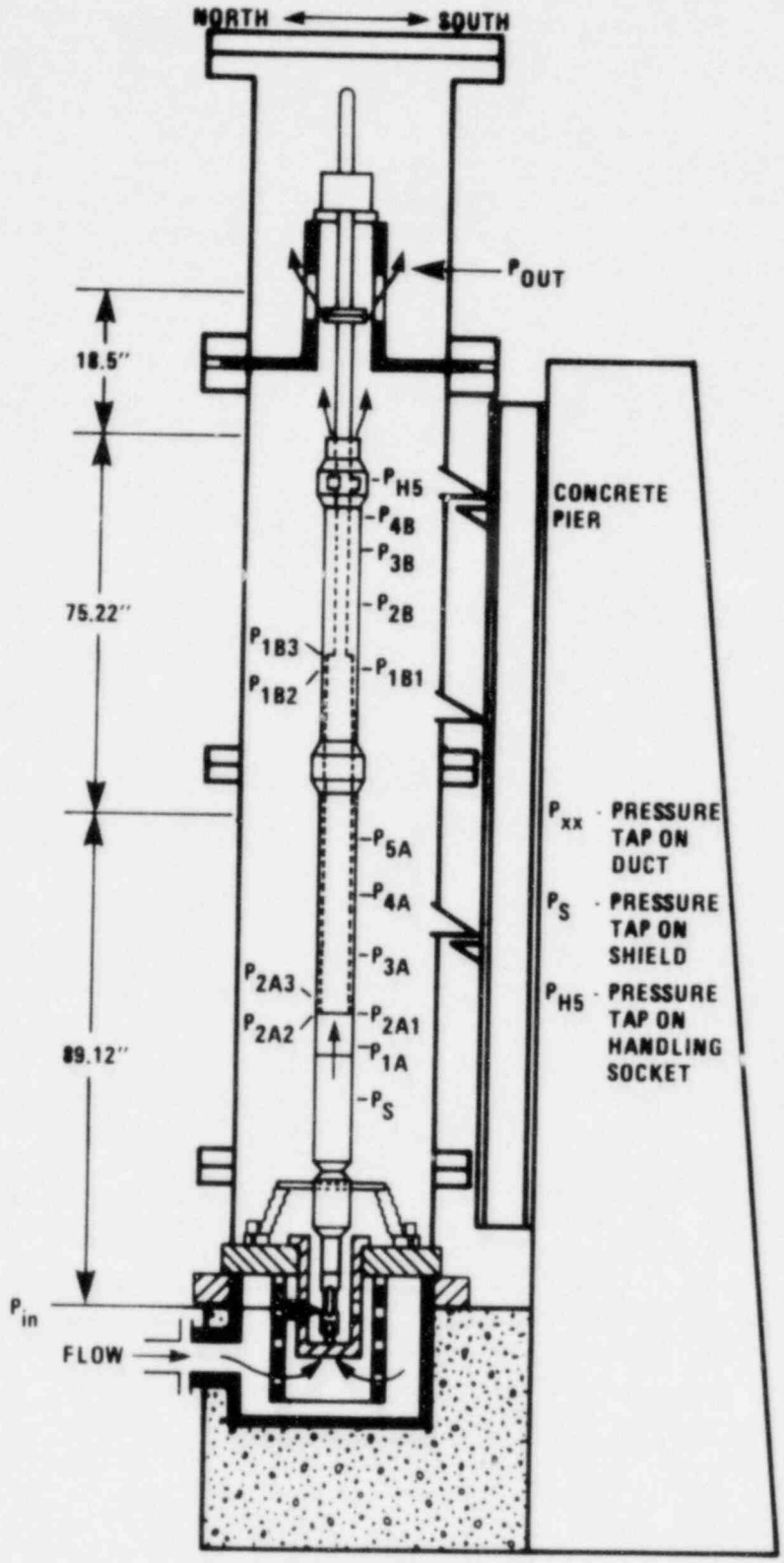

Figure 6. Hydraulic Test Section And Instrumentation Location

7197-6

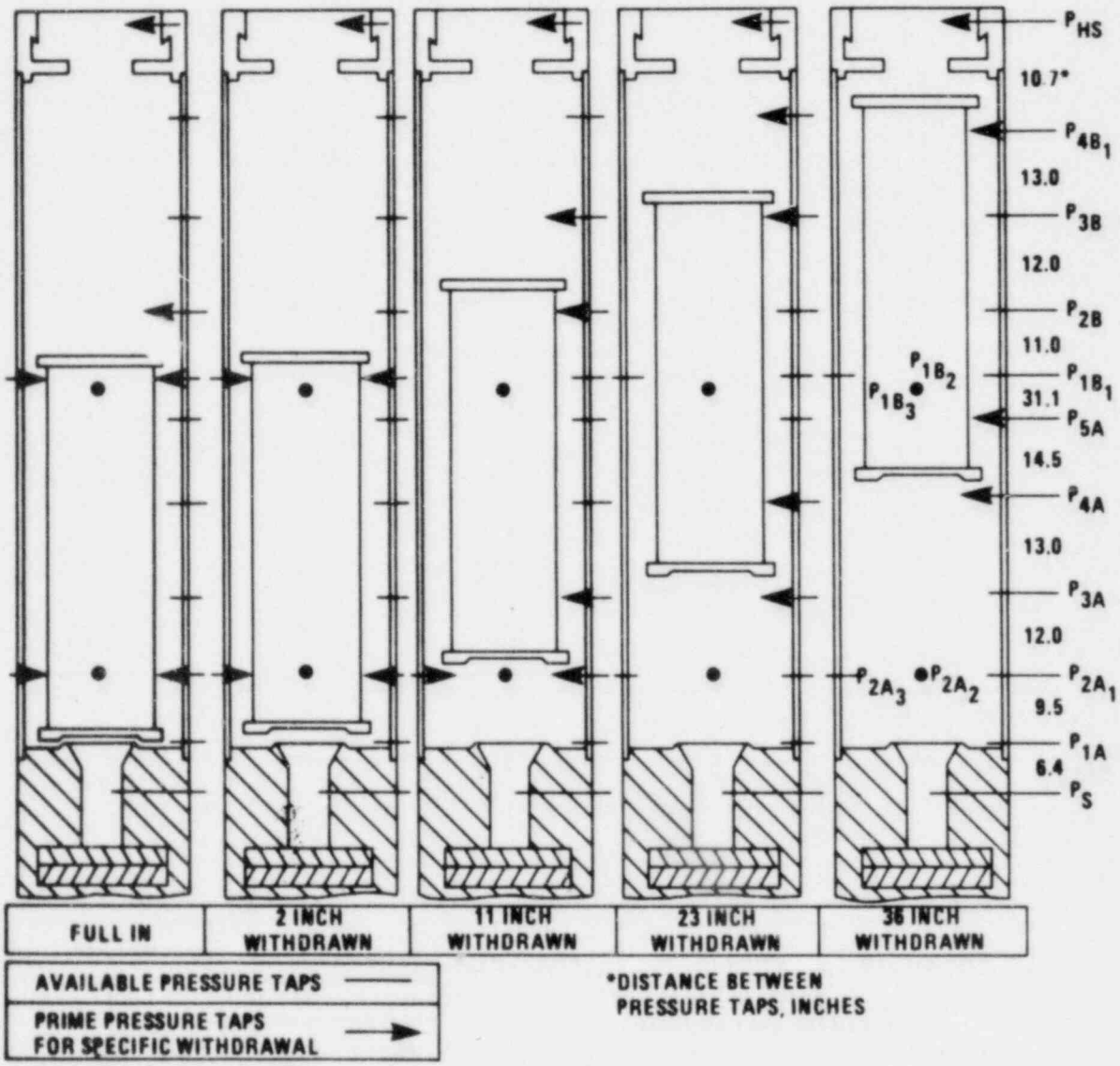

Figure 7. Relative Axial Positions (Withdrawals) of Absorber Bundle Tested

7197-7

the relative location of the pressure taps are reported in Figure 6. The static pressure taps were placed sufficiently far from local flow perturbations to prevent spurious readings and minimize localized effects; for example, the minimum distance between the outer duct pressure taps and the leading edge of the absorber assembly wear pads was 20 hydraulic diameters, while 60 hydraulic diameters was the minimum distance between the nearest downstream pressure tap and the trailing edge of the wear pads.

The flow paths configuration and, consequently, the pressure drops vary depending on the axial position (insertion) of the absorber bundle. Therefore, tests were performed for different withdrawal positions of the absorber bundle: i.e., 0 inches (fully inserted), 11 inches (28 cm) withdrawn, 23 inches (58.4 cm) withdrawn and 35 inches--91.4 cm--(fully) withdrawn. This extensive investigation was aimed at fully characterizing the various components pressure drops as a needed input not only for steady state evaluation (some of the PCAs are fully withdrawn, while others are partially inserted--11 inches withdrawn), but also for analytical representation of the pressure drops and fluid retarding forces throughout the scram. Figure 7 shows in detail the relative position of the pressure taps and the absorber bundle for the various insertions investigated. Not shown in the figure are the pressure taps used to measure the test section inlet and outlet pressure, P_{in} and P_{out}, which are reported in Figure 6. All of the pressure taps of Figure 7 are single taps located on the same flat of the outer duct, except for the P_{2A} and P_{1B} taps. At these locations three pressure taps are located circumferentially (120° apart) around the duct to provide more detailed pressure drop data for the annulus flow between the wear pads, particularly since several misalignment configurations of the bundle within the outer duct were also investigated. Particular attention was focused in characterizing the pressure drop across the wear pads (bottom and upper) and the bypass annulus in addition of course to the total pressure drop across the assembly. Figure 7 identifies the prime pressure taps providing this information for different withdrawal positions.

3.1.2 Assembly and Bypass Pressure Drop Tests

As mentioned in the previous section, pressure drops across the wear pads, the bypass annulus and the total assembly at various flow rates were obtained through differential reading of the appropriate pressure taps. Some typical examples are reported in the following along with the CRAB-II comparison. Figure 8 refers to Phase II (bundle blocked) data at 11 inches withdrawn. The agreement is good for the total assembly and the bottom wear pad ΔP's but CRAB-II tends to overestimate the bypass annulus and the top wear pad ΔP. A similar trend is shown by Figure 9 which refers to the same assembly position (11 inches withdrawn) for Phase IV (unblocked bundle). Predictions still deviate from data for the top wear pad and the bypass annulus but not as much as in the previous case. Even better agreement is shown in Figure 10 (23 inches-58.4 cm--withdrawn, Phase IV), but for the full-out position (Figure 11), only the total pressure drop is correctly predicted; large discrepancies exist in prediction of the individual components ΔP's. The most important result of this analysis was that the total pressure drop across the assembly was predicted consistently for both Phase II and Phase IV tests with good accuracy (generally within 10% of the nominal experimental data and well

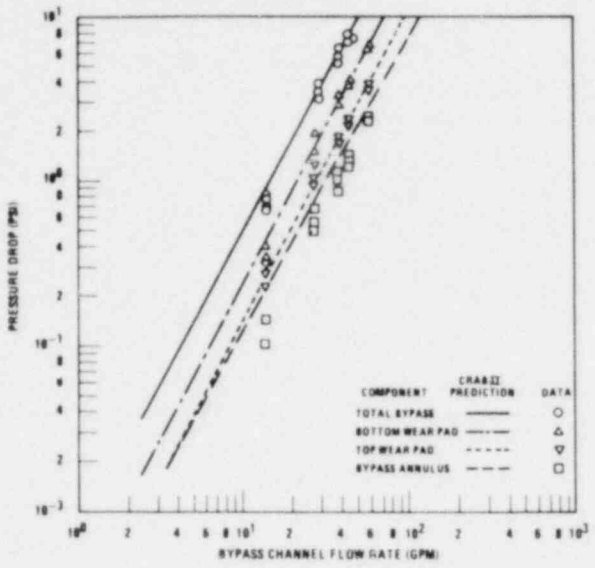

Figure 8. CRAB-II/Data Pressure Drop Comparison: Phase II, 11 Inches Withdrawn

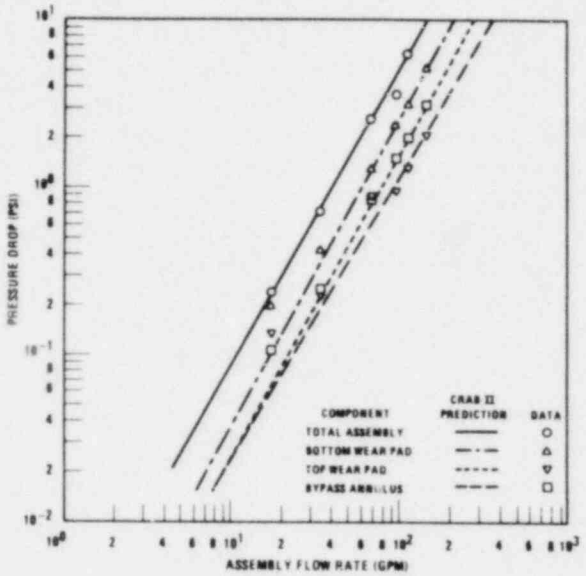

Figure 9. CRAB-II/Data Pressure Drop Comparison: Phase IV, 11 Inches Withdrawn

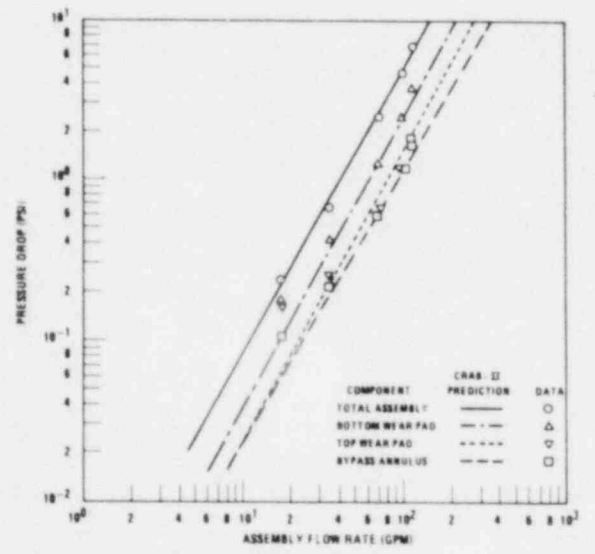

Figure 10. CRAB-II/Data Pressure Drop Comparison: Phase IV, 23 Inches Withdrawn

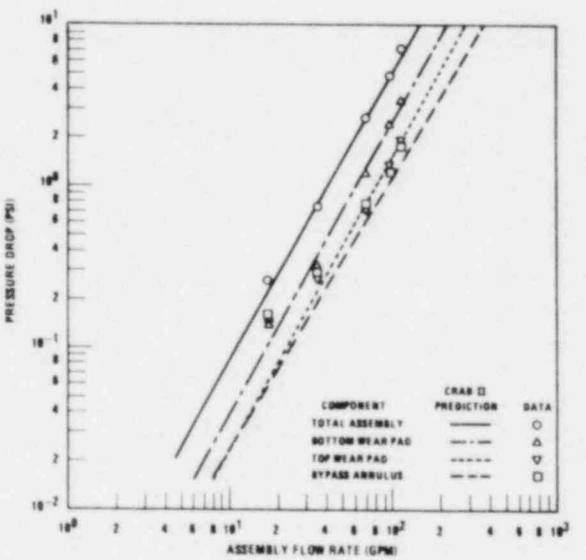

Figure 11. CRAB-II/Data Pressure Drop Comparison: Phase IV, Fully Withdrawn

7197-5

within the 90% confidence experimental error band); in fact, the total pressure drop is the parameter determining the bundle/bypass flow split, the flotation characteristics and the fluid retarding force during scram. While the designer needs were thus well satisfied, from the point of view of the code developer there was the disconcerting fact that some of the individual components ΔP's were poorly predicted. The principal cause for this behavior is that the CRAB-II version used in the comparison did not employ empirical parameters in the calculation of form losses; for example, the pressure drop across the wear pads was calculated with standard contraction/expansion equations based on area ratios, which is obviously inadequate for a complex geometry as a labyrinth wear pad. Thus, K-coefficients were experimentally derived for the losses across the wear pads (bypass flow path) from data obtained in these tests and for the losses across the plates (bundle flow path) from data obtained in the supplemental bundle tests (Section 3.1.3). The comparison between data and predictions was then dramatically improved as shown by two examples reported in Figures 12 and 13. The latest version of CRAB-II incorporates these empirically determined coefficients as a user's option.

3.1.3 Absorber Bundle Tests and Friction Factor Determination

The data reported in the previous section and their comparison with CRAB-II predictions indicated a growing disagreement at low flow conditions. This was due to two reasons: 1) inaccuracy of the pressure measurements at low flow; at ~10 gpm (0.6 l/sec), the measured readings were just a few inches of water and below 10 gpm the measurements were totally inaccurate yielding in most cases negative pressure drops; and 2) the absorber friction factor correlation used in the code was the Novendstern correlation (Reference 3), which had been derived for fuel assemblies (large number of pins--217--and $p/d = 1.25$) at fully turbulent flow. Thus application of the Novendstern correlation to transition/laminar conditions in the absorber bundle (37 pins with $p/d \sim 1.05$) is clearly inadequate. Additionally, the absorber bundle employs a flattened wire in the peripheral channel to reduce the side channels overcooling effects, while a full wire is used in the fuel assembly peripheral channels.

It was therefore decided to perform a special additional test of the pressure drop through a CRBR absorber bundle throughout the entire operating range (turbulent to laminar), paying particular attention to minimizing the experimental error at very low, laminar flow conditions. Performance of this experiment not only resulted in generation of the final information link needed for a full characterization of the PCA hydraulics and validation of the CRAB-II code, but also completed the state-of-the-art regarding experimental determination of the friction factor in rod bundles. In fact, while data and correlations are available for fuel and blanket assemblies (see for example References 4 and 5), none was available until now for the control assemblies.

The test section used in these supplemental tests is shown in Figure 14. The water flow ranged from 1.5 to 120 gpm--0.1 to 7.6 l/sec--(1 to 120% of design flow); two series of tests were conducted, one at high flow (>40 gpm--2.5 l/sec--) with a water temperature of 180°F (82°C), the second at low flows with a water temperature of 80 to 100°F (27 to 38°C). The reason for the

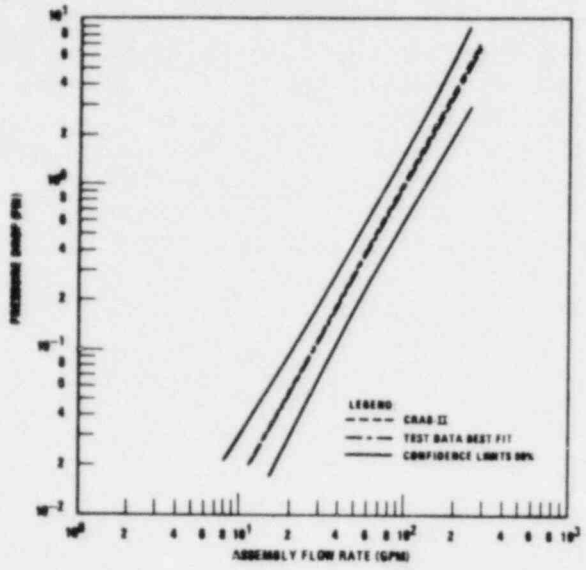

Figure 12. Comparison CRAB-II/Data Following Calibration of Form Losses in CRAB II: Phase IV, 11 Inches Withdrawn, Top Wear Pad

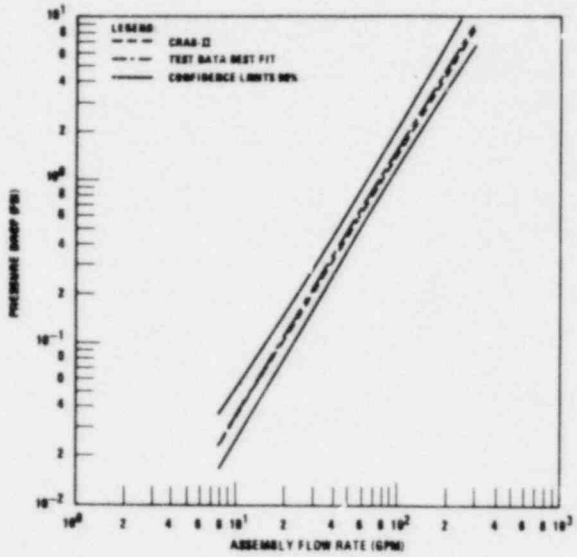

Figure 13. Comparison CRAB-II/Data Following Calibration of Form Losses in CRAB-II: Phase IV, 11 Inches Withdrawn, Bypass Annulus

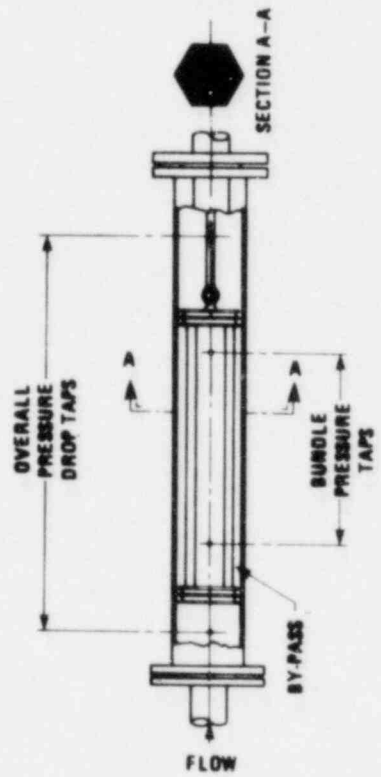

Figure 14. Test Section Used in Absorber Bundle Testing

7197-4

lower water temperature was to yield a Reynolds number as low as possible (the lowest Reynolds number tested being 280). As previously mentioned, particular care was exercised in pressure readings at very low flows: an inclined manometer employing a fluid of 1.75 specific gravity was used and a considerable time interval was allowed before readings were taken of the small manometer differentials. Vertical manometers and calibrated differential pressure gauges were used at higher flow rates. The flow was measured by sharp-edged orifices in series with rotameters and the flow rates were set in increasing and decreasing sequences by rotameter observation. Two series of tests were performed:

1. pressure drop measurements of the absorber bundle alone to determine the bundle friction factor.

2. pressure drop measurements of the total assembly (bundle and bypass) to determine the bundle-to-bypass flow split.

In the first series flanges were attached directly to the ends of the hexagonal duct surrounding the rod bundle. The duct was then assembled into the hydraulic loop. Pressure taps were located in the inlet and outlet pipes and at a 50 inch (1.3 m) vertical distance in the rod bundle zone as shown in Figure 14. Pressure drop data at various flow rates and fluid temperatures were converted into friction factor versus Reynolds number notation and are reported in Figure 15. Experimental uncertainties were 2% or less at high flow, but increased to ~18% at very low flow conditions. A regression analysis of these data provided the following correlations representing the absorber bundle friction factor throughout the entire Reynolds number range:

LAMINAR ($Re \leq 500$)

$$f = \frac{84}{Re}$$

TRANSITION ($500 < Re < 5000$)

$$f = \frac{84}{Re}\sqrt{1 - \Psi} + \frac{0.350}{Re^{0.25}}\sqrt{\Psi}$$

with $$\Psi = \frac{Re - 500}{5000}$$

TURBULENT ($Re \geq 5000$)

$$f = \frac{0.350}{Re^{0.25}}$$

These correlations, except of course for the numerical values of the calibrated coefficients, are consistent with those previously developed for the fuel (Reference 4) and blanket (Reference 5) assemblies.

In the second series of tests, end rings with wear pads were attached to the bundle duct. The duct was centered in the outer duct by set screws and hung from a perforated plate between the upper flanges by a prototypic shaft and

adapter plate. The locations of the overall and bypass pressure taps are shown in Figure 14. Flow split data were obtained as discussed in the next Section 3.1.4. Also, experimental loss coefficients as a function of Reynolds number were obtained for the bottom and top plates; they were used in updating the representation of form losses in CRAB-II as mentioned in the previous Section 3.1.2.

3.1.4 Bundle/Bypass Flow Split

The flow split between absorber bundle and bypass was not obtained directly in the tests, since it was possible to measure only the total assembly flow rate. It was however easily determined from correlation of data obtained in Phase II (rod bundle blocked) and Phase IV (both bundle and bypass open);(*) since the bypass and bundle are parallel channels, the pressure drop through the total assembly, the bundle and the bypass must be equal. Thus, the procedure was to: 1) curve fit the total assembly pressure drop data in ΔP versus flow correlations for both Phase II and Phase IV; 2) select a ΔP and obtain the assembly flow rate (from the Phase IV correlation) and the bypass flow rate (from the Phase II correlation) corresponding to the selected ΔP; 3) calculate the flow split as the ratio of the absorber bundle (total assembly minus bypass) to the total assembly flow rate; 4) repeat steps 2 and 3 to obtain a correlation between flow split and total assembly flow rate.

Data thus obtained are reported in Figure 16 together with the CRAB-II prediction. As shown in the figure, CRAB-II conservatively underpredicts the flow split throughout the entire range. The agreement is quite good at the design flow conditions (code underpredicting by 3%) and in the laminar region of interest to natural circulation analyses (code underpredicting by 2 to 5%). The major discrepancy ($\sim$9%) occurs in the transition region where experimental flow split data are somewhat lacking due to questionable reliability of bypass data as discussed in Section 3.1.2. Since the transition region is not of prime design concern and since the code predictions are conservative, additional experimental investigations were not pursued.

3.1.5 Flotation

In the flotation tests (Phase III of the hydraulic tests) a load cell was installed above the outflow section and connected to the bundle by an extension shaft. The flow through the assembly was increased incrementally above the design value and the load cell output was recorded for each flow increment; pressure drop data were also recorded. A zero load cell reading was taken as the incipient flotation point. It was found that after the initial lifting, the bundle would stop approximately 8-10 inches (20-25 cm) above its initial position due to friction effects and would not freely float until the flow was sufficiently increased to overcome the friction. Flow (and pressure drop) at the initial lifting was taken as indication of flotation conditions. Different initial positions of the bundle (e.g., fully inserted and 11 inches--28 cm--withdrawn) were tested; flotation results qualitatively

---

(*) or first and second series of tests for the supplemental absorber bundle tests reported in Section 3.1.3.

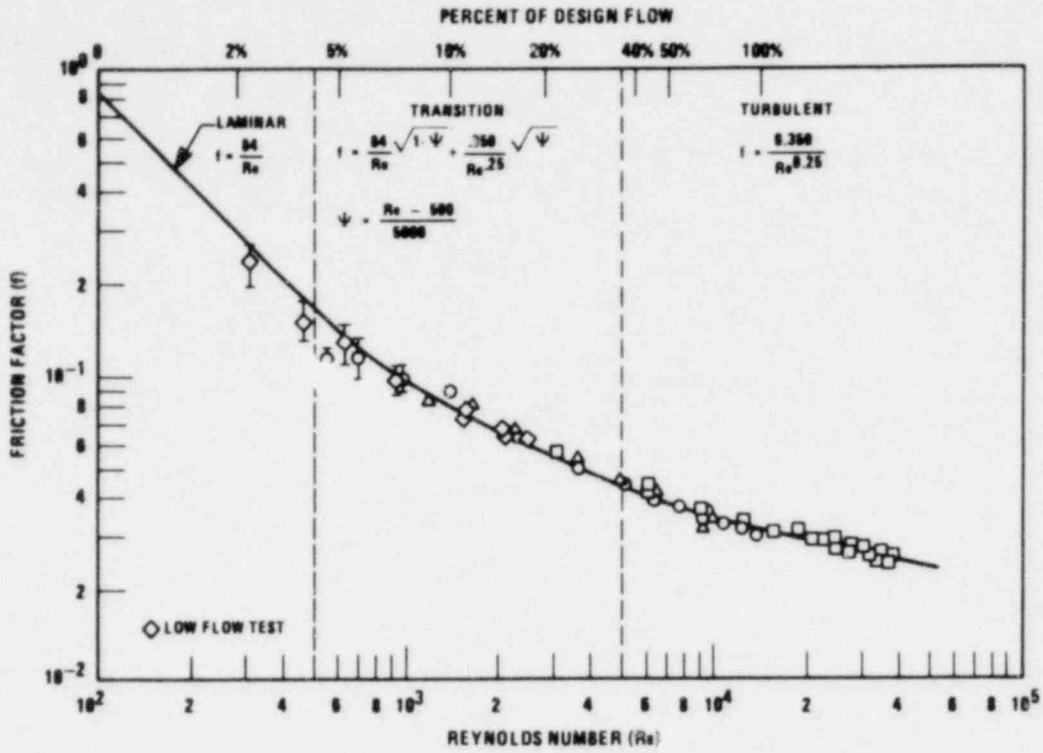

Figure 15. Primary Control Assembly Rod Bundle Friction Factor

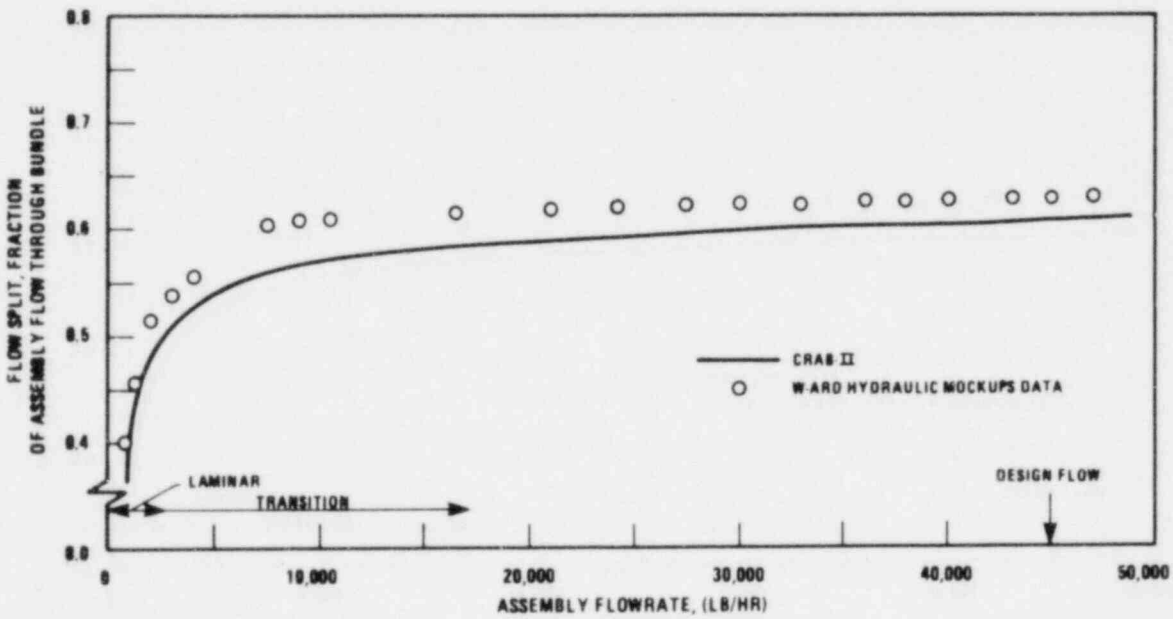

Figure 16. CRBR Primary Control Assembly Flow Split: Comparison CRAB-II Predictions/ ARD Hydraulic Mockups Data

7197-3

confirmed the expected characteristics of the assembly pressure drop. The CRAB-II flotation predictions are reported in Table I along with the range of experimental observations; the agreement is quite favorable, as was previously found in CRAB predictions of the FFTF control assembly flotation characteristics (Reference 1).

TABLE I

COMPARISON FLOTATION DATA/CRAB-II PREDICTIONS FOR CRBR ABSORBER BUNDLE

	Test	CRAB-II
Flotation Flowrate, lb/hr (kg/sec)	55,000-57,500 (6.93-7.24)	55,300 (6.97) (fully inserted) 58,200 (7.33) (11" withdrawn)
Flotation ΔP, psi (atm)	7.2-7.5 (0.490-0.510)	7.5 (0.510) (fully inserted) 7.45 (0.507) (11" withdrawn)

3.2 Scram Tests

Accelerated life tests of the PCA and the Primary Control Rod Drive Mechanism under sodium conditions were conducted at Westinghouse ARD. A major objective was to test the scram behavior of a prototypic control assembly and related mechanisms. The assembly flowrate was varied between 4500 and 51,500 lb/hr (0.57 and 6.5 kg/sec), thus covering from 10% to 115% of the design flow; the range of sodium temperatures tested was from 400°F to 1100°F (204° to 593°C); the control assembly was inserted from the fully withdrawn position and from several intermediate, partially withdrawn positions. Scram assisting and retarding forces were measured; test results for the bellows and the dashpot were reported in Sections 2.2.3 and 2.2.4, respectively. Spring and mechanical friction forces were also experimentally determined and were used in the CRAB-II test predictions. CRAB-II predictions and test data are compared in Figure 17 for a high flow scram from fully withdrawn conditions. As shown in the figure, the agreement is nearly perfect. This was not an isolated case; in fact, excellent agreement between predictions and data was consistently found as graphically depicted in Figure 18, which groups the high temperature, full rod drop tests. Very good agreement was also found for scrams from partially withdrawn conditions as shown in Figure 19. As mentioned in Section 2, perhaps the most significant feature of the CRAB-II model in respect to the original CRAB version is the three control volumes with constant pressure drop boundary condition, which implies a reduction in the assembly flowrate during scram. Code predictions were confirmed by the test data as shown by the example reported in Figure 20. The agreement is indeed remarkable, especially since it was not possible for the test to exactly simulate the "remaining of the core" resistance as a parallel flow path to the control assembly.

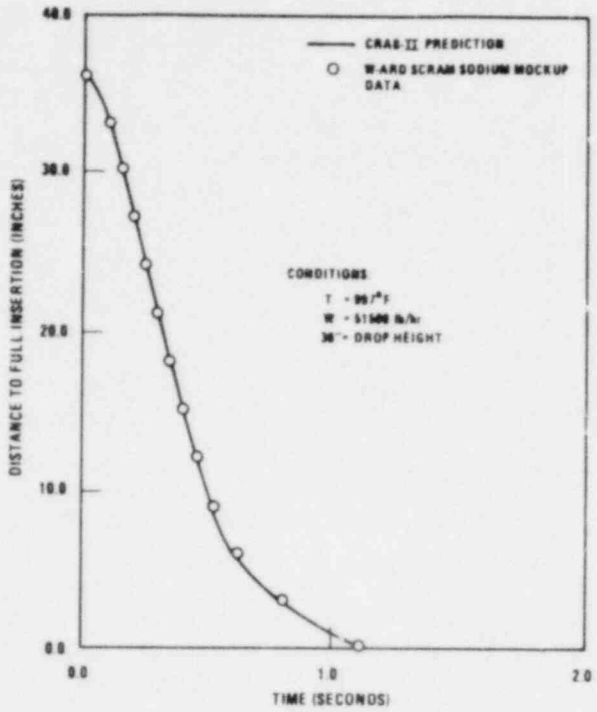

Figure 17. A Comparison Between Scram Predictions by CRAB-II and ARD Sodium Mockup Data

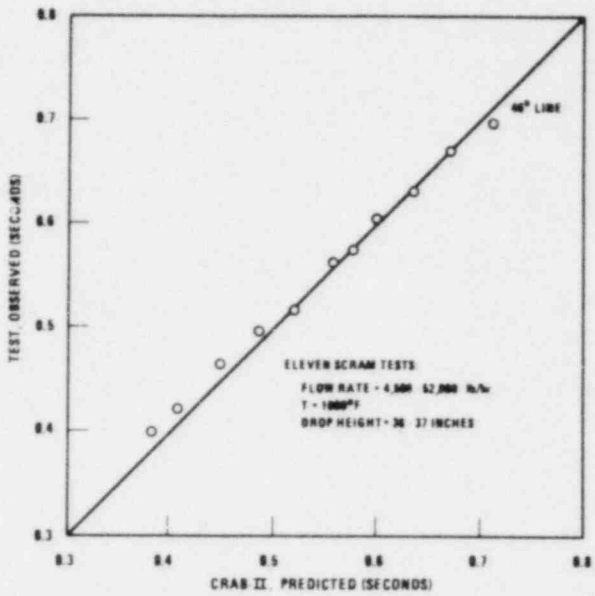

Figure 18. Summary Comparison of the CRAB-II Predicted Versus Test Observed Scram Time to Reach the Dashpot

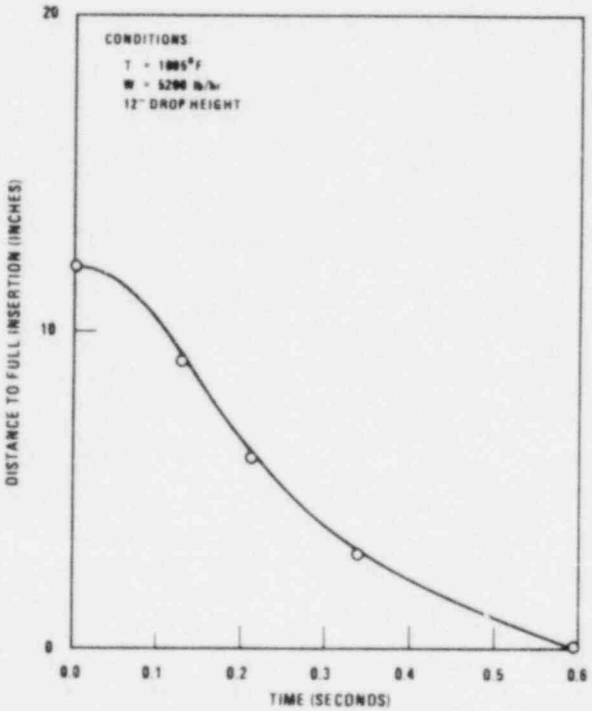

Figure 19. A Comparison of CRAB-II Predictions/Data for Insertion from Partially Withdrawn Conditions

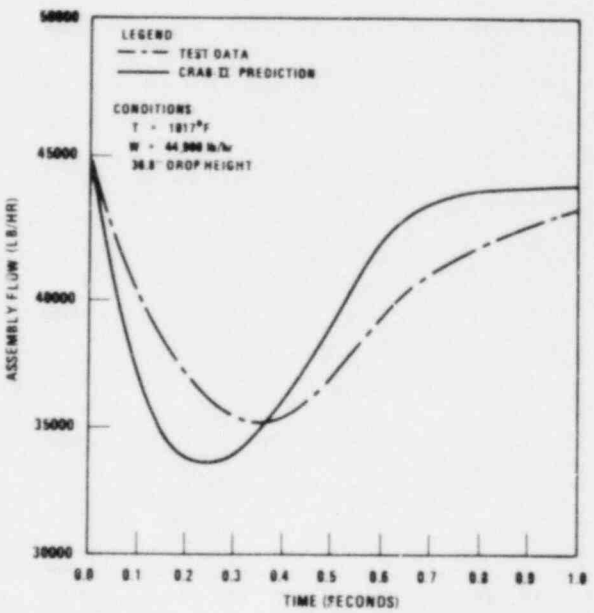

Figure 20. Transient Reduction in Assembly Flowrate During Scram

7197-8

4.0 CONCLUSIONS

The CRAB-II code is a uniquely detailed and realistic analytical tool to predict the steady state and transient (scram) hydraulic behavior of LMFBR control assemblies of the rod bundle type. In addition to providing a very accurate representation of the assembly hydraulic field through its three-control volumes model, the code also features accurate modeling of components, such as bellows and dashpot, which influence the scram behavior. The code running time is, in most cases, only a few seconds, thus making the code ideal for extensive parametric analyses, in addition to its use as a primary design tool. The high reliability of the code's predictions is underlined by the excellent agreement with prototypic test data obtained for the CRBR primary control assembly. The three key design parameters: rod bundle/bypass flow split, flotation characteristics, and scram insertion parameters are predicted within a few percent; the deviation between test data and code predictions is less than the experimental errors. Particularly significant is the excellent accuracy shown by CRAB-II in predicting the scram insertion characteristics, since this is the primary function of the control assemblies and has obviously critical implications on the safe operation of the reactor. The earlier CRAB version had also shown very satisfactory reproduction of test data for the FFTF assembly. It is concluded therefore that CRAB-II is a mature, validated code which can be used with confidence in design and analysis of the CRBR core.

Finally, the reader's attention is called to the absorber bundle friction factor data and empirical correlations which close a gap and complete the state-of-the-art in the characterization of the hydraulics of rod bundles used in LMFBR cores.

ACKNOWLEDGEMENTS

The authors are greatly indebted to all those who performed the experimental testing of the CRBRP PCA and provided the data reported here. Special thanks go to J. G. Akey and J. M. Kovalcik who directed, respectively, the hydraulics and scram dynamics tests, to H. O. Lagally, the CRBRP PCA cognizant engineer and to T. A. Pitterle, the CRBRP PCA cognizant manager.

NOMENCLATURE

A	flow area
D	hydraulic diameter
F	force
f	friction factor, generic function
g	gravitational constant, generic function
K	loss coefficient
L	length
M	mass of absorber bundle and attached hardware
$\dot{m}$	mass flowrate
m	time derivative of flowrate
P	pressure
p/d	pitch-to-diameter ratio
Re	Reynolds number
t	time
U	fluid velocity
V	volume
z	rod bundle position (measured from fully withdrawn)
$\dot{z}$	rod bundle velocity, positive down
$\ddot{z}$	rod bundle acceleration
β', β''	defined in text
ΔP	pressure drop
ρ	fluid density
ψ	intermittency factor, defined in text

Subscripts

A,B,C	control volume A, B, C
a	in the fluid
b	at a solid surface
by	bypass channel
c	corner channel
cg	cover gas
i	inboard channel
rb	rod bundle
s	side channel
sh	shear

Note: other symbols and subscripts, only used once, are defined in the text.

REFERENCES

1. M. D. Carelli, C. W. Bach, and R. A. Markley, "Hydraulic and Scram Dynamics Analysis of LMFBR Control Rod Assemblies," Trans. Amer. Nucl. Soc., 16, 218 (1973).

2. M. D. Carelli, H. W. Brandt, C. W. Bach, and H. D. Kulikowski, "LMFBR Control Rods Scrqam Dynamics, "Trans. Amer. Nucl. Soc., 18, 278 (1974).

3. E. H. Novendstern, "Turbulent Flow Pressure Drop Model for Fuel Rod Assemblies Utilizing a Helical Wire Wrap Spacer System," Nucl. Eng. Design, 22, 218 (1973).

4. D. R. Spencer and R. A. Markley, "Friction Factor Correlation for 217-Pin Wire Wrap Spaced LMFBR Fuel Assemblies," Tans. Amer. Nucl. Soc., 39, 1014 (1981).

5. F. C. Engel, R. A. Markley, and A. A. Bishop, "Laminar, Transition and Turbulent Parallel Flow Pressure Drop Across Wire Wrap Spaced Rod Bundles," Nuclear Sc. Engineering, 69, 290 (1979) and 74, 226 (1980).

A SIMPLE FORMALISM FOR THE CALCULATION OF THE EFFECT OF SODIUM VOIDING ON NEUTRON LEAKAGES IN A FAST REACTOR

P. BENOIST

SUMMARY

A simple formalism for the calculation of the effect of sodium voiding on neutron leakages in a fast reactor is presented. The diffusion coefficients in a plane or 2-D lattice are calculated following a method which is very analogous to the method proposed earlier by the author for the treatment of thermal reactors. The two situations, sodium present, sodium voided, are calculated with the same approximations. It is known that it is impossible, in the situation where the sodium is voided, to calculate buckling-independent diffusion coefficients, for they diverge ; these coefficients are hence calculated, in both situations, at the lowest order of the expansion in terms of the buckling, which introduces a logarithmic term. The calculation is performed in the actual geometry of the lattice, without cylindricalizing the cell. Angular correlation terms appear to be small, if not negligible, in a fast reactor, at least in a rod lattice.

A SIMPLE FORMALISM FOR THE CALCULATION OF THE EFFECT OF SODIUM VOIDING ON NEUTRON LEAKAGES IN A FAST REACTOR

A - INTRODUCTION

The knowledge of the reactivity effect of sodium voiding in fast reactors is very important for their safety. This reactivity change is the resultant of several effects, generally responsible of a positive reactivity injection, except one, the increase of neutron leakages, which is always negative. This particular effect shall be investigated here, first from a general point of view, then in two configurations currently used in practice : plane lattice, bidimensional lattice (triangular or square).

The difficulty of the problem comes from the fact that the classical formulas for the calculation of the diffusion coefficient, if the "image-piles" approximation is assumed, and if only the buckling-independent part of this coefficient is retained, loose any signification when the lattice contains bidimensional void gaps. These void gaps appear generally in a fast reactor when sodium is voided. The diffusion coefficient parallel to these gaps becomes infinite if the above formulas are applied. When the sodium is in, the diffusion coefficient remains finite but, even in this case, the validity of the result remains questionable, due to the relatively high transparency of sodium to neutrons.

Moreover it is extremly important for the determination of the differential effect that both configurations, sodium in, sodium out, are calculated according to the same formalism, involving the same approximations.

A simple method allowing to take advantage anyway of the classical formulation, in the case of a bidimensional lattice, consists in cylindricalizing the cell, which is composed of a central fuel rod, surrounded with sodium or void. This way was investigated by several authors. The diffusion coefficients obtained in such a way keep a finite value when sodium is voided. Nevertheless it is easy to understand that this process juggles away the singularity of the problem, the convergence of the integrals being obtained by a purely artificial change in the physical reality.

One of the most important works about axial streaming in a gas-cooled fast reactors was presented by Köhler and Ligou[1,2]. This work, which takes correctly into account the singularity of the problem, led to the DIFFAX code, which allows to calculate the axial diffusion coefficient in a hexagonal lattice of fuel pins. It does not assume any expansion in powers of the buckling. This code can of course be used in a sodium reactor when the sodium is voided ; in return it cannot be used when the sodium is present ; moreover it deals only with the axial coefficient and in a one-speed theory. Other works on streaming in fast reactors were published in [3,4,5,6].

The purpose of the present work, which is developed in [7], is the following one : starting from the general basis of theory presented earlier by the author [8], we establish for fast reactors calculations a simple formalism analogous to the one proposed for thermal reactor calculations. This formalism involves the concept of directional collision probability, defined in [8,9]. Fischer [6] used also this concept in the calculation of a plane lattice, introducing a "non-leakage factor". Here, the introduction of such a factor is avoided, exactly as in [8]. We limit ourselves, no more at the zeroth order in the buckling $\vec{B}$, which, as we have seen, is impossible in a sodium-voided reactor, but at the lowest order, which is logarithmic, neglecting terms of second order or above. It can be expected that [10], due to the relatively weak heterogeneity of a fast reactor, this order is sufficient in practical cases, the correction taking into account higher order terms being calculated on the homogenized lattice.

Several definitions of the diffusion coefficients exist, each being based on a given equivalence criterion between the lattice and the homogenized medium. In [8], we chose a definition keeping invariant the leakages of neutrons. We prefer here to use the new definition of Deniz [11], based on a perturbation between the lattice and the homogenized medium. This definition leads to the same expression of the diffusion coefficients as in [8], except that the so-called *absorption term* appearing in [8] disappears ; this has the consequence of making the diffusion coefficients independent of the way how the cell is defined. Anyway the deviation between the various definitions of D_k is certainly weak in a fast reactor lattice, the cell of which has a rather small optical thickness. In [7], in addition to the diffusion coefficients in each group, we calculate the migration area, according to the first Deniz theory [12].

The diffusion coefficient parallel to the boundary planes (in the plane case), or the axial diffusion coefficient (in a bidimensional lattice) can be, at a given energy, calculated in a one-speed theory, since it does not depend on the cross-sections at other energies (at least if scattering is isotropic). In other terms, only first flight collision probabilities appear. On the contrary, in the calculation of the perpendicular diffusion coefficient (in the plane case) or of the radial diffusion coefficient (in a bidimensional lattice), *angular correlation* term appear, and introduce a coupling between energies. These terms do not lead to any divergence at the limit $\vec{B} \to 0$ and can therefore, in conformity with our basic hypothesis, be calculated assuming directly $\vec{B} = 0$. In plane geometry, their calculation for general plane lattices is in progress. In a bidimensional lattice, we suggest to calculate these terms for a Wigner-Seitz cell, which for this particular calculation is a reasonable approximation. The MP method [13] is used to calculate these terms, both for isotropic and anisotropic scattering. Numerical values are given in the present paper, and show that their influence is weak, if not negligible, in a fast reactor lattice.

B - BASIC FORMALISM

We assume the image-piles approximation, extending the lattice to infinity. The diffusion coefficient D_k in the direction k (with k = x, y or z), and at a given energy, may be expressed from the leakages $\mathcal{F}(\vec{B})$

$$\mathcal{F}(\vec{B}) = \sum D_k(\vec{B})\ B_k^2$$

where B_k is the component k of the bucking vector $\vec{B}$.

Instead using the definition of $\mathcal{F}(\vec{B})$ proposed in[8], which expresses $\mathcal{F}$ from the *actual* flux and current existing in the lattice, we prefer to start here from the new definition of Deniz[11], which involves the *microscopic* flux and current ; this new definition leads to the same expression as in[8], except that the so-called *absorption term* disappears (this makes D_k independent of the definition of the cell boundaries). This expression is

$$\mathcal{F}(\vec{B}) = - \vec{B} \cdot \frac{\int_V d\vec{r} \int_{4\pi} d\Omega \; \Omega \; h_B(\vec{r},\vec{\Omega})}{\int_V d\vec{r} \int_{4\pi} d\Omega \; g_B(\vec{r},\vec{\Omega})}$$

where V is the volume of the cell. The functions g_B and h_B are defined by

$$f_B(\vec{r},\vec{\Omega}) = g_B(\vec{r},\vec{\Omega}) + i \; h_B(\vec{r},\vec{\Omega})$$

where f_B is the solution of the isotropic scattering transport equation

$$\left[\vec{\Omega}.\vec{\nabla}_{\vec{r}} + \Sigma_t(\vec{r}) + i\vec{B}.\vec{\Omega} \right] f_B(\vec{r},\vec{\Omega}) = \frac{\Sigma^{(s)}(\vec{r})}{4\pi} \int_{4\pi} f_B(\vec{r},\vec{\Omega}) \; d\Omega \qquad (1)$$

In a problem with energy spectrum, the symbol $\Sigma^{(s)}(\vec{r})$ is to be considered as a energy transfer operator taking into account transfers by scattering and by fission ; Eq. (1) is an eigenvalue equation.

Our purpose is to calculate D_k at the lowest order of the expansion in powers of $\vec{B}$. As we have seen, it cannot be the zero-order, but it shall be logarithmic. Neglecting terms of order B^2 and above, we obtain

$$D_k = \frac{\int_{V^\infty} d\vec{r} \int_V d\vec{r}' \; \Omega_k^2 \; \frac{\exp(-\tilde{\Sigma}R)}{R^2} \cos(\vec{B}.\vec{R}) \; g_0(\vec{r}',\vec{\Omega})}{\int_V d\vec{r} \int_{4\pi} d\Omega \; g_0(\vec{r},\vec{\Omega})} \qquad (2)$$

The integration over $\vec{r}$ in the numerator is extended to the whole lattice V^∞. Let us assume the "flat flux approximation", which represents the classical angular flux $g_0(\vec{r},\vec{\Omega}')$ in each medium i of the cell as a uniform and isotropic function ϕ_i. This approximation, which was reasonable in thermal lattices, is surely still better in fast ones. We may now write Eq. (2) as

$$D_k = \frac{1}{3} \; \frac{\sum_i \sum_j V_i \; \phi_i \; \lambda_j \; P_{ij,k}}{\sum_i V_i \; \phi_i} \qquad (3)$$

The summations on i run over all the media of the cell and the summations on j run over all the media of the lattice, V_i is the volume of medium i, ϕ_i the average classical flux in this medium and λ_j the total (or transport) mean free path in medium j. The $P_{ij,k}$ generalize the directional collision probabilities introduced in[8,9].

$$P_{ij,k} = \frac{3}{V_i \lambda_j} \int_{V_j^\infty} d\vec{r} \int_{V_i} d\vec{r}' \, \Omega_k^2 \, \frac{\exp(-\tilde{\Sigma} R)}{4\pi R^2} \cos(\vec{B}.\vec{R}) \qquad (4)$$

The transport probabilities introduced in[8,9] take into account the *angular correlation terms*. We prefer here to treat these terms separately later, as a correction to the principal term represented by Eqs. (3,4)

The $P_{ij,k}$ are linked together by relations which make the calculations easier. The first one is the reciprocity relation

$$V_i \lambda_j P_{ij,k} = V_j \lambda_i P_{ji,k}$$

The second one, the conservation relation

$$\sum_j P_{ij,k} = 1 \qquad (5)$$

is no more valid due to the presence of $\cos(\vec{B}.\vec{R})$ in (4) ; but, if terms of order B^2 and above are neglected in D_k, which is our assumption, it is possible to show that Eq. (5) is rigorous.

These two relations allow to write Eq. (3) under the general practical form given in Eq.(B.5) of [8] or Eq. (18) of [9]. Let us define reduced probabilities

$$P_{ij,k} = \frac{\lambda_j}{r_j} P_{ij,k} \qquad \text{with} \quad r_j = \frac{2 V_j}{S_j} \qquad (S_j = \text{surface of medium } j)$$

If the lattice contains only two media, a fuel u and a coolant c, the practical form reduces to

$$D_k = \frac{1}{3} \lambda_u \left\{ 1 + \frac{V_c \phi_u}{V_t \phi_t} \left(1 - \frac{\lambda_u}{\lambda_c} \right) \left[1 + \frac{r_c}{\lambda_u} \left(\frac{\phi_c}{\phi_u} - \frac{\lambda_u}{\lambda_c} \right) (Q_k + Q_k') \right] \right\} \qquad (6)$$

We have

$$V_t \phi_t = V_u \phi_u + V_c \phi_c$$

and

$$Q_k + Q_k' = P_{cc,k}$$

The term Q_k corresponds, in Eq. (4) to the contribution of paths from $\vec{r}'$ to $\vec{r}$ which do not cross medium u, and the term Q_k' to the contribution of paths crossing u.

The problem is reduced to the calculation of Q_k and Q_k'. The term Q_k', remaining finite at the limit $\vec{B} \to 0$, shall be calculated assuming directly $\vec{B} = 0$. It is impossible for the term Q_k, which shall be calculated keeping $\cos(\vec{B}.\vec{R})$ in Eq. (4).

C - PLANE LATTICES

Let us consider a plane lattice of fuel plates u, with thickness t, separated a by coolant c (sodium or void), with thickness e. Let $\sigma = \Sigma_c$ e. It is easy to show that, in the direction x perpendicular to the plates, and at the limit $\vec{B}e \to 0$

$$Q_x(\sigma) = \frac{1}{\sigma} - \frac{3}{4\,\sigma^2} + \frac{3}{\sigma^2} E_5(\sigma) \tag{7}$$

where $E_n(\sigma)$ is the exponential integral function. For $\sigma = 0$,

$$Q_x(0) = \frac{3}{4}$$

a result already mentioned in [8].

In the direction z parallel to the plates, the situation is more complicated. If $\vec{\alpha} = \frac{\vec{B}}{\Sigma}$, we may write, at the limit $\vec{B}e \to 0$, whatever the value of σ is

$$Q_z(\sigma,\vec{\alpha}) = Q_z(\sigma,0) + \delta Q_z(\vec{\alpha}) \tag{8}$$

with

$$\delta Q_z(\vec{\alpha}) = \lim_{\sigma \to 0} [Q_z(\sigma,\vec{\alpha}) - Q_z(\sigma,0)]$$

The first term in Eq. (8)

$$Q_z(\sigma,0) = \frac{1}{\sigma} - \frac{3}{8\,\sigma^2} + \frac{3}{2\,\sigma^2} [E_3(\sigma) - E_5(\sigma)]$$

diverges at the limit $\sigma \to 0$, but the convergence shall be restored by the term $\delta Q_z(\vec{\alpha})$; Eq. (8) may be written

$$Q_z(\sigma,\vec{\alpha}) = \frac{1}{\sigma} - \frac{3}{8\,\sigma^2} + \frac{3}{2\,\sigma^2} [E_3(\sigma) - E_5(\sigma)] - \frac{3}{8} \ln \frac{1 + \frac{\alpha_z^2}{2} + (1 + \alpha_z^2)^{1/2}}{2}$$

$$- \frac{3}{4\,\alpha_z^2} \left[1 + \frac{\alpha_z^2}{2} - (1 + \alpha_z^2)^{1/2} \right] \tag{9}$$

If the sodium is voided, $\sigma = 0$, $\alpha_z \to \infty$ and Eq. (9) reduces to

$$Q_z(0,\vec{\beta}) = \frac{3}{4} \left(\ln \frac{2}{\beta_z} - \gamma + \frac{1}{2} \right) \tag{10}$$

with

$$\beta_z = B_z\, e \qquad \text{and} \qquad \gamma = .57722...$$

The term Q_K' can be calculated for $\vec{B} = 0$; if τ is the optical thickness of the fuel

$$Q'_x = \frac{3}{\sigma^2}\int_0^1 \mu^3 \left[1 - \exp\left(-\frac{\sigma}{\mu}\right)\right]^2 \frac{\exp\left(-\frac{\tau}{\mu}\right)}{1 - \exp\left(-\frac{\tau+\sigma}{\mu}\right)}\, d\mu \qquad (11)$$

$$Q'_z = \frac{3}{2\,\sigma^2}\int_0^1 (\mu - \mu^3) \left[1 - \exp\left(-\frac{\sigma}{\mu}\right)\right]^2 \frac{\exp\left(-\frac{\tau}{\mu}\right)}{1 - \exp\left(-\frac{\tau+\sigma}{\mu}\right)}\, d\mu \qquad (12)$$

Putting Eqs. (7) and (11), or (9) and (12) in Eq. (6) gives immediately D_x and D_z. In the particular case where sodium is voided, Eqs. (6), (10) and (12) for D_z are rigorously equivalent to the expression obtained by Köhler and Ligou (Eq. (20) of [1]). In the general case ($\sigma \neq 0$ or $\sigma = 0$), the expression obtained by Fischer (Eq. 25 of [6]), which lies on different approximations, is slightly different from Eqs. (6), (9) and (12).

The angular correlation terms, which appear in the case k = x, introduce a coupling between energies. They have been calculated analytically in particular cases in [8] (Appendix IV) ; their general calculation in plane geometry is in progress. They can certainly be neglected for plane cells having a small optical thickness but may be not negligible if this thickness increases.

D - BIDIMENSIONAL LATTICE OF RODS

Calculation of Q_k

Let us consider now a bidimensional lattice (triangular or square) of fuel rods u, infinite in height, imbedded in a coolant medium c. The term Q_k may be written, according to Eq. (4)

$$Q_k = \frac{3}{4\pi\, V_c\, r_c}\int_0^1 \eta\, d\eta \int_0^1 d\xi\, I_k \qquad (12)$$

with, after some transformations

$$I_r = S_c \int_0^{\pi} d\theta \sin^2\theta \int_0^{\infty} d\rho\, g(\rho)\, \rho^2 \exp\left[-\xi\eta\left(\frac{\Sigma_c}{\sin\theta} + i\, B_z \cot g\,\theta\right)\rho\right] \cdot$$

$$\cdot \left[J_0(\xi\,\eta\, B_r\, \rho) - J_2(\xi\,\eta\, B_r\, \rho)\right] \qquad (13)$$

$$I_z = 2\, S_c \int_0^{\pi} d\theta \cos^2\theta \int_0^{\infty} d\rho\, g(\rho)\rho^2 \exp\left[-\xi\eta\left(\frac{\Sigma_c}{\sin\theta} + iB_z \cot g\,\theta\right)\rho\right] J_0(\xi\eta B_r\, \rho) \qquad (14)$$

Here, B_z is the component of $\vec{B}$ in the axial direction and $B_r = (B^2 - B_z^2)^{1/2}$. We introduced the projected chord distribution $g(\rho)$, where ρ is the projection of a chord in medium c, on the xy plane. Choosing

$$\int_0^\infty g(\rho)\, d\rho = 1$$

it can be shown that

$$\bar{\rho} = \int_0^\infty g(\rho)\, \rho\, d\rho = \frac{\pi}{2} r_c$$

Let us see the interest of introducing the distribution $g(\rho)$. If the sodium is voided ($\Sigma_c = 0$) and if $\vec{B} = 0$, the mean square of projected chords appears in Eqs. (12,13,14)

$$\overline{\rho^2} = \int_0^\infty g(\rho)\, \rho^2\, d\rho \qquad (15)$$

This mean square diverges in the case, considered here, where medium c behaves at infinity as two-dimensional gaps ; the behaviour of $g(\rho)$ at infinity is indeed $\frac{A}{\rho^3}$, where A is a constant depending of the lattice. Let us write

$$g(\rho) = g_{(0)}(\rho) + g_{(\infty)}(\rho)$$

with

$$g_{(\infty)}(\rho) = \frac{A}{\rho^3} T(\rho - \rho_1)$$

where ρ_1 is a finite and arbitrary value of ρ and where $g_{(0)}(\rho)$ decreases at infinity faster than $\frac{1}{\rho^3}$.

The term $\frac{A}{\rho^3}$ is responsible of the divergence of $\overline{\rho^2}$ (Eq. (15)). Its contribution $Q_{k(\infty)}$ shall be calculated keeping the dependence in $\vec{B}$ in Eqs. (13,14). To the contrary the contribution of $g_{(0)}(\rho)$ can be calculated for $\vec{B} = 0$. We write, as in plane geometry (Eq. (8))

$$Q_k(\sigma,\alpha_r,\alpha_z) = Q_k(\sigma,0,0) + \delta Q_k(\alpha_r,\alpha_z) \qquad (16)$$

with

$$\delta Q_k(\alpha_r,\alpha_z) = \lim_{\sigma \to 0} \left[Q_{k(\infty)}(\sigma,\alpha_r,\alpha_z) - Q_{k(\infty)}(\sigma,0,0) \right] \qquad (17)$$

and

$$\sigma = r_c \Sigma_c \qquad \alpha_r = \frac{B_r}{\Sigma_c} \qquad \alpha_z = \frac{B_z}{\Sigma_c}$$

We limit ourselves to the case, very common in practice, where, in a triangular lattice, there exists one and only one series of gaps

$$\frac{1}{2} < \frac{2\,a}{s} < \frac{\sqrt{3}}{2}$$

2 a being the rod diameter and s the lattice pitch. Thus the value of the constant A is

$$A = \frac{3\,s\,\varepsilon^2}{\pi\,a}$$

where

$$\varepsilon = s\,\frac{\sqrt{3}}{2} - 2\,a$$

is the thickness of the two-dimensional gaps.

The anaytical expression of $\delta Q_k(\alpha_r,\alpha_z)$ (Eq. (17)) is given as a simple integral in [7]. At the limit $\sigma \to 0$, it leads to a logarithmic dependence versus $\alpha_r = \frac{r_c\,B_r}{\sigma}$ and $\alpha_z = \frac{r_c\,B_z}{\sigma}$.

The term $Q_k(\sigma,0,0)$ appearing in Eq. (16) is also calculated in [7]. Since it is a collision probability, it can be expressed as an integral of the distribution $g(\rho)$. This distribution is the sum of the distributions $g_n(\rho)$ corresponding to the paths extending from the surface of a given rod 0 to the surface of a rod situated in the n^{th} crown of rods surrounding rod 0. For $n \geqslant n_\infty$, where n_∞ is a sufficiently great value of n, the distribution $g_n(\rho)$ may be represented as a Dirac distribution of ρ centered on an average value of the distance from rod 0 to rod u. This allows an analytical treatment of the series from $n = n_\infty$ to ∞, which puts into evidence, in the particular case $\sigma \to 0$, a logarithmic dependence versus σ which cancels the same logarithmic dependence in σ appearing in $\delta Q_k(\alpha_r,\alpha_z)$; there remains a logarithmic dependence in $r_c\,B_r$ and $r_c\,B_z$; if, moreover $B_r = 0$, this leads to the same logarithmic dependence of D_z versus $r_c\,B_z$ as the one obtained in Eq. (13) of [2] for a gas-cooled fast reactor.

For $n < n_\infty$, the series is calculated term by term ; their analytical expression is given in [7].

Calculation of Q'_k

The term Q'_k may be written

$$Q'_k = \frac{\lambda_c}{r_c}\,P'_{cc,k}$$

where λ_c is the total mean free path of the medium c and $P'_{cc,k}$ the directional probability for a neutron born in c to suffer its first collision in c, this neutron being supposed to cross one or several times the medium u. This term, being not singular at the limit $\sigma \to 0$, can be calculated for $\vec{B} = 0$.

The directional probability $P'_{cc,k}$ shall be obtained using an approximation which makes the calculations very easy. This approximation consists in breaking the coupling between paths in medium c and in medium u, assuming that neutrons enter both media according to an angular flux proportional to Ω_k. This generalizes a well-known approximation used to calculate the classical first flight collision probabilities in a lattice, assuming that neutrons enter medium c and u according to a semi-isotropic angular flux. In the present problem, dealing directional probabilities, the necessary continuity of currents is to be replaced by the continuity of *fictitions currents* defined in [8] (Section B). The advantage of this approximation is that directional probabilities corresponding only to medium c, or only to medium u, appear in the formula of Q'_k.

The formula of Q'_k based on this approximation are given in [7] (Section D-II). A much more elaborate approximation is given in [7] (Appendix I).

Angular correlation terms

In the axial coefficient D_z, angular correlation terms cancel, at least if scattering is isotropic. In the radial coefficient D_r, even if scattering is isotropic, they do not cancel and introduce a negative contribution. They can be calculated for $\vec{B} = 0$ since they are regular at this limit. They introduce a coupling between the energy groups.

The principal term D_{k_0}, involving directional first flight collision probabilities, is badly calculated in the Wigner-Seitz cell model, and requires a bi-dimensional treatment as presented above. To the contrary, the cylindricalization of the cell can be considered as a good model for the calculation of the angular correlation terms. The method MP of Yang and Benoist[13] allows to calculate the diffusion coefficients in a cylindricalized cell, using integral transport theory ; the only approximation consists in assuming $\vec{B} = 0$; moreover it allows to treat either isotropic or linearly anisotropic scattering, with any number of groups. The following numerical values are extracted from [13].

Let us consider a circular cell containing a fuel rod surrounded with sodium. We considered also the case where sodium is voided. The dimensions are

Rod radius = 0.635 cm
Equivalent cell radius = 1.495 cm

Let us treat this cell in one-group theory. The code MP has calculated this cell, first with linearly anisotropic scattering (LA) secondly with isotropic scattering, using the corresponding transport cross-sections (IT). This cross-sections are given in table I (Results of multigroup calculations are given in[13], and shown the effect of intergroup coupling).

	Fuel	Sodium
LA	$\Sigma_t = .3734\ cm^{-1}$ $\Sigma_{s_0} = .3612\ cm^{-1}$ $\Sigma_{s_1} = .0898\ cm^{-1}$ $\frac{\nu \Sigma_f}{k_{eff}} = .0125\ cm^{-1}$	$\Sigma_t = .1072\ cm^{-1}$ $\Sigma_{s_0} = .1071\ cm^{-1}$ $\Sigma_{s_1} = .0225\ cm^{-1}$
IT	$\Sigma_{tr} = .3435\ cm^{-1}$ $\Sigma_s = .3312\ cm^{-1}$ $\frac{\nu \Sigma_f}{k_{eff}} = .0125\ cm^{-1}$	$\Sigma_{tr} = .0997\ cm^{-1}$ $\Sigma_s = .0996\ cm^{-1}$

Table I - One group cross-sections

The following values are obtained

		k = x	k = z
Sodium in	$(D_{k_0}^{IT})$	(2.3701)	(2.4094)
	(D_k^{IT})	(2.3670)	(2.4094)
	$D_k^{IT} - D_{k_0}^{IT}$	-0.00303	0
	(D_k^{LA})	(2.3660)	(2.4099)
	$D_k^{LA} - D_{k_0}^{IT}$	- .0040	+ .0005
Sodium out	$(D_{k_0}^{IT})$	(5.9519)	(6.5126)
	(D_k^{IT})	(5.9198)	(6.5126)
	$D_k^{IT} - D_{k_0}^{IT}$	-0.0321	0
	(D_k^{LA})	(5.9215)	(6.5212)
	$D_k^{LA} - D_{k_0}^{IT}$	-0.0304	+0.0086

Table II - One group diffusion coefficients in a fast reactor lattice

As said above, the values of the diffusion coefficients D_k and of their principal term D_{k0} are certainly not good, due to the cylindricalization approximation ; they are given here only as an information and are put into brackets. To the contrary, the values of the difference $D_k^{IT} - D_{k0}^{IT}$, which represent the angular correlation terms, are much more interesting, because they have no reason to be strongly modified by the cylindricalization. Thus we suggest the following procedure. The principal term D_{k0}^{IT} shall be calculated in bidimensional geometry by the method presented above, involving $\vec{B}$ and the transport cross-sections. Then we shall add to this term the correction $D_k^{IT} - D_{k0}^{IT}$ calculated by the code MP in cylindrical geometry, or even better the correction $D_k^{LA} - D_{k0}^{IT}$, which takes exactly in account linearly anisotropic scattering. We see on the table that this correction represents only a small part of the principal term if the sodium is out and an even smaller part if the sodium is in. Its influence on reactivity is certainly very weak.

It is particularly interesting to consider the relative error which should be made on the sodium voiding effect (D_k sodium out - D_k sodium in) if angular correlation terms were simply neglected. Calculating these terms in the LA approximation, this relative error should be - 0.74 % for k = r and + 0.20 % for k = z. Even these relative errors are probably very overestimated, because the difference D_k^{LA} sodium out - D_k sodium in is certainly very underestimated in Table II. Cylindricalization indeed underestimates very probably D_k in the situation sodium in, but even much more in the situation sodium out, for which the effect of bidimensional void studied above takes its maximum importance.

E - CONCLUSION

The formalism presented above, and developed in [7], allows, with simple calculations, to obtain the diffusion coefficients in a plane or bidimensional fast reactor lattice, neglecting terms of order B^2 or above. The case where sodium is in and the case where sodium is voided are calculated according to the same approximations, which is very important to get a correct estimation of the difference effect. Angular correlation terms appear to be small, if not negligible, at least in rod lattices, as shown by numerical values given in Table II. If these terms can be neglected, coupling between energies disappers. Other numerical values for diffusion coefficients shall be given in a future paper.

REFERENCES

1. P. KÖHLER, J. LIGOU - The Axial Streaming in Gas-cooled Fast Reactors, EIR-244, Würenlingen (1973).

2. P. KÖHLER, J. LIGOU - Axial Neutron Streaming in Gas-cooled Fast Reactors, Nucl. Sc. and Eng., 54, 357 (1974).

3. E. EISEMANN - Anisotrope Diffusion bei gasgekühlten schnellen Brutreaktoren, KFK - 1577, Karlsruhe (1972).

4. E.M. GELBARD, D.C. WADE, R.W. SCHAEFER, R.E. PHILIPS - Calculations of Void Streaming in the Argonne Gas-cooled Fast Reactor Critical Experiments, Nucl. Sc. and Eng., 64, 624 (1977).

5. M.J. GRIMSTONE - Methods for the Calculation of Streaming Corrected Diffusion Coefficients for Pin and Plate Cells in Fast Reactors, Proceedings of Lugano Conference : "Homogenization Methods in Reactor Physics", IAEA-TECDOC-231, p. 461 (1980).

6. E.A. FISCHER - Neutron Streaming in Fast Reactor Slab Lattices and in Cylindrical Channels, Nucl. Sc. and Eng., 78, 227 (1981).

7. P. BENOIST - Formalisme pour le calcul de l'effet de la vidange du sodium sur les fuites de neutrons dans un réacteur rapide, CEA-R 5121, Saclay (1981).

8. P. BENOIST - Théorie du coefficient de diffusion des neutrons dans un réseau comportant des cavités, CEA-R 2278, Saclay (1964).

9. P. BENOIST - Streaming Effects and Collision Probabilities in Lattices, Nucl. Sc. and Eng., 34, 285 (1968).

10. T. DURACZ - Private Communication.

11. V.C. DENIZ - The Homogenization Procedure for Lattices, Homogenized Diffusion Coefficients and the Eigen-Coefficient Approach, Proceedings of Munich Conference : "Advances in Mathematical Methods for the Solution of Nuclear Engineering Problems", Vol. 1, p. 161, ANS-ENS (1981).

12. V.C. DENIZ - Study of the Kinetics of Thermalized Neutrons Populations in Multiplying or Non-Multiplying Heterogeneous Media, Nucl. Sc. and Eng. 28, 397 (1967).

13. C. YANG, P. BENOIST - Interaction des fuites de neutrons en réseau hétérogène et de l'anisotropie du choc, CEA Report, to be published, Saclay (1982).

DEVELOPMENT AND VALIDATION OF A METHOD TO TREAT LARGE INTERNAL VOIDS IN REACTOR DESIGN CALCULATIONS

R. M. Lell, R. B. Pond, and S. K. Bhattacharyya
Argonne National Laboratory
9700 South Cass Avenue
Argonne, Illinois 60439

ABSTRACT

A method is presented for the inclusion of an extended void region, the TREAT Upgrade hodoscope slot, in diffusion theory neutronics calculations. A line-of-sight transmission matrix is generated and used to compute the contribution from any mesh interval adjoining the slot to the incoming partial current at any other mesh interval on the slot boundary. This incoming partial current is used to formulate boundary conditions which are embedded in a diffusion theory neutronics treatment. Analytical validation efforts show very good agreement between this method and S_N and Monte Carlo calculations. This method also agrees satisfactorily with experimental measurements of eigenvalue and power distribution.

I. INTRODUCTION

The problem of voids in reactor calculations is an old one in reactor physics. Generally a void is present in a reactor core due to accidental circumstances, e.g., loss of coolant or core collapse, or to the use of gas as a coolant. On rare occasions the void is an integral part of the reactor design as in the cases of the planned TREAT Upgrade reactor[1] and the existing TREAT reactor.[2] For these reactors, a radial rectangular void exists in the core to permit monitoring of target fuel motion during transient tests at the facility performed in support of the LMFBR safety program in the United States.

The presence of a void always complicates reactor physics because neutron streaming in the void causes significant changes in neutron leakage, often in a preferred direction. In TREAT Upgrade the problem is particularly severe because the void is large and localized on one side of the core. The resulting streaming plus the imbalance in the core fuel distribution lead to a strong azimuthal dependence in the core power distribution.

Accurate analysis of the effects of an extended, irregular void such as that in TREAT Upgrade is very often difficult because of problems with all of the standard computational techniques. Traditionally, a core containing such a void is analyzed by transport theory methods, particularly S_N and Monte Carlo However, both cost and time considerations preclude the use of standard transport theory methods for repetitive design calculations such as those required for the TREAT Upgrade design effort.

Standard diffusion theory methods are inadequate for this analysis for various reasons. Classical diffusion theory fails because the diffusion coefficient becomes infinite in the void. Standard cell homogenization techniques, even

those based on anisotropic diffusion coefficients such as the Benoist method,[3] are inapplicable because no basic unit cell exists in TREAT Upgrade.

The simplest solution to the void problem in TREAT Upgrade is to fill the void with a material having a high diffusion coefficient and very little absorption. The material may be fictitious or real, e.g., low density sodium or aluminum. This approach is useful for basic calculations, but its accuracy is limited. Test calculations for TREAT Upgrade with sodium in the void have shown that the eigenvalue and the flux distribution are quite sensitive to the sodium density. Further, even the best of these calculations compared poorly with a corresponding S_N calculation.

An approach that has been used successfully for the void problem involves the use of transport theory methods to generate anisotropic diffusion coefficients for the void. A set of these transport-corrected diffusion coefficients can be used for a family of closely related diffusion calculations. Both Monte Carlo and S_N calculations have been used as a basis for the generation of transport-corrected diffusion coefficients.[4,5] The principal drawback of this method is the necessity for a new transport calculation and regeneration of the diffusion coefficients whenever the diffusion problem configuration varies too much from that of the base transport calculation.

To overcome the drawbacks of the various diffusion coefficient schemes, a transport treatment of the void in TREAT Upgrade was embedded in a diffusion theory treatment of the rest of the core. The void in TREAT Upgrade is a rectangular parallelepiped formed by removing all material from the active fuel length of the central column of fuel elements in a radius from the core center to the northern face of the core. This void will be referred to as a slot hereafter because it is commonly called the hodoscope slot in references to TREAT and TREAT Upgrade.

The concept of coupling a transport theory calculation of a portion of a reactor core with a global diffusion calculation is not new; it has been done in many forms over the years for a variety of purposes.[6-8] In the method adopted here, the transport calculation of neutron streaming in the TREAT Upgrade slot becomes a part of the actual diffusion calculation rather than an auxiliary procedure.

II. LINE-OF-SIGHT (LOS)-DIFFUSION METHOD

The method presented here has been described in greater detail previously.[9] This presentation is only intended to summarize key features for clarity in the following sections. The global calculation for the core is based on the standard finite difference diffusion formulation. Neutron streaming in the slot is accounted for through the use of a line-of-sight transmission matrix which relates the partial current entering the void from any mesh interval on the slot boundary to the partial current entering any other mesh box on the boundary from the slot.

Two assumptions are made in deriving the line-of-sight (LOS) matrix. First, the axial dimension leakage is treated through the assumption of an axial

buckling on the slot surface and in the core. This reduces a three-dimensional calculation to two dimensions. Second, the flux on the surface of the slot is assumed to be isotropic. A more elaborate treatment of the angular dependence is, in principle, possible, but the resulting equations and calculational procedure become much more complex. The net effect of these two assumptions can only be assessed through the validation procedure discussed below.

Define J^m_{in} to be the total partial current entering mesh box m from the slot, J^n_{out} to be the total partial current entering the slot from mesh box n, and J^{mn}_{in} to be that portion of J^n_{out} that streams through the slot and enters mesh box m. Based on the buckling and isotropic flux assumptions, J^{mn}_{in} can be computed for every mesh box on the slot boundary. From the calculation of J^{mn}_{in} for all m and n, one can define a matrix L whose element L_{mn} is such that

$$J^{mn}_{in} = L_{mn} J^n_{out}$$

and, consequently,

$$J^m_{in} = \sum_{n=1}^{N} J^{mn}_{in} = \sum_{n=1}^{N} L_{mn} J^n_{out}$$

where N is the total number of mesh boxes on the slot boundary. L is what is meant by the line-of-sight transmission matrix. Given the basic assumptions about the axial buckling and isotropic flux stated earlier, computation of L is strictly a matter of geometry, depending only on the mesh structure in the diffusion calculation.

In this method, no calculations are actually performed in the slot. J^m_{in} is calculated for each mesh box m on the slot boundary. J^m_{in} is then used to formulate a boundary condition for mesh box m. This boundary condition replaces the partial current that would enter mesh box m from its neighbor in the slot in a conventional calculation. In other words, the normal coupling of mesh box m to its neighbor in the slot is replaced with a coupling to all mesh boxes on the slot boundary through L and the boundary condition.

This procedure, referred to hereafter as the LOS-diffusion method, was implemented in the diffusion module of the DIF3D code.[10] During each inner iteration, fluxes are computed by the standard procedure for all mesh boxes which do not border the slot. For any mesh box m on the slot boundary, the normal iteration procedure is altered to compute J^m_{in}, convert it to the required boundary condition, and include the boundary condition in the equations for the flux in m. All mesh boxes that lie within the actual slot are skipped in the calculation.

The only required parameter for the LOS-diffusion method is the axial buckling on the surface of the slot, B_z. To obtain B_z, an S_N calculation is performed

in the plane normal to the principal axis of the slot. The resulting axial flux profiles are fitted with a cosine shape as a function of distance from the slot. This gives one B_z as a function of position and allows one to determine B_z on the slot surface. For a multigroup calculation, the multigroup B_{zg}'s are collapsed according to the equation

$$B_z^i = \left[\sum_{g=1}^{G} B_{zg}^i \, \phi_g^i \, \sigma_{fg}^i \right] \Bigg/ \left[\sum_{g=1}^{G} \phi_g^i \, \sigma_{fg}^i \right]$$

for position i and group g.

III. VALIDATION OF LOS-DIFFUSION METHOD

a) Analytical

The first step in the validation of the LOS-diffusion method was a series of comparisons with S_N and Monte Carlo calculations for corresponding TREAT Upgrade core models. The core for TREAT Upgrade (referred to as TU hereafter) consists of a 19 × 19 array of four inch square fuel elements surrounded by graphite reflector elements. The fuel in the element consists of UO_2 dispersed in graphite which is then sealed in a 25 mil Inconel can. The uranium concentration in the TU core is strongly position dependent. It varies both with radius and with azimuthal angle from the slot.

Three separate TU core models, A, B, and C, were constructed for the validation. The simplest of these, Model A, is shown in Fig. 1. This model retained most of the key features of TU while dispensing with details. The region labelled DRIVER contains the existing TREAT fuel elements that will be used in TU. TARGET denotes the in-pile test loop and target pins in TU. Regions C1, C2, and C3 are the modified portions of the core. For simplicity, all of the individual fuel elements and compositions were coalesced into C1, C2, and C3 with representative compositions. All region boundaries were made square for convenience.

Axial leakage was neglected in Model A to simplify the S_N calculation. Axial leakage in the S_N calculation is represented by a DB^2 term. For the rest of the core, D is defined, and B^2 is easy to compute. In the slot, however, D is not defined, and it is very difficult to find values for D and B^2 such that both planar and axial components of neutron streaming are accurately treated. This difficulty never arises in the LOS-diffusion method because no calculations are actually performed within the slot. To avoid complications, infinite height was assumed for the comparisons.

Both one-group and four-group calculations were carried out for Model A to test the importance of group structure. For purposes of comparison, the one-group calculation was repeated as a conventional diffusion calculation with varying densities of sodium in the void. The computed eigenvalues are shown in Table I. It is obvious that the LOS-diffusion and S_N eigenvalues do not

differ significantly. The eigenvalues for the conventional diffusion calculations do differ from the S_N case. Further, the eigenvalue in the conventional diffusion calculation changes significantly as the sodium density changes.

The LOS-diffusion method would be of little value for core design purposes if it reproduced eigenvalues well but failed to compute fluxes accurately. The LOS-diffusion fluxes were compared with corresponding S_N fluxes for Model A Figures 2 and 3 show the ratio of the S_N flux to the LOS-diffusion flux for groups 1 and 4 of the multi-group calculations. These contour plots show that the flux agreement is generally good with three localized exceptions. The first is near the outer boundary of the reflector. The disagreement near the outer boundary has nothing to do with the LOS-diffusion method. It is caused by the difference between the vacuum boundary condition in the S_N calculation and the zero flux boundary condition in the diffusion calculation. The error caused by forcing the flux to zero on the boundary propagates into the reflector, causing the error shown. The second exception occurs at the core center. The in-pile test loop in TU is highly absorptive, giving rise to a severe transport effect in the test loop. The size of the effect is increased by the errors introduced by the LOS-diffusion method, but the effect is predominantly a transport effect caused by the increased absorption in the test loop. The third exception is along the border of the slot. This error is a consequence of the approximations in the LOS-diffusion method, particularly the isotropic flux assumption. The error along the slot is small and highly localized. It has little effect on the global calculation. In contrast, the calculations with sodium in the slot showed large flux errors throughout the core and, as one would expect, the size of the errors depended on the sodium density in the slot.

Model B was constructed from Model A to study axial effects. B is identical to A except that B has a height of 161 cm, corresponding to the extrapolated height of the core. Because of the problem with a buckling in the slot, Monte Carlo was used to provide the transport solution. For the LOS-diffusion calculation, axial leakage in the core was accounted for by a DB^2 term; in the slot, the leakage was represented through the B_z parameter in the LOS matrix. Table I shows the eigenvalue comparison between Monte Carlo and LOS-diffusion. Flux comparisons were not possible due to the difficulty in calculating pointwise fluxes by Monte Carlo.

The simplified models of the TU core used for the preceeding calculations neglect many of the finer details of the core, particularly the strong dependence of uranium concentration on position in the TU core and the resulting fine structure in the flux profile. Model C was constructed to asertain how accurately the LOS-diffusion method computes highly localized effects. Model C is an exact representation of the TU core except that the axial leakage is ignored. The LOS-diffusion method was compared with S_N in four group calculations of Model C.[11] The eigenvalue comparison is shown in Table I. A contour plot of the ratio of the pointwise diffusion power density to the S_N power density is shown in Fig. 4. The eigenvalue agreement is excellent, and the agreement between the power distributions is also very good except in the localized regions discussed above.

The agreement between eigenvalues computed with the LOS-diffusion method and corresponding S_N and Monte Carlo eigenvalues is excellent for all of the core models studied. The flux comparisons are also very good globally. The local flux errors along the slot in the LOS-diffusion method are small and easy to compensate for. For TU design calculations, the LOS-diffusion method is an acceptably accurate and economical substitute for the transport calculations that would otherwise be required.

b) Experimental

Validation of the LOS-diffusion method against more accurate computational techniques is necessary but not sufficient for its intended uses. The method is intended for the design of the TU core. To determine whether the actual core will perform according to the analytical predictions, the method must be validated against experimental measurements. Ideally the experimental measurements are made on a critical assembly that mocks up the essential features of the real system. In this case, such a comparison is not possible because no dedicated criticals have been performed for TU. Further, the available experimental measurements are quite limited because the slot geometry that exists in TU is rarely encountered in other reactors. There are measurements available from the initial TREAT configuration[2] and from critical experiments performed on the ZPR-9 facility at Argonne National Laboratory in support of the STF test reactor core design work.[12] The TU spectrum is intermediate between the soft TREAT spectrum and the hard STF-critical assembly spectrum.

The initial TREAT configuration is shown in Fig. 5. The locations within the shaded boundary contain fuel elements; the outer three rings contain reflector elements. TREAT fuel elements are similar to TU fuel elements except that the uranium concentration in TREAT fuel is uniform and that the Inconel can material is replaced by zircalloy in the active fuel region and by aluminum in the reflector regions. The radial half slot was formed by removing elements K1 through K10 from column K of the matrix.

Because of the effects of errors and bias in the basic cross section data and processing, the eigenvalue is of less value than the reactivity worth of the slot as a measure of computational accuracy. For the initial TREAT configuration, the measured worth of the radial half slot is 3.12% Δk. The worth computed by the LOS-diffusion method is 3.27% Δk. More detailed comparisons of local fission rates could not be made because experimental data on fission rate distributions is not available.

The basic reactor layout for the STF-critical is shown in Fig. 6. The fuel elements for this assembly consisted of aluminum drawers containing plates of enriched uranium, iron, and stainless steel. The active fuel length was 182.88 cm; a 27.94 cm axial reflector of iron and steel was placed at each end of the drawer. Each matrix element was 5.5245 cm square. The crosses in the figure denote drawers which contained no uranium. In the reference configuration, all drawer locations were occupied.

Three slotted configurations were studied. A radial single drawer slot was formed by removing the active fuel region from those drawers marked with an H in Fig. 6. Next, a diametral single drawer slot was formed by removing the

active fuel region from all drawers marked H or F. Finally, a radial triple width slot was formed by removing all drawers marked H or T. The slot height was 182.88 cm; the slot did not extend into the axial reflectors.

It was necessary to use the method mentioned above to compute B_z for each slot configuration. Because the S_N calculation is done in a plane normal to the principal axis of the slot, the radial and diametral single drawer slots appear identical in the calculation and have the same B_z. For a narrow slot such as the single drawer slot, the axial buckling is only weakly dependent on position near the slot, and B_z on the slot surface differs by only a few percent from the geometric buckling of 0.013158 cm^{-1}. The three drawer width slot causes a significant decrease in buckling near the slot, reducing B_z to 0.009270 cm^{-1} on the slot surface. These calculated results are in qualitative agreement with experimental fission traverse data that indicate that the slot does cause a slight reduction in buckling nearby.

The worths of the three slot configurations were measured by a source jerk technique. The measured and calculated worths are shown in Table II. It is not clear why the accuracy of the calculation (as measured by C/E) changes so much between the radial and diametral single drawer slots. In the case of the triple width radial slot, the C/E could have been reduced by including the reduced buckling in the calculation for the assemblies near the slot. The calculation was performed without including the local decrease in buckling caused by the slot. If this factor had been included, the calculated slot worth would have decreased, reducing C/E.

Power distributions were measured by fission rate traverses for the radial and diametral single drawer slots. The f^{28}/f^{25} ratio measured at the core center of the reference configuration was used to correct the experimental data for the ^{238}U fission rate in the 93% enriched mapping foils. The calculated data are the ^{235}U fission rates. The calculated and measured data for the two single drawer slot configurations are shown in Figs. 7 and 8. The various symbolic lines represent calculated data; each such line has an associated symbol representing the measured data. All data are normalized to 900 in Row 29/Column 23.

Figures 7 and 8 show that the calculated data follow the shapes of the measured data and even show the same small periodic blips of the measured data. These blips occur where the non-fuel drawers, i.e., those denoted by a cross, are located.

IV. SUMMARY

The LOS-diffusion method agrees quite well with S_N and Monte Carlo calculations. The eigenvalue agreement is excellent; the flux correspondence is quite good except for a small error near the slot boundary. The agreement between measured and calculated slot worths and power distributions is reasonably good. The LOS-diffusion method has proven very effective for TU design and calculations. With some modification, this method should be applicable to other configurations containing large internal voids.

V. REFERENCES

1. S. K. Bhattacharyya, et al., "Physics Design of the Upgraded TREAT Reactor," Proc. ANS Topical Meeting on Advances in Reactor Physics and Shielding, Sun Valley, Idaho, September 14-17, 1980.

2. F. Kirn, et al., "Reactor Physics Measurements in TREAT," ANL-6173, Argonne National Laboratory, October 1960.

3. P. Benoist, "Theorie du Coefficient de Diffusion daus un Réseau Comportant des Cavités," CEA-R2278, Centre d'Etudes Nucléaires-Saclay, 1964.

4. J. P. Odom, et al., "Monte Carlo Diffusion Modeling of Void Effects," Trans. Am. Nuc. Soc., Vol. 23, p. 527 (1976).

5. D. J. Malloy, "Response Matrix Directional Diffusion Coefficients for Application Within Large Cavities," Proc. ANS Topical Meeting on Advances in Reactor Physics and Shielding, Sun Valley, Idaho, September 14-17, 1980.

6. G. Klotzkin, et al., "A Method of Monte Carlo Fitting," Nucl. Sci. Eng., Vol. 57, p. 218 (1975).

7. M. R. Mendelson, et al., "Two-Dimensional Blackness-Theory Boundary Conditions - RZ Geometry," Trans. Am. Nuc. Soc., Vol. 12, No. 1, p. 210 (June 1969).

8. W. Bernnat, W. Klumpp, and P. Holder, "Treatment of Big Cavities in Diffusion Calculations by Monte Carlo Response Matrices," Atomkernenergie, Vol. 26, p. 153 (1975).

9. E. M. Gelbard, et al., "Treatment of Internal Rectangular Voids in Diffusion Theory," Trans. Am. Nuc. Soc., Vol. 35, p. 233 (November 1980).

10. D. R. Ferguson and K. L. Derstine, "Optimized Iteration Strategies and Data Management Considerations for Fast Reactor Finite-Difference Diffusion Theory Codes," Nuc. Sci. Eng., Vol. 64, p. 593 (1977).

11. R. S. May, Private Communication.

12. R. B. Pond and W. R. Robinson, "Gap, Slot, and Fuel Rotation Worths in STF All-Converter Mockup Assembly," Reactor Development Program Progress Report, ANL-RDP-81, pp. 4.8-4.11.

TABLE I. Eigenvalue Validation of LOS-Diffusion Method - Analytical

Configuration	Number of Groups	k_L LOS-Dif.	k_T Transport	k_L/k_T
TU Model A	4	1.2694	1.2711	0.9987
TU Model A	1	1.2422	1.2414	1.0006
TU Model A,[a] 100% T.D. Sodium	1	1.2380[a]	1.2414	0.9973
TU Model A,[a] 10% T.D. Sodium	1	1.2303[a]	1.2414	0.9911
TU Model A,[a] 1% T.D. Sodium	1	1.2187[a]	1.2414	0.9817
TU Model B	1	1.1419	1.1402 ± 0.0022	1.0015
TU Model C	4	1.2830	1.2849	0.9985

[a]Classical diffusion theory with sodium in the slot.

TABLE II. Experimental Validation of LOS-Diffusion Method-Slot Worth

Configuration	B_z, cm^{-1}	Slot Worth Calculated	Slot Worth Measured	C/E
TREAT Initial Core	0.019073	3.27%	3.12%	1.048
STF Critical				
Single Drawer Width Radial Half Slot	0.013158	1.555%	1.608% ± 0.005%	0.967 ± 0.003
Single Drawer Width Diametral Full Slot	0.013158	2.851%	3.219% ± 0.017%	0.886 ± 0.005
Triple Drawer Width Radial Half Slot	0.009270	5.917%	5.180% ± 0.055%	1.142 ± 0.012

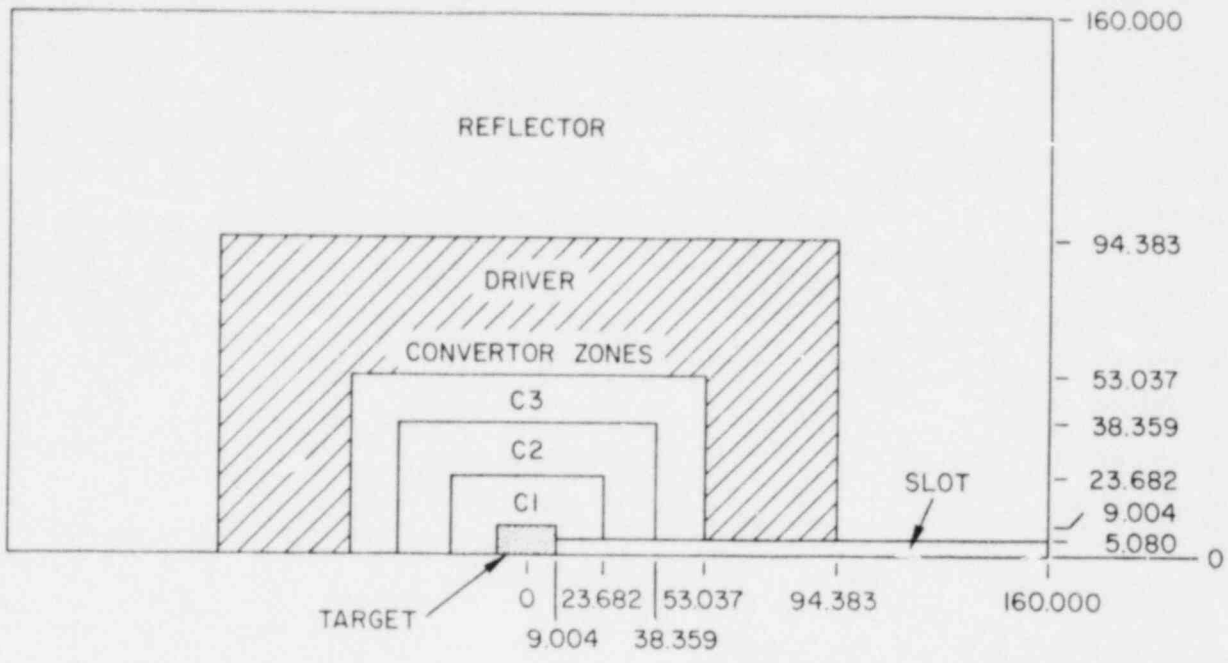

Fig. 1 TREAT Upgrade Core Model A

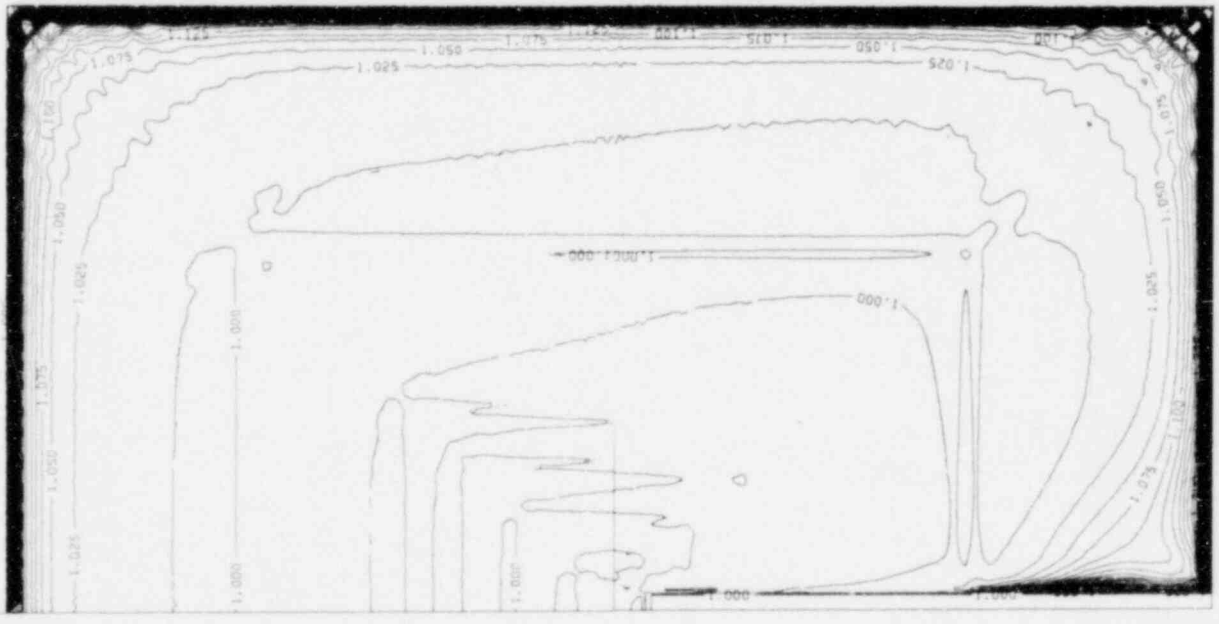

Fig. 2 TU Core Model A - $\phi(S_N)/\phi$(LOS-Dif) for Group 1

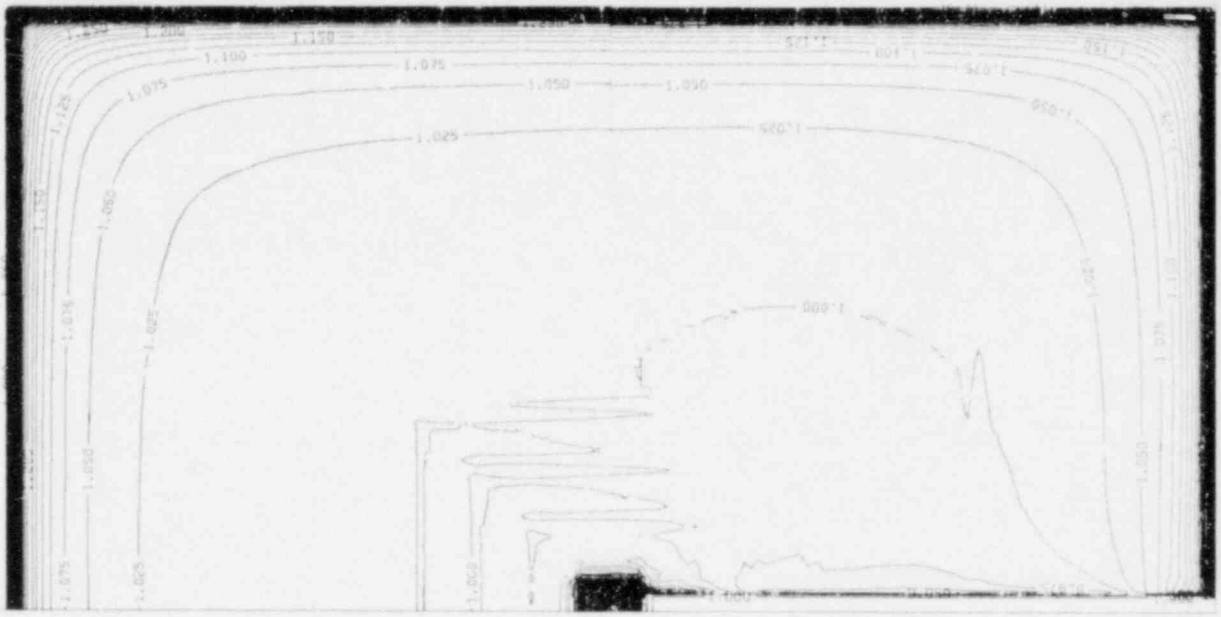

Fig. 3 TU Core Model A - $\phi(S_N)/\phi$(LOS-Dif) for Group 4

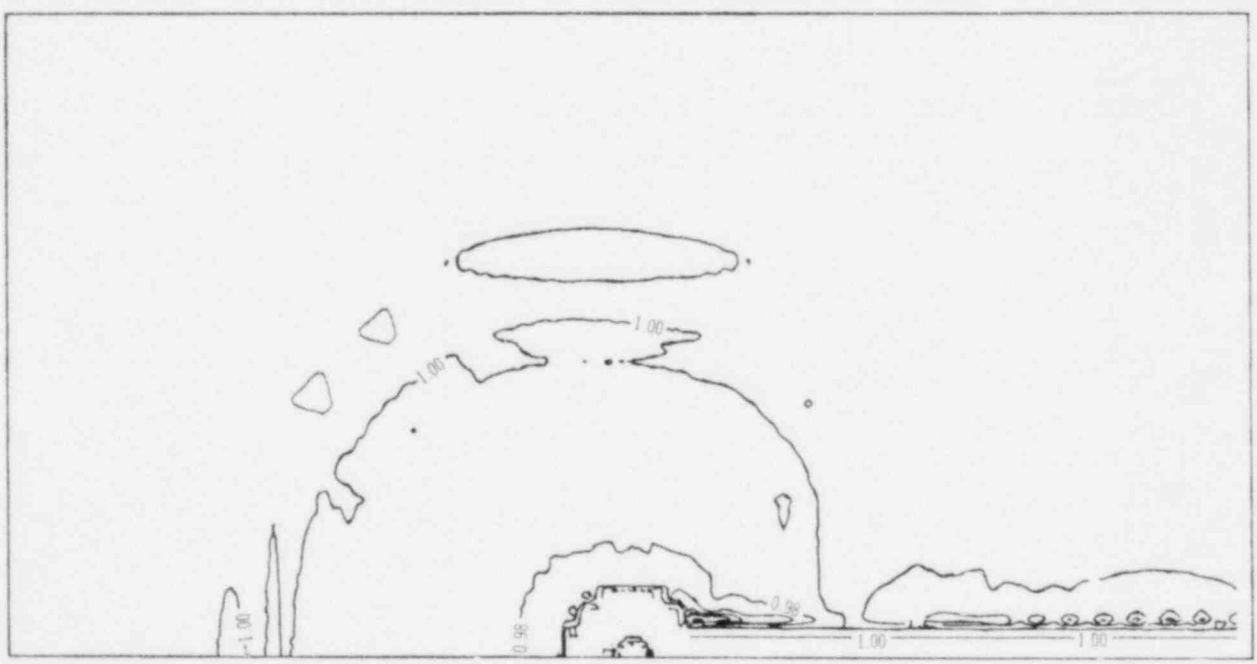

Fig. 4 TU Core Model C - Power Density Ratio, LOS-Diffusion/S_N

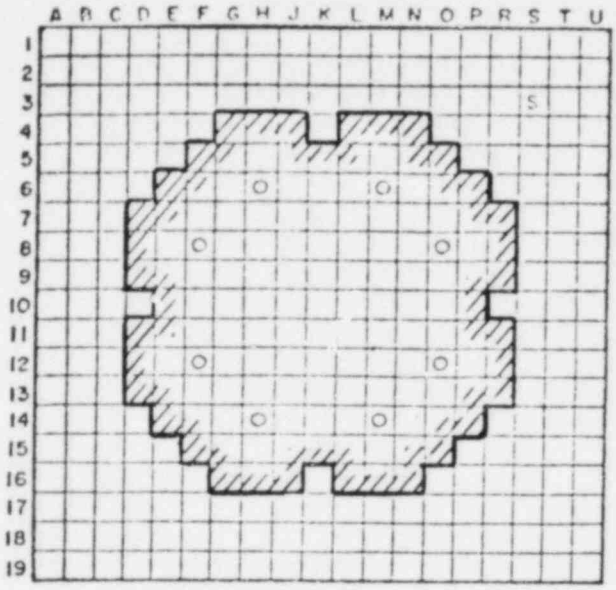

Fig. 5 Initial TREAT Core Configuration

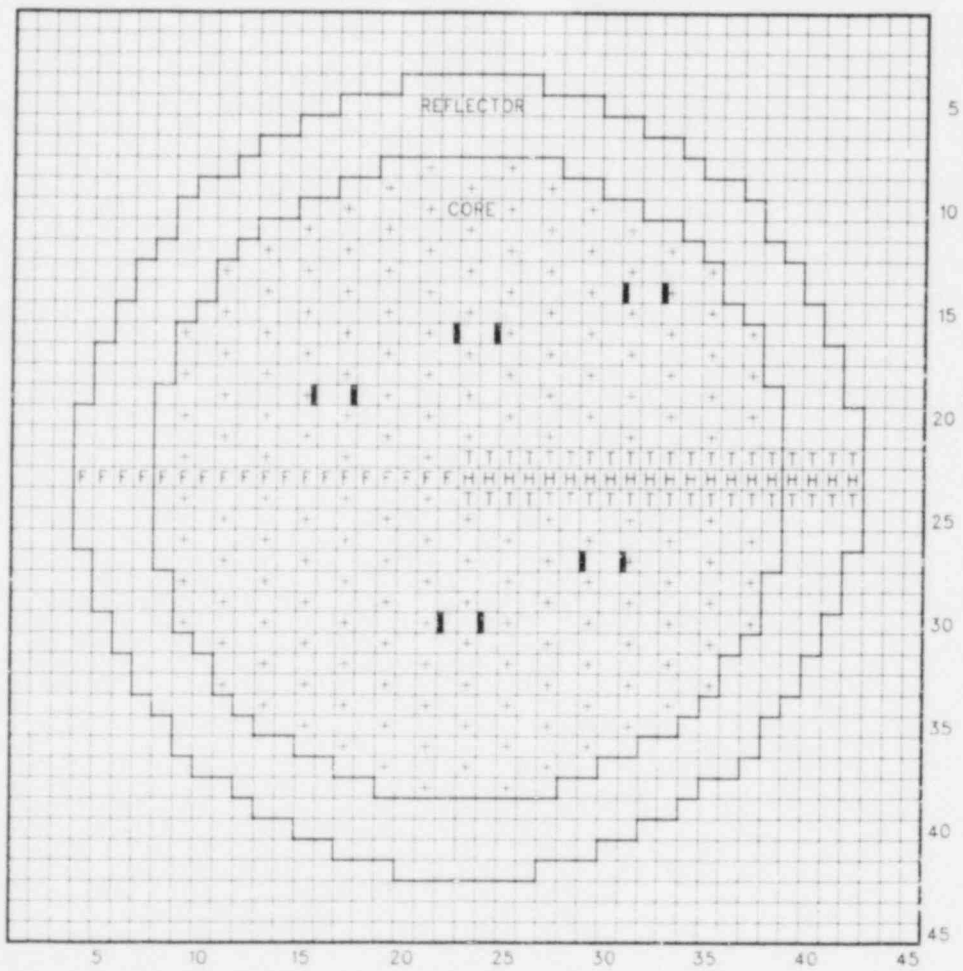

Fig. 6 STF Half-, Full- and Triple-Slot Configurations

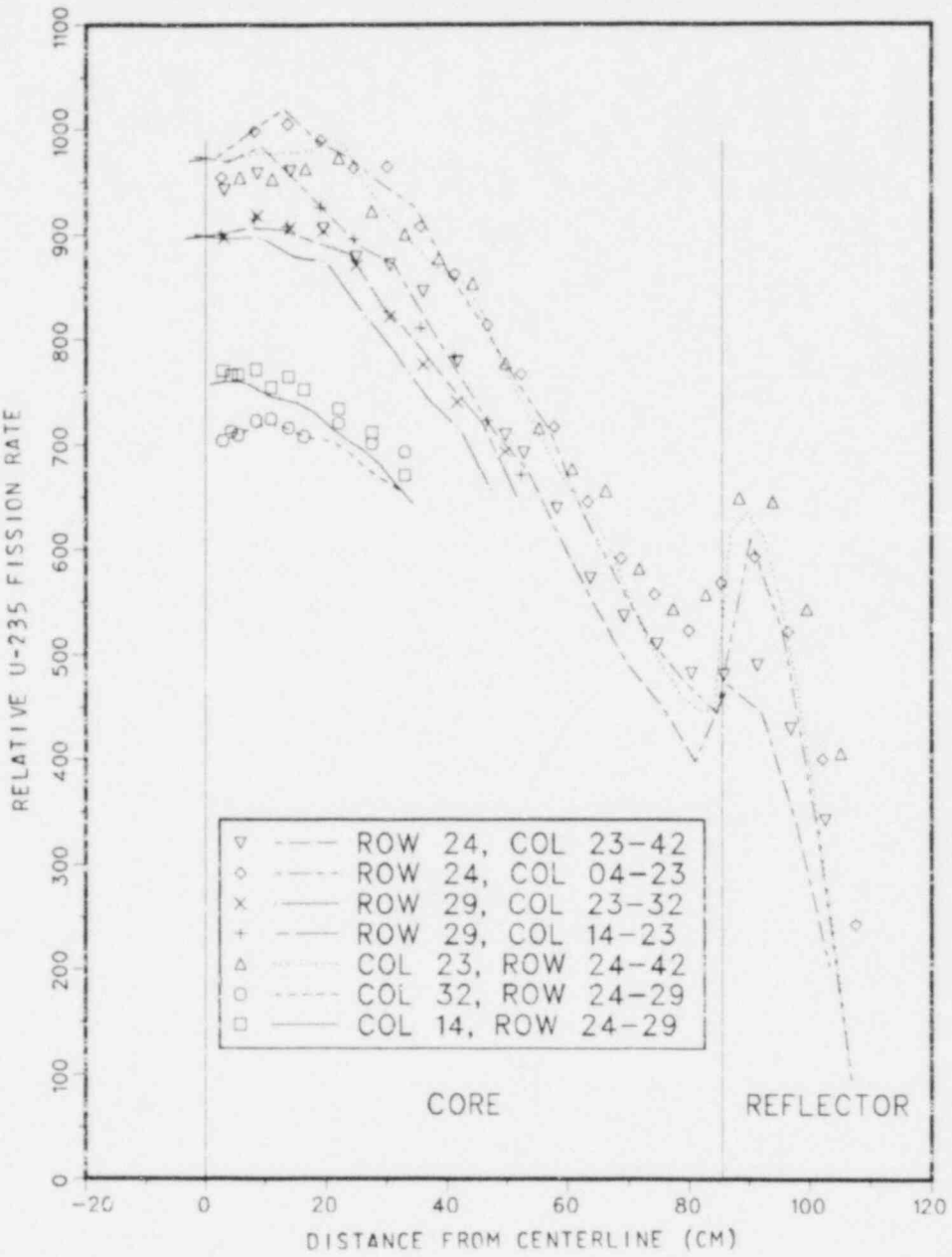

Fig. 7 Relative Fission Rate Distributions in the STF Half-Slot Critical Configuration.

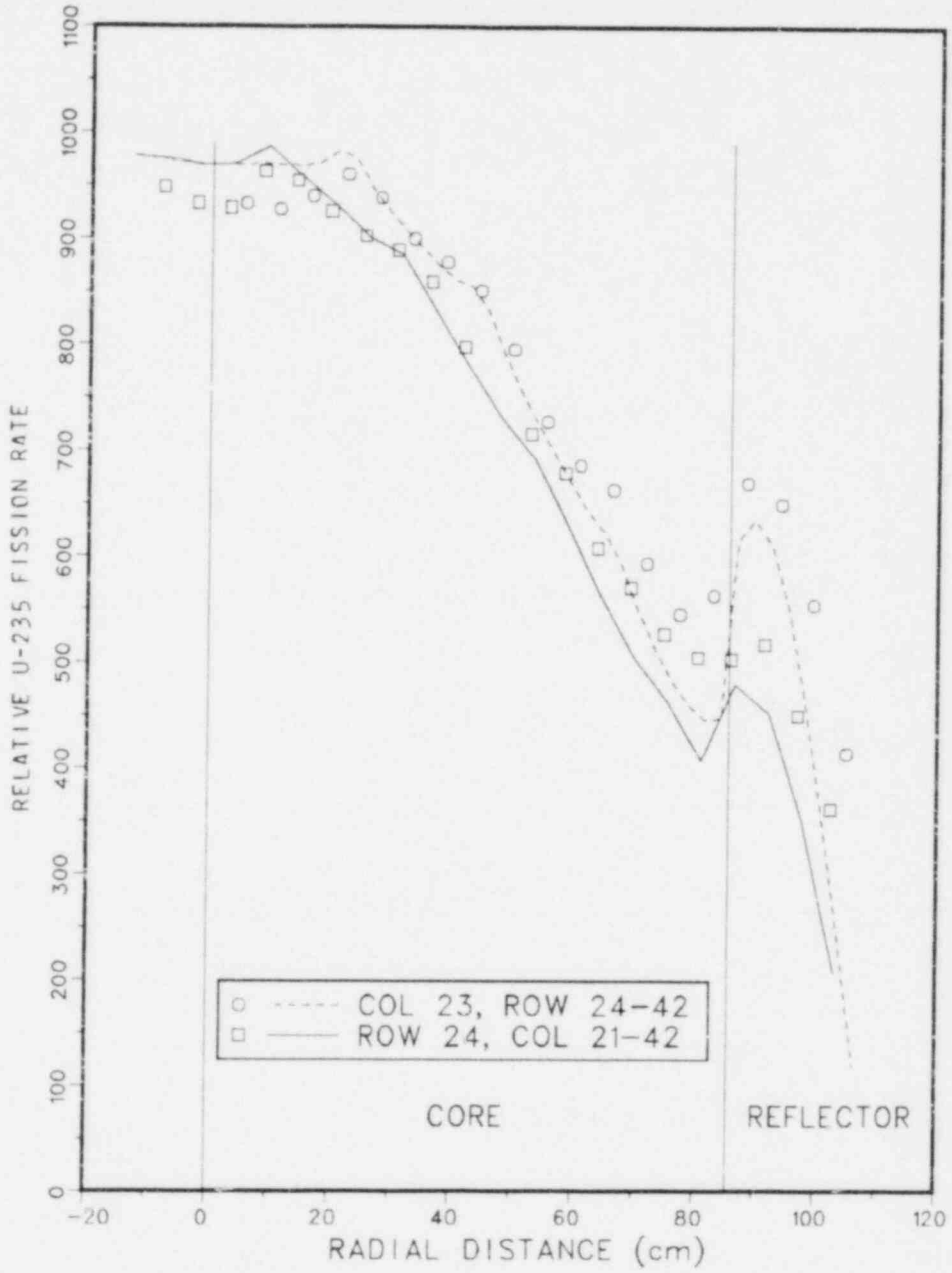

Fig. 8 Relative Fission Rate Distributions in the STF Full-Slot Critical Configuration.

A THEORETICAL METHOD OF ANALYSIS OF NONLINEAR REACTOR DYNAMICS

M. Podowski
Department of Nuclear Engineering
Rensselaer Polytechnic Institute
Troy, New York

ABSTRACT

The analysis of stability in bounded domains of initial perturbations is presented for nonlinear point kinetics models. It is shown that the method proposed can also be used to establish relationships between the magnitude of initial trajectories and that of the reactor responses. In particular, an analytical expression is derived for the peak power of a reactor subjected to a sudden reactivity increase. The results of theoretical evaluation are compared with those of computer calculations, showing a good agreement. Some extensions to nodalized space dependent models are discussed.

1. INTRODUCTION

Due to the fast development of computer techniques in recent years, numerical methods of analysis of reactor dynamics have considerably prevailed over the theoretical ones. In particular, complex computer codes in the time domain, based on sophisticated models for both reactor physics and thermal-hydraulics, have become the dominant tool. Although the accuracy of such codes is very high, such an approach has some considerable limitations inherently built in. One of them is the high computer cost, especially if a general parametric analysis of a reactor is required. Another aspect, perhaps even more significant, concerns the fact that some important system characteristics can be overlooked or misinterpreted if the theoretical analysis is ignored. Particularly, the above applies to the question of reactor stability. Although theoretical methods are very difficult to apply in advanced reactor dynamics, they prove very useful in exploring fundamental characteristics of less sophisticated reactor models [1,2]. The above especially refers to nonlinear models, since the linear stability analysis (in the frequency domain) has been successfully accomplished for quite complex systems [3,4].

The objective of this paper is to show that various problems arising from nonlinear reactor dynamics can be solved by using the analytical method introduced in Ref. 5. The method was originally focused on the analysis of nonlinear stability in bounded domains of initial perturbations for reactor models with arbitrary reactivity feedbacks. As reported in the present paper, the concept proposed in Ref. 5 can be extended to a more general class of problems, such as establishing relationnships between the magnitude of initial trajectories and those of the reactor responses. It is also shown that this method can be combined with that used in Ref.6 and applied to the analysis of nodalized space dependent models.

2. METHOD OF ANALYSIS

Consider a point reactor model,

$$\dot{P} = \frac{\varrho-\beta}{\ell} P + \sum_{i=1}^{K} \lambda_i C_i \tag{2.1}$$

$$\dot{C} = \frac{\beta_i}{\ell} P - \lambda_i C_i \qquad (i=1,\ldots,K) \tag{2.2}$$

with the reactivity, ϱ, given by,

$$\varrho = \varrho_o + \varrho_f \tag{2.3}$$

where the feedback reactivity, ϱ_f, takes the form of a time-invariant, in general - nonlinear functional,

$$\varrho_f(P) = \varrho_f\{P(\tau),\ -\infty<\tau\leq t\} \tag{2.4}$$

Setting $\varrho_f(0)=0$, yields $\varrho_o>0$.

Assuming that P_o is a nonzero steady state solution of Eqs.(2.1)-(2.3), we can rewrite Eq.(2.3) as,

$$\varrho(x) = \varrho\{x(\tau),\ -\infty<\tau\leq t\} \tag{2.5}$$

where $x=(P-P_o)/P_o$, and $\varrho(0)=0$.

Several interesting properties of system (2.1)-(2.3) can be explored by using a Liapunov functional of the form [5],

$$V = F[x(t)] + \sum_{i=1}^{K} (\beta_i/\ell\lambda_i) F[z_i(t)] + [Q(x)](t) \tag{2.6}$$

where*,

$$F(u) = u - \ln(1+u) \tag{2.7}$$

$$z_i(t) = \lambda_i \int_{-\infty}^{t} \exp -\lambda_i(t-\tau)\, x(\tau)\, d\tau \tag{2.8}$$

$$[Q(x)](t) = -\frac{1}{\ell}\int_{-\infty}^{t} \exp\left[-2\mu(t-\tau)\right] x(\tau)\, [\varrho(x)](\tau)\, d\tau \qquad (\mu>0) \tag{2.9}$$

In general, the concept of Liapunov functional can be applied in the analysis of stability of the solution $x(t)=0$ ($P(t)=P_o$). The unique feature of the functional given by Eqs.(2.6)-(2.9) is that by using it we can not only establish conditions for stability, but also evaluate allowable domains of initial functions for which the perturbed trajectories asymptotically return to the original steady state level.

Differentiating Eq.(2.6) with respect to t along any trajectory of system (2.1)-(2.3) yields,

$$\dot{V} = -\sum_{i=1}^{K} (\beta_i/\ell) \frac{(x-z_i)^2}{(1+x)(1+z_i)} - 2\mu[Q(x)](t) \tag{2.10}$$

Let us now assume that there exist such numbers $m_1<0<m_2$ that if $m_1\leq x(t)\leq m_2$ for t $(-\infty,\infty)$, then the inequality holds,

$$[Q(x)](t) \geq 0 \qquad \text{for } t\geq 0 \tag{2.11}$$

(*) An extension of the functional given by Eqs.(2.6)-(2.9), based on a modified stability concept, is discussed in Ref. 7.

It follows from Eq.(2.9) that

$$\left|\left[Q(x)\right](t)\right| \leq \frac{1}{2\mu\ell} \sup_{\tau \leq t} |x(\tau)| \quad \sup_{\tau \leq t} \left|\left[\rho(x)\right](\tau)\right| \leq \Psi(\sup_{\tau \leq t} |x(\tau)|) \tag{2.12}$$

where $\Psi(u)$ is a continuous nondecreasing function, and $\Psi(0)=0$. Hence, it can be shown that any solution $P(t)=P_o\left[1+x(t)\right]$ of system (2.1)-(2.3) with the initial function, $x(t)$ for $t \leq 0$, satisfying the inequality*,

$$F\left[x(0)\right] + \sum_{i=1}^{K} (\beta_i/\ell\lambda_i)\, F\left[z_i(0)\right] + \Psi(\sup_{\tau \leq 0} |x(\tau)|) < \min_{k=1,2} F(m_k) \tag{2.13}$$

approaches the steady state, P_o, as $t \to \infty$. In particular, it follows from Eq. (2.13) that if $\Delta_1 < 0 < \Delta_2$ are such numbers that

$$\left[1 + \sum_{i=1}^{K} (\beta_i/\ell\lambda_i)\right] F(\Delta_2) + \Psi(\Delta_2) < \min_{k=1,2} F(m_k) \tag{2.14}$$

$$F(\Delta_1) = F(\Delta_2) \tag{2.15}$$

then the set $D = \left\{ x(t) \text{ for } t \leq 0 : \Delta_1 \leq x(t) < \Delta_2 \right\}$ belongs to the domain of attraction of the solution $x(t)=0$.

Practical applications of the functional, V, given by Eq.(2.6) can be extended beyond the question of stability itself. It can also be used to establish relationships between the magnitude of initial functions and that of reactor responses. Assuming that $x(t) \in D$ for $t \leq 0$, with Δ_1 and Δ_2 satisfying Eqs.(2.14) and (2.15), we obtain from Eq.(2.6),

$$F\left[x(t)\right] + \sum_{i=1}^{K} (\beta_i/\ell\lambda_i)\, F\left[z_i(t)\right] \leq V(t) \leq V(0) \leq F\left[x(0)\right] + \sum_{i=1}^{K} (\beta_i/\ell\lambda_i)\, F\left[z_i(0)\right] + \Psi(\Delta_2) \qquad \text{for } t \geq 0 \tag{2.16}$$

In particular, Eq.(2.16) yields,

$$F\left[x(t)\right] \leq V(0) \qquad \text{for } t \geq 0 \tag{2.17}$$

where V(0) can be explicitly calculated for any given initial function. Solving Eq.(2.17) for x(t) yields the lower and upper bounds for the perturbed trajectory,

$$\eta_1 \leq x(t) \leq \eta_2 \qquad \text{for } t \geq 0 \tag{2.18}$$

where $\eta_1 < 0 < \eta_2$, and $F(\eta_1) = F(\eta_2) = V(0)$.

In the case of transients for which changes in the concentration of delayed neutrons can be neglected, Eq.(2.16) simplifies to,

$$F\left[x(t)\right] \leq F\left[x(0)\right] + \Psi(\Delta_2) \leq F(\Delta_2) + \Psi(\Delta_2) \tag{2.19}$$

For a reactor with the linear reactivity feedback given by,

$$\rho(x)(t) = \int_0^\infty x(t-\tau)\, dh(\tau) \tag{2.20}$$

the function Ψ can be expressed as,

$$\Psi(u) = \frac{M}{2\mu\ell}\, u^2 \tag{2.21}$$

where $M = \underset{\langle 0, \infty \rangle}{\text{Var}}\, h < \infty$. Thus, Eq.(2.19) can be rewritten as,

---

(*) The rigorous derivation of the criterion for asymptotic stability involves some additional conditions. In particular, $\lim_{t \to \infty} [\rho(x)](t)=0$ must imply $\lim_{t \to \infty} x(t)=0$.

$$F[x(t)] \leq F(\Delta_2) + \frac{M}{2\mu\ell}\Delta_2^2 \tag{2.22}$$

where the number $\mu > 0$ can be explicitly evaluated for any specific function $h(t)$.

The question discussed hitherto was focused on evaluating trajectory bounds for autonomous reactor systems responding initial perturbations belonging to a given set D. However, the method proposed can also be applied to the analysis of nonautonomous models subjected to external actions which do not terminate at any specific time, such as: external reactivity insertion, cold water injection, increase in coolant flow rate, etc. In particular, the evaluation of the reactor peak power following a sudden change in the reactivity due to the control rod withdrawal is presented in the next section.

3. PEAK POWER EVALUATION FOR A REACTOR SUBJECTED TO A SUDDEN REACTIVITY INCREASE

It is widely known that if a reactor undergoes a sudden external action, the largest power departure from the initial steady state occurs in a short time thereafter. The more abrupt is the perturbation of a given magnitude, the higher is the reactor peak power. Hence, it can be assumed for the purpose of the present analysis that a reactor transient is initiated at t=0 by a stepwise change in the core reactivity. Additionally, assuming that the perturbed reactor, originally operating at the power P_o, asymptotically approaches a new equilibrium level, P_1, we can relate the transient to a modified autonomous model. Namely, the unsteady state can be treated as if it was caused by the initial perturbation, $(P_o - P_1)$, from the steady state, $P = P_1$.

Assuming that a reactivity $\rho_{ext} > 0$ was inserted at t=0 into the reactor operating at the steady state, P_o, the total reactivity at $t \geq 0$ is given by,

$$\rho = \rho_{ext} + \rho_o + \rho_f(P) \tag{3.1}$$

Let the equation,

$$\rho_{ext} + \rho_o + \rho_f(P) = 0 \tag{3.2}$$

have at least one steady state solution $P = P_1 > P_o$. Setting,

$$x(t) = (P - P_1)/P_1 \tag{3.3}$$

we assume that the solution x(t)=0 is asymptotically stable, and the initial trajectory $x(t) = (P_o - P_1)/P_1 = \Delta < 0$ for $t \leq 0$ belongs to its domain of stability. Hence, P_1 is indeed the unique asymptotic equilibrium level for the transient originated at the power P_o. If ρ_{ext} is sufficiently large (as in the case of a superprompt critical reactor), delayed neutrons can be neglected, and the peak power reached during the transient can be calculated from,

$$F[(P_{max} - P_1)/P_1] \leq F(\Delta) + \Psi(\Delta) \tag{3.4}$$

As an illustration, let us consider a reactor model with the Doppler reactivity effect. We assume that the feedback reactivity is given by,

$$\rho_f = \rho_f(T) = - r(T)\, T \tag{3.5}$$

where r is the temperature dependent Doppler coefficient of reactivity, and the incremental fuel temperature, T, satisfies the equation,

$$Mc\dot{T} = P - KT \tag{3.6}$$

where M and c are respectively the mass and specific heat of fuel, K is the thermal conductance between fuel and coolant.

Assuming that r is a linear function of T, i.e,

$$r = r_1 + r_2 T \tag{3.7}$$

Eq.(3.1) takes the form,

$$\rho = \rho_{ext} + \rho_o - r_1 T - r_2 T^2 \tag{3.8}$$

where T can be evaluated from Eq.(3.6) as,

$$T = b \int_{-\infty}^{t} \exp\left[-a(t-\tau)\right] P(\tau) d\tau \tag{3.9}$$

with $a = K/(Mc)$, $b = 1/(Mc)$.

In order to find steady state solutions of Eq.(3.2) we will consider three separate cases.

a) $r_2 > 0$, r_1 - arbitrary;

Eq.(3.2) has a unique steady state solution,

$$P_1 = \frac{K}{2}\left\{-\frac{r_1}{r_2} + \left[\left(\frac{r_1}{r_2}\right)^2 + 4\,\frac{\rho_{ext}+\rho_o}{r_2}\right]^{1/2}\right\} > 0 \tag{3.10}$$

b) $r_2 < 0$, $r_1 > 0$;

Assuming that

$$r_1^2 + 4(\rho_{ext}+\rho_o) r_2 \geq 0 \tag{3.11}$$

Eq.(3.2) has two steady state solutions,

$$P_1' = \frac{K}{2}\left\{-\frac{r_1}{r_2} - \left[\left(\frac{r_1}{r_2}\right)^2 + 4\,\frac{\rho_{ext}+\rho_o}{r_2}\right]^{1/2}\right\} > 0 \tag{3.12}$$

$$P_1'' = \frac{K}{2}\left\{-\frac{r_1}{r_2} + \left[\left(\frac{r_1}{r_2}\right)^2 + 4\,\frac{\rho_{ext}+\rho_o}{r_2}\right]^{1/2}\right\} > P_1' \tag{3.13}$$

c) $r_2 = 0$, $r_1 > 0$;

The only positive solution of Eq.(3.2) is,

$$P_1 = K\,\frac{\rho_{ext}+\rho_o}{r_1} \tag{3.14}$$

If $r_2 < 0$ and $r_1 \leq 0$, Eq.(3.2) has no positive steady state solutions.

The next step in the analysis concerns stability of the asymptotic steady state solution, P_1. Inserting Eq.(3.9) into Eq.(3.8), and rearranging, we obtain for case (a),

$$\rho = -k_1 y - k_2 y^2 \tag{3.15}$$

where,

$$y = a \int_{-\infty}^{t} \exp\left[-a(t-\tau)\right] x(\tau) d\tau \tag{3.16}$$

$$k_1 = \frac{1}{K} P_1 (r_1 + 2 \frac{r_2}{K} P_1) \tag{3.17}$$

$$k_2 = \frac{r_2}{K^2} P_1^2 \tag{3.18}$$

with x(t) given by Eq.(3.3). Combining Eqs.(3.10), (3.17), and (3.18), yields,

$$k_1 > k_2 > 0 \tag{3.19}$$

Eq.(3.15) can be substituted into Eq.(2.9), to yield,

$$Q(x)(t) = \frac{1}{\ell} \int_{-\infty}^{t} \exp\left[-2\mu(t-\tau)\right] (k_1 xy + k_2 xy^2) d\tau \tag{3.20}$$

By inserting Eq.(3.16) into Eq.(3.20), and taking into account that $x(t) \geq -1$, we obtain from Eq.(2.11),

$$k_1 a \int_{-\infty}^{t} x_\mu(\tau) d\tau \int_{-\infty}^{\tau} \exp\left[-(a-\mu)(\tau-\theta)\right] x_\mu(\theta) d\theta - (k_2+c) a \int_{-\infty}^{t} y_\mu(\tau) d\tau \int_{-\infty}^{\tau} \exp\left[-(a-\mu)(\tau-\theta)\right]$$
$$x(\theta) d\theta + c \int_{-\infty}^{t} y_\mu^2(\tau) d\tau \geq 0 \tag{3.21}$$

where,

$$x_\mu(t) = \exp(\mu t) x(t) \tag{3.22}$$

with $0 < \mu < a$, and $c > 0$.
Eq.(3.21) can be transformed into the form,

$$\int_0^\infty \left\{ a k_1 H_\mu(j\omega) |X_\mu(t,j\omega)|^2 - a(k_2+c) H_\mu(j\omega) X_\mu(t,-j\omega) Y_\mu(t,j\omega) + a |Y_\mu(t,j\omega)|^2 \right\} d\omega$$
$$\geq 0 \tag{3.23}$$

where,

$$H_\mu(j\omega) = \int_0^\infty \exp\left[-(a-\mu+j\omega)t\right] dt = \frac{1}{a-\mu+j\omega} \tag{3.24}$$

$$X_\mu(t,j\omega) = \int_{-\infty}^{t} \exp(-j\omega\tau) x_\mu(\tau) d\tau \tag{3.25}$$

Replacing Eq.(3.23) by a stronger inequality,

$$\int_0^\infty \left\{ a k_1 \, \mathrm{Re} H_\mu(j\omega) |X_\mu(t,j\omega)|^2 - a(k_2+c) |H_\mu(j\omega)| \, |X_\mu(t,j\omega)| \, |Y_\mu(t,j\omega)| \right.$$
$$\left. + c |Y_\mu(t,j\omega)|^2 \right\} d\omega \geq 0 \tag{3.26}$$

we can readily show that if the inequality is satisfied for all u_1, u_2, and ω,

$$k_1 \frac{a(a-\mu)}{(a-\mu)^2+\omega^2} u_1^2 - (k_2+c) \frac{a}{\left[(a-\mu)^2+\omega^2\right]^{1/2}} u_1 u_2 + c u_2^2 \geq 0 \tag{3.27}$$

then Eq.(3.21) holds for all $t \geq 0$. Eq.(3.27) requires that the inequality,

$$c^2 + 2\left[k_2 - 2k_1(1 - \frac{\mu}{a})\right] c + k_2^2 \leq 0 \tag{3.28}$$

has at least one solution $c > 0$. The last condition is fulfilled if k_1 and k_2 satisfy Eq.(3.19). Thus, we conclude that the solution $x(t)=0$ $(P(t)=P_1)$ is globally asymptotically stable.

In case (b), Eqs.(3.15)-(3.18) can still be used, while Eq.(3.19) must be re-

placed by:

- if P_1 is given by Eq.(3.12),

$$k_1 > 0, \quad k_2 < 0 \tag{3.29}$$

- if P_1 is given by Eq.(3.13),

$$k_1 < 0, \quad k_2 < 0 \tag{3.30}$$

Let us first consider stability of the steady state P_1'. Assuming that $-1 \leq x(t) \leq \eta$ $(\eta > 0)$, and substituting Eq.(3.15) into Eq.(2.11), yields,

$$ak_1 \int_{-\infty}^{t} x_\mu(\tau)d\tau \int_{-\infty}^{\tau} \exp\left[-(a-\mu)(\tau-\theta)\right] x_\mu(\theta)d\theta - a(c-k_2\eta) \int_{-\infty}^{t} y_\mu(\tau)d\tau \int_{-\infty}^{\tau} \exp\left[-(a-\mu)(\tau-\theta)\right]$$
$$x_\mu(\theta)d\theta + c\int_{-\infty}^{t} y_\mu^2(\tau)d\tau \geq 0 \tag{3.31}$$

In the way similar to that used before we find that Eq.(3.31) is satisfied for all $t \geq 0$ if the inequality,

$$k_1 \frac{a(a-\mu)}{(a-\mu)^2+\omega^2} u_1^2 - (c - k_2\eta) \frac{a}{\left[(a-\mu)^2+\omega^2\right]^{1/2}} u_1 u_2 + c\, u_2^2 \geq 0 \tag{3.32}$$

holds for all u_1, u_2, and ω. A sufficient condition for this is,

$$\eta \leq -\frac{k_1}{k_2}\left(1 - \frac{\mu}{a}\right) \tag{3.33}$$

The above proves that the solution $P(t)=P_1'$ is asymptotically stable. The bounds for initial trajectories can be evaluated from Eq.(2.14). Neglecting delayed neutrons, taking into account that

$$\Psi(\Delta_2) = k_1\Delta_2^2 + |k_2|\Delta_2^3 \tag{3.34}$$

and substituting Eq.(3.33) into Eq.(2.14),yields,

$$F(\Delta_2) + \frac{1}{2\mu\ell}\left(k_1\Delta_2^2 + |k_2|\Delta_2^3\right) \leq F\left[\frac{k_1}{|k_2|}\left(1 - \frac{\mu}{a}\right)\right] \tag{3.35}$$

For any given k_1, k_2, and μ, Eq.(3.35) can be solved for Δ_2. Taking the largest value for Δ_2 over $\mu \in (0,a)$, and calculating Δ_1 from Eq.(2.15), yields the allowable range for the magnitude of initial functions.

Concerning the steady state P_1'', it can be easily shown that this solution is unstable (even for the linearized model).

If $r_2=0$ and $r_1>0$ (case (c)), Eq.(3.15) reduces to,

$$\rho = -k_1 y \tag{3.36}$$

where,

$$k_1 = \frac{r_1}{K} P_1 = \rho_{ext} + \rho_o \tag{3.37}$$

It follows that Eq.(2.11) can be rewritten as,

$$\int_{-\infty}^{t} x_\mu(\tau)d\tau \int_{-\infty}^{\tau} \exp\left[-(a-\mu)(\tau-\theta)\right] x_\mu(\theta)d\theta = \frac{1}{\pi}\int_0^\infty \frac{a-\mu}{\left[(a-\mu)^2+\omega^2\right]^{1/2}} |X_\mu(t,j\omega)|^2 d\omega \geq 0 \tag{3.38}$$

Thus, the solution, P_1, given by Eq.(3.14) is globally asymptotically stable.

The analysis performed so far indicates that the initial steady state (stable) operating level of the reactor model under consideration is given by,

$$P_o = \begin{cases} \frac{K}{2}\left\{-\frac{k_1}{k_2} + \left[\left(\frac{k_1}{k_2}\right)^2 + 4\,\frac{\rho_o}{k_2}\right]^{1/2}\right\} & \text{if } k_2 > 0 \\ \frac{K}{2}\left\{-\frac{k_1}{k_2} - \left[\left(\frac{k_1}{k_2}\right)^2 + 4\,\frac{\rho_o}{k_2}\right]^{1/2}\right\} & \text{if } k_2 < 0 \text{ and } k_1 > 0 \\ \frac{K}{k_1}\,\rho_o & \text{if } k_2 = 0 \text{ and } k_1 > 0 \end{cases} \tag{3.39}$$

Hence, we can use Eq.(3.4) to evaluate the reactor peak power for a given external reactivity, ρ_{ext}. For case (a) and (c) , it can be accomplished for an arbitrary $\rho_{ext}>0$, while for case (b) an additional condition must be satisfied, i.e.

$$|\Delta| = (P_1' - P_o)/P_1' \leq |\Delta_1| \tag{3.40}$$

where Δ_1 can be calculated from Eqs.(2.15) and (3.35). For all the cases uder consideration, Eq.(3.4) takes the form,

$$F\left[(P_{max}-P_1)/P_1\right] \leq F(\Delta) + \frac{1}{2\mu\ell}\,(k_1\Delta^2 + |k_2||\Delta|^3) \tag{3.41}$$

In particular, setting $k_2=0$, we obtain,

$$\Delta = (P_o-P_1)/P_1 = -\frac{\rho_{ext}}{\rho_{ext}+\rho_o} \tag{3.42}$$

Since it follows from Eq.(3.38) that $(a-\mu)$ may be made arbitrarily small, Eq. (3.41) reduces to,

$$F\left[(P_{max}-P_1)/P_1\right] \leq F\left(-\frac{\rho_{ext}}{\rho_{ext}+\rho_o}\right) + \frac{\rho_{ext}^2}{2a\ell(\rho_{ext}+\rho_o)} \tag{3.42}$$

The last equation was used to make estimates for the reactor peak power for various ρ_{ext}. The results, compared with those of computer calculations, are given below (also see Fig.1).

ρ_o	ρ_{ext}	Peak Power, $(P_{max}-P_o)/P_o$		Error %
		From Comp. Calc.	From Eq.(3.42)	
$7.775\ 10^{-3}$	1.0β	105.7	109.3	3.4
	1.5β	232.5	238.8	2.7
	2.0β	409.3	418.8	2.3
$3.8875\ 10^{-4}$	1.0β	2030	2149	5.9
	1.5β	4552	4749	4.3
	2.0β	8079	8362	3.5

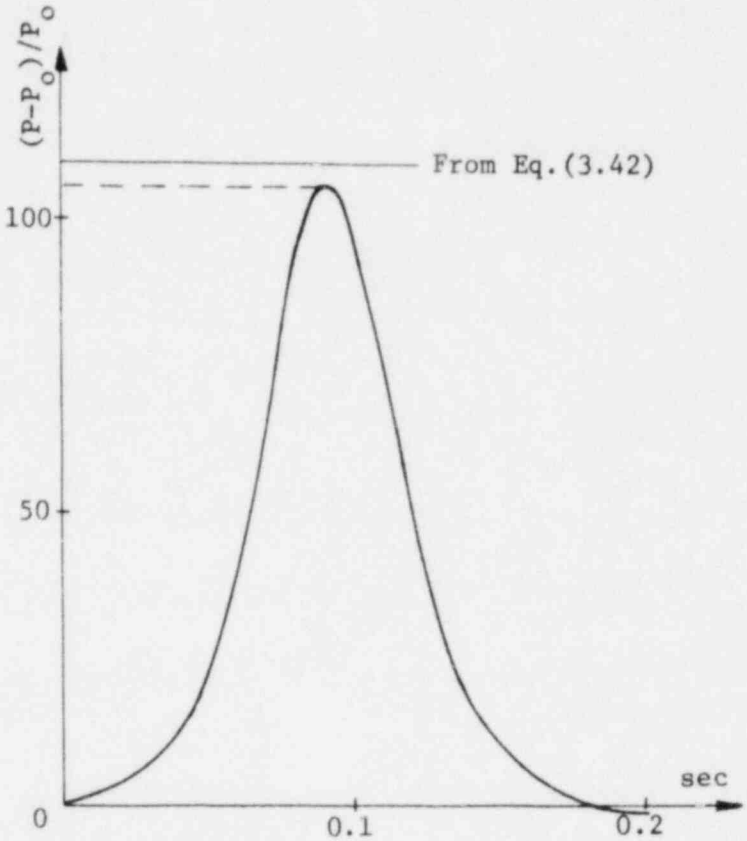

Fig.1. Power vs. time for the reactor model with a fuel temperature coefficient of reactivity; $\rho_o = 7.775\ 10^{-3}$, $\ell = 10^{-4}$sec, $\rho_{ext} = \beta$.

4. STABILITY ANALYSIS FOR A REACTOR WITH NONLINEAR FEEDBACK EFFECTS

The method of stability analysis, discussed in Section 2, is based on the assumption that the reactivity, ρ, can be transformed into the functional form given by Eq.(2.5). In most practical cases, however, the reactivity is related to reactor physical parameters, such as temperature, void fraction, etc. These parameters, in turn, depend on the reactor power (neutron flux) through certain differential equations. As long as these equations are linear, they can be integrated, and the result substituted into the expression for ρ, leading to the required Eq.(2.5). The problem appears to be more complicated in the case of nonlinear equations, when the system variables cannot be separated. In general, the question arises whether Eq.(2.5) can be explicitly derived at all. The objective of this section is to demonstrate that even if the feedback equation cannot be directly integrated, the reactivity can still be transformed into the form given by Eq.(2.5).

Consider a reactor model with the reactivity, ρ, given by,

$$\rho = - k_1 x - k_2 y \tag{4.1}$$

where $x=(P-P_o)/P_o$ (P_o is an operating steady state level of the reactor), and y satisfies the equation,

$$\dot{y} = -(b+c)y + bx - cxy \tag{4.2}$$

with $b>0$.

Eq.(4.2) may assume various physical interpretations. For instance, as shown in the Appendix, it can be used to describe the thermal-hydraulics of a simple boiling water reactor model.

It is readily seen that Eq.(4.2) cannot be explicitly solved for y. However, we can combine this equation with the dimensionless form of Eq.(2.1), i.e.

$$\dot{x} = -\frac{1}{\ell}(k_1 x + k_2 y)(1+x) - \sum_{i=1}^{K}(\beta_i/\ell)(x-z_i) \tag{4.3}$$

where z_i is given by Eq.(2.8), to yield,

$$y = \frac{c\ell}{k_2}x - \int_{-\infty}^{t}\exp\left[-b(t-\tau)\right]\left[\left(\frac{bc\ell}{k_2} - c\frac{k_1}{k_2} - b - \frac{\beta c}{k_2}\right)x(\tau) + \frac{c}{k_2}\sum_{i=1}^{K}\lambda_i z_i(\tau) - c\frac{k_1}{k_2}x^2(\tau)\right]d\tau \tag{4.4}$$

Inserting Eq.(4.4) into Eq.(4.1), and rearranging, we arrive at,

$$\frac{\dot{\varrho}}{\ell} = -\left(\frac{k_1}{\ell} + c\right)x + \int_{-\infty}^{t}\left\{\left(bc - \frac{ck_1+bk_2}{\ell} - \frac{bc}{\ell}\sum_{i=1}^{K}\frac{\beta_i}{b-\lambda_i}\right)\exp\left[-b(t-\tau)\right] + \frac{c}{\ell}\sum_{i=1}^{K}\frac{\beta_i\lambda_i}{b-\lambda_i}\exp\left[-\lambda_i(t-\tau)\right]\right\}x(\tau)d\tau - \frac{c}{\ell}k_1\int_{-\infty}^{t}\exp\left[-b(t-\tau)\right]x^2(\tau)d\tau \tag{4.5}$$

Let $ck_1>0$. Substituting Eq.(4.5) into Eq.(2.9), it can be readily shown that if the inequality holds for all $\omega\in(-\infty,\infty)$,

$$\frac{k_1}{\ell} + c + \left(\frac{ck_1+bk_2}{\ell} + \frac{bc}{\ell}\sum_{i=1}^{K}\frac{\beta_i}{b-\lambda_i} - bc\right)\frac{b-\mu}{(b-\mu)^2+\omega^2} - \frac{c}{\ell}\sum_{i=1}^{K}\frac{\beta_i\lambda_i}{b-\lambda_i}\frac{\lambda_i-\mu}{(\lambda_i-\mu)^2+\omega^2} - \Delta\frac{k_1}{\ell}\frac{c}{b-2\mu} \geq 0 \tag{4.6}$$

where $0<\mu<\min\{b, \lambda_i(i=1,\ldots,K)\}$, then Eq.(2.11) is satisfied for all such x that $\sup_t x(t)<\Delta$ ($\Delta>0$). Thus, the solution $x(t)=0$ is asymptotically stable.

The allowable domain of initial perturbations can be evaluated by combining Eq.(4.6) with Eqs.(2.14) and (2.15), with $m_1>-1$, $m_2=\Delta$.

If $ck_1<0$, we can use Eq.(4.6) assuming that $\Delta<0$, and $\inf x(t)>\Delta$. The domain of initial perturbations can be established similarly as in the previous case, with $m_1=\Delta$, m_2 - arbitrary.

If $k_1=0$, Eq.(4.6) reduces to,

$$c + b\left(\frac{1}{\ell}k_2 + \frac{c}{\ell}\sum_{i=1}^{K}\frac{\beta_i}{b-\lambda_i} - c\right)\frac{b-\mu}{(b-\mu)^2+\omega^2} - \frac{c}{\ell}\sum_{i=1}^{K}\frac{\beta_i\lambda_i}{b-\lambda_i}\frac{\lambda_i-\mu}{(\lambda_i-\mu)^2+\omega^2} \geq 0 \tag{4.7}$$

In particular, assuming one group of delayed neutrons, Eq.(4.7) is satisfied if,

$$c\omega^4 + \left[c\lambda^2 + \frac{1}{\ell} b^2 k_2 + \frac{\beta c}{\ell} (b+\lambda)\right]\omega^2 + \frac{1}{\ell} b^2 \lambda^2 k_2 \geq 0 \quad \text{for} \quad \omega^2 \geq 0 \qquad (4.8)$$

Thus, if $c>0$ and $k_2>0$, then the steady state solution $x(t)=0$ $(P(t)=P_o)$ of the model given by Eqs.(4.2) and (4.3) is globally asymptotically stable.

5. EXTENSION TO MULTI-MODE KINETICS

Point kinetics models constitute a simplified form for more general, space-dependent reactor dynamics. Because of the complexity of the partial differential systems, the time and space dependent models are usually discretized for computational purposes. Among others, the following form can be used as a multimodal representation of nonsteady state spacial reactor kinetics[6],

$$\dot{x}_j = \frac{1}{\ell} \rho_j (1+x_j) - \sum_{i=1}^{K} \frac{\beta_i}{\ell} (x_j - z_{ji}) + \sum_{k\neq j}^{N} \frac{\alpha_{jk}}{\ell} \frac{P_{ko}}{P_{jo}} (x_k - x_j) \quad (j=1,\ldots,N) \qquad (5.1)$$

where $\alpha_{jk} \geq 0$ are the coupling coefficients, P_{jo} are the steady state nodal powers, $x_j=(P_j-P_{jo})/P_{jo}$, and z_{ji} $(j=1,\ldots,N;\ i=1,\ldots,K)$ are given by,

$$z_{ji}(t) = \lambda_i \int_{-\infty}^{t} \exp\left[-\lambda_i (t-\tau)\right] x_j(\tau) d\tau \qquad (5.2)$$

Stability analysis for system (5.1)-(5.2) was performed in Ref.6. Although the method used there proved efficient in establishing conditions for global asymptotic stability, it cannot be applied if stability occurs only in bounded domains of initial functions. However, by combining the approach of Ref.6 with that used in this paper, we obtain a convenient tool for evaluating the magnitude of allowable space dependent initial perturbations.

Briefly, defining the functional V as,

$$V = \sum_{j=1}^{N} P_{jo}^2 \left\{ F(x_j) + \sum_{i=1}^{K} (\beta_i/\ell\lambda_i)\, F(z_{ji}) - \frac{1}{\ell} \int_{-\infty}^{t} \exp\left[-2\mu(t-\tau)\right] x_j \rho_j d\tau \right\} \qquad (5.3)$$

with F given by Eq.(2.7), we obtain,

$$\dot{V} = \frac{1}{\ell} \sum_{j=1}^{N} \left\{ - P_{jo}^2 \sum_{i=1}^{K} (\beta_i/\ell) \frac{(x_j - z_{ji})^2}{(1+x_j)(1+z_{ji})} + \sum_{k\neq j}^{N} \alpha_{jk} P_{jo} P_{ko} \frac{x_k x_j - x_j^2}{1+x_j} \right.$$

$$\left. - 2\mu P_{jo}^2 \int_{-\infty}^{t} \exp\left[-2\mu(t-\tau)\right] x_j \rho_j d\tau \right\} \qquad (5.4)$$

Setting $\alpha_{jk} = \alpha_{kj}$, the second term in Eq.(5.4) yields,

$$\sum_{k\neq j}^{N} \alpha_{jk} P_{jo} P_{ko} \frac{x_k x_j - x_j^2}{1+x_j} = - \sum_{k<j} \alpha_{jk} P_{jo} P_{ko} \frac{(x_j - x_k)^2}{(1+x_j)(1+x_k)} \leq 0 \qquad (5.5)$$

Hence, the inequality,

$$\sum_{j=1}^{N} P_{jo}^2 \int_{-\infty}^{t} \exp\left[-2\mu(t-\tau)\right] x_j \rho_j d\tau \leq 0 \qquad (5.6)$$

implies: $V(t) \geq 0$, and $\dot{V}(t) \leq 0$ for $t \geq 0$

In particular, if $\rho_j = \rho_j(x_j)$, Eq.(5.6) is equivalent to,

$$\int_{-\infty}^{t} \exp\left[-2\mu(t-\tau)\right] x_j \rho_j d\tau \leq 0 \quad \text{for } j=1,\ldots,N \qquad (5.7)$$

Hence, each integral in Eq.(5.7) can be taken separately, and treated in the way used before for point reactor models.

Assuming that Eq.(5.6) is satisfied for all such x_j that $m_{1j} \leq x_j(t) \leq m_{2j}$ $(m_{1j} < 0 < m_{2j})$, $j=1,\ldots,N$, the set of initial perturbations, $D = \{x_j(t)$ for $t \leq 0 : \Delta_{1j} < x_j(t) < \Delta_{2j}\}$, can be evaluated from,

$$\sum_{j=1}^{N} P_{jo}^2 \left\{ 1 + \sum_{i=1}^{K} (\beta_i / \ell\lambda_i)\, F(\Delta_{2j}) + \Psi_j(\Delta_{21},\ldots,\Delta_{2N}) \right\} < \sum_{j=1}^{N} P_{jo}^2 \min_{n=1,2} F(m_{nj}) \tag{5.8}$$

$$F(\Delta_{1j}) = F(\Delta_{2j}) \qquad (j=1,\ldots,N) \tag{5.9}$$

where Ψ_j is a generalization of the function Ψ, given by Eq.(2.12).

CONCLUDING REMARKS

The results obtained in this paper demonstrate that the theoretical approach to nonlinear reactor dynamics, described in Sections 2 and 5, can be successfully applied in the analysis of various reactor models, both one and multidimensional. Although the examples discussed were rather simple, this method can also be used to investigate more complicated reactor models.

REFERENCES

1. D.L. Hetrick, "Dynamics of Nuclear Reactors", The University of Chicago Press, Chicago (1971).
2. Z. Akcasu, G.S. Lellouche, and L.S. Shotkin, "Mathematical Methods in Nuclear Reactor Dynamics", Academic Press, Inc., New York (1971).
3. G.C. Park, J.K. Park, M. Becker, R.T. Lahey, Jr., and M. Podowski, Trans. Am. Nucl. Soc., 39, 1053 (1981).
4. J.K. Park, G.C. Park, M. Becker, M. Podowski, and R.T. Lahey, Jr., Proceedings of the ANS Topical Meeting on Advances in Reactor Physics and Core Thermal Hydraulics (1982).
5. M. Podowski, Trans. Am. Nucl. Soc., 34, 286 (1980).
6. M. Podowski, Nucl. Sci. Eng., 72, 256 (1979).
7. M. Podowski, Trans. Am. Nucl. Soc., 41 (1982).

APPENDIX

Consider the following form for the mass and energy conservation equations, respectively, of a homogeneous two-phase flow model,

$$\frac{\partial \rho_H}{\partial t} + \frac{\partial (\rho_H v)}{\partial z} = 0 \tag{A.1}$$

$$\frac{\partial (\rho_H h)}{\partial t} + \frac{\partial (\rho_H v h)}{\partial z} = q'' \frac{P_H}{A} \tag{A.2}$$

where ρ_H, v, and h are respectively the density, velocity, and enthalpy of the two-phase flow, q" is the surface heat flux, P_H is the heated perimeter, and A is the cross section area for fluid flow.

Eqs.(A.1) and (A.2) can be combined and integrated across the channel length (L_H), to yield ,

$$L_H \frac{d}{dt} (\overline{\rho_H h}) = - \rho_{He} v_e h_e + \rho_i v_i h_i + \overline{q''} \frac{P_H L_H}{A} \tag{A.3}$$

where the subscripts i and e refer to the reactor inlet and exit, respectively, and the bars over the symbols denote length-averaged parameters.

Neglecting the effect of moving boiling boundary, we obtain,

$$v_e = m \overline{q''} + v_i \tag{A.4}$$

Assuming that

$$\overline{\rho_H h} = 0.5(\rho_{He} h_e + \rho_i h_i) \tag{A.5}$$

and combining Eqs.(A.3), (A.4), and (A.5), yields Eq.(4.2) with y defined as,

$$y = \left[(\overline{\rho_H h}) - (\overline{\rho_H h})_o\right] / \left[(\overline{\rho_H h})_o - (\rho_i h_i)\right] \tag{A.6}$$

Introducing the average void fraction,

$$\overline{\alpha} = \frac{\rho_f h_f - \overline{\rho_H h}}{\rho_f h_f - \rho_g h_g} \tag{A.7}$$

and denoting by r_P and r_α the power and void coefficients of reactivity, respectively, yields,

$$\rho = \rho_o - r_P P - r_\alpha \overline{\alpha} = - r_P (P - P_o) - r_\alpha (\overline{\alpha} - \overline{\alpha}_o) = - r_P P_o x - r_\alpha \frac{\rho_i h_i - (\overline{\rho_H h})_o}{\rho_f h_f - \rho_g h_g} y \tag{A.8}$$

Setting,

$$k_1 = r_P P_o \tag{A.9}$$

$$k_2 = r_\alpha \frac{\rho_i h_i - (\overline{\rho_H h})_o}{\rho_f h_f - \rho_g h_g} \tag{A.10}$$

Eq.(A.8) takes the form of Eq.(4.1).

SYMMETRIES APPLIED TO TRANSPORT AND DIFFUISON EQUATIONS

M. Makai
Central Research Institute for Physics
H-1525 Budapest 114, P.O.B.49, Hungary

ABSTRACT

Symmetry considerations allow the formutation of several problems of reactor physics in a geometry independent fashion. First a solution to the transport equation is given in a heterogeneous lattice, made up from square shaped cells. The solution involves a cell problem set and a finite difference scheme with coefficients determined through the cell problem set. Second a coarse mesh solution is derived in hexagonal geometry. The obtained analytical solution yields a response matrix equation set. A HTGR benchmark solution is given along with comparison with other coarse mesh methods. In both problems presented, formulation in the considered geometry is given. The appendix comprises details of the employed group theory.

I. INTRODUCTION

Following the development of various types of reactors the technique for solving reactor physics problems for PWR geometry, is well developed whereas LMFBR, HTGR or WWER geometries have tended to remaine in the shade. A good deal of the sophisticated expedients of the PWR geometry can be transferred to other geometries by means of symmetry considerations.

The application of symmetry considerations is based on expressing the involved quantities(such as flux, partial currents, etc.) with the help of functions invariant under the symmetry transformations of the cell or node. The recipe for finding those eigenfunctions has been established by mathematicans [1,2]. Some details necessary for the present applications are summarized in the Appendix.

This work is devoted to two applications of symmetry considerations to reactor physics. The first problem is concerned with determining the neutron density in a reactor core. The complexity of this problem motivates the search for simpler approximations to the transport equation. How should the coefficients in a diffusions equation be chosen to substitute the transport equation? How should the neutron density be determined at a given place in the approximation selected? There are several answers to these usually posed questions [3-6]. The answers, however, are often based on arbitrarily made assumptions. We evade the first question by showing that the solution to the transport equation is determined by a cell problem set, in which response functions of each cell type are to be determined. A response function is nothing more than the neutron distribution in the cell with a given incoming current distribution at the boundary. In the expression for the neutron density, the boundary condition is separated from the response and it can be shown that the solution of a finite difference scheme yields the boundary condition at every cell boundary. The dependent variable in the finite difference scheme is a vector, in the case of square cells the vector has only two independent components which are essentially different in magnitude, therefore a perturbation method is applicable to their determination.

The second problem is concerned with an analytical coarse mesh solution in hexagonal geometry [7-9]. Symmetry considerations allows us to develop a response matrix equation set, the response matrix elements being determined from the analytical solution. The GA9A1 [10] benchmark problem is solved, the presented results show that our method gives good results even with one point per hexagon.

2. SOLUTION TO THE TRANSPORT EQUATION IN A HETEROGENEOUS LATTICE

Let us consider a core containing several cell types but the cells differ only in the involved materials but not in geometry. Let each cell be square in shape, the inner structure of the cell may again be different but symmetric: if a transformation leaves the cell geometry invariant, it leaves the materials of the cell invariant, too. Such a core may represent a PWR core, the materials involved in a cell are differently enriched fuels with clad and moderator or a control rod with clad and moderator. For simplicity's sake, a cell is assumed as small enough to justify the use of face averaged partial currents.

We follow the line of a typical iterative method. First a suitable initial guess is set up, then we take the cells one by one. First the incoming currents depend on the energy E and the angular variable $\underline{\Omega}$. The dependence on $\underline{\Omega}$ is taken into account by the Legendre expansions:

$$I_j^{(n)}(E,\underline{\Omega}) = \frac{1}{4\pi}\phi_j^{(n)}(E) + \frac{3}{4\pi}\underline{J}_j^{(n)}(E)\cdot\underline{\Omega} + \ldots \qquad (2.1)$$

where $I_j^{(n)}(E,\underline{\Omega})$ is the incoming current at the j-th face of the n-th cell, $\phi_j^{(n)}(E)$ and $\underline{J}_j^{(n)}(E)$ are the corresponding face averaged flux and net current respectively. The independent variables E and $\underline{\Omega}$ will not be taken into consideration unless they have an explicit role.

It is well known that in the considered approximation the neutron density in the cell is uniquely determined [11]. Let us decompose the incoming current vector consisting of the four incoming currents at the four faces, into eigenfunctions of the square's symmetry transformations shown in Fig.1. The result is

$$\begin{vmatrix} I_1^{(n)} \\ I_2^{(n)} \\ I_3^{(n)} \\ I_4^{(n)} \end{vmatrix} = X_1^{(n)} \cdot \begin{vmatrix} 1 \\ 1 \\ 1 \\ 1 \end{vmatrix} + X_2^{(n)} \cdot \begin{vmatrix} 1 \\ 0 \\ -1 \\ 0 \end{vmatrix} + X_3^{(n)} \cdot \begin{vmatrix} 0 \\ 1 \\ 0 \\ -1 \end{vmatrix} + X_4^{(n)} \cdot \begin{vmatrix} 1 \\ -1 \\ 1 \\ -1 \end{vmatrix} \qquad (2.2)$$

where

$$X_1^{(n)} = (I_1^{(n)}+I_2^{(n)}+I_3^{(n)}+I_4^{(n)})/4 \qquad (2.3)$$

$$X_2^{(n)} = (I_1^{(n)}-I_2^{(n)})/2 \qquad (2.4)$$

$$X_3^{(n)} = (I_2^{(n)} - I_4^{(n)})/2 \tag{2.5}$$

$$X_4^{(n)} = (I_1^{(n)} - I_2^{(n)} + I_3^{(n)} - I_4^{(n)})/4. \tag{2.6}$$

As is shown in the Appendix, the symmetry properties of the flux and of the normal component of the net current are the same. If $\underline{\Omega}$ is measured from the normal to the cell face in Eq. (2.1) then the subscript j of the variable $X_j^{(n)}$ in Eqs. (2.3)-(2.6) does not refer to the j-th face but to the symmetry properties. The first vector on the RHS of Eq. (2.2) represents a homogeneous surrounding: the entering neutron distribution is the same at the four cell faces. The second and third vector represents a streaming along the x and y axis respectively. Such a streaming may be represented by a surrounding where $\phi=0$ and either $J_x=0$, $J_y=1$ or $J_x=1$, $J_y=0$. The fourth vector represents a cross flow: neutrons enter through faces 1 and 3, and leave through faces 2 and 4. According to Eq. (2.2) any boundary condition can be built up from those four cases. It is worth noting that when the incoming currents are space dependent along the cell faces, further terms appear in Eq. (2.2), but they are not essentially different from the four considered terms.

Before proceeding, the transport equation in the n-th cell has to be written. Let us write it as

$$T^{(n)}\psi^{(n)}(\underline{r},E,\underline{\Omega}) = 0 \tag{2.7}$$

where

$$T^{(n)} = \underline{\Omega}\,\underline{\nabla} \star + \Sigma^{(n)}(\underline{r},E)\star - \int_0^\infty \int_{4\pi} \Sigma_s^{(n)}(\underline{r},E;\underline{\Omega}'\to E,\underline{\Omega})\star\, d\underline{\Omega}'dE' - \frac{\chi^{(n)}(\underline{r},E)}{k_{eff}} \int_0^\infty \int_{4\pi} \nu\Sigma_f^{(n)}(\underline{r},E')\star d\Omega'dE' \tag{2.8}$$

and k_{eff} is the eigenvalue taken from the previous iteration; the cross sections have the standard meaning. As $T^{(n)}$ does not involve an external source, the operator $T^{(n)}$ is linear.

The solution to Eq. (2.7) with the boundary condition given by the LHS of Eq. (2.2) is sought. Owing to the linearity of $T^{(n)}$, the sought neutron density $\psi^{(n)}$ is unequivocally determined by the four solutions of Eq. (2.7) with the four vectors of Eq. (2.2), in turn, as boundary condition. Let us denote these solutions by $u_1^{(n)},\ldots,u_4^{(n)}$. According to the remarks following Eq. (2.6), the four functions $u_j^{(n)}$ have physical meaning as follows: $u_1^{(n)}$ is the neutron density in the n-th cell when it is imbedded into a homogeneous surrounding; the incoming currents at the four faces are equal; $u_2^{(n)}$ and $u_3^{(n)}$ express the neutron density in the n-th cell when it is imbedded into an x or y directed streaming, respectively; $u_4^{(n)}$ is the neutron density in the n-th cell, when it is imbedded into a cross flow. Our result can be summarized as

$$\psi^{(n)}(\underline{r},E,\underline{\Omega}) = \sum_{i=1}^{4} X_i^{(n)} u_i^{(n)}(\underline{r},E,\underline{\Omega}) \tag{2.9}$$

Before passing on to the determination of $X_i^{(n)}$, we would mention that the $u_i^{(n)}(\underline{r},E,\underline{\Omega})$ functions are eigenfunctions to every symmetry transformation of the cell, thus $u_i^{(n)}(\underline{r},E,\underline{\Omega})$ is invariant under symmetry transformations, whereas $u_2^{(n)}(\underline{r},E,\underline{\Omega})$ changes sign under the $x\to x$ transformation but remains invariant under the $y\to -y$ transformation and so forth.

The incoming currents of the n-th node are the outgoing currents of the adjacent nodes in the sense of our iterational strategy. Since from now on our analysis is concerned with the relationship between adjacent cells, a new notation is introduced, see Fig.2. Because of Eqs. (2.3)-(2.6) the coefficient $X_1^{(o)}$ of the central cell is expressible with the help of the outgoing currents of the adjacent cells:

$$X_1^{(0)} = (J_3^{(1)}+J_4^{(2)}+J_1^{(3)}+J_2^{(4)})/4 \tag{2.10}$$

$$X_2^{(0)} = (J_3^{(1)}-J_1^{(3)})/2 \tag{2.11}$$

$$X_3^{(0)} = (J_4^{(2)}-J_2^{(4)})/2 \tag{2.12}$$

$$X_4^{(0)} = (J_3^{(1)}-J_4^{(2)}+J_1^{(3)}-J_2^{(4)})/4 \tag{2.13}$$

Let $r_i^{(n)}$ denote the face averaged outgoing currents determined from the $u_i^{(n)}$ functions. By means of the linearity of both the symmetry transformations and the operations forming the ougoing current from the neutron density, the outgoing current in the n-th cell can be decomposed as

$$\begin{vmatrix} J_1^{(n)} \\ J_2^{(n)} \\ J_3^{(n)} \\ J_4^{(n)} \end{vmatrix} = X_1^{(n)} r_1^{(n)} \begin{vmatrix} 1 \\ 1 \\ 1 \\ 1 \end{vmatrix} + X_2^{(n)} r_2^{(n)} \begin{vmatrix} 1 \\ 0 \\ -1 \\ 0 \end{vmatrix} + X_3^{(n)} r_3^{(n)} \begin{vmatrix} 0 \\ 1 \\ 0 \\ -1 \end{vmatrix} + X_4^{(n)} r_4^{(n)} \begin{vmatrix} 1 \\ -1 \\ 1 \\ -1 \end{vmatrix}$$

$$n = 0,1,2,\ldots \tag{2.14}$$

Comparing the lines of both sides of Eq. (2.14) we have an expression for $J_1^{(n)}$ through $X_i^{(n)}$. Substituting the obtained expression into Eqs. (2.10)-(2.13) we get:

$$X_1^{(0)} - 1/4 \sum_{i=1}^{4} X_1^{(i)} r_1^{(i)} = Q_1^{(0)} \tag{2.15}$$

where the source $Q_1^{(0)}$ is given by

$$Q_1^{(0)} = X_2^{(3)} r_2^{(3)} - X_2^{(1)} r_2^{(1)} + X_3^{(4)} r_3^{(4)} - X_3^{(2)} r_3^{(2)} + X_4^{(1)} r_4^{(1)} - X_4^{(2)} r_4^{(2)} + X_4^{(3)} r_4^{(3)} - X_4^{(4)} r_4^{(4)} \tag{2.16}$$

For the other components:

$$X_2^{(0)} - 1/4\left(X_2^{(1)}\cdot(-r_2^{(i)}) + X_2^{(3)}\cdot(-r_2^{(3)})\right) = Q_2^{(0)} \tag{2.17}$$

$$Q_2^{(0)} = 1/2\left(X_1^{(1)} r_1^{(1)} - X_4^{(1)} r_4^{(1)} - X_1^{(3)} r_1^{(3)} - X_4^{(3)} r_4^{(3)}\right) \tag{2.18}$$

$$X_3^{(0)} - 1/2\left(X_3^{(2)}\cdot(-r_3^{(2)}) + X_3^{(4)}\cdot(-r_3^{(4)})\right) = Q_3^{(0)} \tag{2.19}$$

$$Q_3^{(0)} = 1/2\left(X_1^{(2)} r_1^{(2)} - X_4^{(2)} r_4^{(2)} - X_1^{(4)} r_1^{(4)} + X_4^{(4)} r_4^{(4)}\right) \tag{2.20}$$

$$X_4^{(0)} - 1/4 \sum_{i=1}^{4} X_4^{(i)} r_4^{(i)} = Q_4^{(0)} \tag{2.21}$$

$$Q_4^{(0)} = 1/4\left(X_1^{(1)} r_1^{(1)} - X_2^{(1)} r_2^{(1)} - X_1^{(2)} r_1^{(2)} + X_3^{(2)} r_3^{(2)} + X_1^{(3)} r_1^{(3)} + X_2^{(3)} r_2^{(3)} - \right.$$
$$\left. - X_1^{(4)} r_1^{(4)} - X_3^{(4)} r_3^{(4)}\right) \tag{2.22}$$

The source term $Q_1^{(0)}$ in Eq. (2.15) depends on $X_2^{(n)}, X_3^{(n)}$ and $X_4^{(n)}$, n=1,...,4. This finite difference scheme updates $X_1^{(n)}$ in both directions. The source term in Eq. (2.17) is updated from the solution of Eq. (2.15). The $X_2^{(n)}$ values are updated only in the x direction. It is noteworthy that $X_2^{(n)}$ and $X_3^{(n)}$ seem independent: $Q_2^{(0)}$ does not depend on $X_3^{(0)}$ nor does $Q_3^{(0)}$ depend on $X_2^{(0)}$. We can update the fourth component $X_4^{(n)}$ from Eq. (2.21) along both directions. All in all Eqs. (2.15)-(2.22) are a selfconsistent set of equations; we can solve the involved finite difference equations in the usual way. The coefficients included in Eqs. (2.15),(2.17),(2.19) and (2.21) depend only on the microfunctions $u_i^{(n)}$, i=1,...,4, n=1,...,4.

Our results can be summarized as follows. Our assumptions concerned only the material distribution within the square cell. It has been shown that in a heterogeneous lattice composed of several cell types neutron density is expressed by Eq. (2.9). We may consider the quantities $X_i^{(n)}$ as a finite difference representation of the macroflux whose components are determined by finite difference equations (2.15)-(2.22). The microfunctions $u_i^{(n)}$ give the neutron distribution within the n-th cell when the cell is imbedded into a well determined surrounding. Our analysis is based on only the transport equation and its symmetry properties, hence the obtained results are fairly general. The derivation is given in cartesian geometry for simplicity's sake but the development in hexagonal or triangular geometry is straightforward though tedious.

To find the relationship with other methods, the fission source term is determined in the n-th cell; using group structure in the energy variable:

$$S_g^{(n)} = \frac{\chi_g^{(n)}}{4\pi k_{eff}} \sum_{g'} \nu\Sigma_{fg'}^{(n)} \sum_{i=1}^{4} \bar{X}_{ig'}^{(n)} \cdot \bar{u}_{ig'}^{(n)} \tag{2.23}$$

where the bar denotes integrated quantities over the angle variable. $X_{ig}^{(n)}$ is determined from the finite difference form (2.15). As we have seen,

$X_{1g}^{(n)}$ expresses a macroflux denoted by ψ_m into which the cell is imbedded, the other $X_{ig}^{(n)}$ terms express gradients in the macroflux, thus the first three terms in Eq. (2.23) can be considered as a discretized form of

$$S_g^{(n)} = \psi_m u_1^{(n)} + \frac{\partial \psi_m}{\partial x} u_2^{(n)} + \frac{\partial \psi_m}{\partial y} u_3^{(n)} \qquad (2.24)$$

where $u_i^{(n)}$ are periodic functions composed of cross section and microfunctions. It is well known that the first term in Eq. (2.18) is the Wigner-Seitz [12] approximation, extended to heterogeneous lattices. At the same time (2.24) is and extension of the source form assumed by Benoist [3], Bonalumi [4] and Deniz [5], thus Eq. (2.9) is an extension of the assumptions used in well known codes [13,14]. On the other hand, it has long been recognized that the above assumptions give satisfactory results even in heterogeneous lattices. The coefficients $X_i^{(n)}$ usually decrease with i thus there is definitely a point in approximating the sum in Eqs. (2.2) and (2.9) by the first term only. In some cells, however, the second, third or even the fourth term may be important. This is the case if the cell has drastically different neighbours. We go on showing that the second and third components of the macrofunction, i.e. $X_2^{(n)}$ and $X_3^{(n)}$, are always expressible with the help of the first and fourth component, in contrast with the method of Laletin and Elshin [15].

To this end let us write the continuity of the incoming-outgoing currents at the i-th face of the cell marked with zero:

$$I_i^{(0)} = J_{i'}^{(i)} \qquad i' = \mathrm{mod}(i+1,4)+1 \qquad (2.25)$$

$$J_i^{(0)} = I_{i'}^{(i)} \qquad (2.26)$$

From Eqs. (2.14) and (2.2) the partial currents are expressed by $X_i^{(n)}$ and we have:

$$\sum_{k=1}^{4} c_k^{(i)} X_k^{(0)} = \sum_{k=1}^{4} c_k^{(i')} r_k^{(i')} X_k^{(i')} \qquad i=1,\ldots,4 \qquad (2.27)$$

$$\sum_{k=1}^{4} c_k^{(i)} X_k^{(0)} r_k^{(0)} = \sum_{k=1}^{4} c_k^{(i')} X_k^{(i')} \qquad (2.28)$$

and the coefficients $c_k^{(i)}$ are read out from Eq. (2.2) as $c_k^{(i)}$ is the i-th element of the k-th vector. For a given i only three $c_k^{(i)}$ is not zero, thus Eqs. (2.27) and (2.28) allow us to express the third $X_k^{(n)}$ with the help of $X_1^{(n)}$ and $X_4^{(n)}$. Furthermore $X_1^n >> X_4^n$ for most cells, hence the joined equation for $X_1^{(n)}$ and $X_4^{(n)}$ can be solved by the perturbation method, which is important for effectiveness. The components $X_2^{(n)}$ and $X_3^{(n)}$ are eliminated from the finite difference scheme.

3. GEOMETRY INDEPENDENT COARSE MESH METHOD

Although in carthesian geometry several techniques have been elaborated for solving the few group diffusion equation, the range of methods applicable to hexagonal or triangular geometry is rather narrow. This situation is partially due to the restriction on the cross leakage concept [16].

The iteration strategy of the previous section is applicable to the coarse mesh method as well. Starting from a suitable initial guess, we can take the nodes one by one, the incoming currents are known from the outgoing currents of the adjacent nodes. We seek a formula to express the node averaged flux and the outgoing currents with the help of the incoming currents. Thus we have to solve the few group diffusion equation in a node with a given boundary condition, i.e. with given face averaged incoming currents. As we have seen in the previous section, we can construct the solution to a boundary condition problem from the "responses" of the node. A response of the node is the solution of the diffusion equation in the node with given symmetric boundary condition, i.e. with symmetric incoming currents. In this section a geometry independent coarse mesh method is presented but instead of giving a general development, an explicit derivation is given for hexagonal geometry [7-9] assuming a homogenized node. The few group diffusion equation is written as

$$\langle D\rangle \nabla^2 \underline{\phi}(\underline{r}) + \Sigma \underline{\phi}(\underline{r}) = 0 \tag{3.1}$$

where $\langle D\rangle$ is a diagonal matrix with entries D_g (diffusion coefficient in group g); Σ is a matrix composed of cross sections as

$$\Sigma_{gg'} = \Sigma_{rem,g} - \frac{\chi_g}{k_{eff}} \nu\Sigma_{fg'} + \Sigma_{g'\to g} \tag{3.2}$$

and in Eq. (3.2) arbitrary up- or downscattering is allowed. The flux will be expressed by means of the eigenfunctions of the Laplace operator; to this end we have to solve the eigenproblem

$$(\langle D^{-1}\rangle \Sigma)\ \underline{t}_i = -\lambda_i^2 \underline{t}_i \tag{3.3}$$

with i=1,...,G (number of energy groups). There are standard techniques for solving this eigenvalue problem [17,18]. Using eigenvalues λ_i^2 we can form elementary solutions $\underline{f}_{ij}$, which satisfy Eq. (3.1) within the node:

$$\underline{f}_{ij} = e^{\lambda_j \underline{e}_i \cdot \underline{r}}\, \underline{t}_j \qquad i=1,\ldots,6;\ j=1,\ldots,G. \tag{3.4}$$

Here $\underline{e}_i$ is the normal vector to node face i. In contrast with the previous section where the response functions $u_j^{(n)}$ were determined by numerical procedures, and the symmetry properties of the response functions were determined by the boundary condition, now an analytical solution is possible and we can determine the response functions by decomposing the solution into eigenfunctions of the node's symmetries. As is shown in the Appendix the symmetry properties of the solution determine the symmetry of the incoming current. The response functions $\underline{h}_{kj}$,k=1,...,6; j=1,...,G are determined from Eqs. (3.4) and (A3):

$$\underline{h}_{kj} = \sum_{i=1}^{6} \omega_{ki} \underline{f}_{ij} \tag{3.5}$$

the matrix ω is

$$\omega = \begin{vmatrix} 1/6 & 1/6 & 1/6 & 1/6 & 1/6 & 1/6 \\ 1/6 & -1/6 & 1/6 & -1/6 & 1/6 & -1/6 \\ 2/\sqrt{12} & -1/\sqrt{12} & -1/\sqrt{12} & 2/\sqrt{12} & -1/\sqrt{12} & -1/\sqrt{12} \\ 0 & 1/2 & -1/2 & 0 & 1/2 & -1/2 \\ 2/\sqrt{12} & 1/\sqrt{12} & -1/\sqrt{12} & -2/\sqrt{12} & -1/\sqrt{12} & 1/\sqrt{12} \\ 0 & 1/2 & 1/2 & 0 & -1/2 & -1/2 \end{vmatrix} \quad (3.6)$$

The nodal flux $\underline{\phi}$ is expressed as a linear combination of the response functions $\underline{h}_{kj}$:

$$\underline{\phi}(\underline{r}) = \sum_{k=1}^{6} \sum_{g'=1}^{G} c_{kg'} \underline{h}_{kg'}(\underline{r}) \quad (3.7)$$

Averaged fluxes and incoming currents determined from $\underline{\phi}$ are as follows:

$$\bar{\underline{\phi}} = \frac{1}{V} \int_V \underline{\phi}(\underline{r}) dr \quad (3.8)$$

$$\underline{I}_i^{(k)} = \frac{1}{F_i} \int_{F_i} \sum_{g'=1}^{G} c_{kg'} \cdot \frac{1}{4} [\underline{h}_{kg'}(\underline{r}) + 2D \frac{\partial \underline{h}_{kg'}}{\partial n_i}] dr \qquad k=1,\ldots,6;\ i=1,\ldots,6 \quad (3.9)$$

where F_i is the surface of the i-th node face, n_i denotes the outward normal. A here not detailed analysis shows that the average flux is zero unless the response functions corresponding to k=1 are considered [7]. The same analysis shows that the partial currents corresponding to $\underline{h}_{kj}$ at the six node faces are proportional to the k-th row vector in the matrix ω and the arbitrary vector of six elements can be decomposed according to the rows of matrix ω. Let us decompose the six incoming current vectors at the six node faces:

$$\underline{I} = (\underline{I}_1, \underline{I}_2, \underline{I}_3, \underline{I}_4, \underline{I}_5, \underline{I}_6) \qquad \underline{I} = \sum_{k=1}^{6} \underline{m}_k \cdot \bar{\omega}_k \quad (3.10)$$

$\underline{m}_k$ - is a linear expression of the incoming currents [8].

It is clear that the incoming currents obtained from (3.9) should equal $\underline{m}_k$ which gives 6G equations for the 6G unknowns $c_{kg'}$. The equations with different k do not mix, thus Eq. (3.10) disintegrates into 6 sets with G unknowns in each set. After solving Eq. (3.10) we determine the outgoing currents and average fluxes from the analytical solution (3.6). We update the incoming current vector and pass on to the next node.

The presented method can be summarized as follows. First the eigenvalues λ_i^2 of the cross-section matrix are determined, see Eq. (3.3). There are, in general, G eigenvalues of which some may be complex. From the eigenvalues and the eigenvectors space dependent elementary solutions are formed,

see Eq. (3.4). These elementary solutions $\underline{f}_{ij}$ include different eigenvectors (index j) and six different arbitrarily chosen vectors $\underline{e}_i$ (index i). In the function set $\underline{f}_{ij}$ the vector notation refers to the energy groups. From this function set eigenfunctions of the symmetry transformations of the node are formed, this procedure is carried out with the help of matrix ω, determinable from Eq. (A3). There are 6 such eigenfunctions (index k) which may involve one of the G eigenvalues (index j): $\underline{h}_{kj}$ denotes those eigenfunctions. The flux $\underline{\phi}(\underline{r})$ is a linear combination of the eigenfunctions $\underline{h}_{kj}$, see Eq. (3.7). According to a here not detailed analysis [7] the incoming currents determined from $\underline{h}_{kj}$ inherit the symmetry properties of the eigenfunction $\underline{h}_{kj}$. We can decompose the incoming currents at the node faces into eigenvectors of the symmetry operations, see Eq. (3.10). The so obtained eigenvectors are the same as the ones determined from the k-th component of the flux $\underline{\phi}(\underline{r})$, see Eq. (3.7) using definition (3.9). Thus 6G equations are given to determine the 6G unknowns c_{kg}, in Eq. (3.7).

The coarse mesh programs working in hexagonal geometry are essentially different from the here presented one. Polynomial approximations [19] and nodal expansion method [20] are in use. Approximation by exponential functions is implemented in the SIXTUS code [21].

The above developed idea has been implemented in the HEXAN computer code. Results for the GA9A1 test problem show the efficiency of the HEXAN code. The eigenvalue and the maximum error in power density obtained by several programs are given in Table 1. The reference eigenvalue is 1.1183±0.0001, obtained by extrapolating to zero mesh size [24]. Power density by HEXAN is given in Table 2, compared with a finite difference solution with 48 points per hexagon [10]. The maximum error is 2.2%, in good agreement with the only assumption made in HEXAN: nodes are connected by the continuity of face averaged quantities which causes some error in the eigenvalue. The HEXAN code is successfully being used for WWER calculations. At present only two acceleration methods are built into the code: asymptotic extrapolation and overrelaxation with restraint [25].

APPENDIX. PRIMER ON SYMMETRIES

Symmetry transformations of a given cell geometry constitute an abstract structure called group [1]. The operation defined between symmetry transformations is their consecutive application and is called product. Every symmetry transformation has an inverse, the product of two symmetry transformations is again a symmetry transformation, the "unit" among the symmetry transformations is the $\underline{r} \to \underline{r}$ transformation.

Symmetries of a given cell geometry are summarized in the literature [1,2]. The symmetries of a regular cell with n faces form a group called C_{nv}; if the cell is cylindrical, the group is C_∞. For our purposes only the eigenfunctions of the symmetry transformations are needed and a method for determining them. Every symmetry transformation changes the coordinates, and is represented by a matrix P:

$$\underline{r}' = P\,\underline{r} \qquad (A1)$$

A function f transforms under the coordinate transformation as

$$P\,f(\underline{r}) = f(P^{-1}\underline{r}). \qquad (A2)$$

That is the inverse matrix to P is applied to the coordinates. The transformation of a vector amounts to nothing other than a permutation of the elements. For example, the permutation rule of the vector formed from the n incoming currents can be found from the transformation rule of the cell faces.

The symmetry transformations are classified [1]; the different eigenfunctions of the symmetry transformations are called irreducible representations. There are as many irreducible representations as there are classes. The number of classes is given in the so called character table of the group [1,2]. It may happen, however, that some representations can not be represented. This is the case when one uses face averaged partial currents. To represent every irreducible representation a vector of m element should be used, where m is the sum of the first column in the character table. The irreducible representations are projected out by

$$f_i(r) = \frac{\ell_i}{h} \sum_{P \in G} [\chi^{(i)}(P)]^* \cdot Pf(\underline{r}) \qquad (A3)$$

where ℓ_i is the first number in the i-th row of the character table, h is the number of symmetry transformations of the cell $\chi^{(i)}(P)$ denotes the character table as matrix [2]. From the character table of a square cell, given in Table 3, it is easy to derive Eq. (2.2). From the character table of a hexagonal cell, given in Table 4, the elements of the matrix ω can be determined, see section 3.

Any function is decomposable into irreducible representations. Irreducible representations are orthogonal, hence they do not mix together when applying linear transformations to them. In both problems discussed, the below derived properties of the transport and diffusion equation were employed. Let $\hat{O}$ denote the operations of the transport or diffusion equation and let $\hat{B}$ denote the operations forming the incoming currents from the flux or neutron density.

The neutron density in a cell satisfies the equations

$$\begin{aligned} \hat{O}\psi(\underline{r}) &= 0 \qquad \underline{r} \in V_{cell} \\ \hat{B}\psi(\underline{r}) &= I(\underline{r}) \qquad \underline{r} \in \partial V_{cell} \end{aligned} \qquad (A4)$$

where $I(\underline{r})$ is a given function. The solution to Eq. (A4) is given by

$$\psi(\underline{r}) = \sum_k c_k \psi_k(\underline{r})$$

where index k runs over the possible irreducible representations and the functions ψ_k are the solutions of

$$\begin{aligned} \hat{O}\psi_k(\underline{r}) &= 0 \qquad r \in V_{cell} \\ \hat{B}\psi_k(\underline{r}) &= I_k(\underline{r}) \qquad \underline{r} \in \partial V_{cell} \end{aligned}$$

The coefficients c_k are determined by the irreducible components of $I(\underline{r})$ as

$$I(\underline{r}) = \sum_k c_k I_k(\underline{r}) \quad .$$

In section 3 we used the fact that the symmetry properties of the solution to (A4) and those of the function $I(\underline{r})$ may not be different.

REFERENCES

[1] L.D. Landau, E.M. Lifsitz: Theoretical Physics, Vol. 3, Quantum Mechanics, Chapter 12, Pergamon Press, London (1959)

[2] L.M. Falicov: Group Theory and its Physical Applications, Univ. of Chicago Press, Chicago (1966)

[3] P. Benoist: Theorie du Coefficient de Diffusion des Neutrons dans un Reseau Comportant des Cavites, Report CEA-R-2278, Centre d'Etudes Nucleaires, Saclay, (1964)

[4] R.A. Bonalumi: Nucl.Sci.Eng. 59, 445 (1976)

[5] V. Deniz: A New Consistent Definition of the Homogenized Diffusion Coefficient of a Lattice, Report BARC-989, Bhabha Atomic Research Centre, Trombay, (1978)

[6] E.M. Gelbard: Nucl.Sci.Eng. 54, 327 (1974)

[7] M. Makai: Symmetries and the Coarse Mesh Method, Report EIR-414, Eidg. Institute für Reaktorforschung, Würenlingen, (1980)

[8] M. Makai, J. Arkuszewski: Trans.Am.Nucl.Soc. 38, 347 (1981)

[9] M. Makai: Symmetries Applied to Reactor Calculations, to be published

[10] Argonne Benchmark Problem Book, ANL-7416, Suppl. 2, (1977)

[11] K.M. Case, P.F. Zweifel: Linear Transport Theory, Addison-Wesley, Reading, Mass. (1967)

[12] G.I. Bell, S. Glasstone: Nuclear Reactor Theory, p. 163, Van Nostrand, New York, (1970)

[13] J. Bussac, P. Reuss: Traité de Neutronique, Hermann, Paris, (1978)

[14] A. Hoffmann et al.: APOLLO - Code Multigrouppe de Resolution de l'Equation du Transport pour les Neutrons Thermiques et Rapide, Report SERMA S No. 1. 193, Centre d'Etudes Nucleaires, de Saclay, (1973)

[15] N.I. Laletin, A.V. Elshin: Derivation of Finite Difference Equations for Heterogeneous Reactor, Report ИАЭ-3280/5, Kurchatov Institute, Moscow, (1980), in Russian

[16] H. Finnemann et al.: Atomkernenergie, 30, 123 (1977)

[17] IMSL Reference Manual, 2, pE-1, IMSL Public Service, Houston, (1980)

[18] B.T. Smith et al.: Matrix Eigensystem Routines EISPACK Guide, Lecture Notes in Computer Science, 6, p. 41, Springer, Berlin, (1976)

[19] P. Siltanen et al.: HEXBU, Report 14, Nuclear Engineering Laboratory, Technical Research Centre of Finland, Helsinki, (1974)

[20] T. Duracz: A Nodal Method in Hexagonal Geometry, Proc.Int. Topical Meeting on Advances in Mathematical Methods for the Solution of Nuclear Engineering Problems, Münich, 1, 423, (1981)

[21] J. Arkuszewski: SIXTUS-A 2D Diffusion Theory Code in Hexagonal Geometry, Report EIR-410, Eidg. Institute für Reaktorforschung, Würenlingen, (1980)

[22] W.R. Davison: BUGI80/HTGR,A 2D Triangular Mesh Multigroup Diffusion Burnup Code for Use in the Design of 180° Rotationally Symmetric HTGR Cores, Report GA-A12674, General Atomics, San Jose, (1975)

[23] D.R. Vondy et al.: VENTURE, Report ORNL-5062, Oak Ridge, (1976)

[24] R. Steinke: Personal Communication (1981)

[25] D.R. Vondy, T.B. Fowler: Nucl.Sci.Eng. 67, 415, (1978)

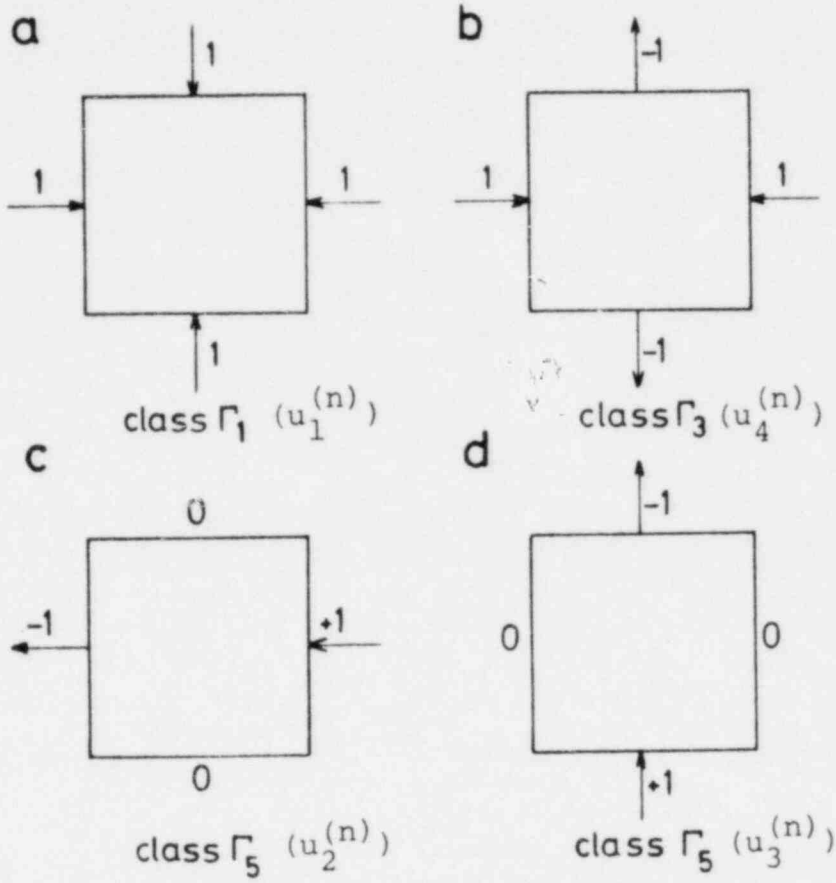

Fig.1. Boundary conditions to determine response functions $u_1^{(n)}$, $u_2^{(n)}$, $u_3^{(n)}$ and $u_4^{(n)}$

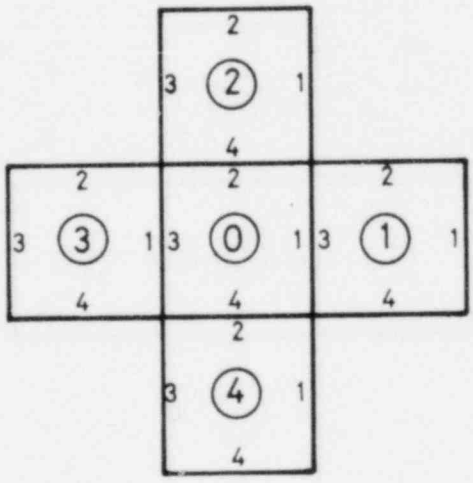

Fig.2. Numbering of cells and cell faces

TABLE 1. Comparison of GA9A1 Benchmark Results

Program	k_{eff}	Points/Node	ΔP(%)	Δφ	Time (sec)	Machine	Ref.
BUG 180	1.11815	48	0.0	10^{-5}	9600	UNIVAC-1108	[22]
GRIMHX	1.11863	6	3.1	10^{-5}	26	IBM 360/195	[10]
VENTURE	1.11860	54	-	10^{-5}	270	IBM 360/195	[23]
VENTURE	1.12725	1	-	10^{-5}	37.2	IBM 360/91	[23]
VALE	1.11596	3	3.3	10^{-5}	17	IBM 360/91	[24]
DIFGEN	1.11700	38	4.7	7.10^{-5}	780	CYBER 174	[24]
M 2	1.11824	1	-	-	-	-	[20]
HEXAN	1.11888	1	2.2	3.10^{-5}	537.3	EC-1040	

1 sec IBM 360/195 = 2 sec IBM 360/91 = 4 sec CYBER 174
(≃ 11 sec UNIVAC 1108) = 30 sec EC-1040

TABLE 2. Power densities obtained by HEXAN for the GA9A1 problem

Node	Power	Error(%)	Node	Power	Error(%)
1	0.366	2.2	23	0.907	0.2
2	1.065	0.0	24	0.722	0.2
3	0.836	0.3	25	0.965	0.4
4	1.234	0.0	26	1.091	0.1
5	1.287	0.3	27	1.059	0.2
6.	1.279	0.1	28	0.889	0.2
7	1.301	0.3	29	0.644	0.5
8	1.251	0.4	30	0.856	0.2
9	1.254	0.2	31	0.947	0.1
10	0.774	0.5	32	1.006	0.3
11	1.167	0.0	33	1.083	0.0
12	1.147	0.1	34	1.066	0.1
13	1.220	0.1	35	0.9166	0.1
14	1.182	0.0	36	0.644	0.5
15	1.155	0.0	37	0.854	0.2
16	1.166	0.0	38	0.958	0.0
17	0.329	1.6	39	1.093	0.1
18	0.837	0.3	40	1.047	0.2
19	0.935	0.2	41	1.001	0.0
20	0.998	0.0	42	0.917	0.3
21	1.016	0.0			
22	0.979	0.1			

TABLE 3. Character table of the C_{4v} group

Repr./Class	C	$2C_a$	$2C_d$	C_b	$2C_c$
Γ_1	1	1	1	1	1
Γ_2	1	-1	-1	1	1
Γ_3	1	1	-1	1	-1
Γ_4	1	-1	1	1	-1
Γ_5	2	0	0	-2	0

TABLE 4. Character table of the C_{6v} group

Repr./Class	C_1	C_2	$2C_3$	$2C_4$	$3C_5$	$3C_6$
Γ_1	1	1	1	1	1	1
Γ_2	1	1	1	1	-1	-1
Γ_3	1	-1	1	-1	1	-1
Γ_4	1	-1	1	-1	-1	1
Γ_5	2	2	-1	-1	0	0
Γ_6	2	-2	-1	1	0	0

SIMULATION OF NEUTRON SPECTRA IN AXIAL SLICES USING SPACE AND ENERGY DEPENDENT BUCKLINGS*

K. N. Grimm and D. Meneghetti
EBR-II Project
Argonne National Laboratory
Argonne, Illinois 60439

ABSTRACT

The method of space and energy dependent bucklings was used to model the axial dimension of a fast reactor RZ calculation using one-dimensional analysis. This analysis has been done using transport theory or diffusion theory. Considered were cases where the axial one-dimensional slice was a full-height core, a partial-height core or a non-core region. Negative bucklings, resulting from axial reflector regions, can lead to numerical instabilities. These stability problems were circumvented by using a regional pseudo-scattering or regional pseudo-fission source to model net inward leakages.

INTRODUCTION

Experimental Breeder Reactor No. II (EBR-II) contains a heterogeneous core region, upper and lower steel axial reflectors, a steel radial reflector, and a fertile radial blanket. Run-to-run neutronic calculations are currently done in XY geometry using the discrete-ordinates transport code DOT-II (Ref. 1) with the S_4 approximation. The axial leakage is modeled by an axial leakage cross section $D_g B^2$, where D_g is the diffusion coefficient for energy group g and B^2 is the gross-region energy-dependent buckling. This leakage cross section is added to the transport and absorption cross sections for each region and energy group. The gross regions for which the bucklings are assumed constant in space and energy are the core, radial reflector, and radial blanket. The current XY calculations assume an energy-independent buckling value of 0.0023 cm^{-2} in the core, 0.00085 cm^{-2} in the radial reflector, and 0.0023 cm^{-2} in the radial blanket.

Use of buckling values in this manner gives satisfactory eigenvalues and high-energy reaction rates. However, large errors occur in neutron-flux spectra at low energies, where the flux levels are small. These errors are shown in the following figures. Figures 1 and 2 show the core-full-height, volume-integrated fluxes when the reference run (see Appendix A) is calculated using an RZ model in the DOT-IV (Ref. 2) transport code and by a one-dimensional (1D) model with the above constant bucklings in the 1D transport code ANISN (Ref. 3). Figure 3 shows the 1D flux error (relative to the RZ calculation) in reflector row 9 and blanket row 12. Although the differences are not as striking as for the core, they still are large.

The large flux errors at the lower energies are mainly due to the assumption of energy-independent, regionally constant buckling. A regionally constant positive buckling implies a net outward current. In the core region, the neutron leakage is outward for the higher energy groups, but because of the axial reflectors, the leakage is inward for the lower energy groups. In this buckling methodology, an outward net leakage implies a positive buckling, whereas an inward net leakage implies a negative buckling.

*Work supported by the U.S. Department of Energy.

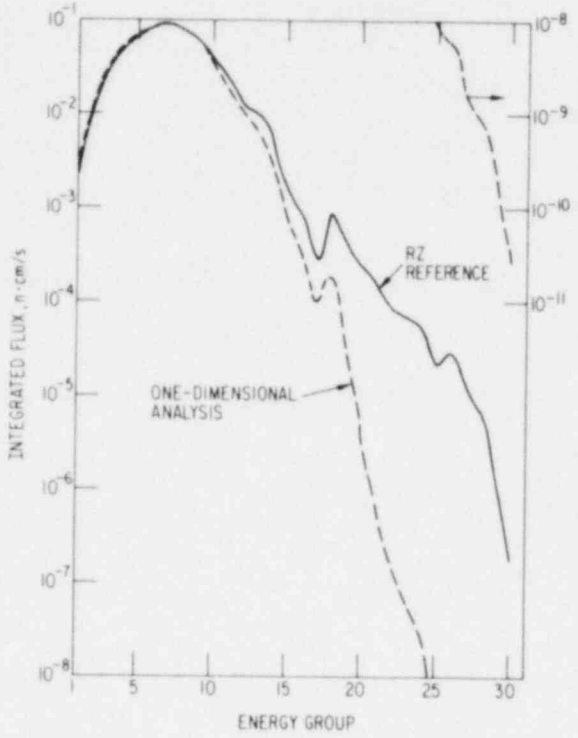

Fig. 1. Volume-integrated Flux in EBR-II Core Row 1 for RZ Reference Calculation and for One-dimensional (1D) Calculation with Full-height Constant Buckling

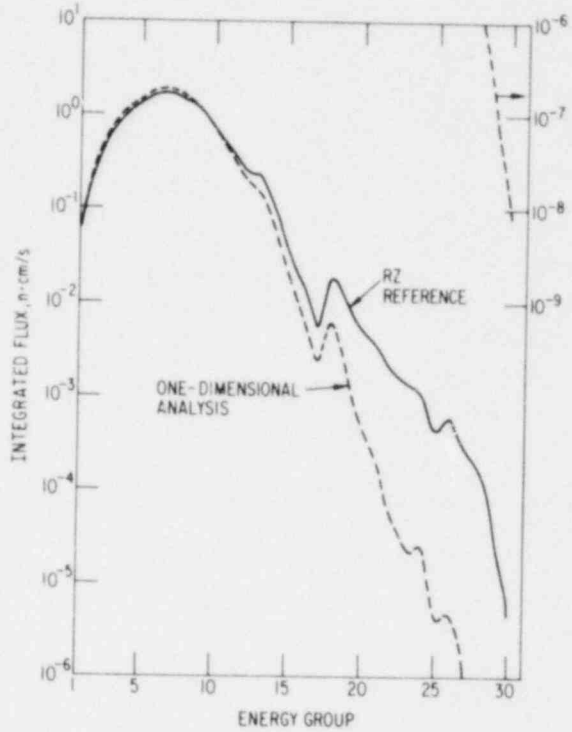

Fig. 2. Volume-integrated Flux in EBR-II Core Row 5 for RZ Reference Calculation and for 1D Calculation with Full-height Constant Buckling

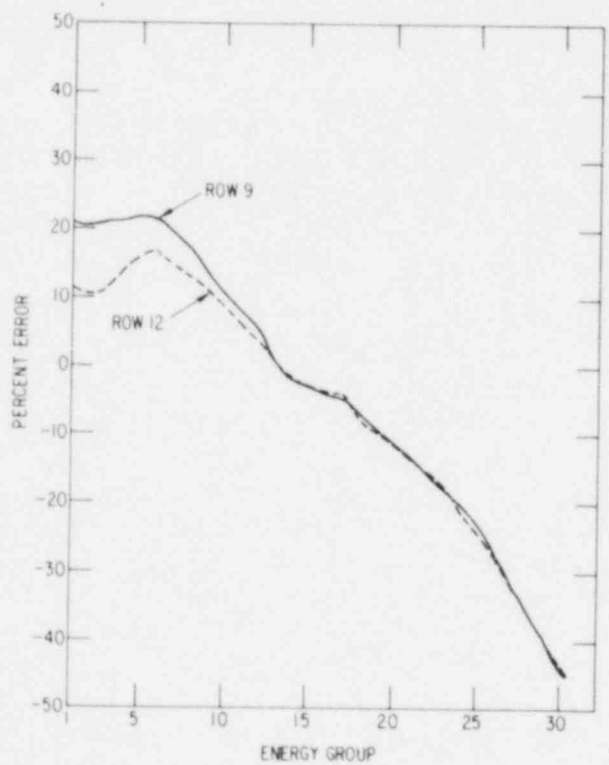

Fig. 3

Percent Error (Relative to RZ Reference Calculation) When Using a 1D Model with Full-core-height Constant Buckling: Reflector Row 9 and Blanket Row 12

In our analysis, the bucklings, which can be positive or negative, were then calculated for each row, using boundary currents. Sometimes, however, the use of these negative bucklings resulted in calculational instabilities.

To circumvent the difficulties associated with a negative buckling (a negative outward-leaking source), these leaking-in neutrons were modeled by either an additional fissioning source (the χ_g method) or an increased downscatter source [$\Sigma_s(1\rightarrow g)$]. This report describes the two methods and compares the results of their use to the results from a reference RZ calculation.

BUCKLING CALCULATION

In general, a buckling for energy group g and region R is calculated as if it is an additional removal by equating the integrated DB^2 leakage over the region volume (V_R) with the integrated normal axial currents ($\bar{J}\cdot n$) at the axial surfaces of the region, viz.,

$$\int_{V_R} D_g B_g^2 \phi_g \, dV = \int_S \bar{J}_g \cdot \bar{n} \, dA,$$

where

D_g is the diffusion coefficient for group g,

B_g^2 is the groupwise buckling,

ϕ_g is the groupwise scalar flux,

$\bar{J}_g$ is the groupwise current,

and

$\bar{n}$ is the unit vector normal to the regional axial surface S.

Hence, for a specific region and energy group, if we know the diffusion coefficient, and can obtain the scalar flux and the boundary angular fluxes from a reference calculation, the bucklings can be calculated. To show the usefulness of these bucklings in equivalent 1D cylindrical transport calculations with space- (region-) and energy-dependent bucklings, the resultant fluxes will be compared to the fluxes from the reference 2D RZ calculation. Our version of the 1D transport code ANISN had to be modified to accept space- and energy-dependent bucklings. Any axial reactor portion (slice) for the reference RZ calculation can be modeled in this way. The output flux times volume from the 1D calculation is equal to the flux times volume from the 2D calculation for the appropriate RZ slice.

The portion of the reference RZ calculation chosen for initial testing was a full-core-height 34.49-cm (13.5-in.) slice of the core, radial reflector, and radial blanket. The radial mesh spacing used in the ANISN calculation was identical to the radial mesh spacing in the core slice of the RZ reference calculation. (Throughout this report that all 1D calculation radial mesh spacings reflect the corresponding radial mesh spacing in the RZ reference calculation.) Table I shows representative bucklings for core rows 1 and 5, reflector row 9, and blanket row 12 for this one-slice problem.

TABLE I. Regional Bucklings for 34.49-cm (Core-height) Axial Slice Buckling, cm^{-2}

Energy Group[a]	Core Row 1	Core Row 5	Reflector Row 9	Blanket Row 12
1	4.17-3[b]	4.48-3	4.34-3	2.45-3
2	4.21-3	4.52-3	4.15-3	2.20-3
3	3.92-3	4.21-3	3.46-3	2.25-3
4	3.38-3	3.62-3	2.82-3	2.24-3
5	3.03-3	3.27-3	2.31-3	1.90-3
6	2.69-3	2.87-3	1.89-3	1.57-3
7	2.13-3	2.20-3	1.53-3	1.39-3
8	1.77-3	1.87-3	1.38-3	1.26-3
9	1.36-3	1.23-3	1.13-3	1.16-3
10	6.61-4	5.33-4	1.00-3	1.04-3
11	-3.70-4	-5.09-4	8.84-4	9.53-4
12	-1.52-3	-1.89-3	7.54-4	9.12-4
13	-3.43-3	-3.51-3	5.19-4	8.33-4
14	-6.85-3	-7.54-3	3.89-4	7.93-4
15	-1.35-2	-1.38-2	3.60-4	7.69-4
16	-2.07-2	-2.46-2	4.73-5	7.52-4
17	-3.30-2	-3.68-2	3.20-5	8.01-4
18	-3.38-2	-3.48-2	-2.13-6	6.05-4
19	-6.82-2	-6.74-2	-2.24-4	5.10-4
20	-1.08-1	-1.09-1	-5.29-4	3.40-4
21	-1.27-1	-1.27-1	-8.71-4	1.96-4
22	-2.03-1	-2.05-1	-1.24-3	1.47-5
23	-2.12-1	-2.21-1	-1.66-3	-2.06-4
24	-1.87-1	-1.85-1	-2.15-3	-5.78-4
25	-4.62-1	-4.75-1	-2.72-3	-1.70-3
26	-4.06-1	-4.09-1	-3.85-3	-8.44-4
27	-4.59-1	-4.45-1	-5.37-3	-3.16-3
28	-1.43-1	-1.51-1	-7.28-3	-1.71-3
29	-2.71-1	-2.71-1	-9.25-3	-2.47-3
30	-1.05+0	-9.85-1	-1.23-2	-7.11-3

[a] Group energies given in Appendix A.

[b] Read 4.17-3 as 4.17×10^{-3}.

Severe calculational instabilities resulted when these bucklings were used in a 1D ANISN calculation. Although the effective transport cross section never became negative, the effective removal cross section (i.e., the effective transport cross section less the in-group scattering) became negative in some regions and energy groups. To circumvent these programmatic difficulties it was decided to use the positive bucklings as bucklings and transform the negative buckling terms into sources. Two methods which can be used to model these pseudo-sources will now be discussed.

The neutron-transport equation is just a statement of neutron conservation (losses = sources). The normal transport source term contains a fission source term and a scattering source term. When a negative-buckling (negative-loss) term is transposed from the loss side to the source side of the trans-

port equation, algebraically it may be disguised as either a fission source or a scattering source. With the χ_g method, negative bucklings are modeled by additional fission sources; with the $\Sigma_s(1\rightarrow g)$ method, they are modeled by additional scattering sources. The actual forms of the two methods are discussed below.

A. The χ_g Method

For a specific region R, the total fission-neutron source for energy group g is

$$\frac{\chi_g}{k} \sum_{i\epsilon R} \sum_{h=1}^{N} \nu_h^i \Sigma_{fh}^i \phi_h^i V_i,$$

where

χ_g is the fission spectrum for group g,

k is the system eigenvalue,

ν_h^i is the number of neutrons per fission for energy group h at mesh point i,

Σ_{fh}^i is the macroscopic fission cross section for energy group h at mesh point i,

ϕ_h^i is the scalar flux in energy group h at mesh point i,

and

V_i is the volume associated with mesh point i.

The meshwise source due to group-h fissions ($\nu_h^i \Sigma_{fh}^i \phi_h^i V_i$) has been summed over all N energy groups and over all mesh points (i) in region R.

An incremental fission spectrum ($\Delta\chi_g$) for energy group g is defined as

$$\Delta\chi_g \equiv \frac{\sum_{i\epsilon R} D_g^i |B_{g,i}^2| \phi_g^i V_i}{\frac{1}{k} \sum_{i\epsilon R} \sum_{h=1}^{N} \nu_h^i \Sigma_{fh}^i \phi_h^i V_i}$$

for energy groups in which there are negative buckling values, then the modified fission spectrum ($\chi_g + \Delta\chi_g$), when multiplied by the flux as was done above, will model both the fission neutrons and the neutrons axially leaking in. Although the incremental fission spectrum is dependent on the reference calculation, it should be relatively insensitive to run when the run-to-run modifications are small. If the run-to-run modifications are large, new incremental fission spectra have to be calculated.

As seen by the definition, the incremental fission spectrum is region dependent, so our version of the 1D transport code ANISN had to be modified to

:cept a region-dependent fission spectrum. The major effect of this modification was to slightly increase the code container size needed to run a roblem.

ince the denominator must not be zero if $\Delta\chi_g$ is to be defined, further adustments have to be made to model leakage of neutrons into nonfissioning egions. To accomplish this, in the reference calculation a small amount 10^{14} atoms/cm^3) of ^{235}U was inserted into what were originally nonfissionng regions. The choice of ^{235}U was arbitrary; any fissionable material ill suffice. The amount of fissionable material used in the nonfissioning egions, although arbitrary, should be kept small so that it does not alter he flux values or the system eigenvalue. The same number density of issionable material that appears in regions of the reference calculation as to appear in the equivalent regions of the 1D model.

3. The Σ_s (1→g) Method

For a specific region R, the total neutron scattering source for energy group g, assuming isotropic scattering, is

$$\sum_{i\epsilon R} \sum_{j=1}^{N} \Sigma^i_{j\to g} \phi^i_J V_i,$$

where $\Sigma^i_{j\to g}$ is the macroscopic scattering cross section for scattering between group j and group g at meshpoint i. A set of pseudo scattering cross sections ($\Sigma^R_{j\to g}$, j = 1, N) that model the axial in-leakage for region R and energy group g can be defined as follows:

$$\sum_{i\epsilon R} \sum_{j=1}^{N} \Sigma^R_{j\to g} \phi^i_j V_i = \sum_{i\epsilon R} D^i_g |B^2_{g,i}| \phi^i_g V_i.$$

For convenience, all the pseudo scattering was put into the transfer from group 1 to group g; hence,

$$\Sigma^R_{1\to g} = \frac{\sum_{i\epsilon R} D^i_g |B^2_{g,i}| \phi^i_g V_i}{\sum_{i\epsilon R} \phi^i_1 V_i}.$$

When multiplied by the flux, as was done above, these pseudo scattering cross sections model the axial in-leakage of neutrons. As with the incremental fission spectra in the χ_g method, these cross sections are region dependent even for a region-independent negative buckling. Once these cross sections are calculated, they are put into the 1D transport calculations by normal cross-section input/mixing methods. The Σ_s(1→g) method involves more numbers (cross-section sets) than the χ_g method does, but there is no code modification involved.

RESULTS

The quantitative comparisons between the reference RZ flux spectra and the 1D flux spectra calculated with bucklings and either the χ_g method or $\Sigma_s(1\rightarrow g)$ method are presented here in four different sections. The first section (Sec. IV.A) details the differences between the row-wise flux spectra calculated with the χ_g method and the $\Sigma_s(1\rightarrow g)$ method when the full-height core region is used as the calculational slice for the buckling. When a finer axial spectral definition is required, several axial slices may have to be used for the calculations. Section IV.B considers the case where the full-height core is described by three axial slices. The third section (Sec. IV.C) considers two axial noncore-slice calculations: one in the lower axial reflector, and one in the upper axial reflector.

All the above results are based upon angular fluxes obtain from transport theory analysis. In Section IV.D the results of the Sections IV.A-I.C are compared with results using fluxes calculated using diffusion theory.

A. One Slice Consisting of Full Core Height

This section compares the RZ reference flux spectra with the 1D flux spectra calculated using bucklings and either the χ_g or the $\Sigma_s(1\rightarrow g)$ method. The full-height core was the calculational slice. When each region is a full-core- height row, the representative directly calculated bucklings are as was shown in Table I. Tables II and III show, respectively, the additional fission spectra ($\Delta\chi_g$), and the pseudoscattering cross sections [$\Sigma_s(1\rightarrow g)$] that were calculated from the negative bucklings given in Table I.

Figures 4-7 show the percent errors in group flux (relative to the RZ reference flux) for core rows 1 and 5, reflector row 9, and blanket row 12 when using the χ_g method and the $\Sigma_s(1\rightarrow g)$ method. These figures show that the difference between the results from the two methods are small when compared to the types of differences seen in Figs. 1-3.

The flux values for row 9 (radial reflector), calculated using 1D analysis, have the highest errors in the first few energy groups. The errors then moderate. This effect is irrespective of calculational slice. These errors result from use of axial out-leakage values obtained from highly anisotropic flux distributions as though the out-leakage values arose from a diffusion theory angular distribution. This error is caused by trying to model a highly anisotropic axial out-leakage by an isotropic buckling. This error, although occurring in all regions, is largest in regions where there is no high-energy source and, hence, the high-energy angular flux is quite directional. The error, however, is not limited to high energies. Whenever an isotropic effect (fissioning or scattering) is used to simulate an anisotropic in-leaking source, a flux error will result even if the angular flux is derived from diffusion theory.

Since the differences between the χ_g and the $\Sigma_s(1\rightarrow g)$ methods are shown here, the negative bucklings are modeled only by the χ_g method in Sections IV.B and IV.C.

B. Three Slice Across Full Core Height

If a finer axial flux distribution is desired, multi-slice buckling calculations have to be done. A 1D flux calculation, with appropriate bucklings, has to be done for each required slice. This has been done for three core axial slices of the reference problem. The top and bottom core slices were 13.3 cm thick, whereas the middle slice was 7.9 cm thick.

TABLE II. Regional Additional Fission Spectra for 34.49-cm (Core-height) Axial Slice

Energy Group	Core Row 1	Core Row 5	Reflector Row 9	Blanket Row 12
1	4.17-3[a]	4.48-3	4.34-3	2.45-3
2	4.21-3	4.52-3	4.15-3	2.20-3
3	3.92-3	4.21-3	3.46-3	2.25-3
4	3.38-3	3.62-3	2.82-3	2.24-3
5	3.03-3	3.27-3	2.31-3	1.90-3
6	2.69-3	2.87-3	1.89-3	1.57-3
7	2.13-3	2.20-3	1.53-3	1.39-3
8	1.77-3	1.87-3	1.38-3	1.26-3
9	1.36-3	1.23-3	1.13-3	1.16-3
10	6.61-4	5.33-4	1.00-3	1.04-3
11	0.0	0.0	8.84-4	9.53-4
12	0.0	0.0	7.54-4	9.12-4
13	0.0	0.0	5.19-4	8.33-4
14	0.0	0.0	3.89-4	7.93-4
15	0.0	0.0	3.60-4	7.69-4
16	0.0	0.0	4.73-5	7.52-4
17	0.0	0.0	3.20-5	8.01-4
18	0.0	0.0	0.0	6.05-4
19	0.0	0.0	0.0	5.10-4
20	0.0	0.0	0.0	3.40-4
21	0.0	0.0	0.0	1.96-4
22	0.0	0.0	0.0	1.47-5
23	0.0	0.0	0.0	0.0
24	0.0	0.0	0.0	0.0
25	0.0	0.0	0.0	0.0
26	0.0	0.0	0.0	0.0
27	0.0	0.0	0.0	0.0
28	0.0	0.0	0.0	0.0
29	0.0	0.0	0.0	0.0
30	0.0	0.0	0.0	0.0

[a]Read 4.17-3 as 4.17×10^{-3}.

TABLE III. Regional Pseudoscattering Cross Sections for 34.49-cm (Core-height) Axial Slice

		Additional Fission Spectrum ($\Delta\chi_g$)			
Group	Original χ	Core Row 1	Core Row 5	Reflector Row 9	Blanket Row 12
1	2.18-2[a]	0.0	0.0	0.0	0.0
2	9.99-2	0.0	0.0	0.0	0.0
3	1.97-1	0.0	0.0	0.0	0.0
4	2.27-1	0.0	0.0	0.0	0.0
5	1.85-1	0.0	0.0	0.0	0.0
6	1.22-1	0.0	0.0	0.0	0.0
7	7.08-2	0.0	0.0	0.0	0.0
8	3.79-2	0.0	0.0	0.0	0.0
9	1.93-2	0.0	0.0	0.0	0.0
10	9.55-3	0.0	0.0	0.0	0.0
11	4.64-3	8.98-4	1.32-3	0.0	0.0
12	2.23-3	1.81-3	2.38-3	0.0	0.0
13	1.06-3	4.04-3	4.65-3	0.0	0.0
14	5.05-4	2.96-3	3.71-3	0.0	0.0
15	2.40-4	1.35-3	1.84-3	0.0	0.0
16	1.13-4	9.06-4	1.13-3	0.0	0.0
17	5.36-5	3.61-4	4.30-4	0.0	0.0
18	2.54-5	2.08-3	2.51-3	2.97+1	0.0
19	1.20-5	2.06-3	2.45-3	2.18+3	0.0
20	5.66-6	1.63-3	1.91-3	3.83+3	0.0
21	2.68-6	1.24-3	1.43-3	4.80+3	0.0
22	1.26-6	1.01-3	1.16-3	5.34+3	0.0
23	5.97-7	8.09-4	9.28-4	5.60+3	1.01-4
24	2.82-7	6.02-4	6.97-4	5.59+3	4.57-4
25	1.33-7	4.60-4	5.39-4	5.29+3	4.00-4
26	9.27-8	6.24-4	7.36-4	8.58+3	7.75-5
27	2.07-8	3.03-4	3.62-4	5.21+3	2.17-4
28	4.62-9	6.65-5	8.64-5	2.25+3	3.98-5
29	1.03-9	2.13-5	2.74-5	5.63+2	2.18-5
30	1.03-9	6.97-6	8.94-6	2.09+2	6.14-6

[a]Read 2.18-2 as 2.18×10^{-2}.

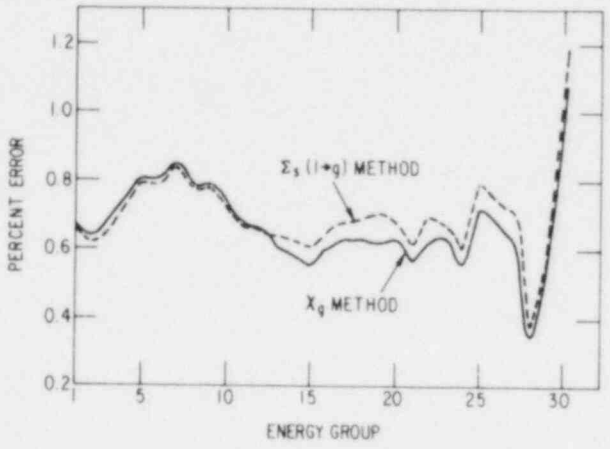

Fig. 4. Percent Error (Relative to RZ Reference Calculation) When Using a 1D Model with Variable Buckling and the χ_g and $\Sigma_s(l\to g)$ Methods: Full Core Height, Core Row 1

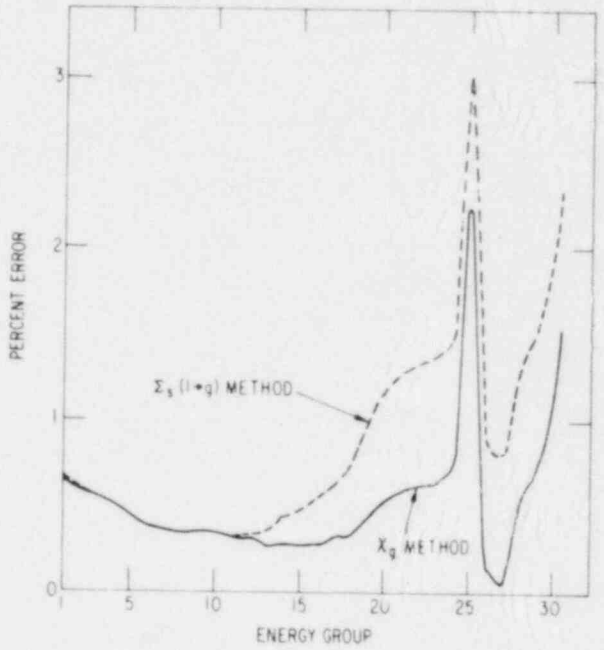

Fig. 5. Percent Error (Relative to RZ Reference Calculation) When Using a 1D Model with Variable Buckling with the χ_g and $\Sigma_s(l\to g)$ Method.: Full Core Height, Core Row 5

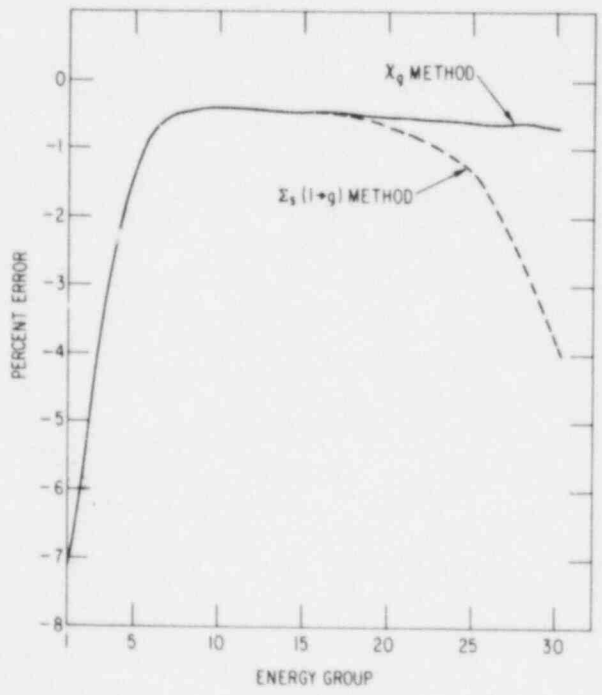

Fig. 6. Percent Error (Relative to RZ Reference Calculation) When Using a 1D Model with Variable Buckling with the χ_g and $\Sigma_s(l\to g)$ Methods: Full Core Height, Reflector Row 9

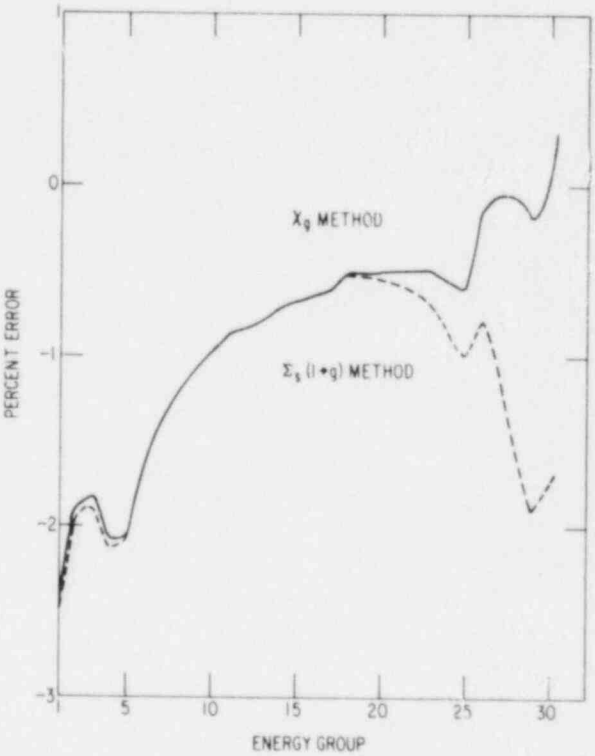

Fig. 7. Percent Error (Relative to RZ Reference Calculation) When Using a 1D Model with Variable Buckling with the χ_g and $\Sigma_s(l\to g)$ Methods: Full Core Height, Blanket Row 12

Figures 8 and 9 show the errors in group flux (relative to the RZ reference flux) for the middle and bottom slices of core rows 1 and 5, reflector row 9, and blanket row 12 when using the χ_g method. The flux errors for rows 1 and 5 are within a few percent until energy group 20. After group 20, the error becomes oscillatory and relatively large. This large error is due to an unsatisfactory mesh spacing for the lower-energy groups and the relative hardness of the lower-energy source in the middle slice. The low-energy source for the middle slice is mainly a combination of transport (leaking in) and downscatter, not fission. These low-energy neutrons [as represented by the $\Delta\chi_g$ or the $\Sigma_s(1\rightarrow g)$ method] see a relatively large removal cross section (about half the transport cross section). In the low-energy groups, these neutrons are removed mostly by absorption. Because of the large removal cross section, a fine mesh is needed to follow the rapidly varying low-energy spatial source and flux. (The results for the top slice are not shown since, due to symmetry, top slice results are nearly identical to bottom slice results.) A 13-axial-slice case was also done. Thirteen-axial slices correspond to one calculational slice per axial mesh interval in the reference calculation. The results for this case are not shown because they are similar to the three-slice-case.

C. Slice Across Lower and Upper Axial Reflectors

This series of calculations modeled an axial slice one mesh interval wide in each axial reflector. (See Fig. 1-A in the Appendix for the relative location of the axial reflectors.) The axial slice in the lower reflector went through 7-1/2 rows of lower reflector, 3-1/2 rows of radial reflector, and 4+ rows of radial blanket (blanket rows 15 and 16 are not full rows). Figure 10 shows the flux errors in core rows 1 and 5, reflector row 9, and blanket row 12 of the lower-reflector slice when the χ_g method was used to model axially incoming neutrons. (Recall that a small amount of ^{235}U was put into all nonfissioning regions so that the χ_g method could be used in these regions.) As in the other slices, the errors in the high-energy groups are due to modeling anisotropic leakage by isotropic buckling.

The axial slice in the upper axial reflector went through four rows of upper reflector followed by one row (row 5) composed of a radial smear of axial reflector and seven boron carbide control rods, 1-1/2 more rows of upper reflector, 3-1/2 rows of radial reflector, and 4+ rows of radial blanket. Because of cylindricization and self-shielding effects, the ^{10}B was put only into the outer zone of row 5. To conserve atoms, ^{11}B was substituted for ^{10}B in the inner zone. Figure 11 shows the flux errors in core rows 1 and 5, reflector row 9, and blanket row 12 of the upper-reflector slice when the χ_g method was used to model axially incoming neutrons. Again, the errors in the high-energy groups are due to modeling anisotropic leakage by isotropic buckling. The relatively high errors in the lower-energy group in the outer zone of the row-5 control-rod section are due to mesh spacing problems in the highly absorbing ^{10}B-containing zone. Much of the error in the lower-energy groups of the inner (non-^{10}B-containing) zone of row 5 is a result of the error in the outer zone of that row. Figures 10 and 11 show that even noncore axial slices can be modeled if adequate care is taken in setting up the reference calculation.

D. Diffusion Theory Flux Estimates

The only difference between transport calculated parameters and diffusion calculated parameters is in how the axial leakage is calculated.

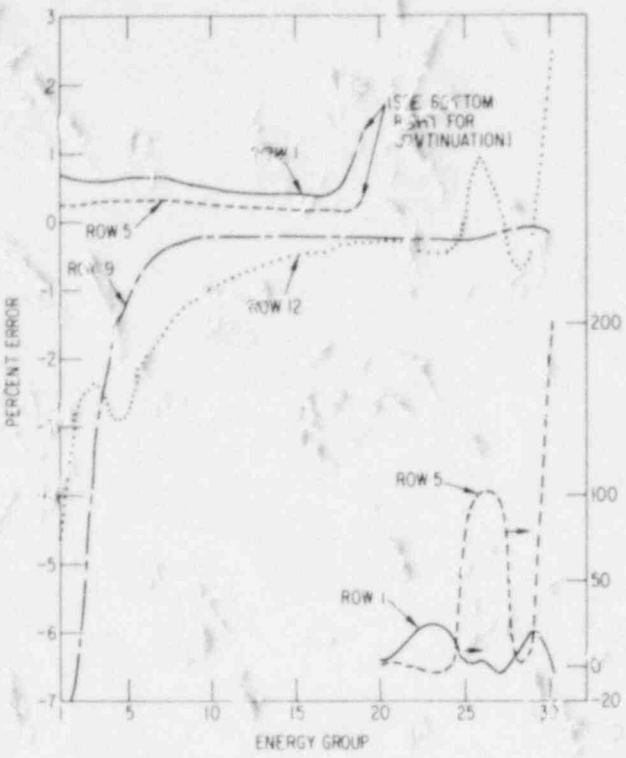

Fig. 8. Percent Error (Relative to RZ Reference Calculation) When Using a 1D Model with Variable Buckling and the χ_g Method: Middle Slice of Three-slice Problem

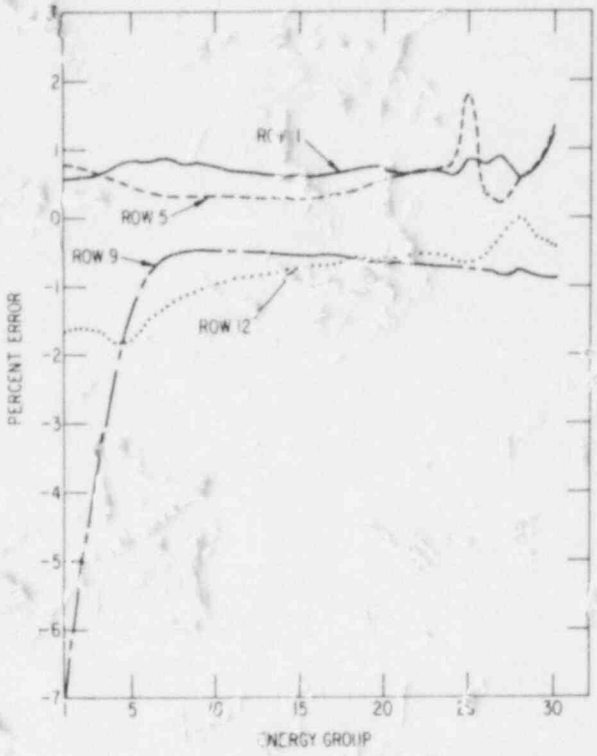

Fig. 9. Percent Error (Relative to RZ Reference Calculation) When Using a 1D Model with Variable Buckling and the χ_g Method: Bottom Slice of Three-slice Problem

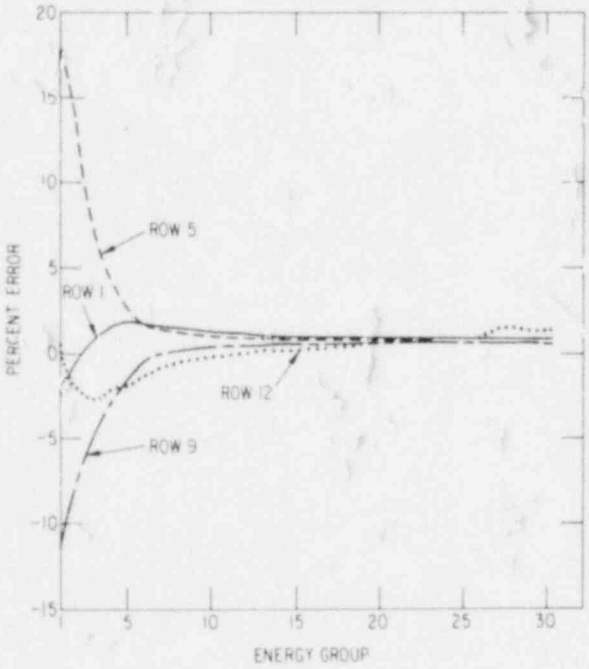

Fig. 10. Percent Error (Relative to RZ Reference Calculation) When Using a 1D Model with Variable Buckling and the χ_g Method: Lower-reflector Slice

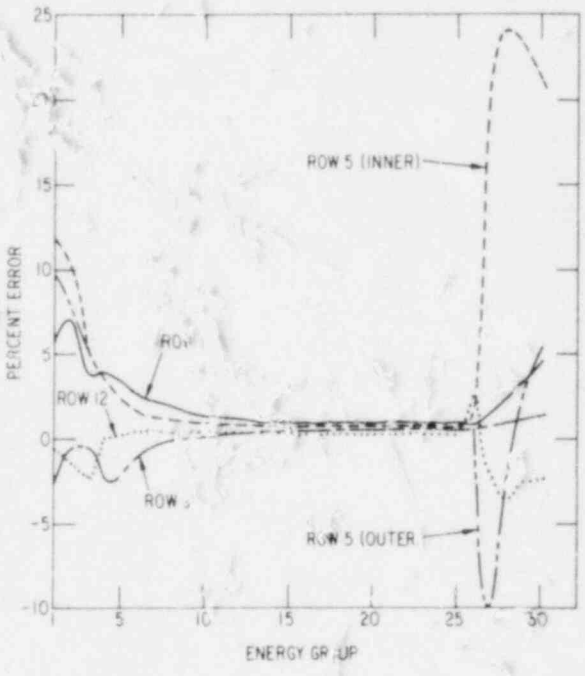

Fig. 11. Percent Error (Relative to RZ Reference Calculation) When Using a 1D Model with Variable Buckling and the χ_g Method: Upper-reflector Slice

The transport-analysis method uses transport boundary angular fluxes to calculate the axial leakage, whereas the diffusion method uses flux-differencing methods and diffusion fluxes. Although transport methods more accurately describe actual boundary phenomena, the flux error between 2D diffusion and 1D diffusion [with diffusion-calculated parameters of buckling, χ_g and $\Sigma_s(1\rightarrow g)$] should be smaller than the flux error between 2D transport and 1D transport (with transport-calculated parameters), because Fick's Law (the diffusion approximation) was assumed to apply in developing the bucklings and the χ_g and $\Sigma_s(1\rightarrow g)$ methods. This does not imply that the diffusion error should be smaller.

The diffusion theory calculations were done with the CITATION (Ref. 4) diffusion theory code. Only the $\Sigma_s(1\rightarrow g)$ method was used in diffusion analysis, because it was the easier method to incorporate in our diffusion-analysis codes. Besides, the transport results shown in Figs. 4-7 indicate that χ_g method gives results similar to those from the $\Sigma_s(1\rightarrow g)$ method.

Figures 12-15 are Figs. 4-7 with the percent error for the $\Sigma_s(1\rightarrow g)$ method using diffusion theory superimposed. The results show that indeed the diffusion RZ flux is easier to approximate than the transport flux. (It should be pointed out that the diffusion calculation with the negative bucklings left as buckling terms converged, but the relative flux errors were much larger than those shown in Figs. 12-15.) The three slice case shows similar improvement. Whereas the transport middle-slice calculation (see Fig. 8) has a maximum error approaching 200% and the end-slice calculation (see Fig. 9) has a maximum error approaching -7%, the diffusion middle-slice and end-slice calculations maximum errors are, respectively, 1.5% and 0.6%.

The upper- and lower-reflector slice diffusion cases are not shown because of problems with the diffusion $\Sigma_s(1\rightarrow g)$ cross sections used in the flux calculations. In these regions negative bucklings, thus the $\Sigma_s(1\rightarrow g)$ cross sections, are in the high energy groups. But in the CITATION code, the in-group transfer is ignored, hence no leakage-in source could be put into group one. This problem could be overcome by using the χ_g method.

CONCLUSIONS

The results show that good agreement can be obtained between the transport groupwise fluxes calculated with RZ geometry and those calculated with 1D geometry using bucklings calculated from transport theory boundary angular fluxes, with either the χ_g or the $\Sigma_s(1\rightarrow g)$ method substituting for negative bucklings. One-dimensional diffusion theory results, using bucklings calculated from RZ diffusion fluxes, show improved agreement with diffusion RZ fluxes. This results from use of the relation between bucklings and leakages which is valid for diffusion theory but has been assumed valid also for use with the transport theory flux and leakage solutions. Whether transport or diffusion theory is used, adequate mesh spacing must be used in regions of relatively high absorption and low sources. Even if the reference calculation is adequate for the buckling calculation, a small error will be introduced because anisotropic leakage is modeled by an isotropic effect. This built-in error is usually largest in the high-energy groups of nonfissioning regions.

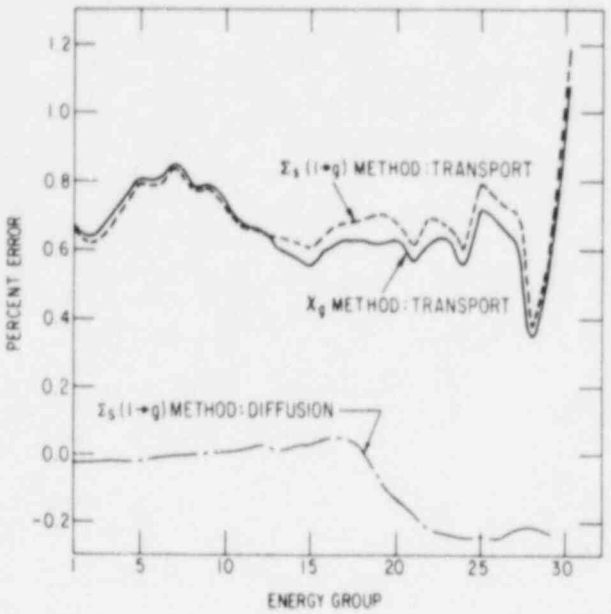

Fig. 12. Percent Error (Relative to RZ Reference Calculation) in Flux from 1D Calculations Using Full-height Variable Buckling and the χ_g and $\Sigma_s(1\rightarrow g)$ Methods: Core Row 1

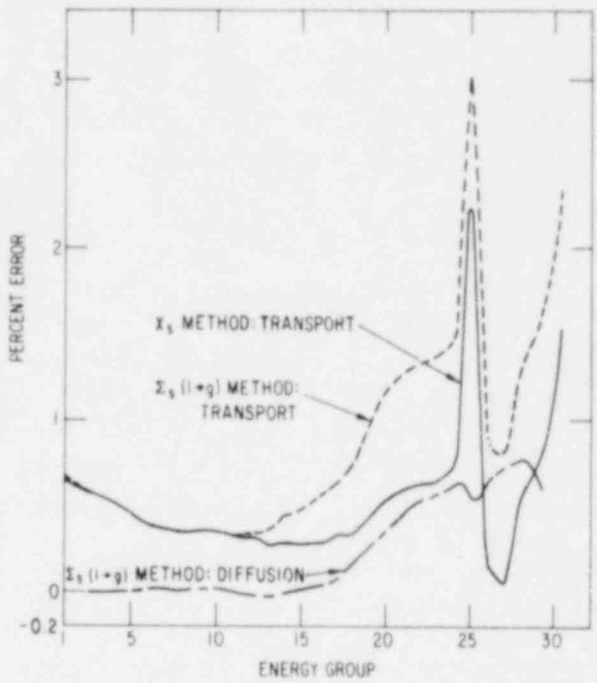

Fig. 13. Percent Error (Relative to RZ reference Calculation) in Flux from 1D Calculations Using Full-height Variable Buckling and the χ_g and $\Sigma_s(1\rightarrow g)$ Methods: Core Row 5

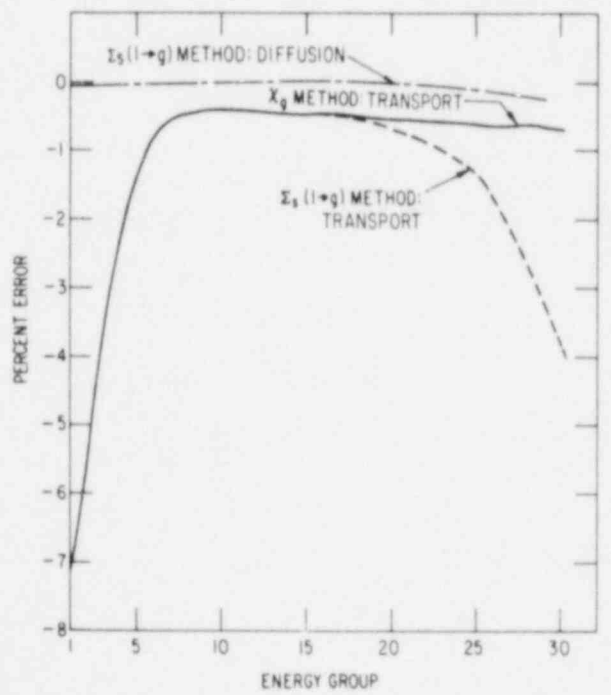

Fig. 14. Percent Error (Relative to kZ Reference Calculation) in Flux from 1D Calculations Using Full-height Variable Buckling and the χ_g and $\Sigma_s(1\rightarrow g)$ Methods: Reflector Row 9

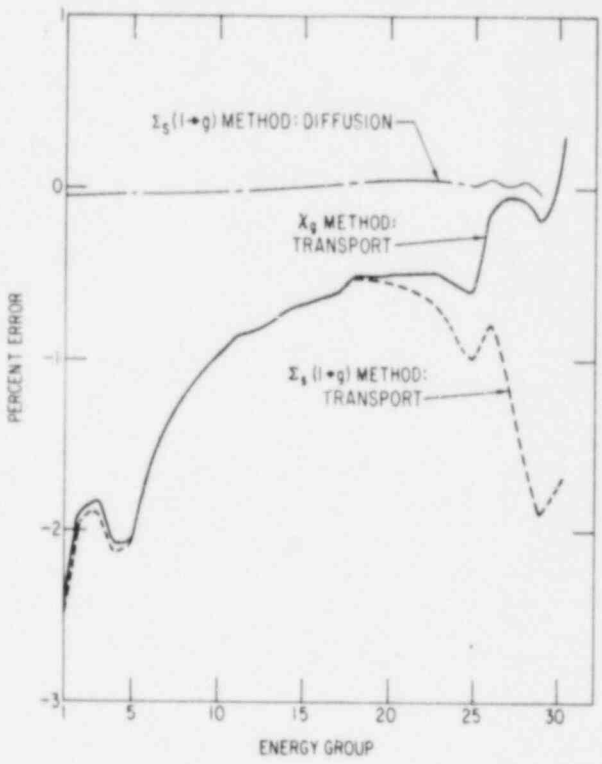

Fig. 15. Percent Error (Relative to RZ Reference Calculation) in Flux from 1D Calculations Using Full-height Variable Buckling and the χ_g and $\Sigma_s(1\rightarrow g)$ Methods: Blanket Row 12

APPENDIX A

Reference Calculations

The RZ configuration used throughout this study as the reference was based on an EBR-II loading similar to run 105A. Figure A-1 shows the RZ geometrical configuration. The radial mesh spacing was $\sim$ 2.7 cm (two mesh intervals per radial row). The core axial mesh spacing was $\sim$ 2.7 cm. The axial mesh spacing in noncore regions varied, however, it was always less then 3.5 cm. The XY configuration for which the row-wise atom-density smearing was done is shown in Fig. A-2. The reference transport calculation was normalized so that the total integrated fission-neutron source was 1 neutron/s. The reference diffusion calculation was normalized so that the total integrated neutronic power was 57.25 MW.

The neutron cross sections used in the transport calculations are a 30-energy-group, transport-approximation P_0 set generated by the MC^2 code (Ref. 5) from ENDFB/Version III data. Table A-I shows the 30-energy-group structure. The neutron cross sections used in the diffusion calculations are a 29-energy-group set generated from ENDFB/Version I data. The 29-energy-group structure is the first 29-energy-group of the 30-energy-group structure.

REFERENCES

1. F. R. Mynatt, *DOT, A Two-dimensional Discrete-ordinates Transport Code*, K-1694, Radiation Shielding Information Center, Oak Ridge National Laboratory.
2. W. A. Rhoades, D. B. Simpson, R. L. Childs, and W. W. Engle, Jr., *The DOT-IV Two-dimensional Discrete-ordinates Transport Code with Space-dependent Mesh and Quadrature*, ORNL-TM-6529, Oak Ridge National Laboratory (August 1978).
3. W. W. Engle, Jr., *A Users Manual for ANISN--A One-dimensional Discrete Ordinates Transport Code with Anisotropic Scattering*, K-1693, Oak Ridge National Laboratory (June 1973).
4. T. B. Fowler and D. R. Vondy, *Nuclear Reactor Core Analysis Code: CITATION*, ORNL-TM-2496, Oak Ridge National Laboratory (July 1970).
5. B. J. Toppel, A. L. Rago, and D. M. O'Shea, *MC^2, A Code to Calculate Multigroup Cross Sections*, ANL-8318 (June 1967).

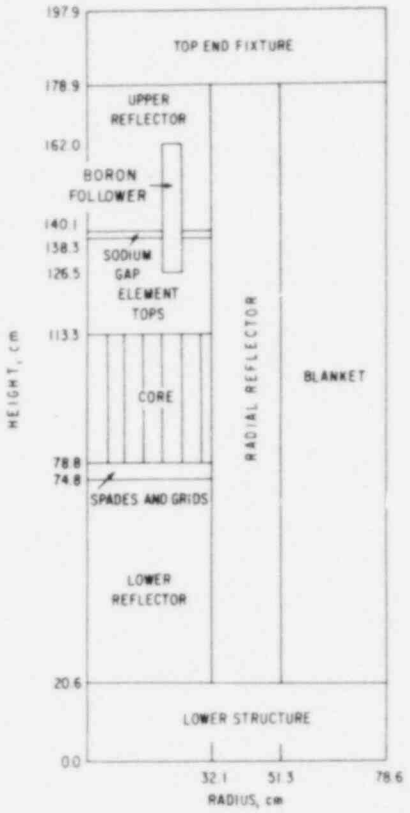

Fig. A.1. Geometrical Configuration for RZ Reference Calculation

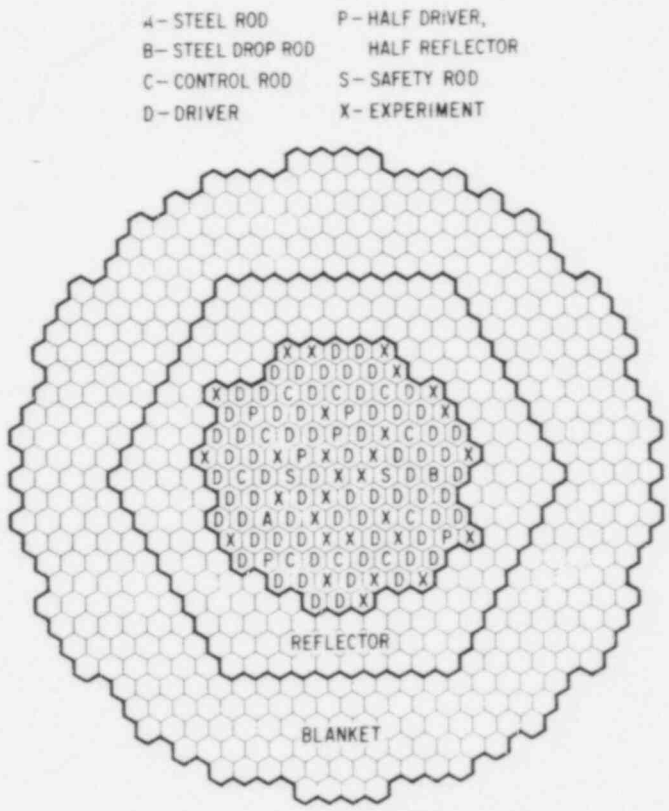

Fig. A.2. Core Loading Configuration for Proposed EBR-II Run 105A

TABLE A-1. Thirty-group-set Energy Structure Used in Neutronic Calculations for EBR-II Runs

Group No.	Upper Energy, eV	Lethargy Width
1	0.10000+8[a]	0.5
2	0.60653+7	0.5
3	0.36788+7	0.5
4	0.22313+7	0.5
5	0.13534+7	0.5
6	0.82085+6	0.5
7	0.49787+6	0.5
8	0.30197+6	0.5
9	0.18316+6	0.5
10	0.11109+6	0.5
11	0.67379+5	0.5
12	0.40868+5	0.5
13	0.24788+5	0.5
14	0.15034+5	0.5
15	0.91188+4	0.5
16	0.55308+4	0.5
17	0.33546+4	0.5
18	0.20347+4	0.5
19	0.12341+4	0.5
20	0.74852+3	0.5
21	0.45400+3	0.5
22	0.27536+3	0.5
23	0.16702+3	0.5
24	0.10130+3	0.5
25	0.61442+2	0.5
26	0.37267+2	1.0
27	0.13710+2	1.0
28	0.50435+1	1.0
29	0.18554+1	1.0
30	0.68256+0[b]	∞

[a] Read 0.10000+8 as 0.10000×10^{8}.

[b] Lower energy of group 30 = 0.0 eV.

BACKGROUND CROSS-SECTION METHOD FOR EPITHERMAL SPECTRUM CALCULATION IN THERMAL REACTORS

Yung-An Chao and Aquilino Senra Martinez*
Nuclear Science and Engineering Division
Carnegie-Mellon University
Pittsburgh, PA 15213

ABSTRACT

To improve Bondarenko's background cross-section method for thermal reactor applications, a more accurate homogenization of the cells than using Wigner's equivalence theorem is needed. A scheme of resolving this problem was suggested by the authors, based on the moment expansion approximation to collision probabilities developed by the authors. The scheme, further refined and simplified, is now tested numerically against benchmark calculations of the EPRI OZMA code. The expected error of the order of magnitude of 1% from spatial homogenization for each individual resonance, is confirmed. Independent of the question of homogenization, however, resonance interference from differen t isotopes affecting the proper definition of the background cross-section is found to be a dominating source of error in the background cross-section method. A method to resolve this difficulty is devised. The overall effect of the errors on the k-effective is found to be 0.03% for a typical PWR core.

INTRODUCTION

Aiming at developing an accurate background cross-section method applicable to thermal reactor calculations, we have recently published a series of articles ranging from a moment expansion scheme of calculating escape probabilities[1] and Dancoff corrections,[2] to a new formulation of equivalence theorem and background cross-section method.[3] In this paper we report numerical results of test calculations for the proof of principle. The formulation of Ref.(3) is further refined and simplified in the following aspects. (1) The two correction terms to the conventional background cross-section flux is reduced to one with no loss of accuracy. (2) The Dancoff correction is incorporated in a more natural and accurate way. (3) The effect of the absorptive component of the conventionally defined background cross-section on the flux suppression is accounted for. (4) The formulation is further generalized to include a third cladding ring. The proof of principle calculations are done for typical PWR lattices in the MUFT 54 group structure and compared against benchmark calculations using the EPRI OZMA code,[4] which uses (point by point) experimental cross-section profiles and solves the integral transport equation.

The theoretical refinements will be discussed first, and the numerical result of the test calculations follows. Errors of all major approximations are individually identified and estimated. It is found that the most difficult problem is that the very assumption of a background cross-section itself may contribute to the dominating (large) error in the presence of interference of resonances of different isotopes. Granting the validity of the assumed background cross-section, the error from spatial homogenization is well confirmed to be of the order of magnitude of one per cent for each of the fine groups as the

* Permanent address: Universidade Federal do Rio de Janeiro, COPPE/Nuclear Engineering Program, Rio de Janeiro, R.J. 20000, Brazil.

analysis of Ref.(3) indicates. To resolve the difficulty of resonance interference from different isotopes, a method is devised to build a separate interference file which is consistent with the scheme of homogenization and compatible to the use of the background cross-section files. With this interference file, the overall error for averaged cross-sections and reaction rates in each fine energy group can be kept satisfactorily small. The collective contribution of these errors from epithermal groups to the k-effective is found to be 0.03% for a typical PWR lattice.

THEORY

According to the analysis given in Ref.(3), for a two region (fuel-moderator) cell, the flux in the fuel region, Φ_f, can be decomposed into two terms,

$$\Phi_f = \Phi_0(\Sigma_0) + \alpha\Sigma_e^2 \Phi_1(\Sigma_0) \tag{1}$$

the constant parameter α and the effective geometry cross-section Σ_e both depend only on the geometry of the lattice. The flux spectrum as a function of energy is determined through Φ_0 and Φ_1 which satisfy the following integral equations.

$$(\Sigma_t^A + \Sigma_0)\,\Phi_0 = \int_E^{E/\alpha_A} \frac{\Sigma_s^A \Phi_0}{(1-\alpha_A)E'}\,dE' + \Sigma_0/E \tag{2a}$$

$$(\Sigma_t^A + \Sigma_0)\,\Phi_1 = \int_E^{E/\alpha_A} \frac{\Sigma_s^A \Phi_1}{(1-\alpha_A)E'}\,dE' + (\Sigma_t^A + \Sigma_0)^{-1}\,(1/E-\Phi_0) \tag{2b}$$

which both involve Σ_0 as the only parameter for a given cross-section profile of the absorber A. The parameter Σ_0 is defined as

$$\Sigma_0 = \Sigma_b + \Sigma_e \tag{3a}$$

where

$$\Sigma_b = \text{the background cross-section} \tag{3b}$$

The above equations are improved over those of Ref.(3) with the reduction of three flux components to two. This is possible due to a more concise treatment of the terms containing escape probability. It is realized that all the approximations made to the escape probability and Dancoff correction can be summarized in the following single equation,

$$\Sigma_t^f P_f/(1-P_f) = \Sigma_e(1+\alpha P_w) \tag{4}$$

where Σ_e is the Dancoff corrected geometry cross-section, P_w is Wigner's rational approximation, $\Sigma_e/(\Sigma_e+\Sigma_t^f)$, and α is a constant geometry parameter which depends very simply (essentially linearly) on the Dancoff correction. The validity of the approximation, Eq.(4), has been examined over all the ranges of optical length and lattice pitch.

The background cross-section Σ_b is conventionally defined simply as the group averaged sum of all the fuel cross-sections except for that of the absorber under consideration. Such a definition of Σ_b induces two errors in

Eq.(2). One is the neglect of any interference between resonances of the absorber and other fuel isotopes contributing to Σ_b. The other is the unproper normalization of the flux solved from Eq.(2). The former is a much tougher problem and will be discussed later. The latter does not affect the calculation of averaged cross-sections, but does affect very significantly the calculation of reaction rates. We will discuss this problem and its remedy first. The normalization of the slowing down density for Eq.(2) is 1/E. If the absorption cross-section of isotope A were set at zero, the flux solved from Eq.(2) would be 1/E. However, we know that even if $\Sigma_a^A=0$, Σ_b may still contain absorption from other isotopes and therefore the flux should be smaller that 1/E. The mistake is that the right hand side of Eq.(2) provides slowing down sources and should not have the appearance of any absorption cross-sections of the other fuel isotopes. In other words, it should be something smaller than Σ_b instead of Σ_b itself on the right hand side. However, it is not simply Σ_b subtracting the absorptive part of Σ_b either; the question of the validity of narrow resonance approximation for other fuel isotopes arises too. A more accurate treatment is to replace Σ_b on the right hand side of Eq(2) by Σ_b', and determine Σ_b' by the following consistency requirement. If we go back to the exact flux integral equation prior to the introduction of background cross-section, and replace all energy dependent cross-sections by their group averaged values, we will find explicitly the flux as, say, C/E. Now we go to Eq.(2), replace Σ_b on the right by Σ_b' and replace Σ_t^A and Σ_s^A by their group averaged values $\bar{\Sigma}_t^A$ and $\bar{\Sigma}_s^A$. Then we find the flux explicitly as, say C'/E where C' is a function of Σ_b'. Setting C' equal to C for consistency we can determine Σ_b'. The result of this correction is that

$$\Phi_F' = ((\Sigma_0' + \bar{\varepsilon})/(\Sigma_0 + \bar{\varepsilon}))\ \Phi_F(\Sigma_0) \tag{5}$$

where $\Phi_F(\Sigma_0)$ is the solution of Eqs.(1) and (2),

$$\bar{\Sigma}_0' = \Sigma_b' + \Sigma_e \tag{6a}$$

$$\bar{\varepsilon} = \alpha\Sigma_e^2/(\Sigma_e + \bar{\Sigma}_t^A) \tag{6b}$$

$$\Sigma_b' = (\Sigma_b - \Sigma_{ba})(\Sigma_e + \bar{\varepsilon})/(\bar{\Sigma}_a^A + \Sigma_{ba} + \Sigma_e + \bar{\varepsilon}) \tag{6c}$$

with Σ_{ba} defined as the absorptive part of Σ_b.

We have also generalized the formulation to three regions to include a cladding. Starting with three flux integral equations in the three regions, we make several approximations to the collision probabilities to arrive at the result that the cladding included flux is equal to Φ_F' multiplied by a factor generally less than one and equal to one in the limit of vanishing absorption in the cladding or vanishing thickness of it. The Dancoff correction for a three region lattice is also worked out in a simple yet sufficiently accurate approximation. We will omit the presentation of the three region analysis here because it is somewhat involved. In any case, for typical PWR lattices, a straightforward homogenization of the cladding and the moderator by volume weighting is found to be sufficiently accurate that the use of the more accurate three region treatment has not been found to be really necessary.

The use of the above scheme to develop background cross-section files and the use of the files go as follows. First one solves Eq.(2) for Φ_0 and Φ_1

for values of Σ_0 and tabulates against Σ_0 the averaged cross-sections and reaction rates that are calculated with ϕ_0 and ϕ_1 separately. To use the files one starts with estimated initial values of averaged cross-sections of the isotopes in question, from which an initial value of Σ_0 results. To this initial value of Σ_0, corresponding values of cross-sections and reaction rates contributed by ϕ_0 and ϕ_1 are fetched from the tabulated files. The ϕ_0 and ϕ_1 contributions are then linearly combined according to Eq.(5) to give updated cross-sections of the isotopes, from which the updated Σ_0 is obtained. This iteration continues until convergent results are reached.

Such a scheme is superior to the original Bondarenko's in three ways. One is the much more accurate and fudge-parameter independent method of spatial homogenization. The other is that Eq.(2) is solved exactly for the fluxes, while Bondarenko used 1/E fluxes. The third is that reaction rates in addition to group averaged cross-sections are tabulated as well, so that essentially all the useful information from epithermal spectrum calculation is stored in the background cross-section files.

However, there still remains one most important assumption, that is, in Eq.(2) all cross-sections except for that of the absorber under consideration are replaced by energy independent, group averaged cross-sections.

TEST CALCULATIONS

To check the accuracy of the various approximations made and examine the feasibility of the method, a series of proof of principle calculations are carried out. As we have repeatedly emphasized, the theory we have developed deals with the problem of spatial homogenization and improvements over Wigner's equivalence theorem. However, even if we were to consider a truly homogeneous medium so that no homogenization is needed, the very basic idea itself of background cross-section, namely assuming constant group averaged cross-sections for "background" isotopes may not be valid. This invalidity arises if the background isotopes have strong resonances overlapping with those of the particular isotope under consideration. Thus to separate the issue of spatial homogenization from interference of resonances of different isotopes, we first check the validity of the very assumption of constant cross-sections for the background isotopes. We consider a typical two-region PWR lattice (neglecting the cladding at the moment for simplicity) with 3% enriched uranium metal as fuel. The benchmark epithermal calculation for this lattice is done with the code OZMA, which can handle a heterogeneous cell by dividing each region up to ten sub-regions and solving the integral transport equation numerically. The cross-section profiles are constructed from point-to-point experimental data instead of resonance parameters. With the benchmark solution available, the correct values of group averaged cross-sections of the isotopes can be computed. We then test the validity of the notion of background cross-section by running OZMA again, however, with cross-section profiles of "background" isotopes replaced by their group averaged cross-sections. If the result of this second run of OZMA disagrees with that of the benchmark calculation, then the notion of background cross-section is not valid. Since no other approximations are made, this disagreement directly reflects the effect of resonance interference between background isotopes and the isotope under consideration. The findings of this test calculation can be summarized as follows.

1) The errors associated with U^{238} are generally much smaller than those associated with U^{235}. This is easy to understand because flattening the resonance profiles of the 97% u^{238} will have a large effect on the spectrum, while flattening that of the 3% U^{235} affects the spectrum much more mildly.

2) For most of the resonance present groups (groups 27 to 54 of the MUFT groups) the errors are quite small. The ones with error greater than 2% are listed in Table 1.

3) The most troublesome groups are the 41st, 45th and 46th.

The lattice of this example is a hexagonal one with a fuel rod radius of 0.5199 cm and a pitch distance of 1.99967cm. The symbols R and Σ refer to reaction rate and cross-section, the subscripts A and S refer to absorption and scattering, and the superscript 5 and 8 refer to U^{235} and U^{238}.

Group	R_A^5	R_S^5	R_A^8	R_S^8	Σ_A^5	Σ_S^5	Σ_A^8	Σ_S^8
34	4.5	4.5	--	--	--	--	--	--
36	--	--	--	--	-2.95	--	--	--
38	--	3.64	--	--	-3.59	--	--	--
39	-2.27	6.89	--	--	-6.10	2.71	--	-2.26
41	15.94	5.94	--	-2.62	12.69	2.97	--	-3.11
45	25.07	7.78	--	--	19.54	3.01	--	--
56	44.42	--	4.70	--	45.00	--	5.55	--

Table 1. Percentage errors from the sole approximation of using group averaged cross-sections for "background" isotopes. These errors directly reflect resonance interference between the two isotopes.

To see how important these errors are, we convert the errors in reaction rates in Table 1 to the corresponding errors in the total reaction rates from all the twenty-eight groups between the 27th group and the 54th group. As listed in Table 2, we conclude that the basic idea of background cross-sections breaks down for groups 41st, 4th and 46th. Additional refinements must be made to these three groups to account for the resonance interference effect.

Group	R_A^5	R_S^5	R_A^8	R_S^8
34	.12	.12	--	--
38	--	.07	--	--
39	-.13	.19	--	--
41	.73	.14	--	-.06
45	.33	.13	--	--
46	1.23	.01	.52	-.02

Table 2. Contributions of the errors in Table 1 to percentage errors in the total reaction rates of all the groups between the 27th and the 54th group.

To assess the accuracy of our homogenization method, summarized in Eqs. (1) and (5), we compare the solution to these equations against the heterogeneous OZMA calculation with the same group averaged cross-sections for the background isotopes. The percentage errors of the comparison are presented in Table 3, together with the corresponding errors of using Wigner's rational approximation, i.e., setting α=0 in Eqs. (1) and (5). Only groups with errors for our method greater than 2% are shown in the table. It confirms very well the theoretical estimation that in general the errors should be of the order of magnitude of one per cent. The errors are a little larger for U^{235} than U^{238}; however, the absolute contribution from U^{235} is also much smaller because of its low number density.

Group	R_A^5	R_S^5	R_A^8	R_S^8	Σ_A^5	Σ_S^5	Σ_A^8	Σ_S^8
33	-- (-2.99)	-- (-2.99)	-- (-9.28)	-- (-2.24)	-- (--)	-- (--)	-2.01 (-7.23)	-- (--)
39	-- (-10.14)	-- (-9.25)	3.11 (-5.57)	-- (-4.42)	-- (--)	-- (--)	-- (--)	-- (--)
41	2.72 (-10.86)	-- (-11.89)	2.07 (-8.19)	-- (-8.11)	2.94 (--)	-- (--)	-- (--)	-- (--)
43	2.81 (-5.93)	-- (-4.63)	-- (-4.51)	-- (-4.51)	-- (-2.01)	-- (--)	-- (--)	-- (--)
44	4.10 (-5.21)	-- (-5.94)	-- (-6.20)	-- (-5.77)	3.60 (--)	-- (--)	-- (--)	-- (--)
46	-- (-12.04)	-- (-9.92)	-- (-12.01)	3.92 (-6.35)	-- (-2.49)	-- (--)	2.31 (-4.89)	-- (--)
47	2.17 (-3.84)	-- (-2.68)	-- (--)	-- (--)	-- (--)	-- (--)	-- (--)	-- (--)

Table 3. Percentage errors resulting from our method of homogenization as compared to heterogeneous OZMA calculation neglecting resonance interference between isotopes. In parentheses are the corresponding errors of using Wigner's rational approximation.

Now we come back to the problem of resonance interference. It should be emphasized that the interference here is referring to that between resonances of different isotopes, not that among the resonances of the same isotope. For the isotope whose reaction rate is to be computed from the solutions of Eq. (2), its exact cross-section profile is used in the equation and the interference among its own resonances are all automatically accounted for. This is quite different from classical approximations such as narrow resonance approximation, which assumes no interference between adjacent resonances so that the flux recovers to 1/E shape between the resonances. The uniquely attractive feature of a background cross-section method is that the flux

depends only on the cross-section profile of the isotope under consideration and is independent of what the background isotopes are and how their cross-section profiles behave. As soon as interference is included, the flux necessarily depends on the cross-section profile of the interferring isotope as well, and the attraction of a background cross-section method is immediately lost. Therefore, the interference problem really lies outside the scope of background cross-section methods. To bring in interference is essentially to give up the idea of background cross-section method.

Whatever method to account for resonance interference is introduced to supplement a background cross-section method, some sort of resonance interference file involving parameters of the interferring isotopes must be introduced. Fortunately, not interference from any two isotopes must be included. Usually the spectrum is dominated by one major isotope, e.g., U^{238} for LWR. It may suffice to include interferences between other minor isotopes and the major isotope, not interferences among the minor isotopes. We suggest one way to account for the interference effect between the minor isotopes and the major one, and demonstrate it with the same example discussed previously. In this example, U^{235} and U^{238} resonances overlap considerably in groups 41, 45 and 46. The flux shape in these three groups tend to be dominated by U^{238} resonance and should not be very sensitive to the enrichment of U^{235}, given the small range of enrichment of practical interest. Therefore the flux used for background cross-section method may be obtained approximately by adding the cross-section profile of 2% U^{235} to that of U^{238} and, to compensate for the addition, subtract from the number density of U^{235} appearing in its group averaged macro-scopic cross-section the amount of 2% U^{235}. This flux is then used for both U^{238} calculations and U^{235} calculations as well. When we modify in this way the previous heterogeneous OZMA calculation with group-averaged cross-sections, we find that the errors in Table 1 are now reduced to the ones shown in Table 4.

Group	R_A^5	R_A^5	R_A^8	R_S^8	Σ_A^5	Σ_S^5	Σ_A^8	Σ_S^8
41	8.35	1.69	--	-1.03	8.56	-1.90	--	-0.83
45	1.35	-0.13	--	--	1.51	0.02	--	--
46	2.49	--	1.38	--	2.81	--	1.70	--

Table 4. New percentage errors after resonance interference correction, corresponding to those in Table 1.

There are of course other ways of correcting for interference effects. One way is to divide the troubling groups into smaller ones. The other is to calculate the interference directly by employing some simple flux spectrum. For example, a calculation with group 41 split into two sub-groups, reduces R_A^5 from 8.35% to 1.71% and Σ_a^5 from 8.56% to 1.19%. But we think the 2% U^{235} adjustment method is simpler and may be accurate enough.

In the above example, only two regions (fuel and moderator) are considered. Now we include a third cladding. As mentioned in the previous section, the method has been generalized to the three region case. However, a straightforward homogenization of the cladding and the moderator works very well for practical cases, that the further improvement born out by the three region

generalization is not really called for. As a second example, we considered a standard PWR square lattice with the following parameters: fuel rod radius=0.4095 cm, cladding outer radius=0.47 cm, and pitch distance=1.25 cm. The fuel is 2.6% enriched uranium oxide, and the cladding material is zircaloy. The accuracy of the calculation for this example is found to be just about the same as that of the previous example.

We carry the analysis of this second example further to calculate the k-effective with the HAMMER code[5]. Two calculations with HAMMER are done. One uses the benchmark epithermal constants calculated by OZMA as input, the other uses the epithermal constants obtained by our background cross-section method. The difference in k-effective is found to be .03%.

ACKNOWLEDGEMENT

We are very grateful to Dr. Odelli Ozer for making the codes HAMMER/OZMA accessible to us. We want to thank Dr. J. Barhen for several very helpful explainations on the operation of OZMA, Drs. W. Rothenstein and P. Rose for helping us to understand the EPRI version of HAMMER. And we also feel much obliged to Mr. Li Erkang for his generous assistance on computation and some very useful discussions. This work is supported in part by Westinghouse Electric Corporation.

REFERENCES

(1) Y.A. Chao and A.S. Martinez, Nucl. Sci. Eng. 66, 254 (1978); and Y.A. Chao, Nucl. Sci. Eng. 69, 443 (1979).

(2) Y.A. Chao, M.B. Yarbrough and A.S. Martinez, Nucl. Sci. Eng. 78, 89, (1981). NOTE: Eqs.(12) and (13), and Table III of this paper contain a mistake. The correct result (better) will be submitted to Nucl. Sci. Eng. as a corrigendum.

(3) Y.A. Chao and A.S. Martinez, Nucl. Sci. Eng. 80, 401 (1982).

(4) Barhen, J. and W. Rothenstein (1981), OZMA code, EPRI NP 926.

(5) Barhen, J., W. Rothenstein, and E. Taviv, (1978), The HAMMER code System, EPRI NP-565.

Implementation And Application of RCP System at BNL*

L.D. Eisenhart
M. Todosow
Brookhaven National Laboratories

Abstract

We will discuss the implementation of the RCP01 Monte Carlo system at the Brookhaven National Laboratory Central Scientific Computing Facility. Initial benchmarking experience and an LWR core physics application will be described.

1. Introduction

The RCP01[1] program is a generalized three dimensional continuous energy Monte Carlo program suitable for thermal reactor benchmark calculations. A library preparation program (RCPL1)[2] exists for creating Doppler broadened cross section profiles for use in RCP01 after they have been processed from ENDF/B source tapes. These programs were written at the Bettis Atomic Power Laboratory (BAPL) and first distributed in the late 1970's through the National Energy Software Center at Argonne.

2. Implementation

2.1 XAP Cross Section Data From ENDF/B

The XAP data base concept frees the casual RCP01 user from the complexities of the ENDF/B storage and processing programs. Data is arranged into two distinct structures (fast and thermal) before any Doppler broadening of resonances occur. Thus, any given isotope need only be processed once from ENDF/B to each XAP database. Modified versions of the standard programs ETOG,[3] ETOT,[4] and FLANGE[5] are used for this transformation. Since XAP uses AFM (See 2.3) which in turn uses standard software, these databases can be stored online when constructing specific libraries. Currently, at BNL we have 20 nuclides and 5 kernels on our XAP databases. It has been our policy only to add nuclides to the databases on an "as needed" basis. The information in XAP when needed by RCPL1 is retrieved by random access read routines based on isotope, energy group, reaction type and subtype (if any). A backup to the random database consists of UPDATE files necessary to regenerate the information. Thus, once all the nuclides needed for a study are contained in XAP only a single RCPL1 library generation job will provide the needed broadened pointwise library in AFM format.

The overall structure of what we will call the RCP system is shown in Figure-1. The modified versions of the standard ENDF/B processing codes given in Level I of Figure-1 provide data to the XAP libraries of Level II. The XAP thermal and epithermal libraries then provide multigroup cross section data and resonance parameters which may be used by other calculational tools as well as by RCP01. The XAP libraries contain epithermal multigroup averaged and thermal mid-group cross sections, as well as parameters needed to calculate resonance cross section profiles for resonance nuclides. RCPL1 then prepares

* This work was performed under the auspices of the U.S. Nuclear Regulatory Commission

the cross section job library for RCP01 by using data in the XAP libraries. It accesses the resolved resonance parameters and forms profiles by whatever formalism is dictated and then Doppler broadens them. It creates an unresolved resonance distribution based on a Porter-Thomas distribution. Appropriate thermal kernels and smooth data are also digested.

2.2 Cross Section Data For RCP01

The data produced by RCPL1 consists of both multigroup and point data. Smooth integral cross sections are given as multigroup sets within a relatively arbitrary energy structure (in practice, the epithermal data is given for 54 multigroups and the thermal data is given for 25 multigroups). Doppler broadened cross sections for resonance nuclides are obtained from unresolved and either (symmetric or asymmetric as appropriate) Breit-Wigner single-level, or Adler-Adler or Reich-Moore, multi-level parameters. These cross sections are tabulated on a user prescribed fine energy mesh within the RCP group structure. The fine energy mesh is nuclide independent. The energies selected for the pointwise resonance cross sections are uniformly spaced between the energy breakpoints of the group. Unresolved resonance regions are treated by generating a random sample cross section set on a fine energy mesh, in a preprocessor stage, which is then handled in a manner that is similar to the resolved resonance data in RCP01 but preserves the characteristics of the Porter-Thomas distribution that was used to sample the unresolved structure. Pointwise data includes microscopic capture, elastic scattering and fission cross sections. Each XAP resonance nuclide may be a multi-isotope mixture of as many as 25 components. This considerably simplifies the representation of structural materials such as Zircaloy, stainless steel, etc.

Differential nuclear data is usually in a multigroup form with the multigroups related to the group structure used in the RCP01 calculation. Inelastic scattering (permitted only in the highest energy groups) is assumed to be isotropic in the center-of-mass system (CMS) and is treated via multigroup scattering matrices. Elastic scattering is described by the first four Legendre components of the differential cross section in the CMS. Elastic scattering may be anisotropic in the inelastic scattering groups, but is assumed to be isotropic in the CMS in all other epithermal groups. Scattering from bound Hydrogen is assumed to be from a free proton at rest in the epithermal groups, except for the Special Epithermal Treatment which may extend over some of the lowest epithermal RCP groups. In that case the bound Hydrogen target is treated kinematically as a free proton target with a Maxwellian distribution of velocities corresponding to an effective "source" temperature.

In the thermal group, P-3 25 group scattering kernels are used for the treatment of neutronic interactions with up to two non-resonance nuclides. Each kernel consists of four transfer matrices describing the scattering of neutrons among the thermal subgroups. However, only one kernel is allowed in a given material.

2.3 Software Implementation

The specialized system required for this environment[6] is not the standard CDC-7600 suplied software. The BAPL environment can for the most part be simulated on standard CDC operating systems by using the MODEL[7] environment. The major BNL programming effort involved (a) writing an advanced file manager (AFM) simulator to interface with standard CDC permanent filing and (b) writing the data base retrieval routines (XAP) to interface with AFM in a truly random read-write capability for cross section and parameter isotopic information.

RCP01 needs AFM both to read the cross section library and to write and read files for restart and editing. No other major changes in the program environment were necessary for execution on a CDC 7600 except the interface to a plotting package. Minor inadequacies in the SCOPE 2.1.5 overlay loader necessitated some trivial changes in the overlay structure of RCP01 enabling the entire system to enter a preproduction Q/A phase at BNL.

3. Applications

The RCP01 system described above has been used in various applications in BNL's Light Water Reactor Safety activities. The system performance was first evaluated by simulating some experimental and calculational benchmarks. Results were then compared either to the experiments or to the results obtained from other Monte Carlo analyses. These calculations verified that the cross section generation procedures and the Monte Carlo simulation had been properly implemented, and that consistent results were obtained. After the successful benchmarking, a calculation of incore detector activation and local fission rate distribution was performed for a typical PWR assembly. RCP01 results were then compared to results obtained from deterministic design codes.

3.1 Benchmarking

Calculations of critical experimental benchmarks are often used to qualify a specific computational approach for the solution of a class of problems whose characteristics are similar to those of the experimental configuration. Comparison of the calculated and experimental results helps to quantify the deviation of the calculated result from experimentally measured "truth."

Benchmarking calculations were performed for the Cross Section Evaluation Working Group (CSEWG) TRX-1 unit cell benchmark and two Battele Pacific Northwest Lab (PNL) fuel storage rack critical experiments.[8] Cross section job libraries were generated at room temperature for the required isotopes using ENDF/B-V based data and the procedures described previously.

3.1.1 TRX-1 Unit Cell

The TRX-1 critical benchmark experiment was performed years ago at the Bettis Atomic Power Laboratory. It consisted of a uniform hexagonal lattice of slightly enriched (1.3 wt.% U-235) Uranium metal rods in a H_2O moderator. The rods were clad in Aluminum and had a 0.5753 cm O.D. on a 1.806 cm triangular pitch. The experiment was done at room temperature. This simply buckled configuration has long been used as a standard for testing spectrum codes and is one of the most heavily used benchmarks by the CSWEG.

In the RCP01 calculations we modelled one-third of the unit cell, with the fuel, gap and clad explicitly represented, and with ENDF/B-V based nuclear data. Approximately 38,000 neutron histories were processed. The results obtained for the infinite multiplication factor and for various measured reaction rate ratios are shown in Table-1. The breakpoint between "fast" and "thermal" energies was assumed to be 0.625 eV. The quoted 1σ uncertainties assume no correlation between the estimates for the reaction rates. Table-1 also shows the experimentally measured quantities, as well as the results obtained from two other state-of-the-art Monte Carlo codes - SAM-CE[9] and MCNP[10] also using ENDF/B-V. The principal differences between these codes is in the modelling of nuclear data - both SAM-CE and MCNP use essentially pointwise data and explicit treatments of thermal scattering ($S(\alpha,\beta)$) while the RCP01 nuclear data are based on mixed group and point formalisms as described above.

The results show excellent agreement between the results from the three Monte Carlo codes, and good agreement with experiment. It should be noted that the indicated levels of agreement with experiment generally represent considerable improvement over the comparable results obtained with ENDF/B-IV based nuclear data.[11]

3.1.2 Fuel Storage Pool Criticals

The storage pool experiments that were simulated involved the determination of the critical separation between three clusters of UO_2 rods arranged in a linear array, both with and without 1.1 wt % borated stainless steel absorber plates located between the clusters.[8] The clusters consisted of 15 x 8 arrays of 4.31 wt % enriched UO_2 rods (clad in Aluminum) at a lattice pitch of 2.54 cm. With this fuel and lattice spacing, a critical configuration can be achieved with a single 8 x 16.37 $\pm$ 0.03 cluster. The configurations that were examined therefore represent a loosely coupled system, and are a strigent test for any calculational approach.

The analyses were performed with two continuous energy Monte Carlo programs, SAM-F (the Monte Carlo component of the SAM-CE system) and RCP01, using nuclear data based on ENDF/B-V. The cross setion library for SAM-F was obtained from the National Nuclear Data Center. The experimental configurations were modelled in detal with both programs (i.e. fuel-gap-clad, absorber plates, and the surrounding water filled tank). The structural materials within the tank, and the tank itself were not explicitly modelled, but this omission is expected to have a negligible effect on the calculated results. Approximately 20,000 neutron histories were processed for each simulation.

The results obtained for the critical configuration in the absence of the poison plates, and with the borated stainless steel plates present are presented in Tables 2 and 3, respectively. The SAM results utilize the Maximum Likelihood Estimator.[11] The number of neutron histories processed per minute on a CDC-7600 are presented for the SAM and RCP results as a measure of the efficiency of the Monte Carlo simulation. Results obtained with KENO-IV (from Ref. 12) using three cross section libraries (27-group ENDF/B-IV; 123-group GAM-THERMOS; 16-group Hansen-Roach) are also presented. The KENO calculations involved the processing of approximately 30,000 neutron histories, but no information is available on the computing times.

3.1.3 Conclusions From Benchmark Calculations

The results shown in Tables 1-3 support the following conclusions about the performance of RCP01, with ENDF/B-V data, for systems similar to those encountered in analyses of light water reactors (LWRs):

1. RCP01 performs well relative to experiment, and relative to other Monte Carlo codes that are available for LWR related analyses.

2. RCOP1 is approximately twice as fast, for comparable accuracy, as SAM-CE (cf.Table-2).

3.2 Calculation of Fission Rates For Typical PWR Assembly

Following the successful benchmarking of RCP01 for LWR related systems, a comparison was made between results obtained from different calculational approaches for the in-core detector activation rate-to-local and global fission rates in a typical PWR assembly. The objective of the study was to compare results from standard design codes to results obtained from a detailed calculation performed with a continuous energy Monte Carlo program (RCP01) with ENDF/B-V based nuclear data.

Calculations were performed for a typical PWR type assembly at BOL using three distinct calculational methods:

1. Use of a transport theory based multigroup spectrum code to obtain spatially homogenized, energy condensed cross sections for distinct regions in the lattice, followed by a few-group diffusion theory calculation for a partially homogenized assembly. This approach is embodied in the use of the EPRI-CELL[13] and PDQ-7II[14] programs, and is typical of the methods generally used to perform this type of calclation.

2. Similar to (1), except that the assembly calculation utilizes transport theory. This approach is embodied in the CASMO[15] program, and represents a more sophisticated treatment of the problem.

3. A Monte Carlo calculation for the assembly which retains all the spatial and energy detail. This approach is available in the RCP01 program. Since it involves minimal approximations, it serves as the reference calculation.

Fission rates for the assembly and for the fission chamber detector are summarized in Table 4. Results are normalized to a total production rate of unity for the assembly, and are presented separately for the fissioning isotopes, and for the fast and thermal energy ranges, as well as the sum over all energies.

Fission rate distribution and eigenvalue results are presented in Figure-2. The total 1σ uncertainties from RCP01 associated with each of the local fuel rod fission rates are shown. The quoted uncertainties consist of two components: 1) the uncertainity in the Monte Carlo estimate of the fuel rod fission rate, and 2) an estimate of the uncertainty associated with the eigenfunction. Note that the uncertainties for locations not on the symmetry axes are lower than the values on the vertical and 45° axes. This is because fissions in two symmetrically located rods are involved in the estimates for these loctions. Figure 2 also shows the percent differences between the RCP01 mean estimates for the normalized local fission rates, and the results from the deterministic methods. Although there are some locations where these differences are greater than the 1σ uncertainty in the Monte Carlo results, when a 2σ range is considered (corresponding to approximately a 95% confidence interval) the results from the three calculations "agree" in most locations.

RCP01 predicts the highest eigenvalue for the configuration, consistent with the use of ENDF/B-V data. The PDQ-7II eigenvalue is lower (as expected since pre-ENDF/B-V data are involved) but is within the 1 uncertainty on the Monte Carlo results. The CASMO eigenvalue is the lowest of the three. This result is consistent with the level of agreement that was observed in an earlier study between PDQ-7II and the CPM program (which is very similar, in terms of results, to CASMO).[16]

The Monte Carlo results involved the processing of 99,710 neutron histories, resulting in 1 uncertainities of $\sim$1.5-3.0% (cf. Figure-2) for the individual fuel rod fission rates and $\sim$7-8% for the detector fission rate.

There is generally good agreement between the results from the three methods in terms of the integrated fission rate for the assembly as a function of both isotope and energy (cf. Table 4). There is also reasonable agreement between all three methods in terms of the fission rate distribution for the assembly (cf.Fig. 2).

Agreement between E-CELL/PDQ-7II and CASMO for the detector fission rate is also good, but both methods predict a much higher fission rate than does RCP01 (~15-19% higher). There are a number of possible reasons for this discrepancy, including differences in modelling the assembly geometry, and differences in the treatment of nuclear data (especially at the assembly level). In particular, the modelling differences give rise to a much larger absorption rate in the instrument thimble surrounding the detector in the RCP01 model (by 14%); hence fewer thermal neutrons are available to cause fissions in the U-235 in the detector location.

The results obtained during the course of this study provide increased confidence that fission rate distributions for PWR assemblies are being well calculated by standard design techniques. The discrepancies observed between results from Monte Carlo calculations, and those obtained from standard design codes for the detector fission rate, suggest that further studies in this area are desirable.

4. Conclusions

Thus, in its first years since its release from the cloistered environment of the BAPL operating system, we have successfully implemented RCP01 on standard CDC software, benchmarked it, and begun to use it in mission oriented LWR safety work. In the future as the needs arise, the databases will be enlarged to encompass more isotopes. Geometry decks of various common configurations will be generated and available. At that time the RCP01 package will be available to quickly answer safety problems with a high quality solution.

References

1. N.R. Candelore et al., "RCP01 - A Monte Carlo Program for Solving Neutron and Photon Transport Problems in Three-Dimensional Geometry With Detailed Energy Description," WAPD-TM-1267, Bettis Atomic Power Laboratory (August 1978).

2. A.V. Dralle et al., "RCPL1 - A Program to Prepare Neutron and Photon Cross Section Libraries for RCP01," WAPD-TM-1268, Bettis Atomic Power Laboratory (August 1978).

3. D.E. Kusner and R. A. Dannels, "ETOG-1, A Program to Process Data from the ENDF/B File to the MUFT, GAM and ANISN Formats", WCAP-3845-1, ENDF-114, Westinghouse Electric Corporation (1969); Supplement (1973).

4. C.L. Beard and R.A. Dannels, "ETOT-A Fortran IV Program to Process Data from the ENDF/B File to Thermal Library Format," WCAP-7363, Westinghouse Electric Corporation (1970).

5. H.S. Honeck and D.R. Finch, "FLANGE-II (Version 71-1), A Code to Process Thermal Neutron Data From an ENDF/B Tape," DP-1278, Savannah River Laboratory (October 1971).

References (Continued)

6. W.R. Cadwell, editor, "Reference Manual-Bettis Programming Environment" WAPD-TM-1181, Bettis Atomic Power Laboratory (Sept. 1974).

7. L.A. Boelter, "MODEL-Modified Environmental Library," Control Data Corporation (May 1972).

8. S.R. Bierman, et al., "Critical Separation Between Subaritical Clusters of Low Enriched UO_2 Rods With Fixed Neutron Poisons, "Nuclear Technology, 42, 237 (March 1979)

9. H. Lichtenstein et al., "The SAM-CE Monte Carlo System For Radiation Transport and Criticality Calculations in Complex Configurations (Revision 7.0)," EPRI-CCM-8, Electric Power Research Institute (July 1979).

10. W.L. Thompson, editor, "MCNP - A General Monte Carlo Code for Neutron and Photon Transport," LA-7396-M, Revised, Los Alamos Scientific Laboratory (Nov. 1979).

11. M. Beer and P. Rose, "Implementation of the SAM-CE Monte Carlo Benchmark Analysis Capability for Validating Nuclear Data and Reactor Design Codes," EPRI-NP-1791, Electric Power Research Institute (April 1981)

12. R.M. Westfall, J.R. Knight, "Scale System Cross-Section Validation with Shipping Cash Critical Experiments," Trans. Am. Nuc. Soc., 33, 368 (Nov. 1979).

13. W.J. Eich, "Advanced Recycle Methodology Program," Part II Chapter 5, Research Project 118-1, Electric Power Research Institute (1976).

14. C.J. Pfeifer, "PDQ-7 Reference Manual II", WAPD-TM-947 (L), Bettis Atomic Power Laboratory (1971)

15. A. Ahlin et al., "CASMO-A Fuel Assembly Burnup Program," AE-RF-76-4158 (Rev. Ed.), Studsvik Energiteknik ABN (1978)

16. J.W. Herczeg, et al., "Simulation of a PWR First Cycle With the ARMP System," BNL-NUREG-25607, Brookhaven National Laboratory (1979)

TABLE-1

RESULTS FOR TRX-1 CELL
BENCHMARK
ENDF/B-V NUCLEAR DATA

PARAMETER	EXPERIMENT	RCP01
k_∞	--	1.1840 + 0.0030
ρ_{28}	1.311 ± 0.02	1.312 ± 0.010
δ_{25}	0.0981 ± 0.001	0.0969 ± 0.0012
δ_{28}	0.0914 ± 0.002	0.0912 ± 0.0008
C*	0.792 ± 0.008	0.786 ± 0.002

	SAM-CE*	MCNP*
k_∞	1.1847 ± 0.0012	1.1800 ± 0.0008
ρ_{28}	1.300 ± 0.007	1.318 ± 0.005
δ_{25}	0.0947 ± 0.0004	0.0966 ± 0.0003
δ_{28}	0.0913 ± 0.0004	0.0912 ± 0.0004
C*	0.782 ± 0.002	0.788 ± 0.002

* COMMUNICATED BY E. SCHMIDT - BNL-NNDC

TABLE 2

MONTE CARLO RESULTS FOR
SIMULATION OF UNPOISONED
CRITICAL

METHOD	$K_{EFF} \pm 1^{\sigma}$	# NEUTRON HISTORIES / MIN.
RCP01	0.9996 ± 0.007	1413
SAM-F	1.0052 ± 0.007	694
KENO-IV		
LIBRARY 1*	0.989 ± 0.005	
LIBRARY 2*	0.984 ± 0.004	NOT
LIBRARY 3*	0.997 ± 0.004	AVAILABLE

*KENO-IV LIBRARIES ARE ALL MULTIGROUP (RESULTS ARE FROM REFERENCE 5)

LIBRARY 1 - 27-GROUP ENDF/B-IV

LIBRARY 2 - 123-GROUP GAM-THERMOS (ENDF/B-II)

LIBRARY 3 - 16-GROUP HANSEN-ROACH

TABLE 3

MONTE CARLO RESULTS FOR
SIMULATION OF POISONED
CRITICAL

METHOD	$K_{EFF} \pm 1^{\sigma}$	#NEUTRON HISTORIES / MIN.
RCP01 +	1.003 ± 0.009	1404
SAM-F	0.996 ± 0.004	734
KENO-IV		
LIBRARY 1*	0.982 ± 0.004	
LIBRARY 2*	0.987 ± 0.004	NOT
LIBRARY 3*	1.001 ± 0.004	AVAILABLE

* KENO-IV LIBRARIES ARE ALL MULTIGROUP (RESULTS ARE FROM REFERENCE 5)

LIBRARY 1 - 27-GROUP ENDF/B-IV

LIBRARY 2 - 123-GROUP GAM-THERMOS (ENDF/B-II)

LIBRARY 3 - 16-GROUP HANSEN-ROACH

+ RESULTS FOLLOWING PROCESSING OF 9500 NEUTRON HISTORIES

TABLE 4

Summary of Detector And Assembly Fission Rates

	RCP01	CASMO	PDQ-7II
Assembly Fission Rates			
U-235 Fission Rate			
Fast*	5.76(-2)+	5.93(-2)	5.84(-2)
Thermal*	3.21(-1)	3.22(-1)	3.22(-1)
Total*	3.79(-1)	3.81(-1)	3.81(-1)
	(± 0.33% 1σ)		
U-238 Fission Rate			
Fast	2.74(-2)	2.70(-2)	2.70(-2)
Thermal	1.18(-7)	0.0	0.0
Total	2.74(-2)	2.70(-2)	2.70(-2)
	(± 0.42% 1σ)		
U-235 + U-238 Fission Rates			
Fast	8.50(-2)	8.64(-2)	8.54(-2)
Thermal	3.21(-1)	3.22(-1)	3.22(-1)
Total	4.06(-1)	4.08(-1)	4.08(-1)
	(± 0.31% 1σ)		
Dectector Fission Rates			
U-235 Fission Rate			
Fast	2.21(-11)	2.22(-11)	2.27(-11)
Thermal	1.03(-10)	1.27(-10)	1.22(-10)
Total	1.25(-10)	1.49(-10)	1.45(-10)
	(± 7% 1σ)		

*Fast refers to energy range 10 MeV-0.625 eV
Thermal refers to energy range 0.625 eV-0.0 eV
Total refers to energy range 10 MeV-0.0 eV

+ Read as 5.76×10^{-2}

FIGURE 1

RCP ENDF/B DATA FLOW

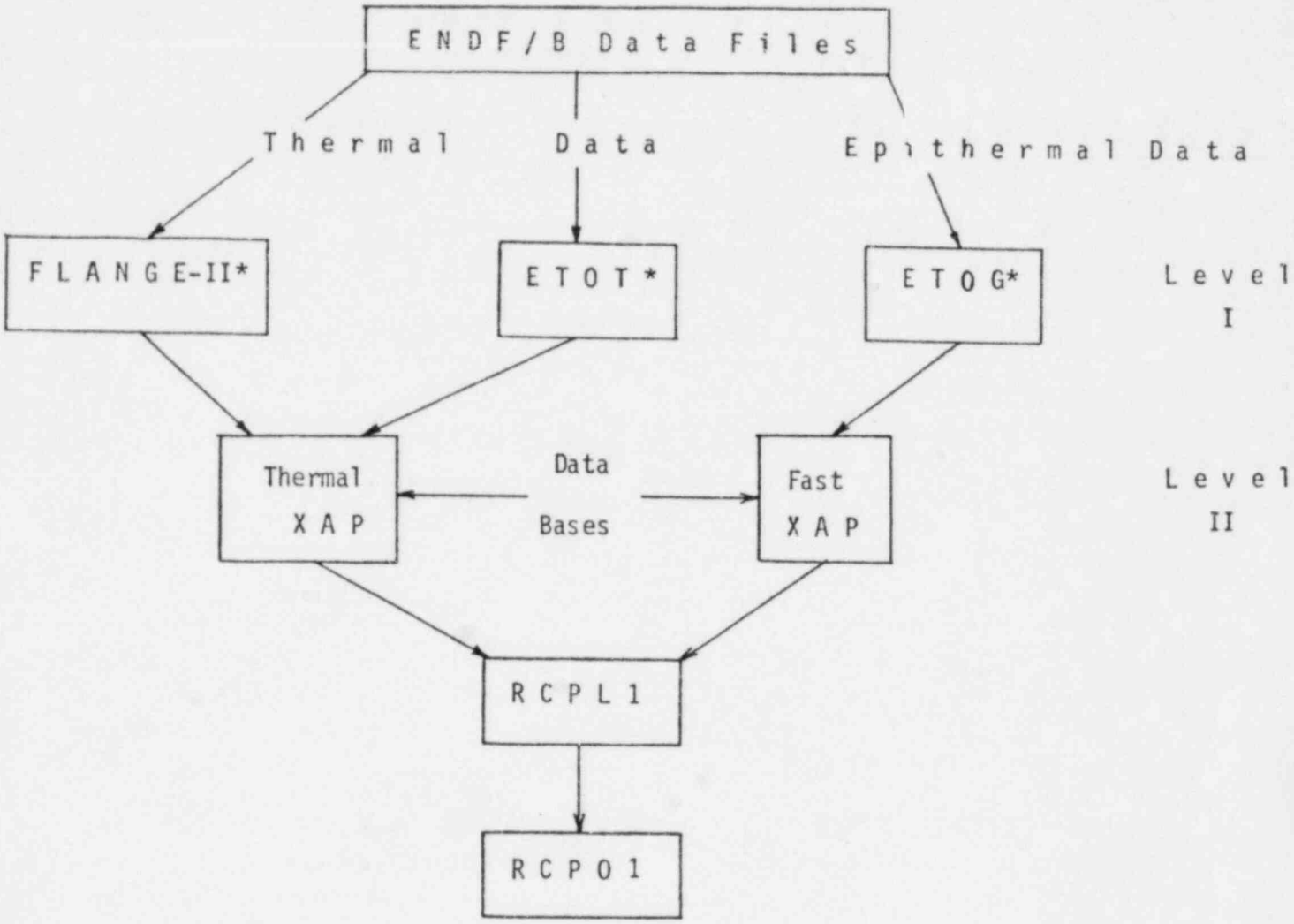

FIGURE 2

One Standard Deviation Uncertainties On RCP01 Local Fission Rates; and Percent Differences Between RCP01 Mean Estimates For Normalized Fission Rates and CASMO and PDQ-7II Results

2.7 0.5 1.0	2.7 -0.1 0.4	% % %	RCP01 Difference CASMO vs. RCP Mean Estimate Difference PDQ vs. RCP Mean Estimate					
2.7 2.6 3.3	1.6 -0.6 0.0	2.6 -1.2 -0.4						
	1.9 1.6 1.1	1.9 -2.1 -2.2						
2.6 0.5 0.5	1.9 -0.9 -0.1	1.7 2.6 3.6	2.2 -1.7 -1.4	2.7 4.6 6.6				
2.6 0.7 1.6	1.9 -1.4 -0.6	1.9 -2.4 -1.5	1.9 -1.3 -1.0	2.2 -0.6 0.2				
	2.2 -0.5 -1.0	1.9 -0.8 -1.1		1.6 0.8 1.2	1.6 -0.7 -1.0	2.7 -1.2 -1.0		
2.6 0.0 0.3	1.7 3.2 3.6	2.0 -0.1 0.2	1.9 -2.9 3.4	2.0 -0.5 -0.2	2.0 -2.8 -3.2	1.7 1.9 1.1	2.8 0.1 -1.0	
2.7 0.8 0.8	2.0 0.3 -0.1	1.7 1.0 0.4	1.7 1.8 1.2	2.3 -4.1 -4.8	1.7 -0.4 -1.4	2.1 2.2 1.1	1.8 2.8 1.4	2.8 3.6 2.0

k RCP01) = 1.131 + 0.002
k (CASMO) = 1.122
k (PDQ-7) = 1.129

LIGHT WATER REACTOR COUPLED NEUTRONIC AND THERMAL-HYDRAULIC CODES*

David J. Diamond
Department of Nuclear Energy
Brookhaven National Laboratory
Upton, N.Y. 11973

ABSTRACT

An overview is presented of computer codes that model light water reactor cores with coupled neutronics and thermal-hydraulics. This includes codes for transient analysis and codes for steady state analysis which include fuel depletion and fission product buildup. Applications in nuclear design, reactor operations and safety analysis are given and the major codes in use in the USA are identified. The neutronic and thermal-hydraulic methodologies and other code features are outlined for three steady state codes (PDQ7, NODE-P/B and SIMULATE) and four dynamic codes (BNL-TWIGL, MEKIN, RAMONA-3B, RETRAN-02). Speculation as to future trends with such codes is also presented.

INTRODUCTION

The neutron flux, and hence the power, in a light water reactor (LWR) is (among other things) a function of the fuel pellet temperature and the water temperature and density. These thermal-hydraulic variables are in turn a function of the power. In many applications it is necessary to have this coupling explicitly represented throughout the core. The codes that have been developed to satisfy this requirement are of two general types.

The first type includes the effect of fuel depletion and fission product buildup and hence is useful for steady state calculations at different points in the life of a fuel cycle as well as for calculations of slow transients due to changing xenon concentration. These calculations have significance in fuel management, operations and safety. Codes for these applications which represent the core in three dimensions are frequently called core simulators. One dimensional codes will not be considered in this paper because of their limited use in the aforementioned applications.

The second type of code couples time dependent neutronics and thermal-hydraulics in order to determine core behavior under accident or operational transient conditions. This is a much more difficult analysis problem with fewer applications and hence there is less experience available. The codes that are used may be either one, two or three dimensional and are called core dynamics codes.

We consider each type of code separately in the following. For both core simulators and core dynamics codes we first discuss applications, and then

---

* This work was performed under the auspices of the U.S. Nuclear Regulatory Commission.

identify the major codes in use in the USA. Characteristics of selected codes are then summarized. This includes the neutronics and thermal-hydraulics modeling as well as other features. Finally something is said about future trends relative to code development.

APPLICATIONS OF CORE SIMULATORS

Core simulators are used for incore fuel management (or equivalently for nuclear design). Fuel enrichment requirements, loading patterns, and cycle length can be determined with the help of these codes. For predictive calculations, assumed operating conditions are input to the code whereas for core-follow calculations the actual operating history is used. The codes are also used to help determine spent fuel composition.

Applications with operational significance are closely related to the above fuel management examples. Core simulators are useful for determining operating strategies for fuel preconditioning and for load following and in general for determining critical statepoints. These functions can be done at the plant site with fast running codes if the proper hardware is available. On-line monitoring with such a code also allows for the detection of anomalous behavior in the reactor.

Calculations with operational safety significance include those to determine the reactor protection system setpoints, the thermal margins as a function of different operating conditions (either directly or by supplying data to another code) and the differential and integral control rod (or bank) reactivity worths. Core simulators are also used to generate core-average delayed-neutron data and reactivity functions to describe control rod motion and thermal-hydraulic feedback, all of which are needed in safety calculations done with a point kinetics model.

MAJOR CORE SIMULATORS

Table 1 lists the major pressurized water reactor (PWR) and boiling water reactor (BWR) core simulators in use in the USA. The principal user and appropriate references are also given. Codes A.1-A.4 and B.1-B.2 are used by the five U.S. fuel vendors and do not have a wide circulation. PRESTO (Code A.5 and B.3) is a foreign product which has recently been made available to utilities in this country via the University Computing Co. The CORE code is a general LWR code, however, its application to BWRs is most notable.

The codes which have had the most widespread use by the utility industry are NODE-P/B (Codes A.6 and B.4), SIMULATE (Codes A.7 and B.5) and PDQ7 (Codes A.8) and they will be discussed further in the next section. NODE-P/B has many variants e.g. SUPERNODE-P/B is the equivalent Control Data Corp. product and NAI3D-P/B is the equivalent Nuclear Associates International product. SIMULATE is of particular interest because its support by the Electric Power Research Institute gives it the potential for an even larger number of users than it already has.

Although PDQ7 (or PDQ8) can be used as a core simulator for both PWRs and BWRs it has had no such application to BWRs and its use as a PWR simulator has been

TABLE 1
LWR Core Simulators

	Code	Principal User	Reference
A.	PWR Codes		
1	PALADON	Westinghouse (W)	C1
2	ROCS	Combustion Engineering (C-E)	O1,O2
3	FLAME 3	Babcock & Wilcox (B&W)	M1
4	XTG	Exxon Nuclear (ENC)	S1
5	PRESTO	Scandpower (ScP)	S2
6	NODE-P	Utilities, Brookhaven Nat'l Lab (BNL)	R1
7	SIMULATE	Yankee Atomic (YAEC), Utilities	V1
8	PDQ7, PDQ8	Bettis Lab, B&W, BNL	P1,P2
B.	BWR Codes		
1	GEBS (PANACEA)	General Electric (GE)	W1
2	XTGBWR	Exxon Nuclear	E1
3	PRESTO	Scandpower	S2
4	NODE-B	Utilities, BNL	K1
5	SIMULATE	YAEC, Utilities, BNL	V1,V2
6	CORE	TVA	F2

limited. Its widespread use by the industry has been primarily for two dimensional (X-Y plane) calculations needed for fuel assembly or core calculations. In these applications there is generally no direct coupling between the neutronics and thermal hydraulics. Hence, PDQ7 is not an important core simulator (primarily because its finite difference algorithm makes computation time large for a detailed three dimensional calculation); nevertheless, it is an important reactor analysis code and hence is discussed below in further detail along with NODE-P/B and SIMULATE.

SUMMARY OF CORE SIMULATOR CHARACTERISTICS

Table 2 summarizes the characteristics of PDQ7, NODE-P/B and SIMULATE. In particular the neutronics and thermal-hydraulics methodology are outlined and information is given on the burnup calculation and other features of the code which are of interest to a core analyst. An important difference between PDQ7 and the latter two codes is the use of nodal methods by NODE-P/B and SIMULATE which allow them to be relatively fast running. SIMULATE in turn is slower running than NODE-P/B; a penalty imposed by the slightly more sophisticated modeling and the improved features summarized in Table 2. A basic difference between the two nodal codes is the use of one neutron energy group in NODE-P/B and two groups in SIMULATE. Since SIMULATE only treats the thermal group approximately, however, this is generally referred to as a 1-1/2-group method.

Both NODE-P/B and SIMULATE rely on user supplied correlations to obtain thermal-hydraulic variables of interest. Auxiliary calculations are therefore necessary. The use of input correlations extends to steam table information required by the calculation.

Table 2
LWR core depletion code characteristics

	PDQ7	NODE-P/B	SIMULATE
Neutron flux calculation			
Geometry	Flexible[a]	X,Y,Z; 1 node/assembly	X,Y,Z; 1 or 4 nodes/assembly
Symmetry	Mirror, rotational	Mirror, rotational	Mirror, rotational
Boundary condition	Fixed flux	Core-reflector leakage	Core-reflector albedo
Energy groups	1 - 5	One	1, 1-1/2
Solution algorithm	Finite differencing	FLARE nodal method	Several nodal options
Searches	Control rod position, poison concentration	Soluble boron, Haling burnup	Control rod position, power, flow, soluble boron, Haling burnup
Depletion/Fisson products	Any user specified linear chain, e.g. Xe, Sm, actinides	Explicit I,Xe exposure void and control dependence history	Explicit I,Xe,Pm,Sm exposure and void history dependence
Thermal-hydraulics methodology			
Fuel temperature	Conduction model or correlation[b]	Proportional to power[b]	Quadratic correlation with power[b]
Flow distribution	Input; cross flow allowed in (R,Z) geometry	Quadratic correlation with power[b]	Linear correlation with power[b]
Coolant temperature/density	Uses vapor generation and slip correlation	PWR: temperature from quadratic correlation with quality.[b] Density from quadratic correlation with temperature.[b] BWR: void fraction from quality using slip correlated with exit quality and inlet velocity. Subcooled voids from correlation.	PWR: density from quadratic correlation with quality[b] BWR: same as NODE-B
Other features	Flux synthesis Adjoint flux Incore detector responses	Fuel shuffling Incore detector response[b] Normalization recommended CHFR calculated	Fuel shuffling Incore detector response[b] Normalization recommended BWR inlet subcooling, bypass voiding calculated
Availability[c]	NESC,UCC,CYERBNET	EPSC,UCC,CYBERNET	EPSC
References	P1,P2,S3,B1,R2	R1,R3,K1,B2,D1	V1,V2,V3

a Rectangular, cylindrical, spherical or hexagonal geometry in 1,2 or 3 dimensions with variable mesh size
b User must supply correlations
c NESC: National Energy Software Center; UCC: University Computing Company; CYBERNET: Control Data Corp; EPSC: Electric Power Software Center

Under "Other Features" in Table 2 it is noted that normalization of the calculation to measurements made at operating plants is recommended. Although this diminishes the mechanistic nature of the calculation it has proven to be important in enabling these codes to be successful as core simulators. This might not be the case if the codes were used for abnormal situations far removed from the operating conditions at which they were normalized.

FUTURE TRENDS WITH CORE SIMULATORS

Since current core simulators have a long history of successful application it seems unlikely that new codes will be written or that major neutronic or thermal-hydraulic modeling changes will be incorporated into existing codes. However, note the exceptions to this. An improved two-phase flow model (L1) is already being incorporated into SIMULATE. Improved methods (based on two-group nodal techniques) also exist for the neutronics and, for example, the method used in the QUANDRY code (G4) could be the basis for a new core simulator.

Instead of concentrating on totally new modeling there may be refinements to existing models and the incorporation of additional models from auxiliary codes into the core simulators. Examples of refinements are: making albedos a function of local water density and having the correction for thermal neutron diffusion dependent on the presence of control blades and void fraction. Examples of models that exist in auxiliary codes that might be incorporated include a thermal margin calculation for SIMULATE and a flow distribution calculation for NODE-P/B or SIMULATE.

Most of the future effect is expected to be in areas that directly affect the core analyst. Improving the linkage to other codes is very important (L2). This includes both the streamlining of the data generation process required for the core simulator and the automatic generation of data by the simulator for use in neutron kinetics calculations. An allied concern is improved documentation that provides the user with procedures for generating the data he needs. There is also an interest in computational speed - of particular interest in codes that may be used for on-line monitoring.

APPLICATIONS OF CORE DYNAMICS CODES

If there is a situation in which the power distribution changes rapidly in time i.e. the spatial and temporal changes are non-separable, then a code which uses spatial neutron kinetics must be employed - preferably with coupling to the thermal-hydraulics. For a PWR the most obvious situation in which this is necessary is a rod ejection accident (REA). For this accident a full three dimensional representation is necessary.

In most PWR transients initiated by perturbations in the thermal-hydraulics (as opposed to a reactivity initiated accident such as the REA) the changes in the core power distribution are relatively slow and spatial kinetics is not necessary. Exceptions to this rule can be found. If there is a failure of control rods to insert after a reactor trip initiated by some transient (an ATWS event or a stuck rod situation) then the core behavior becomes important and spatial kinetics may be necessary. Reference B10 demonstrates this for a transient initiated by a loss-of-feedwater. In a steam line break in a plant

using a once-through steam generator the rapid depressurization of the primary and the lack of shutdown in an assembly due to a stuck-rod could cause thermal limits to be exceeded. However, the evidence as to whether spatial kinetics is needed (B10,N1) is inconclusive.

In the case of BWRs it is clear that because of the strong coupling between void and power there are many transients initiated by thermal-hydraulic perturbations in which spatial neutron kinetics coupled with a thermal-hydraulics calculation is necessary. This is certainly the case for ATWS events and for overpressurization transients. In the latter case reactor trip may be initiated only when the core is already experiencing a power surge. In these types of transients it is usually changes in the axial power shape that are significant - frequently the radial shape does not change much. In such a case a one dimensional neutron kinetics solution may be adequate. If there is an interest in following the hot channel or if there is only a partial control rod insertion then a three dimensional representation is necessary.

The reactivity initiated accident of concern in a BWR is a rod drop accident. As in the case of the REA in a PWR this requires a three dimensional core representation or at least an (R,Z) geometry.

MAJOR CORE DYNAMICS CODES

A list of coupled time dependent neutronic and thermal-hydraulic codes is given in Table 3 for application to both PWRs and BWRs. The principal user, appropriate references and the number of dimensions in the spatial neutron kinetics formulation is also given. Codes A.1-A.4, A.8, B.1 and B.2 are used by the five U.S. fuel vendors and, with the exception of MEKIN (A.3), are not expected to have further circulation. TITAN (A.5 and B.5) is a combination of the QUANDRY neutron kinetics code and the THERMIT thermal-hydraulics code and is still under development. TWIGL (A.6) has had limited PWR application and there is no documentation of any FX2-TH (A.7) applications. FIESTA (A.8) is for the special application of calculating scram reactivity. RETRAN-02 (A.9) also has not yet been applied to PWRs (with its spatial kinetics option) in a documented study.

TABLE 3
LWR Core Dynamics Codes

	Code	Dimensions	Principal User[a]	Reference
A.	PWR codes			
1	HERMITE	3	C-E	R4,R5
2	TWINKLE	3	W	B3
3	MEKIN	3	B&W, BNL	A1,B4,B5
4	XTRAN	2	ENC	E1
5	TITAN	3	MIT	G1,G2
6	TWIGL	2	Bettis,C-E	Y1
7	FX2-TH	2	ANL	S5
8	FIESTA	1	C-E	D2
9	RETRAN-02[b]	1	EPRI/EI	M2

TABLE 3 (cont.)
LWR Core Dynamics Codes

	Code	Dimensions	Principal User[a]	Reference
B.	BWR Codes			
1	ODYN[b]	1	GE	A2,S4
2	COTRAN	2	ENC	P1
3	RAMONA-3B[b]	3	BNL	D4
4	MEKIN	3	BNL	A1,B4
5	TITAN	3	MIT	G1,G2
6	BNL-TWIGL	2	BNL	C2,D3
7	RETRAN-02[b]	1	EPRI/EI,TVA	M2

a See Table 1 for definition of abbreviations. Also: ANL, Argonne; EI, Energy Incorporated
b Also models nuclear steam supply system.

Since the applications to BWR safety analysis are more extensive than to PWR analysis we consider the BWR codes in more detail. We eliminate consideration of the (proprietary) fuel vendor codes and the TITAN code with which there is limited experience. In the next section, therefore we consider BNL-TWIGL, MEKIN, RAMONA-3B and RETRAN-02.

SUMMARY OF CORE DYNAMICS CODE CHARACTERISTICS

Table 4 summarizes the important characteristics of the four codes of interest for BWR core dynamics. The following text comments on the entries (sequentially) in the table.

Each code has a different set of field equations for the two-phase water system. Although a mixture momentum equation is written for RAMONA-3B in the vessel it is integrated around the flow path resulting in one integrated momentum equation for each channel through the core. The RAMONA-3B and BNL-TWIGL formualtions are therefore similar by virtue of having a single pressure for the entire core.

BNL-TWIGL and RAMONA-3B are also similar in that they both use slip correlations to obtain relative phasic velocities. Specifically, RAMONA-3B has two options (Bankoff-Malnes and Bankoff-Jones) for this correlation and also uses a fixed bubble rise velocity whereas BNL-TWIGL uses the Bankoff-Jones correlation and no bubble rise velocity. The so-called dynamic slip model in RETRAN-02 is based on the drift flux formulation and was not available in the original version of the code. (Homogeneous flow or an algebraic slip are also available in RETRAN-02). Each code has a different subcooled boiling model indicated by the developer's name in the table.

RETRAN-02 with its 16 heat transfer regimes is clearly more sophisticated than the other three codes in this regard. Note also that RETRAN-02 is the only

one of the four codes that allows for superheated steam and a metal-water reaction.

BNL-TWIGL has no need for a two-phase friction multiplier because it does not solve a momentum equation. Another consequence of this is that the flow distribution must be specified for BNL-TWIGL.

The calculation of critical heat flux is done in RAMONA-3B with the RELAP4/MOD7 correlation while with RETRAN-02 the user has several options. Both of these codes have specific models for post-CHF flow and heat transfer. Although BNL-TWIGL does allow for heat transfer with very high void fractions that model has not been fully validated for the post-CHF regime.

One of the most important distinctions between these codes is the fact that RAMONA-3B and RETRAN-02 model the entire nuclear steam supply system (NSSS) whereas MEKIN and BNL-TWIGL model only the core. The inlet flow rate, temperature and pressure therefore must be input into the latter two codes whereas for the codes that model the NSSS this is calculated by the code using boundary conditions elsewhere in the system.

Although RETRAN-02 is capable of calculating a flow distribution this is a moot point since it is a one-dimensional neutron kinetics model and hence it is most likely that only one thermal-hydraulic channel would be used to represent the in-channel flow.

The bypass channel can be represented in RAMONA-3B and RETRAN-02 in order to properly calculate the hydraulic conditions in the core. However, the water density in the bypass region is not used as feedback to the neutron cross sections for use in obtaining the neutron kinetics solution.

The conduction model limitation referred to for BNL-TWIGL is not serious and results in not knowing the temperature distribution through the pellet. For RAMONA-3B the limitation is that fuel rod properties (geometry, conductivity etc.) cannot be different in different channels.

A hot bundle representation is essential in a one dimensional core code such as RETRAN-02 and theoretically should not be necessary with a more detailed geometry such as is found in the other three codes. Nevertheless, there are situations when those codes might be used with only one dimension represented or with such a coarse radial mesh that a hot bundle calculation would be very useful.

A major distinction between the four codes with regard to neutron kinetics is the use of a finite difference algorithm in BNL-TWIGL and MEKIN as opposed to the use of a nodal method in RAMONA-3B and a space-time factorization method in RETRAN-02. The latter two approaches are meant to improve the computational speed. The coarse-mesh method in RAMONA-3B (related to the steady state algorithm used in PRESTO and SIMULATE) has proven to be relatively fast running. The fact that albedo boundary conditions are used rather than an explicit reflector also helps improve the computational speed of RAMONA-3B. The space-time factorization method used in RETRAN-02 has had successful application in FX2-TH and FIESTA but little experience has been collected to determine whether it will be more efficient for BWR applications than, for example,

TABLE 4
Core Dynamics Code Characteristics[a]

	BNL-TWIGL	MEKIN	RAMONA-3B	RETRAN-02
Core Thermal Hydraulics				
Field Eqns - number	3	3	4	3
Mass	Mixture	Mixture	Vapor, Mixture	Mixture
Energy	Liquid,Vapor	Mixture	Mixture	Mixture
Momentum	No	Mixture	Mixture	Mixture
Relative Phasic Velocities	Bankoff-Jones (BJ) Slip	Homogeneous	Bankoff-Malnes/ (BJ) Slip	Dynamic Slip
Subcooled Boiling	Lellouche	Levy	Rakstad	Lellouche/ Zolotar
Heat Transfer Regimes	3	2	4	16
Two-Phase Friction Multiplier	No	3 Options	Yes	3 Options
CHF Calculation	No	No	RELAP4/MOD7	4 Options
Post-CHF Modeling	Some	No	Yes	Yes
Superheated Steam	No	No	No	Yes
Inlet Conditions	Input	Input	Calculated	Calculated
Flow Distribution	Input	Calculated	Calculated	Calculated
Bypass Channel	No	No	Yes-Not coupled to neutronics	Yes-Not coupled to neutronics
Conduction Model Limitations	Only average pellet temp.	--	Only one rod type	--
Direct Energy Deposition	Clad & Coolant	Coolant	Coolant & Bypass	Coolant & Bypass
Metal-Water Reaction	No	No	No	Yes
Hot Bundle	No	No	No	Yes

a See text for explanation

TABLE 4 (cont.)
Core Dynamics Code Characteristics[a]

	BNL-TWIGL	MEKIN	RAMONA-3B	RETRAN-02
Neutron Kinetics				
Dimensions (Geometry)	2:(R,Z)[b]	3:(X,Y,Z)[b]	3:(X,Y,Z)[b]	1:(Z)
Energy Groups[c]	2	2	1-1/2	2
Delayed Neutron Precursor Groups[c]	6	6	6	6
Solution Algorithm	Finite Difference	Finite Difference	Nodal Method	Space-Time Factorization
Boundary Conditions	Zero Flux or current	Zero Flux, Albedo	Albedo	Zero Flux
Miscellaneous				
Decay Heat[d]	No	$F(t_o,t)$	$F[t_o,P(t),t]$	$F[P(t),t]$
Feedback Dependence[e]	U,T_C,T_F,	U,T_C,T_F, N_X	U,T_C,T_F,N_X,C_B, (E,U_E)	U,T_C,T_F
Reactivity Edits	Yes	Yes	No	No
Single or Multiple Rod Groups Per Channel	Multiple	Single	Single	Multiple
References				
Modeling	C2,D3,Y1	A1,B4,R6	B8,B9,D4	M2,M3
Application/ Qualification	C3,C4	B7,C5	B6,D4	F1,G4

a See text for explanation
b Reducible to one dimension
c Maximum number
d Pre-transient operating time, t_o; time, t; instantaneous power, P(t).
e Moderator density, U; coolant temperature, T_C; fuel temperature, T_F; xenon number. density, N_X; boron concentration, C_B; exposure, E; void history, U_E.

a finite difference method. Note also that RAMONA-3B uses a 1-1/2 group method while all the other codes use a two group method.

Three of the codes have models for decay heat whereas BNL-TWIGL which was originally designed for fast transients has none. The models in RAMONA-3B and RETRAN-02 are suitable for the analysis of ATWS events because the decay heat is a function of instantaneous power whereas the decay heat model in MEKIN is for shutdown situations.

All four codes allow for cross sections to be a function of the three thermal-hydraulic variables moderator density and temperature and fuel temperature; although in most BWR transients the dependence on moderator temperature can be neglected. RAMONA-3B and MEKIN also allow for the cross section to be a function of the equilibrium xenon concentration. RAMONA-3B is the only code in which the cross sections may depend on boron concentration - essential for considering ATWS events. Although the cross section may also in theory be a function of exposure and void history in RAMONA-3B, the practice at BNL has been to use data that represent the reactor at a fixed point in the fuel cycle.

In a single channel core representation it is necessary to be able to represent more than one bank or group of rods in a dynamic way. Without this capability the rods can only be represented as all in or all out. With this capability (as in BNL-TWIGL and RETRAN-02) the rods are represented with a control rod density between zero and one which varies axially depending on the rod pattern. Having this capability may also be important when the radial dimension is represented in a coarse fashion.

FUTURE TRENDS WITH CORE DYNAMICS CODES

Of the four codes considered for BWR analysis it is clear that the NSSS codes RAMONA-3B and RETRAN-02 have an advantage over the other two codes. The former code can be used for the rod drop accident and both codes can be used for system transients. MEKIN is too long running and does not offer any advantages over RAMONA-3B to be used for BWR calculations. BNL-TWIGL can only be used at BNL and again does not offer any significant advantages over RAMONA-3B. Although these four codes have been highlighted in this paper, work on the advanced code TITAN is progressing and results of that effort will be watched closely to determine whether TITAN or a similar advanced code can replace any of the existing codes.

The major emphasis in the near term with RAMONA-3B and RETRAN-02 is expected to be further code assessment in order to delineate the limitations and capabilities of the codes. Separate effects tests, numerical benchmarks and plant data will be used. This process has already identified deficiencies which can be remedied. The application of the codes to accident analysis is also important as it identifies what reactor behavior is expected and consideration can then be given to whether the modeling for that specific behavior is adequate.

Changes to the core thermal-hydraulics in RAMONA-3B that have already been identified include the improvement of the calculation under reverse flow

conditions and the addition of channel dependent fuel rod types for the heat conduction calculation. Naturally, with both RAMONA-3B and RETRAN-02 there will be many modifications that relate to the thermal-hydraulics outside of the core - indeed these problems will be the major preoccupation of future code development. New thermal-hydraulic modeling will also be important for improving computational speed.

Although there has been considerable research in recent years to develop different nodal methods for solving the neutron kinetics equation it is not clear in these times of limited resources if there is sufficient incentive to replace the method used in either code - and in the process give RETRAN-02 a three dimensional neutron kinetics capability. The major motivation would have to be considerably faster computational speed. There is some motivation to enable RAMONA-3B to automatically calculate one dimensional (1D) cross section data from a three dimensional steady state (RAMONA-3B) calculation in order to expedite the use of the code in a 1D mode for certain transient analysis. Analysts interpreting results from both of these codes would benefit by having reactivity edits available.

REFERENCES

A1. A.L. Aronson, H.S. Cheng, D.J. Diamond and M.S. Lu, "MEKIN-B: The BNL Version of the LWR Core Dynamics Code MEKIN," BNL-NUREG-28071 Brookhaven National Laboratory (1980).

A2. G.A. Alesii, S.P. Congdon, B.S. Shiralkov and R.B. Linford, "One Dimensional Core Transient Model," NEDO-24154, General Electric Co. (1978).

B1. R.J. Breen, O.J. Marlowe and C.J. Pfeifer, "HARMONY: System For Nuclear Reactor Depletion Computation," WAPD-TM-478, Bettis Atomic Power Lab. (1965).

B2. R.W. Bowring, "Physical Model, Based on Bubble Detachment, and Calculation of Steam Voidage in the Subcooled Region of a Heated Channel," HPR 29, OECD Holden Reactor Project, Norway (1962).

B3. R.F. Barry and D.H. Risher, "TWINKLE-A Multi-Dimensional Neutron Kinetics Computer Code," WCAP-8028A, Westinghouse Electric Co. (1975).

B4. R.W. Bowring, J.W. Stewart, R.A. Shober and R.N. Sims, "MEKIN: MIT-EPRI Nuclear Reactor Core Kinetics Code," EPRI-CCM-1, Vol. 1 and EPRI 227 Electric Power Research Institute (1975).

B5. G.F. Malan and W.M. Herwig, "BWKIN Development and Validation," Trans. Amer. Nucl. Soc. June (1982).

B6. S. Børresen and L. Moberg, "Qualification of the Neutronics Model in RAMONA-III," Trans. Amer. Nucl. Soc. June (1982).

REFERENCES (cont.)

B7. R.W. Bowring et al., "MEKIN: MIT-EPRI, Nuclear Reactor Core Kinetics Code, RP 227, Program Development Notes," Volumes 1 and 2.2, EPRI CCM-1, Electric Power Research Institute (1975).

B8. P. Bakstad and K.O. Solberg, "A Model For the Dynamics of Nuclear Reactors with Boiling Coolant With a New Approach to the Vapour Generating Process," KR-121, Institutt For Atomenergi, Norway (1967).

B9. S. Borresen, "A Simplified Coarse-Mesh Three Dimensional Diffusion Scheme for Calculating the Gross Power Distribution in a Boiling Water Reactor," Nucl. Sci. & Engr, 44, 37 (1971).

B10. S. Bian, G.F. Malan and G.A. Schwenk, "Multidimensional Analysis of PWR Accidents Using the BWKIN (MEKIN) Code," Trans. Amer. Nucl. Soc., 34, 315 (1980).

C1. T.M. Camden, P.J. Kersting and W.R. Carlson, "PALADON -Westinghouse Nodal Computer Code," WCAP-9486, Westinghouse Electric Co. (1978).

C2. H.S. Cheng, "The Thermal-Hydraulic Model of BNL-TWIGL," BNL-NUREG-28787, Brookhaven National Laboratory (1980).

C3. H.S. Cheng and D.J. Diamond, "Analyzing the Rod Drop Accident in a Boiling Water Reactor," Nucl. Tech., 56, 40 (1982).

C4. H.S. Cheng and D.J. Diamond, "Core Analysis of Peach Bottom 2 Turbine Trip Tests," BNL-NUREG-24903, Brookhaven National Laboratory (1978).

C5. H.S. Cheng, A.L. Aronson, J.W. Herczeg and D.J. Diamond, "The Use of MEKIN-B for Light Water Reactor Transient Calculations," BNL-NUREG-28785, Brookhaven National Laboratory (1980).

D1. D.L. Delp, D.L. Fischer, J.M. Harriman and M.J. Stedwell, "FLARE-A Three-Dimensional Boiling Water Reactor Simulator, GEAP-4598, General Electric Co. (1964).

D2. U. Decher, "FIESTA - A One-Dimensional, Two-Group Space-Time-Kinetics Code For Calculating PWR Scram Reactivities," CEN-122(F), Combustion Engineering Inc. (1979).

D3. D.J. Diamond, Ed. "BNL-TWIGL, A Program For Calculating Rapid LWR Core Transients," BNL-NUREG-21925, Brookhaven National Laboratory (1976).

D4. D.J. Diamond et al., "Water Reactor Safety Research Division, Quarterly Progress Reports," Jan. 1979 - Dec. 1981, NUREG/CR-0821, 1035, 1248, 1403, 1506, 1618, 1800. 1960, 2160, 2381, Brookhaven National Laboratory.

E1. Exxon Nuclear Co. proprietary code.

REFERENCES (cont.)

F1. S.L. Forkner et al., "BWR Transient Analysis Model Utilizing the RETRAN Program," TVA-TR81-01, Tennessee Valley Authority (1981).

F2. S.L. Forkner, G.H. Meriwether and T.D. Beu, "Three-Dimensional LWR Core Simulation Methods," TVA-TR78-03A, Tennessee Valley Authority (1979).

G1. D.P. Griggs, A.F. Henry and M.S. Kazimi, "Development of a Three-Dimensional Two-Fluid Code With Transient Neutronic Feedback For LWR Applications," MIT-EL-81-013 Massachusetts Institute of Technology Energy Lab. (1981).

G2. D.P. Griggs, M.S. Kazimi, and A.F. Henry, "Development of an Advanced Three-Dimensional Coupled Neutronics/Thermal Hydraulics Code for Light Water Reactor Safety Analysis," Proceedings of ANS Topical Meeting on Reactor Physics and Core Thermal Hydraulics, Kiamesha Lake (1982).

G3. G.C. Gose and J.A. Naser, "RETRAN-02 Spatial Kinetics Methods," Trans. Amer. Nucl. Soc. June (1982).

G4. G. Greenman, K. Smith and A.F. Henry, "Recent Advances in an Analytic Nodal Method for Static and Transient Reactor Analysis," Proceedings of the Topical Meeting in Computational Methods in Nuclear Engineering, Williamsburg (1979).

K1. E.D. Kendrick, Jr. and J.R. Fisher, "EPRI-NODE-B" in "Advanced Recycle Methodology Program System Documentation," EPRI-CCM-3, Part II, Chapter 15, Electric Power Research Institute (1977).

L1. G.S. Lellouche and B.A. Zolotar, "Mechanistic Model for Predicting Two-Phase Void Fraction for Water in Vertical Tubes, Channels and Red Bundles," EPRI NP-2246-SR, Electric Power Research Institute (1982).

L2. G.S. Lellouche et al.,"RASP, An Integrated Reload Analysis and Safety Program," Proceedings of Conference on Reactor Physics and Core Thermal Hydraulics, Kiamesha Lake (1982).

M1. C.W. Mays and M. Furtney, "FRAME3 -A Three-Dimensional Nodal Code for Calculating Core Reactivity and Power Distributions," B&W-10124, Babcock & Wilcox (1976).

M2. J.H. McFadden et al. "RETRAN-02 - A Program For Transient Thermal-Hydraulic Analysis of Complex Fluid Flow Systems," EPRI NP-1850, Electric Power Research Institute (1981).

M3. D.A. Meneley, K.O. Ott and E.S. Wiener, "Fast Reactor Kinetics - The QXI Code," ANL-7769 Argonne National Laboratory (1971).

N1. P. Neogy, D. Diamond and J. Carew, "A Spatial Kinetic Analysis of a PWR Core Response to Steam Line Break," BNL-NUREG-29336, Brookhaven National Laboratory (1981).

REFERENCES (cont.)

O1. T.G. Ober, J.C. Stark, I.C. Rickard and J.K. Gasper, "Theory, Capabilities and Use of the Three-Dimensional Reactor Operation and Control Simulator (ROCS): Nucl. Sci. Eng. 64, 605 (1977).

O2. T.G. Ober, R.P. Bandera, W.B. Terney and J.C. Stark, "Extension of the ROCS Simulator to Two Energy Groups," Trans. Amer. Nucl. Soc. 28, 763 (1978).

P1. C.J. Pfeifer, "PDQ-7 Reference Manual II," WAPD-TM-947 (L), Bettis Atomic Power Lab. (1971).

P2. C.J. Pfeifer and C.J. Spitz, "PDQ-8 Reference Manual," WAPD-TM-1266, Bettis Atomic Power Lab. (1978).

P3. D.W. Pruitt, "COTRAN: A Coupled Neutronic and Thermal Hydraulic Transient Analysis Code," Trans. Amer. Nucl. Soc. June (1982).

R1. B.M. Rothleder and J.R. Fisher, "EPRI-NODE-P" in "Advanced Recycle Methodology System Documentation," EPRI-CCM-3, Part II, Chapter 14, Electric Power Research Institute (1977).

R2. B.M. Rothleder, "PDQ7/HARMONY User's Manual," EPRI Draft Report, Electric Power Research Institute (1979).

R3. B.M. Rothleder, R.A. Blake, J.R. Fisher and E.D. Kendrick, "PWR Core Modelling Procedures for Advanced Recycle Methodology Program," EPRI Draft Report, Electric Power Research Institute (1979).

R4. P.E. Rohan, S.G. Wagner and S.E. Ritterbusch," HERMITE, A Multi-Dimensional Space-Time Kinetics Code For PWR Transients," CENPD-188, Combustion Engineering (1976).

R5. P.E. Rohan and S.G. Wagner, "PWR Spatial Kinetics at Combustion Engineer," Trans. Amer. Nucl. Soc. June (1982).

R6. D.S. Rowe, "COBRA IIIC: A Digital Computer Program for Steady State and Transient Thermal-Hydraulic Analysis of Rod Bundle Nuclear Fuel Elements," BNWL-1695, Battelle Northwest Laboratories (1973).

S1. R.B. Stout, "XTG: A Two-Group Three-Dimensional Reactor Simulator Utilizing Coarse Mesh Spacing and Users Manual (PWR Version)" XN-CC-28 Rev. 4, Exxon Nuclear Co. (1976).

S2. T.O. Sauar, S. Børresen, J. Hangen, E. Nitteberg, H.K. Haess and T. Skardhamar, "A Multilevel Data-Based Computer Code System for In-Core Fuel Management in Light Water Reactors," Proc. 4th U.N. Int'l. Conf. IAEA, A/Conf. 49/P/293, Vol. 2 (1972).

REFERENCES (cont.)

S3. J.N. Sorensen, "Thermal Feedback Calculations in the PDQ-5 Few Group Neutron Diffusion-Depletion Computer Program," WAPD-TM-639, Bettis Atomic Power Lab. (1967).

S4. S.A. Sandoz, S.P. Congdon and R.B. Linford, "Simulation of BWR Transients," Proc. Conf. Simulation Methods for Nuclear Power Systems, EPRI WS-81-202, Electric Power Research Institute (1981).

S5. R.A. Shober, T.A. Daly and D.R. Ferguson, "FX2-TH: A Two Dimensional Nuclear Reactor Kinetics Code with Thermal-Hydraulic Feedback," ANL-78-97 Argonne National Laboratory (1978).

V1. D.M. Ver Planck, "Manual For the Reactor Anaylsis Program SIMULATE," YAEC-1158, Yankee Atomic Electric Co. (1978).

V2. D.M. Ver Planck, "Methods For the Analysis of Boiling Water Reactors Steady State Core Physics," YAEC-1238, Yankee Atomic Electric Co. (1981).

V3. D.M. Ver Planck, "SIMULATE Procedures Manual," YAEC-1159, Yankee Atomic Electric Co. (1978).

W1. J.A. Wooley, "Three-Dimensional BWR Core Simulator," NEDO-20953, General Electric Co. (1976).

Y1. J.B. Yasinsky, M. Natelson, L.A. Hageman, "TWIGL - A Program to Solve the Two Dimensional, Two-Group, Space-Time Neutron Diffusion Equations With Temperature Feedback," WAPD-TM-743 (1968).

VALIDATION OF RECORD/PRESTO AGAINST GAMMA SCAN AND EXPERIMENTAL VOID LOOP DATA

S. Børresen
Scandpower Inc., Bethesda, Maryland

and

H. K. Naess
Scandpower A/S, Kjeller, Norway

SUMMARY

This paper describes results of validation of the FMS program PRESTO (Reference 1) against the Hatch γ-scan data, using lattice physics data from RECORD (Reference 2), and against experimental void loop data (Reference 4).

PRESTO is the 3-D LWR simulator program with coupled neutronics and thermal hydraulics models. RECORD is a 2-D fuel assembly homogenization and burnup code.

The basic reactor physics model of RECORD has been independently benchmarked against available critical lattice experimental data, isotopic analysis data, gamma scan data, and other special measurements.

RECORD/PRESTO applications in numerous core follow studies have rendered a significant amount of comparisons with in-core detector measurements, such as TIP and LPRM recordings.

The Hatch gamma scan results were analyzed with the objective of qualifying both the 3-D nodal power distribution model of PRESTO as well as the in-assembly local power distribution predicted by combining the results of RECORD and PRESTO. The total nodal standard deviation between measured and calculated La-140 distributions was 6.4%.

Comparisons of axial pin-power distributions for the wide-wide and the narrow-narrow corner pins for selected Hatch assemblies showed very good agreement.

The combined neutronics and thermal hydraulics model of PRESTO relies on methods derived from first principles of reactor physics and thermal hydraulics with no artificial adjustment of the modelling to improve the overall agreement with plant data.

Independent qualification of the thermal hydraulics model was obtained by analysis of the FRIGG experimental void loop data. The measurements were performed in a full scale, electrically heated mock up of a BWR fuel assembly with surrounding flow channel. A total of 31 different experimental conditions, covering the typical BWR operating range of power, flow and subcooling data, were analyzed with PRESTO's thermal hydraulics model.

The standard deviation between calculated and measured void, for a total of 243 points, was 2.1%.

METHOD OF ANALYSIS, HATCH GAMMA SCANS

This analysis of the Edwin I. Hatch gamma scan data was performed by Scandpower as part of a general benchmarking effort of PRESTO using RECORD lattice physics data. The work was funded by members of the European FMS User Group, Institutt for Energiteknikk, Norway and Scandpower A/S, Norway.

Gamma scan measurements of 106 bundles of the initial Edwin I. Hatch BWR core were performed by General Electric at EOC-1 in a program jointly sponsored by EPRI and GE.

Seventy-five of these bundles comprised a complete octant of the core. The additional 31 bundles were located in four-bundle cells, around real or pseudo instrument locations symmetric to those in the octant.

All 106 bundles were measured at a minimum of 12 axial positions corresponding to the midpoints of the odd numbered PRESTO nodes. Partially controlled bundles were measured at additional positions in the vicinity of the control blade tip.

Six bundles were measured at 24 or 27 axial elevations to obtain a detailed profile of the axial La-140 shape. Four of these were disassembled for single rod scanning to obtain local power distribution measurement.

The uncertainty in the measurements was determined from repeated measurements of the standard bundle. The total uncertainty in nodal La-140 intensity quoted was 1.7%.

The reactor operation through the first cycle was simulated with PRESTO with the objective of predicting the EOC La-140 distribution for comparison with the corresponding measured distribution.

The calculation was carried out using 33 burnup steps. Operating data, characterizing each step, were obtained from Reference 5.

All core dimensional data, and core specific thermal hydraulic parameters, required for the PRESTO core model were obtained from Reference 5.

A complete nuclear cross section data bank was generated with RECORD based on the published fuel design data.

The data bank consisted of the following:

- Two group macroscopic cross sections, diffusion coefficients pin-power peaking factors as functions of burnup, exposure weighted void and instantaneous void.
- A perturbed cross section set, assuming 15% void in the water gaps at 70% in-channel void. (No water gap voidage at 0% and 40% in-channel void.)

The perturbed dataset was used to account for bypass flow boiling caused by plugging of the bypass flow holes in the core support plate. This dataset was used after the core average burnup had reached 4000 MWD/TU corresponding,

approximately, to the time when the bypass plugging was performed. The reactivity effect of the assumed water gap void fraction (15%) was 0.8% Δk at 70% in-channel void.

- Coefficients for the influence of control rods, xenon, Doppler, samarium and spacer grids on the basic cross section set.

The xenon, Doppler and samarium models in PRESTO account for differential effects relative to the corresponding equilibrium values. The control rod and spacer grid effect are included as additive terms to the thermal group absorption cross section.

A 1/4-core, symmetric, core model was set up to generate the reflector boundary conditions at EOC-1. First, an approximate EOC condition was obtained by running through the 33 burnup steps with a 1/4-core model using typical BWR reflector boundary conditions. Then, the ALBMO procedure (an option within PRESTO) was used to generate a specific set of boundary conditions for the EOC condition. The latter data was not significantly different from the data used in the 33 burnup steps. Then, the 33 burnup steps were recalculated using a 1/2-core model with the specific reflector data derived as explained above.

The 1/2-core model was used to enable exact representation of all control rod patterns associated with each of the burnup steps.

The nodal distribution of Ba-140 was automatically tracked through the 33 steps and the EOC distribution was saved on a file for comparison with the corresponding experimental La-140 distribution.

Detailed simulation, using an option in PRESTO where each burnup step is further subdivided into time steps, was performed for the last three months of operation to assure proper integration of the Ba-140 nodal concentration distribution.

Comparison of Calculated and Measured La-140 Distributions

The time from the reactor was shut down to the actual measurement was sufficiently long to justify the assumption that the measured La-140 intensities were in equilibrium with the corresponding Ba-140 concentrations. Thus the two distributions would be proportional.

In order to compare calculated and measured data, normalization was performed in the following way:

The calculated nodal Ba-140 concentrations were normalized to unity over all nodes, N, of the 75 fuel assemblies in the core octant:

$$\frac{1}{N} \cdot \sum_{\text{octant}} P_{\text{calc}} = 1 \qquad (1)$$

A normalization factor, c, was defined for the measured data:

$$\frac{c}{N} \cdot \sum_{\text{octant}} P_{\text{meas}} = 1 \qquad (2)$$

The nodal standard deviation (σ) was calculated using the RMS prescription.

The top nodes (no. 24) were excluded in the calculation of the standard deviation, since only a few assemblies were actually measured at this elevation.

The standard deviation thus calculated was 6.4%. Separating controlled and uncontrolled nodes, the following result was obtained:

Type of Node	# Nodes	Std. Dev. (%)
Controlled	290	6.4
Uncontrolled	1435	6.5
Total	1725	6.4

An overview of the nodal comparison for all bundles of the core octant is shown in Figure 1. Examples of individual bundle plots are shown in Figure 2.

Bundle-wise ratios between calculated and measured, axially integrated curves are shown in Figure 3. This representation illustrates the average radial, or bundle power, comparison. Excluding three bundles where a normalization problem was suspected, the following statistics were obtained for the bundle power comparison:

	# Bundles	Average Ratio	Std. Dev. (%)
Rodded bundles	22	1.012	1.8
Unrodded bundles	50	.992	1.8
Core periphery bundles	8	1.005	1.0
Core interior bundles	64	.997	1.9
Total	72	.998	1.8

Comparisons of calculated and measured axial, pin-wise, La-140 distribution were performed for four different fuel pins (the narrow-narrow and wide-wide corner pins of assemblies, Nos. 373 and 393).

The calculated pin-wise axial distributions were obtained by multiplying the nodal distributions calculated by PRESTO with pin-to-node power peaking factors obtained from the RECORD data bank. Peaking factors for each axial node were calculated by interpolating to the nodal exposure and exposure weighted void among the values tabulated in the data bank. Different sets of peaking factors were used for the rodded and the unrodded condition. Results are shown in Figure 4.

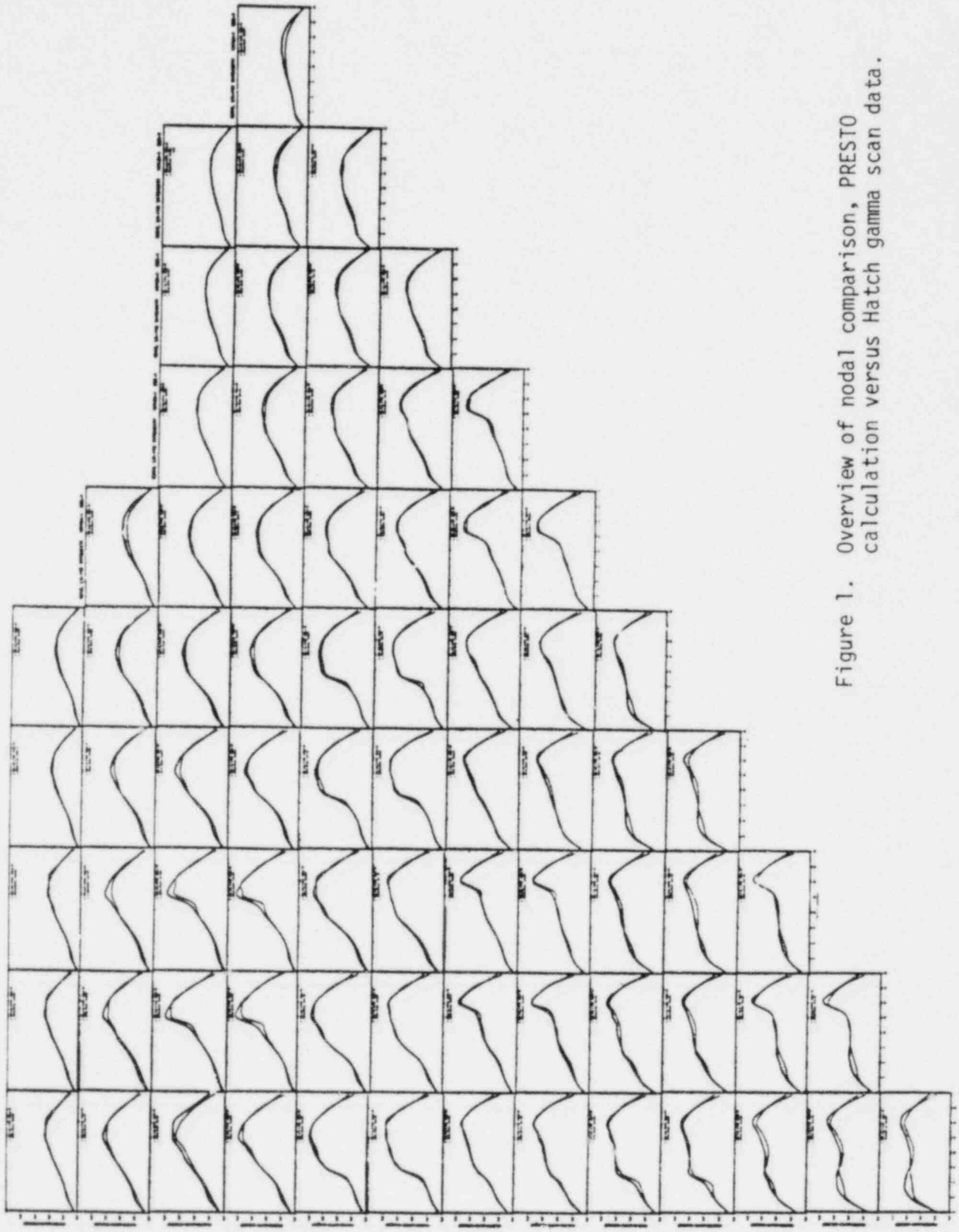

Figure 1. Overview of nodal comparison, PRESTO calculation versus Hatch gamma scan data.

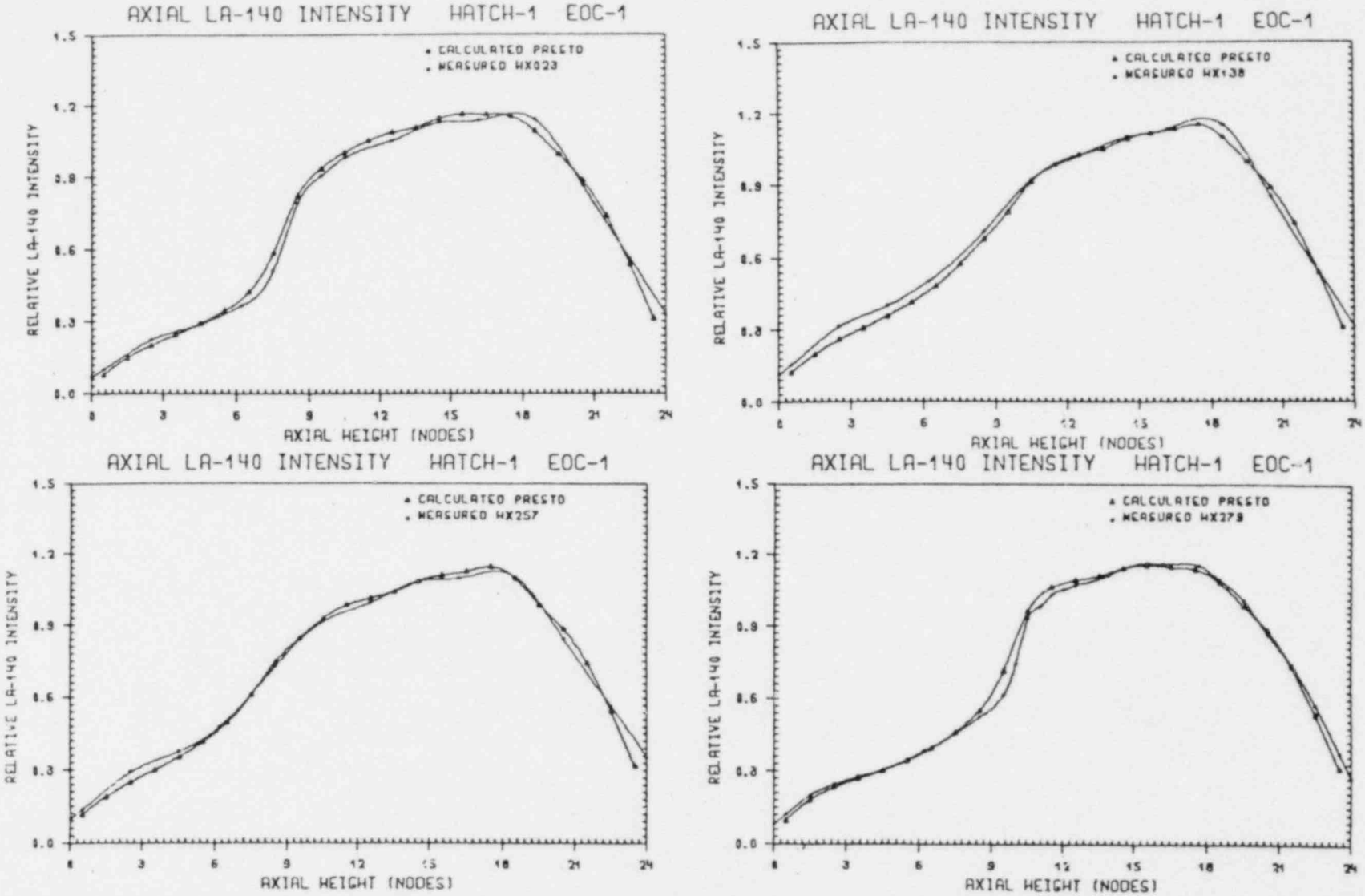

Figure 2. Examples of comparisons of bundle-wise La-140 distributions, PRESTO versus gamma scan data

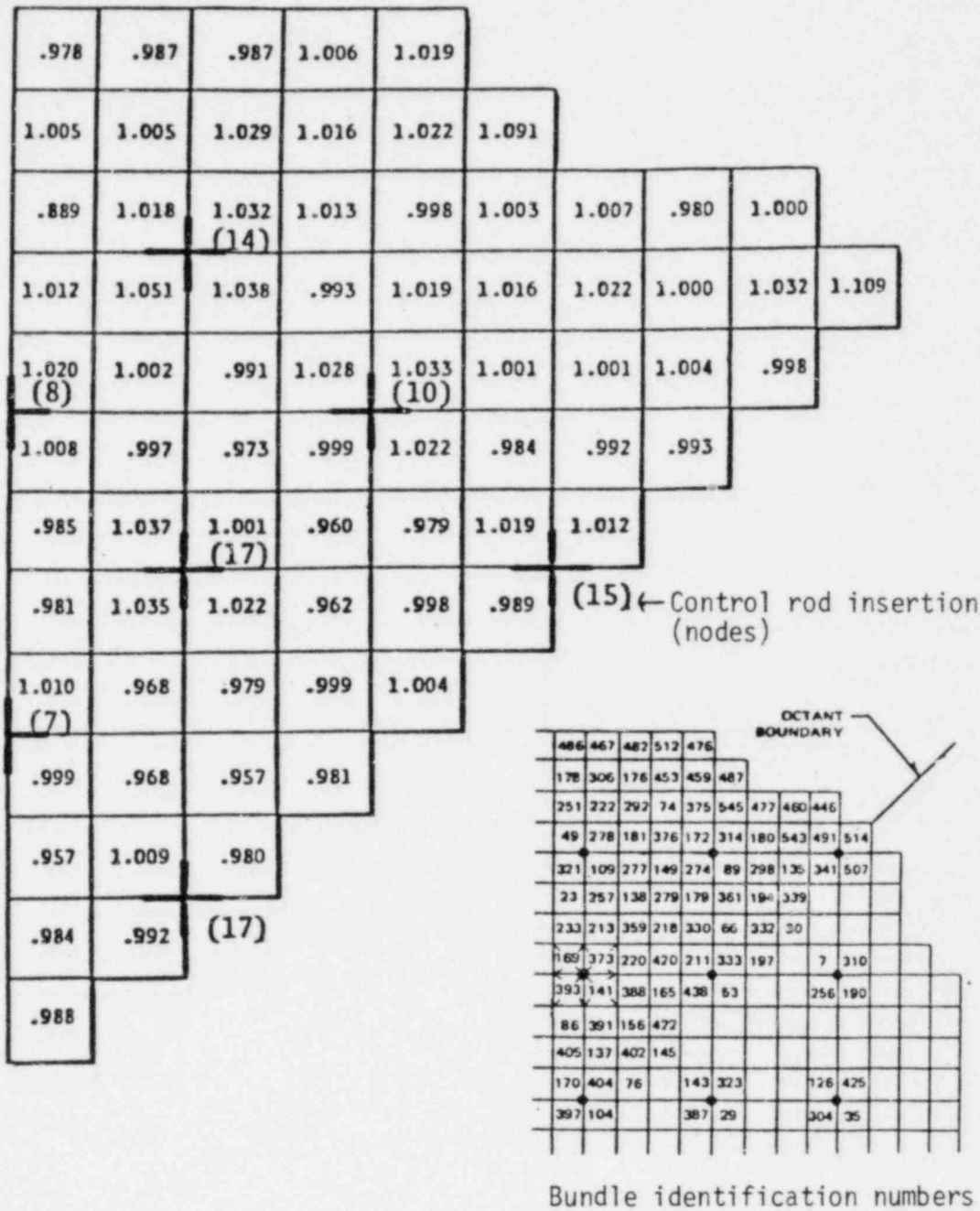

Bundle identification numbers

Figure 3. Bundle-wise ratios of calculated and measured, axially integrated, La-140 distributions

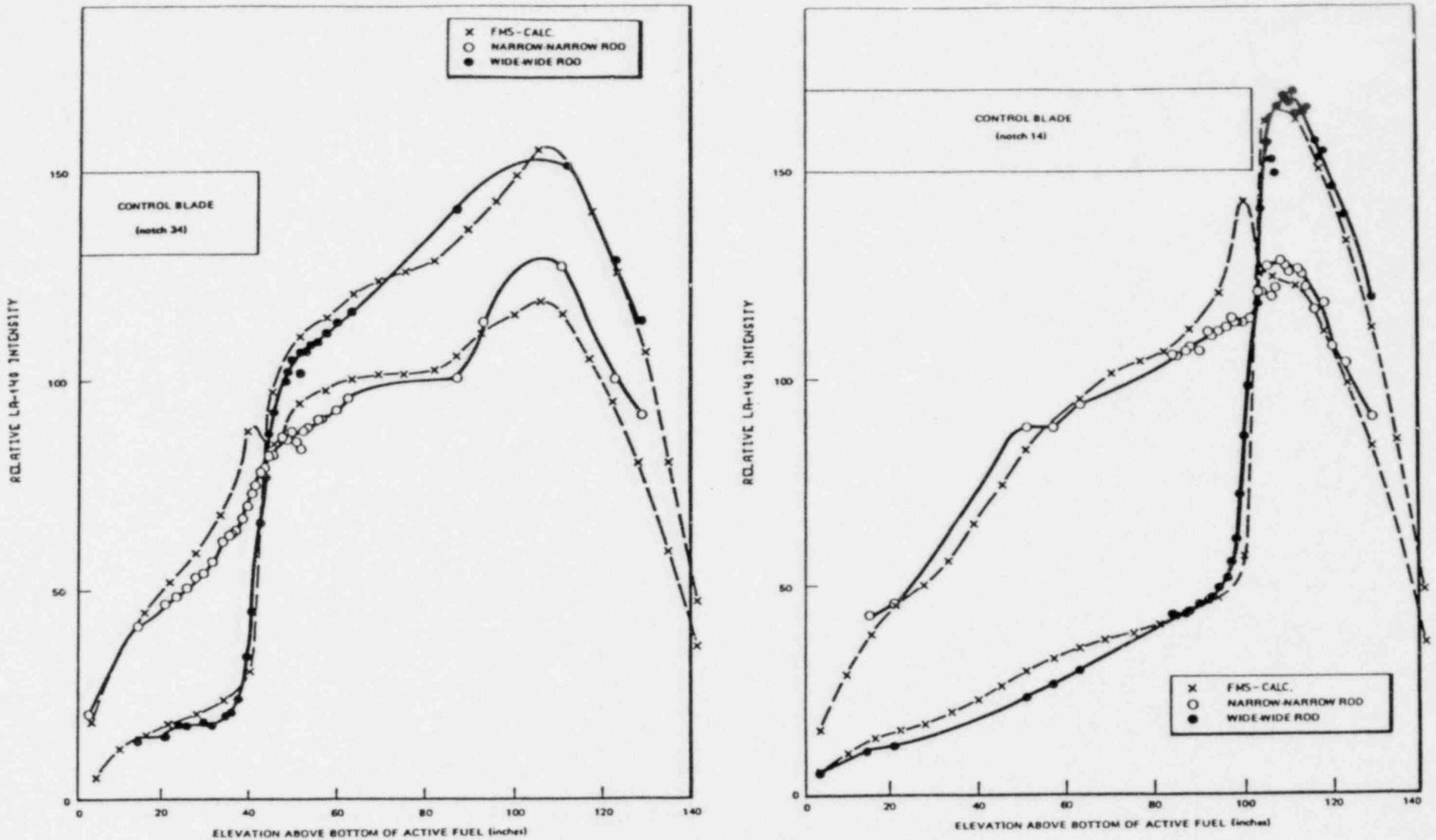

Figure 4. Calculated and measured axial La-140 relative distributions in the N-N and W-W corner pins of Hatch bundles HX393 (left) and HX373 (right)

In general, very good agreement was obtained in comparing calculated and measured axial La-140 shapes. Although not shown in this paper, it was found that the calculated La-140 distribution agreed well with the calculated EOC power distribution. Thus, the conclusions drawn are valid fo the power distribution as well.

The discrepancies seen may be grouped into two categories, as follows:

- In the center region of the core, where the power distribution is relatively flat, with a tendency to double hump, the measurement shows a depression of the "bottom hump," which is not seen in the calculation. This may be due to inaccuracies in the calculated EOC exposure distribution resulting from approximations in power distribution modelling during the cycle or due to unidentified problems with the experimental data.

- A slight over-prediction of the power peak is observed for some of the sharply top peaked distributions in the outer region of the core. This phenomenon does not correlate with control rod insertion, and is probably related to exposure distribution inaccuracies.

The following observations and conclusions are made:

- The influence of partially inserted control rods (both deep and shallow insertion) on the axial power distribution in surrounding fuel assemblies is very well predicted by PRESTO. This is true for the four assemblies immediately adjacent to the control blade, as well as for those located in the next "ring" away from the blade. Both power shape and the rodded-to-unrodded power step are in good agreement with measurement.

- The axial power shape in the throttled periphery bundles (see Figure 1) are as good as in the unthrottled bundles.

- The general agreement between calculated and measured "bundle power" is very good.

- There are no systematic radial tilts.

- Periphery bundle power is calculated with the same precision as core interior bundles.

- Rodded bundle powers are in good agreement with measurements.

- In general, the pin-wise axial shapes are well reproduced. Especially, the ratio between the power levels in the "rodded" and "unrodded" portions of the pins agrees very well.

COMPARISON OF CALCULATED AND MEASURED AXIAL VOID DISTRIBUTION

The FRIGG void loop experimental data (Reference 4) were analyzed with the objective of obtaining qualification of the thermal hydraulics model of PRESTO independently of any neutronics to thermal hydraulics coupling.

The measurements were performed in a full-scale coolant loop containing electrically heated, BWR mockup, fuel rods. The operating conditions of the experiment covered a wide range in power, flow rate and subcooling. The loop operating data, expressed in percent of typical BWR bundle operating data, is shown in Table 1.

Table 1. FRIGG Loop Operating Data in Percent of Typical BWR Data

Pressure	96 - 98%
Power	50 - 120%
Flow rate	30 - 140%
Subcooling	100 - 400%

A total of 31 different experimental conditions, involving various combinations of operating data were analyzed with the thermal hydraulics model of PRESTO.

Results showing calculated and measured axial void profiles for typical cases are shown in Figures 5 and 6.

The total, point-wise standard deviation (RMS) of the difference between calculated and measured void was 2.15% with an average deviation of 0.58% void.

Statistical analysis was also performed for each of three data groups obtained by subdividing the data according to flow range. These results are shown in Table 2.

Table 2. Average Deviation and Standard Deviation in Percent Void, PRESTO Hydraulics Model Versus FRIGG Void Loop Data

	# Cases	Average Dev. (%)	Std. Dev. (%)
Low flow	12	0.28	1.75
Normal flow	13	0.33	1.95
High flow	6	1.76	3.10
Total	31	0.58	2.15

The point-wise correlation between calculated and measured void data is shown in Figure 7. The linear regression slope coefficient of the correlation is 0.97 demonstrating very good agreement over the investigated void range (0-80% void).

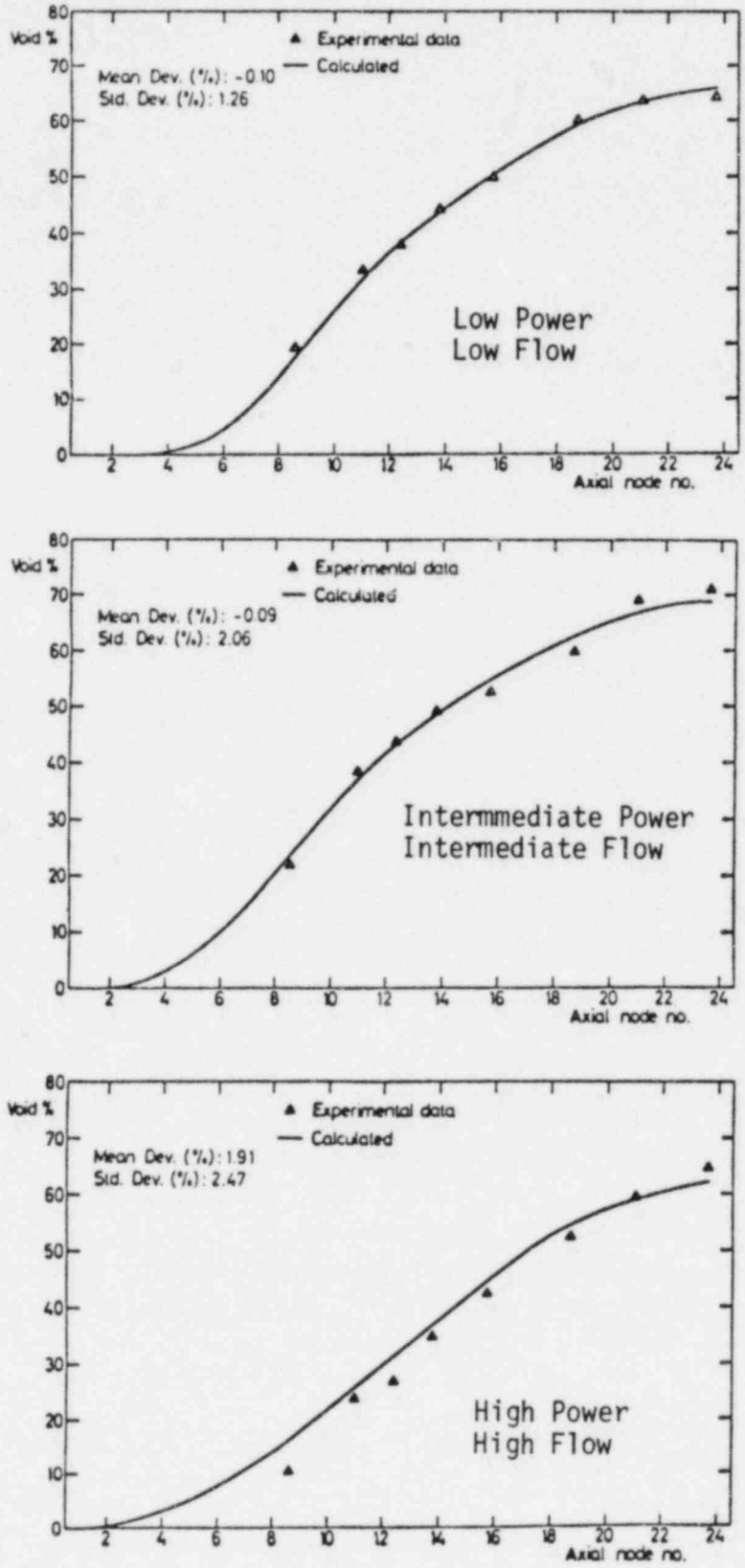

Figure 5. Comparison of calculated and measured axial void distributions. PRESTO model versus FRIGG data.

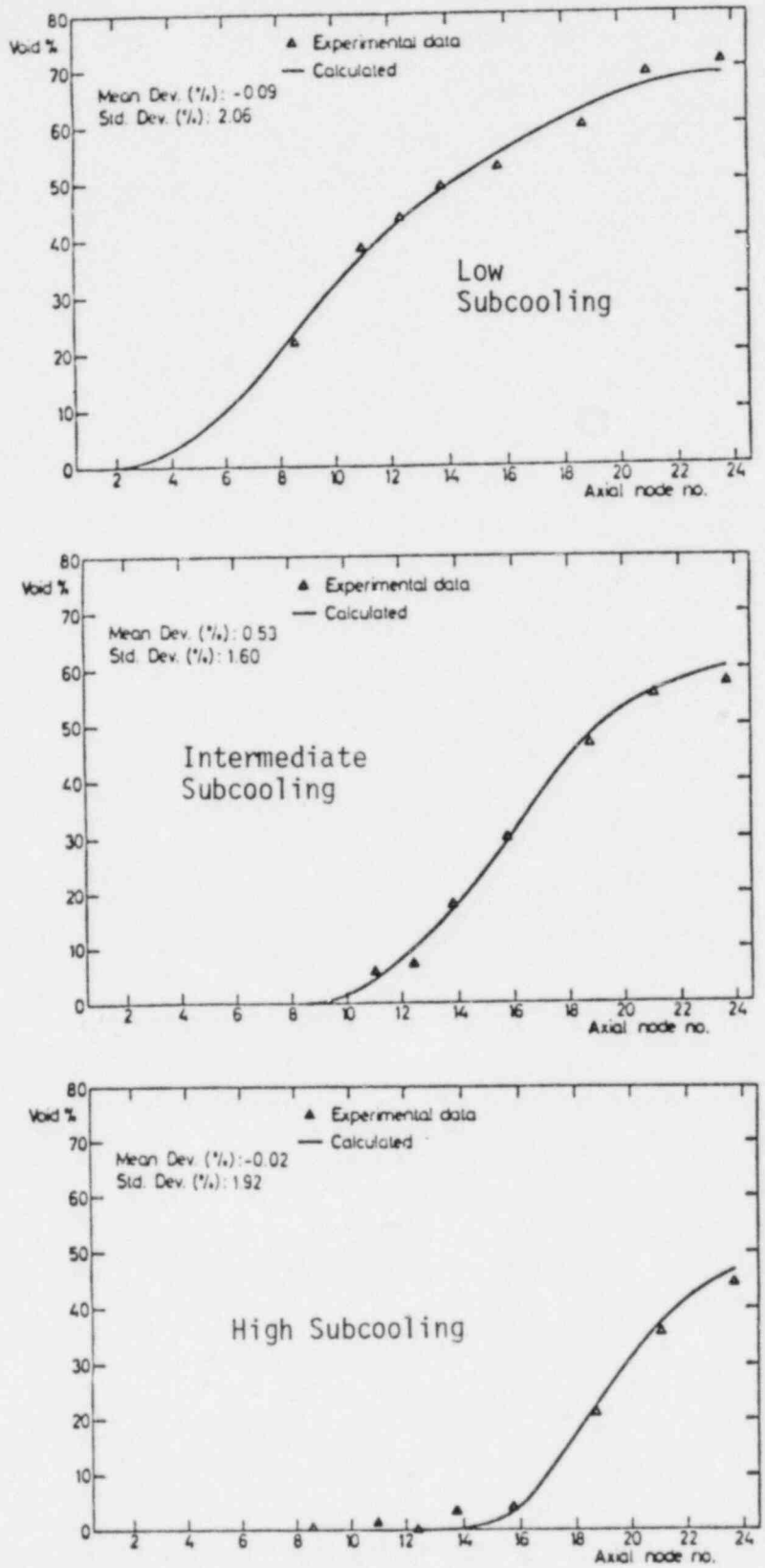

Figure 6. Comparison of calculated and measured axial void distributions. PRESTO model versus FRIGG data

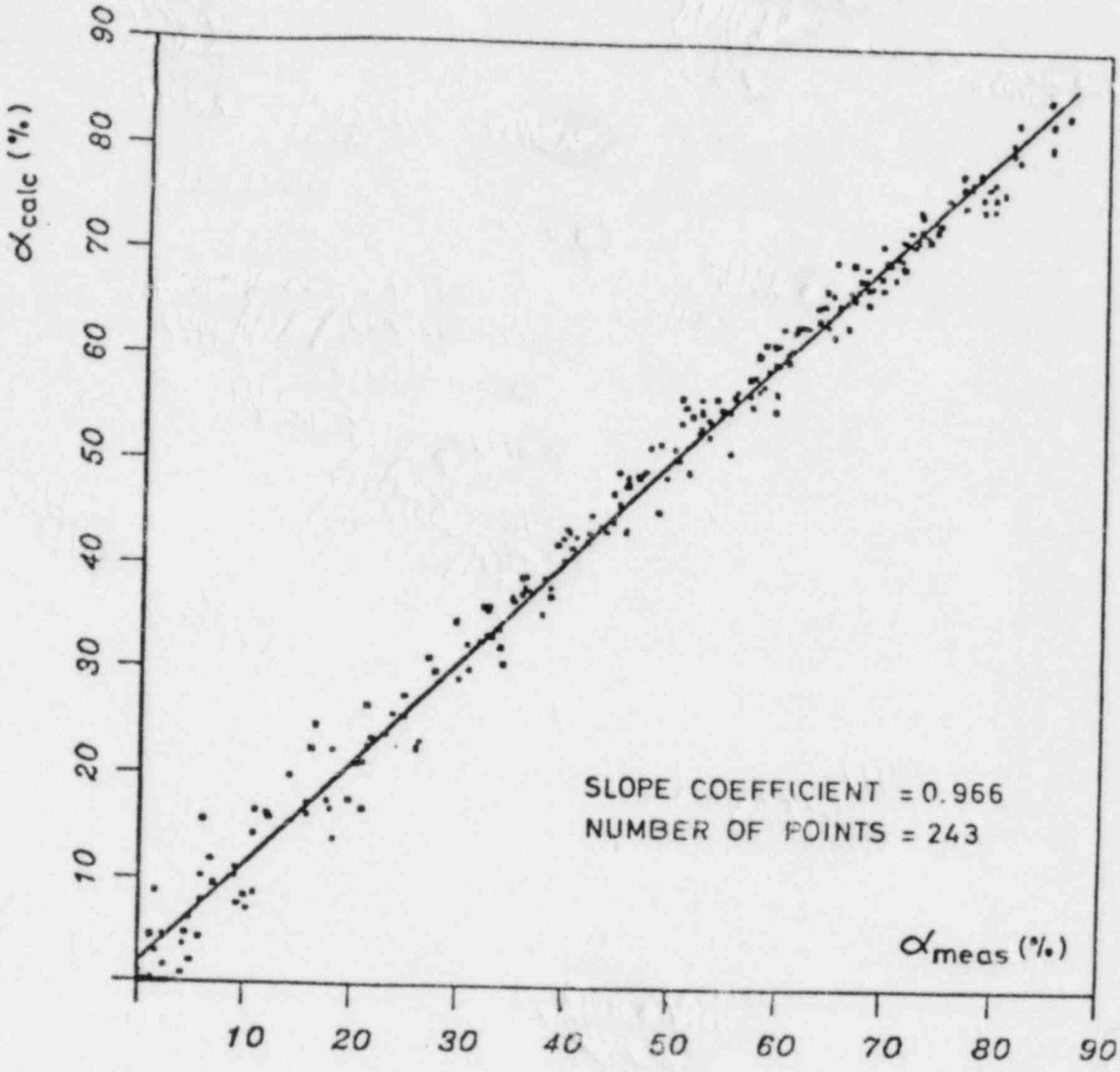

Figure 7. Correlation between calculated measured void

CONCLUSIONS

Results of comparisons of PRESTO with experimental gamma scan data and with experimental in-channel void data both show agreement close to the experimental uncertainties.

The applied model is independent of any reactor specific adjustment and is therefore well suited for true predictive calculations.

With previous uncertainties in the thermal hydraulics model largely removed, it is concluded that the void feedback effect on the neutronics model, as reflected in the axial power shape, is well represented based on RECORD lattice data.

It is also concluded that the applied model reproduces closely the experimental data for the following detailed effects:

- The influence of partially inserted control rods on the bundle power distribution, the axial power shape in bundles adjacent to the blades and in individual fuel rods within such bundles.

- The power generated in core periphery bundles versus that of the core interior bundles.

The small discrepancies observed in the gamma scan comparison may be caused by approximations in the representation of the reactor operating history.

A fully detailed core follow, as will be obtained in on-line applications of PRESTO, will eliminate this uncertainty in future studies.

REFERENCES

1. S. Børresen, T. Skardhamar, S. Wennemo-Hanssen, "Applications of FMS RECORD/PRESTO for Analysis and Simulation of Operating LWR Cores," Proc. NEA Specialists Mtg., Paris, (Nov., 1979).

2. S. Børresen, "A Simplified, Coarse Mesh: Three-Dimensional Diffusion Scheme for Calculating the Gross Power Distribution in a Boiling Water Reactor," Nucl. Sci. & Eng., 44 (1971), p 37.

3. L. M. Shiraishi, G. R. Parkos, "Gamma Scan Measurements at Edwin I. Hatch Nuclear Plant, Unit 1, Following Cycle-1," EPRI NP-511, Research Project 130-3, Final Report, (August, 1978).

4. O. Nylund, et al, Confidential FRIGG reports on experiments and results (1969, 1970).

5. N. H. Larsen, J. G. Goudey, "Core Design and Operating Data for Cycle 1 of Hatch-1," EPRI NP-562, (1979).

TITAN: AN ADVANCED THREE-DIMENSIONAL NEUTRONICS/THERMAL-HYDRAULICS CODE FOR LIGHT WATER REACTOR SAFETY ANALYSIS

D.P. Griggs, M.S. Kazimi, A.F. Henry
Department of Nuclear Engineering
Massachusetts Institute of Technology*

ABSTRACT

The initial development of TITAN, a three-dimensional coupled neutronics/thermal-hydraulics code for LWR safety analysis, has been completed. The transient neutronics code QUANDRY has been joined to the two-fluid thermal-hydraulics code THERMIT with the appropriate feedback mechanisms modeled. A detailed steady-state and transient coupling scheme based on the tandem technique was implemented in accordance with the important structural and operational characteristics of QUANDRY and THERMIT. A two channel sample problem formed the basis for steady-state and transient analyses performed with TITAN. TITAN steady-state results were compared with those obtained with MEKIN and showed good agreement. Null transients, simulated turbine trip transients, and a rod withdrawal transient were analyzed with TITAN and reasonable results were obtained.

INTRODUCTION

A state-of-the-art code capable of calculating three-dimensional steady-state and transient neutronics and thermal-hydraulics has been developed. The code has been named TITAN [1], an acronym for three-dimensional integrated thermal-hydraulics and neutronics.

The TITAN code was developed using existing programs for the calculation of core thermal-hydraulics and neutronics. The THERMIT code [2] was selected for the thermal-hydraulics portion and the QUANDRY code [3] was selected for the neutronics portion. The two codes were combined and the appropriate feedback mechanisms were modeled. Neutronics and thermal-hydraulic calculations are performed in tandem for a representation of a nuclear reactor core in three-dimensional Cartesian coordinates. The core model consists of calculational volumes having horizontal cross sectional areas equal to that of a fuel assembly. Either PWR or BWR cores may be modeled. Transients may be initiated by perturbations of cross sections or of the coolant flow, temperature, or pressure boundary conditions. Feedback is calculated by approximating the nuclear cross sections as linear functions of fuel temperature, moderator temperature and moderator density.

THERMAL-HYDRAULICS

The thermal-hydraulics portion of TITAN is THERMIT, a two-fluid thermal-hydraulics code capable of performing steady-state and transient analyses of water-cooled nuclear reactors in three dimensions. The two-fluid model uses separate partial differential equations expressing conservation of mass, momentum and energy for each individual fluid phase (liquid and vapor). As a result, both thermal and mechanical nonequilibrium between the phases can be modeled. The fluid dynamics model is a distributed resistance (or porous body) model and is well suited for either subchannel or core-wide analyses. Both PWR and BWR models may be ana-

*work supported by Boston Edison, Northeast Utilities, Yankee Atomic, PSE & G, and LILCO.

lyzed in Cartesian coordinates. THERMIT can handle complex fluid dynamics conditions, such as natural circulation, blowdown, flow reversal and phase separation. A heat transfer package is included which can determine appropriate regimes based on a complete boiling curve. A flexible fuel pin model solves the radial conduction equation for fuel temperatures, with one average fuel rod modeled per node. Built in correlations for temperature dependent fuel and clad properties as well as a variable gap heat transfer coefficient model are options in the fuel pin calculation.

In addition to having an advanced two-phase flow model, THERMIT also has a very flexible and reliable solution method. A semi-implicit technique is used which is a modification of the I.C.E. method [4]. This method is not limited by the speed or direction of the flow and is thus well suited for severe transients. However, there is a stability limit on the allowed time step size, governed by the Courant condition:

$$\Delta t < \left| \frac{\Delta X}{V_{max}} \right| , \qquad (1)$$

where ΔX is the mesh spacing and V_{max} is the largest fluid velocity. The semi-implicit transient solution scheme guarantees convergence of the numerical method (provided a real solution exists). An important restriction of the method is that the steady-state conservation equations cannot be solved directly. As a result, there is no convenient way to generate a steady-state solution with THERMIT. Steady-state solutions are obtained by running an unperturbed transient from an initial guess of thermal-hydraulic conditions. This procedure eventually results in a solution which changes little from time step to time step.

THERMIT permits considerable flexibility in the specification of boundary conditions. Either pressure or velocity boundary conditions may be specified at the inlet or outlet. Inlet temperatures and void fractions are also required by THERMIT. These boundary conditions may have arbitrary radial shapes. During a transient, time-dependent forcing functions can be applied to the top and bottom boundary conditions and to the inlet temperatures. The forcing functions apply a constant multiplier to the given steady-state boundary conditions, thus retaining the initial spatial profiles.

The THERMIT code has undergone considerable testing and verification [2,5]. The combination of a two-fluid model with suitable constitutive relations and a reliable numerical method allows for the most detailed analysis of two phase flow currently available and offers the possibility of being more generally applicable and more accurate than other models.

NEUTRON KINETICS

The neutronics portion of TITAN is based on the QUANDRY code [3], which uses an analytic nodal method to solve space-dependent reactor transients. The two-group diffusion theory approximation to the neutron transport equation is utilized and the reactor is modeled as an array of homogenized regions (or nodes), for which equivalent diffusion theory parameters must be determined [6]. The nodal method uses node-averaged fluxes as the primary unknowns rather than calculating fine mesh fluxes and then averaging to give node-averaged fluxes. Given that the homogenized two-group parameters can be determined, the only approximation made is that the neutron leakages in each node transverse to the Uth direction (U = X, Y, or Z) can be represented by a quadratic function of the coordinate U.

The coefficients of these quadratic functions are determined iteratively as part of the flux solution, obviating the need for user-supplied adjustable parameters or albedoes.

A considerable amount of computational time is saved by the nodal approach. Indeed, the computational efficiency of QUANDRY has been shown to be at least two orders of magnitude greater than that of finite difference methods [3]. It was this characteristic that made QUANDRY an excellent choice for a coupled code. In addition, QUANDRY has proven to be highly accurate for both static and transient solutions. The accuracy of QUANDRY has been tested extensively by comparison with the results of numerical benchmark problems [7].

The QUANDRY solution method provides for direct calculation of the static and transient nodal neutron diffusion equations. The static (steady-state) solution procedure performs the eigenvalue search with or without thermal-hydraulic feedback. Transients are initiated by cross section perturbations or variations in core inlet flow or inlet temperature. Each node may be perturbed by an instantaneous cross section change or by a single continuous linear perturbation over a specified period of time. A cusping correction is applied to cross section changes of this type [7]. The "θ" time integration method allows the transient equations to be solved explicitly, implicitly, or any combination of these.

COUPLING METHODOLOGY

The coupling methodology used in TITAN was devised after reviewing other coupled codes and after considering many of the important characteristics of QUANDRY and THERMIT. A review of other coupled codes indicated that most of them use some form of the tandem coupling method, in which the neutronics and thermal-hydraulics calculations are performed alternately, with feedback information passed between each segment as required. This approach seemed particularly appropriate for TITAN since QUANDRY and THERMIT were completely independent codes having rather different solution schemes. The basic philosophy behind the development of the coupling strategy was that the common support functions, such as input, restart, initialization and editing, would be integrated while the dissimilar computational functions would be linked only by the feedback information.

TITAN was designed to operate in two modes: steady-state and transient. As a result, there are two coupling schemes employed. For a steady-state calculation, the static neutronic solution of QUANDRY is linked to the transient THERMIT solution. For a transient calculation, the transient neutronic solution of QUANDRY is linked to the transient THERMIT solution. As a result, TITAN has been programmed to operate as a two step, interactive process. When a steady-state solution has been obtained, the calculation is terminated by the user and the steady-state conditions are stored on a disk file. The transient calculation is a separate problem, beginning with reading the initial conditions from the disk file. This two step method allows the user to monitor the steady-state convergence and ensure that an appropriate set of initial conditions are used in the transient calculation. In addition, a number of transient calculations can be done using the same steady-state solution.

For both the steady-state and transient modes of operation, the links between neutronics and thermal-hydraulics are the two sets of feedback information.

The neutronics portion of TITAN provides the nodal powers which drive the heat transfer calculation, while the thermal-hydraulics portion provides the parameters necessary to calculate the nodal neutron cross sections. The nodal cross sections are assumed to have a linear dependence on the node average fuel temperature, moderator temperature, and moderator density. The macroscopic cross section of type α for node (i,j,k) is calculated by an equation of the form:

$$\Sigma_{\alpha(i,j,k)} = \Sigma^{*}_{\alpha(i,j,k)} + \left(\frac{\partial\Sigma_\alpha}{\partial T^c}\right)\left(T^c_{(i,j,k)} - T^{c*}\right) + \left(\frac{\partial\Sigma_\alpha}{\partial T^f}\right)\left(T^f_{(i,j,k)} - T^{f*}\right)$$

$$+ \left(\frac{\partial\Sigma_\alpha}{\partial \zeta^c}\right)\left(\zeta^c_{(i,j,k)} - \zeta^{c*}\right) , \qquad (2)$$

where T^c and T^f are node average coolant and fuel temperatures, respectively, and ζ^c is the node average coolant density. Quantities marked with * indicate user-supplied reference values. Reference cross sections and feedback coefficients are supplied for each unique neutronic composition. A linear relationship of this type can describe cross sections accurately over limited ranges of temperatures and densities. However, the current version of TITAN assumes that the linear functional form is valid over the entire range of thermal-hydraulic variables so that, if the reference cross sections and partial derivatives are known, the thermal-hydraulic feedback model can be completely specified. A second feedback model in which the moderator density contribution is represented as a quadratic function is being added to TITAN. The feedback logic requires that the same geometric model be used for both neutronics and thermal-hydraulics calculations.

STEADY-STATE OPERATION

The major task of the TITAN steady-state coupling methodology is to provide a mechanism for generating a set of neutronic and thermal-hydraulic parameters which correspond to a steady-state condition for the reactor modeled. The code uses the static neutronics solution method of QUANDRY in tandem with the THERMIT solution method to accomplish this task. The approach used is to perform periodic static neutronics calculations while the thermal-hydraulics solution is converging. Each static neutronics calculation uses the latest thermal-hydraulic data (and corresponding cross sections) as its starting point and converges to a steady-state solution with no feedback updates. No external perturbations are applied to either the neutronics or thermal-hydraulics. This approach takes advantage of the speed and economy of the QUANDRY static solution method and recognizes that convergence of the thermal-hydraulics solution is the more difficult and time-consuming process. Convergence is attained when the flow and energy balances have been attained to the order of 10^{-4} to 10^{-5} and the nodal powers are nearly constant. The number of thermal-hydraulic time steps per static neutronic calculation can be varied as the convergence progresses. The utility of this feature is that the frequency of neutronic calculations can be matched to the rate at which the feedback parameters are changing. Hence, the user may quite appropriately use one thermal-hydraulic time step per static neutronic calculation initially and increase to ten thermal-hydraulic time steps per static neutronic calculation during the latter stages of convergence. Judicious use of this feature can reduce CPU time as much as 50% without affecting the results.

An important subsidiary task of the steady-state mode of TITAN is the processing of input data. This task is one of the support functions that was consolidated when THERMIT and QUANDRY were merged. In addition to the usual geometrical data, neutronic data and boundary conditions that one might expect to provide as input, the solution method of THERMIT requires that a set of initial thermal-hydraulic conditions be supplied by the user. These initial conditions include the pressure, void fraction, vapor temperature, and vapor axial velocity for each node. If, as in TITAN, a heat transfer calculation is being performed, the initial clad surface temperature for each node is also required. The user must therefore determine appropriate initial conditions from some auxiliary calculation or simply make a reasonable guess. Experience with THERMIT has not shown that there is much sensitivity of running time or steady-state solution to these initial conditions. However, it seemed likely that the convergence of TITAN might be more sensitive to the initial conditions, since the fuel temperatures, moderator temperatures, and moderator densities are also feedback parameters. Therefore, a simple thermal-hydraulics model [8] was incorporated into TITAN to eliminate the need for providing these initial thermal-hydraulics conditions as input. The model assumes homogeneous equilibrium flow, neglects pressure drop, and models the fuel with a lumped capacity approximation. This simple model is capable of supplying reasonable initial values for the average fuel temperature and the average coolant temperature, in each node. The pressure and axial vapor velocity must still be supplied.

The TITAN code is designed to be used interactively, with the user controlling the operation remotely at a terminal. The steady-state coupling procedure takes advantage of this fact, allowing the user to monitor and alter the convergence procedure. An outline of this procedure is as follows:

1) Read in input data from an on-line data file. Free format is used; data arrays are placed in a large container array and a pointer system is used to locate individual subscripted variables. This permits object-time dimensioning, if desired.

2) Perform initializations. The initial thermal-hydraulic conditions are calculated with a simple model and the initial cross sections are calculated.

3) An entire static neutronics calculation is calculated with the current cross sections. No feedback updates are performed during the static convergence.

4) The nodal powers are calculated and these are passed to the thermal-hydraulics segment.

5) A thermal-hydraulics calculation is performed for one or more unperturbed time steps (time step size determined by the code). The average nodal thermal-hydraulic feedback parameters and the new cross sections are calculated.

6) The current transient time is checked to see if the end of the current time domain has been reached. If the time domain end has not been reached, return to 3) and continue until the end of the time domain. If the end of the last time domain has been reached, the

code will do one of two things, depending on the input option selected. One option is for the calculation to end, writing the steady-state conditions on a disk file if desired. The other option is for the user to be prompted at the terminal for additional time domain information to continue the convergence procedure. If the energy and flow errors displayed at the terminal indicate satisfactory convergence, the user can end the calculation, saving the steady-state conditions on disk file for a transient calculation. If not, the specification of new time domain information will continue the procedure (return to 3).

This procedure is summarized in Figure 1. It has been demonstrated for the problems analyzed that this tandem method converges to a good steady-state solution with a reasonable amount of computational effort.

TRANSIENT OPERATION

The primary task of the transient coupling logic in TITAN is to provide the necessary structure to permit the neutronic and thermal-hydraulic analysis of a variety of types of transients. The transients of interest may be initiated by changes in reactivity, core flow rate, inlet temperature, reactor pressure or combinations of these. Proper coordination of thermal-hydraulic and neutronic time steps is also required.

The tandem coupling scheme developed for TITAN uses a staggered approach in which it is assumed that the transient is initiated by either neutronics or thermal-hydraulics. The first transient time step is calculated for that segment of the code, subject to the user-supplied forcing functions and with no feedback contribution included. Following this initial time-step (or time-steps), the relevant feedback information is calculated and, together with any applied forcing functions, constitutes the perturbation which is applied in advancing the other segment to the same transient time.

As in the steady-state mode, transients are designed to be run interactively. Steady-state conditions must have been previously generated and stored on an on-line disk file in order to do a transient analysis. Additional input data required includes time-dependent pressure and flow boundary conditions and/or cross section perturbations. Cross section perturbations may be applied instantaneously or over a continuous time interval. Only one cross section perturbation per node is allowed during a transient. For the initial coupling, it was assumed that the neutronic and thermal-hydraulic time steps were identical. The transient procedure is as follows:

1) Read common blocks and container array from steady-state disk file,

2) Read transient input from data file,

3) Perform any needed initializations,

4) Calculate the time steps, subject to Courant numerical stability limitations and user-supplied upper and lower bounds,

5) Determine whether the transient is initiated in the neutronics segment or in the thermal-hydraulics segment. If neutronics, go to 6). If thermal-hydraulics, go to 7).

6) Perform one complete feedback loop, beginning with the transient neutronics calculation. Calculate the new nodal powers and update these in the thermal-hydraulics calculation for the same time period. Calculate the average feedback parameters and the new cross sections. Go to 8)

7) Perform one complete feedback loop, beginning with the thermal-hydraulics calculation. Calculate the average feedback parameters and new cross sections. Perform the transient neutronics calculations for the same time period. Calculate the new nodal powers and update them in the thermal-hydraulics segment.

8) Check for the end of the current time domain. If the end has not been reached, return to step 4). If the time domain has ended, the calculation ends or the user is prompted for new time domain information.

CODE APPLICATIONS

A) Sample Problem

A sample problem was devised to serve as a basis for preliminary applications of TITAN. The problem consists of two adjacent part-length (1.524m) boiling water reactor fuel assemblies. Each assembly is controlled by an independent homogeneous control rod. A zero flux boundary condition on one vertical face produces large horizontal flux tilts. The sample problem is partitioned into 20 nodes, 10 in each channel, and has seven different neutronic compositions. The cross sections and feedback coefficients were obtained from Rodriquez-Vera [9], as was a steady-state solution produced with the MEKIN code [10]. This problem was intended to provide a useful model for the testing, debugging and verification of the TITAN code. The important descriptive parameters pertaining to the sample problem are given in Table 1. All analyses presented in this article relate to this sample problem.

B) Steady-State Results

The TITAN code was applied to the sample problem and successfully obtained a converged steady-state solution. A MEKIN solution to the same problem was provided by Rodriquez-Vera. The TITAN analysis used constant fuel and clad thermal conductivities and gap heat transfer coefficients in order to duplicate the MEKIN analysis as closely as possible. Figure 2 shows the axial power shapes calculated by MEKIN and TITAN. The TITAN results compare well with those obtained by MEKIN. Slight differences in the powers in the top nodes reflect the fuel temperature feedback effect. The built-in thermal-conductivities in TITAN were lower than those used in the MEKIN analysis, resulting in higher average fuel temperatures in the TITAN analysis. The higher average fuel temperatures in the TITAN analysis depressed the power slightly in the upper nodes. In all other respects, the two codes showed good agreement.

C) Transient Results

Several preliminary transient results have been produced with TITAN. All of these used steady-state results calculated for the sample problem. A set of null transients were performed for both boiling and non-boiling problems. These indicated that the solution procedure could maintain the steady-state

TABLE 1

Sample Problem Characteristics

Total power	6077.6	kw
Number of fuel assemblies	2	
Assembly length	152.4	cm
Number of fuel rods per assembly	64	
Average fuel power density	366.38	w/cm^3
Average linear heat generation rate	9.496	kw/ft
Fuel rod diameter	1.226	cm
Clad thickness	.0813	cm
Gap thickness	.0114	cm
Inlet temperature	548	°K
Total flow rate	31.703	kg/s
Channel 1 flow velocity	1.946	m/s
Channel 2 flow velocity	2.511	m/s
Outlet pressure	7.136	MPa
Channel flow area	93.5	cm^2
Channel 1 control rod insertion distance	76.0	cm
Channel 2 control rod insertion distance	121.6	cm

in the absence of applied forcing functions. A simulated turbine trip transient analysis was successfully performed. Time-dependent inlet flow and outlet pressure forcing functions were applied to drive the transient. The two-assembly "reactor" was initially at full power. No scram was modeled. Figure 3 shows the forcing functions and the calculated reactor power as a function of time during the transient. The magnitude and duration of the power peak are similar to those obtained for real reactors [11], though no solution exists against which the TITAN results could be checked. Nevertheless, the results seem reasonable, as the power rise closely follows the inlet flow boundary condition.

A control rod withdrawal transient has been analyzed with TITAN and preliminary results obtained. The transient consists of a continous withdrawal of the Channel 2 control rod at a rate of 1.276 m/s. This withdrawal rate removes the rod entirely in 1.0 seconds. The transient was designed to be a benchmark calculation for three-dimensional coupled codes [9]. The preliminary results obtained with TITAN cannot be conclusively judged, since no reference solution for this problem exists to date. However, the analysis serves to show that the logic for a neutronically initiated coupled analysis has been exercised.

SUMMARY

TITAN, a three-dimensional coupled neutronics/thermal-hydraulics code, has been developed. The code combines the nodal neutron kinetics code QUANDRY with the two fluid nonequilibrium thermal-hydraulics code THERMIT. A tandem coupling methodology and a linear feedback model allows TITAN to perform steady-state and transient analyses of LWR cores in three dimensions. Several steady-state analyses have been performed with good results. Comparison of TITAN results to those obtained with MEKIN shows good agreement. A few preliminary transient analyses indicate that the transient coupling methodology is reliable, though further evaluation is needed. The combination of state-of-the-art models both for neutronics and thermal-hydraulics in TITAN offers the promise of both accuracy and generality of application in LWR safety analysis.

References

1. D. P. Griggs, A. F. Henry and M. S. Kazimi, "Advanced Methods Development for LWR Transient Analysis, Final Report: 1981-1982", M.I.T. Energy Laboratory Report No. MIT-EL-82-021, May 1982.

2. J. E. Kelly, S. P. Kao and M. S. Kazimi, "THERMIT-2: A Two-Fluid Model for Light Water Reactor Subchannel Transient Analysis," M.I.T. Energy Laboratory Report No. MIT-EL-81-014, April, 1981.

3. G. Greenman, K. S. Smith and A. F. Henry, "Recent Advances in an Analytic Nodal Method for Static and Transient Reactor Analysis", ANS Proceedings of the "Topical Meeting on Computational Methods in Nuclear Engineering," Williamsburg, Virginia, Vol. 1, pp. 3-49 (April 1979).

4. F. H. Marlow and A. A. Amsden, "A Numerical Fluid Dynamics Calculation Method for All Flow Speeds," Journal of Computational Physics, 8, p. 197, (1971).

5. J. E. Kelly and M. S. Kazimi, "Development and Testing of the Three Dimensional, Two-Fluid Code THERMIT for LWR Core and Subchannel Applications," M.I.T. Energy Laboratory Report No. MIT-EL-79-046 (1979).

6. K. S. Smith, A. F. Henry and R. A. Loretz, "Determination of Homogenized Diffusion Theory Parameters for Coarse Mesh Nodal Analysis," ANS Topical Meeting, Sun Valley, Idaho, September 1980.

7. K. S. Smith, "An Analytic Nodal Method for Solving the Two-Group, Multidimensional, Static and Transient Neutron Diffusion Equations", Nuclear Engineering Thesis, Department of Nuclear Engineering, M.I.T., Cambridge, MA (March 1979).

8. H. Khalil, "A Static, Two-Phase, Thermal Hydraulic Feedback Model for the Nodal Code QUANDRY", MITNE-235, Department of Nuclear Engineering, M.I.T., (1980).

9. F. J. Rodriquez-Vera, "Some Benchmark Calculations by Using the Computer Code MEKIN", Nuclear Engineering Thesis, Department of Nuclear Engineering, M.I.T. (1982).

10. R. Bowring, et al., "MEKIN: MIT-EPRI Nuclear Reactor Core Kinetics Code," CCM-1, EPRI Report RP228 (1975).

11. "Preliminary Safety Analysis Report, Duane Arnold Energy Center," Iowa Electric Light and Power Company (1968).

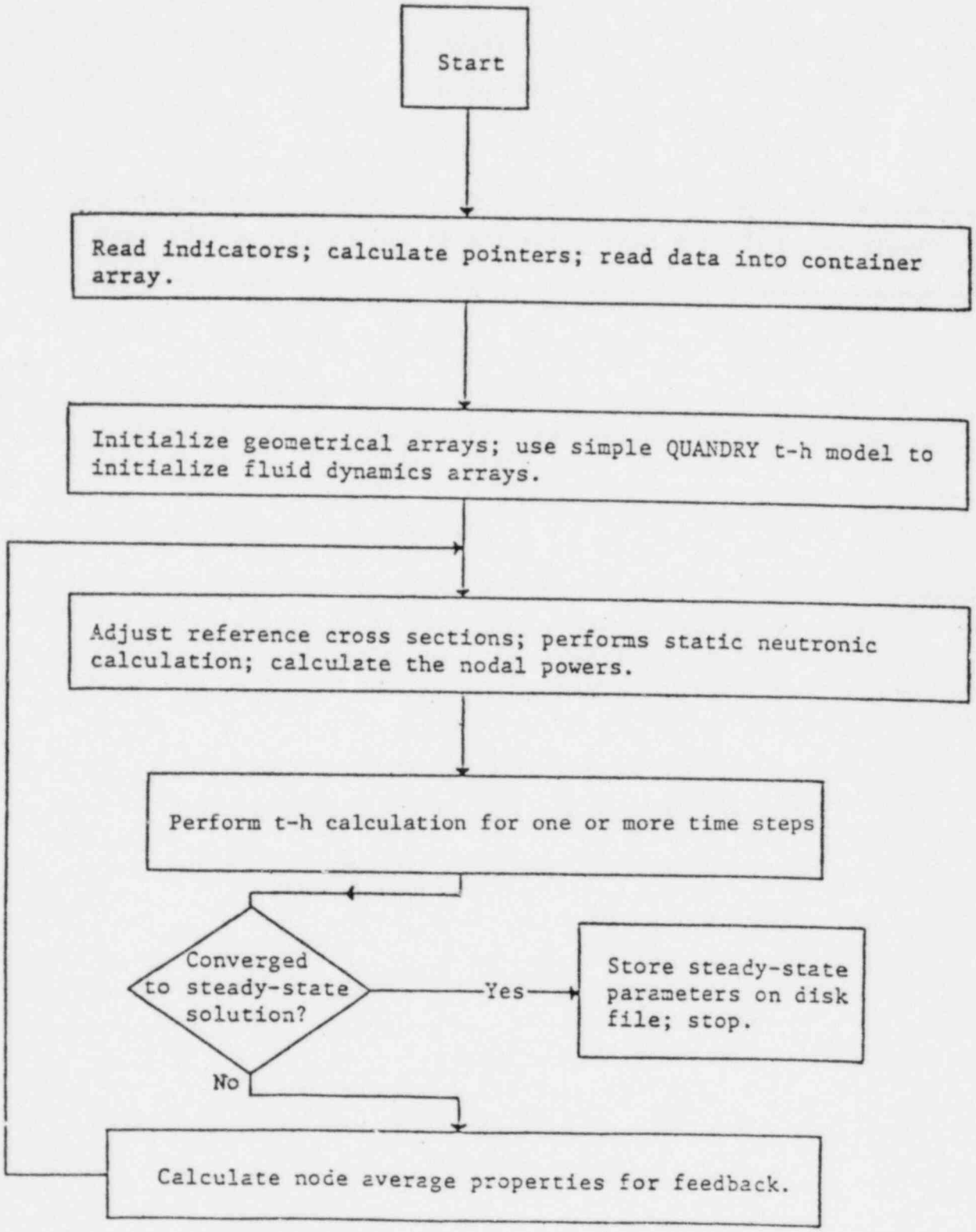

Figure 1: Steady-State Coupling Strategy

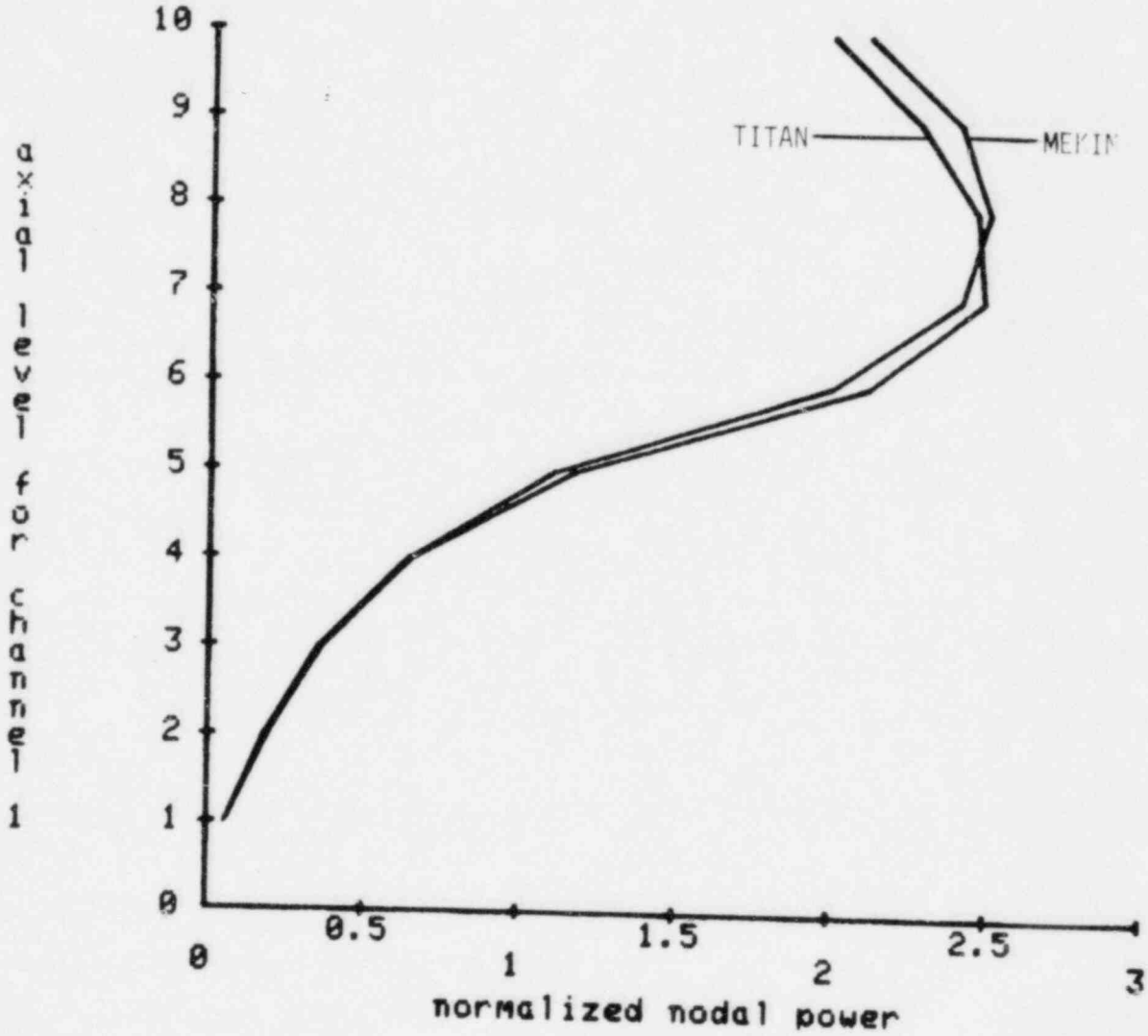

Figure 2: Steady-State Axial Power Shape, Channel 1

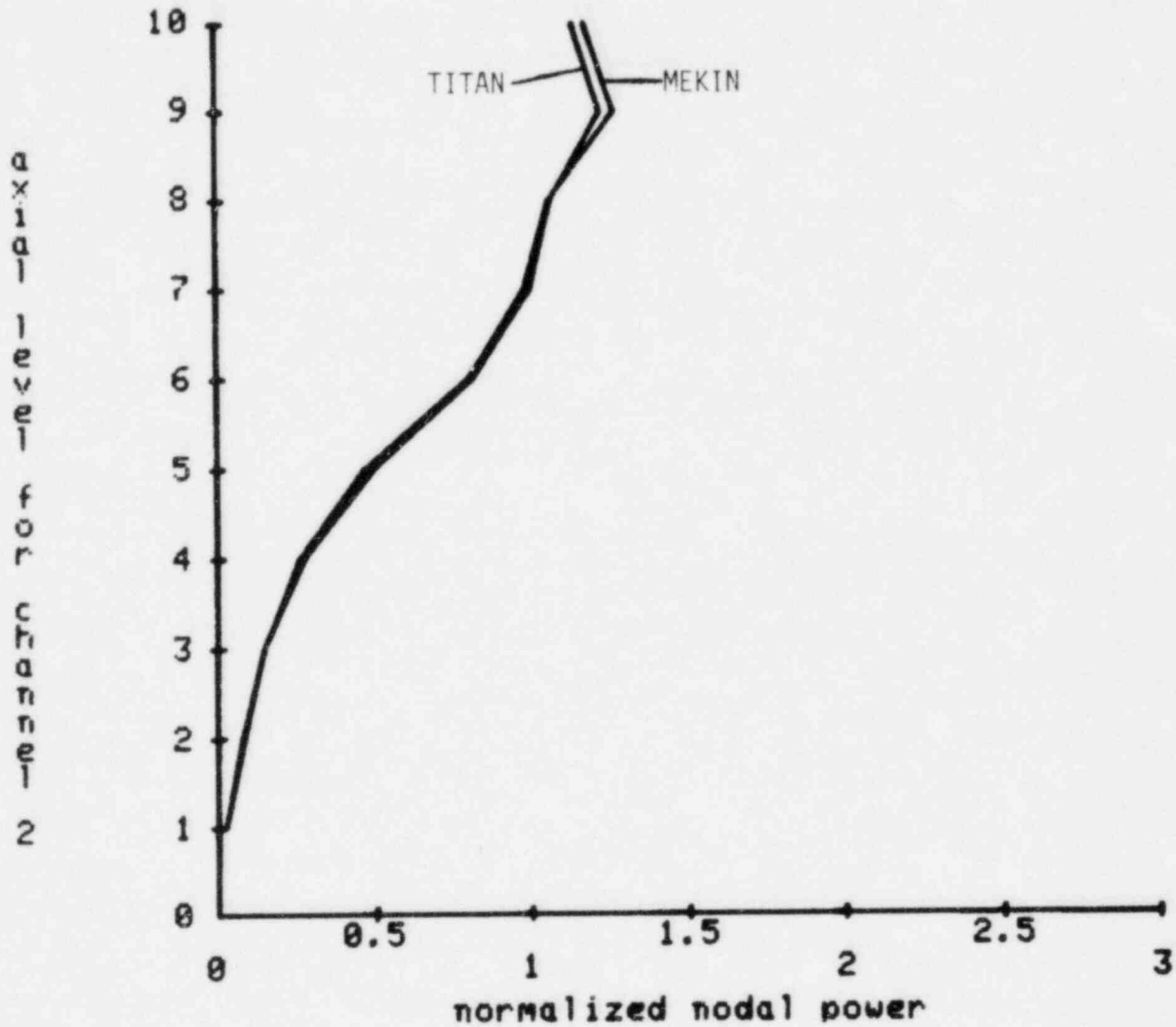

Figure 3: Steady-State Axial Power Shape, Channel 2

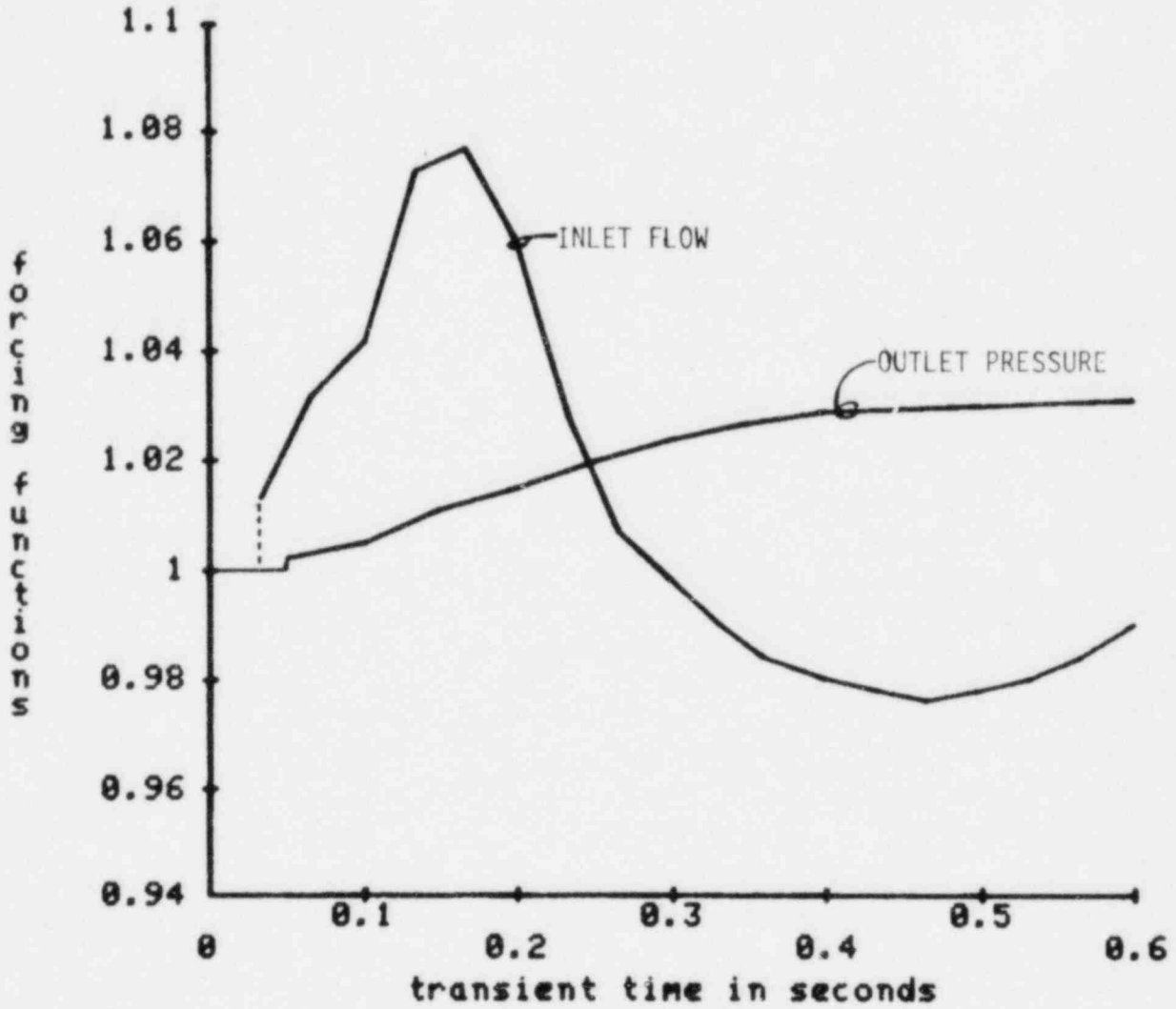

Figure 4: Forcing Functions for Simulated Turbine Trip Analysis

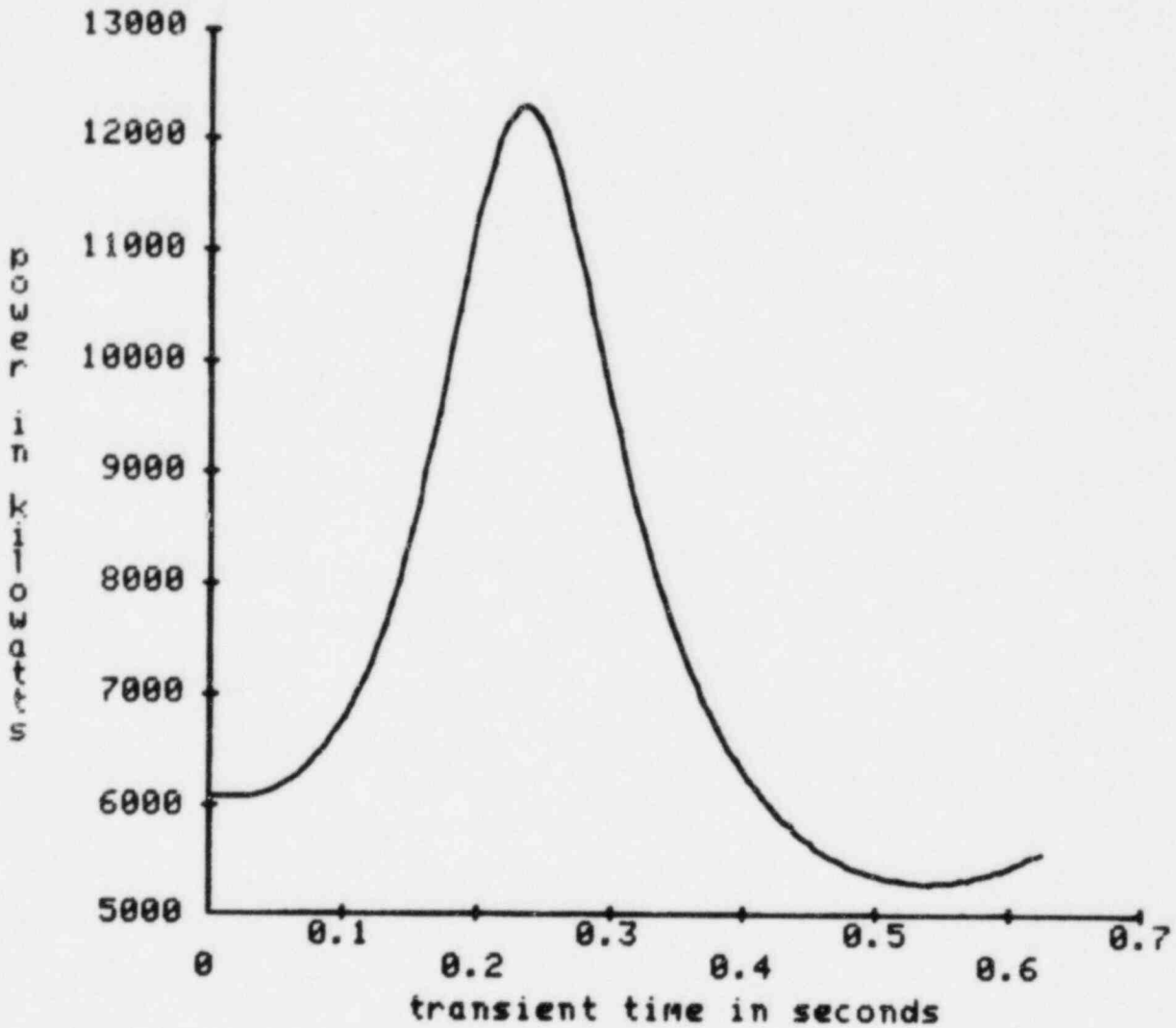

Figure 5: "Reactor" Power During Simulated Turbine Trip

THE NEUTRON KINETICS AND THERMAL-HYDRAULIC TRANSIENT COMPUTATIONAL MODULE OF THE NEPTUNE SYSTEM : CRONOS

A. Kavenoky, J.J. Lautard
Département des Réacteurs à Eau
Service d'Etudes des Réacteurs et de Mathématiques Appliquées
Centre d'Etudes Nucléaires de Saclay
91191 Gif sur Yvette Cedex (France)

1. INTRODUCTION

The NEPTUNE system had been designed to provide all the computational modules needed for a PWR calculation including design fuel management and reactivity accidents ; NEPTUNE provides 2D transport assembly calculations and steady state diffusion computations in 1D, 2D, 3D geometries. The steady state diffusion modules include standard finite difference codes and specific modules using the finite element method. The most recently added module is devoted to steady and transient calculations needing coupled neutronics and thermal-hydraulics calculations : it is named CRONOS ([1 to 7]).

CRONOS accounts for detailed transient calculations : at each time step the moderator density and the fuel temperature are determined by a refined thermal-hydraulic calculation ; these parameters are used as feed-back in the neutron-kinetics equations. The treatment of the 3D space dependent kinetics equation is based on the finite element method.

This paper is divided into four parts : § 2. presents the finite element treatment of the neutron kinetics equation, § 3. is devoted to the thermal-hydraulic model implemented in Flica 3 and to the numerical treatment, § 4. briefly describes the ARIANE data processing system specially designed for NEPTUNE and in the last part numerical results are presented for a full size rod ejection calculation for a 900 Mwe PWR (Fessenheim 2).

2. FINITE ELEMENT APPROXIMATION OF THE NEUTRON KINETICS EQUATION

The well-known time dependent neutron diffusion equations is used under the standard format :

$$\frac{1}{V_g}\frac{\partial \phi_g}{\partial t} = \nabla D_g \nabla \phi_g - \Sigma_{tg}\phi_g + \sum_{g'=1}^{g} \Sigma_{r\, g'\to g}\phi_{g'}$$

$$+ \chi_g \sum_{g'=1}^{G} (1-\beta_{g'})\, \nu \Sigma_{f\, g'}\phi_{g'} + \sum_{\ell=1}^{L} \chi_{\ell g}\lambda_\ell C_\ell$$

$$C_\ell(r,t) = C_\ell^o(r)\, e^{-\lambda_\ell t} + \int_o^t e^{-\lambda_\ell (t-s)} \left(\sum_{g'=1}^{G} \beta_{\ell\, g'}\, \nu \Sigma_{f\, g'}\phi_{g'} \right) ds$$

In this formula $C_\ell(r,t)$ represents the density of ℓ^{th} group of precursors. In order to solve this system of equations a finite element representation of the flux spatial variation is used :

$$\phi_g(r,t) = \sum_{i=1}^{N} \alpha_{ig}(t)\ P_i(r) \qquad (1)$$

$P_i(r)$ is a finite element basis and $\alpha_{ig}(t)$ are the expansion coefficients ; in the next paragraph the specially developped basis is presented.

2.1. The spatial finite element basis |8|

For this calculation, the 3D reactor core is divided into rectangular parallelepiped elements : on each element the flux is expanded over a truncated polynomial basis. A large number of polynomial approximations are provided from which the more used are the Lagrange basis : in 3D the Lagrange basis provides a factorized polynomial basis :

$$P_i(r) = \prod_{j=1}^{j=3} P_i^j(x_j)$$

For each variable x_j, the user may choose the degree of the polynomial P_i^j between 1 and 3 ; the elements available in CRONOS are presented in § 2.1.3.

The weak form of the diffusion equation involves integrals of products of the basis functions :

$$M_{ij}^k = \int P_i^k(x)\ P_j^k(x)\ dx \qquad (2)$$

$$S_{ij}^k = \int \nabla\ P_i^k(x)\ .\ \nabla\ P_j^k(x)\ dx \qquad (3)$$

Two major improvements have been added to the standard calculations : choice of a basis reducing the number of terms to be accounted for and numerical integration.

2.1.1. Refined basis

In order to fasten the numerical solution, the P_i^k polynomials are chosen in order to minimize the number of M_{ij}^k non equal to zero : our basis beeing factorized the treatment is presented in 1D. If the standard Lagrange polynomials are used (corresponding to the nodes) not any alement of M_{ij}^k is equal to zero : in our treatment the polynomials corresponding to the edges of the element core kept and the other are replaced by orthogonal linear combinations of themselves which are chosen to be orthogonal to the first two ones.

Figure 1 presents the third order M_{ij}^k matrix corresponding to the standard and modified basis : the number of terms is reduced from 16 to 6.

$$\begin{bmatrix} * & * & * & * \\ * & * & * & * \\ * & * & * & * \\ * & * & * & * \end{bmatrix} \qquad \begin{bmatrix} * & * & & \\ * & * & & \\ & & * & \\ & & & * \end{bmatrix}$$

Standard Lagrange M_{ij}^k Matrix (1D - 3rd order)

Modified M_{ij}^k Matrix (1D - 3rd order)

2.1.2. Numerical integration providing super-convergence

The standard finite element method is based on analytical calculation of Eqs (2) and (3) ; some theoretical attempts had shown that better results may be obtained if these integrals are computed using Gauss formula ; all the polynomials of our basis beeing of the same order q, the Gauss formula using q integration points had to be used. This formula integrates rigorously polynomials of order 2 q-1 ; the S^k_{ij} matrix is exact but an integration error remains for M^k_{ij} (the order of the integral beeing 2q).

Some theoretical results have proved that this procedure gives a superconvergence on the function gradient at the Gauss points. Our experience may shown that this superconvergence is also achevied on the function itself.

For instance, for the third order polynomials, the 3 point Gauss formula is used for the choice of the basis (the polynomials are defined to be orthogonal using the non rigorous numerical integration scheme).

2.1.3. Set of implemented elements

The 3D elements are product of 2D xy elements by 1D axial elements :

a) Two-dimensional finite element

LINEAR

- Linear Lagrange 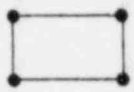 (LL4)

- Linear Lagrange with numerical integration 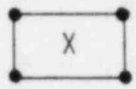 (LL4#)

- 9 nodes standard Lagrange 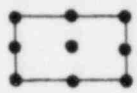 (PL9)

- Orthogonalized Lagrange with numerical integration 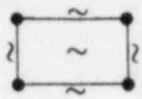 (PL9#)

CUBIC

- 16 nodes standard Lagrange  (CL16)

- Orthogonalized Lagrange with numerical integration  (CL16#)

b) Axial elements

LINEAR

- Linear Lagrange  (LL2)

- Linear Lagrange numerical integration 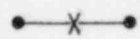 (LL2#)

PARABOLIC

- 3 nodes Lagrange (PL3)

- Orthogonalized Lagrange-Numerical integration (PL3#)

2.2. Representation of the $\alpha_{ig}(t)$

For the numerical calculation the interval [0,T] is divided into S time steps $[t_p, t_{p+1}]$ and :

$$t \in [t_p, t_{p+1}] \quad \alpha_{ig}(t) = \alpha_{ig}^{p}\ \omega_p(t) + \alpha_{ig}^{p+1}\ \omega_{p+1}(t)$$

Where $\omega_p(t)$ and $\omega_{p+1}(t)$ are polynomials defined on $[t_p, t_{p+1}]$. In the CRONOS module, two options are provided :

a) $\omega_p(t) = \ell_p(t) \qquad \omega_{p+1}(t) = \ell_{p+1}(t)$

Where ℓ_p and ℓ_{p+1} are the linear functions with value of 1 (resp. 0) at t_p and 0 (resp. 1) at t_{p+1} : this representation is the standard Crank Nicholson scheme.

b) $\omega_p(t) = 0 \qquad \omega_{p+1}(t) = 1$

This scheme provides the standard Backwards Euler formula.

2.3. Numerical resolution

With the finite element spatial representation of § 2.1. and the time representation of § 2.2., the linear system to be solved may be written as :

$$A_{p+1}\ \vec{\alpha}_{p+1} = -\ A_p\ \vec{\alpha}_p + \vec{R}_p \qquad (4)$$

In this equation, the vector $\vec{\alpha}_p$ denotes the expansion presented in Eq. (1) for the flux at time t_p, $\vec{R}_p$ is a source vector representing the neutron yielded by the precursors.

If the total number of spatial unknowns is N and the number of energy groups is G, the order of the matrix A_p is NxG : the block structure of a matrix A_p is given in Fig. 2.

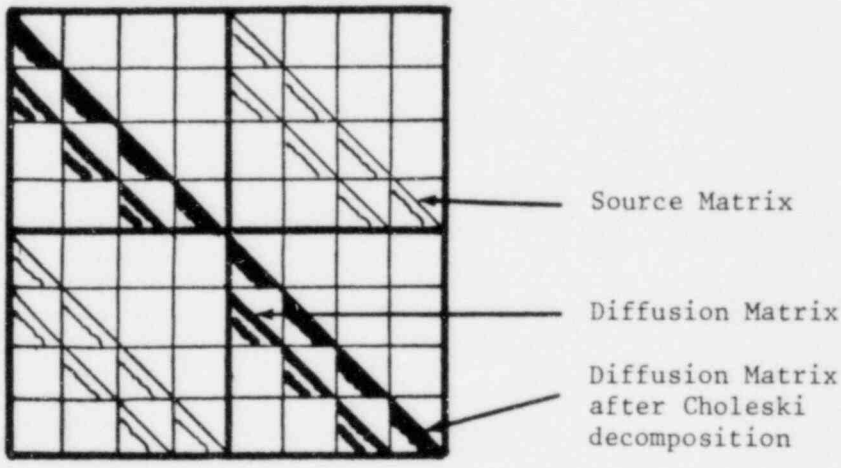

Fig. 2 - 2 groups, 4 planes. Matrix Structure

Each diagonal block is corresponding to a plane of the axial discretization.

The numerical solution is performed using a special Block-SOR method. The diagonal blocks corresponding to each plane are solved and an outer iteration is performed and accelerated by minimization of the L^2 remaining.

The solution of the linear systems involved in the diagonal blocks is computed by the LDU algorithm.

2.4. Cross section representation

CRONOS being devoted to transient calculations for PWR, accurate representation of the thermal hydraulic feedback are mandatory : cross sections depend explicitly on the fuel temperature and moderator density.

In CRONOS, tables of cross sections depending on any number of parameters may be stored as NEPLIB : for usual computations, at least three parameters are accounted for : irradiation, fuel temperature and moderator density. At run time the macroscopic cross sections corresponding to the state of each element are interpolated in these tables and a few less important isotopes are stored as microscopic cross sections (i.e. Boron or Xenon).

The APOLLO module of the NEPTUNE system provides an automatic generator of these NEPLIB libraries : in one APOLLO run a complete NEPLIB is determined depending on any number of parameters.

3. THE THERMAL-HYDRAULIC TRANSIENT MODULE FLICA AND THE COUPLED CALCULATIONS

3.1. The FLICA 3 model

A special version of the subchannel analysis code FLICA 3 had been introduced in CRONOS for steady state and transient calculations.

Starting for the diffusion finite element geometry, vertical channels are defined as sets of cylindrical regions of the reactor ; for example a channel may be one or a few fuel assemblies ; each channel is divided vertically into cells.

The thermal-hydraulic model of FLICA 3 is based on a generalization of the standard HEM model.

A set of balance equations are used for each cell :

- mass balance equation
- vertical momentum balance equation
- projection of the momentum balance equation on the axis orthogonal to the cell interface
- mean energy balance equation.

A second energy equation is added for the treatment of subcooled boiling : it is the liquid energy equation.

A standard finite difference discretization is applied in the z direction and the equations are solved level after level.

The results of the FLICA calculation are maps of fuel temperature and moderator density : they are used as state variables for the diffusion calculation.

3.2. Coupling of neutron kinetics and thermal-hydraulic calculation

The CRONOS system is implemented using a special data processing language named ARIANE (described in § 4.) which allowes the user to define himself the iterative procedure ; for the first calculations a complicated iterative scheme had been used and now the simple procedure described below has proved to provide a sufficient accuracy.

a) The thermal-hydraulic state being given at time t, a neutron kinetics calculation is performed for a time step δt assuming steady cross sections.

b) The thermal-hydraulic calculation is done assuming a linear variation of the power distribution during δt.

For design calculations this procedure gives accurate results : these results will be presented in § 5.2.

4. THE ARIANE DATA PROCESSING SYSTEM

The CRONOS modules are managed by the ARIANE data processing system which has been designed to make easier development, maintenance and operations of scientific programs : ARIANE is divided into three elementary functions :

a) A pre-compiler processses a super-set of FORTRAN allowing virtual memory simulation (LAGD translator) and the OTOMAT library is used at run-time to perform the storage management.

b) A dynamic loader is used at run time to load, one by one, the binary modules which are called and to solve the external references : using the dynamic loader, no linkage-editor step has to be run and no overlay to be built.

This dynamic loader allowes to call any module which is stored in a direct access library.

c) The logical chaining of the computation modules is controlled by the ARIANE language : the user submits to the ARIANE compiler a program describing the logical algorithm to be performed and the compiler output is executed. The ARIANE system had been designed for IBM computers running under OS/VS1 or VS2 ; a Cray version running with COS had been generated and is now operational.

The use of the ARIANE in CRONOS cancels any limit on the size of the problem to be solved and allowes the user to define himself his solving algorithm.

5. NUMERICAL RESULTS

The CRONOS code is currently running on IBM and Cray 1 computers ; a very refined full size calculation had been done on an IBM 3033 computer ; it is presented in § 5.2. A simpler benchmark had been run on Cray 1 in order to measure the efficiency of this computer for LDU calculations.

5.1. Benchmark calculation

The efficiency of our routines had been measured on IBM and Cray 1 computers : a linear system of order 1296 with a half matrix of 48545 stored terms was solved 800 times.

The computing time on IBM was 104.91 s and on Cray 1 it was 9.82 s : in this way the Cray computer is 10.7 times faster than the IBM one.

In this calculation the total number of floating point operations performed is about 157.4×10^6 : the measured power on this benchmark is about 1.50 Mflops for the IBM and 16.03 Mflops for the Cray 1 computer.

These numbers allow to assume that the CRONOS resolution is 10 times faster on the Cray.

5.2. Rod ejection calculation [9]

A 3D rod ejection calculation had been performed for the Fessenheim 2 reactor at beginning of cycle 2 ; all the control rods were inserted at their operationnal position for a power of 1 MWth ; the most efficient totally inserted C control rod is ejected in 0.1 s.

The ejected rod being on a symetry axis of the reactor, one half of the reactor was described : a mesh grid of 17x9 modified parabolic Lagrange elements were used in xy and 20 linear elements axially, the 2D reactor map is given on Fig. 3. The cross sections were represented by a two group NEPLIB.

Fig. 4 presents the axially averaged steady state power distribution. Fig. 5 the mean axial power distribution at time t=0. Fig. 6 is a representation of total power of the reactor during the transient. The maximum power achieved is 4200 MWth at time t=0.32 s. At this time the element peak factor is 6.3 : the plane power distribution corresponding to this peak is given on Fig. 7 (plane z = 295).

The axial variation of the power distribution for the peak time and the peak assembly is plotted on Fig. 8 and the fuel temperature for the same conditions are presented on Fig. 9.

Finally the mean axial power distributions are given on Fig. 10 for various times during the transient.

6. CONCLUSION

The CRONOS module of the NEPTUNE system has proved to provide an efficient computation tool for coupled neutronic and thermal-hydraulic transients. The complete rod ejection calculation has needed 8 CP hours on IBM 3033 ; 72% of the time was used in the iteration part of the computation (5.76 h). The 28% remaining are sequential calculations very difficult to vectorize (2.24 h).

The computing time for the same calculation on Cray may be estimated as :

Iteration	5.76 h on IBM	speed ratio 10.7 → 0.54 h
Remaining	2.24 h on IBM	speed ratio 3.0 → 0.75 h

The total computing time may be about 1.3 h on Cray 1.

In this way CRONOS allowes to perform refined 3D kinetics calculation for standard design work.

REFERENCES

|1| A. KAVENOKY
NEPTUNE - A Modular Scheme for the Calculation of Light Water Reactors.
Meeting ANS, Charleston (USA), Avril 1975

|2| J. BOUCHARD, A. KAVENOKY, P. REUSS
NEPTUNE - Un système modulaire pour le calcul des réacteurs (à eau légère).
European Nuclear Conference, Paris 1975

|3| J. BOUCHARD, A. KAVENOKY, P. REUSS
Development and Assessment of the NEPTUNE Light Water Reactor Calculation System.
European Nuclear Conference, Hamburg, May 6-11, 1979

|4| A. KAVENOKY, J.J. LAUTARD, A. MANUEL, D. ROBEAU
NEPTUNE - Les modules ELECTRE et CRONOS pour les calculs stationnaires et transitoires de distribution de puissance avec prise en compte des contre-réactions thermohydrauliques.
Conférence OCDE - Paris 26-28 Novembre 1979

|5| A. KAVENOXY, J.J. LAUTARD, P. REUSS
Modeling of Feedback Effects : the Development of the CRONOS Code.
Congrès ANS, Atlanta (USA), 3-6 Juin 1979

|6| M.F. FOURQUET, A. KAVENOKY, D. ROBEAU
Le système ARIANE.
G.A.M.N.I. - IIè Congrès International sur les Méthodes Numériques dans les Sciences de l'Ingénieur - PARIS - 1-5 Décembre 1980

|7| A. KAVENOKY, M.F. ROBEAU
Un système d'aide à la programmation scientifique : ARIANE.
Colloque A.F.C.E.T. - PARIS, 8-10 Juin 1982

|8| J.J. LAUTARD
New Finite Element Representation for 3D Reactor Calculations.
ANS/ENS Meeting - MUNICH, 27-29 April 1981

|9| R. LENAIN
Modélisation axiale d'un coeur de réacteur à eau pressurisée pour l'étude d'un accident de réactivité : Ejection d'une barre de contrôle.
Thèse 3ème Cycle, ORSAY, 1982

Ejected control rod

RFLR : radial reflector

E325 : 3.25% enriched assembly

E31P : 3.21% enriched assembly

E31N : 3.21% enriched assembly with black control rod

E26P : 2.6% enriched assembly

E26N : 2.6% enriched assembly with black control rod

Fig. 3 - Radial Map of the Core

					.0	.0	.0	
			.0	.0	.0	.6830	.7365	
		.0	.0	.9304	1.261	1.265	.5531	
	.0	.0	.8541	1.487	1.117	1.021	.9206	
.0	.0	.8541	.8781	.9770	1.018	1.292	1.256	
.0	.9302	1.487	.9769	1.064	.8615	1.066	1.156	
.0	1.261	1.117	1.018	.8614	.5767	.8543	.6751	
.0	.6829	1.265	1.021	1.292	1.066	.8543	.9533	.9178
.0	.7364	.5530	.9205	1.256	1.156	.6751	.9178	.7629
.0	.6829	1.265	1.021	1.292	1.066	.8543	.9533	.9178
.0	.0	1.261	1.117	1.018	.8614	.5767	.8543	.6751
	.0	.9302	1.487	.9769	1.064	.8615	1.066	1.156
	.0	.0	.8541	.8781	.9769	1.018	1.292	1.256
		.0	.0	.8541	1.487	1.117	1.021	.9206
			.0	.0	.9303	1.261	1.265	.5530
				.0	.0	.0	.6830	.7365
					.0	.0	.0	

Fig. 4 - Axially Averaged Steady State Power Distribution

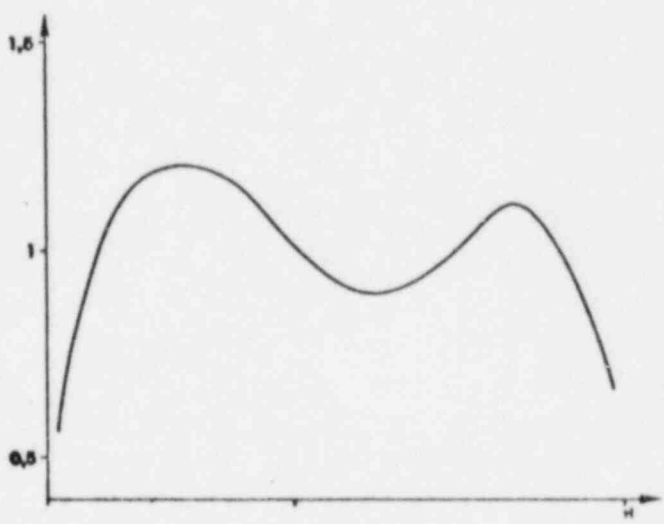

Fig. 5 - Mean Axial Steady State Power Distribution

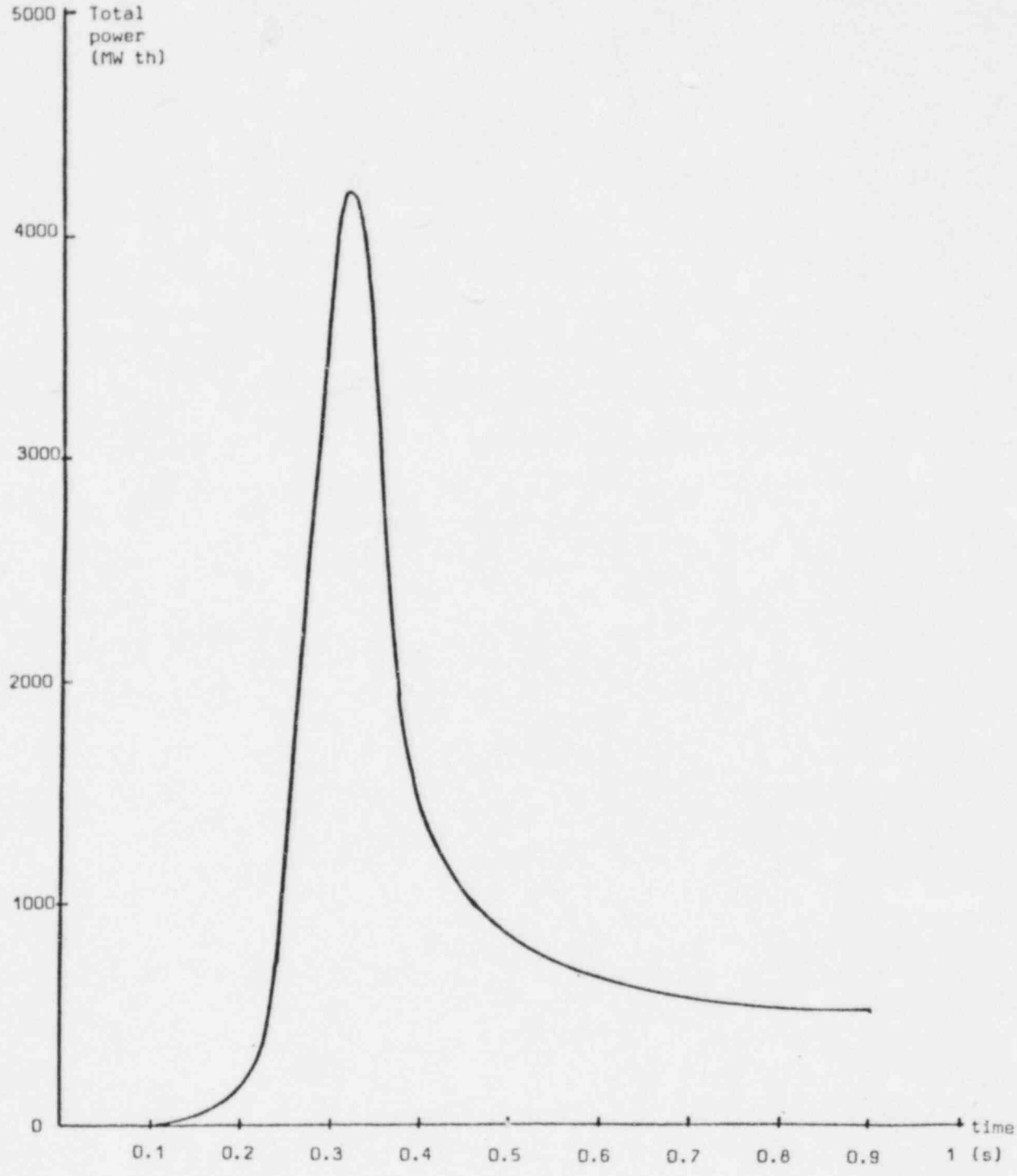

Fig. 6 - Total Power after a Rod Ejection

					.0	.0	.0
			.0	.0	.0	3.829	4.763
		.0	.0	2.734	4.616	6.307	4.747
	.0	.0	1.661	3.748	3.457	3.854	3.901
	.0	.0	.9418	.9927	1.944	2.577	3.725	3.762
	.0	.9326	1.557	1.160	1.698	1.749	2.415	2.653
.0	.0	1.192	1.093	1.089	1.069	.8464	1.326	.8485
.0	.5692	1.100	.9021	1.186	1.014	.8552	1.023	.9775
.0	.5721	.4367	.7361	1.022	.9216	.4353	.7790	.6756
.0	.5367	.3973	.6766	.9416	.8364	.3773	.6739	.5866
.0	.4623	.8284	.6667	.8648	.6974	.5227	.5943	.5716
.0	.0	.7376	.6319	.5719	.4758	.3042	.4171	.2563
	.0	.4898	.7294	.4381	.4735	.3783	.4534	.4752
	.0	.0	.3472	.2475	.3570	.3987	.5174	.5035
		.0	.0	.2799	.5250	.4114	.3858	.3521
			.0	.0	.3321	.4609	.4690	.2042
				.0	.0	.0	.2508	.2703
						.0	.0	.0

Fig. 7 - Radial Power Distribution
at the Power Peak (plane z=295, t=0.32 s)

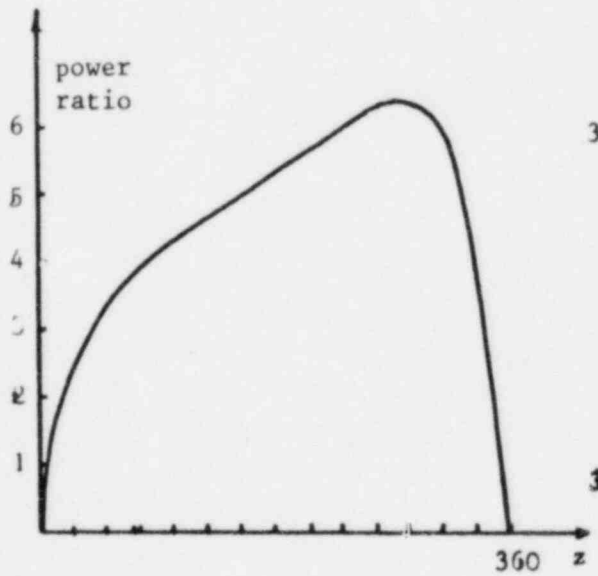

Fig. 8
Axial Power Distribution
for the Hot Assembly
at Time t=0.32 s

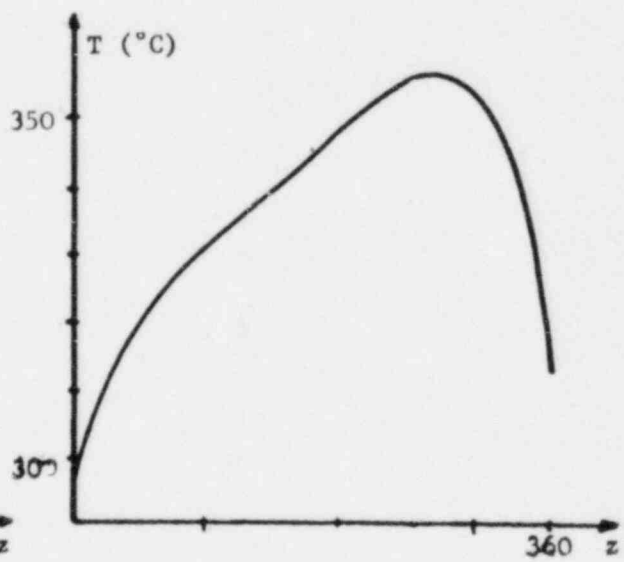

Fig. 9
Axial Fuel Temperature
for the Hot Assembly
at Time t=0.32 s

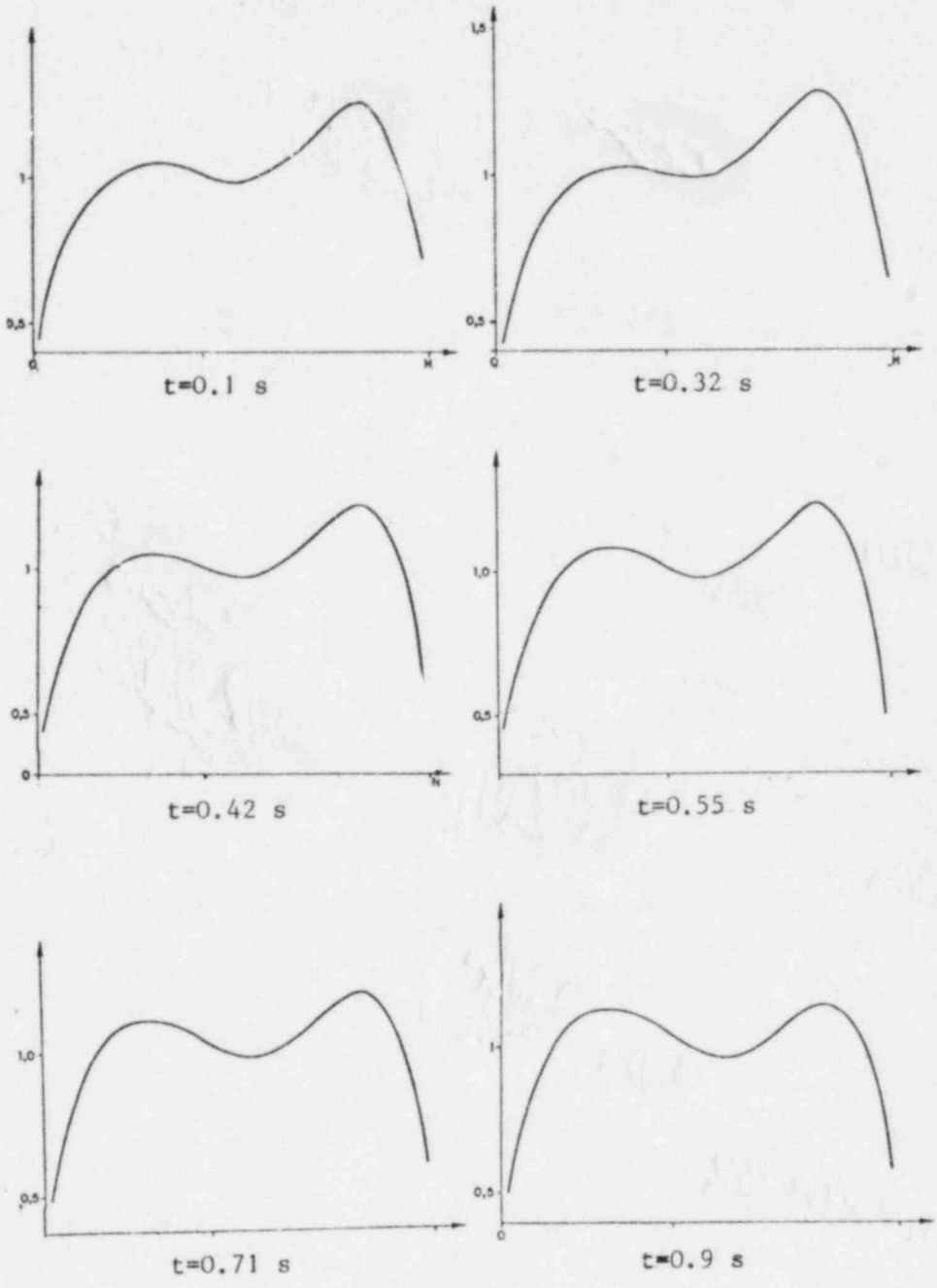

Fig. 10 - Mean Axial Power Distribution
for Various Time

SIMULATION OF SELF-LIMITING POWER TRANSIENTS IN ENRICHED NUCLEAR REACTOR CORES USING A THERMODYNAMIC NON-EQUILIBRIUM AXIAL FLOW MODEL FOR THE WATER COOLANT

A.W. Dalton
Australian Atomic Energy Commission
Lucas Heights Research Laboratories
Lucas Heights, NSW, 2234, Australia

ABSTRACT

The computer code NAIADQ has been developed to investigate the behaviour of water steam-mixtures subjected to induced rapid changes in pressure or enthalpy such as those which can occur in power transients and loss of coolant accidents in water-cooled nuclear reactors.

The effects of thermodynamic non-equilibrium are accommodated in the model by an equation which specifies the rate at which mass is transferred between the two phases. To compensate for the deviation from the equilibrium rate of vapour generation it is assumed that the water can superheat, that the density and enthalpy of the vapour are at saturation and that the two phases mix homogeneously.

At present, the capabilities of the code extend only to the description of reactivity-induced power transients in water-cooled nuclear reactors which utilise enriched ^{235}U fuel in the form of thin metal plate arrays. For this the code is coupled to a point neutron kinetics and reactivity feedback subroutine. Good agreement was obtained between the calculations and published measurements over a wide range of coolant conditions, including those in which steam generation was observed.

OBJECTIVES AND PRINCIPLES OF METHOD USED

This paper describes a model for simulating the course and consequences of non-destructive reactivity accidents in experimental water-moderated nuclear reactor cores. It is basically a coupled neutron kinetics-hydrodynamics-heat transfer model which uses point kinetics and one-dimensional thermal-hydraulics equations.

In this model the core is represented as a single fuel channel operating in the mean core flux with mean core coolant flow. The physical behaviour of the coolant as a function of time and axial location in this channel is modelled by a set of equations for the conservation of the mass, momentum and energy of the water-vapour mixture and the conservation of the mass of the vapour at a number of nodal points along the flow path. It is assumed that the two phases are mixed homogeneously, are at equal pressure, have equal velocities and that the vapour is always in a saturated state, the liquid being allowed to superheat.

Coupled to these equations is a detailed heat transfer model which determines the partitioning of the energy generated in the fuel between the fuel element and the coolant fluid. In the nucleate boiling regime, heat transfer is represented by either a transient conduction, forced convection model. When the water adjacent to the fuel surface reaches saturation, a surface boiling model is used to calculate the heat transfer. The associated increased rate of the latter is described in terms of the rapid propagation of a superheated temperature front into the coolant. It is assumed that vapour is generated in this expanding superheated layer at a non-equilibrium rate.

The energy generation rate in the fuel is calculated from the instantaneous values of the excess core reactivity using a point reactor kinetics model. The excess core reactivity at any instant is derived from the sum of the initial excess reactivity changes produced in the core region up to that instant by the energy input to the system. The reactivity feedback mechanisms included were fuel rod expansion, and changes in the moderator density and neutron temperature in the core region.

The conservation equations are represented as a set of partial differential equations which are solved numerically using a first order, finite difference method, the time-space mesh for the latter being defined by the nodal points and the sequential time steps used in the calculations. Because the method used is stable for all time step sizes, the latter are continuously varied in response to specified criteria for accuracy requirements in the calculations. The solution to these equations, which form the bulk of the calculations, yield the fuel surface temperature and the state properties of the coolant at each nodal position at each time step.

Data produced by these numerical calculations are used in the analytical prediction of the movement of the temperature front in the coolant and also the rate of vapour generation in the superheated region behind it at each node during each time step. The total reactivity feedback was also estimated at the end of each time step from the changes in the channel properties predicted by both the finite difference calculations and the analytical vapour generation model.

DETAILS OF THE CALCULATIONS

The Hydraulics Model

The axial flow of the coolant along the channel is described by four conservation equations, similar to those proposed by Zuber |1|. The quantities involved are vapour mass, mixture mass, mixture momentum and mixture energy. These equations, together with the following assumptions, permit thermodynamic non-equilibrium effects of the coolant to be calculated:

(i) the vapour is always in a saturated state, the liquid is allowed to superheat;

(ii) the two phases are homogeneously mixed;

(iii) the pressures in the two phases are equal; and

(iv) the mass-transfer rate between the two phases is proportional to their area of contact and the deviation of the liquid temperature from its saturation level.

The conservation equations are one-dimensional in the axial direction, z, of the flow path, and variables at each axial position are expressed in terms of the averages of the local mixture properties over the flow area. The equations are

(i) Vapour Mass

$$\frac{\partial(C\rho)}{\partial t} + \frac{1}{a}\frac{\partial(CW)}{\partial z} = \Gamma \quad , \qquad (1)$$

(ii) Mixture Mass

$$\frac{\partial \rho}{\partial t} + \frac{1}{a}\frac{\partial W}{\partial z} = 0 \quad , \tag{2}$$

(iii) Mixture Momentum

$$\frac{1}{a}\frac{\partial W}{\partial t} + \frac{1}{a}\frac{\partial M}{\partial z} + \frac{\partial P}{\partial z} + F + \rho g \sin\theta = 0 \quad , \tag{3}$$

(iv) Mixture Energy

$$a\frac{\partial}{\partial t}\left(\rho H - P + \frac{M}{2a}\right) + \frac{\partial E}{\partial z} - pq + Wg \sin\theta = 0 \quad , \tag{4}$$

The assumptions are incorporated into a set of constitutive equations.
Note: The set notation appearing in this paper is defined in the appendix.

(a) The properties of the vapour phase are a function of pressure alone, that is

$$\rho_V = \rho_V(P), \quad T_V = T_S(P), \text{ etc.} \tag{5}$$

The properties of the liquid phase are a function of both the pressure and the enthalpy in the sub-cooled region and this is assumed to be the case also in the superheated state, hence

$$\rho_L = \rho_L(H_L,P) \text{ and } T_L = T_L(H_L,P), \text{ etc.} \tag{6}$$

Tables containing the properties of water, including an extrapolation into the superheated region, are stored in a sequential data set |2|. In the NAIADQ code the state properties of the two phases are obtained from these tables by interpolation.

(b) The assumption of homogeneous flow allows the properties of the mixture to be expressed as linear combinations of the two phases, for example

$$H = C\,H_{SV} + (1 - C)\,H_L \quad . \tag{7}$$

(c) Because the vapour phase is assumed to be at saturation, all interphase energy transfer mechanisms are implicitly included in the vapour generation equation. The only heat transfer mechanism required by the code is an overall wall to coolant correlation of the form

$$h = f(X, T_{FS}) \quad . \tag{8}$$

(d) The pressure drop resulting from frictional losses for turbulent flow of any liquid in a pipe is given by Fanning's formula

$$F = K_f \rho u^2 \quad , \tag{9}$$

where $K_f = f\,L/De$ for straight pipes; (10)

where f is a function of the Reynolds number ($G\,De/\mu$), various relationships being used to cover a wide range of values |2|.

Heat Transfer

To calculate the power distribution between the fuel and the coolant, a one-dimensional fuel model is used in which

$$q = Q - A\, dT_{FC}/dt \quad , \tag{11}$$

where $$q = h_T(T_{FC} - T_L) = h_F(T_{FC} - T_{FS})$$

$$= h\,(T_{FS} - T_L) \tag{12}$$

and $$h_T = h\, h_F/(h + h_F) \quad . \tag{13}$$

The fuel surface temperatures and the heat transfer to the coolant fluid were estimated from these relationships, in each of the time step cycles of the finite difference calculations.

Non-boiling heat transfer

For zero or low mass flow (Re <2000), heat is assumed to be transferred by thermal conduction. For Re >2000, the flow is assumed to be turbulent and heat to be transferred by forced convection.

The transient thermal conduction model is based on slab geometry and an exponentially rising heat flux;

$$h = \kappa^2\, B\, S/(B\, S/\tanh(B\, S) - 1) \quad , \tag{14}$$

where $$B = (\rho\, c/\kappa\, \tau_o)^{1/2} \quad . \tag{15}$$

For turbulent flow, a number of forced convective surface heat transfer correlations were used, all having the form

$$h = K(\kappa/De)\, Re^n\, Pr^m \quad , \tag{16}$$

where the value of the constant K and the indices n and m depend on the option used |3|.

Boiling heat transfer

When the fuel surface temperature exceeds the saturation temperature of the coolant, the surface heat transfer correlation of Forster and Zuber |4| is used:

$$h_{NB} = 0.0015\, (\kappa/R)\, Re^{0.62}\, Pr^{0.33} \quad , \tag{17}$$

where Re and Pr are the Reynolds and Prandtl numbers for the 'flow system' associated with the bubble agitation in the superheated layer at the fuel coolant interface. A correlation taken from Redfield |5| was used to estimate the heat flux at which a departure from nucleate boiling occurred.

Selection of heat transfer correlation

Selection of the heat transfer correlation to be used in the equations at a given nodal point at any given time is based on the following:

(1) If the fuel surface temperature is less than the saturation temperature of the water, a non-boiling correlation is automatically used in the calculations. If Re >2000, the code automatically selects the forced convective option giving the largest value for h.

(2) When the fuel surface temperature calculated on the basis of the non-boiling option used in (1) exceeds the saturation temperature of the water, surface heat fluxes are calculated for both the non-boiling and boiling boundary conditions. If the heat flux for nucleate boiling is the greater, then it is used in the calculation; if it is smaller, then the non-boiling value of h is used. The temperature at which the switch to nucleate boiling occurs is referred to as the trigger temperature for vapour generation.

Vapour Generation Model

Propagation of the temperature front

When the fuel surface temperature exceeds the saturation temperature of the water, it is assumed that a temperature front is propagated into the water, normal to the fuel surface, coincident with the large increase in the heat flux associated with the switch from non-boiling to boiling heat transfer |6|. From the time t_1 at which this occurs, the layer of water behind this temperature front is assumed to absorb the total surface heat flux and that its temperature, $T_\chi(t)$, is assumed equal to that of the fuel surface. The distance advanced by the temperature front, $\chi(t)$, measured from the fuel surface, at any later time t, is given by

$$\frac{\chi(t)}{S} = \frac{\rho_L(t)\, c_L(t) \cdot \{T_L(t) - T_L(t_1)\}}{\rho_\chi(t)\, c_\chi(t) \cdot \{T_\chi(t) - T_L(t_1)\}} \quad . \tag{18}$$

The fuel surface temperature and bulk coolant properties used in this equation are obtained during each time step cycle of the thermal-hydraulics calculations. The specific heat c_χ and the density ρ_χ of the superheated water are obtained from standard functions in the code |7|.

Vapour generation

When the temperature of the superheated water reaches the trigger level, the bubbles which form at the surface of the fuel begin to grow, become detached, then rapidly increase in size. The rate at which vapour is generated is assumed to be given by the formula |8|

$$\Gamma_\chi = \lambda_N\, \alpha_\chi^{2/3}(1 - \alpha_\chi)(T_S R_U)^{1/2}\, (T_\chi - T_S)/T_S \quad . \tag{19}$$

To produce vapour generation when the trigger temperature is exceeded, a 'seeding' value, for α, of 1×10^{-4}, is used in the calculations.

Reactor Kinetics

The time dependent behaviour of the reactor power is determined by using the KINET subroutine |9| available within the NAIADQ code to solve the reactor kinetic equations:

$$\frac{d\phi(t)}{dt} = \left[k(t)(1 - \beta) - 1\right] \frac{\phi(t)}{\ell} + \sum \lambda_i C_i(t) \quad , \tag{20}$$

$$\frac{dC_i}{dt} = k(t)\beta_i \frac{\phi(t)}{\ell} - \lambda_i C_i \quad . \tag{21}$$

The delayed-neutron data used in these equations |10|, which include a condensed representation of the D2O photo-neutron data of Bernstein |11|, are also available within NAIADQ.

The neutron multiplication factor k(t), is coupled to the temperature distribution in the fuel channel via the heat transfer correlation equation and is given by

$$k(t) = k_0 + \sum_0^t \Delta k(t) \quad . \tag{22}$$

A value for Δk is calculated at each nodal point along the flow path in each successive time step cycle. The nodal contributions are spatially weighted and summed to yield the total value of Δk in a given time step. In the non-boiling regime, the effects include fuel plate expansion, moderator expansion and neutron temperature changes in the core region,

$$\Delta k(t) = B_1 \Delta T_{FS} + B_2 \Delta T_L + B_3 \Delta \rho_L / \rho_0 \quad ; \tag{23}$$

in the boiling region, the feedback is augmented by the decrease in the density of the expanding superheated layer and the generation of steam voids.

$$\Delta k(t) = B_1 \Delta T_{FS} + B_2 \Delta T_\chi + B_3 \left[\omega\alpha + \frac{\chi}{S} \frac{\Delta \rho_\chi}{\rho_0} + \left(1 - \frac{\chi}{S}\right) \frac{\Delta \rho_L}{\rho_0} \right] . \tag{24}$$

Boundary Conditions

In the present finite difference scheme, two boundary conditions are required, for the equations of mixture mass and momentum, throughout the simulation of a transient and independent of the direction of fluid flow. These may be specified in terms of either the pressure or the flow rate at one end of the flow path. For the equations of mixture energy and vapour mass, boundary conditions are required only when the direction of flow is inward. For these equations, the number of boundary conditions can be 0 (outward flow at both ends), 2 (inward flow at one end, outward at other end) or 4 (inward flow at both ends).

During a transient, the number of boundary conditions required can vary if changes occur in the flow direction of the coolant at the ends of the flow path. When flow reversal occurs, the code automatically adjusts the number of boundary conditions required.

Time Step Control

The magnitudes of the time steps used in the NAIADQ calculations are selected on the basis of the maximum changes, in either P or H over all nodes, that the user considers to be acceptable. The overall maximum and minimum time step size and the maximum increase to be allowed in successive time step cycles must also be specified.

COMPARISON WITH EXPERIMENT

Experimental Principles

The capabilities of the model have been checked against a series of experimental

power transients on the SPERT II reactor |12|. In these tests, the reactor core was subjected to very large and rapid power changes by the injection of a range of excess core reactivities. The low heat capacity and the high thermal conductivity of the thin, metal fuel plates ensured that the changes in the fuel surface temperatures were also large and in phase with the power changes. The range of initiating conditions used in the tests ensured that the coolant was subjected to transient heat transfer conditions covering both the non-boiling and the boiling regimes. The excess core reactivity, which was measured continuously throughout the transients, provided a sensitive indication of the rapid physical changes which occurred in the water coolant.

Experimental Details

The SPERT II fuel plate consisted of a fuel alloy section, 62 mm x 0.51 mm x 610 mm, enclosed by cladding, 69 mm x 0.51 mm x 640 mm. These plates were assembled in parallel arrays, separated by 24 mm, in square sectioned fuel boxes with 760 mm sides. The number of fuel plates per box was 18 and the number of fuel boxes in the core was 68, this being denoted in SPERT nomenclature by B18/68. The core structure was immersed in heavy water contained in a 3m o.d. reactor vessel.

The close packing of the fuel in this core caused it to be very undermoderated, such that the maximum flux was at the boundary of the core, the ratio of the maximum to mean core flux being 2.5:1. To provide an indication of the fuel surface temperatures reached in the region of the maximum flux, thermocouples were located on fuel plates at the core boundary close to the axial mid-plane.

Power transients were initiated by the rapid ejection, of a centrally located control rod, from the core to bring the reactor into the required supercritical state. In all the transients the initial reactor power was low enough so that the control rod movement was completed before a significant amount of energy was released in the core. During the transients, both the power and the fuel surface temperatures were measured continuously.

The core of 68 fuel channels was represented axially by a single flow path operating in the mean flux with mean coolant flow rate. The geometrical properties of this channel were represented one-dimensionally at 11 axial points along its length, the fuelled section being defined by seven equally spaced (0.087 m) nodes. The geometrical and physical properties of the materials needed for the calculations were taken from reference 12. The boundary conditions for pressure were specified as constant at both ends of the flow path throughout all transients. Constant values of enthalpy and quality were specified initially at the inlet end.

Experimental Results

In this paper the numbering system of reference 12 is used to identify the transients. The test conditions are specified in Table 1 and a comparison of the calculated and measured values of some parameters at peak power is given. The observed changes in the magnitudes of these parameters reflect the increasing contributions arising from surface boiling heat transfer effects, which are more efficient than non-boiling mechanisms, in terms of reactivity feedback per unit energy released in the fuel.

The measured time dependence of the reactivity compensation after peak power was used to determine the rate of vapour void formation in all the transients. Table 2 lists the data relevant to the calculated vapour generation for all the transients in which the trigger temperature was exceeded. The wide variation in the generation rates is reflected in the contribution to the reactivity compensation arising from the vapour voids which are formed in the coolant. For the

TABLE 1

COMPARISON OF EXPERIMENTAL AND CALCULATED DATA

Run No.	Pressure (MPa)	Mass Flow (kg s^{-1})	Inverse Period (s^{-1})	Initial Temp. (K)	Core Power (MW)			$\varepsilon_{tm}/\tau_0\ \phi_{max}$		
					Expt	Calc.	Ratio	Expt	Calc.	Ratio
8	0.110	0	2.17	295	16	17	0.95	2.32	2.13	1.09
9	0.110	0	4.40	295	42	39	1.08	2.09	2.40	0.87
10	0.110	0	6.30	295	106	108	0.98	1.51	1.62	0.93
11	0.110	0	9.07	295	189	195	0.97	1.39	1.41	0.99
12	0.110	0	11.4	295	237	270	0.88	1.45	1.39	1.04
13	0.110	0	13.5	295	287	351	0.82	1.47	1.35	1.08
14	2.58	0	3.5	293	38	37	1.03	2.01	2.00	1.01
15	2.58	0	5.5	295	79	88	0.89	2.08	1.96	1.06
16	2.58	0	4.0	295	47	48	0.98	2.01	2.00	1.00
17	2.58	0	6.4	294	97	126	0.77	1.96	1.91	1.03
18	2.58	0	10.3	295	241	318	0.76	1.71	1.73	1.01
20	1.48	0	10.0	295	-	298	-	-	1.67	-
21	1.48	0.37	11.0	295	266	261	1.02	1.64	1.60	1.03
23	1.48	1.2	11.0	295	265	268	0.99	1.72	1.61	1.07
25	1.48	3.0	11.0	297	257	273	0.94	1.81	1.61	1.12
26	1.48	6.0	10.0	300	263	273	0.96	1.15	1.64	1.06
39	1.48	12.0	9.5	313	248	239	1.04	2.09	2.06	1.01

TABLE 2

MAXIMUM VALUES OF VAPOUR GENERATION PROPERTIES DURING THE TRANSIENTS

Run No.	Generation Rate (kg m^{-3} s^{-1})	Void Fraction	Reactivity Compensation ($)	
			Voidage	Total
10	1.5	0.34	2.57	3.15
11	2.4	0.52	3.93	5.42
12	3.3	0.65	4.91	5.81
13	4.2	0.71	5.37	6.64
18	0.036	0.0004	0.003	2.42
20	0.100	0.0024	0.0018	2.36
21	0.094	0.0022	0.0017	2.42
23	0.079	0.0019	0.0014	2.41
25	0.068	0.0017	0.0013	2.40

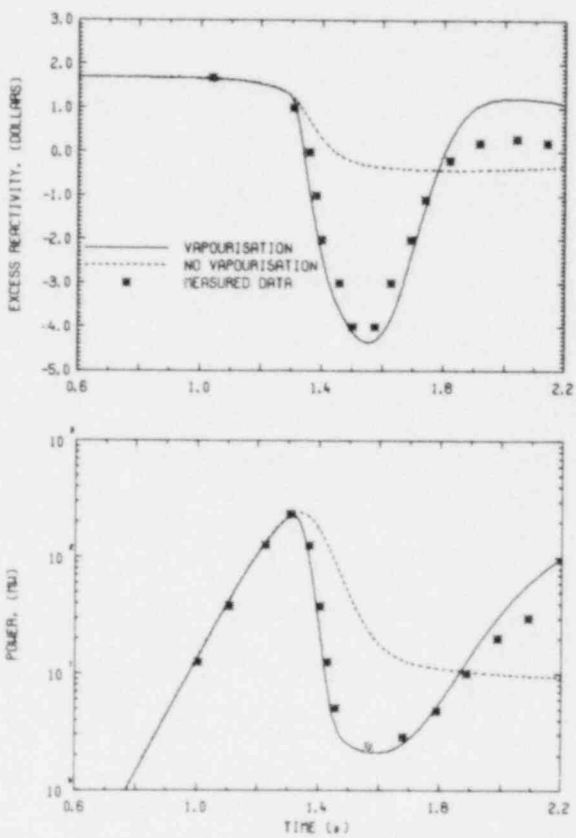

FIGURE 1: EFFECTS OF VAPORISATION

no-flow tests at atmospheric pressure (Runs 10-13), the voidage formation accounts for the major part of the total measured reactivity feedback. This is illustrated in Figure 1, where the calculated power and reactivity changes, both with and without vapourisation are compared with the measured data for run 12. The main effect of an initial forced coolant flow rate on the reactor power (runs 23, 25, 26 and 39) is seen in its behaviour after the first power peak in Figure 2 (where the lines correspond to the calculated, and the points to the measured data). Both the post-power level and the damping of the power oscillations are observed to be greater, the larger the initial rate of coolant flow. The calculations reproduced these features quite well.

The calculated vapour generation rates and void ratios at axial nodes 3 to 9 are shown in Figures 3 and 4 for run 12. The whole core vapour generation rates in the supercritical transients (runs 10 - 13) correspond to a range of values from 90 to 250 litres per second, the same order of magnitude as the rates fitted by Connolly |6| to the SPERT I transients. For the remainder of the transients listed in Table 1 in which vapour generation occurred the voidage accounted for only a very small fraction of the total reactivity compensation (Table 2), vapour generation being suppressed in these tests by the higher pressures and turbulent flow. The difference between the total reactivity compensation and that arising from vapour voids is accounted for by the reactivity feedback from changes in the density of the water, the temperature of the fuel and the neutron temperature in the core region of the reactor.

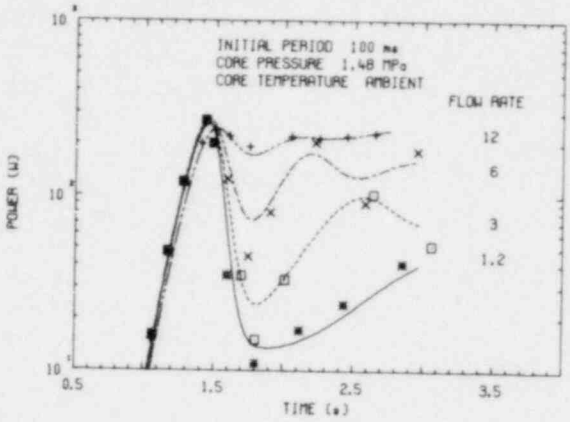

FIGURE 2: POWER CHANGES IN FLOW TESTS

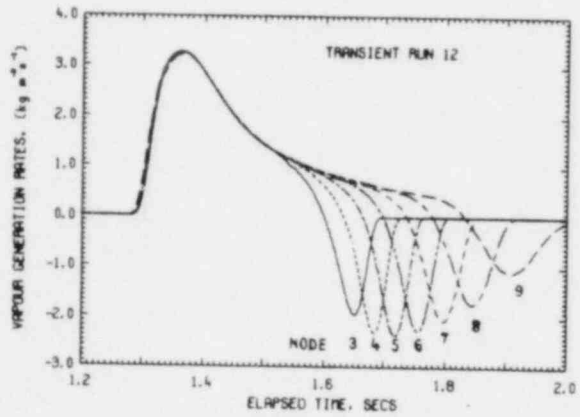

FIG. 3: PREDICTED VAPORISATION RATES

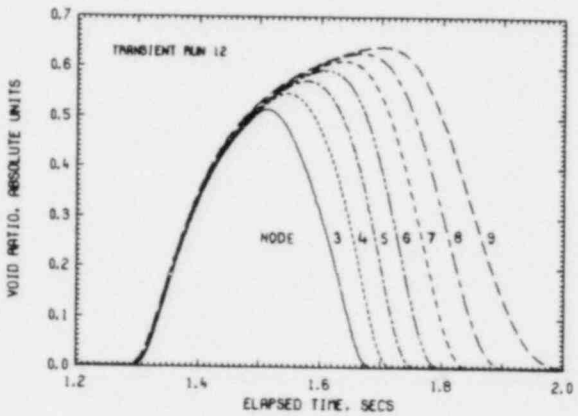

FIG. 4: PREDICTED VOID RATES

The calculations also produced a detailed description of the time dependence of the coolant flow rates induced in all the transients. With zero initial flow and large vapour generation rates the flow behaviour is quite complicated, Figure 5 (run 12). A significant flow out of both ends of the channel is

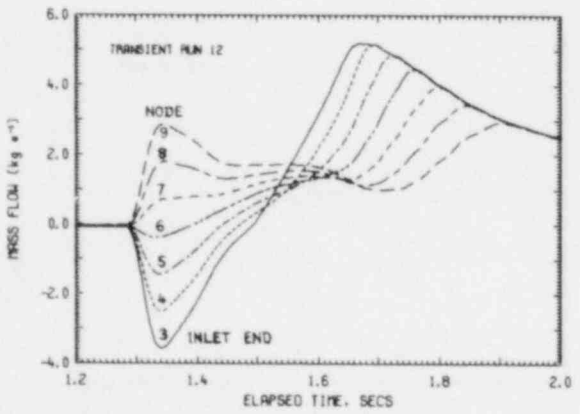

FIG. 5: PREDICTED MASS FLOW RATES

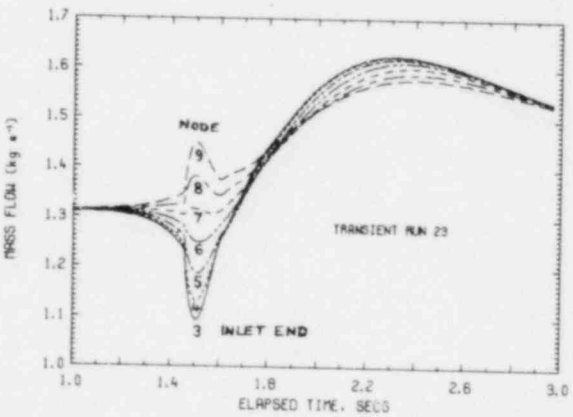

FIG. 6: PREDICTED MASS FLOW RATES

produced initially by the generation of vapour within it. The subsequent rapid condensation of the vapour produces a flow reversal at the inlet end and an ultimate convective flow rate up the channel. The dependence of the induced flow rate on the changing void ratios at different axial positions along the channel can be seen by comparing Figures 4 and 5. For the forced flow tests similar but much smaller effects were produced in flow behaviour, the changes being superimposed on the initial flow rate as illustrated in Figure 6 (run 23).

The calculated mean channel heat fluxes (Table 3) indicated that the critical heat flux is exceeded only in the maximum rated channels of the most rapid transient (Run 13). Fuel burnout was observed in the peripheral channels in the corresponding experimental test.

TABLE 3

CALCULATED FUEL SURFACE TEMPERATURES AND HEAT FLUXES

Run No.	T_S (K)	T_{tr} (K)	T_{max} (K)	$T_{max} - T_{tr}$ (K)	$T_{max} - T_S$ (K)	Heat Flux (MW m^{-2})	
						Max.	Critical
8	375.5	-	367.2	-	-	0.07	4.6
9	"	-	387.3	-	-	0.21	3.8
10	"	394.0	403.0	9.0	27.5	1.0	3.3
11	"	"	411.3	17.3	35.8	1.6	3.7
12	"	"	416.7	22.7	40.1	2.1	4.2
13	"	"	421.5	27.5	45.9	2.7	4.8
14	499.2	-	377.5	-	-	0.21	13.1
15	"	-	448.3	-	-	0.45	9.8
16	"	-	404.6	-	-	0.26	12.2
17	"	-	484.2	-	-	0.63	7.7
18	"	513.5	522.3	8.8	23.1	2.7	11.1
20	470.8	486.0	496.5	10.5	25.7	2.5	7.1
21	"	484.4	495.0	10.4	24.2	2.1	7.3
23	"	486.3	494.5	8.2	23.7	2.2	8.2
25	"	488.6	494.0	5.4	23.2	2.1	10.8
26	"	-	473.0	-	2.2	1.9	13.0
39	"	-	424.9	-	-	1.9	16.0

Discussion

The uncertainty in the reactor power calibration of the SPERT cores has been quoted as ± 10 to 15 per cent |13| and the estimated accuracy of the calculated reactivity feedback coefficients is better than ± 20 per cent |6|. On this basis, the agreement between the calculated and measured parameters indicate that both the feedback coefficients and the heat transfer correlations used in the analyses were essentially correct.

The agreement obtained for the flow transients, in which the observed effects were primarily a consequence of the rate of energy removal from the core region by the forced coolant flow and the heat transfer in nucleate boiling, provides

good support for both the thermal-hydraulics calculation and the use of the steady state heat transfer correlations for turbulent flow during rapid transient conditions. The agreement obtained for the no-flow transients, in which large peak values of reactivity compensation were observed, provides support for the use of the non-equilibrium vapour generation model for transients in which rapid changes in heat transfer rates occur during subcooled nucleate boiling.

A more complete comparison could have been made if the coolant temperatures, pressures and mass flow rates in the core had been included in the published data, that calculated by the code being much more extensive. In particular, the heat transfer correlations and the vapour generation model used in the present analysis could have been checked more directly. A confirmation of the induced effects observed in the calculated flow rates of the coolant in all the transients would have provided good support for the thermal hydraulics calculations.

CONCLUSIONS

The model used in the present analysis gave good agreement with the published experimental data for both the boiling and the non-boiling transients over a wide range of flow conditions including zero flow. This analysis indicated that, even for power transients in which the fuel surface temperature rose rapidly through the saturation temperature, the ensuing reactivity compensation produced by nucleate boiling at the fuel surface was sufficient to ensure that such transients can be self-limiting before the formation of large vapour voids in the bulk coolant flow. For the zero flow transients, in which large vapour voids were produced, the calculations showed that their occurrence coincided with the return of the reactor power to a very low level following the rapid rise to peak value, and hence were not instrumental in the termination of the excursion.

That this agreement with the measured data was obtained using a vapour generation and hydraulics model similar to that successfully applied in depressurisation codes used to simulate loss of coolant accidents |3,8,14| adds to the generality and validity of this method of analysis. On the basis of the agreement obtained in these simulations, the NAIADQ code appears to be a promising method for investigating thermodynamic non-equilibrium in two-phase flow.

ACKNOWLEDGEMENTS

The author wishes to thank W.J. Turner and J.W. Connolly for their assistance in the development of the code, G.D. Trimble and W.J. Turner for the provision of the hydraulics code on which the present code is based, and B.E. Clancy for his assistance with the utilisation of the point reactor kinetics code.

REFERENCES

|1| Zuber, N. (1967). Symposium on Two Phase Flow, Eindhoven, Sept. 4-9. EUR 4288e, pp. 1091-1109.

|2| Trimble, G.D. and Turner, W.J. (1976). NAIAD - A Computer Program for Calculation of the Steady State and Transient Behaviour (LOCA) of Compressible Two-phase Coolant in Networks. AAEC/E378.

|3| Dalton, A.W. (1982). NAIADQ - A Thermodynamic Non-equilibrium Computer Code for the Calculation of the Transient Behaviour of Two-phase Flow. AAEC/E report (in preparation).

|4| Forster, H.K. and Zuber, N. (1955). Dynamics of Vapour Bubbles and Boiling Heat Transfer. A.I.Ch.E.J., 1, pp. 531-535.

|5| Redfield, J.A. (1965). CHIC-KIN - A Fortran Program for Intermediate and Fast Transients in a Water Moderated Reactor. WAPD-TM-479.

|6| Connolly, J.W. (1977). A Simple Method of Transient Heat Transfer and Its Application to Power Excursions in Water Moderated Nuclear Reactors. Second Australasian Conference on Heat and Mass Transfer. University of Sydney, Feb. 1977, pp. 485-492.

|7| Houghtaling, J.E., Sala, A. and Spano, A.H. (1964). Transient Temperature Distributions in the SPERT I D-12/25 Fuel Plates During Short-period Power Excursions. IDO-16884.

|8| Rivard, W.C. and Torrey, M.D. (1975). Numerical Calculations of Flashing from Long Pipes Using a Two-Field Model. LA-6104-MS.

|9| Clancy, B.E (1982). ZAPP - A Computer Program for the Simulation of Power Reactor Transients. AAEC/E report (to be published).

|10| Harries, J.R. (1978). Inverse Kinetics Reactivity Measurements on the Materials Testing Reactor, HIFAR. AAEC/E456.

|11| Bernstein, S., Preston, W.M., Wolfe, G. and Slattery, R.E. (1947). Yield of Photo-Neutrons from ^{235}U Fission Products in Heavy Water. Phys. Rev. 11, p. 573-582.

|12| Johnson, R.L. Lawson, H.A., McClure, J.A. and Norberg, J.A. (1965). An Analysis of the Excursion Behaviour of a Highly Enriched Plate - Type D_2O - Moderated Core in SPERT II. IDO-17109.

|13| Obenchain, C.F. (1969). PARET - A Programme for the Analysis of Reactor Transients. IDO-17282.

|14| Hirt, C.W. and Romero, N.S. (1975). Application of a Drift - Flux Model to Flashing in Straight Pipes. LA-6005-MS.

APPENDIX

NOTATION

SI units are used for all variables.

Description	Symbol
Heat capacity per unit wetted area	A
Flow area of flow path	a
Core reactivity feedback coefficients	
fuel expansion	B_1
neutron temperature	B_2
coolant expansion	B_3
Specific heat	c
Precursor concentrations	C_j
Quality of coolant (non-equilibrium)	C
Equivalent diameter of coolant channel	De
Energy flux of mixture	E
The Fanning friction factor	f
Frictional pressure gradient	F
Acceleration due to gravity	g
Mass velocity	G
Surface heat transfer coefficient of fuel	h
Bulk heat transfer coefficient of fuel	h_F
Enthalpy	H
Multiplication factor for core flux	k
Prompt neutron lifetime	ℓ
Half fuel plate separation	L
Momentum of mixture × flow area	M
Pressure	P
Heated perimeter of fuel	p
Prandtl number	Pr
Heat flux at fuel surface	q
Power generated per unit heated area	Q
Mean bubble radius	R
Universal gas constant	R_u
Reynolds number	Re
Equivalent length of flow path	S
Temperature	T
Real time	t
Velocity	u
Mass flow rate	W
Vector whose components are W, P, H and C	X
Axial distance along flow path	z
Void fraction in coolant	α
Delayed neutron fraction	β
Fission energy release	ξ
Thermal conductivity	κ
Vapour generation rate in coolant	Γ
Relaxation constants of delayed neutrons	λ_j
Constant in vapour generation formula	λ_N
Viscosity	μ
Reactor power	ϕ
Material density	ρ
Angle of elevation	θ
Asymptotic period of power transient	τ_0
Spatial weighting for void reactivity	ω
Thickness of superheat water layer	χ

Subscripts

FC	Fuel centre	tm	Time of peak power
FS	Fuel surface	tr	Trigger
L	Bulk liquid	T	Total
max	Maximum	V	Vapour
NB	Nucleate boiling	X	Superheated region
S	Saturated state	0	Time zero

RASP: An Integrated Reactor Analysis Support Package

by

G. S. Lellouche, L. Agee, W. Eich, J. Naser

Electric Power Research Institute

INTRODUCTION

Over the last eight years EPRI has produced, benchmarked, and validated two major code packages; ARMP and RETRAN. These codes serve the purpose of providing design and analysis capabilities for coupled core physics/thermal hydraulics and for systems response. With the exception of the recommended (default) ARMP LWR sequences, the early development of the various EPRI methodologies did not stress user convenience or consistency between code systems. They allowed very general input capability and did not foresee the need to couple (hence be consistent) with other, seemingly disparate, codes. In this sense the thermal-hydraulic models and their concomitant heat transfer correlations were not uniform from code to code. In the same sense, the output of ARMP, for example, could not be used directly as input to either COBRA 3C-MIT or RETRAN.

During this period of time extensive upgrading of both code packages has continued both in the physics and engineering areas. Two years ago, two major projects were initiated to:

- o produce VIPRE, a 3-D time-dependent thermal-hydraulic code,
- o proceed with RASP, a reactor analysis support package which fully integrated ARMP, RETRAN, and VIPRE using linking codes and the DATATRAN data base manager.

With the initiation of the VIPRE and RASP developments, the incompatibilities were felt more seriously. As a result, modifications in ARMP and RETRAN were initiated to allow both increased user convenience and code-to-code consistency. This paper will discuss the current status of RASP, the envisioned future developments to the package, including a short description of the developmental versions of ARMP, RETRAN, and VIPRE (see Appendix).

Reactor Analysis Support Package (RASP)

The purpose of the RASP activity is to tie together the computer codes developed by EPRI in the area of thermal-hydraulics, neutronics, fuel management and fuel behavior. The results of this effort will produce a verified and validated package, including guidelines that can be used by the utility industry for both reload and safety analysis to:

1. Perform fuel management
2. Design cores within cycle-dependent envelopes
3. Analyze design base accidents

4. Determine protection system setpoints

5. Define limiting conditions of operation

The current EPRI activity associated with the RASP package is: 1) linking the main production codes ARMP, RETRAN and VIPRE together; 2) assuring consistency between the physics and modeling of the various codes, and 3) writing guidelines on the proper use of the entire package. The conceptual view of the linked RASP system is shown in Figure 1. The solid lines denote linkage codes which were developed under RASP. The broken lines denote linkage codes envisioned in the future.

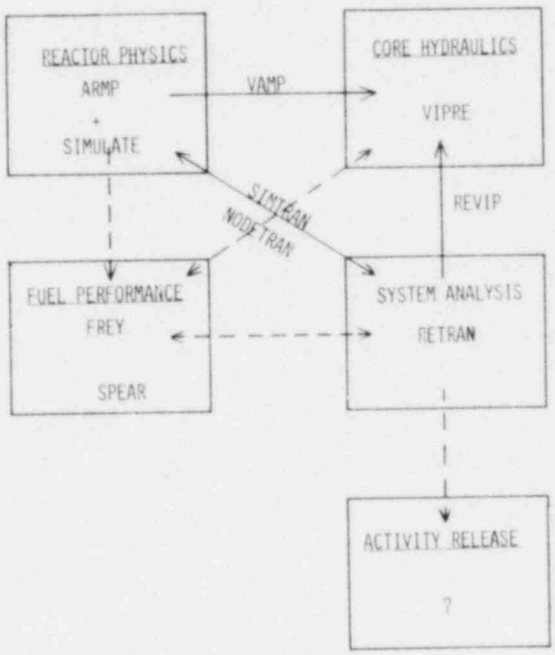

Figure 1. RASP CODES AND LINKAGES

The linkage of the three central codes will have produced a useable product (denoted as RASP-01) which is expected to be pre-released in late 1982. While the utilities are testing and in effect performing a "shakedown" of the basic code package, the fuel performance code FREY will be integrated into the package and updated and advanced versions of ARMP, RETRAN and VIPRE will be incorporated and pre-released in late 1983 as RASP-02.

The goal of the RASP-01 project has been to produce a code package that is adequate to perform the required analyses. The intent has not been to develop a new state-of-the-art package but one that could do the job efficiently and effectively. While other EPRI projects continued to generate state-of-the-art codes which could be used to supplement or benchmark the RASP-01 package, the code package itself has been geared toward economical everyday use by the utilities. The developmental activity associated with each major code package is discussed in the Appendix. The second objective of the RASP project is to generate the documentation required.

GUIDELINE DEVELOPMENT

The guidelines developed for RASP have been broken into five separate areas:

1. plant model building
2. preparation of user model qualification reports
3. analysis of SAR Chapter 15, Operational Transients, with special emphasis on Design Base Accidents
4. reload safety evaluation document
5. setpoint (including uncertainty) analysis

There is insufficient space to discuss all of these guidelines in detail; however, a brief description of each guideline is given below:

1. Plant Model Building Guideline

The purpose of this guideline is to assist the utility engineer in the general use of ARMP, SIMULATE*, RETRAN and VIPRE to model NSSS plants. Because there is considerable difference in what is required between the different code types, each must be discussed separately.

ARMP/SIMULATE Modeling

The use of the ARMP program for PWR fuel management application is well understood and adequately documented in "PWR Core Modeling Procedures for Advanced Recycle Methodology Program." In the midterm it will be upgraded to: 1) describe application for transient analysis, and 2) describe SIMULATE application.

A similar document is being prepared for BWR application. The current expected availability date of the BWR procedures is early 1983.

VIPRE MODELING

The use of the VIPRE code in the context of RASP is currently limited to core analysis. The detailed description of the input is described in the

*Note that at this time we separate SIMULATE from ARMP. With the release of ARMP-02 in 1983, SIMULATE will be fully incorporated into the ARMP system and not be differentiable as such.

VIPRE Computer Code Manual. These input instructions are adequate to describe the use of the code once the geometrical detail of the core is decided upon. The questions addressed in the guidelines for a PWR are: 1) is the core symmetrical; if so, to what degree (i.e., ½ core, ¼ core, ½ core), 2) in what degree of detail to represent the assemblies and pins, and 3) how much axial resolution is required. Only the second and third considerations apply to the BWR plants since BWRs must be represented in full core.

RETRAN MODELING

The general RETRAN modeling guideline will attempt to describe to an experienced RETRAN user how to model a previously unmodeled event. The transient analysis guidelines for RETRAN will be directed to the inexperienced user and attempt to describe existing modeling experience. These guidelines will be based on current experience and upgraded as additional information becomes available.

2. User Model Qualification Guideline

The object of this document is to give guidance in the following areas:

a. A description of how specific utility models are qualified: for example, comparison to plant data, performance of benchmark calculations and comparisons to vendor results are possible approaches.

b. A demonstration of the capabilities and experience on the part of the utility staff that is needed to show qualification to use the models.

c. A suggested process for a reload licensing analysis including a decision process for what analyses are needed, how studies are performed, how and what results are reported and how quality assurance is carried out.

3. Analysis of SAR Chapter 15 Operational Transients and Design Base Events

The general guidelines discussed earlier identify the basic Modeling Methodology. The activity in this area is expected to give a brief indication of what case specific parameters, code options, etc., should be used for 1) Best Estimate and 2) Conservative Analysis. The justification for this will be based on The Code Specific Qualification Reports; in most cases, the RETRAN Qualification Report (Volume 4, NP-1850, for RETRAN-02).

4. Preparation of Reload Safety Evaluation Documentation

For each reload the utility must reconsider all of the FSAR (Chapter 15) events. This reconsideration can range from a complete reanalysis of the FSAR events to merely checking the updated physics parameters to ensure that they remain within bounds set by prior analyses. In practice, reanalyzing all of the FSAR events for a reload is quite rare; however, it is common to reanalyze a few of the more limiting transients, particularly for the first few reload cycles. For the later reload cycles, a Reload Safety

Evaluation (RSE) consisting of little more than a comparison of cycle-specific data to that used in the analyses of record to demonstrate their continued applicability is possible if parameter operating ranges and starting points do not change.

5. Setpoint Analysis

EPRI expects to develop setpoint methodology in 1983, and currently has a summary report on setpoint analysis.

LINKING CODES

The linking codes currently under development are:

- o REVIP
- o VAMP
- o NODETRAN/SIMTRAN

The purpose of REVIP and VAMP is to produce a more detailed thermal-hydraulic analysis of the core using VIPRE than is allowed by either the ARMP nodal codes or RETRAN (for transients). There is nothing especially novel in linking codes. However, the links between ARMP and RETRAN present a somewhat more interesting problem. Basically, the question is how to reduce the three-dimensional information in the nodal codes to the one-dimensional form in RETRAN. The collapsing problem has been with us for many years and there are a number of potential solutions. Remembering that we must also collapse the feedback equations (power, temperatures, flow), we have chosen to use flux-adjoint collapsing for cross sections, diffusion coefficients, inverse velocities, and reactivity feedback, and volume averaging for physical parameters (power).

DATATRAN is a data base management and executive program that acts as a host for scientific and engineering programs. It evolved from a development tool to an efficient software production system in the period from 1966-1977 and is now being modified by EPRI to support data and program exchange between CDC and IBM equipment. Experience has shown it to be a contributing factor to the implementation of standardized input, standardized documentation, and reduction of software duplication.

DATATRAN is an extension to FORTRAN that supplements input/output functions and program control functions. It is a language extension that allows full FORTRAN capability. Concepts employed are not really new, but are simply packaged conveniently. The two central concepts are:

1. Communication to a data pool with named collections of data called data sets, and
2. Program units called modules that communicate only with each other through the data pool by way of the named data sets. Modules vary in length between 500-8000 source statements (2000 statement average) and normally represent a fairly significant computation.

Note that there is no direct user-module or module-module communication. DATATRAN performs no computations itself - modules do the computing.

These two concepts are packaged so that they can be utilized at the input level vis-a-vis FORTRAN.

APPENDIX

ARMP

As indicated by the words on which the acronym is based, the original intent of the various research projects whose output comes under the generic heading of ARMP (Advanced Recycle Methodology Program) was the generation of a unified system for LWR core simulation that would encompass plutonium recycle as well as uranium assembly designs. The general unavailability of reprocessing in this country has practically foreclosed the plutonium recycle option. Nevertheless, application of the ARMP system to uranium-loaded LWR cores has been widespread among domestic utilities. Several DOE laboratories also utilize ARMP.

At the present time the nodal and concomitant thermal-hydraulic codes for each LWR scheme and distinct versions tailored to pressurized and boiling water reactor systems respectively are: NODE-P and -B, THERM-P and -B. The PWR lattice and the BWR multi-bundle lattice codes were PDQ/HARMONY (P/H). The pin-cell code of the PWR sequence was EPRI-CELL: a unique linking of the GAM, THERMOS and CINDER codes. The single-bundle lattice code of the BWR sequence was initially the multigroup collision probability code, CPM. Many utilities have opted for the faster and easier-to-use CASMO code and for the first version of the SIMULATE code in place of EPRI-NODE-B. EPRI-CELL and its ENDF/B-II library with a V. I U-238 and selected V. III isotopes had been benchmarked against assorted isotopics and critical experiments. The CPM V. III library, particularly the U-238, has been normalized against hot full power EPRI-CELL runs on consistent infinite lattice bases.

In summary of the present status, the ARMP system is more well defined and mature in its PWR side. A draft PWR Procedures Manual has been available for over two years which provides step-by-step instructions for the preparation both of 3-D nodal simulations and also quarter core (XY) P/H depletion runs. A draft P/H Manual, which provides substantial clarification of the Bettis documents, has also been distributed. One deficiency, however, (soon to be remedied by the PSEUDAX enhancement to P/H) has been the unavailability of a 2-D fine mesh code with thermal-hydraulic feedback such as the Westinghouse TURTLE code. In most other aspects, however, the ARMP system is tantamount to those of the PWR vendors and, perhaps, superior in lumped absorber treatment.

The development of the BWR side has lagged somewhat in that the nodal code requirements are substantially greater than those for PWRs. With the existence of SIMULATE-1 and particularly the imminent availability of SIMULATE-2, with extensions of existing codes to allow calculations at cold conditions as well as margin calculations, and with improved thermal hydraulics integreated into the nodal solution, the upgrading of the BWR sequence to parity with that for PWRs can be seriously expected.

In view of projects, the release of whose accomplishments is imminent, and in view of other development contractually in place, it is more useful in a review paper of this type to describe the ARMP core analysis methodology in terms of its 1983 status.

Figure 2 schematically summarizes the interrelationship of the major PWR codes; in Fig. 2 and 3, processing codes which link the output of one physics module to the input of another are indicated by asterisks.

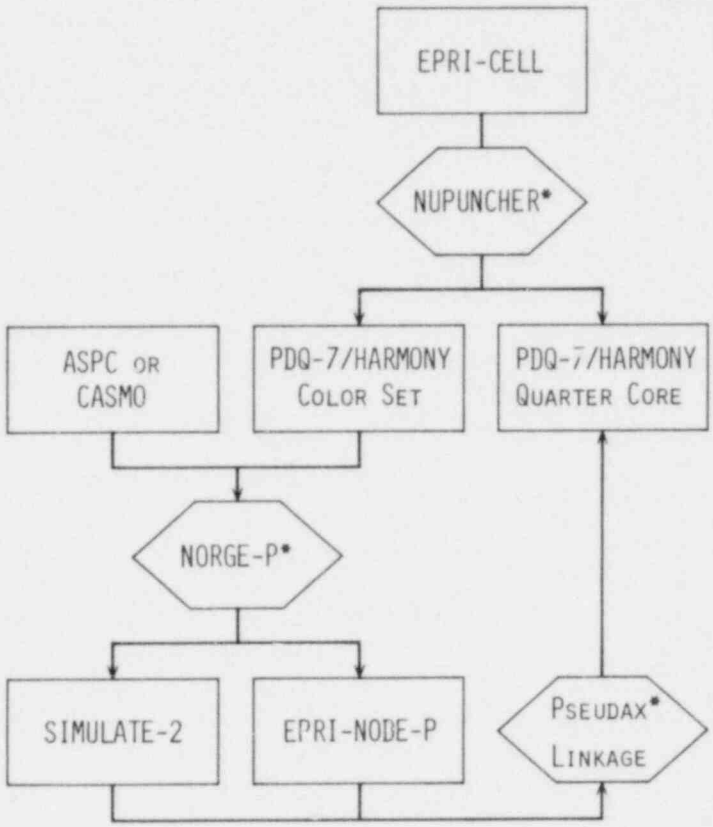

FIGURE 2.
FLOW OF DATA FOR EPRI'S PWR REACTOR PHYSICS CALCULATIONS

Virtually every code module shown in Fig. 2 will be new or will have been substantially revised from initial ARMP releases. EPRI-CELL has already been the object of programming, physics and engineering modifications. The Bettis-derived machine language environmental routines have been replaced by FORTRAN statements. The installation of Pershagen's slicing technique in the THERMOS portion, in place of the original ray tracing, has produced up to 70% run time reduction by virtue of minimal spatial mesh requirements. Even cases involving gadolinia-loaded fuel benefit both in accuracy and reduced mesh from this change. Auxiliary linkages not shown in Fig. 2 automate to a high degree the preparation of P-H input for both gadolinia-loaded fuel and discrete boron lumped absorbers. The input requirements of restart problems will be greatly simplified. The ratio of the number of branch calculations (which utilize restart) to ordinary depletion runs increases somewhat with PSEUDAX and significantly with reload licensing

requirements. A predictor-corrector depletion capability will reduce depletion run times even further.

The PDQ-7/HARMONY (P/H) code has undergone such extensive modifications under EPRI projects that, to satisfy the strictures of Naval Reactors, EPRI has become a secondary distributor of the code. Some of the more significant changes are a predictor-corrector depletion capability (PCDC), a standardized environmental library, a HARMONY table file and important modifications for the PSEUDAX capability. The PCDC should allow savings in total run time for depletion problems of 30 to 50%. The same environmental library used in RETRAN is now being installed in the various versions of P/H. The HARMONY file should simplify input (thus improving QA) as well as reduce run time since, currently, the input is processed at every timestep.

In a PWR, assembly averaged power either axially averaged or edited at a particular axial location, can show significant shifts between hot zero power (HZP) and hot full power (HFP) conditions. Cores as disparate in age as Ginna Core 1 and Comanche Peak 1 show about 15% net power shifts (defined as the sum of the reduction of the peak assembly plus the increase in the lowest power assembly in going from HZP to HFP). The original version of P/H as incorporated in the ARMP system did not account for moderator density and resonance temperature feedbacks which are responsible for these net power shifts. To remedy this and provide other capabilities, the PSEUDAX methodology has been developed, involving changes to EPRI-CELL NUPUNCHER, both nodal codes and, principally, to P/H. The changes to the nodal codes, EPRI-NODE-P and SIMULATE, have been HARMONY format edits for assembly average power from each axial plane of the XYZ solution. Besides power (implicitly the resonance temperature), these edits include the local water density. This information is then presented to P/H as input. Through a succession of fixed source runs, P/H then produces a fine mesh power and flux distribution, which on the assembly average, matches the specified input power.

ASPC is a development of CPM that will be faster than the latter code for comparable problems; it will be easier to use and that will incorporate several improvements. For instance, a free format input with maximum use of default entries will replace the current fixed field input. Assorted thermal expansion calculations will be performed, an echo check, optional processing of input only, etc. Restart information will be read from and written to the same tape, instead of two tapes being used; other application and QA aspects of restart will be improved. Most of the run time of CPM is expended in the collision probability solution, in up to 12 neutron groups, for the XY assembly representation. This solution will be replaced, by user option, with an S_4 calculation. Utilization of this option should not only produce a substantial run time improvement for the assembly geometry now utilized by CPM (diagonal half of a BWR, octant of a PWR) but should also allow much more complete geometric representations of single or multiple assembly geometries which are impractical within the framework of the current CPM solution. For consistency and to reduce known poor data comparisons, the group structure will be upgraded to that of E-CELL.

NORGE-P is a flexible data processing code that will accept the output of ASPC, CASMO or P/H color sets (the adjacent quadrants of 4 assemblies which

are differentiated by enrichment and burnable poison complement, each unique such combination being a color). For use in this path, the P/H output files have been altered from machine language.

SIMULATE-2 designates a significantly improved version of the SIMULATE nodal code which had been released by EPRI in 1978. The SIMULATE code is notable for the several neutronic options it contains: flare-type, coarse mesh diffusion theory (CMDT), modified CMDT (or PRESTO-type model). The new version adjusts radial edge leakage corrections depending on the migration length of the outermost nodes. It accommodates different "A" factors for rodded and unrodded nodes. It will be faster running than the original release and incorporates other significant user-oriented improvements as well as the new EPRI void model.

Likewise, EPRI NODE-P in 1983 will be substantially improved over the original release version. The improvements here will mostly be in the area of basic programming efficiency. One significant methodological change will be an optional three-moderator temperature history capability. This option will be added in connection with the code linking NODE-P to RETRAN, dubbed NODETRAN.

The draft PWR Procedures Manual will be upgraded to include those accretions to the methodology made since the issuance of the original draft. Along with upgraded and new code manuals as necessary, the Revision-0 of this PWR Manual will be issued.

Figure 3 schematically summarizes the interrelationship of the major BWR codes. MICBURN is a special code, auxiliary to ASPC and CASMO, which treats a gadolinia-loaded fuel pin in some geometrical detail within the pellet. Multigroup macroscopic cross-sections are edited and then input to the respective assembly analysis codes.

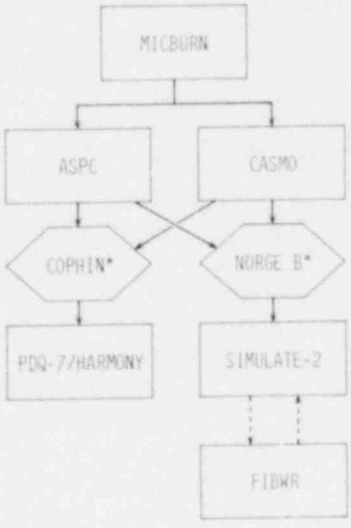

FIGURE 3.

FLOW OF DATA FOR EPRI'S BWR REACTOR PHYSICS CALCULATIONS

NORGE-B is a processing code similar in function to NORGE-P. Not shown is a branch to EPRI-NODE-B, mainly for the benefit of the BWR version of the PSMS. NORGE-B will differ from the extant NORGE code not only in the link to NODE-B but also in its extension to modeling both rodded and unrodded cold BWR configurations (68°F to 200°F). In conjunction with this methodological extension to cold conditions, a simple perturbation theory approach will be implemented in SIMULATE to estimate the worth of control rods.

The COPHIN code processes the depletion dependent output of the indicated assembly analysis codes into input for P/H. It was originally generated to allow the representation with depletion of more than one BWR assembly. It utilizes macroscopic depletion for the most part; only I-135 and Xe-135 are treated microscopically as are two pseudo-isotopes used as independent variables.

The dashed lines in Fig. 3 between FIBWR and SIMULATE-2 represent a two-level linking of FIBWR methodology into SIMULATE-2. FIBWR is the counterpart of SIMULATE in the thermal-hydraulic area in that it accurately computes channel flows, pressure drops, void fractions and water densities, given the detailed power distribution. From the computing point of view, it is not practical to incorporate FIBWR itself as a subroutine in SIMULATE. The FIBWR methodology, however, will be incorporated in two ways. In one, parametric curve fits would provide bundle pressure drops, for a series of typical channels, over a range of axial and radial powers and channel flow rates and subcooling. In the other more expensive way, not likely to be used on a day-to-day core follow basis, models from FIBWR which compute single channel pressure drop and void fraction would be incorporated in a core flow distribution algorithm in SIMULATE. Table lookup bypass flows in SIMULATE would also be utilized.

Finally, a draft BWR Procedures Manual will be released. This manual will serve as a guide to the various code manuals utilized in the BWR sequence and will provide background information and procedures for effective modeling of the core. This manual will serve as a suggested starting point for BWR users for about two years; with use it is expected to develop into a formal document analagous to its PWR correspondent.

VIPRE-1

VIPRE-1 was developed on the strengths of the COBRA code series, most notably COBRA-IIIC, COBRA-IIIC/MIT and COBRA-IV-I, with improvements to the flow solution numerics adapted from COBRA-WC. A large part of the developmental work on VIPRE-1 consisted of tailoring the code to the utilities' analytical requirements, upgrading the code's capabilities and improving the flexibility of its use. Some of the more important improvements were:

- Expanded choice of correlations for Critical Heat Flux (CHF), including the new EPRI-1 methodology*, Critical Power Ratio (CPR),

*EPRI-1 is a benchmarked subchannel CHF correlation; it is likely that EPRI-2, a benchmarked assembly CHF correlation, will be added at a later date.

two-phase flow and heat transfer, with provision for user-programmed correlations in each category.

- o Several input options tailored for one-pass hot channel analysis.
- o Iteration capability for setpoint analysis.
- o Ability to vary the shape of the fuel rod axial power profile during transients.
- o Generalized rod conduction model for nuclear fuel rods, electric heater rods, hollow tubes and walls. (A dynamic gap conductance model is available with nuclear fuel rods.)
- o Capability to compute flow reversal and recirculation.
- o Compact storage scheme and several flow solution options.
- o Free field input.
- o Output options for line printer plots and a postprocessor for CALCOMP plots.
- o Implemented functional fits of water properties.

These new features make VIPRE-1 flexible and easy to use, and enable it to perform many simulations that current codes cannot.

VIPRE-1 predicts the three-dimensional velocity, pressure, and thermal energy fields for single- and two-phase flow in PWR and BWR cores. It solves the finite difference equations for mass, energy and momentum conservation for an interconnected array of channels assuming incompressible homogeneous flow. Although the formulation is homogeneous, nonmechanistic models are included for subcooled boiling and vapor/liquid slip in two-phase flow.

The VIPRE-1 modeling structure is based on subchannel analysis. The core or section of symmetry is defined as an array of parallel flow channels with lateral connections between adjacent channels. A channel may represent a true subchannel within a rod array, a closed tube, or large flow area representing several subchannels or rod bundles. The shape and size of the channels and their interconnections are essentially arbitrary. The user has a great deal of flexibility for modeling reactor cores or any other fluid flow geometry.

A particularly useful application of this flexibility is the ability to do one-pass hot channel analysis for PWRs. The hottest region of the hot assembly is modeled in great detail with individual subchannels, while the remainder of the hot assembly is modeled by lumped channels comprising a larger segment of the rod array. The remainder of the core is modeled on an increasingly coarser mesh, with very large channels comprised of several fuel assemblies. An example is shown in Figure 4. This technique is probably the most efficient and realistic way to simulate a reactor core.

VIPRE-1 has been designed to easily accommodate this generalized core geometry through flexible, user-selected input options.

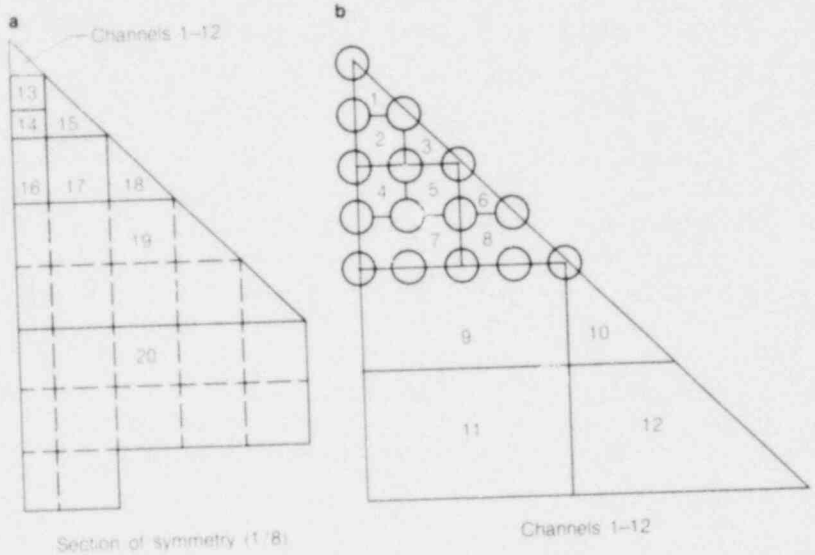

FIGURE 4.
EXAMPLE OF PROGRESSIVE CORE MODELING

VIPRE-1 can also be used for BWR analysis on a lumped channel basis, where each bundle is treated as a one-dimensional flow channel. This approach is useful for Critical Power Ratio (CPR) analysis in a BWR core, since the CPR correlations are generally correlated to the bundle-average conditions. The axial distribution of the bundle-average void fraction in the hot bundle is also a parameter of interest in BWR analysis. This can readily be calculated with VIPRE-1.

Further improvement of VIPRE-1's BWR modeling capabilities is underway. This involves installing a more realistic model to compute the bypass flow between bundles.

VIPRE-1 will compute the detailed flow field in the core using boundary conditions from the RETRAN systems code and power distributions from the ARMP neutronics package. Input will be passed between them by linkage programs, but the codes themselves will run independently. As far as practical, VIPRE-1 contains similar empirical correlations and logic to make it consistent with RETRAN for this application.

Although more work remains, the code has been verified against a wide variety

of experimental data for conditions relevant to its intended application. This includes void fraction data for subcooled and saturated boiling, heat transfer experiments over the entire boiling curve, a large body of critical heat flux data, and single phase velocity measurements around blockages in rod bundles. Sensitivity studies were done to investigate the effect of different correlations, variations in geometric detail, timestep size and solution convergence parameters. The results of most of these tests confirmed that the code performs accurately and efficiently in a wide variety of situations.

VIPRE-2

VIPRE-2 is an advanced two-fluid version of VIPRE-1, currently under development. The basic two-fluid model in VIPRE-2 is being adapted from the COBRA type steam generator analysis code developed at EPRI. This code was designed to model once-through or U-tube PWR steam generators, including the primary tubes, downcomers and separator. It can also examine a smaller segment of the steam generator in very close detail, and can resolve the individual phase velocity and temperature profiles within a single subchannel. VIPRE-2 will have these capabilities in addition to those of VIPRE-1.

The VIPRE-2 two-fluid model computes the three-dimensional velocity and temperature fields of each phase separately as well as the local pressures and vapor volume fractions. It uses essentially the same subchannel analysis techniques as VIPRE-1. The two-fluid model computes the relative phase motion and nonequilibrium directly, rather than through correlations for subcooled voids and slip as is required in VIPRE-1. The interaction of the two phases is computed by empirical models for interfacial drag, heat transfer, and mass exchange.

A major effort in the VIPRE-2 development will be to enhance the speed and reliability of the numerical solution. At present, the steady-state simulations can become quite time-consuming and potentially are impractical. Additional work will involve making the present VIPRE-1 CHF, CPR, and heat transfer correlations compatible with the two-fluid model. The interfacial drag and vapor generation models will also be improved by incorporating the subcooled boiling model developed under the EPRI void model and an interfacial drag model consistent with the drift flux model implicit in the EPRI void model.

Pre-Release RETRAN Version

From a systems applications point of view, RETRAN is most limited by the assumption of thermal-equilibrium (i.e., both phases of a two-phase mixture are at the same temperature). Preliminary evidence indicates that nonequilibrium effects are important in some operational transients, particularly in the pressurizer of a PWR and in the core of a BWR. RETRAN models (such as the pressurizer and separator models) exist that address these specific requirements. Some analysts are using the nonequilibrium pressurizer model in the upper head of both PWR and BWR plants to account for postulated nonequilibrium effects as well as in the downcomer of a BWR.

Developmental versions of RETRAN exist that address this problem directly; they have five and/or six field equations. The additional equations remove the restriction that both phases are at saturation (5-Equation Model) or have full nonequilibrium capability (6-Equation Model). (The fifth equation is the conservation of vapor mass; the sixth equation is the conservation of liquid energy; closure of the system of equations of both models is facilitated by using a nonequilibrium equation of state). RETRAN-5 EQ* is the current pre-release version of RETRAN.

*RETRAN-5EQ is one of three potential candidates for an advanced systems code tentatively entitled EPRI Advanced Systems Code (EASY-C), all of which will allow for 5 and 6 equation representations of two-fluid thermal hydraulics.

SOME REACTOR PHYSICS EFFECTS RELATED TO RECENT TRENDS IN IN-CORE FUEL MANAGEMENT

A. Jonsson, M. W. Crump, P. H. Gavin, S. F. Grill, R. A. Loretz, W. B. Terney

Combustion Engineering Inc., Windsor, Connecticut

ABSTRACT

This paper examines some of the reactor physics aspects of recent in-core fuel management trends (higher burnups and longer fuel cycles) and describes related considerations and changes for Combustion Engineering (C-E) design methods. The following specific effects are discussed:

Effects related to higher enrichments:

- The use of enrichment zoning.
- The use of burnable absorbers in reloads.
- The use of gadolinium to replace boron as a burnable absorber.

Effects related to higher burnup and the larger reactivity contrast between new and old fuel:

- Potentially more non-uniform flux and burnup distributions within coarse mesh nodes.
- Increased inter-nodal leakage influencing the performance of coarse mesh neutronics.
- Impact on the in-core instrumentation system.

INTRODUCTION

Fuel management trends in LWR's over the past fifteen to twenty years have been characterized by efforts to extend discharge burnups and more recently to improve fuel utilization. For PWR's there has been a continued increase in the average discharge burnup from about 12 MWd/kg in the 1960's to about 26 MWd/kg in the late 1970's. Currently, the industry average is around 33 MWd/kg. Goals of reaching 45 MWd/kg have been set for DOE sponsored development programs[1] while fuel management studies and individual rod burnups in experimental irradiations have reached over 50 MWd/kg.

The trend to higher burnups and longer fuel cycles has led to many important lattice modifications. Higher initial enrichments are needed, typically 4.4 wt % U-235 for the feed in an equilibrium cycle reaching 50 MWd/kg. The consequences of higher enrichment are potentially higher power peaking factors on the local as well as on the global scale. These, in turn, have led to the use of enrichment zoning and the increased use of burnable absorbers in reloads.

The latter use is also a direct consequence of the need to limit the soluble boron concentration at the beginning of each cycle to prevent a positive moderator temperature coefficient. Other lattice modifications include the possible use of annular fuel for improved fuel utilization and performance.

Several important areas that have impact upon reactor physics methods and procedures must be dealt with in order to realize these goals for current fuel management strategies. Enrichment zoning impacts physics methods for PWR assembly and lattice calculations while the higher contrast between new and old fuel puts a higher demand on the capabilities of coarse mesh methods for 2D and 3D core analysis. The increased need for burnable absorbers has led to renewed interest in gadolinium for PWR applications. This has required additional attention to depletion and transport methods used in assembly and lattice codes.

The following considerations have been examined and in some instances have led to modifications and extensions of C-E reactor physics design methods and procedures.

- Increased power splits between fresh and burned fuel may require improvements in the definitions of coarse mesh few-group constants either via appropriately defined diffusion coefficients [2] or heterogeneity factors[3,4] in order to obtain correct inter-nodal leakages.

- Increased power splits lead to larger axial variations in the coupling coefficients (part of the software used by in-core instrumentation systems) which are used to perform the extrapolation of power in instrumented fuel to power in uninstrumented fuel and to predict local peaking factors. This leads to greater emphasis on 3D methods (coarse mesh and fine mesh) for the generation of such software.

- The use of enrichment zoning within individual fuel assemblies increases the complexity and size of fine mesh cross section table sets used in the diffusion theory calculations. In order to obtain reliable results, the fine mesh diffusion calculations must be carefully modeled on the basis of assembly or lattice calculations using multi-group transport theory. The degree of complexity can be reduced by performing the fine mesh calculations linked with the coarse mesh by the imbedded method [2,5,6].

- Gadolinium burnable absorbers pose relatively stringent requirements on calculative accuracy since the PWR power distribution is sensitive to reactivity errors. Group condensation methods have been found to place a lower limit on the number of energy groups that can be used in assembly transport calculations. Other important considerations include the effects of azimuthally non-uniform flux distributions in the gadolinium and in adjacent fuel pins. The latter effect alone can be worth as much as 0.5% $\Delta\rho$ on an assembly average basis. Time stepping techniques for both assembly/lattice depletions and core calculations have been modified to account for the rapidity with which the flux level changes in the presence of gadolinium.

The first part of this paper examines some reactor physics aspects related to the use of higher enrichments (enrichment zoning, burnable absorbers in reloads including the use of gadolinium. In the second part of the paper, selected high-burnup aspects of reactor physics methods are discussed namely those related to the increased contrast between new and old fuel.

REACTOR PHYSICS CONSIDERATIONS RELATED TO THE USE OF HIGHER ENRICHMENTS

Use of Enrichment Zoning

As mentioned in the Introduction, the consequences of higher fuel enrichment are potentially higher peaking factors on the local as well as on the global scale. To counteract higher local peaking, C-E often employs enrichment zoning, i.e., lower enrichment pins are located in higher flux areas of the assembly (usually near waterholes). This new design feature has placed additional requirements on the reactor physics procedures that generate and use few-group cross sections as outlined below.

Assembly averaged as well as cellwise few group cross sections are generated by the two-dimensional transport code DIT [7] under the various operating conditions encountered by each fuel assembly. Cellwise cross sections are transferred into fine mesh diffusion theory models such as PDQ which are used to predict the evolution of the radial power distribution and more specifically, the maximum radial peaking factors, as well as the evolution of the incore detector response.

A basic requirement of the cross sections used in a diffusion theory code is that they reproduce the fine mesh flux structure and local reaction rates of the transport code that generated them. Two problems must be addressed in order to satisfy these requirements. The first one is a consequence of the mesh cornered finite difference approximation to the diffusion equation used in PDQ, which cannot reproduce the large flux gradients present in the neighborhood of the assembly water holes. The second problem is due to the impracticality of assigning unique cross sections sets to each cell in a fuel assembly. By necessity, many if not all cells of the same type are given the same cross sections. In order to maintain the required level of accuracy in the diffusion theory solution, the following features are introduced: first the combined effects of lower enrichment and spectrum softening of the fuel cells adjacent to water holes are explicitely taken into account. Then a fitting of all non-fuel cell cross sections is performed so as to reproduce, in the diffusion theory flux, the reaction rates of the transport solution. Finally, the thermal diffusion coefficients in and around the water holes are fitted to preserve the pin to assembly power peaking factor.

A very general representation of the cross sections is used in the PDQ fine mesh as well as in coarse mesh diffusion theory codes. Cross sections are functionalized versus five variables viz. exposure, fuel enrichment, soluble boron concentration, moderator and fuel temperatures. These cross sections are then applicable regardless of the cycle, exposure, feed enrichment and operating conditions.

With enrichment zoning, the number of necessary cross section table sets grows toward the limit of computer capacity. To counteract this, the complexity must be reduced. This is being achieved by performing the fine mesh calculations linked with the coarse mesh by the imbedded method. The detailed cross section functionalization described above is retained in the coarse mesh thus permitting the power history dependent isotopics to evolve on a node average basis. The imbedded, fine mesh calculation for each coarse mesh node on the other hand is performed with a macro-model. The cross sections are still functionalized as described above but since there are fewer of them, more individual pin type cross section sets can be used to model the details of the assembly design.

The Use of Burnable Absorbers in Reloads

The use of higher feed enrichments leads to utilization of burnable absorbers in reloads for the reasons mentioned in the Introduction. Also, low leakage fuel management designs seek to improve uranium utilization over conventional fuel management by reducing core neutron leakage. This would enable reduction in enrichment requirements for equivalent power output of the core cycle. Low leakage loading patterns usually have burned fuel located at the core periphery and use burnable absorbers in reload fuel to control power peaking. In analyzing such designs it is important that errors in the leakage and burnable absorber calculations are sufficiently small to ensure that the predicted gains are real.

The accuracy of C-E methods for shimmed reload cores is supported by core follow analyses. These data indicate an overall reactivity error, including the capability to calculate both leakage and shim absorption, of about 0.3 per cent independent of burnup. The calculative accuracy for the depletion of B_4C burnable absorber rods is being separately verified by measurments performed at the Advanced Reactivity Measurement Facility (ARMF) for individual shim rods taken from a partially depleted core.

Analyses for low leakage fuel mangement with C-E cores predicted reductions in core leakage corresponding to about 1% excess reactivity or 0.12 wt % reduction in average enrichment per batch. The predicted gains are supported by the accuracy of C-E methods for cores using B_4C shims.

The Use of Gadolinium

The use of gadolinium as a replacement to B-10 as a burnable absorber has led to the need to modify methods and procedures. Time stepping techniques for the depletion routines of both the DIT assembly spectrum code and the ROCS, 3D, coarse mesh code[8] have been modified to eliminate the well known need for extremely short time steps. Two other aspects will be discussed here since they are less well known and appear to be significant sources of reactivity error. Since the PWR core power distribution is sensitive to local reactivity errors these aspects may be of interest in the current environment of evolving gadolinium design methods for PWR's. These two aspects are: a) the choice of the group structure for the few-group assembly calculation performed to obtain coarse mesh average cross sections and b) the choice of mesh structure inside

the gadolinium pin cell when performing the flux calculation and the depletion. The first of these two may be of importance to assembly codes with spectrum calculations accurate enough to permit the spatial assembly calculation to be performed in a minimum of energy groups. The DIT code [7] is this class of codes. For normal applications (including B_4C shims) its assembly calculation can be performed in as few as 4 energy groups (1 thermal group) because the spectrum calculation preceding the group condensation represents essentially all relevant spatial detail in the environment of the cell for which few-group cross sections are being calculated. For gadolinium, however, it was found, when varying the number of groups to which condensation was made, that substantial reactivity errors are incurred with only 4 groups. Fig. 1 shows this error for a 16-shim assembly with a modest gadolinium loading of 2 wt %.

FIGURE 1

SENSITIVITY OF k_∞ vs ASSEMBLY GROUP STRUCTURE

16 x 16 ASSEMBLY WITH 16 Gd_2O_3/UO_2 SHIMS AT 2 Wt% Gd LOADING

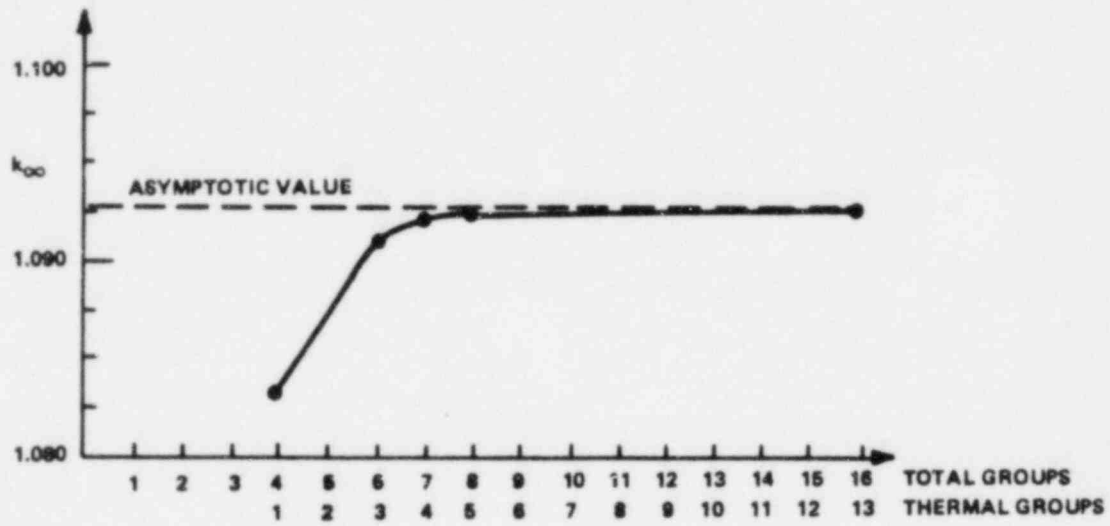

It indicates that seven energy groups (four thermal) are necessary for modeling gadolinium loaded assemblies. Most assembly codes do normally use this number of groups or more but it is felt that the reason for this requirement may be of interest for theoretical reasons and to those who operate with highly accurate spectrum calculations. In the case of gadolinium, a highly accurate spectrum calculation does not allow one to reduce significantly the number of energy groups used for the assembly calculation. A reactivity analysis identified the problem as being located in the group condensation process itself. The absorption cross section, as is normally done, was condensed linearly using 85-group spectra which were space dependent with high resolution inside the pellet. The thermal absorption rate was still incorrect by some 6% for the gadolinium cells as shown in Table 1.

TABLE 1

Thermal Absorption Rate and Flux Level Inside a Gd_2O_3/UO_2 Pellet

Annular Region	Absorption Rate 4 group	Absorption Rate 16 group	δ	Flux Level 4 group	Flux Level 16 group	δ
1	.007008	.005445	+29%	.008196	.00625	+31%
2	.007735	.006210	+25%	.008284	.006503	+27%
3	.008701	.007175	+21%	.008384	.006790	+23%
4	.010062	.008558	+18%	.008507	.007138	+19%
5	.012150	.010720	+13%	.008670	.007580	+14%
6	.015768	.014545	+ 8%	.008937	.008181	+ 9%
7	.023338	.022736	+ 3%	.009365	.009105	+ 3%
8	.047718	.048965	- 3%	.010758	.011023	- 2%
Total	.132479	.124355	+6.5%			

δ = % error in the 4-group results

It is clear from Table 1 that it was the flux level itself in the interior parts of the pellet (and not the cross-section) that caused an overall 6.5% error; i.e., the transport equation solved before and after group condensation gave substantially different flux profiles in the pellet when linear condensation was used. Although the flux in the deep interior of the pellet is relatively small the flux errors were large enough to cause substantial overall reaction rate errors.

The second aspect which can cause substantial reactivity errors is related to the non-symmetric flux distribution inside gadolinium pellets that are located in overall flux gradients.

For conventional light water reactor analysis, the assumption is usually made that the flux and the isotopics within fuel pins are independent of the azimuthal angle around the fuel pellets. This reduction in model complexity leads to more efficient calculations, both from the standpoint of computer time and computer storage. Recent and preliminary evidence, however, has suggested that azimuthal tracking of isotopics may be required for modeling the burnup characteristic of gadolinium shims in the vicinity of waterholes.

Figures 2 and 3 show typical flux contours for the thermal energy region of an 8 wt% Gd_2O_3/4 wt% U-235 pin located on the corner of a large C-E waterhole at beginning of life (BOL). These flux profiles show that radial gradients dominate the spatial shape of the flux and that, although the gadolinium has its full density, the strong absorbtive nature of the odd gadolinium isotopes tends to symmetrize the flux azimuthally. This indicates that near BOL, the pellet isotopics do not require azimuthal tracking.

FIGURE 2

THERMAL FLUX CONTOURS IN A GADOLINIUM FUEL PIN IN THE ENERGY RANGE 0.251 eV TO 0.625 eV AT BEGINNING OF LIFE

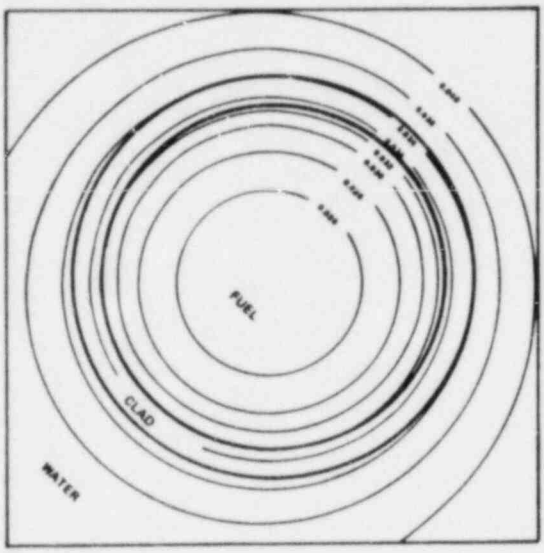

FIGURE 3

THERMAL FLUX CONTOURS IN A GADOLINIUM FUEL PIN IN ENERGY RANGE 0.000 eV TO 0.030 eV AT BEGINNING OF LIFE

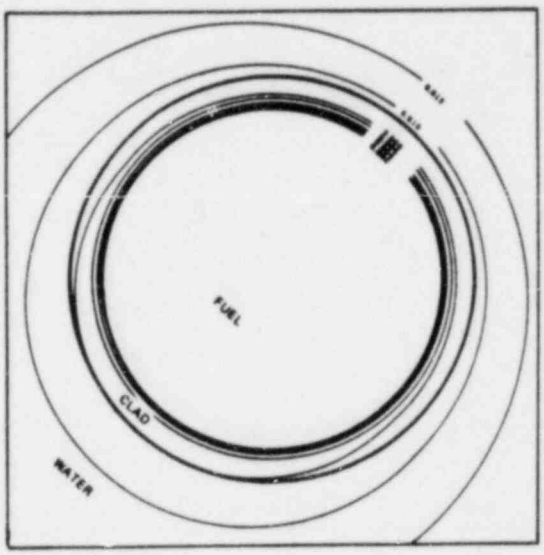

Figures 4 and 5, however, show the flux contours for the Gd_2O_3/UO_2 pin at 16 MWd/kg (the time at which most of the gadolinium has been depleted). These contours show a strong skew of the flux as a function of angle, indicating that azimuthal depletion effects may be of importance in the later stages of gadolinium depletion for the correct determination of assembly reactivity.

FIGURE 4

THERMAL FLUX CONTOURS IN A GADOLINIUM FUEL PIN IN THE ENERGY RANGE 0.251 eV TO 0.625 eV AT 16 MWD/Kg BURNUP

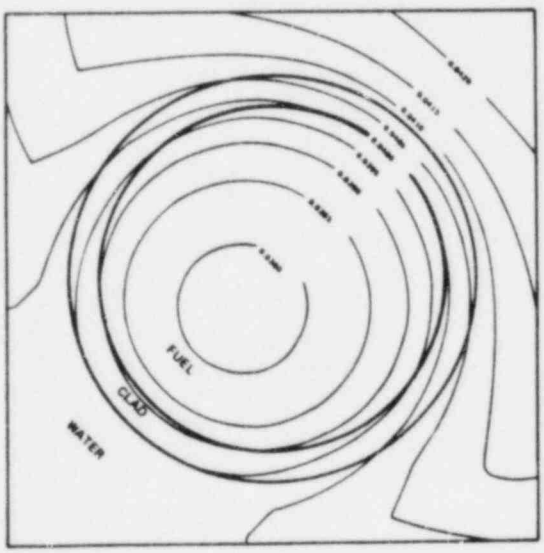

FIGURE 5

THERMAL FLUX CONTOURS IN A GADOLINIUM FUEL PIN IN THE ENERGY RANGE 0.000 eV TO 0.030 eV AT 16 MWD/Kg BURNUP

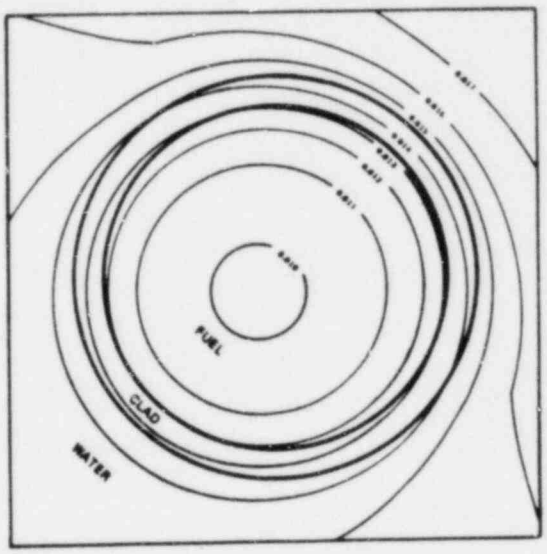

For illustrative purposes, the magnitude of the reactivity error made in not tracking isotopics azimuthally was determined for the geometries of Fig. 6. These cases were calculated assuming both azimuthal and symmetric tracking of the gadolinium isotopics. Eight energy groups were used to account for spectral effects.

FIGURE 6

AZIMUTHAL TRACKING TEST ASSEMBLY GEOMETRIES

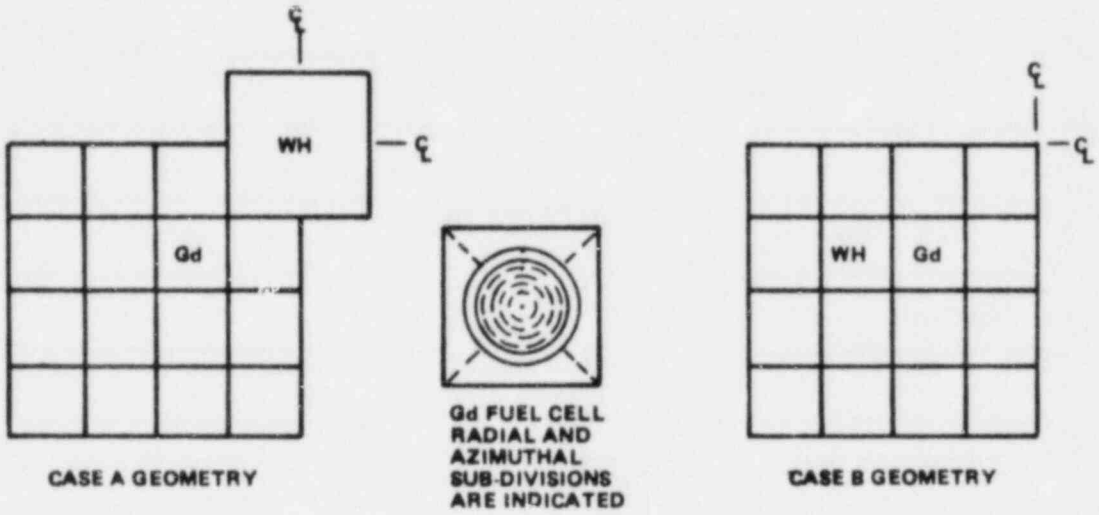

Figures 7 and 8 show the reactivity bias observed for the two cases shown in Fig. 6. As indicated above, based on DIT calculations, there is little effect on k_∞ seen near BOL using azimuthal tracking. However, as the gadolinium reaches its peak burnout rate, errors of the order of 0.7% Δk_∞ are observed between the cases of azimuthal and symmetric tracking.

FIGURE 7

CASE A REACTIVITY BIAS vs BURNUP BETWEEN AZIMUTHAL AND SYMMETRIC TRACKING OF GADOLINIUM ISOTOPICS

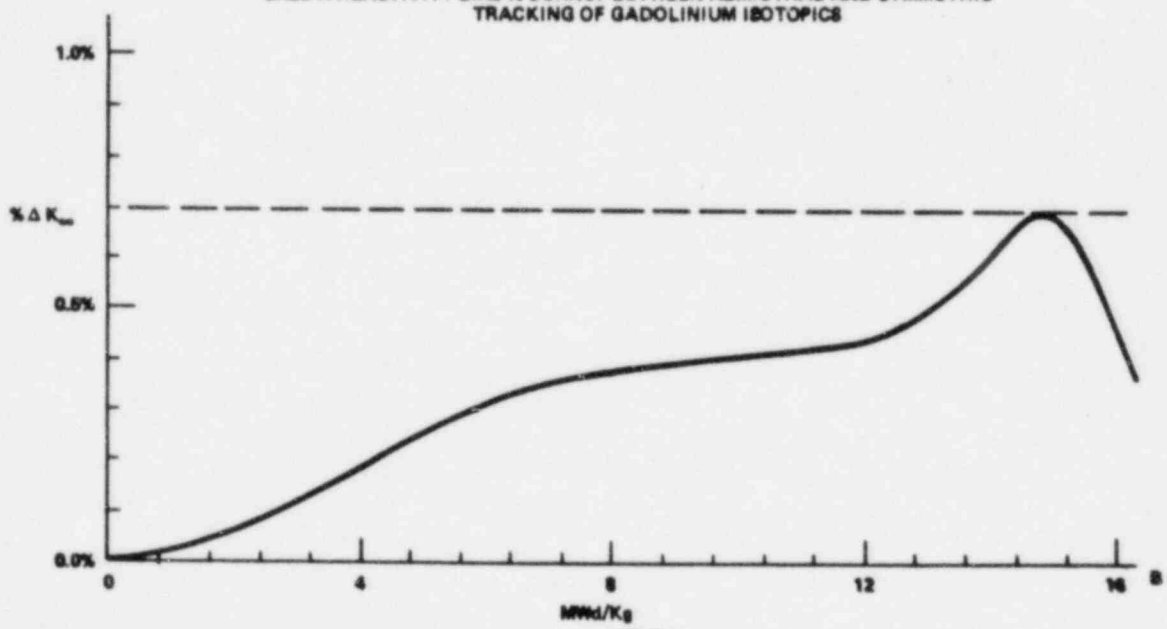

FIGURE 8

CASE B REACTIVITY BIAS vs BURNUP BETWEEN AZIMUTHAL AND SYMMETRIC TRACKING OF GADOLINIUM ISOTOPICS

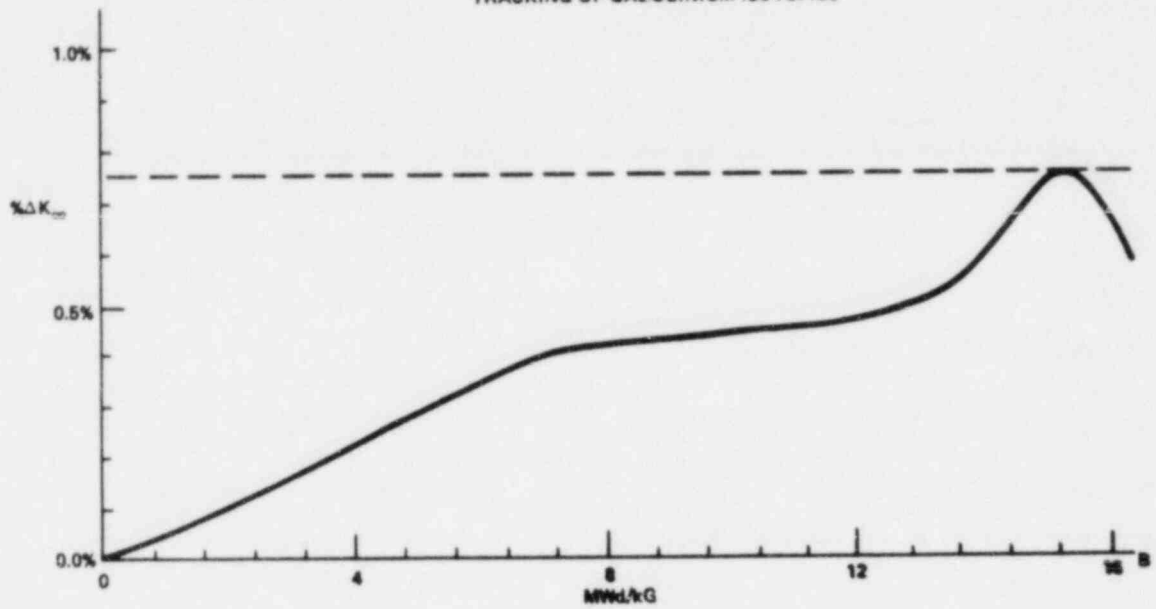

In addition to the magnitude of the reactivity effect noticed, the azimuthally depleted case is seen to peak approximately 0.5 MWd/kg sooner than the non-azimuthal depletion case. The combined errors in reactivity and in timing of gadolinium depletion will affect both the global and the local power distributions.

Although the tracking of gadolinium isotopics azimuthally is important for reactivity determination at the end of life of the absorber, the azimuthal shape of the flux influences the calculated value of reactivity throughout life. DIT has the capability to model azimuthal variation of the flux within each cell.

In order to assess the importance of this capability, DIT was also used with a zeroth order Fourier mode option for the spatial two-dimensional assembly transport calculation at beginning of life (BOL). This option assumes an azimuthally symmetric flux profile within the pin. Use of this option, compared to a higher order flux calculation, resulted in an overall higher thermal flux level, and therefore, higher absorption rates in the gadolinia. The smoothing of flux levels depressed the flux in the surrounding fuel, lowering their reaction rates. The net effect was a 0.5% $\Delta\rho$ reduction in reactivity for the zeroth Fourier mode calculation.

In conclusion this preliminary analysis indicates an incentive for placing the gadolinia fuel pins away from waterholes or other strong thermal gradients in order to minimize modeling uncertainties related to azimuthal depletion. This design criteria can be accommodated in the C-E lattice designs. Additionally, it is concluded that it is necessary to properly model the azimuthal dependence of the flux distribution within uranium fuel pins located

near gadolinium pins regardless of the location and degree of depletion of the gadolinia.

REACTOR PHYSICS CONSIDERATIONS RELATED TO HIGH BURNUP

In this section we discuss three specific, selected questions related to increased burnup and the consequent higher contrast between new and old fuel. Larger flux gradients and increased leakage at the interfaces between new and old fuel are potential sources of error for coarse mesh calculations. The more non-uniform flux distributions tend to make the coarse mesh average cross sections more problem dependent while the increased net flow of neutrons across node boundaries may make the neutronics of coarse mesh codes less accurate. Power distributions associated with high burnup also lead to a larger range of values for so called coupling coefficients used to infer the power level in uninstrumented fuel. This has led to a need to modify incore instrumentation system software.

Increased Leakage Between New and Old Fuel

The coarse mesh (CM) code ROCS[8] employed by C-E for design calculations uses a higher order difference method based on Taylor expansion. In application, for conventional fuel management, this method has proven accurate when compared with both in-core measurements and with fine mesh calculations using the PDQ-7 code [9,10]. In high-burnup fuel management both power splits and inter-nodal leakages increase beyond this data base. The accuracy of the Taylor expansion technique has been confirmed relative to fine mesh calculations using consistent cross sections. Figure 9 shows power splits in a portion of a cycle 8 core loading with the large burnup differential typical of high burnup fuel management.

FIGURE 9
ACCURACY OF ROCS COARSE MESH (CM) CODE AT HIGH BURNUPS

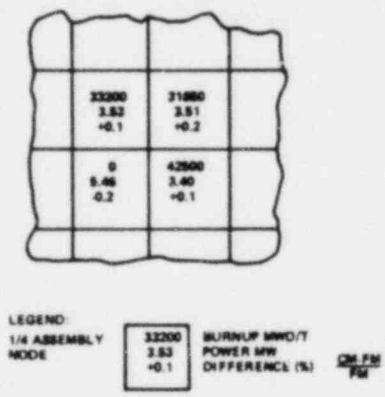

In this case CM cross sections were taken from the fine mesh (FM) calculation to eliminate any effects due to a possible need for so called rehomogenization. It is clear from Fig. 9 that the ROCS Taylor expansion technique yields highly accurate power split calculations even for high burnup fuel management.

The need for rehomogenization in high burnup situations is discussed next. It is well-known that conventionally generated CM cross sections, ie. with $J_{net}=0$ as a boundary condition for the assembly calculations, can lead to typically 5% power distribution errors particularly for fuel located at the core periphery [7,11]. Table 2 shows the effect upon local k_∞ of rehomogenization for a number of CM nodes (1/4 assemblies) located in environments similar to the one illustrated in Figure 9 but which do not originate from edge locations where strong burnup gradients are generated.

TABLE 2

REHOMOGENIZATION EFFECTS ON LOCAL K_∞

Node	Burnup (MWd/kg)	$k_\infty(J_n=0)$	$k_\infty(J_n\neq0)$	Δk_∞
43	14.372	1.06775	1.06729	-.00046
63	42.515	.87512	.87559	+.00047
113	16.163	1.05279	1.05229	-.00050
129	8.444	1.11962	1.11917	-.00045

One concludes from Table 2 that an additional need for rehomogenization does not exist as a result of higher burnups in fuel depleting in in-board locations.

Impact on In-Core Instrumentation System

With the trend to longer cycles and higher burnups, there is a larger contrast between new and old fuel. This contrast leads to larger power splits between new and old fuel and also to larger axial variations of the power splits over that experienced with the more conventional fuel management schemes. This causes a larger axial variation of the precalculated coupling coefficients used by the in-core instrumentation system software to extrapolate the power in instrumented assemblies to uninstrumented assemblies.

Historically a single library set, of coupling coefficients has been generated for the mid-detector level and used for all in-core detector levels, evaluated at the appropriate assembly burnup at that level. Figure 10 shows the results of a comparison of 3-D calculated box power distributions at each plane to those synthesized from in-core detector powers taken from the same 3-D calculation using single-level coupling coefficients generated for the mid-plane. The large variation of the standard deviation towards the top and bottom of the core is caused by the axial variation of the coupling coefficients. This is due to the axial variation of burnup differences and reactivity between new and old fuel. When multi-level coefficients are evaluated at each of five detector levels, and used in the extrapolation from instrumented to uninstrumented assemblies, the errors are substantially decreased as shown in Figure 10.

Although the incentive to use multi-level coefficients is strong even for conventional fuel management, high burnup fuel has accentuated this need. The CECOR [12] software for the C-E in-core instrumentation system is designed to conveniently handle multi-level coefficients for coupling, pin peaking and the signal to power conversion. The use of single-level coefficients gives highly conservative values of the peaking towards the core ends. The over-conservatism is removed when using multi-level coefficients.

FIGURE 10

COMPARISON OF ROCS-CECOR PLANAR BOX POWER SYNTHESIS ERRORS USING SINGLE AND MULTI-LEVEL COEFFICIENTS (NEAR BOC)

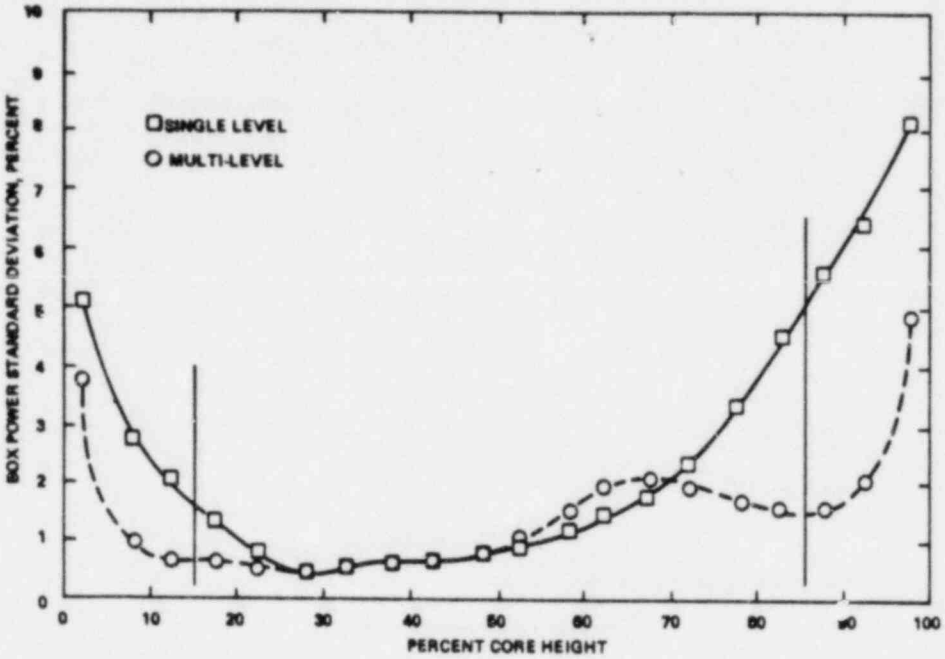

CONCLUSION

The accuracy of C-E physics design methods has been reviewed in the light of the requirements of recent fuel management trends. The low leakage fuel management gains are found to be of significant size when compared with observed reactivity biases for shimmed reloads.

Increased interest in the use of gadolinium as a burnable absorber has required a number of important changes in the design methods. Additional changes may prove necessary to account for non-uniform azimuthal depletion effects within Gd absorbers.

The ROCS, coarse mesh, design code remains accurate for high-burnup fuel management applications. High-burnup has not increased the need for using rehomogenized coarse mesh cross sections.

Higher fuel burnup has increased the benefits of going to so called multi-level coefficient libraries for the incore instrumentation software by removing over-consevatism.

REFERENCES

1. U. Decher, "The Evaluation and Demonstration of Methods for Improved Nuclear Fuel Utilization," First Annual Reports DOE/ET/34013-1, CEND-384 October 1980 and COO-34010-1, CEND-382, June 1980.

2. A. Jonsson and R. L. Hellens, "Recent Improvements in PWR Physics," ANS Conference 1980 Advances in Reactor Physics and Shielding, September 14 - 17, 1980, Sun Valley, Idaho.

3. A. Y. Cheng, C. L. Hoxie and A. F. Henry, "A Method for Determining Equivalent Homogenized Parameters," ANS/ENS Topical Meeting on Advances in Mathematical Methods of Nuclear Engineering Problems, April 27 -29, 1981, Munich.

4. K. Koebke, "Advances in Homogenization and Dehomogenization," ANS/ENS Topical Meeting on Advances in Mathematical Methods of Nuclear Engineering Problems, April 27 -29, 1981, Munich.

5. S. F. Grill, A. Jonsson and J. R. Rec, "A Nodal Imbedded Method to Recover Local Power Peaking from Coarse Mesh Reactor Calculations," Trans. Am. Nucl. Soc., 35 . 580, 1980.

6. A. Jonsson, S. F. Grill and J. R. Rec, "Nodal Imbedded Calculation for Retrieval of Local Power Peaking from Coarse Mesh Reactor Analysis," ANS/ENS Topical Meeting on Advances in Mathematical Methods of Nuclear Engineering Problems, April 27 - 29, 1981, Munich.

7. A. Jonsson, J. R. Rec and U. N. Singh, "Verification of a Fuel Assembly Spectrum Code Based on Integral Transport Theory," Combustion Engineering Inc. paper TIS-5815 presented at the ANS Annual Meeting, June 1978, San Diego, Trans. Am. Nucl. Soc., 28 , 778, 1978.

8. T. G. Ober et. al., "Extension of the ROCS Coarse Mesh Physics Simulator to Two Energy Groups," Trans. Am. Nucl. Soc., 28 , 763, 1978 and C-E paper TIS-5856.

9. W. B. Terney et. al., "Qualification of C-E's 3-D Spatial Neutronics Code for PWR Analysis," Trans. Am. Nucl. Soc., 30 , 227, 1978 and C-E paper TIS-6011.

10. R. P. Bandera et.al., "Evaluation of Coarse Mesh Methods in Calculation of Safety Related Parameters," Trans. Am. Nucl. Soc., 35 , 560, 1980.

11. M. R. Wagner, K. Koebke and H. J. Winter, "A Non-Linear Extension of the Nodal Expansion Method," ANS/ENS Topical Meeting on Advances in Mathematical Methods of Nuclear Engineering Problems, April 27 - 29, 1981, Munich.

12. A. Jonsson, W. B. Terney, M. W. Crump, "INCA/CECOR Power Peaking Uncertainty-Evaluation of Uncertainty in The Nuclear Power Peaking Measured by the Self-powered, Fixed In-core Detector system," CENPD-153-NP, May 1980.

REACTOR PHYSICS AND IN-CORE FUEL MANAGEMENT FOR SWEDISH REACTORS

Malte Edenius, STUDSVIK OF AMERICA, 99 Pond Ave,
BROOKLINE, MASS 02146

1 INTRODUCTION

Nuclear fuel costs depend strongly on bundle and core design as well as on operating strategy. Improvements of the in-core fuel management can result in multi-million dollar savings for each cycle. The Swedish utilities have therefore found it important to have full in-house capability in the field. This requires efficient and accurate methods for reactor physics analysis, and the development of advanced computer programs is an important task for the utilities and the supporting industry.

Sweden has three nuclear utilities - OKG, Sydkraft and The Swedish State Power Board (SSPB) - with seven operating BWRs of ASEA-ATOM design and two Westinghouse PWRs. One more PWR is ready for start-up and two BWRs are under construction. Fuel for the BWRs has been supplied by ASEA-ATOM and Exxon and for the PWRs by KWU and Westinghouse.

This paper will briefly describe the main reactor physics codes used by the utilities and give some examples of in-core fuel management (ICFM) activities. The intent is not to review the Swedish ICFM but rather to demonstrate some activities where the interaction between reactor physics methodology and ICFM is of importance.

2 REACTOR PHYSICS PROGRAMS

The major reactor physics programs being used by the utilities to support the in-core fuel management are shown in Figure 1. They are: CASMO-2 (Ref 1,2) for bundle calculations, POLCA (Ref 3) for the three-dimensional core calculations, MBS (Ref 4) for two-dimensional diffusion theory calculations and CYCLE (Ref 5) for multi-cycle scoping studies. Linking between the various programs is done using highly automatic interface codes.

CASMO is a two-dimensional multi-group transport theory program for BWR and PWR assembly calculations. It generates few-group cross sections to be used in the core calculations and is capable of handling all heterogeneities that occur in today's LWR fuel such as gadolinia rods, water holes, water gaps, cruciform or cluster control rods, etc.

CASMO 2 is an extended version of the original CASMO (Ref 6) program. The physics model is the same in the two versions, but CASMO-2 allows a much more flexible geometry and several new options have been developed.

POLCA is a three-dimensional nodal code for BWR applications. The SSPB has modified POLCA for PWR calculations. The neutronics calculation is a 1.5 group model with thermal neutron coupling between nodes.

25 axial nodes are used in both BWRs and PWRs, and PWR bundles are divided into four nodes in the x-y plane. Two-group cross section data are given as three-dimensional tables in input.

The MBS program is used to calculate pin powers in a PWR. Cross sections are taken from CASMO-2, either individually for each pin

type or smeared over a larger zone. Normally, bundle homogenized data are used. MBS also reads the calculated internal power distribution within the bundle from the CASMO output file and superimposes the fine structure power distribution on the smoothed distribution calculated by the diffusion theory routine in MBS. This feature utilizes the fact that the pin power distribution already has been calculated in CASMO and does therefore allow a coarser mesh in MBS.

There is no need to make a microscopic depletion with isotopic burnup chains in MBS because the depletion in CASMO has already been carried out with individual pin spectra where the influence of, e.g. water holes and burnable poison rods have been accounted for. The MBS burnup calculation is therefore done using macroscopic cross sections.

Thus, utilizing the extra information and detail of the CASMO bundle calculation compared to the limited information from a pin cell code, MBS can be run with coarser mesh and macroscopic depletion without any significant loss of accuracy. This results in reduced computer costs and less input data so that input and QA are simplified.

CYCLE is used for multi-cycle analyses. It contains a one-dimensional two-group diffusion theory model for the neutronics calculation. The program can estimate cycle lengths, enrichments, number of bundles to be loaded, etc. over many cycles. CYCLE can be coupled to an economics module, SURPRIS, for analysis of the fuel costs under various economic assumptions.

Many auxiliary programs have been developed by the utilities and are used together with the main programs listed above. Two examples are: CHACAL (Ref 7), which facilitates the design of core loadings in BWRs with diagonal loading patterns and AVESTA (Ref 7), which

determines the locations of control modules with the smallest shut down margins in a BWR core.

3 IN-CORE FUEL MANAGEMENT

In-core fuel management at the Swedish utilities is split between the headquarters and the core group at the specific plant. Fuel demand, neutronics bundle design, loading patterns, master BWR control rod sequences, etc. are normally determined at the headquarters. The plant core group makes calculations to determine, e.g. the detailed startup and operation of the reactor. BWR control rod patterns may be modified by the plant personnel if thermal margins are too small or too big.

3.1 Assembly Calculations

A proper analysis of a power reactor involves many calculational steps and transfer of much data between codes. Thus, the ease in using the codes is of great importance. For example, few-group data for POLCA are tabulated as function of many independent parameters (exposure, void, fuel and moderator temperature, boron concentration, control rod, hot zero power or cold conditions, etc) and several CASMO depletion runs with branch calculations are needed for each fuel type in order to include burnup history effects.

Void and control rod history are important in BWR calculations and are accounted for in POLCA. Void history is by far the most important of the two effects. Control history for nodes next to a control rod can be substantial as illustrated by Figure 2, but the overall influence on k_{eff} is less important, because only a fraction of the control rods are inserted during a cycle. However, control history is quite important for the internal power distribution within a bundle (Figure 3).

Moderator temperature history takes the place of void history in PWR analysis. The effect is smaller, about 1 % in k_∞ at 30 MWd/kg going from inlet to outlet temperatures (Figure 4), but influences the calculated axial power distribution and is therefore always included in our calculations.

Other burnup history effects, such as boron concentration and fuel temperature, have been found to be of less importance as long as an adequate average value is used in the depletion calculations. This is demonstrated by the results in Table 1. The reference case followed a boron let down curve for the first cycle and case 2 was calculated with a constant boron concentration equal to the average concentration of the boron let down curve. The results are very close to each other. We have therefore chosen to use a constant boron concentration in CASMO burnup calculations, since this simplifies the tabulation of data in POLCA. It is however, important that a proper average concentration is used. Case 3 shows that the boron history effect is 0.5 % on k_∞ at 30 MWd/kg going from 400 to 800 ppm boron.

Case 4 demonstrates the fuel temperature effect if the decrease in temperature versus exposure is followed in the assembly calculation. Compared to burnup at constant fuel temperature this results in 0.1 % higher k_∞ at average burnup and 0.1 % lower k_∞ at EOL, which is neglibible in core calculations with a mixture of different burnups. CASMO depletion calculations are normally done at constant bundle average fuel temperature.

The need to cover the various depletion histories in the assembly calculations requires that 100-250 reactivity points are calculated with CASMO for each fuel type. Typical sets of reactivity points are shown in Figures 5 and 6. Poison rod history from boron or gadolinia rods is always accounted for by treating each type of burnable poison bundle as a separate fuel type.

3.2 Core Calculations

Most core calculations are done with POLCA which exists in different versions for BWRs and PWRs. MBS is used for PWR core calculations for pin by pin power predictions.

Core follow calculations with POLCA and MBS have generally given results in good agreement with operating data. We normally do not make any adjustments of input data between cycles. Albedo values, e.g. are kept the same cycle after cycle. An exception from the good core follow results have been observed, however, in an initial BWR cycle, where the axial TIP readings were poorly predicted. A new model for the thermal neutron coupling between nodes in POLCA has recently been developed and is expected to improve the results for the initial cores, which contain very heavy absorbers and therefore are sensitive to the thermal leakage between nodes.

Cold shut down margins in BWRs have been found to be calculated with good accuracy using POLCA. Shut down margins with one control rod withdrawn are measured at start up of each cycle. The calculated k_{eff} level is consistently almost 1 % higher than at operating conditions but cycle independent. The higher k_{eff} at cold conditions is consistent with observations from analysis (Ref 8) of hot and cold criticals in the Studsvik KRITZ facility.

3.3 Examples of Special Studies

Current optimization focuses on low leakage loadings, burnable poison designs, extended burnup, cycle length and coast down for both reactor types. The BWR optimization effort also involves fine tuning of the diagonal loading scheme (Ref 9, 10) and control rod patterns, spectral shift operation and reconstitution of discharged assemblies for reinsertion (Ref 11).

The diagonal loading scheme was first used in Oskarshamn 1 1976 and is used in all Swedish BWRs since 1978. An example of the loading pattern is shown in Figure 7. Only one control rod sequence per cycle is needed because every second control module is free of fresh fuel, so the rods can be operated next to low reactivity fuel.

We have frequently allowed one year old fuel in modules with the control rod inserted during a large part of the cycle. The control history is somewhat different from that shown in Figures 2 and 3 because the bundle has always been burnt at least one cycle without an adjacent control rod. Therefore, a control rod is never inserted before the gadolinium is depleted and a typical control history is illustrated by Figures 8 and 9. The bundles are designed so that the internal power peak does not increase with control history. However, the power in fuel rods next to the control rod increases substantially when the control rod is withdrawn at the end of a cycle. Therefore, some extra shuffling is usually done at reloads, so that bundles next to the last rods to be withdrawn are at least two years old. Power mismatch is increased and reactivity decreased when one is forced to avoid one year old fuel in control modules, so there is an incentive to use one year old fuel where it does not lead to increased risks for fuel failure.

A recent study for the Barseback BWR showed that, compared to a pure diagonal loading, four to six extra fresh assemblies were needed in a reload with several control cells with two years old or older fuel.

The calculational volume for diagonal loadings is reduced significantly because the extra effort to find several rod withdrawal sequences is avoided and also because thermal margins are improved. Our experience is that the existing programs predict the behaviour of diagonal core loadings accurately. No program modifications were needed when we changed loading scheme four years ago.

Reconstituted assemblies have been inserted in several of the Swedish BWRs. Oskarshamn 2 loaded 10 assemblies made up of previously irradiated fuel rods 1978. In 1979-80 assembly reconstitutions were made by rebuilding two initial assemblies into one with increased reactivity. Five water holes were introduced in the assembly, and the assembly k_∞ gain was 7.5 %. However, k_∞ decreases faster with burnup in the rebuilt assemblies than in normal fuel, and after irradiation for one cycle the k_∞ gain is reduced to 6 %. 21 reconstituted assemblies were loaded 1980. 78 more rebuilt assemblies were inserted 1981, this time reconstituted from three year old assemblies of the second reload batch. The k_∞ gain was 4.5 %.

98 rebuilt assemblies with a moderate k_∞ increase of 1.5-2.0 % are expected to be loaded 1982. These will reduce the fresh fuel load by about 8 bundles. The long term saving is expected to about half of that, i.e. 4 fresh bundles.

Examples of bundle designs are shown in Figures 10 and 11. The extra water holes are introduced to further increase k_∞ . The internal power peaking in reconstituted bundles is much larger than in normal bundles. Also the detector-to-power ratio is quite different. Therefore, rebuilt assemblies are not loaded in high power positions or adjacent to detectors.

An auxiliary code, MOVEROD, was developed for CASMO-2 so that shuffling of burnt fuel rods can easily be done within and between bundles in the calculations. Because of the axial burnup distribution of the fuel rods MOVEROD-CASMO calculations need to be done at several exposure values. The extra effort is not negligible, but the fuel savings are significant when initial bundles can be reconstituted. Figure 12 shows some results for k_∞ versus exposure. The methodology for design and analysis of reconstitution is now well established and a routine part of the ICFM.

It is essential that the reactor physics methods can predict differential results from alternative bundle and core designs, operating strategies, etc, accurately. One important example is the end-of-cycle residual in burnable poison rods. Too high gadolinium or boron concentrations can result in additional fuel costs of a million dollars or more per cycle. The minimization of burnable poison end-of-cycle residual is a major challenge, which requires accurate calculations involving both CASMO and POLCA. Axial shaping of gadolinium is used in most Swedish BWR reloads (Ref 12) adding to the degree of freedom (Figure 13).

Swedish utilities optimize the burnable poison design for each loading so that the residual reactivity penalty is kept to a minimum. The amount of gadolinia used in BWR assemblies varies from 3 rods with 1.5 % Gd_2O_3 up to 7 rods with 5 % Gd_2O_3 depending on the power density in the reactor and the cycle length. ASEA-ATOM provides axially distributed Gd in all reload fuel. This helps to shape the axial power distribution and keeps the residual reactivity down compared to uniform Gd loadings. The cycle individual design is such that the end-of-cycle penalty in the high absorbing isotopes Gd-155 and Gd-157 is very small. The residual from the even isotopes which remains in the fuel throughout its life is calculated to 150 pcm and 1200 pcm in the 3x1.5 % and the 7x5 % Gd fuel, respectively. A 1200 pcm residual needs to be compensated either by increasing the U-235 enrichment by a little more than 0.1 % or by loading about 5 % more fresh bundles each cycle. Thus, there is a very strong economic incentive to minimize the amount of burnable poison to what is needed for safe operation of the reactor.

Comparisons between various fuel management schemes frequently require multi-cycle analyses. Such calculations are easiest done with CYCLE. A simplified model like the one in CYCLE cannot pre-

dict leakage or power peakings very well but seems otherwise to be quite useful to predict differential results (enrichment, number of fresh assemblies, influence of coast down, etc). Comparison of schemes with different leakage like in-out or out-in PWRs requires more accurate models and are best done with POLCA calculations for several cycles.

4 CODE MODIFICATIONS

New designs require from time to time modifications in existing computer programs. Current examples are the new SVEA (Ref 13) BWR bundle design and annular fuel in both BWRs and PWRs.

Test assemblies of ASEA-ATOM's SVEA design (Figure 14) with a central water cross in 8x8 BWR bundles have been loaded in Ringhals 1. For analysis of this new design a new model had to be developed for CASMO. This was finished in early 1982 and the SVEA bundles can now be calculated as easily as standard fuel. Analyses performed by Sydkraft indicate a reactivity gain of about 2.5 % at BOL for the same average enrichment as standard fuel. It seems likely that BWR fuel costs can be reduced by up to 10 % using the SVEA design.

The introduction of annular fuel pellets has also recently lead to program development. The void fraction of the central hole in the pellets is usually in the range 10-20 % and it has been demonstrated (Ref 14) that a simple volume homogenization of the UO_2 pellet can be done under such circumstances, so that the fuel can be analysed with standard cell codes. The use of Gd in annular fuel requires, however, that the correct geometry is preserved when performing the Gd depletion calculation. The MICBURN code (Ref 15) which is used in conjunction with CASMO for Gd calculations has been modified to accomodate this new geometry. Simultaneously MICBURN was made more user oriented and flexible also for other purposes such as microscopic depletion calculations of boron burnable poison rods in PWRs.

Other new concepts like Gd in PWRs or new boron rod designs did not require any program changes but can be handled using existing methodology (Ref 16). The introduction of Gd in PWRs demonstrates the advantage in using, as far as possible, the same methods for BWR and PWR analysis, so that experience from one reactor type directly can be transferred to the other one. It is important that the methodology used for in-core fuel management is based on a good theoretical basis and is accurate enough that the analyses can be trusted also for new designs.

Program modifications sometimes are initiated as a result of observed discrepancies between predictions and measurements. An example is the comparisons of measured TIP traces and gamma scans with calculations in BWRs, which led us to include a model for non-uniform void distribution in CASMO in order to improve the calculation of detector readings (Ref 17).

The fission chamber detector reading predictions at high void fractions were found to be sensitive to the possible existense of a thin water film inside the channel wall. The water film may increase the detector reaction rate by as much as 10 % at the top of the core as shown in Table 2. Few group cross sections and k_∞ values are usually insensitive to the in-channel void distribution.

5 CONCLUDING REMARK

Major goals for in-core fuel management are to reduce fuel costs, increase operating flexibility and provide reliable data for safety related work. To reach these goals it is essential that the engineer can spend most of his time analysing results of calculations rather than performing the calculations. This requires easy-to-use and reliable computer codes within a well integrated fuel management system. The continued Swedish effort focuses on further

improvements of efficiency and accuracy in the existing system of programs.

ACKNOWLEDGEMENT

The author likes to thank S E Larsson, Sydkraft; T Lefvert, SSPB, and G Wiksell of OKG for material used in this paper.

REFERENCES

1 M EDENIUS, A AHLIN and H HAGGBLOM
"CASMO-2 User's Manual". STUDSVIK/NR-81/3 (1981)

2 A AHLIN and M EDENIUS
"CASMO-2 for generation of effective PDQ cross sections", presented at the ANS National Meeting in Los Angeles, June 1982

3 ASEA-ATOM Proprietary Code

4 O NORINDER and K OLSON
STUDSVIK Internal Memo

5 L LARSSON and A AHLIN
STUDSVIK Internal Memo

6 A AHLIN and M EDENIUS
Trans. Am. Nuc. Soc., 26, 604 (1977)

7 G WIKSELL, OKG Internal Memo

8 M EDENIUS
"Temperature Effects in Light Water Lattices"
Trans. Am. Nucl. Soc., 30, 711 (1978)

9 M EDENIUS
"A Note on Refueling Schemes for BWR Cores"
Trans. Am. Nucl. Soc., 28, 388 (1978)

10 M EDENIUS, S LARSSON and G WIKSELL
"Diagonal loadings in Swedish BWRs"
Trans. Am. Nucl. Soc., 38, 183 (1981)

11 P LINDGREN, O BERNANDER, S HELMERSSON and A JOHANSSON
"Fuel Reconstitution as a Method for Improving Uranium Utilization"
Trans. Am. Nucl. Soc., 39, 136 (1981)

12 E TENERZ and O BERNANDER
"Trends in the Flexibility of BWR Core Operation"
Trans. Am. Nucl. Soc., 33, 801 (1979)

13 O NYLUND, B FREDIN and A JOHANSSON
"SVEA - A New BWR Fuel Assembly Concept for Improved Fuel Utilization"
ANS Topical Meeting: Technical Basis for Nuclear Fuel Policy, Newport, September 1981

14 Session on: "Fuel Utilization Aspects of Annular Pellets", Trans. Am. Nucl. Soc., 38, 145 (1981)

15 A AHLIN and M EDENIUS
"MICBURN-CASMO/CPM for Analysis of Assemblies with Gadolinium",
Paper presented at the ANS Annual Meeting in Los Angeles, June 1982

16 K EKBERG, E JONSSON, V GUSTAVSSON and O NORINDER
"A Study of Long PWR Cycles Using Gadolinia"
Trans. Am. Nucl. Soc., 38, 184 (1981)

17 M EDENIUS
"Analysis of BWR Bundles with Nonuniform Void Within the Channel"
Trans. Am. Nucl. Soc., 35, 543 (1980)

Table 1 k_∞ versus exposure with different boron and fuel temperature history. (15x15 PWR)

Exposure MWD/kg	Boron let down C=800-0 T_f=900 Case 1 (Ref).	Const. Boron C=400 T_f=900 Case 2	Const. Boron C=800 T_f=900 Case 3	T_f hist C=400 T_f=1100-700 Case 4
0	1.23642	-	-	-
10	1.12070	1.12015	1.12106	1.12073
20	1.03532	1.03503	1.03786	1.03630
30	0.96288	0.96274	0.96771	0.96364
40	0.90134	0.90124	0.90834	0.90032

Note: All k -values in the table are branches to C=400 ppm boron and T_f=900 K, i.e. the table shows only the "history effect".

C=Boron history conc. in ppm

T_f=Fuel temp. history in K

Case 1 was calculated with a linear decrease of boron from 800 ppm at BOL to 0 ppm at 20 MWd/kg and then with a constant conc. of 400 ppm.

Case 4 was calculated with a linear decrease of fuel temp. from 1100 K at BOL to 700 K at 40 MWd/kg.

Table 2 k_∞ detector constants and power in narrow/narrow corner pin for 8x8 Gd bundle

Void distr.	0 MWd/kg		20 MWd/kg	
	0 %	75 %	0 %	75 %
	k_∞			
Flat void W film	1.02772	.97828 - .00307	1.00158	.99378 + .00043
	Detector constant			
Flat void W film	3.97	3.56 +8.7 %	4.53	3.36 +9.2 %
	Power in narrow/narrow corner			
Flat void W film	1.203	1.077 +4.1 %	1.112	1.031 +4.0 %

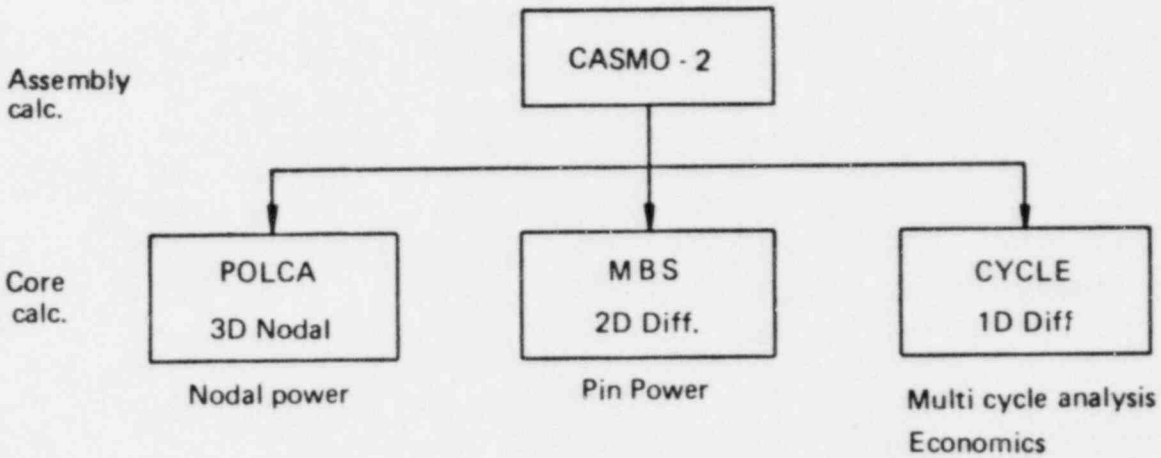

Figure 1. MAIN CODES USED BY SWEDISH UTILITIES

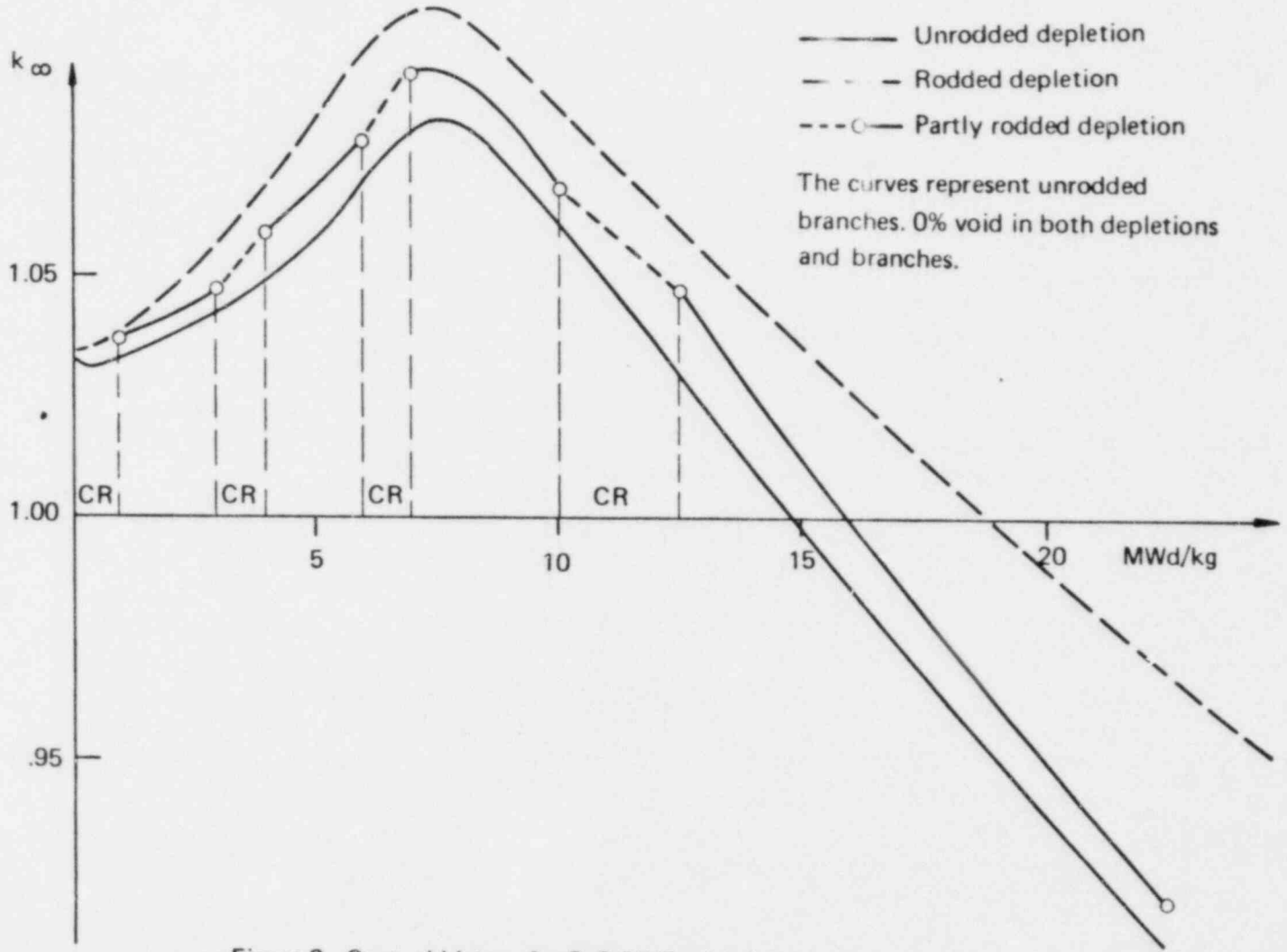

Figure 2. Control history for 8x8 BWR with 4 Gd rods.

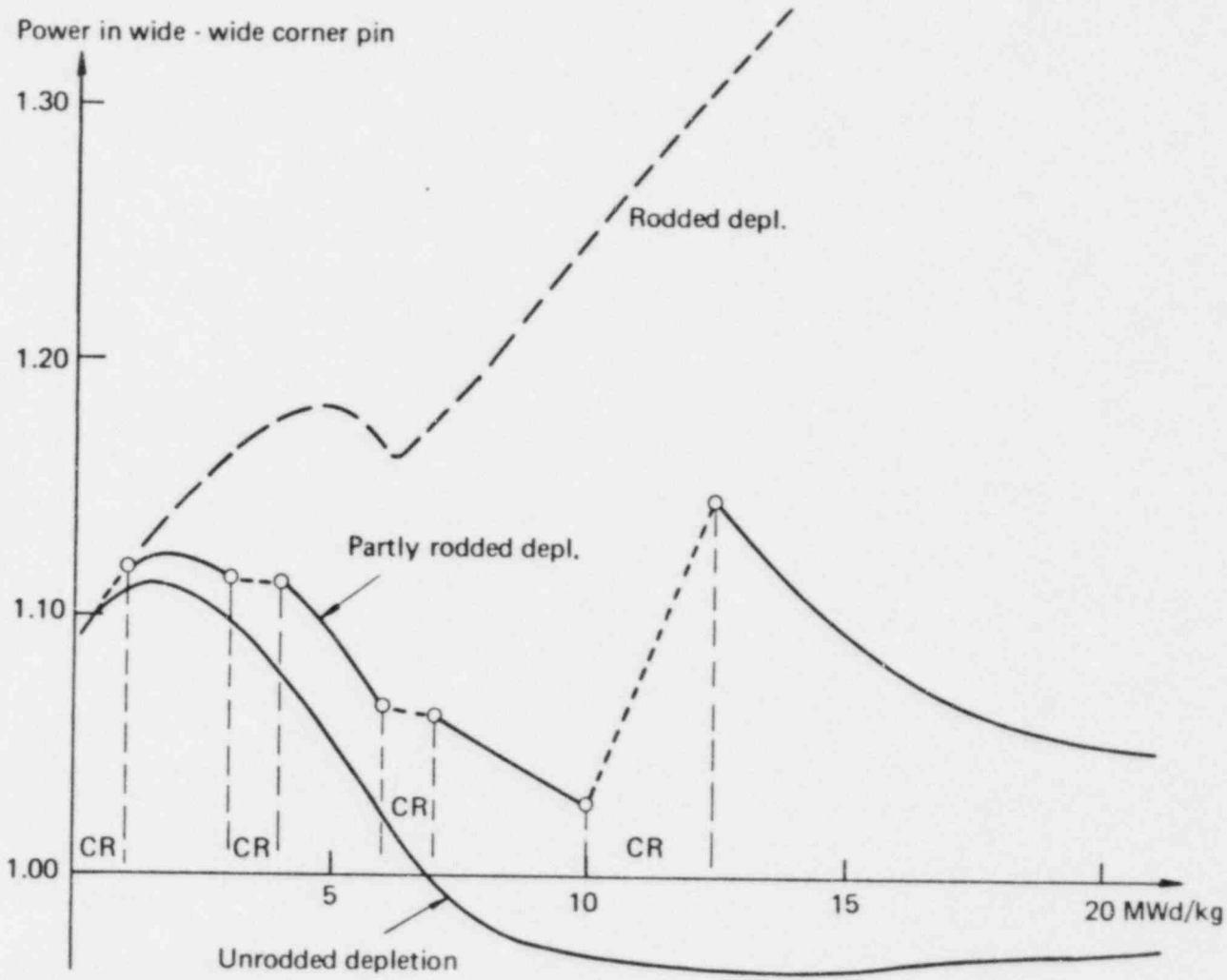

Figure 3. Power in corner pin for various control histories. 8x8 BWR with 4 Gd rods.
(The curves represent unrodded branches.)

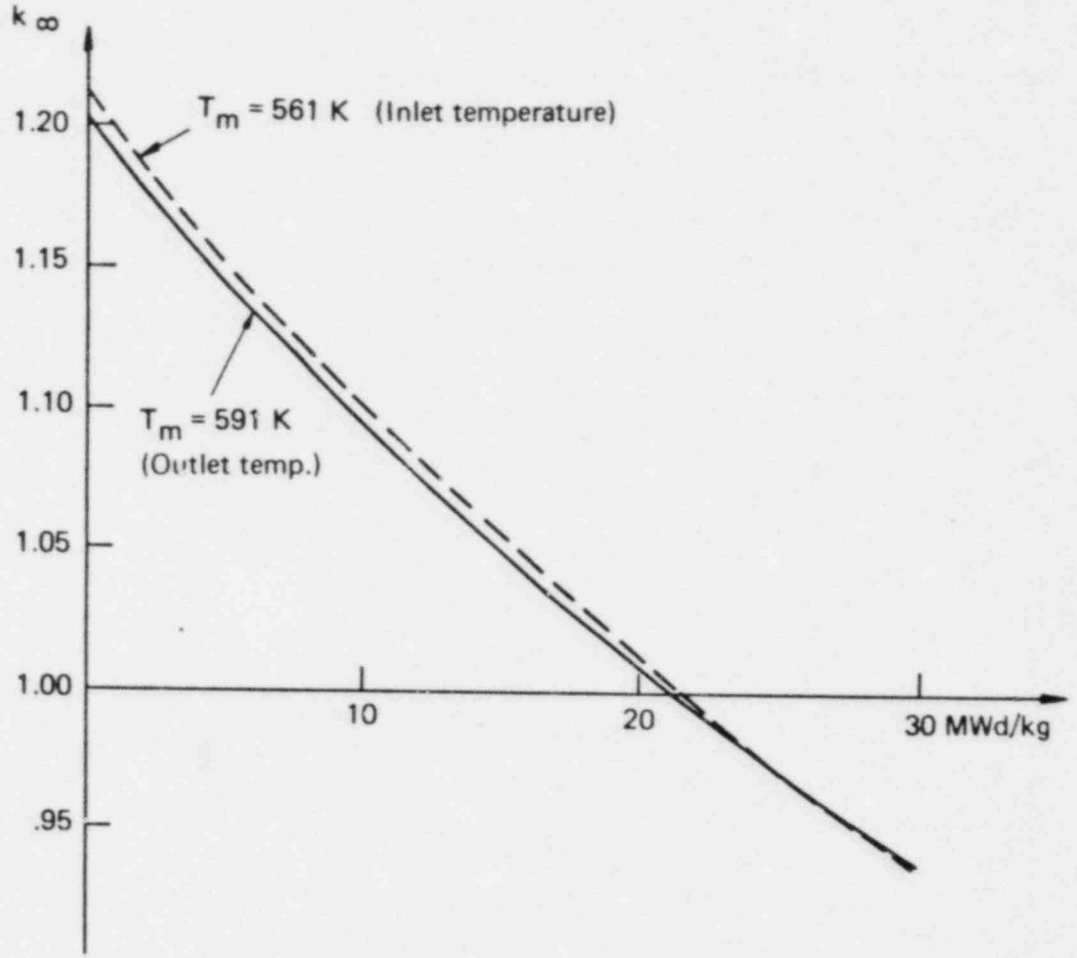

Figure 4. 17x17 PWR depletion with different moderator temperatures

Figure 5 Reactivity points for BWR assembly

Depletion condition	Branch	Exposure in MWd/kg 0	5	10	15	20	25	30
V0	U0	xxoxoxoooo xoooox	x x x x	x x x x	x	x
	U40	x x	x	x	x
	U70	x x	x	x	x
	TF	x x	x	x	x
	CT	x x x o	x	x	x
	C	x x x o	x o	x	x
	C+CT	x x x o	x	x	x
V40	U0	x x	x	x	x
	U40	xxoxoxoooo xoooox	x x x x	x x x x	x
	U70	x x	x	x	x
	TF	x x	x	x	x
	CT	x x x o	x	x	x
	C	x x x o	x o	x	x
	C+CT	x x x o	x	x	x
V70	U0	x x	x	x	x
	U40	x x	x	x	x
	U70	xxoxoxoooo xoooox	x x x x	x x x x	x
	TF	x x	x	x	x
	CT	x x x o	x	x	x
	C	x x x o	x o	x	x
	C+CT	x x x o	x	x	x
V0 CT	U0	x x o	x	x	x
	U0+CT	xxoxoxoooo xoooox	x x x x	x x x x	x

x = reactivity point for all assemblies
V = Void history
U = Instantaneous void
o = additional point for Gd-assembly (example)
TF = Fuel temp
CT = Control rod
C = Cold

Figure 6 Reactivity points for PWR assembly

Depl. cond.	Branch	Exposure in MWd/kg							
		0	5	10	15	20	25	30	35
V576	C0	x	x	x		x		x	
	U576/C400	xxx x x	x x	x x	x x	x	x	x	x
	C800	x	x	x		x		x	
	U591		x	x		x		x	
	TF	x	x	x		x		x	
	CT+C0	x	x	x		x		x	
	CT	x	x	x		x		x	
	CT+C800	x	x	x		x		x	
V591	C0	x	x	x		x		x	
	U591/C400	xxx x x	x x	x x	x x	x	x	x	x
	C800	x	x	x		x		x	

V = Moderator temp history (K) U = Instantaneous moderator temp (K) CT = Control rod

C = Boron concentration (ppm) TF = Fuel temperature

Note: Reactivity points for hot zero power (HZP) and also for V 561 and U 561 are frequently added to those shown in the figure.

Figure 7. BARSEBÄCK UNIT-2. HALF-CORE BASIS

F = FRESH FUEL
1 = CYCLE 1 (ONCE BURNED) FUEL
2 = CYCLE 2 (TWICE BURNED) FUEL
R = REINSERT (ONCE BURNED) FUEL

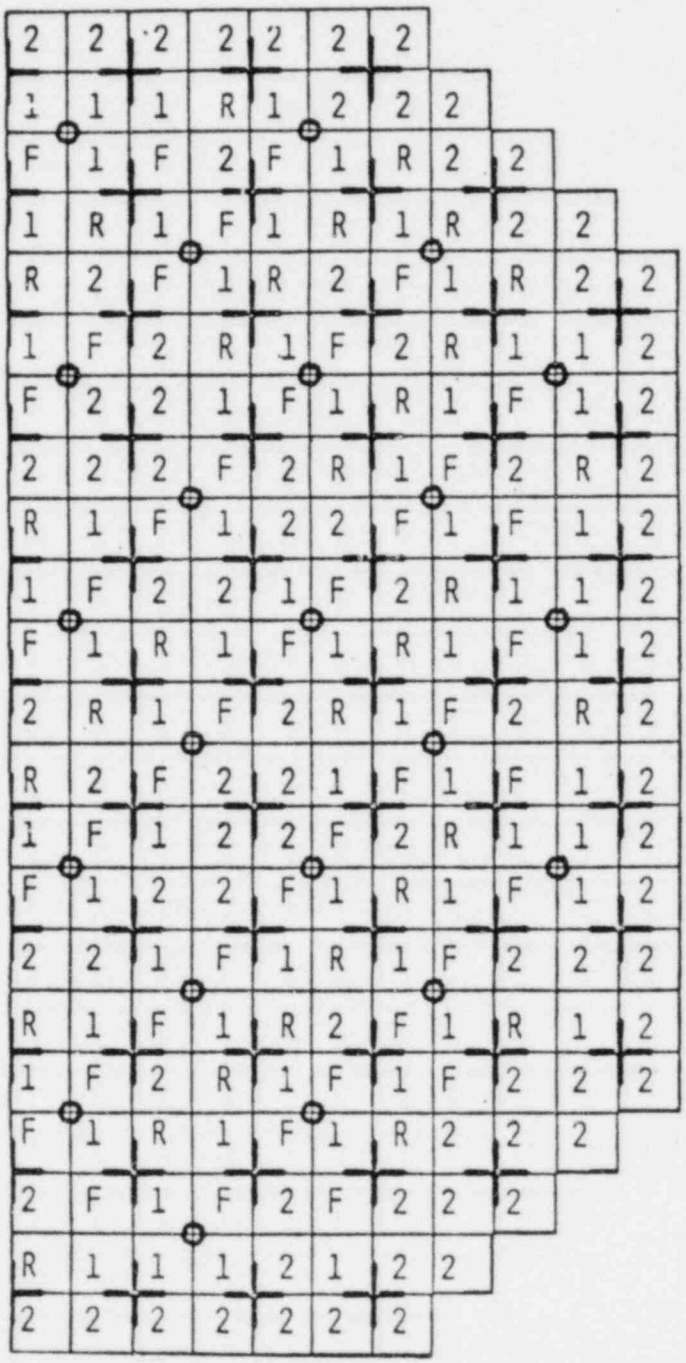

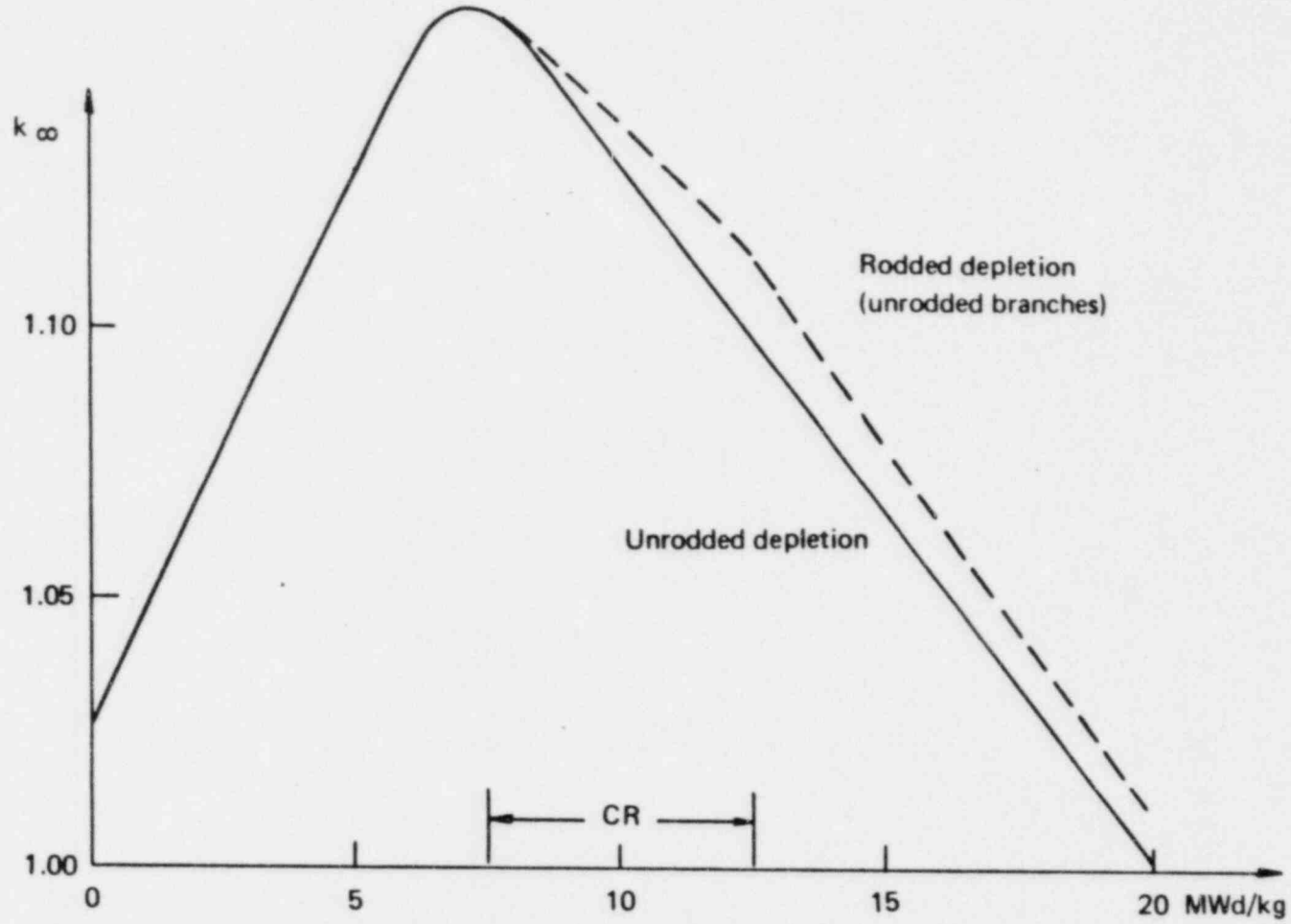

Figure 8. Control history in 8x8 bundle in diagonal loading. k_∞ versus burnup.

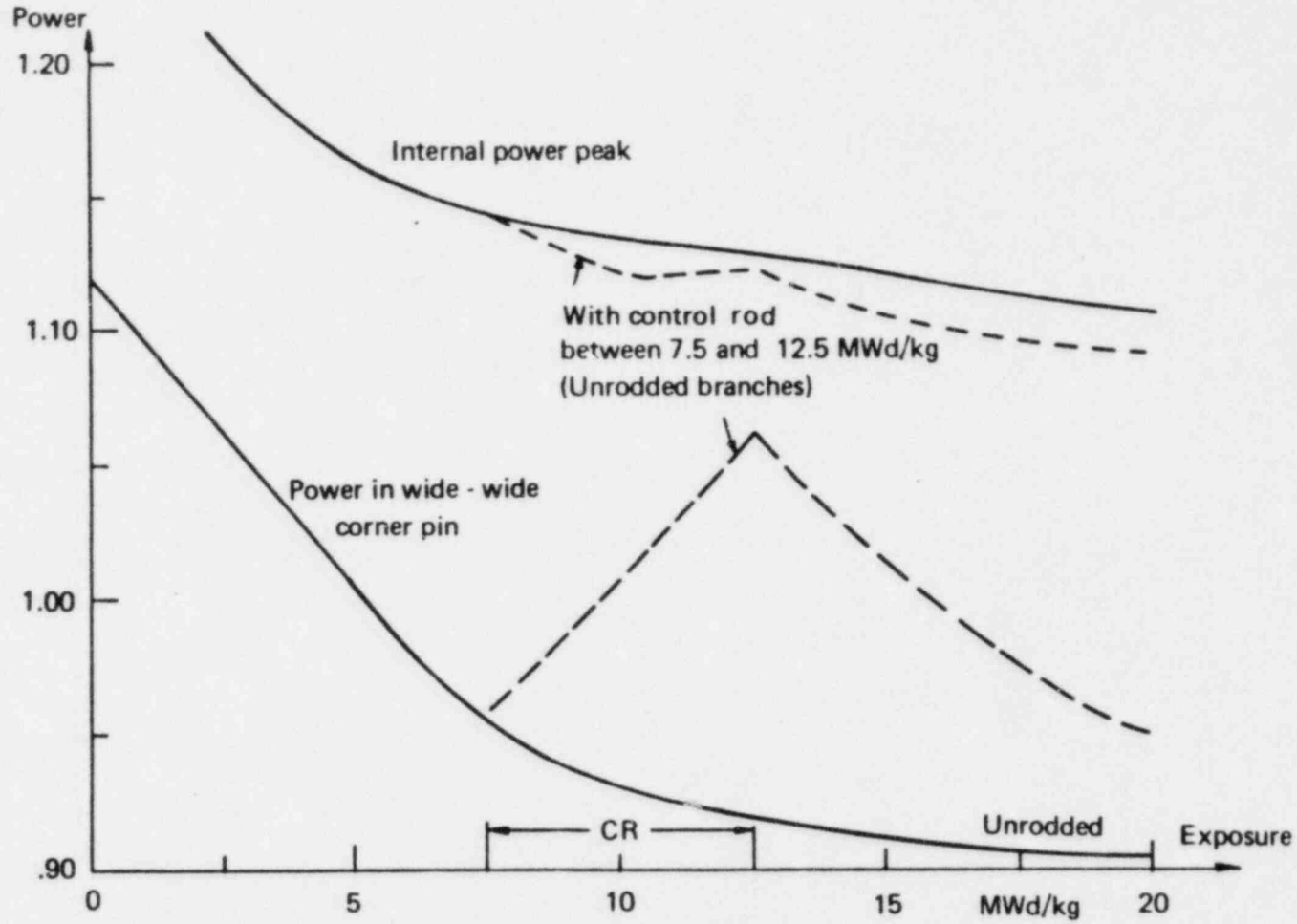

Figure 9. Control history in 8x8 bundle in diagonal loading
Power versus burnup

Figure 10 RECONSTITUTION OF FUEL

Oskarshamn 2 initial fuel at 18 MWd/kg U (0.92 w/o)

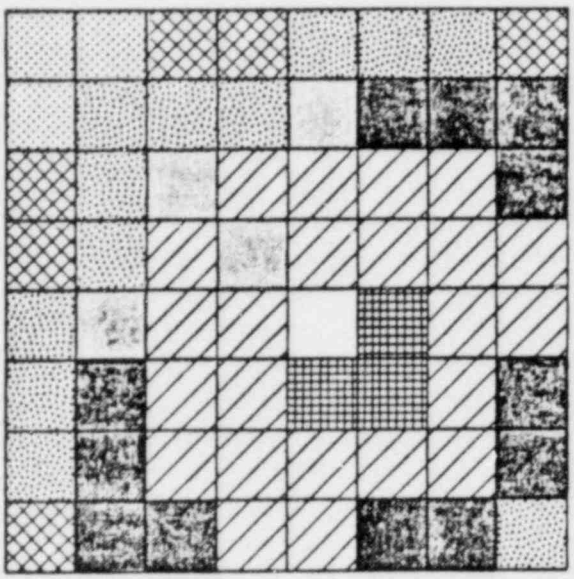

After reconstitution (1.17 w/o)

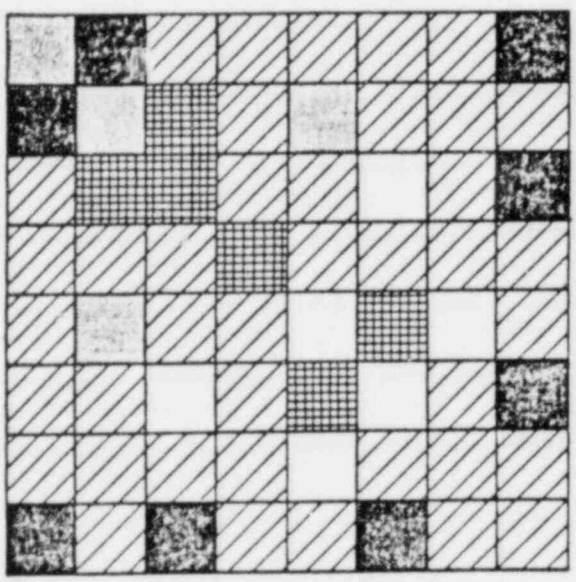

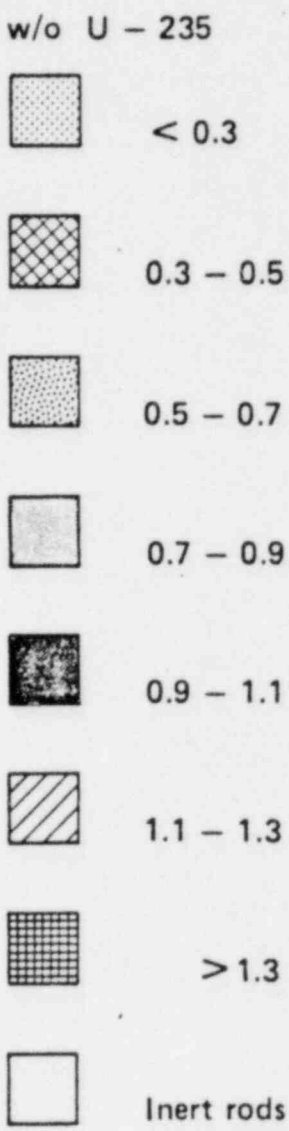

Reactivity Gain 8% Δk_{∞}

Figure 11. FUEL RECONSTITUTION IN OSKARSHAMN 2, 1982

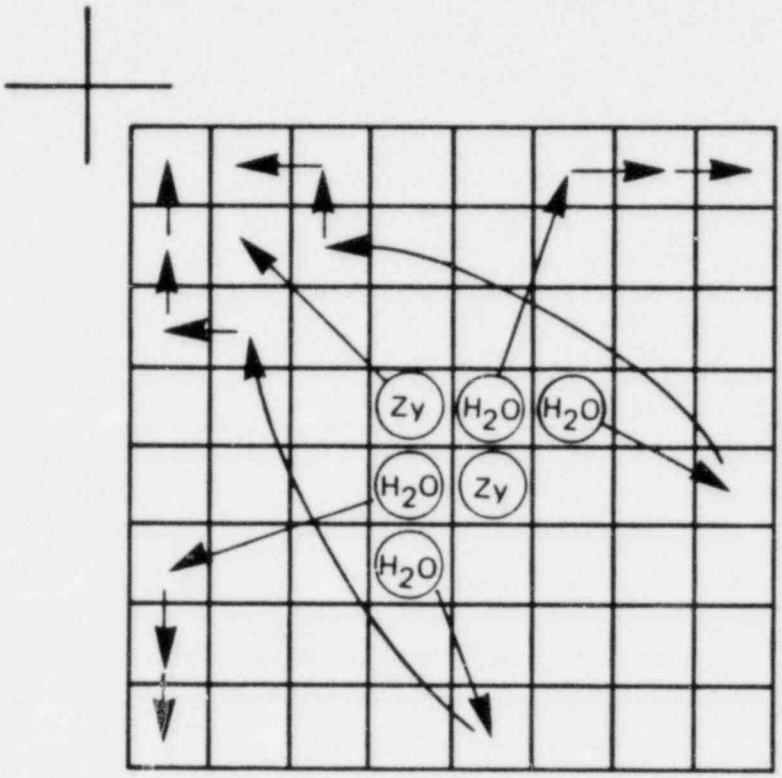

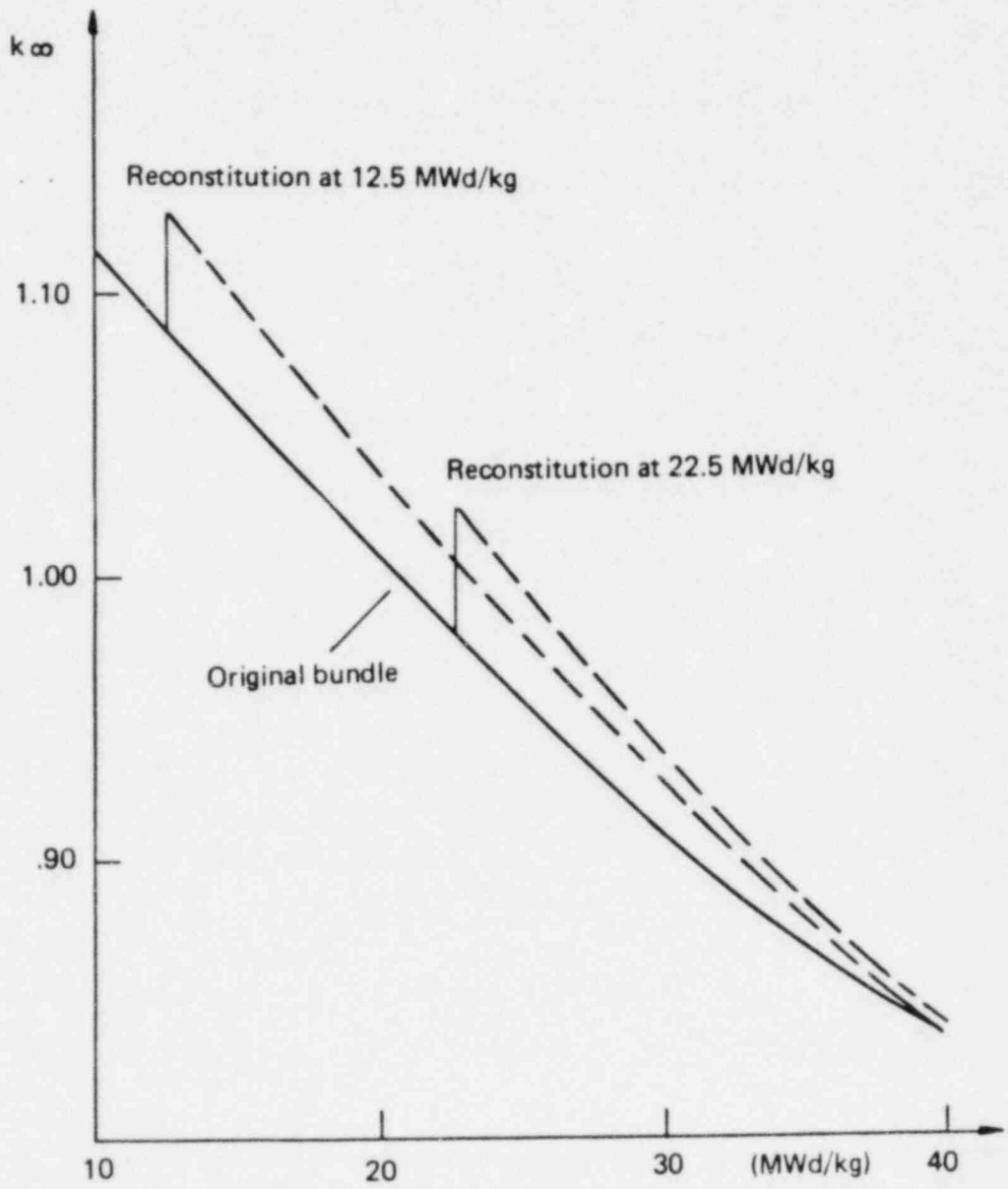

Figure 12. OSKARSHAMN 2
k_∞ before and after reconstitution.
Void = 40 %

Figure 13 Axial Burnable Absorber (BA) Grading in ASEA–ATOM Reload Fuel

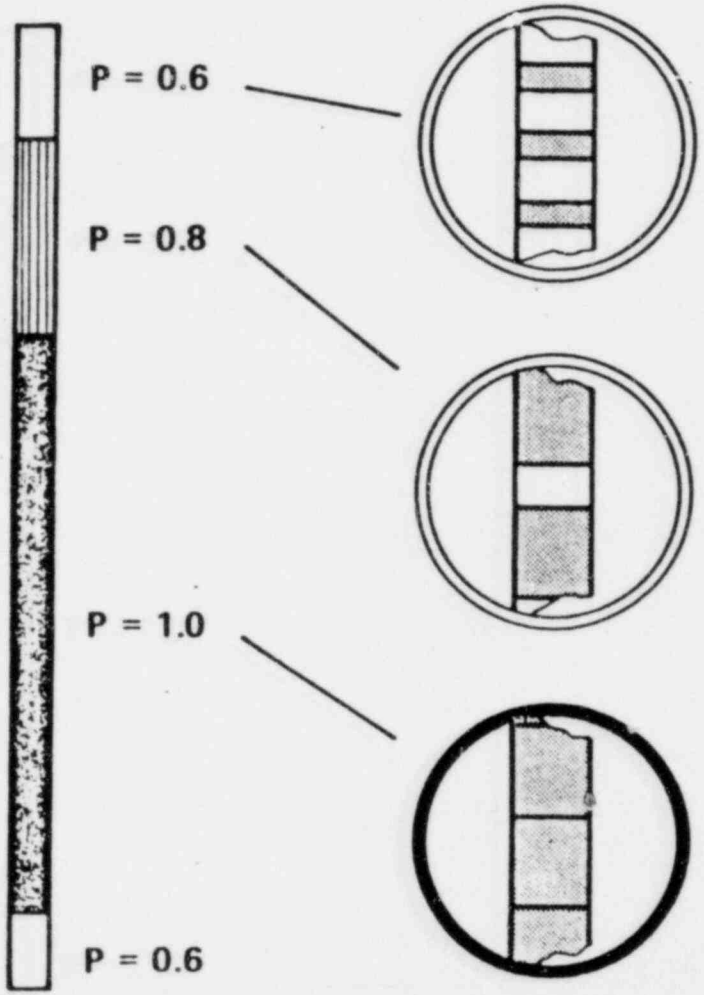

- Same Gd_2O_3 concentration in all BA pellets
- All BA rods can be identical
- Assists in axial power shaping
- Small residual Gd reactivity due to simultaneous burnup .

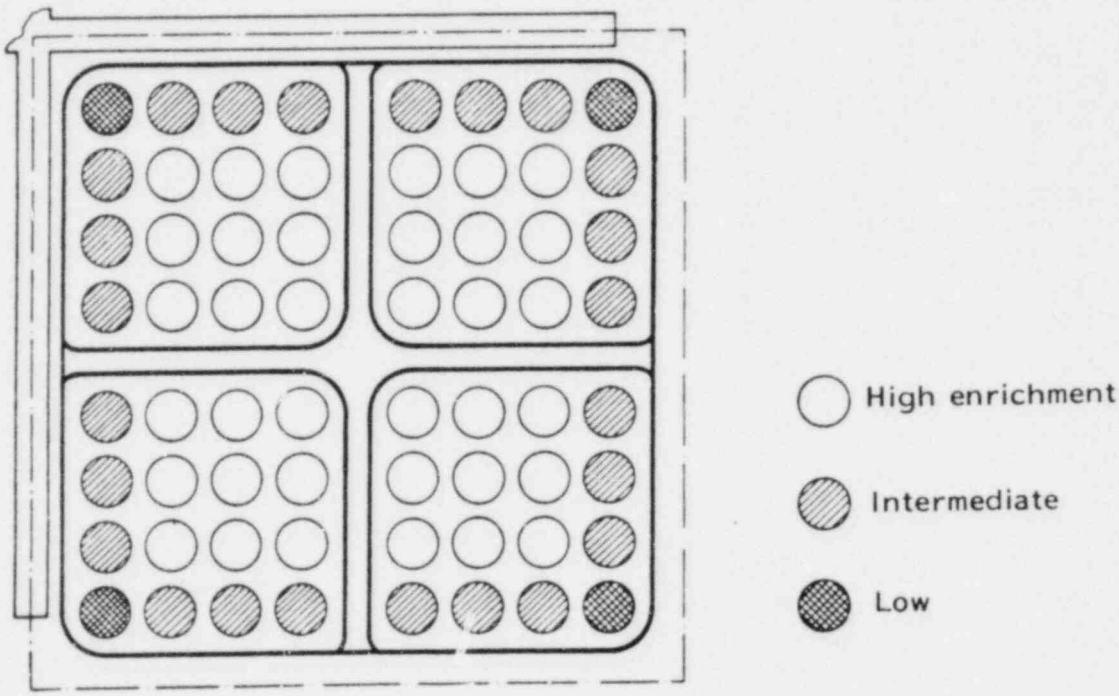

Figure 14. Cross section of a SVEA assembly cell with symmetric outer water gaps.

NEACRP LMFBR BENCHMARK CALCULATION INTERCOMPARISON FOR FUEL BURN-UP PRELIMINARY ANALYSIS

G. Palmiotti, M. Salvatorès, B. Ruelle
Centre d'Etudes Nucléaires de Cadarache
Boîte Postale N° 1
F.13115 - Saint-Paul-Lez-Durance
France

ABSTRACT

The paper presents a preliminary summary of the results of the international intercomparison of burn-up benchmark calculations for a LMFBR, proposed by the NEACRP. Ten solutions from eight different organizations were submitted.

The spread of the results is analysed in terms of spread on basic data, whenever possible.

1. INTRODUCTION

A burn-up calculation has been proposed |1|, on the LMFBR benchmark model |2|, and an intercomparison of the calculation results has been sponsored by NEACRP. In this paper, some preliminary consideration are presented on some major features of the exercise. In particular, the reactivity loss for the proposed fuel cycle (320 days), and the isotope build-up have been analysed, by means of same simplified sensitivity calculations. The spread of the results obtained is compared to same target accuracy requirements. When possible, basic data accuracy is analysed, using the one-group averaged cross-sections, provided by the benchmark participants.

Internal breeding gain and sodium void effect evolution from the beginning to the end-of-cycle value are also briefly analysed.

2. REQUIREMENTS OF DATA ACCURACY

Before analysing the benchmark calculation results it is useful to recall some of the data accuracy requirements that have been made for the so-called major and minor actinides in the past. These requirements have been made in general with respect to core integral parameter target accuracy requirements (see e.g. ref. |3| and |4|), but they have been specified also directly in connection with fuel burn-up requirements |4,5,6,7|. Moreover, the present state of the art has been reviewed in detail in ref. |8| and |9|. For what concerns fission product data, the proceedings of the Specialists' meeting on neutron cross-sections of fission-product nuclei, held in BOLOGNA, December 12-14, 1979, ref. |10|, summarize most of the present state of the art. For what concerns the heavy isotope data,

table I summarizes some of the required accuracies, some indications of the present uncertainties and the spread of the one-group data supplied by the benchmark participants. The cross-sections taken into account are the capture and fission cross-sections. The (n,2n) data will be presented separately. Some of the basis for the data accuracy requirements are also presented in table I, as they are stated by different authors. Table II summarized similar data concerning the pseudo-fission product cross-section data.

3. REACTIVITY LOSS RESULTS

The model and the description of the burn-up problem have been specified in ref. |1| and |2|.

One of the requirement for the participants was to supply the reactivity loss breakdown into the components :

ρ_1 : reactivity variation due to core heavy isotope concentration variation,
ρ_2 : reacitivity loss due to fission product build-up,
ρ_3 : reactivity gain due to heavy isotope build-up in the blankets.

Obviously, the total reactivity loss ρ is given by :

$$\rho = \rho_1 + \rho_2 + \rho_3$$

The results of the benchmark calculations are given in table III.

To analyse these results, a simplified one-group sensitivity calculation was performed, based on perturbation theory at first order.

3.1. Reactivity variation due to core heavy isotopes

The simplified sensitivity study was based on the following expression :

$$\rho_1 = \sum_i \delta N_i \, (\nu\sigma_f^i - \sigma_a^i \phi)\phi = \sum_i \rho_i \qquad (1)$$

(only U-238, Pu-239 and Pu-241 were considered in the sum over the isotope index i). To analyse the origin of the spread of the results of table III, the following expression was used :

$$\frac{\delta\rho_1}{\rho_1} \simeq \sum_i \frac{\rho(\delta N_i)}{\delta N_i} \frac{\rho_i}{\rho_1} + \sum_i \frac{\delta(\nu\sigma)^i}{\nu\sigma_f^i} b_F^i + \sum_i \frac{\delta(\sigma_a)^i}{\sigma_a^i} b_a^i \qquad (2)$$

The b_F^i and b_a^i are straightforward coefficients.

The $\delta(\nu\sigma_f)^i/\nu\sigma_f^i$ and $\delta(\sigma_a)^i/\sigma_a^i$ values can be obtained from the

data in table I. The $\delta(\delta N_i)/\delta N_i$ values can be related to data uncertainties by means of time dependent perturbation expressions [11] :

$$\frac{\delta(\delta N_i)}{\delta N_i} = \sum_{j,k} s_{ijk} \frac{\delta\sigma_{jk}}{\sigma_{jk}} \qquad (3)$$

where the build-up of isotope i is affected by the uncertainties of cross-sections type k of isotope j.

The main sensitivity coefficients s_{ijk} relevant to the U-238, Pu-239 and Pu-241 isotope density variations were calculated and are given in table IV.

Using expression (2), and the one-group data spread of table I, we were able to reproduce fairly well the standard deviation obtained using the direct K_{eff} calculation results of table III : ± 0.4% ΔK/K against the ± 0.5% ΔK/K value of table III.

It was possible to point out the relative contribution of the different data uncertainties to the overall data uncertainty. The results are given in table V.

For the benchmark data, the major role is played by U-238 σ_c and Pu-240 σ_c spread, followed by the σ_f spread of Pu-241 and Pu-239. To check if the data of the benchmark where representative of a more general situation, we also used the required data accuracies of table I. In this case, the standard deviation on ρ_1 would have been similar by slightly higher (± 0.5% ΔK/K), and the relative contribution of separate data would have been different, as it is indicated in table V. The major role is played by σ_c of U-238 and, complementary, by Pu-239 σ_f and it seems that a very stringent requirement is actually needed only for the σ_f of Pu-241, but that a somewhat more relaxed requirement (± 5 ÷ 8%) is needed for the σ_c of Pu-240 and Pu-241.

We have made a further test on the fuel burn-up reactivity effect ρ_1 in a large LMFBR of the SUPER-PHENIX type, with a fuel cycle of 480 days and using two different hypothesis on the origin of the Plutonium (gas-graphite or PWR reactors). Using the two set of uncertainties on data, one from benchmark data spread and the other from the most severe data accuracy requirements of table I, we obtained the results of table VI, which confirm the results of the benchmark calculations and the conclusions drawn above.

In summary, even stringent data requirements on heavy isotopes, cannot reduce the uncertainty of the component of the reactivity loss due to heavy isotope concentration variations to less than ∿ ± 0.5 ÷ 0.7% ΔK/K. To reduce this uncertainty, it would be essential a further reduction on the σ_c of U-238 accuracy requirements, which seems at present difficult to be met.

3.2. Reactivity loss due to FP build-up

One of the fairly surprising result of the benchmark calculations, is related to the relatively high spread of the results for the FP component of the reactivity loss, ρ_2.

Table II indicates a standard deviation, with respect to the mean value, of the one-group capture cross-section of the pseudo-fission product of ± 16.2%. The individual values of the σ_c^{FP} of the pseudo FP are shown in table VIII. On the contrary, the individual isotope cross-section data are not being analysed here.

Table III results indicate a spread on the mean value of ρ_2, corresponding to a standard deviation of ± 16%. Since in principle the discrepancies of ρ_2 should be attributed mainly to the discrepancy in the σ_c of FP, this result seems consistent.

However, a closer look to the data shows that not only the discrepancy on the one-group σ_c^{FP} plays a role, buth there is evidence for important spectral effects. For example, the discrepancy between the ANL and the CEA-2 solutions on ρ_2 is + 12.7%, and the discrepancy on σ_c^{FP} is + 24%. This effect can be due to :
1) pseudo-fission product cross-section characteristics (spectral shape of σ_c^{FP}, self-shielding, inelastic cross-sections) and low energy spectrum ; or,
2) to effects on ρ_2 due to the other cross-sections.

Sensitivity calculations based on generalized perturbation theory indicate that, e.g. the effects on ρ_2 due to U-238, Pu-239, Oxygen, stainless-steel and Na cross-sections variations of 10% should be of the following order of magnitude (values of $\delta\rho_2/\rho_2$ in percentage) :

Effect due to 10% variation of :	U-238	Pu-239	Oxygen	Na	SS
σ_a	- 3.4	- 2.6	0	0	- 0.5
$\sigma_{scatt.}$	+ 1.0	+ 0.1	+ 2.2	+ 1.0	+ 1.2

These effects are fairly small and should not contribute in a significant way to explain the above mentioned effect. Further investigation would then be needed in this field, in particular related :
1) to the spectral shape of the σ_c^{FP} used by the particpants ;
2) possible effects due to FP inelastic cross-sections.
It is worth noting that, if the benchmark results are confirmed, they would show some differences with the conclusions of the BOLOGNA Meeting [10] and would cast same doubts on the present ability to predict ρ_2 with an accuracy of ± 10%.

As a final remark, we think useful to remind that at CEA, a ± 16% uncertainty on ρ_2 is announced at present on design calculations, based on the combination of the following main uncertainties (partially correlated) :

σ_c^{FP} : ± 10%

yield : ± 8%

migration of gaseous FP : ± 3%

4. SODIUM-VOID RESULTS

Sodium-void reactivity coefficient evolution with burn-up is presented in table VIII. The spread of the results at EOC is very similar to that, already small, obtained for BOC data (∿ 8%). In this way, the results of ref. |1| are confirmed, as it is confirmed the result of some integral experiment analysis, in which the E-C/C on the sodium-void effect was found independent from, e.g. the Pu-240 content of the core |12|.

It is also confirmed that the σ_c^{FP} uncertainty affects the Na void effect in a relatively small way (according to ref. |13|, ± 30% on σ_c^{FP} would produce ± 1.7% on the non-leakage component of the Na void in a large LMFBR).

However, some remarks can ben made to explain some of the most discrepant results.

The average percentage value of the increase of the Na void effect is ≃ + 22%. Some solutions (CEA, JAERI) exibit a lower value. This result could be correlated to a low σ_c^{FP} value. In fact, this is the case only for the CEA solution. A further explanation can be found in the hardening of spectrum at EOC which makes the positive Na void component more positive. Actually, the F8/F5 ratio shows the smaller increase, between BOC and EOC, in the case of the CEA and JAERI solutions. Furthermore, both solutions were characterized by a less steep slope of the adjoint function at high energies |1|. All these factors explain the lower increase of the Na void effect between BOC and EOC.

5. OTHER INTEGRAL PARAMETERS

For this preliminary analysis, we should indicate that other integral parameters considered in the intercomparison, like reactions rate ratios, were not affected strongly by burn-up and no unforeseen supplementary uncertainties did show-up. As an example, the internal breeding gain value, which was affected at BOC by an absolute spread of approximately ± 0.03, has a similar spread at EOC (or slightly less).

6. ACTINIDE BUILD-UP

As a part of the benchmark exercise, a simplified burn-up calculation was requested, concerning the higher transactinides. Some of the results are summarized in table IX, where the results obtained for the build-up of Np-237, Pu-236, Pu-238, Pu-242, Am-241, Am-243, Cm-242 and Cm-244, are compared.

The dispersion of the data obtained is often of the order of magnitude of some target accuracy requirements |6,7|.

However, the case of Pu-236 is worth noting. The build-up of this isotope is directly related to the ^{237}Np(n,2n) data.

On this data, a large spread of values is presently observed, and this is reflected in the large dispersion obtained among the benchmark results ($\sim \pm 180\%$).

For all the previously mentioned isotopes, a sensitivity analysis was performed based on expressions of the type of (3), and some results are shown in table X.

Am-243

This data is strongly dependent on Pu-242 σ_c. A $\pm 20\%$ dispersion on this data is observed among the benchmark participants, and this correlates well with the $\sim \pm 22\%$ standard deviation observed.

Cm-242

A $\pm 12\%$ contribution to the observed standard deviation on the isotope build-up ($\sim \pm 26\%$) is due to Am-241 σ_c observed dispersion among participants. A complementary role is played by λ_β of Pu-241 (sensitivity coefficient s = 0.98), and λ_α of Cm-242 (sensitivity coefficient s = 0.39).

Cm-244

The uncertainties on σ_c of Pu-242 and σ_c of Am-243 are the most important contributors. If the observed spread of the benchmark data (incomplete in the case of Am-243 σ_c) is used, an approximate 24% contribution of the total $\sim 40\%$ observed deviation is found. More complete data on σ_c of Am-243 would be needed in this case.

Pu-238

In absence of detailed data on (n,2n) and λ data, the observed standard deviation ($\sim \pm 16\%$) is obtained if one uses the supplied data dispersion for σ_c of Np-237 ($\pm 9\%$), for σ_c of Am-241 ($\pm 13\%$), and estimated uncertainties of $\pm 30\%$ on the (n,2n) values of U-238 and Pu-239 and $\pm 10\%$ on λ_α of Cm-242. A more precise insight on the Pu-238 build-up will be obtained when more detailed informations on (n,2n) and λ data will be available.

7. CONCLUSIONS

At the present stage, only partial conclusions can be drawn. In particular, the fission product data spread and their effects on the reactivity loss during the cycle should be further investigated, and the rules used to prepare the lumped fission product capture cross section clarified. Moreover, it will be useful to identify the possible role of the fission product inelastic scattering data on the reactivity. As far as the reactivity loss due to the heavy isotope density variations, it seems that the present data accuracies (often inside the target specified by the various laboratories) are such that a not negligible uncertainty should be associated to this data, of the order of at least ± 0.5% ΔK/K.

Finally, for what concers the higher actinide data and the impact of their uncertainties, no definite suggestion can be made on the need of higher accuracy. The problem of Np-237 (n,2n) cross-section, leading to the production of Pu-236, is more related to the reaction branching ratio, which is presently being assessed by the different laboratories. However, comparison with experimental data (from irradiated full experiments in particular) should confirm that the type of spread observed in the benchmark, is also representative of the observed calculation/experiment discrepancies.

-o0o-

REFERENCES

|1| - L.G. Lesage et al., ANL-80-78 (NEACRP-L-243), (1980)
|2| - P. Hammer, NEACRP-A-439, (1980)
|3| - J. Rowlands, Int. Conf. on Neutron Physics and Nucl. Data Harwell, (1978)
|4| - P. Hammer, Int. Conf. Nucl. Data and Technology, Knoxville (1979)
|5| - P. Hammer, Int. Conf. on Neutron Physics and Nucl. Data, Harwell, (1978)
|6| - B. Patrick and H. Sowerby, NEANDC-174A, (1980)
|7| - L. Usachev et al., Int. Conf. on Neutron Physics and Nucl. Data, Harwell, (1978)
|8| - H. Küsters, Int. Conf. Nucl. Data and Technology, Knoxville, (1979)
|9| - J. Hirota and H. Mitani, Annals of Nucl. En. 7, 439, (1980)
|10| - Proc. Spec. Meeting on Neutron Cross-Sections of Fission Product Nuclei, Bologna, (1979). In particular, Report of Working-Group 1
|11| - See for example, A. Gandini, M. Salvatorès and L. Tondinelli, Nucl. Sci. Eng. 62, 339, (1977)
|12| - F. Lyon et al., Int. Conf. on Fast Reactor Physics, Aix-en-Provence, (1979)
|13| - A. Bultand, Int. Conf. on Fast Reactor Physics, Aix-en-Provence, (1979)

Isotope		Required accuracy (1σ)	Achieved accuracy (present uncertainty), (often quoted at 1σ)	Spread of Benchmark one-group data (1σ), (From references |1| |8| and |9|)
U-238	σ_c	3%(a,e)	8%(e)	2.1%
	σ_f	4%(e)	5%(e)	3.7%
Np-237	σ_c	10%(a) - 30%(b) - 15%(e)	50%(e) - 25%(c)	8.7%
	σ_f	50%(b)	10%(e) - 10%(c)	3.5%
Pu-238	σ_c	20%(b)	50%(c)	25.6%
	σ_f	7%(b) - 4%(d)	20%(c)	9.0%
Pu-239	σ_c	3%(a,e)	10%(e)	2.5%
	σ_f	2%(e) - 4%(e)	4%(e)	1.2%
Pu-240	σ_c	>3%(a) - 3%(d) - 4%(e)	20%(e) - 3%(b)	13%
	σ_f	>2%(a) - 3%(d) - 10%(e)	10%(e) - 5%(b)	3.2%
Pu-241	σ_c	>3%(a) - 5%(d) - 7%(e)	20%(e) - 20%(c) - 4%(b)	10.3%
	σ_f	>2%(a) - 2%(d) - 5%(e)	8%(e) - 5%(c) - 2%(b)	2.2%
Pu-242	σ_c	10%(a) - 15%(e)	50%(e) - 10%(c)	21%
	σ_f	10%(a) - 5÷10%(d) - 30%(e)	30%(e) - 5%(c)	6.1%

(a) J. Rowlands, Harwell 1978, Ref. |3|
(b) P. Hammer, Harwell 1978, Ref.|5|
(c) B. Patrick and H. Sowerby, NEANDC (174A), Ref. |6|
(d) P. Hammer, Knoxville 1979, Ref. |4|
(e) L. Usachev, Harwell 1978, Ref.|7|
(f) J. Hirota and H. Mitami, Annals of Nucl. En. 7, 439, 1980, Ref. |9|
(g) H. Küsters, Knoxville 1979, Ref. |8|

TABLE I

Isotope		Required accuracy (1σ)	Achieved accuracy (present uncertainty), (often quoted at 1σ)	Spread of Benchmark one-group data (1σ), (From references |1| |8| and |9|)
Am-241	σ_c	10%(a) - 5%(d) - 15%(e) - 8÷10%(c)	15%(e) - 20%(c)	13.3%
	σ_f	10%(a) - 3%(d) - 15%(e)	15%(e) - 10%(c)	18.8%
Am-243	σ_c	10%(a) - 10%(b) - 20%(e) - 10%(c)	50%(e) - 25%(c)	13.3%(f,g)
	σ_f	10%(a) - 30%(b) - 50%(e)	50%(e) - 10%(c)	7.9%(f,g)
Cm-242	σ_c	10%(a) - 50%(b) - 50%(e)	50%(e) - 50%(c)	10.3%(f)
	σ_f	10%(a) - 25%(b) - 50%(e)	50%(e) - 50%(c)	47%(f)
Cm-244	σ_c	10%(a)	50%(c)	23.7%(f,g)
	σ_f	10%(a)	20%(c)	6.6%(f,g)

Basis for requirements :

(a) Control-rod requirement : ±5% (±0.5% ÷ 1% in K_{eff} for irradiated fuel). Decay heat : 2 ÷ 5%
(b) ±5% on decay heat ; inherent source ±20% ; internal breeding gain ±0.02
(c) Production of : Pu-236, Am-241, Am-243, Cm-242, Cm-244 : ±100%(2σ). Production of Pu-238 : ±20%. α decay heat : ±5%
(d) Reactivity loss per cycle : ±0.5% ΔK/K (including FP effects). (Uncertainty in core critical mass for higher transactinides : ±0.2% ΔK/K and ±0.01% in internal breeding gain)
(e) Build-up requirements for (target accuracy) : Pu-236 ±30% (From various fast reactor fuel cycle particularities)
Pu-238 ±20%
Pu-240 ± 5%
Pu-241 ± 4%
Pu-242 ±10%
Am-241 ± 5%
Am-243 ±20%
Cm-242 ±20%
Cm-244 ±40%

TABLE I (followed)

Pseudo FP one-group σ_c	Required accuracy Ref. [1]	Spread of Benchmark one-group data (1σ)
	+10% (±5% for future cores)	± 16.5 %

TABLE II

ORGANIZ.	δKEFF(1)	δKEFF(2)	δKEFF(3)	δKEFF(4)
ANL	-0.01003	0.00565	-0.01940	0.00484
AUSTRAL.	-0.00541	0.00569	-0.01692	0.00690
CEA-2	-0.01275	0.00595	-0.01722	-0.00056
ENEA	-0.00678	0.00547	-0.01611	0.00666
EIR-1	-0.00735	0.00535	-0.01269	0.00065
JAERI	-0.01474	0.00561	-0.01870	-0.00074
KFK-1	-0.01582	0.00562	-0.02207	-0.00172
KFK-2	-0.01940	0.00487	-0.02181	-0.00239
KFK-3	0.0	0.0	0.0	0.0
UKAEA	-0.01727	0.00575	-0.02124	-0.00113
MEAN	-0.01217	0.00555	-0.01868	0.00139
ST. DEV.	0.00501	0.00031	0.00295	0.00370

δKEFF(1) global reactivity loss per cycle
δKEFF(2) reactivity gain due to Pu build-up in blankets
δKEFF(3) reactivity loss due to FP build-up
δKEFF(4) reactivity variation due to the core heavy isotope burn-up

TABLE III

Build-up of	Sensitivity to					
	σ_c(U-238)	σ_c(Pu-239)	σ_f(Pu-239)	σ_c(Pu-240)	σ_c(Pu-241)	σ_f(Pu-241)
U-238	- 0.86	-	-	-	-	-
Pu-239	6.65	- 1.48	- 4.43	-	-	-
Pu-241	-	-	-	0.52	- 0.18	- 0.99

Sensitivity coefficients s_{ijk}, according to equation (3)

TABLE IV

Hypothesis data uncertainties (Table I)	U-238	Pu-239		Pu-240	Pu-241	
	σ_c	σ_c	σ_f	σ_c	σ_c	σ_f
From benchmark data spread	.42	.03	.08	.34	.02	.11
From data accuracy requirements	.72	.03	.16	.01	.01	.07

TABLE V

RELATIVE CONTRIBUTION TO STANDARD DEVIATION ON ρ_1 (*)

(*) Contribution for cross-section i defined as :

$$f_i = \Delta_i^2/\Delta^2 \qquad \text{and} \qquad \text{St. dev.} \equiv \Delta = \sqrt{\sum_i \Delta_i^2}$$

$\Delta = \pm$ 0.4% $\Delta K/K$ for benchmark data and $\pm$0.5% $\Delta K/K$ when the most severe data accuracy requirements of Table I are used.

Type of fuel	Hypothesis of data uncertainties (Table I)	U-238	Pu-239		Pu-240	Pu-241	
		σ_c	σ_c	σ_f	σ_c	σ_c	σ_f
Gas-Graph. origin	From benchmark	.45	.06	.16	.17	0	0
	Accuracy Req.	.66	.05	.28	0	0	0
PWR origin	From benchmark	.41	.10	.09	.29	.02	.09
	Accuracy Req.	.67	.10	.17	.01	0	.05

TABLE VI

RELATIVE CONTRIBUTION TO STANDARD DEVIATION

ON ρ_1 (*)

(*) see footnote to Table V.

Standard deviations (depending on hypothesis of data uncertainties) on ρ_1 :

a) GG < ± .28% ΔK/K / ± .36% ΔK/K

b) PWR < ± .43% ΔK/K / ± .73% ΔK/K

ORG.	ANL	AUST.	CEA	ENEA	EIR	JAERI	KFK-1	KFK-2	KFK-2	UK	MEAN	ST. DEV.
Pseudo FP σ_c	.547	.375	.44	.43	.398	.561	.577	.579	.574	.52	.500	.0806

TABLE VII

PSEUDO-FISSION PRODUCT σ_c (barns/fission)

ORGANIZ.	SODIUM VOID		
	BOC	EOC	EOC-BOC / BOC
ANL	0.02278	0.02877	0.26295
AUSTRAL.	0.02305	0.02842	0.23297
CEA-2	0.02255	0.02600	0.15299
ENEA	0.02331	0.02943	0.26255
EIR-1	0.02428	0.03045	0.25412
JAERI	0.02710	0.03254	0.20074
KFK-1	0.02321	0.02851	0.22835
KFK-2	0.02025	0.02495	0.23210
KFK-3	0.0	0.0	0.0
UKAEA	0.02058	0.02514	0.22157
MEAN	0.02301	0.02825	0.22759
ST. DEV.	0.00201	0.00252	0.03455

TABLE VIII

INNER CORE SODIUM VOID WORTH

(ΔK/K)

ORGANIZ.	NP-237	PU-236	PU-238	PU-242	AM-241	AM-243	CM-242	CM-244
ANL	9.581E-07	2.082E-12	2.848E-07	3.238E-05	3.868E-06	2.059E-06	2.596E-07	1.837E-07
AUSTRAL.	1.878E-06	0.0	3.838E-07	3.258E-05	3.959E-06	1.739E-06	2.587E-07	1.104E-07
CEA-2	1.807E-06	2.414E-12	5.108E-07	3.195E-05	3.677E-06	2.766E-06	2.603E-07	3.507E-07
ENEA	1.500E-06	1.900E-11	3.600E-07	4.053E-05	3.900E-06	2.000E-06	2.900E-07	1.800E-07
EIR-1	1.230E-06	8.900E-18	3.490E-07	3.262E-05	3.946E-06	1.745E-06	2.830E-07	1.560E-07
JAERI	1.582E-06	6.821E-18	3.735E-07	3.306E-05	3.959E-06	1.650E-06	1.187E-07	0.0
KFK-1	1.582E-06	0.0	3.789E-07	3.273E-05	3.886E-06	2.211E-06	2.777E-07	0.0
KFK-2	1.558E-06	0.0	3.335E-07	3.330E-05	3.898E-06	2.857E-06	1.657E-07	1.196E-07
KFK-3	1.549E-06	0.0	3.285E-07	3.325E-05	3.911E-06	2.821E-06	1.638E-07	1.173E-07
UKAEA	1.286E-06	7.896E-13	4.089E-07	3.458E-05	3.826E-06	1.896E-06	2.747E-07	1.198E-07
MEAN	1.493E-06	4.048E-12	3.712E-07	3.370E-05	3.883E-06	2.174E-06	2.352E-07	1.672E-07
ST. DEV.	2.724E-07	7.396E-12	6.006E-08	2.503E-06	6.383E-08	4.721E-07	6.140E-08	7.970E-08

TABLE IX

HIGHER ACTINIDES BUILD-UP

Build-up of	Sensitivity to :					
Np-237	(n,2n) U-238	σ_c Np-237				
	0.97	- 0.11				
Pu-236	(n,2n) U-238	(n,2n) Np-237	σ_f Pu-236	λ_α Pu-236		
	0.98	1.00	- 0.12	- 0.07		
Pu-238	(n,2n) U-238	σ_c Np-237	(n,2n) Pu-239	λ_β Pu-241	σ_c Am-241	λ_α Cm-242
	0.38	0.36	0.31	0.30	0.28	0.21
Pu-242	σ_c Pu-241	σ_f Pu-241	σ_c Pu-242			
	0.23	- 0.05	- 0.10			
Am-241	σ_c Pu-240	σ_f Pu-241	λ_β	σ_c Am-241		
	0.10	- .20	0.97	- 0.17		
Am-243	σ_c Pu-241	σ_c Pu-242	σ_c Am-243			
	0.14	0.94	- 0.13			
Cm-242	λ_β Pu-241	σ_f Pu-241	σ_c Am-241	λ_α Cm-242	σ_f Cm-242	
	0.98	- 0.15	0.87	- 0.39	- 0.09	
Cm-244	σ_c Pu-242	σ_c Am-243				
	0.96	0.92				

Main sensitivity coefficients s_{ijk} according to equation (3)

TABLE X

IMPROVEMENT OF LINEAR REACTIVITY METHODS AND APPLICATION TO LONG RANGE FUEL MANAGEMENT

R. A. Woehlke and B. L. Quan

Yankee Atomic Electric Company
1671 Worcester Road
Framingham, Massachusetts 01701

ABSTRACT

The original development of the linear reactivity theory assumes flat burnup, batch by batch. The validity of this assumption is explored using multicycle burnup data generated with a detailed 3-D SIMULATE model. The results show that the linear reactivity method can be improved by correcting for batchwise power sharing.

The application of linear reactivity to long range fuel management is demonstrated in several examples. Correcting for batchwise power sharing improves the accuracy of the analysis. However, with regard to the sensitivity of fuel cost to changes in various parameters, the corrected and uncorrected linear reactivity theories give remarkably similar results.

INTRODUCTION

The linear reactivity method has been used previously to develop fuel management recommendations[1, 2, 3]. The derivation of the linear reactivity relationship[4] assumes that each batch of fuel receives the same burnup split (power share) during each cycle of residence in the core. This assumption is approximately true in most cases. The authors suspect that this is due to licensing constraints: An individual batch cannot be peaked high above reactor average. To do so would violate operating limits. Strictly speaking, however, the batch peaking (power share) does affect the cycle length and, therefore, the linear reactivity relationship.

The effect of batch power peaking on the linear reactivity relationship was studied by using a detailed 3-D SIMULATE model with two-group cross sections derived from CASMO[5]. Using BWR/3 fuel types, multiple cycles of full, half, third and quarter core reloads were depleted until equilibrium was achieved. The results of this study show that the linear reactivity relationship (core average burnup versus enrichment) is sensitive to the batch power sharing. This sensitivity may be reduced by modifying the linear reactivity equations with a batch peaking term. This modification has the effect of collapsing the linear reactivity relationship into a narrower band valid for a large spectrum of batch peaking and batch sizes. Correcting for batch peaking in this simple way improves the accuracy of linear reactivity methods by about 5% without requiring a lot of cumbersome detail.

To assess the impact of this improvement, several applications of linear reactivity were analyzed. A computer code OPTDIS was developed to generate fuel cycle economics based on either the corrected or uncorrected linear reactivity relationship. The sensitivity of the fuel cycle costs to all the major economic and operational parameters was studied.

In absolute terms, the peaking-corrected equation gives more accurate economic results. However, the fuel cost sensitivities generated from both the corrected and uncorrected linear reactivity equation are remarkably similar. Thus, previous studies which employed uncorrected linear reactivity theory remain generally valid.

IMPROVEMENT OF LINEAR REACTIVITY THEORY

A previous paper[2] generated a plant specific linear reactivity relationship from actual plant data. In retrospect, this method has two soft spots: First, statistically the equation generated was not well supported; only four cycles of data were available at the time. Second, the data came from transition cycles of changing fuel design, enrichment and batch size. It does not necessarily follow that the results were applicable to equilibrium cycles.

A second method of developing the linear reactivity relationship is to use detailed calculations. This overcomes the two major drawbacks of the previous method:

1) Any number of cycles of various enrichments may be generated.

2) The depletion may be repeated until equilibrium is reached.

The only question remaining is: How well does the detailed calculation compare with reality? In this study, a detailed 3-D SIMULATE model was used with two-group cross sections derived from CASMO. This specific model has been benchmarked[5] satisfactorily against eight cycles of Vermont Yankee and two cycles of Quad Cities operating data. It also compares closely with the Quad Cities gamma scans.

This study used four typical 8x8 BWR/3 fuel types of different enrichments and gadolinium loadings. Taking each fuel type individually; full, half, third and quarter core reloads were depleted to the end of full power life using the Haling option of SIMULATE. The process was repeated until equilibrium. Equilibrium was assumed to be reached when the cycle exposure varied by less than 50 MWD/MTU between successive reloads. Table 1 illustrates the resulting equilibrium burnups for each fuel type. Notice the small effect in core average burnup due to the variation in gadolinium content between the 2.74 w/o low Gd fuel (L) and the 2.74 w/o high Gd (H) fuel. This effect is small compared to the effect of batch peaking. Generally, smaller reloads (large n) have higher initial batch peaking; and core average burnup increases with initial batch peaking.

Least-square fitting the core average burnup from Table 1 gives the band of linear reactivity relationships enclosed by the two solid lines in Figure 1. The broadening due to batch peaking implies that detailed knowledge about the intended reload must precede any use of linear reactivity. This is not necessarily true: The cycle exposure and discharge exposure are not as sensitive to batch peaking as the core average exposure suggests. One may modify the linear reactivity equations by a batch power peaking correction term, C. For example:

$$\text{Batch Discharge Exposure, } B_d = \frac{2n}{n+1} CB_1 = \frac{2n}{n+1} B_{eff}$$

$$\text{Equilibrium Cycle Exposure, } B_c = \frac{2}{n+1} CB_1 = \frac{2}{n+1} B_{eff}$$

where B_1 is the core average burnup, and n is the number of reload batches per core. B_{eff} is called the "effective core average burnup". The correction factor, C, may be derived algebraically by weighting the batch power shares.

The dashed line in Figure 1 illustrates the improvement caused by using B_{eff}. The large uncertainty in the linear reactivity relationship has now been collapsed into a narrower region good for various values of n and initial batch peaking from 1.0 to 1.3. Beyond 1.3, the core would probably have difficulty getting licensed.

Table 1: Equilibrium burnups for typical BWR/3 fuel types and core loadings generated with SIMULATE.

Core Description		EOFPL Exposure (GWD/MTU)			Batch Relative Power Peaking		
Reload Size	Fuel Enrich.	B_C Cycle	B_l Core	B_d Disch.	Initial Peak	C Factor	B_{eff} (GWD/MTU)
Full:	2.190	9.414	9.414	9.414	1.0	1.0	9.414
n=1	2.740 (L)	15.198	15.198	15.198	1.0	1.0	15.198
Batch	2.740 (H)	15.023	15.023	15.023	1.0	1.0	15.023
	2.893	17.270	17.270	17.270	1.0	1.0	17.270
Half:	2.190	6.309	9.610	12.525	1.060	.981	9.429
n=2	2.740 (L)	10.419	16.083	20.817	1.089	.971	15.621
Batches	2.740 (H)	10.277	15.849	20.518	1.088	.972	15.402
	2.893	11.755	18.215	23.521	1.098	.968	17.637
Third:	2.190	4.901	9.976	14.033	1.163	.950	9.476
n=2.875*	2.740 (L)	8.282	17.203	23.785	1.208	.932	16.038
Batches	2.893	9.293	19.407	26.720	1.222	.928	18.006
Quarter:	2.740 (L)	6.454	17.520	25.818	1.288	.921	16.136
n=4	2.893	7.193	19.613	28.783	1.306	.917	17.986
Batches							

* Core studied was not exactly divisible by 3.

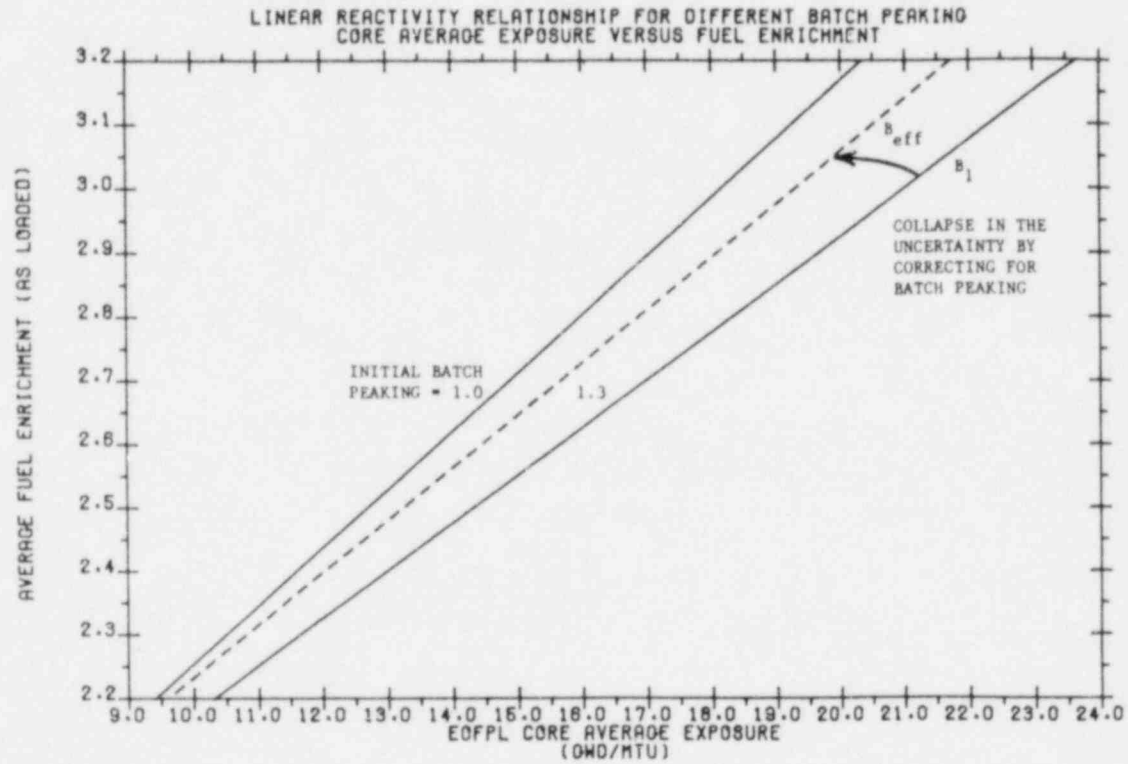

Figure 1: The solid lines show the uncertainty in linear reactivity caused by batch power peaking. The dashed line shows the improvement using B_{eff}.

APPLICATION TO LONG-RANGE FUEL MANAGEMENT

Linear reactivity methods are useful in long-range fuel management since they ignore fuel design and core loading details. This is at once a weakness and a strength. Linear reactivity would not be suitable for generating burnup data for safety and licensing. Its strength lies in detecting differences or trends between one operational strategy and some perturbed alternative. In this application it works cheaply and well.

A computer code, OPTDIS, was developed to study the fuel cycle economics of long-term (equilibrium) fuel management schemes. In the following studies, OPTDIS uses the corrected linear reactivity equation to generate any necessary burnup data. It has the capability of varying the economic parameters, number of batches, cycle length, discharge burnup, refueling period, etc. The output consists of direct and indirect nuclear fuel costs, plant and system energy costs (including replacement energy), outage costs and resource requirements.

A typical study using OPTDIS is the comparison of a standard 12-month cycle with various alternatives. This study uses the unit cost data shown in Table 2. These are typical economic parameters for a plant reaching equilibrium in the mid-1980's. The replacement energy costs are typical of a system loader dominated by oil.

Table 2: Typical economic parameters for a 500 MWe BWR in the mid-1980's.

Economic Parameter	Unit Price
U_3O_8 ($/lb)	50
Conversion ($/lbU)	4
Enrichment ($/SWU)	160
Fabrication ($/KgU)	220
Disposal ($/Kg HM)	280
Scheduled Replacement Energy Cost ($/MWhe)	60
Unscheduled Replacement Energy Cost ($/MWhe)	90
Incore Carrying Charge (%/yr)	15
AFUDC Interest Rate (%/yr)	15
Cost of Refueling ($Millions/Refueling)	10
Capital Expenses ($Millions/Year)	60

The standard base case is an equilibrium 12-month cycle, 4-batch core of approximately 2.85 w/o enrichment. A 92% capacity factor while operating and a 7-week refueling outage are assumed. The alternatives to be considered are extending the cycle length to 18 months, and/or, changing the number of batches.

The results are shown in Figure . For the 12-month cycle, decreasing the batch size relative to the base case causes the discharge burnup to increase. This better utilization of the fuel causes the total plant energy cost (total nuclear + operation and maintenance + refueling + capital cost) to decrease. The significant decrease in the 18-month cycle cases is mainly due to fewer refueling outages. At $10 million per refueling, not including replacement energy, the savings is substantial.

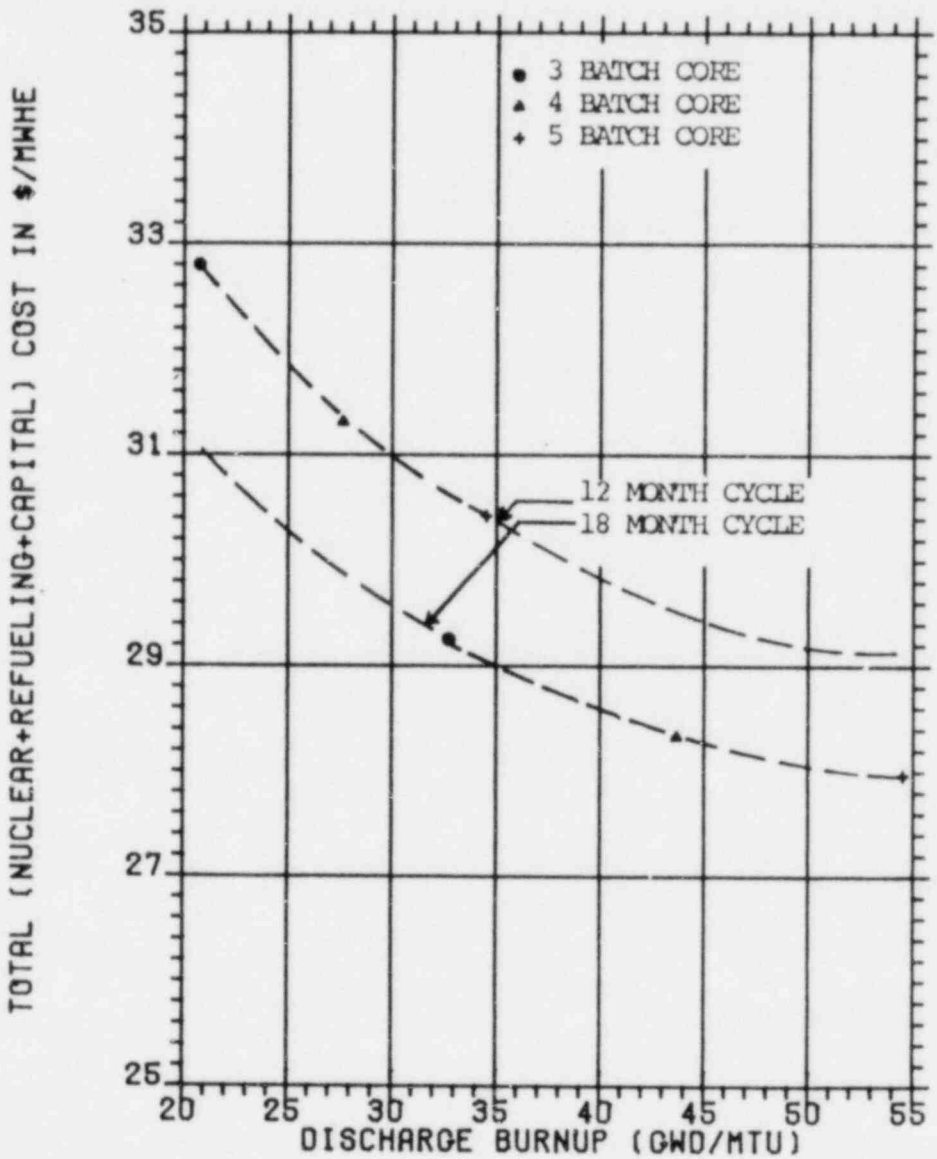

Figure 2: Total plant energy cost as a function of discharge burnup for various cycle lengths and batch sizes.

Studies of the preceding type use linear reactivity to define the gross differences between alternatives. This is only the first step. The feasibility of loading this type of cycle must be determined with detailed 3-D calculations.

Another use of OPTDIS which is well suited to linear reactivity theory, is exploring the sensitivity of fuel costs to changes in various parameters. By definition, the perturbation from the base case is very small in a sensitivity study; the core characteristics are similar. Again, using the same base case: It is observed in Table 3 that the U_3O_8 price has more impact on the fuel cost than the price of SWU. However, the operational capacity factor overshadows all other parameters in importance.

Table 3: Sensitivity of nuclear fuel cycle cost, plant and total system energy cost to various parameters.

	Fractional Change in Cost Per Fractional Change in Input Parameter				
	Case A	Case B	Case C*	Case D	Case E*
Total Nuclear Fuel Cycle Cost ($/yr)(1)	.403	.352	-.138	.348	+.865
Total Plant Energy Cost ($/yr)(2)	.157	.136	-.054	.135	+.336
Total System Energy Cost ($/yr)(3)	.149	.132	.222	.129	-2.427

(1) Includes Direct Nuclear, AFUDC and Incore Carrying Charges.

(2) Defined here as Total Nuclear Fuel Cycle Cost + O&M Cost + Refueling Cost + Capital Cost in $/yr.

(3) Defined here as Total Nuclear Fuel Cycle Cost + Refueling Cost + Replacement Energy Cost in $/yr.

Base Case: 4-batch, 12-month cycle described previously in text.

Case A: Change U_3O_8 Price.

Case B: Change SWU Price.

Case C: Change Refueling Time Period.

Case D: Change AFUDC and Incore Interest Rates.

Case E: Change Capacity Factor.

* Maintaining constant discharge burnup and cycle length as base case.

DISCUSSION AND CONCLUSIONS

This study shows that the linear reactivity relationship (core average burnup versus enrichment) is, in fact, a broad band of equations sensitive to batch peaking. This sensitivity can be significantly reduced by defining an effective core average burnup. The resulting corrected linear reactivity relationship is much more narrow. Its use does not require detailed core and fuel design data.

The method of applying linear reactivity theory to economic analysis is important. Linear reactivity is best applied to situations where a familiar base case is compared to some perturbed alternative. In this way, there is an implied similarity between the fuel designs and reloading characteristics. This is typically the case due to licensing constraints. This is always the case in sensitivity studies, for which, linear reactivity methods are well suited.

Regarding past work based on the uncorrected linear reactivity relationship: The correction is not large enough to change the outcome of past studies. This is due to the fact that the corrected and uncorrected linear reactivity relationships have similar slopes. In any sensitivity or perturbation application the differences are a function of the slope. For example, linear reactivity might typically be applied to determine the cost benefits of a proposed new fuel design. How much increased fuel fabrication cost could be absorbed if the new fuel design increases discharge exposure limits from 28,000 to 32,000 MWD/MTU? This problem was tackled using OPTDIS with both the corrected and uncorrected linear reactivity relationships. The results are presented in Table 4.

Table 4: Savings in total nuclear fuel costs achievable by increasing discharge burnup exposure limits. The three cases were generated by OPTDIS using three different linear reactivity relationships.

Case	Description	Batch Burnup GWD/MTU	Total Nuclear Cost (M$/Year)	Fuel Design Change Savings (M$/Year)
I	Flat Batch Peaking = 1.0	28.0 32.0	41.645 39.549	2.096
II	Initial Batch Peaking = 1.3, B_{eff} Correction	28.0 32.0	40.461 38.269	2.192
III	Initial Batch Peaking = 1.3, No Correction	28.0 32.0	38.897 36.583	2.314

Assuming that batch peaking is flat (Case I) underestimates the savings by about $100,000. Not correcting for batch peaking (Case III) overestimates the savings by about $120,000. Accounting for batch peaking by correcting core average burnup B_1 to yield B_{eff} (Case II) improves linear reactivity accuracy by about 5%. However, these small changes are not significant compared to the overall savings of two million dollars per year. The final decision would be the same regardless of the linear reactivity equation used.

ACKNOWLDGEMENT

We wish to thank Dr. Edward E. Pilat for his invaluable assistance and expert consultation on this paper. This study was undertaken in support of the Vermont Yankee Nuclear Power Station.

REFERENCES

1. H. Y. Watt and E. E. Pilat, "Optimal Coastdown Duration for Yankee Rowe," Trans. ANS, Vol. 22 (321), 1975.

2. P. Antonopolous and R. A. Woehlke, "Vermont Yankee 18 and 12-Month Cycle Economics," Trans. ANS, Vol. 32 (408), 1979.

3. B. L. Quan, et al., "Sensitivity Analysis of Equilibrium Fuel Cycles with Power Coastdown," Trans. ANS, Vol. 35 (75), 1980.

4. E. E. Pilat, "Session 15 - Fuel Reload Synthesis," NUS Fuel Management Workshop, May 7, 1973.

5. D. M. VerPlanck, Methods for the Analysis of BWR Steady-State Core Physics, YAEC-1238, March 1981.

EFFECTS OF TRANSITION TO LUMPED BURNABLE POISON EIGHTEEN-MONTH RELOAD CYCLES ON THE AGREEMENT OF MEASURED AND PREDICTED CORE PHYSICS PARAMETERS

J. J. Woods, A. R. Long, D. D. Shelburne, G. E. Hanson
Nuclear Power Generation Division
Babcock & Wilcox

In recent years, the majority of B&W's customers have converted to the more economical 18-month fuel cycle. The 18-month cycles reduce the number of refuelings and offer greater capacity factors resulting in lower system operating costs. The 18-month fuel cycle, however, requires an increased fuel loading necessitating the placement of some fresh assemblies in the core interior and the use of lumped burnable poisons (LBP). To further improve the economics of 18-month cycles, B&W has provided its customers with the advanced low leakage in-out-in fuel management strategy that we pioneered in the late 1960's. With this strategy, all the fresh assemblies are loaded in the core's interior and contain LBP clusters. Surrounding the fresh assemblies are twice-burned assemblies, while the once-burned assemblies are loaded on the core periphery, giving a low radial leakage.

This strategy places additional demands on the core physics models. In particular, the worth of the LBP must be precisely modeled. In addition, the flux gradients and spectral interaction between fresh and twice-burned fuel, within the fresh assemblies and the core periphery, must be correctly predicted by two-group diffusion theory models to provide the same highly accurate calculations that characterize our non-LBP cycle designs.

This paper demonstrates that the standard physics models B&W used on its first nine 18-month, LBP fuel cycle designs accurately predicted the neutronic characteristics of the cores.

The comparison of calculated physics parameters to data measured during startup testing has been used to verify core operation, to verify design input to safety analysis, and to improve core physics analysis techniques. This is especially true when considering low leakage fuel management, longer cycle length, and the additional variable of added LBP. All of the factors impact hot zero power physics parameters and the hot full power radial power distribution. Comparisons in this paper include: all rods out critical boron, differential boron worth, control rod worth, temperature coefficients and full power radial power distributions.

Figure 1 presents a comparison of measured and predicted hot zero power all rods out critical boron concentrations (AROCBC's). Critical boron concentrations were calculated with a two-dimensional homogenized assembly PDQ model. Nuclide concentrations were obtained from two-dimensional pin by pin assembly calculations. The solid line in Figure 1 represents ideal agreement between the measured and predicted AROCBC's. The agreement for both LBP and non-LBP cores is very good. The average difference between measured and predicted AROCBC's is only 3 ppmb for non-LBP cores and -8 ppmb for LBP cores. All non-LBP predictions are within ±31 ppmb of the measurements. This is much less than the acceptance criterion on critical boron concentrations of 1% $\Delta\rho$ (delta reactivity), or about 100 ppmb. The standard deviation of the non-LBP data is ±17 ppmb, which is close to the estimated measurement uncertainty of ±15 ppmb.

Predictions for LBP reloads were within ±44 ppmb with a standard deviation of ±26 ppmb. The somewhat greater spread in the data for the LBP reloads reflects the added complexity of modeling the interfaces between LBP and non-LBP regions in the homogenized model.

Comparison of measured and predicted differential boron worths (DBW's*) is illustrated in Figure 2. Measured boron worth is determined from data obtained during control rod worth measurements. Boron worth is calculated using the same homogenized assembly model used to predict AROCBC. All measured and predicted differential boron worths agree within the estimated measurement uncertainty of 10% and are well within the 15% acceptance criterion for the test. The observed standard deviations of the data are less than the measurement uncertainty. DBW's for LBP cores appear to be slightly underpredicted but the magnitude of this difference is insignificant. The excellent agreement between measured and predicted boron worths demonstrates the accuracy of the calculational models for LBP as well as non-LBP shuffle schemes.

Measured and predicted total worths of control rod banks 5-7 at hot zero power are compared in Figure 3. Control rod worths are predicted with the PDQ pin by pin model to best represent the interface between rodded and non-rodded regions within the fuel assembly. As seen in Figure 3, this model predicts rod worth very accurately for both LBP and non-LBP cores. The average differences of -0.119 and 0.051% $\Delta\rho$ for non-LBP and LBP reloads, respectively, correspond to only 3.5% and 1.5% of the measured total worths. None of the differences between the measured and predicted worths for LBP cores exceeded the estimated measurement uncertainty of 7.1% of the non-LBP cores; all were within the 10% acceptance criteria. The actual observed standard deviations for both LBP and non-LBP cores were even less than the 7.1% measurement uncertainty.

The comparison of measured and predicted ejected rod worths (ERW's) is shown in Figure 4. Ejected rod worth is calculated with the same 2-D PDQ pin by pin model that is used to predict control rod worth. All measured worths are within the B&W recommended acceptance criteria of .2% $\Delta\rho$ of the predictions. In all but two cases the measured and predicted worths agreed to within .14% $\Delta\rho$. The observed standard deviations of the data are similar for the LBP and non-LBP cores. The ERW's tend to be slightly overpredicted for LBP cores but no bias is apparent for cores with no LBP.

Isothermal temperature coefficients are measured at hot zero power with control rod Groups 5-7 fully withdrawn and with Groups 5-7 inserted. The coefficients are predicted with the homogenized assembly PDQ model. Figure 5 compared measured isothermal temperature coefficients to predictions. In all cases, measured and predicted worths are well within the test acceptance criterion of ±.4% $\Delta\rho$ and in most cases are within ±.2% $\Delta\rho$. The agreement between measured and predicted coefficients is similar for LBP and non-LBP cores for both rods-out and rods-in conditions. The predictions show a slight but insignificant negative bias for both types of cores.

Power distribution comparisons are made during startup at 40, 75 and 100% power. The calculation for the comparisons are made with the three-dimensional nodal code FLAME. A comparison of an LBP rodded beginning of cycle (BOC) radial power distribution is shown in Figure 6. Note the excellent agreement between

*DBW - change in reactivity/change in boron

the measured and predicted relative power density in the peak assembly at core grid location H, 11. The overall standard deviation of 2.4% for all radial peaks also shows excellent agreement. Similar agreement has been noted for all LBP reload cycles. Figure 7 is a comparison of a typical non-LBP reload radial power distribution. This comparison is very similar to the LBP core with excellent agreement not only in the peak location but also in the overall distribution.

Power distribution comparisons are also made between calculated and measured values throughout the core lifetime. Figure 8 shows a typical end of cycle (EOC) comparison for an LBP core. This comparison shows a decrease in the standard deviation of the radial peaks with cycle lifetime. This is typical of most cases. Table 1 summarizes the standard deviation from a sampling of several plants. This data shows a slightly better agreement with LBP cores than with non-LBP cores. This trend is attributed to the fact that the later LBP cycles contain improved incore detectors compared to those present in the non-LBP cycles.

Table 2 summarizes the agreement between the PDQ predictions and measured physics parameters in progressing from non-LBP reloads to LBP reloads.

Data from B&W's continuing results engineering effort demonstrate that, even with the use of LBP low leakage fuel management, B&W's two-group diffusion theory codes and models accurately predict core performance. The correct treatment of the flux gradients and spectral interaction between fresh and twice-burned fuel, within the fresh assemblies and on the core periphery, has been confirmed. The results also provide added confidence that these same models will be adequate when applied to more advanced fuel cycle strategies such as axial blankets and extended burnup.

Table 1

Radial Power Distribution Comparisons

	Non - LBP Cycles			LBP Cycles			
Plant	A	B	C	D	E	F	G
BOC Radial RMS	2.62	4.04	4.33	3.04	2.66	3.23	1.86
MOC Radial RMS	2.76	3.88	3.84	2.79	1.82	2.62	1.87
EOC Radial RMS	2.83	2.75	3.70	2.77	----	2.25	1.82
Overall Average RMS		3.42		2.42			

Table 2

Average Differences Between Predicted and Measured

Physics Parameters for LBP and Non-LBP Reloads

	Non-LBP Reloads		LBP Reloads	
	Average Difference*	Standard Deviation	Average Difference*	Standard Deviation
All rods out critical boron, ppm	3	17	-8	26
Differential boron worth, $\%\Delta\rho/100$ ppm	.010	.030	-.021	.021
Control Rod banks 5-7 total worth, $\%\Delta\rho$	-.119	.143	.051	.096
Ejected control rod worth, $\%\Delta\rho$	-.008	.093	.020	.099
Temperature coefficient, $X10^{-4}\Delta\rho°F$				
All rods out	-.06	.16	-.13	.08
Banks 5-7 in	-.06	.09	-.03	.06

*Predicted-Measured

Figure 1

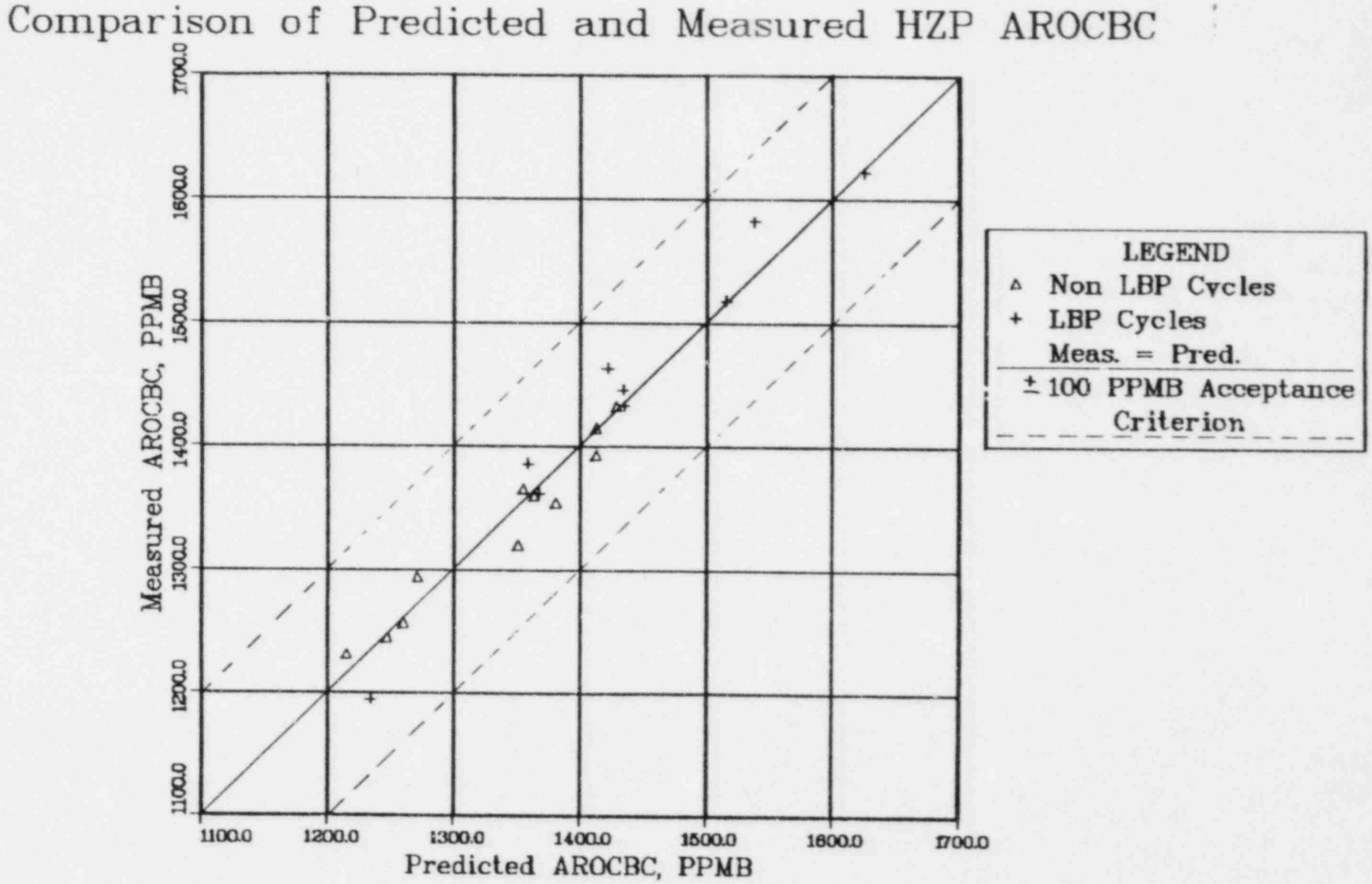

8911.1768

Figure 2

Comparison of Measured and Predicted HZP DBW

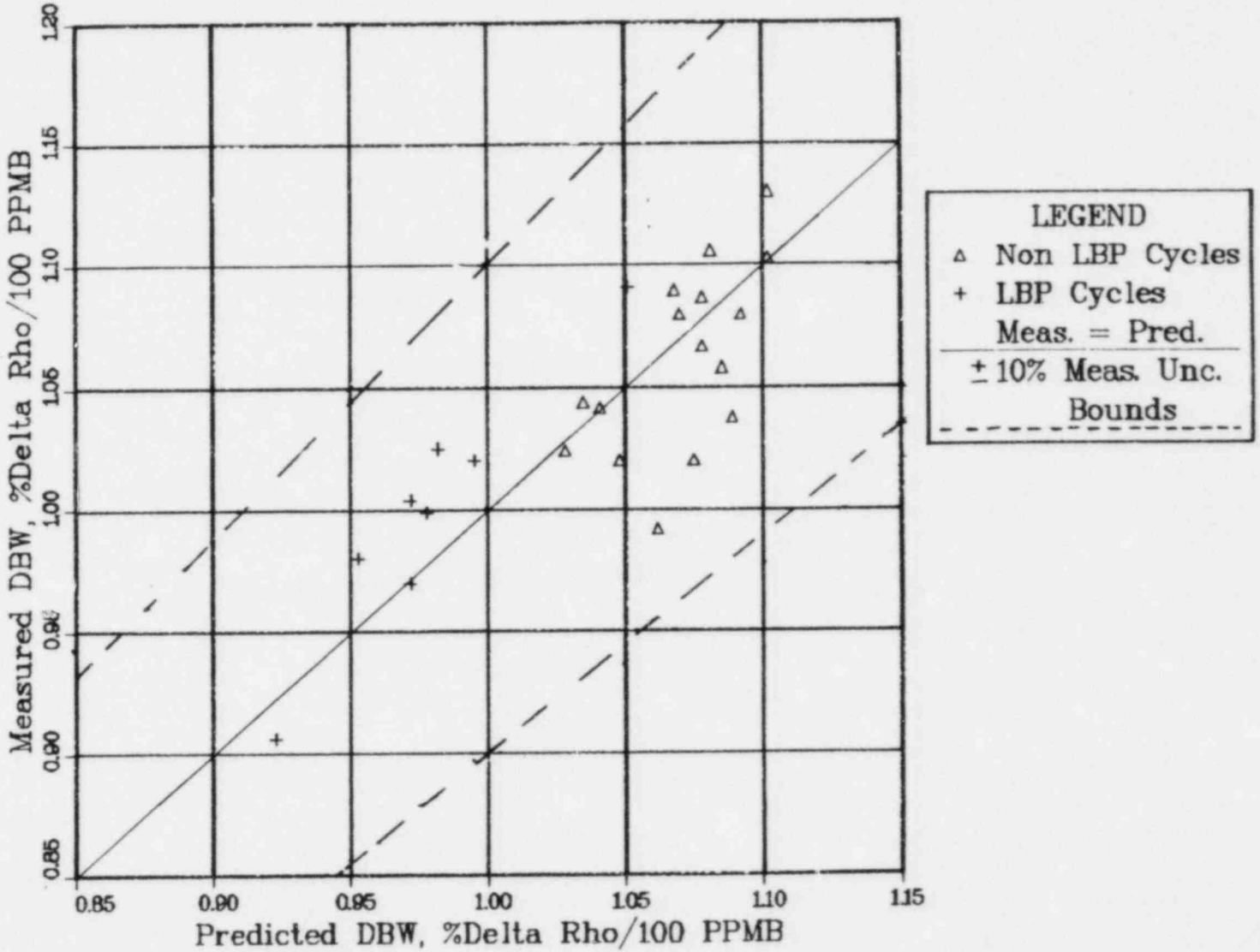

Figure 3

COMPARISON OF PREDICTED,MEASURED HZP REG BANK WORTHS

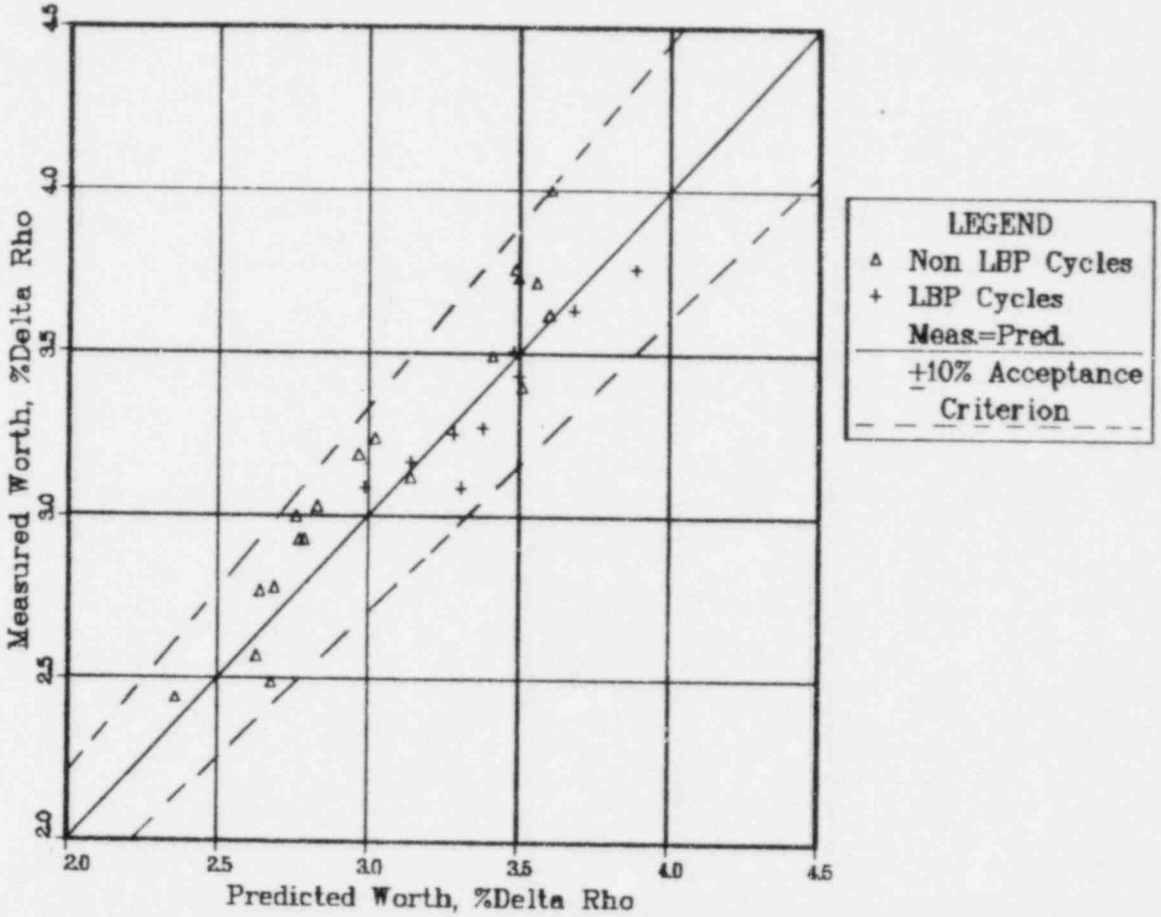

Figure 4

Comparison of Predicted and Measured HZP ERW

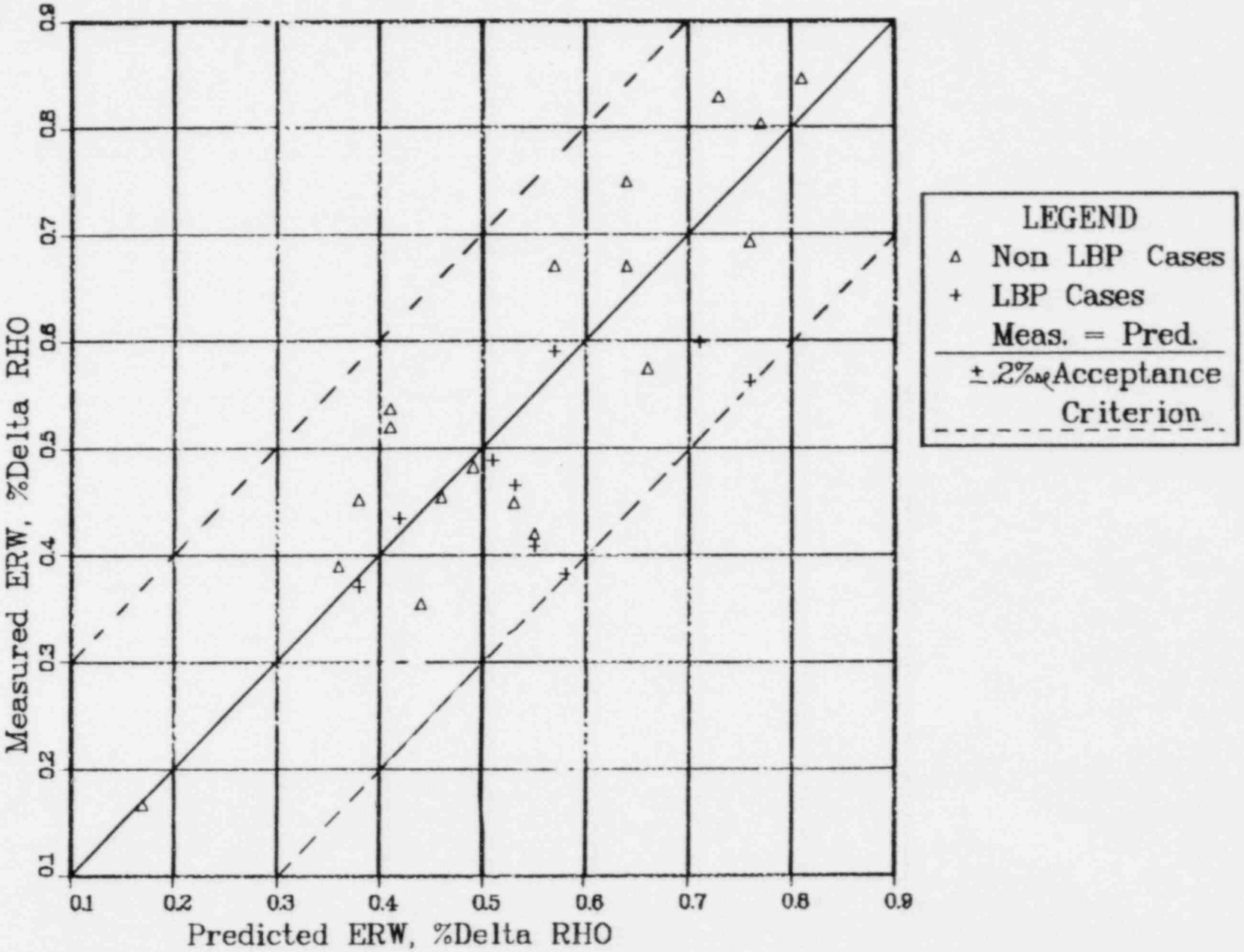

Figure 5

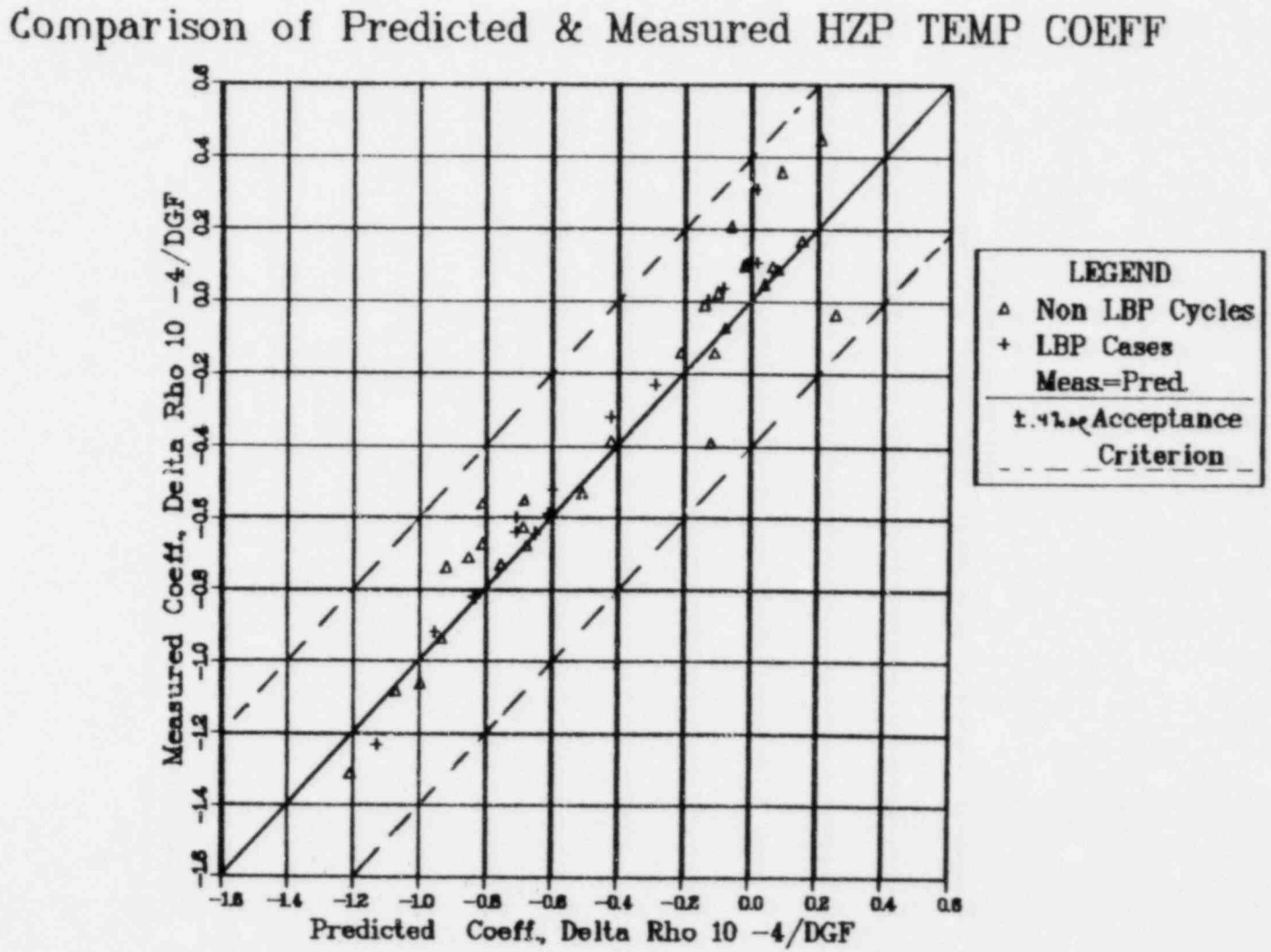
Comparison of Predicted & Measured HZP TEMP COEFF
Measured Coeff., Delta Rho 10 -4/DGF
Predicted Coeff., Delta Rho 10 -4/DGF
-1.6 -1.4 -1.2 -1.0 -0.8 -0.6 -0.4 -0.2 0.0 0.2 0.4 0.6
LEGEND
Non LBP Cycles
LBP Cases
Meas.=Pred.
Acceptance
Criterion

	8	9	10	11	12	13	14	15
H	1.10 1.11 -1.0	1.21 1.23 -1.7	1.14 1.19 -3.7	1.30 1.31 -0.2	1.14 1.13 1.1	1.20 1.16 3.8	.57 .58 -1.5	.45 .46 -2.3
K	1.24 1.26 -1.8	1.24 1.25 -0.8	1.19 1.18 0.1	1.27 1.22 3.6	1.09 1.07 2.4	.97 1.01 -3.8	.51 .53 -3.5	
L	.78 .82 -4.0	1.25 1.22 2.7	1.01 1.03 -2.4	1.27 1.25 1.5	1.00 1.00 -0.2	.44 .46 -3.3		
M	1.17 1.15 1.8	1.24 1.23 0.9	1.12 1.09 2.8	.88 .92 -4.3				
N	1.04 1.05 -0.5	1.08 1.07 0.7	.52 .51 1.1					
O	.61 .60 2.0	MEASURED PREDICTED % DIFFERENCE						

668

Figure 6

Comparison of Predicted and Measured Radial Power Distributions for a Rodded LBP Reload (BOC)

Standard Dev. of Radial Peaks = 2.4 in per-cent
= .02 in RPS

Pred. Radial Peak = 1.30 at H-11

Meas. Radial Peak = 1.31 at H-11

Per-cent Diff. = -0.2

	8	9	10	11	12	13	14	15
H	.93 .91 -2.2	1.09 1.06 -2.8	1.12 1.15 2.7	.99 1.00 1.0	1.15 1.18 2.6	.97 .93 -4.1	.81 .87 7.4	.71 .72 1.4
K		1.13 1.14 0.9	1.27 1.29 1.6	1.22 1.20 -1.6	1.09 1.08 -0.9	1.09 1.09 0.0	.88 .89 1.1	.71 .70 -1.4
L			1.09 1.10 0.9	1.07 1.09 1.9	1.09 1.10 0.9	1.11 1.09 -1.8	1.14 1.12 -1.8	.61 .61 0.0
M				1.18 1.19 0.8	1.07 1.10 2.8	.94 .94 0.0	.90 .89 -1.1	
N					.94 .88 -6.4	1.08 1.08 0.0	.66 .66 0.0	
O						.74 .72 -2.7	MEASURED PREDICTED % DIFFERENCE	

Figure 7

Comparison of A Non-LBP Reload (BOC)

Standard Dev. of Radial Peaks = 2.6 In Per-Cent
= .02 In RPD

Calc. Radial Peak = 1.27 At K-10

Meas. Radial Peak = 1.29 At K-10

	8	9	10	11	12	13	14	15
H	.98 .99 1.0	1.24 1.27 2.4	.99 .98 -1.0	1.25 1.21 -3.2	1.03 1.02 1.0	1.29 1.30 0.8	1.12 1.10 -1.8	.73 .74 1.4
K		1.03 1.04 1.0	.95 .97 2.1	1.02 1.02 0.0	.88 .90 2.3	1.09 1.10 0.9	1.20 1.20 0.0	.72 .71 -1.4
L			1.13 1.11 -1.8	1.25 1.28 2.4	.98 .99 1.0	1.25 1.24 -0.8	1.00 .96 -4.0	.56 .55 -1.8
M				1.01 1.05 4.0	1.24 1.27 2.4	1.05 1.04 -1.0	.76 .76 0.0	
N					1.03 1.03 0.0	1.08 1.06 -1.9	.59 .57 -3.4	
O						.69 .68 -1.4	MEASURED PREDICTED % DIFFERENCE	

Figure 8

Comparison of an LBP Reload (EOC)

Standard Dev. of Radial Peaks = 1.82 In Per-Cent
= 0.013 In RPD

Calc. Radial Peak = 1.29 At H-13

Meas. Radial Peak = 1.30 At H-13

COMPARISONS OF CALCULATED AND MEASURED PARAMETERS FOR A Pu-FUELED LWHCR LATTICE

R. Chawla, K. Gmür, H. Hager, E. Hettergott*, J.M. Paratte
R. Seiler and D. Stahel
Swiss Federal Institute for Reactor Research
5303 Wuerenlingen
Switzerland

ABSTRACT

The lack of suitable integral experiments for Pu-fueled LWHCR lattices renders it difficult to assess the adequacy of calculational methods and data being applied to the physics design of such reactors. The current paper presents results for the first of a series of Cores being investigated in the PROTEUS reactor at Wuerenlingen to help fill the gap - a PuO_2/UO_2 fueled test lattice with an effective Pu enrichment of 7 % and a fuel/moderator ratio of 2.0. The measurements reported include core-centre reaction rate ratios involving the capture rate in ^{238}U and fission rates in ^{235}U, ^{238}U, ^{239}Pu and ^{241}Pu. Infinite-dilution reaction rates in the lattice were determined for the $^{10}B(n,\alpha)$ reaction and for ^{232}Th, ^{233}U fission. Also measured were various radial and axial reaction rate traverses across the test zone to provide material-buckling, and hence k_∞, related data. Comparisons of the measured parameters have been made with calculations based on the use of several different lattice codes and their associated cross-section libraries, viz. WIMS-D, EPRI-CPM and BOXER. For several of the calculated parameters, a strong dependence has been observed on the available data sets. These are discussed in the light of the experimental results, as also the unusual spectrum characteristics of the test lattice.

1. INTRODUCTION

A reactor concept which has been receiving increasing attention from the viewpoint of improved uranium utilization is the homogeneous-design LWHCR (Light Water High Converter Reactor)/1-6/. The possibility suggested is that of providing a current-day type of PWR with a Pu-fueled, tight-pitch core, thereby hardening the neutron spectrum and achieving a conversion ratio ≥0.9. Hardly any experiments exist in the open literature, however, for assessing the calculational methods being applied to the thermal hydraulics and the reactor physics of LWHCRs.

The latter aspect is particularly important in the context of the void coefficient of reactivity (k_{eff}) which must, in all circumstances, be designed to be negative. Depending on the methods and data used for the physics analysis, conflicting calculational results can be obtained which may differ, not only in the magnitude of the coefficient, but also the sign. This may be explained by the fact that the k_∞ void coefficient, in a given case, is made up of several, partially cancelling contributions from individual reaction rates, all of which must be adequately predicted at each voidage step /7/.

A programme of measurements has been initiated at the PROTEUS zero-energy reactor facility at Wuerenlingen, with the broad aim of helping to fill the current gap in benchmark experiments for the reactor physics of LWHCRs /8/. Measurements in

*under contract from EPRI, Palo Alto, CA

Core 1, involving a reference test lattice with full-density H_2O, have been completed. Subsequent Cores will simulate H_2O-voidage in this lattice. The current paper discusses the experimental results obtained in Core 1 for central reaction rate ratios, as well as radial and axial reaction rate traverses across the test zone. Comparisons have been made with calculations based on the use of several alternative lattice codes and data sets.

2. EXPERIMENTAL CONFIGURATION AND TYPES OF MEASUREMENTS

The PROTEUS facility essentially consists of a central test region driven critical by annular thermal driver zones /9/. Figs. 1 and 2 give horizontal and vertical sectional views of the PROTEUS reactor as used for the current experiments. As indicated, the D_2O- and graphite-moderated driver zones are separated from the test lattice by an annular buffer zone consisting of natural-uranium metal rods. The net influence of the outer reactor regions on the neutron spectrum at the centre of the test zone is minimal, the principal reaction rate ratios being affected by typically <2 %.

In selecting the lattice arrangement for the test lattice, a practical constraint was the required utilization of existing fuel materials, viz. 6.70 mm-diameter rods of 15 % PuO_2/UO_2 and depleted UO_2, canned in steel tubes of outer diameter 8.22 mm. The PuO_2/UO_2 rods, which had been welded to specifications for a future fast-reactor experiment, had small quantities of steel washers distributed along their length. A subsidiary assessment confirmed, however, that the effects of the additional steel were small and that these could be adequately taken into account in the measurements as well as the calculations.

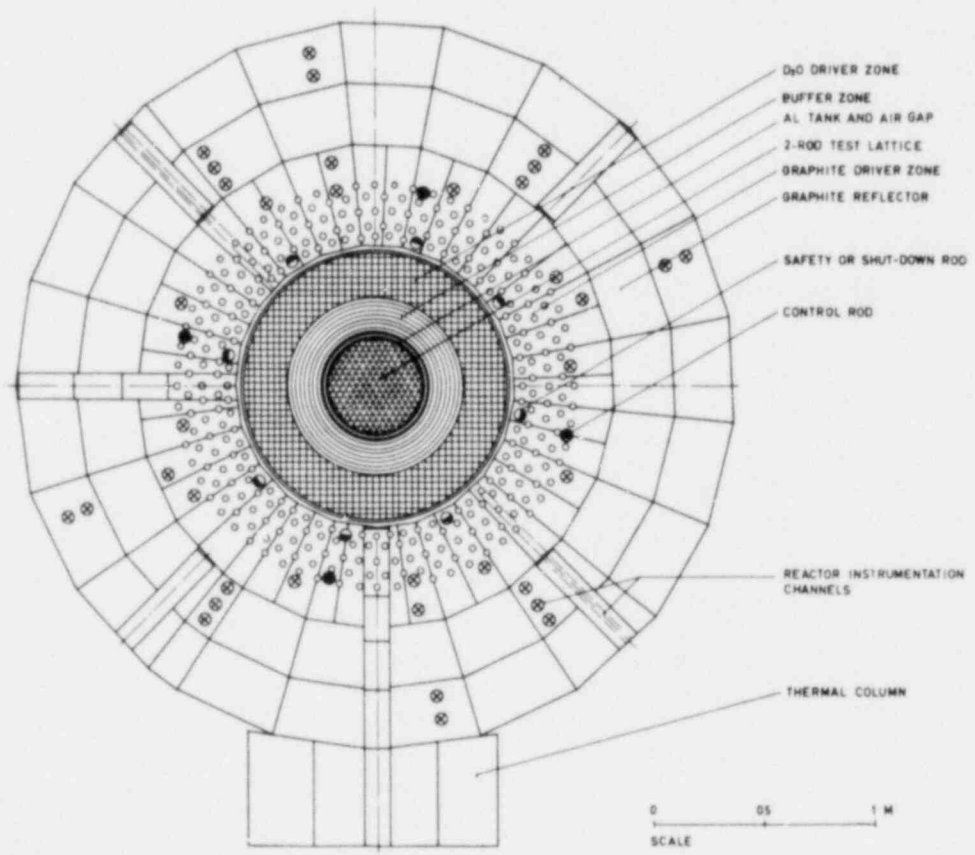

FIGURE 1: HORIZONTAL SECTIONAL VIEW OF THE PROTEUS REACTOR

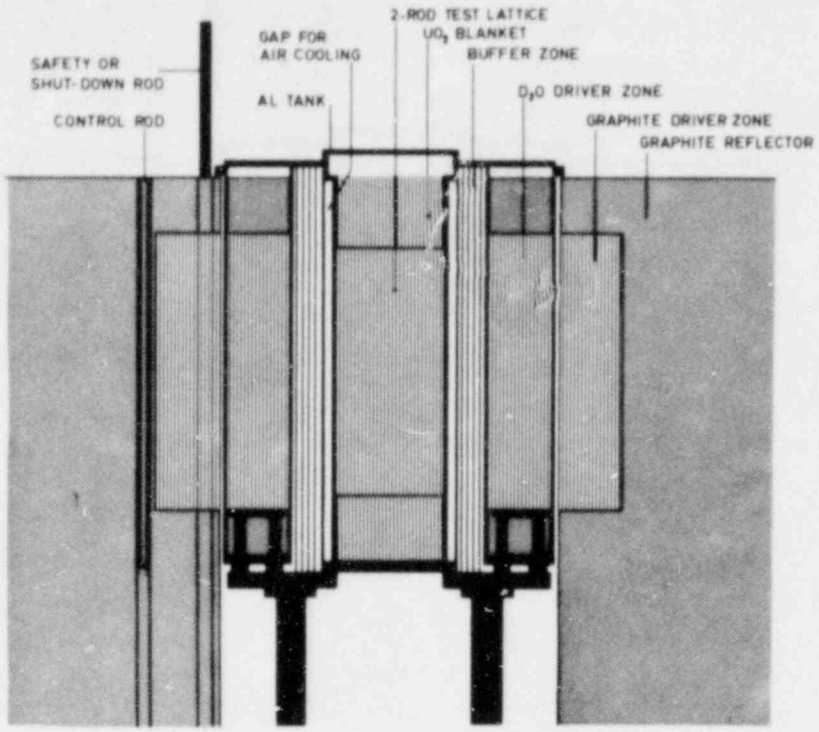

FIGURE 2: VERTICAL SECTIONAL VIEW OF THE PROTEUS REACTOR

Since the principal aim of the current experiments is to provide integral data relevant to LWHCRs of homogeneous design, the test lattice was constructed as a 1:1 mixture of the two different types of available fuel rods so that a mean total-Pu enrichment of about 7 % could be simulated. Fig. 3 shows the lattice arrangement used, the two rod types forming alternate, parallel rows of hexagonal cells with the 9.00 mm pitch providing a fuel/moderator (F/M) ratio of ~2.0. A total of about 2100 rods were thus needed to make the central test zone upto a diameter of 0.43 m. Nuclide number densities used in the cell calculations for the 2-rod test lattice (PROTEUS-LWHCR Core 1) are given in Table 1.

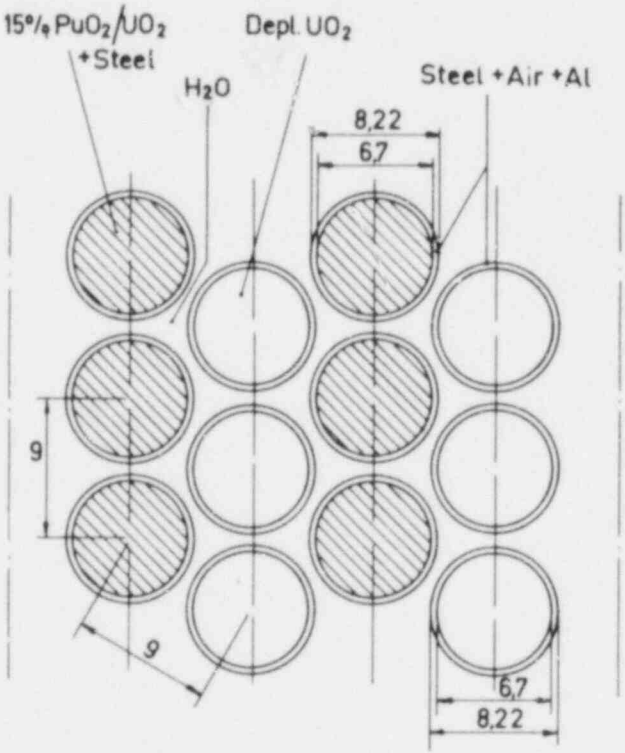

FIGURE 3: SCHEMATIC LAYOUT OF THE TEST LATTICE (dimensions in mm)

Reaction rate measurements were carried out in the test lattice using, for the main part, foil-activation techniques that have been described elsewhere (e.g. /9/) in the context of earlier experimental programmes on PROTEUS. Each type of core-centre reaction rate ratio measurement was, wherever possible, carried out using more than one experimental technique. Thus, for example, the important ratio of ^{238}U capture to ^{239}Pu fission in the lattice was determined by both

TABLE 1: NUCLIDE DENSITIES ($x10^{30}$ m^{-3}) FOR MATERIALS IN THE PROTEUS-LWHCR CORE 1 TEST LATTICE

Material 1 (Fuel 1, 15 % PuO_2/UO_2 + Steel):			
^{235}U ..7.781-5*	^{238}U ..1.839-2	^{239}Pu..2.580-3	^{240}Pu..5.699-4
^{241}Pu..5.675-5	^{242}Pu..1.256-5	^{241}Am..3.833-5	O ..4.346-2
H ..2.005-4	Al..3.683-4	Fe..2.600-3	Cr..6.843-4
Ni..3.301-4	Mn..5.376-5	Si..3.286-5	Mo..8.123-6
Material 2 (Fuel 2, Depl. UO_2):			
^{235}U ..9.851-5	^{238}U ..2.328-2	O ..4.677-2	Al..3.827-4
Material 3 (Clad, Steel + Air + Al):			
Al..6.080-3	Fe..3.125-2	Cr..8.536-3	Ni..5.118-3
Mn..1.001-3	Mo..7.354-4	Si..8.124-4	N ..1.323-5
Material 4 (Moderator, H_2O at 32°C):			
H ..6.652-2	O ..3.326-2		

* to be read as 7.781×10^{-5}

absolute and thermal-comparison methods. Use was also made of fission track recorders (SSTRs) to provide some check on the foil/chamber measurements of fission rate ratios. The core-centre reaction rates determined were ^{235}U fission (F_5), ^{238}U capture and fission (C_8, F_8), ^{239}Pu fission (F_9) and ^{241}Pu fission (F_1), which together account for ~70 % of neutron absorptions in the test lattice. Also monitored as spectral indices for the lattice were the $^{10}B(n,\alpha)$ reaction (B_α), ^{232}Th fission (F_2) and ^{233}U fission (F_3).

The experimental accuracy for the measured reaction rate ratios was, in most cases, about ± 2 %. This error is slightly greater than that achieved in earlier fast-reactor experiments in PROTEUS and resulted from several factors. These were, principally, the much larger foil/pellet heterogeneity effects in the intermediate neutron-energy spectrum of the LWHCR lattice, the need to correct for the presence of steel washers in the PuO_2/UO_2 fuel, and the fact that measurements had to be conducted for two different fuel-rod types.

In order to obtain material-buckling, and hence k_∞, related data for the test lattice, axial and radial reaction rate traverses were measured across the central zone. This was done for the principal reaction rates (F_5, C_8, F_8, F_9) and also for the Rh(n,n') reaction, a fast-neutron detector with a lower threshold than F_8.

3. CALCULATIONAL METHODS AND DATA

Several different cell codes with their associated data libraries have been applied to the analysis of the Core 1 measurements. These include the U.K. code WIMS-D1 /10/, the U.S. code EPRI-CPM /11/ with largely ENDF/B-3 based data, and the Swiss code BOXER /12/ which uses a library derived from ENDF/B-4 for all nuclides except ^{238}U. Each of these codes could be used to model the experimental 2-rod lattice, although with different approximations. Thus, for example, the BOXER and EPRI-CPM routes used a combination of chequer-board and parallel-row square-cell arrangements to simulate the actual hexagonal geometry. The

WIMS-D calculation, while able to model the experimental lattice arrangement somewhat better through appropriate collision probabilities, suffered from other limitations such as that each individual cell-type was considered in isolation at the level of resonance-group cross-section preparation.

Table 2 provides a useful criterion for assessing the sensitivity of calculated parameters to the multicell modeling. This is a comparison made, using each code separately, of results obtained for the 2-rod lattice with those of an "equivalent" single-rod lattice, i.e. one with the same cell dimensions as indicated in Fig. 3 but with a fuel region consisting of a homogeneous mixture of the actual fuel materials (Table 1). Also indicated are results based on a set of Monte Carlo calculations carried out using the SAM-CF code /13/. It is seen that the 2-rod heterogeneity effects calculated by the various methods are quite similar. Further, except for F_5/F_9 (a not very important ratio from the neutron balance viewpoint), the magnitude of the effects is generally <5 % for the various integral parameters. The 2-rod nature of the PROTEUS-LWHCR test lattice should not, therefore, seriously detract from its usefulness as a benchmark experiment for homogeneous-design LWHCRs /14/.

TABLE 2: COMPARISON OF 2-ROD/SINGLE-ROD CALCULATIONS*

Method	WIMS-D	EPRI-CPM	BOXER	Monte Carlo
k_∞	1.004	1.008	1.004	1.001
F_5/F_9	1.211	1.159	1.173	1.183
C_8/F_9	1.034	1.032	1.033	1.032
F_8/F_9	1.006	1.024	1.001	1.001
F_1/F_9	1.053	1.043	1.038	1.031

* results for the 2-rod lattice, relative to values obtained from single-rod (homogenised fuel) calculations

Comparisons of calculational and experimental results, in any given case, reflect shortcomings in both the theoretical model as well as the data library used. In the WIMS-D calculations it was possible to apply different data options for a few of the nuclides. Thus, although most of the results currently being reported employed the "latest" data available on the standard WIMS library tape /15/, a useful "feel" for the sensitivity of calculated parameters could be obtained by using certain "older" options. Table 3 shows, separately, the effects of changing the ^{235}U resonance tabulations, the ^{238}U resonance data, the ^{238}U fast-group cross-sections and finally, the ^{239}Pu fast data. It is clear that the sensitivity of calculated parameters to the available WIMS data options is much higher for the type of neutron spectra being investigated in the current experiments than generally encountered in thermal reactor lattices /16/. The calculated percentage of epithermal events (>4 eV) in the Core 1 test lattice was as high as 62 % for F_5, 95 % for C_8 and 48 % for F_9.

A basic point of interest was confirmed through other subsidiary calculations, viz. that the relative effects of alternative data options of the type indicated above for the 2-rod test lattice were very similar to corresponding effects in single-rod (homogenised fuel) calculations. This provided further justification for the benchmark nature of the experimental lattice.

TABLE 3: SENSITIVITY OF WIMS-D CALCULATED CORE 1 PARAMETERS TO ALTERNATIVE DATA OPTIONS*

Changed Data	^{235}U Reson.	^{238}U Reson.	^{238}U Fast	^{239}Pu Fast
Changed El.No.	235.2	2238.2	238.4	1239.1
k_∞	0.996	0.975	0.994	1.011
F_5/F_9	0.922	1.000	1.001	0.993
C_8/F_9	1.000	1.096	1.001	0.990
F_8/F_9	1.000	1.030	0.947	0.992
F_1/F_9	1.000	0.998	1.002	0.994

* results quoted relative to values obtained with "latest" available options, viz. El. Nos. 235.4, 2238.4 and 3239.1 for ^{235}U, ^{238}U and ^{239}Pu, respectively.

In order to calculate the finite effects of the outer reactor zones (Section 2) on reaction rate ratios at the centre of the test lattice, a 1-D whole-reactor model for PROTEUS was set up using the SN-1D code, a modified version of ANISN /17/. This model was also used for the interpretation of measured radial reaction rate traverses across the test zone (Section 4.2). 28-group cross-section sets for the buffer, driver and reflector zones were available from earlier PROTEUS studies /9/. Data for the test lattice, as well as for the new interface zones, were generated in the same 28-group structure by appropriate condensation of cross-sections derived from WIMS-D.

4. RESULTS AND DISCUSSION

4.1 Central Reaction Rate Ratios

Table 4 shows comparisons of experimental (E) and calculated (C) core-centre values of F_5/F_9, C_8/F_9, F_8/F_9 and F_1/F_9 in PROTEUS-LWHCR Core 1. Each reaction rate has been considered per atom for the test lattice, i.e. represents a mean value weighted with the appropriate nuclide densities in the two rod types. Thus, for example, F_5/F_9 is the ^{235}U-weighted average ^{235}U fission rate for the two rod-types, relative to the ^{239}Pu fission rate in the PuO_2/UO_2 rod alone (Table 1). The C-values for each reaction rate ratio have been corrected for the effects of neutron spectrum perturbation by the outer reactor zones, using the 1-D whole-reactor model mentioned in Section 3. The corrections, i.e. departures from fundamental-mode (k_{eff}=1) values for the test lattice, were negligible ($\lesssim$0.2 %) for all measured reaction rate ratios except F_8/F_9 and F_2/F_9, for both of which a correction of -2 % was applied.

From the viewpoint of the neutron balance, as also of course the conversion ratio, C_8/F_9 is the most important single parameter in Table 4. The EPRI-CPM calculation is seen to underpredict this reaction rate ratio by $\sim$7 %, while the BOXER result appears too high by $\sim$4 %. Agreement between the measured and WIMS-calculated values, on the other hand, is excellent. This, however, could be fortuitous considering the sensitivity indicated in Table 3 to the WIMS ^{238}U resonance tabulations and the fact that the more recently recommended data /16/ are not available on the standard library tape /15/. Evidence confirming the unusually high resonance component of C_8 in the lattice is provided by Fig. 4 which shows the results of fine structure measurements across the fuel diameter. (The

results for the two different rod types are seen to be identical within the experimental errors).

TABLE 4: COMPARISONS OF EXPERIMENTAL (E) AND CALCULATED (C) RATIOS FOR REACTION RATES OCCURRING IN THE TEST LATTICE

Ratio	Experimental Value	C/E		
		WIMS-D	EPRI-CPM	BOXER
F_5/F_9	0.988 ± 2 %	1.096	0.984	1.011
C_8/F_9	0.0691 ± 2 %	1.002	0.926	1.036
F_8/F_9	0.00987 ± 2 %	0.974	1.019	1.113
F_1/F_9	1.92 ± 4 %	1.012	0.949	0.889

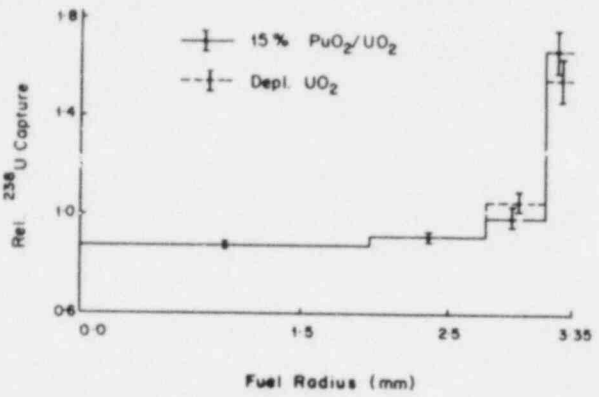

FIGURE 4: FINE STRUCTURE MEASUREMENTS FOR C_8 IN CORE 1

Fast fissions in the lattice (F_8/F_9) appear to be adequately predicted by both EPRI-CPM and WIMS-D, but are ∿11% too high with BOXER. This suggests that the adjustment to ^{238}U fission cross-sections carried out in the otherwise ENDF/B-4 based BOXER library (Section 3) may be in error.

Agreement between measured and calculated values for F_5/F_9, a reaction rate ratio somewhat more sensitive than the others to the 2-rod nature of the test lattice (Table 2), is quite satisfactory with EPRI-CPM and BOXER. WIMS-D, on the other hand, overestimates this ratio by nearly 10 %. Use of the "older" ^{235}U resonance tabulations in WIMS, however, would largely remove this over-prediction (Table 3).

Finally, F_1/F_9 is seen to be well predicted by WIMS-D, while EPRI-CPM and BOXER results appear too low by 5 % and 11 %, respectively. The larger experimental error on this ratio should, however, be borne in mind. It resulted from the non-availability of ^{241}Pu activation foils for the fission rate measurements, the quoted experimental result being based on SSTR measurements alone (Section 2).

Three other reaction rate ratios were measured in the centre of Core 1, viz. F_2/F_9, F_3/F_9 and B_α/F_9. The numerator terms, in each case, represent average infinite-dilution reaction rates for the two rod types, the corresponding nuclides not occurring in the test lattice. F_9, as before, denotes the ^{239}Pu fission rate per atom in the PuO_2/UO_2 rod. While F_2/F_9 and F_3/F_9 could be measured directly in the fuel rods through the combined use of activation foils and fission chambers /9/, there was no technique available for monitoring the $^{10}B(n,\alpha)$ reaction rate in a rod. Recourse was taken to a calculational adjustment of B_α/F_9 measurements made using a specially constructed double-chamber. A

thermal-comparison technique was applied (Fig. 5), and although an accuracy of better than ± 2 % could be achieved for the chamber result itself, the net accuracy for B_α/F_9 in the lattice as defined above was ± 5 %.

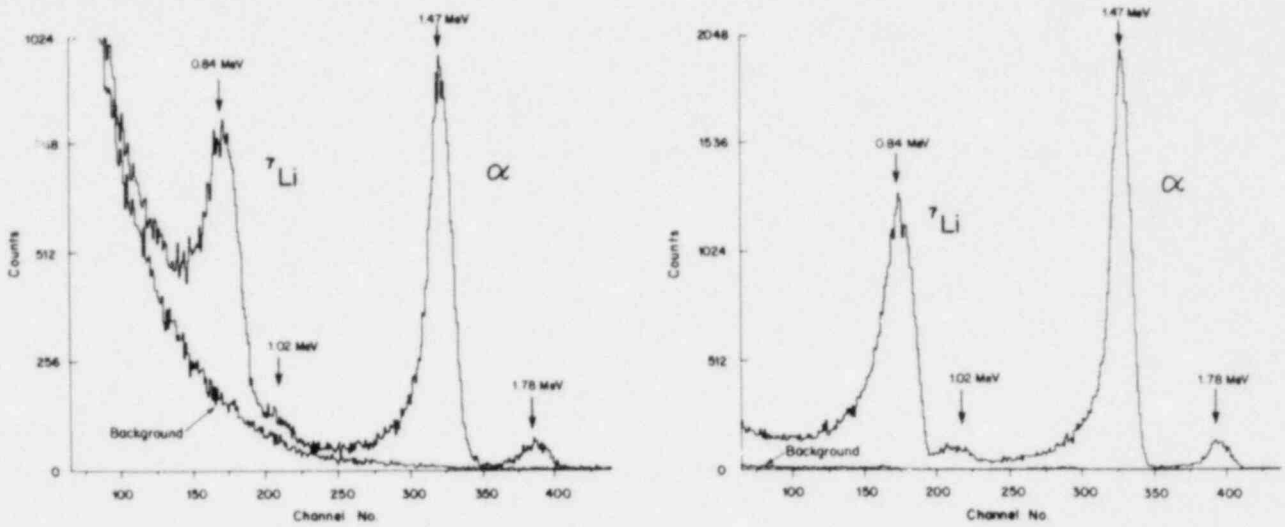

FIGURE 5: PULSE-HEIGHT SPECTRA FOR THE $^{10}B(n,\alpha)$ CHAMBER MEASUREMENTS IN (a) THE LATTICE, (b) THE THERMAL COLUMN

Table 5 gives comparisons of measured and calculated values for the three reaction rate ratios. It is seen that F_2/F_9 is strongly underpredicted by both WIMS-D and BOXER. This is qualitatively consistent with results from fast-reactor experiments which suggest that the ^{232}Th fission cross-sections in current use are too small. F_3/F_9 is calculated ∿10 % too high with WIMS, but appears somewhat too low in BOXER. Finally, for B_α/F_9, agreement with measurement is within the experimental error for WIMS-D, while BOXER seems to underpredict the ratio by ∿11 %.

TABLE 5: COMPARISONS FOR REACTION RATE RATIOS MEASURED AS SPECTRAL INDICES IN CORE 1

Ratio	Experimental Value	C/E	
		WIMS-D	BOXER
F_2/F_9	0.00254 ± 2 %	0.890	0.924
F_3/F_9	1.900 ± 2 %	1.096	0.962
B_α/F_9	5.30 ± 5 %	1.026	0.890

4.2 Reaction Rate Traverses, B_m^2 and k_∞

The reaction rates represented by the experimental results in Table 4 account for ∿70 % of total absorptions in the test lattice. In order to provide some check on the non-measurable reaction rates (principally, capture in the Pu isotopes and in steel), an estimation of material buckling - and hence k_∞ - was attempted via measurements of various radial and axial reaction rate traverses

across the test zone.

It was found that, in the axial direction, the different reaction rate profiles could be all fitted to the same cosine function as long as points within about 50 mm of grid plates and core/blanket boundaries were not considered. After applying a slight correction for the presence of intervening grid plates, the axial-buckling value, α^2, was determined to be (7.2 ± 0.4) m^{-2}.

Along the radial direction, however, it was found that the measured reaction rate traverses fell into two separate categories. These were (i) F_8 and Rh(n,n'), with a sensitivity to fast (MeV) neutrons only, and (ii) F_5, C_8 and F_9, each of which was sensitive to neutrons of median energy in the range 5-80 eV. For reaction rates of a given category radial-buckling values (β^2), deduced from Bessel-function fits across the central 0.25 m-diameter portion of the test zone, were the same within experimental errors. Between the two categories, however, the difference in average β^2-values was as high as $\sim$13 m^{-2}. Clearly, the equilibrium neutron spectrum at the centre of the test zone did not extend significantly in the radial direction, as it did in the axial. The situation was somewhat analogous to buckling measurements in fast-reactor criticals where spectrum-perturbation effects of blanket zones have to be taken into account /18/.

The 1-D whole-reactor model (Section 3), with an input axial buckling for the test zone equal to the measured value (7.2 m^{-2}), was used for calculating the various reaction rate traverses. Radial buckling values, deduced from Bessel-function fits, displayed characteristics very similar to those for the experimental traverses. The theoretical radial buckling given by $\beta^2=B_m^2-\alpha^2$ (where B_m^2 is the material buckling from the cell calculation for the test lattice and α^2 is the measured axial buckling fed as input to the calculation) was found to be $\sim$3 m^{-2} less than the value for the Category (i) reaction rates and $\sim$11 m^{-2} greater than for that for Category (ii). Several numerical checks were made with the calculational model to confirm that simulating changes in the theoretical β^2 for the test zone (e.g. using cross-section data derived from an alternative cell calculation) resulted in the β^2-value for each reaction rate type being modified by a similar amount. Table 6 compares experimental and calculational results for the radial reaction rate traverses and indicates how a "measured" value of β^2 $(=B_m^2-\alpha^2)$ was estimated.

TABLE 6: ESTIMATION OF RADIAL BUCKLING FROM REACTION RATE TRAVERSES

	Calcn.	Expt.	E-C
$\beta^2_{F8,Rh}$ (m^{-2})	2.3	3.7 ± 1.5	1.4
$\beta^2_{F5,C8,F9}$ (m^{-2})	-11.6	-9.0 ± 1.5	2.6
$\beta^2=B_m^2-\alpha^2$ (m^{-2})	- 0.7	1.3 ± 2 *	2.0 *

* estimated from the mean (E-C) values for the two reaction rate categories

Combining the experimental values for α^2 and β^2, the material buckling for the Core 1 test lattice was deduced to be (8.5 ± 2) m^{-2}. This is compared in Table 7 with B_m^2 values calculated by WIMS-D, EPRI-CPM and BOXER. Also shown are the corresponding results for k_∞ (defined as productions/absorptions in the fundamental-mode spectrum). The B_m^2 -based experimental value for k_∞ is shown as having an uncertainty of $\pm$ 1 %, with the theoretical migration area of $5.3 \cdot 10^{-3}$ m^2 assumed to contribute negligibly to the error.

TABLE 7: COMPARISONS OF EXPERIMENTAL AND CALCULATED VALUES OF B_m^2 AND k_∞

	Expt.	WIMS-D	EPRI-CPM	BOXER
B_m^2 (m^{-2})	8.5 ± 2	6.5	10.9	5.8
k_∞	$1.045\pm1\%$	1.035	1.058	1.031

It is seen that WIMS-D and BOXER appear to be somewhat low on k_∞, while EPRI-CPM is too high. Comparing Tables 4 and 7, the k_∞ trend for WIMS-D, together with the rather satisfactory C/E-values for the principal reaction rate ratios, provides some indication that the non-measurable capture rates (in ^{239}Pu, ^{240}Pu, etc.) may be overpredicted. For BOXER, as well as for EPRI-CPM, certain compensating effects due to individual reaction rates may be discerned.

5. SUMMARISED CONCLUSIONS

The currently reported measurements in PROTEUS-LWHCR Core 1 have been shown to provide stringent tests to the adequacy of calculational methods and data that may be applied to the physics design of LWHCRs. With the unusually high percentage of events at epithermal energies, the sensitivity of calculated parameters to alternative data options was much greater than generally encountered in thermal reactor lattices.

On the basis of the various types of comparisons made with experiment, each of the methods applied to the lattice calculations was found to have certain weaknesses. Thus, for example, EPRI-CPM underpredicted the important ratio C_8/F_9 by $\sim$7 %, while BOXER, overestimated fast fissions in the lattice by $\sim$11 %. WIMS-D results, though apparently satisfactory for the principal reaction rate ratios, did indicate possible inadequacies in the calculated spectrum with F_5/F_9 and F_3/F_9 both overpredicted by $\sim$10 %. As regards k_∞, WIMS-D and BOXER results were indicated as being somewhat low, while the EPRI-CPM value was too high.

Subsequent Cores in the current PROTEUS-LWHCR programme of experiments will simulate H_2O-voidage in the Core 1 test lattice. Comparisons of calculated and measured parameters for these other Cores, together with the currently reported results, should provide useful evidence for the adequacy of calculated reactivity variations with voidage for homogeneous-design LWHCRs.

Acknowledgements:

The authors are grateful to Dr. R. Brogli, Mr. M. Jermann, Dr. R. Richmond and Prof. W. Seifritz for their active support of the current research programme. Thanks are also due to Messrs. H. Graf, P. Bourquin, T. Steiner and P. Thomy for operating the reactor so efficiently, as well as for helping out with some

of the measurements.

Contractual support by EPRI, Palo Alto, which enabled one of the authors (EH) to participate in the programme, is gratefully acknowledged, as is also the keen interest in the experiments shown by the following other organisations - MIT, ORNL and GAC, USA, and KWU, KfK and TUB, W. Germany.

References:

1. M.C. Edlund
"High Conversion Ratio Plutonium Recycle in PWRs"
Ann. Nucl. Energy, 2, 801 (1975)

2. F. Correa, M.J. Driscoll and D.D. Lanning
"An Evaluation of Tight-Pitch PWR Cores"
Report MITNE-227 (1979)

3. H.H. Hennies and H. Märkl
"Ueberlegungen zur Modifizierbarkeit eines LWR im Hinblick auf eine bessere Uranausnutzung"
Jahrestagung Kerntechnik, Berlin (1980)

4. W. Keller and F.J. Spalthoff
"Reactor Programs Incorporating the Use of LWRs"
Proc. 11th World Energy Conf., Munich (1980)

5. H.D. Berger and W. Oldekop
"Neutronenphysikalische Aspekte eines fortgeschrittenen Druckwasserreaktors"
Atomkernenergie, 39, 128 (1981)

6. V.O. Uotinen, W.L. Bloomfield, M.A. Haghi, H.M. Jones, J.H. Jones, E.C. Toops, M.C. Edlund and R.J. Florian
"Technical Feasibility of a PWR Design with a Low-Water-Volume-Fraction Lattice"
Report EPRI-NP-1833 (1981)

7. R. Chawla
"Breakdown of the k_∞ Void Coefficient of a LWHCR Lattice"
Atomkernenergie, 37, 303 (1981)

8. R. Chawla, R. Richmond and R. Brogli
"Proposed Programme of Tight-Pitch LWR Physics Experiments in the PROTEUS Reactor"
2nd NEA Meeting on the Improvement of Fuel Utilization, Paris (1980)

9. R. Chawla, K. Gmür, M. Jermann, R. Richmond and U. Schmocker
"Fast Reactor Experiments with Thorium at the PROTEUS Facility"
Report EIR-444 (1981)

10. J.R. Askew, F.J. Fayers and P.B. Kemshell
"A General Description of the Lattice Code WIMS"
J. Brit. Nucl. Energy Soc., 5, 564 (1966)

11. "Advanced Recycle Methodology Program (ARMP), System Documentation"
Internal EPRI Report (1977)

12. C. Maeder and J.M. Paratte
"Calculation of LWR Fuel Elements Containing Burnable Poisons and Plutonium"
Trans. Am. Nucl. Soc., 20, 359 (1975)

13. O. Ozer, private communication

14. R. Chawla, K. Gmür, H. Graf, E. Hottergott, R. Richmond and D. Stahel
"The PROTEUS-LWHCR Experiments: 2-Rod Heterogeneity Effects"
Trans. Am. Nucl. Soc., 40, 213 (1982)

15. C.J. Taubman
"The WIMS 69-Group Library Tape 166259"
Report AEEW-M1324 (1975)

16. J.R. Askew
"The Current UK Position on ^{238}U Resonance Captures in Thermal Reactors"
Report AEEW-R1006 (1975)

17. W.W. Engle, Jr.
"A User's Manual for ANISN, a One-Dimensional Discrete Ordinates Code with Anisotropic Scattering"
Report K-1693 (1967)

18. W. Scholtyssek
"Physics Investigations of Sodium-Cooled Fast Reactors: SNEAK Assembly 9C"
Report KFK-2361 (1977)

MONTE CARLO ANALYSIS OF BWR BYPASS HEATING, GAMMA TIP RESPONSE, AND GAMMA REDISTRIBUTION FACTORS

M. J. Hebert, D. R. Harris*, D. M. Kapitz, and E. E. Pilat

Yankee Atomic Electric Company

*Rensselaer Polytechnic Institute

ABSTRACT

Gamma rays and neutrons deposit energy at locations and times different from those of the reactions giving rise to them. Methods are under development for carrying out the numerous routine calculations that are required for BWR bypass heating, gamma TIP response, and gamma redistribution factors in LOCA and in normal operation. The KENO-IV multigroup Monte Carlo program, in modified form, is used for transport. Coupled neutron and gamma ray cross section sets are employed with appropriate prompt and delayed gamma sources. When delayed gamma sources are required they are synthesized from the operating history using sums of exponential expressions. These are prepared from activation data and from delayed fission gamma data from CINDER fitted at LASL. The Monte Carlo results for TIP response and redistribution are processed first as Green's functions, ie, effects produced in various regions due to unit source in a fuel pin. These Green's functions then are combined with power shapes calculated by normal core analysis methods.

I. INTRODUCTION

Gammas and neutrons can deposit energy at places and times that are different from those of the reactions which give rise to them. The assumption that the energy deposition occurs at the location of the parent reaction is overly conservative in some applications and is inappropriate in other cases. Methods are under development for carrying out the numerous routine calculations that are required for BWR bypass heating, gamma TIP responses, and gamma redistribution factors in LOCA and in normal operation.

Gamma-ray cross sections and transport are well understood, and powerful calculational tools are available. In particular, continuous energy Monte Carlo codes which track neutrons, gammas, and electrons together have been used(1,2) for these applications and tested satisfactorily (1) against

appropriate measurements (3,. There are, however, a great many routine calculations of these effects required for core physics analysis for each cycle for each reactor. The objective of the present work is to develop and validate methodology for routine utility calculations of these effects. Approximations necessarily are employed and these are considered.

Briefly, the methodology utilizes the KENO-IV(4) multigroup Monte Carlo program which many utilities maintain and use for criticality analyses of spent and fresh fuel. This is used with coupled neutron-gamma multigroup cross section sets. These were usually developed for shielding applications and their use for in-core analysis must be demonstrated. Electron transport is ignored except when this is implicit in gamma flux-to-effect conversions. Delayed gamma production is determined taking into account the reactor operating history. Both prompt and delayed gamma production can take into account the current power shape as determined from normal core analysis methodology. Gamma transport Green's functions are determined for beginning-of-exposure compositions. This is justified because the gamma transport cross sections do not change greatly with depletion. Gamma transport is appreciably affected in BWR's by coolant void fraction and by presence or absence of control rods, so these effects are included as distinct reactor conditions. Preliminary accounts of the work have been presented(5,6).

II. BWR BYPASS HEATING

BWR bypass heating is important in the analysis of the flow split between active and bypass channels, in the determination of core response to rapid reactivity transients, and in the calculation of MCPR thermal limits. The direct bypass heating is not large, one or two Mev per fission, and is largely from neutron interactions but with a significant gamma component. Knockon protons from neutron interactions deposit essentially all of their energy in the bypass, and knockons from the channel walls contribute negligibly to bypass heating. Thus neutron kerma in the bypass represents the neutron-induced heating there. The electrons from gamma interactions in the bypass can deposit appreciable energy in the channel walls, however, and electrons from the channel can emerge into the bypass. We justify later the exclusion of electron transport in this application.

Neutron and gamma transport was calculated by KENO-IV using the the CASK(7) coupled 22 neutron group/ 18 gamma group cross section set. This cross section set accounts for gamma production from neutron captures and inelastic scattering as well as for the prompt and equilibrium delayed gammas from fission. The Vermont Yankee fuel bundles were adequately represented by the KENO-IV geometry routine(8). Axial

variations were not modeled, and zero current boundary conditions were used at the bundle periphery. Beginning-of-exposure conditions with 0%, 40%, and 70% void were used in the bundle. The bypass regions were taken to be unvoided. In order to properly account for the neutron source distribution within a bundle, the neutron cross sections were adjusted to account for resonance self-shield.ng based on shielded CLOSEUP cross sections which were prepared by ORNL for Yankee using the SCALE code package(9).

Neutron and gamma fluxes were calculated on a region-by-region basis after the neutron source distribution settled into a converged fission distribution. Because there is no neutron production by gammas in the coupled cross section sets the convergence on the fission distribution is the same as if gammas were not being tracked. The pin-by-pin power shapes were appreciably worse than in our previous Monte Carlo work(8) based on CASMO cross sections, presumably reflecting inadequacies in the CASK neutron cross sections. Energy depositions in the bypass regions were obtained by saving the KENO-generated fluxes and multiplying them in a postprocessor code by neutron and gamma kermas.

Figure 1 shows a typical distribution of gamma energy depositions in the bypass regions of a typical BWR bundle at 40% void, as well as in individual fuel pins. Table 1 shows the variation of neutron and gamma energy deposition in the bypass for various reactor conditions. About 50000 neutron histories were used in each calculation. For these computations the statistical uncertainties were about 2% to 3% in the narrow bypass region and about 1% to 2% in the wide bypass regions. For energy deposition in individual fuel pins the uncertainty was about 2% to 3% for off-diagonal fuel pins, and about 3% to 4% for fuel along the diagonal. This degree of accuracy appears to be adequate for the application. These results are in general agreement with those of other workers (10,11).

This methodology, and the related one described in the next section, involve a number of approximations which are made in the interest of calculation efficiency. Some of these are taken up here and some are considered in the next section. The use of multigroup cross sections for gamma ray transport is adequate in view of the slowly-varying nature of gamma cross sections. Gamma cross sections can vary rapidly at K-, L-, and other edges, but these occur at low gamma energies where the gamma mean-free-path is short. Gamma cross sections are well understood, but neutron cross sections are not. Thus a multigroup set of gamma ray cross sections coupled to a multigroup neutron cross section set validated for in-core analysis would appear to be useful and feasible. The limitation of KENO-IV to P-0 and P-1 scattering patterns is under investigation. The approximate representation of BWR bundle

features by the KENO-IV geometry has only a negligible effect on the results.

The neglect of axial variation is justified in certain circumstances. When the gamma source is simply buckled in the axial direction (eg, varying as cosBz) then the gamma energy deposition can be shown to be also, and with the same buckling B. This occurs when the gamma source-to-effect kernel is a displacement kernel depending only on the displacement between the source and effect locations. The axial gamma source shape does not usually have this simple shape in a BWR, and in addition the gamma kernel is not precisely a displacement kernel because of the slowly increasing amount of void axially. Integrations of axial power shapes with approximate gamma kernels indicates that axial smearing effects are not large, presumably because in addition to the shape invariance for simple buckling the range of the gamma kernel is usually small compared with the axial scale of variation.

Finally we consider the neglect of electron transport. The average energy of electrons from fission product beta decays is about 0.4 Mev. The average equilibrium fission product gamma ray energy is about 0.9 Mev, and Compton scattering of such gammas produces electrons with about 0.4 Mev average energy. Electrons from photoelectric interactions are somewhat softer and electrons from pair production may be somewhat harder than 0.4 Mev. The range of 0.4 Mev electrons is about 0.12 grams per square centimeter or about 0.011 cm in uranium dioxide, 0.018 cm in Zircaloy, about 0.16 cm in hot liquid water, and about 0.55 cm in 70% voided coolant. Thus fission product electrons and gamma-induced electrons which are born in fuel will deposit essentially all of their energy in fuel. A small fraction of the energy of the electrons emitted in clad and structure is deposited in coolant, while a larger fraction of the energy of the electrons produced in coolant is deposited in adjacent clad or structure.

For simple representations of the electron range-energy dependence, it is possible to compute analytically the energy escape fraction for electrons born uniformly and isotropically in a body. When the thickness (T) of the body is at least twice the electron range (R), and if a linear range-energy approximation is used, then the escape fraction is proportional to R/T. The electron range is approximately proportional to A/Zd, where for the body material A is the atomic weight, Z is the atomic number, and d is the density. Thus the energy escape fraction is proportional to A/ZTd. But the electron energy production rate by Compton scattering of gammas in the body is proportional to ZTd/A. Consider a repeating array of channel walls and bypass regions. The rate of electron energy production in channel wall times the energy escape fraction for the wall equals the rate of electron energy production in the

bypass region times the energy escape fraction for the bypass. Thus these balance, and the electron transport need not be tracked. The narrow-narrow and wide-wide bypass regions are about 1 cm and 2 cm thick, respectively, so noting the electron ranges cited earlier it can be seen that a water-filled bypass is more than twice the eletron range, but a voided bypass is not. For bodies thinner than the electron range the energy escape fraction is more complicated so that the conditions of the energy transport balance are not satisfied. In this case it may be necessary to track electrons as well as gammas. We return to this matter when considering TIP response.

III. GAMMA TIP RESPONSE AND REDISTRIBUTION

The reactor operating state is inferred from, among other data, the incore fixed and traversing detectors. Formerly these were usually neutron detectors, with less than about 5% gamma sensitivity, but there is increasing use of gamma detectors--thermal(2), self powered(13), or voltage driven(14). These have various minor neutron sensitivities, but their signals do not depend so much on the precise location of the detector as may be the case for thermal neutron detectors. Gamma detectors offer advantages in accuracy and hence in increased margins to thermal limits and reduced detector asymmetry (15). Reconstruction of the reactor operating state from the gamma detector signals requires knowledge of the gamma energy production nearby, of gamma transport to the detector, and of the gamma energy deposition as it is converted into heat, differential current, or ionization. It may be noted that gamma detectors respond promptly to the local gamma flux, in contrast, eg, to rhodium and certain other self-powered neutron detectors. However the local gamma flux component which has originated from fission or activation product decay reflects earlier operating states. About one-third of the gamma production during power operation is from delayed fission and activation products, and the resulting lag in gamma detection of power changes can be appreciable for some hours(2).

Gamma radiation from one fuel pin can deposit energy in other fuel pins and structure of an assembly or even in another assembly. These "smearing" effects are not insignificant in normal operation where about 11% of the energy release is in the form of gammas, but they become major effects in a LOCA where up to about half of the energy release is in the form of gammas. Our calculation method deals with gamma redistribution and TIP response together.

KENO-IV was first modified at Yankee to carry out one-iteration fixed source problems. This required a number of changes to the code, including a starter-by-starter error estimator rather than the normal generation-by-generation error estimator. Gammas were started in a selected fuel pin of the

8x8 fuel assembly and the resulting region fluxes were determined using track length estimators. Unit prompt and unit delayed gamma sources were employed and their region-by-region effects, referred to as Green's functions, were later combined with pin-by-pin power distributions from CASMO calculations to determine the effects of prompt and delayed gammas together. Energy deposition effects were computed from the gamma fluxes and flux-to-kermas. TIP response was determined by multiplying gamma fluxes in the TIP region (from a track length estimator) by the iron kerma and by a TIP response function supplied by the manufacturer. The interelectrode region in the TIP is thin compared with the electron range, and as was discussed in the previous section it would be necessary to track electrons in this region in order to determine the response. In the calculation described in Ref. 2 the detector was modeled explicitly and electrons were tracked as well as gammas to determine the response.

The 27 neutron group/18 gamma group cross section library CLOSEUP(8) was reformatted for the Yankee KENO-IV. Prompt gamma ray spectra were determined from this library reaction-by-reaction and combined according to the reaction rates in the pins. Delayed gamma spectra and yields were determined by LASL on the basis of CINDER calculations, first in the form of time-dependent fine-energy group gamma yields versus time after a fission pulse (PEPFYD(16)), then in the form of sums of exponentials from FITPULS(17) calculations. The sums of exponential calculations are applied at Yankee by the code CLOBUG to produce delayed gamma yield spectra for given operating histories and cooling times. Starting gammas were selected to be uniform in the fuel pin.

Figure 2 shows representative pin-to-TIP Green's functions for a typical 8x8 Vermont Yankee fuel assembly at hot, 40% void operating conditions near beginning of exposure. Between 80000 and 160000 histories were calculated for each starting fuel pin, depending on location. Adjoint transport calculations, starting the gammas with the TIP flux-to-response spectrum in the TIP region, would have been more efficient for TIP response, but were not used because the results of the forward calculations also can be used for gamma redisribution analyses. The pin-to-TIP Green's functions shown in Fig. 3 fall off rapidly from the pin adjacent to the TIP. Because zero-current boundary conditions are used it is advisable to employ multiple assembly geometries (8) for calculating pin-to-effect Green's functions for outside pins in an assembly. The source gamma spectra and the resulting pin-to-TIP Green's functions appear to be insensitive to depletion.

The gamma transport medium used for these calculations is for beginning of exposure. The primary effect of depletion in the reactor fuel is to convert actinides to neutron-rich

fission products. These transmute by neutron emission and by negatron emission. When the emitted neutrons are captured the residual nuclei also may decay by negatron emission. In either case nuclear neutrons are converted into protons and the betas become atomic electrons to maintain charge balance. Thus the electron density increases in the fuel with accompanying changes in gamma transport properties. The net change in cell-average electron density is estimated to be of order 0.3% over the fuel exposure. Compton scattering cross sections vary as electron density, photoelectric cross sections vary roughly as the cube of the electron density, and pair production cross sections vary as the square of the electron density. The overall effect is to increase the gamma cross sections by 0.3% to 0.9 % in various energy regions. The overall effect on TIP response and gamma redistribution can be estimated by recalculating the pin-to-TIP Green's functions for transport in end-of-exposure material, but this has not been done because changes would be difficult to distinguish from statistical fluctuations.

Pin power distributions from a CASMO depletion for a 40% void fuel assembly were combined with the calculated pin-to-TIP Green's functions to produce the relative gamma TIP detector responses shown in Fig. 4. The TIP response for a four-bundle fuel cell is then calculated from the local power-weighted bundle TIP responses.

IV. CONCLUSIONS

The methodology described here utilizes available transport codes and cross section libraries. The characterization of gamma source spectra and yields is improved, particularly for delayed gammas. Recent LASL work indicates that delayed gamma data for cooling times below 1000 seconds can be improved(18), but the format of data presentation is maintained. The necessary Monte Carlo calculations are costly, but the insensitivity of the Green's functions to depletion suggests that relatively few calculations may be required. This methodology is being examined by comparison with Vermont Yankee results for application to Vermont Yankee operation.

REFERENCES

1. H. Steinberg, H. Lichtenstein, and M. O. Cohen, "An Analysis of Post LOCA Gamma Ray Effects in Representative Light Water Reactors", EPRI NP-425, 1976.
2. L. Bourdet, C. Cladel, O. Hoclet, A. Le Dieu de Ville, and J. C. Nimal, "Studies Relative to the Heating of the Gammma Thermometer", SERMA/T/No. 358.
3. R. B. Bass and W. R. Johnson, "Spatial Distribution of Fission Product Gamma-Ray Energy Deposition in Light Water

Reactor Fuel Elements", EPRI NP-672, Vol. 1, 1978.
4. L. M. Petrie and N. F. Cross, "KENO-IV, An Improved Monte Carlo Code", ORNL-4948, Oak Ridge National Laboratory, 1975.
5. M. J. Hebert, D. R. Harris, and E. E. Pilat, "Monte Carlo Analysis of Bypass Heating in a BWR", Trans. Am. Nuc. Soc. 41,589(1982).
6. M. J. Hebert, D. R. Harris, D. M. Kapitz, W. J. Morse, and E. E. Pilat, "Analysis of Gamma TIP Response in a Boiling Water Reactor", Trans. Am. Nuc. Soc. 41, 610(1982).
7. R. W. Roussin,"CASK, 40-Group Coupled Neutron and Gamma-Ray Cross Section Data", ORNL/RSIC, DLC-23, Oak Ridge National Laboratory, 1974.
8. M. J. Hebert, E. E. Pilat, D. M. Kapitz, D. R. Harris, J. A. Meyer, and M. Edenius, "Monte Carlo Validation of Integral Transport and Diffusion Theory Methods for BWR Core Analysis", Trans. Am. Nuc. Soc. 38,684(1981).
9. Private communication, M. Westfall. J. A. Bucholz, SCALE: A Modular Code System for Performing Standardized Computer Analyses for Licensing Evaluation", NUREG/CR-0200, 1980.
10. G. J. Scatena and G. L. Upham, "Gamma Heating Distribution in a BWR Lattice During Normal Operation and Accident Conditions", NEDO-20214, 73NED110, General Electric Company, 1973.
11. J. A. Naser and B. R. Sehgal, "Monte Carlo Calculations of Direct Moderator Heating for BWR's", Trans. Am. Nuc. Soc. 34, 485(1980).
12. C. L. Martin, "Nuclear Basis for ECCS (Appendix K) Calculations", NEDO-23729, 77NED306, General Electric Company, 1977.
13. N. P. Goldstein and W. H. Todt, "A Survey of Self-Powered Detectors-Present and Future", IEEE Sym. on Nuclear Power Systems, 1978.
14. "Gamma Traversing Incore Probe (TIP) System", General Electric Company, 1980.
15. J. L. Goudey and J. J. Chromik, "Special TIP and Gamma Scan Comparisons for Hatch-1", EPRI-NP-562, Electric Power Research Institute, 1979.
16. R. J. Labauve, T. R. England, D. C. George, and M. G. Stamatelatos, "The Application of a Library of Processed ENDF/B-IV Fission-Product Aggregate Decay Data in the Calculation of Decay-Energy Spectra", LA-7483-MS, Los Alamos National Lab. (1978).
17. R. J. Labauve, D. C. George, and T. R. England, "FITPULS, a Code for Obtaining Analytic Fits to Aggregate Fission-Product Energy Spectra", LA-8277-MS, Los Alamos National Lab. (1980).
18. D. C. George, R. J. Labauve, and T. R. England, "Application of Adjusted Data in Calculating Fission-Product Decay Energies and Source Spectra", LA-9362-MS, 1982.

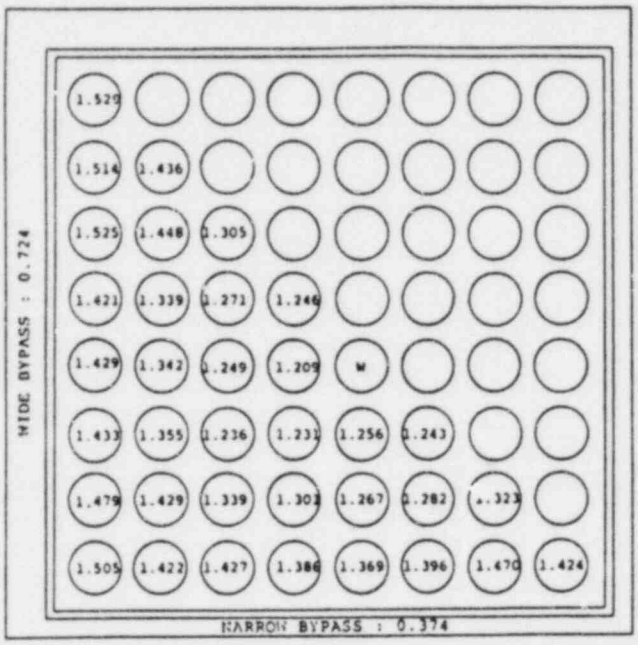

FIGURE 1: Percent of total gamma deposition in the fuel pins and bypass regions of a typical BWR fuel bundle.

					PROMPT DELAYED		
			W	.286±.093 .465±.194			
			.595±.171 .299±.077	.973±.210 1.062±.283	2.072±.501 .538±.149		
			1.627±.330 .865±.263	2.634±.490 1.195±.289	3.677±.657 1.053±.208	3.741± .602 2.128± .370	
		1.381±.362 .214±.135	2.006±.594 1.025±.226	3.139±.594 1.936±.285	5.139±.830 2.615±.377	6.749±1.001 5.723± .790	17.180±1.213 8.949± .634

PROMPT AND DELAYED PIN-TO-TIP GREEN'S FUNCTIONS

FIGURE 2

TABLE 1

Neutron and Gamma Energy Deposition for a Typical 8x8 BWR Bundle Under Varying Void Conditions. (Mev/fission)

	gamma deposition	neutron deposition	total deposition
0% VOID	0.45	0.81	1.26
40% VOID	0.48	1.08	1.56
70% VOID	0.51	1.44	1.95

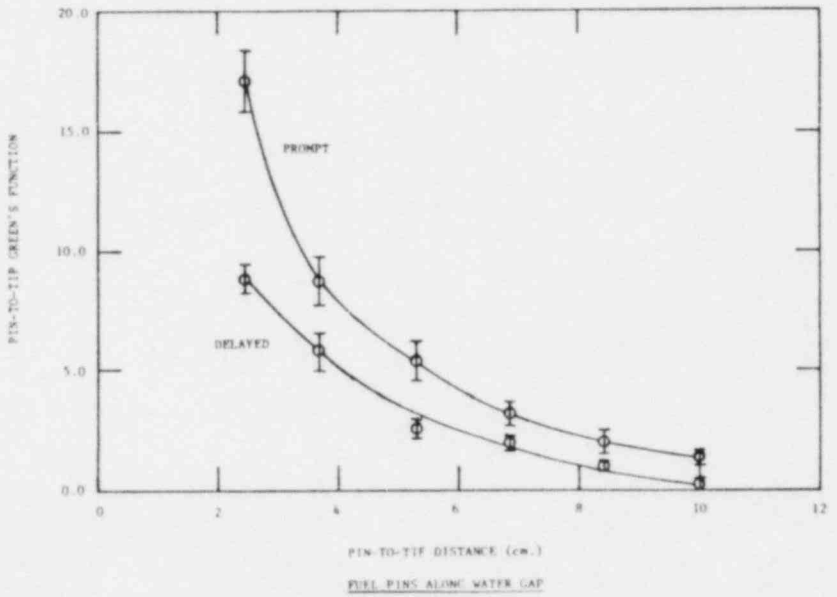

FUEL PINS ALONG WATER GAP

FIGURE 3

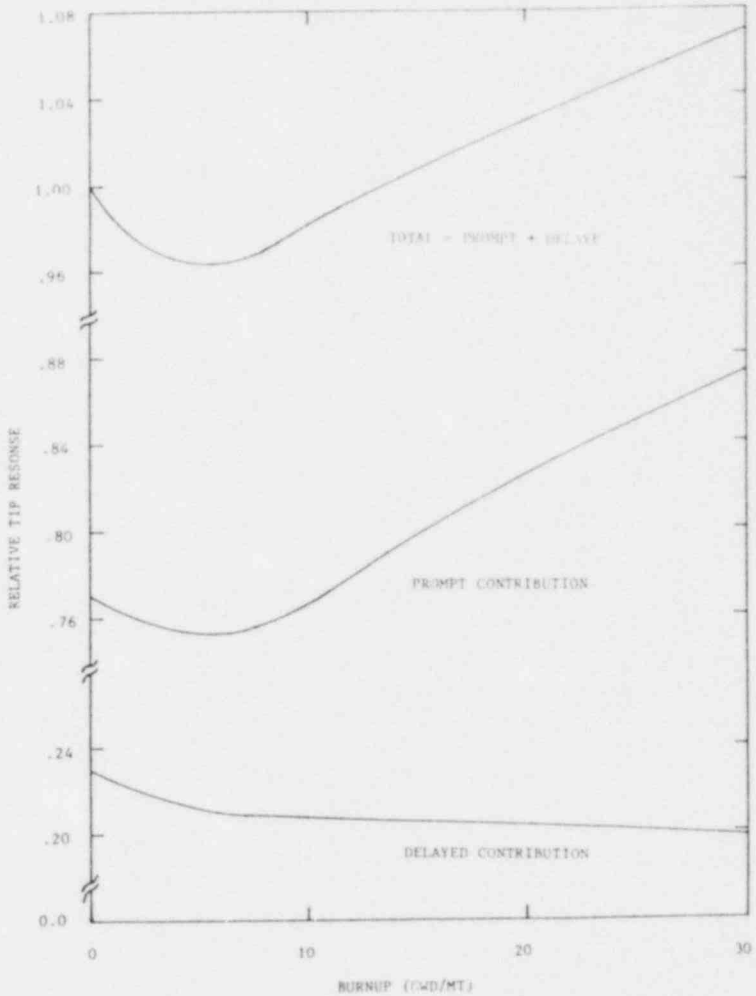

FIGURE 4 TIP RESPONSE BY BURNUP

STATISTICAL METHODS USED IN QUANTIFYING THE ACCURACY OF EPRI-NODE-P AT OCONEE

L. H. Flores
Duke Power Company
Charlotte, NC

Abstract

In reload design applications, accuracy factors must be derived which can benchmark design code predictions to in-core measurements. A statistical methodology is presented wherein Observed Nuclear Reliability Factors (ONRF)[1] were derived for the nodal simulator EPRI-NODE-P[2]. Comparisons of calculated and measured power distributions were performed for Cycles 1 through 5 of the Oconee Unit 1 reactor. Based on these comparisons, ONRFs were derived for assembly radial (2-D) and assembly peak (3-D) power predictions.

Procedural Outline

The derivation of ONRFs required a three step procedure:

1) Assemble in-core power measurements into a measurement (M) data base.

2) Assemble EPRI-NODE-P power predictions into a calculated (C) data base.

3) Statistically combine C and M data to yield ONRFs.

The C and M data bases consisted of assembly radial (R) powers and assembly peak (P) powers. ONRFs were then derived separately for R and P data.

Measurement Data Base

The Oconee reactor's in-core power is monitored by 52 strings of fixed self-powered neutron detectors. Each string contains seven equally spaced rhodium emitters. These strings form a spiral pattern which can be collapsed to effectively instrument each assembly in an octant.

Figure 1 displays the number of detector strings for each assembly folded into an octant. All symmetrically located detectors were algebraically averaged to:

1) minimize power variations due to tilts, signal aberrations, etc.

2) provide compatability with EPRI-NODE-P, which calculates eighth core symmetric power distributions.

All power measurements were taken at approximately equilibrium Xenon conditions and at full rated thermal power (2568 Mwt). Table 1 presents a cycle by cycle description of measurement data.

Unit 1 operated in the rodded mode during cycles 1 through 3, and in a nonrodded (only part-length rods inserted) mode for cycles 4 and 5. During cycle 3, a large enough number of individual detectors were failed to disqualify these power measurements from the final M data base.

EPRI-NODE-P Calculations

EPRI-NODE-P is a nodal code which is similar to the FLARE[3] code. The Oconee calculations were performed in a "core-follow" type mode where the reactor's power and control rod positions were replicated. All power distribution calculations were performed at equilibrium Xenon conditions since the core was approximately at equilibrium during the measurements.

Variable Definitions

The following equations define the variables which were used in the ONRF derivation. The algebraic difference variable was defined:

$$D_i = C_i - M_i \qquad (1)$$

where: D is the i^{th} difference; $1 \leq i \leq N$

C is the i^{th} calculated value (R or P)

M is the i^{th} measured value (R or P)

R is the assembly power relative the core average assembly power.

P is the assembly maximum axial power relative to the core average power

The mean of the difference is defined:

$$\bar{D} = \bar{C} - \bar{M} \qquad (2)$$

where:

$$\bar{C} = \left(\sum_{i=1}^{N} C_i \right) \div N \qquad (3)$$

$$\bar{M} = \left(\sum_{i=1}^{N} M_i \right) \div N \qquad (4)$$

$$\bar{D} = \left(\sum_{i=1}^{N} (C_i - M_i) \right) \div N \qquad (5)$$

N = number of observations in sample

From equation 2, it can be assumed that the variable D is random; and furthermore that D is normally distributed.

Normality Test Results

The frequency distributions of the variable D were examined for sixteen different groups. The ANSI D' Test[4] was used with a 5% level of significance as the normality criterion. This test is a two-sided one, having critical high and low values. A test statistic (D') is formulated, then the distribution is judged normal if D' falls between the critical values.

As shown in Table 2, nine groups passed the test. The remaining seven were judged nearly normal for two reasons:

1) All D' statistics were within 2% of the critical values.

2) An ocular examination of these distributions indicated that they behaved more like normal distributions than others, e.g., uniform.

Figures 2 and 3 are examples of nearly normal and normal distributions as determined by the D' Test.

ONRF Formulation

The following presents a statistical derivation of the Observed Nuclear Reliability Factor by employing one-sided upper tolerance limit (OSUTL) methodology. For a normal random variable X with mean $\bar{X}$ and standard deviation S, the OSUTL of X is defined by:

$$OSUTL(X) = \bar{X} + K \times S \tag{6}$$

where:

$$\bar{X} = \left(\sum_{i=1}^{N} X_i\right) \div N \tag{7}$$

$$S = \left[\left(\sum_{i=1}^{N} (X_i - \bar{X})^2\right) \div (N-1)\right]^{\frac{1}{2}} \tag{8}$$

In equation 6, K is the one-sided tolerance factor. Equation 6 is formulated such that a predetermined proportion of the population (Pr) is below the OSUTL with a confidence factor (α)[5]. K is a function of N, Pr, and α.

Following industry practice, Pr = 95% and α = 95%.

Similarly, the OSUTL for D is given:

$$OSUTL(D) = \bar{D} + K \times S(D) \tag{9}$$

Since C is a deterministic variable, only an upper limit can be estimated by:

$$UL(C) = \bar{M} + OSUTL(D) \tag{10}$$

or:

$$UL(C) = \bar{M} + \bar{D} + K \times S(D) \quad (11)$$

or:

$$UL(C) = \bar{C} + K \times S(D) \quad (12)$$

From equation 12, we see that the upper limit is a function of the variable C and the standard deviation depends upon the difference distribution.

Since more concern is given to underprediction of powers rather than overprediction, equation 11 is modified by changing the sign of $\bar{D}$.

$$UL(C) = \bar{M} - \bar{D} + K \times S(D) \quad (13)$$

Another conservatism, mentioned earlier, was decreasing the number of observations per reactor state point to 29. This increases the value of K, for example:

$$K\ (.95, .95, 290) = 1.80 \quad (14)$$

while $$K\ (.95, .95, 520) = 1.76 \quad (15)$$

Finally, the ONRF is defined as:

$$ONRF = UL(C) \div \bar{M} \quad (16)$$

The ONRF is used as a multiplicative (safety) factor with calculated powers such that:

$$ONRF \times C \leq M \quad (17)$$

for 95% of the population with a confidence factor of 95%.

ONRF Calculation Procedure

ONRFs were calculated separately for R or P data. Corresponding C and M data were paired into observations. Observations were deleted for which C or M were not greater than or equal to 1.0. This was an engineering judgment that only those powers greater than or equal to the core average were to be the primary area of concern.

Results

Tables 3 and 4 display difference statistics for R and P data, respectively. Then using equation 16, the following ONRFs were derived:

		Radial ONRF	Peak ONRF
1.	Rodded (1, 2)	1.03	1.10
2.	Unrodded (4, 5)	1.03	1.04
3.	Combined	1.04	1.08

Presently, all three Oconee Units are operating in the unrodded mode. Therefore, the unrodded ONRFs will be used for future analyses. As an additional conservatism, these factors were increased such that ONRF(R) = 1.05 and ORNF(P) = 1.075.

Verification

The 1.05 radial factor was tested by comparing the product of 1.05 x calculated maximum radial to the measured maximum radial for all 46 state points (cycles 1, 2, 4, 5). Similarly, the 1.075 peak factor was tested versus the measured peaks.

The 1.05 radial factor satisfied equation 17 for all rodded and unrodded cases. The 1.075 peak factor was satisfactory for 96% (26/27) of the rodded cases and all unrodded cases.

Summary

Data bases of measured and calculated assembly relative powers were assembled covering 5 cycles of Oconee-1 operation. Difference distributions from measured and calculated data were verified as either normal or nearly normal. Normal distribution theory was then employed to formulate an Observed Nuclear Reliability Factor (ONRF). ONRFs were calculated and tested for acceptability.

Table 1

Oconee Unit 1 Operation History

Cycle	Mode	EFPD	Control Bank Movement (EFPD)	Number of State Points
1	Rodded	310	92 (RI)[1] 196 (RI)	17
2	Rodded	292	53 (RI) 237 (RW)[2]	10
3	Rodded	304	100 (RI) 246 (RW)	10
4	Unrodded[3]	246	-	9
5	Unrodded[3]	304	-	10

Notes:

1. RI: Bank 7 Pattern Change
2. RW: Bank 7 Withdrawn
3. Bank 7 ~ 80 - 100% Withdrawn During Cycle

Table 2
Difference Distribution Normality Tests
For C,M $\geq$ 1.0 - 5% Level of Significance

Assembly Radial Power

Cycle	N	D'(P = .025)	D'	D'(P = .975)	Remarks
1	308	1504.2	1471.7	1540.0	nearly normal
2	147	492.7	495.0	509.8	normal
3	119	357.4	365.9	371.2	normal
4	144	477.4	483.1	494.1	normal
5	131	414.1	423.1	429.3	normal
1,2	455	2707.5	2660.1	2760.8	nearly normal
4,5	275	1267.5	1285.9	1300.0	normal
1,2,4,5	730	5516.5	5430.7	5602.0	nearly normal

Assembly Peak Power

Cycle	N	D'(P = .025)	D'	D'(P = .975)	Remarks
1	377	2039.7	2034.4	2083.4	nearly normal
2	235	1000.2	998.8	1027.6	normal
3	211	850.3	819.1	874.9	nearly normal
4	199	777.8	789.5	801.0	normal
5	216	880.6	909.5	905.8	normal
1,2	612	4230.8	4172.6	4302.6	nearly normal
4,5	415	2357.5	2397.5	2405.8	normal
1,2,4,5	1027	9220.0	9061.1	9340.2	nearly normal

Table 3

Difference Means and Standard Deviations

for Radials (C,M $\geq$ 1.0)

Cycle	N	$\bar{D}$	S(D)	$\overline{ABS(D)}$	$\overline{S(ABS(D))}$
1	308	-.018619	.038282	.032867	.027010
2	147	-.013606	.050752	.039850	.034107
3	119	-.004970	.053062	.043281	.030844
4	144	-.000243	.029224	.022964	.017974
5	131	.008747	.031790	.026906	.018926
1,2	455	-.016999	.042718	.035123	.029633
4,5	275	.004040	.030748	.024842	.018505
1,2,4,5	730	-.009074	.039949	.031250	.026466

Table 4

Difference Means and Standard Deviations

for Peaks (C,M $\geq$ 1.0)

Cycle	N	$\bar{D}$	S(D)	$\overline{ABS(D)}$	$\overline{S(ABS(D))}$
1	377	.004010	.077792	.061397	.047834
2	235	-.022739	.061448	.049263	.043104
3	211	.014339	.085612	.062537	.060055
4	199	-.018769	.053858	.044837	.035132
5	216	-.012163	.048515	.041721	.027453
1,2	612	-.006262	.073073	.056737	.046416
4,5	415	[illegible]1	.051191	.043215	.031371
1,2,4,5	1027	[illegible]09926	.065246	.051273	.041524

FIGURE 1

OCONEE FUEL ASSEMBLY MAP

NUMBER OF DETECTOR STRINGS PER ASSEMBLY
IN EIGHTH-CORE GEOMETRY

H	1	1	1	1	1	1	1	1
K	1	2	8*	2	2	2	1	
L	1	2	2	8*	2	1		
M	1	2	2	1				
N	1	1	1					
O	1							

* SYMMETRICALLY LOCATED STRING

Figure 2

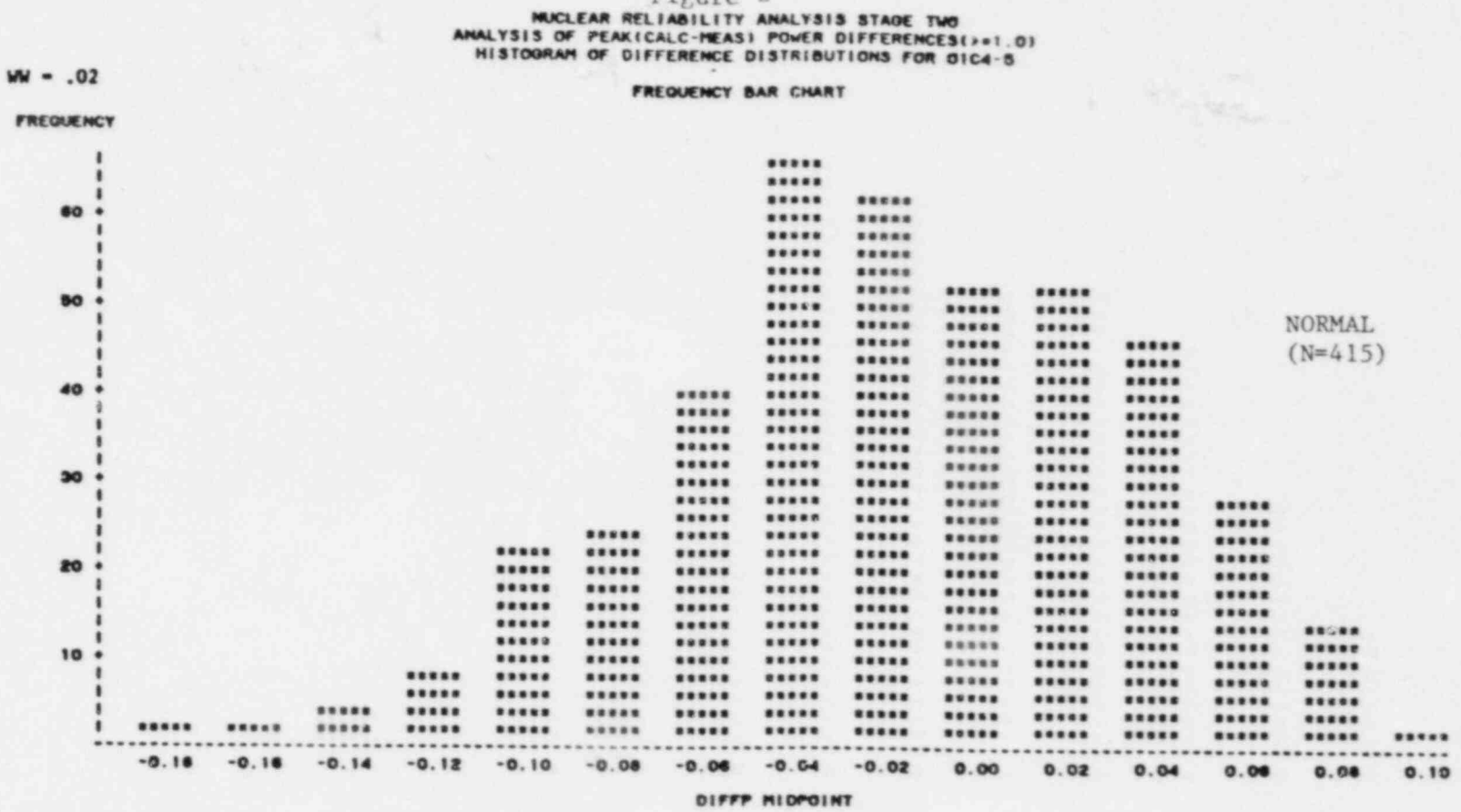
NUCLEAR RELIABILITY ANALYSIS STAGE TWO
ANALYSIS OF PEAK(CALC-MEAS) POWER DIFFERENCES(>=1.0)
HISTOGRAM OF DIFFERENCE DISTRIBUTIONS FOR 01C4-5
FREQUENCY BAR CHART
WW = .02
FREQUENCY
60
50
40
30
20
10
NORMAL
(N=415)
-0.18
-0.16
-0.14
-0.12
-0.10
-0.08
-0.06
-0.04
-0.02
0.00
0.02
0.04
0.06
0.08
0.10
DIFFP MIDPOINT

Figure 3

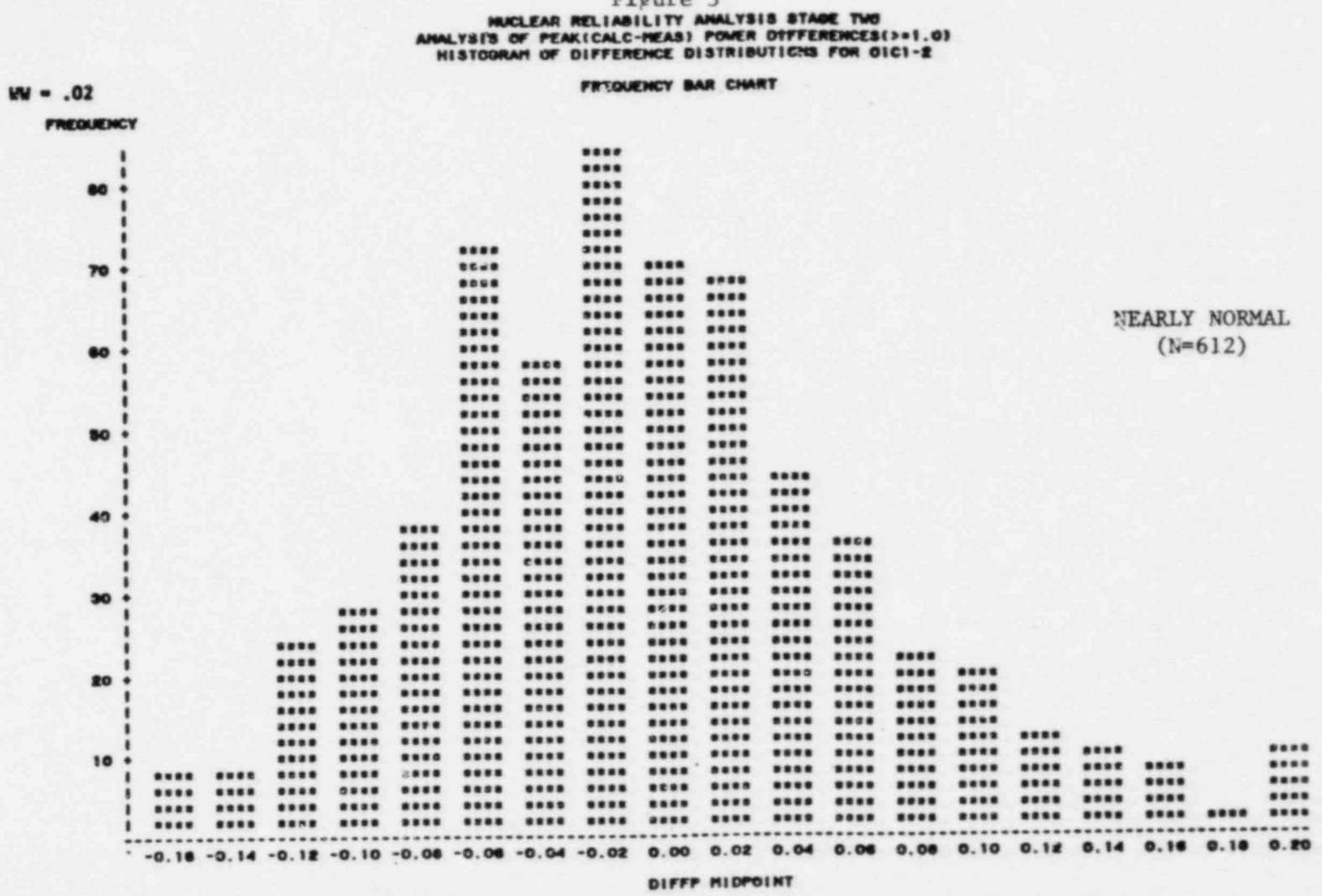
NUCLEAR RELIABILITY ANALYSIS STAGE TWO
ANALYSIS OF PEAK(CALC-MEAS) POWER DIFFERENCES(>=1.0)
HISTOGRAM OF DIFFERENCE DISTRIBUTIONS FOR OIC1-2
FREQUENCY BAR CHART
WW = .02
FREQUENCY
80
70
60
50
40
30
20
10
-0.16 -0.14 -0.12 -0.10 -0.08 -0.06 -0.04 -0.02 0.00 0.02 0.04 0.06 0.08 0.10 0.12 0.14 0.16 0.18 0.20
DIFFP MIDPOINT
NEARLY NORMAL
(N=612)

References

1. Duke Power Company, "Oconee Nuclear Station Reload Design Methodology," NFS-1001, April 1979.

2. B. M. Rothleder, J. R. Fisher, "EPRI-NODE-P," EPRI-ARMP System Documentation, Part II, Chapter 14, September 1977.

3. D. L. Delp, D. L. Fisher, J. M. Harriman, M. J. Stedwell, "FLARE A Three-Dimensional Boiling Water Reactor Simulator," GEAP-4598, July 1964.

4. American National Standards Institute, Inc., "Assessment of the Assumption of Normality (Employing Individual Observed Values)," ANSI N15.15-1974, 1974.

5. D. B. Owen, "Factors For One-Sided Tolerance Limits And For Variable Sampling Plans," SCR-607, Sandia Corporation Monograph, March 1963.

EXPERIMENTAL QUALIFICATION OF THE CALCULATED SUBCRITICALITY IN HIGH DENSITY FUEL STORAGE

A. SANTAMARINA *et al.*

Commissariat à l'Energie Atomique - Département des Réacteurs à Eau
CEN. CADARACHE - B.P. n°1 - 13115 - Saint Paul lez Durance - FRANCE

At various steps the fuel cycle of PWR reactors necessitates assembly storage either fresh or burned. Economic criteria lead to a minimization in the volume of the storage pools, brought about by reducing the fuel assembly lattice pitch ; on the other hand safety criteria define that the storage must always be subcritical ($k_\infty < 0.95$).

In this context, the CRISTO experiment has been conceived in order to qualify the calculation schemes of these storage lattices and to validate criticality calculations in accidental configurations : this experiment provides the multiplication factor of subcritical lattices for which a traditional critical experiment is not feasible. Cosponsored by CEA and FRAMATOME, CRISTO was realized in the EOLE reactor at Cadarache, CEA Center.

The first experiment, CRISTO I, using a wide pitch (water gap = 8 and 10 cm) and a grey absorber (2 and 4 mm stainless steel) was performed in 1978 ; description of the facility as well as some results has already been published /1/. The aim of the CRISTO II experiment (1980-1981) presented here, is the study of high density storages : water gap e_{H_2O} = 4,5 cm and 6,5 cm. The experiment allows the comparison of the antireactivity introduced by various kinds of neutron absorber plates (stainless steel, borated steel, cadmium...) . Moreover the experiment provides the k_∞ curve (and consequently the saturation point) as a function of the increase of the absorber efficiency (from 0 to 20 mg/cm^2 of ^{10}B).

THE CRISTO EXPERIMENT

The storage area is simulated by a section, containing four bundles of 14 x 14 UO_2 pins, loaded in a square cavity (Figure 1). The fuel characteristics are similar to those of a 17 x 17 PWR with 3 % ^{235}U - enriched UO_2 rods. The cavity is surrounded by a MTR driver core which enables the reactor criticality ; progressively larger loading of enriched U-Al plates, allows us to investigate absorbers which are increasingly strong in the test zone : stainless steel, borated steel plates doped at 2.5, 5 and 10 mg/cm^2 in ^{10}B, B_4C, cadmium.

This facility enables various kinds of measurements :

- Radial and axial fission distributions in both test zone and driver core (γ-scanning and fission chamber measurements)
- Thermal flux measurements inside the water gap (Mn detectors)
- Spectral indices (depleted and enriched U detectors).

These measurements allow us, on the one hand to validate the interpretation core calculations and on the other hand to point out the causes of an eventual discrepancy between experiment and calculation on the k_∞ of the concerned storage lattices.

This integral parameter k_∞^{sto} is defined from an equivalence with a regular lattice (same UO_2 rods, but the pitch lattice is 1.58 cm) which is loaded in the whole cavity and poisoned with boric acid until the criticality of the reactor is reached. The k_∞^{reg} of this "equivalent" regular lattice is inferred from radial and axial buckling measurements.

This method which "weighs" the k_∞^{sto} through a regular lattice would be directly exploitable if the interaction effects between the Test Zone (T.Z.) and the Driver Zone (D.Z.) remained the same in both kinds on core. In fact these effets differ : variation of the spectral coupling effects and of the relative weights between T.Z. and D.Z., and modification of the leakage rate between the two kinds of experimental core.

We have therefore been led to define a very accurate calculation scheme of these cores : the interpretation calculations, thus performed, allow us to eliminate the parasitic effects which are linked to the presence of the driver core. These calculated corrections only introduce an acceptable uncertainty which is the same size as the uncertainty associated with the k_∞^{reg} measurement of the regular lattice.

CORE CALCULATION SCHEME

This scheme is exclusively based on the use of the transport theory :

- the first step of homogeneization of the fissile media is carried out through infinite lattice calculations with APOLLO (first probability collision method)
- the second step in obtaining collapsed-groups cross-sections (from 99 groups to 6 groups) is realized from local spectra computed by APOLLO on the radial geometry of the core
- the accurate core calculations (real XY geometry, R and RZ calculations) are performed with the DOT 3.5 code in S_4 quadrature.

THE INTERPRETATION PRINCIPLE

Determination of the experimental k_∞^{sto}

The decomposition of the keff reactor by neutron balance /2/ gives the following :

$$\frac{keff^{sto} - keff^{reg}}{keff^{reg}} = \frac{\Delta\, keff}{keff} = P_{rel}^{TZ} \cdot \left(\frac{\Delta k_\infty}{k_\infty}\right)^{TZ} + \frac{\Delta X}{X} \qquad (1)$$

where : $P_{rel}^{TZ} = \dfrac{Prod^{TZ}}{Prod^{TZ} + Prod^{DZ}}$ relative production in the Test Zone.

$\frac{\Delta X}{X}$ symbolizes the difference in contributions, of the various interaction effects TZ/DZ, between the two types of experimental cores.

Supposing that $\frac{\Delta X}{X}$ is correctly computed by core calculations, the formula (1) becomes :

$$\left(\frac{\Delta keff}{keff}\right)_{meas} - \left(\frac{\Delta keff}{keff}\right)_{calc} = P_{rel}^{TZ} \left[\left(\frac{\Delta k_\infty}{k_\infty}\right)_{meas}^{TZ} - \left(\frac{\Delta k_\infty}{k_\infty}\right)_{calc}^{TZ} \right]$$

in other terms:

$$\left(\frac{k_\infty^{sto} - k_\infty^{reg}}{k_\infty^{reg}}\right)_{meas} = \left(\frac{\Delta k_\infty}{k_\infty}\right)_{calc} + \left[\left(\frac{\Delta keff}{keff}\right)_{meas} - \left(\frac{\Delta keff}{keff}\right)_{calc} \right] \Big/ P_{rel}^{TZ} \qquad (2)$$

The analysis of the various interaction effects contributing to the $\frac{\Delta X}{X}$ term and the estimation of the associated calculation inaccuracies, enable us to obtain the imprecision introduced into the $\frac{\Delta keff}{keff}$ calculated value, and thereby the associated uncertainty of the k_∞^{sto} experimental value.

Interpretation calculations

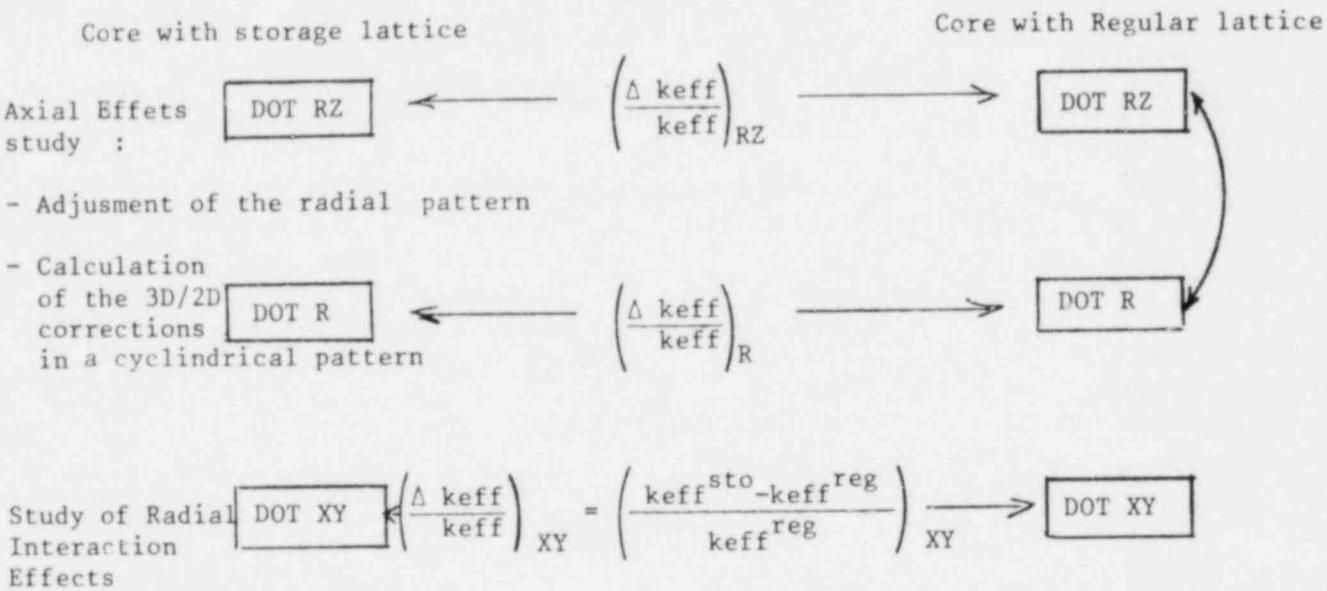

These consecutive calculations provide the $\left(\frac{\Delta keff}{keff}\right)_{calc}$ term, necessary to the (2) formula, as follows :

$$\left(\frac{\Delta keff}{keff}\right)_{calc} = \left(\frac{\Delta keff}{keff}\right)_{XY} + \underbrace{\left(\frac{\Delta keff}{keff}\right)_{RZ} - \left(\frac{\Delta keff}{keff}\right)_{R}}_{\text{3D/2D correction}}$$

The core calculations, performed in the regular lattice configuration, also provide the spatial corrections to be applied to the measured bucklings : the elimination of the perturbations brought about by the driver zone (entering current, difference in height between the Test and Driver Zones) put these measurements back onto the fundamental mode ; these corrected measurements can then be adjusted by the eigen functions of Laplace's operator and therefore supply the associated

geometrical bucklings of each axis. The k_∞^{reg} is deduced with a 200 pcm uncertainty (which is one standard deviation), Moreover this precision allows these measurements to become references for the qualification studies of cell or assembly PWR codes.

QUALIFICATION OF CRITICALITY CALCULATIONS OF INFINITE LATTICE STORAGE

The k_∞ experimental values obtained in the most compact configurations, 4.5 cm interassembly watergap, are shown figure 2,

The corresponding interpretation values are devided from the APOLLO-DOT scheme that we set up for the calculation of these lattices. The experiment/calculation discrepancy remains less than 400 pcm. Alone, the grey absorber (2 mm stainless steel plate) is not accurately calculated ; the 1000 pcm overestimation of k_∞ by calculation is corroborated through another experiment without any absorber. The observed experiment/calculation discrepancy originates from a calculated underestimation of the strong thermal flux increase in the watergap : this is clearly pointed out through the interpretation of the thermal flux radial measurements in the cavity (Figure 3).

Our studies show that the numerical errors, linked to the DOT discretization of the Boltzmann equation variables, can only improve the results by about 100 pcm. In fact the error is likely to be linked to the UO_2 cell homogeneization at the fuel assembly/watergap boundary ; this assumption is now being checked,

REFERENCES

/1/ - J. BOUCHARD et al
"Some Recent Studies on Light Water Reactor Physics"
ANS 1980 - Advances in reactor Physics and Shielding.
Sun Valley September 1980

/2/ - A. SANTAMARINA
"Some problems related to the small zone experiment analysis".
23rd NEACRP meeting, at Argonne National Laboratory West, Idaho (USA)
22-26 September 1980.

Figure 1 : "CRISTO II" EXPERIMENT

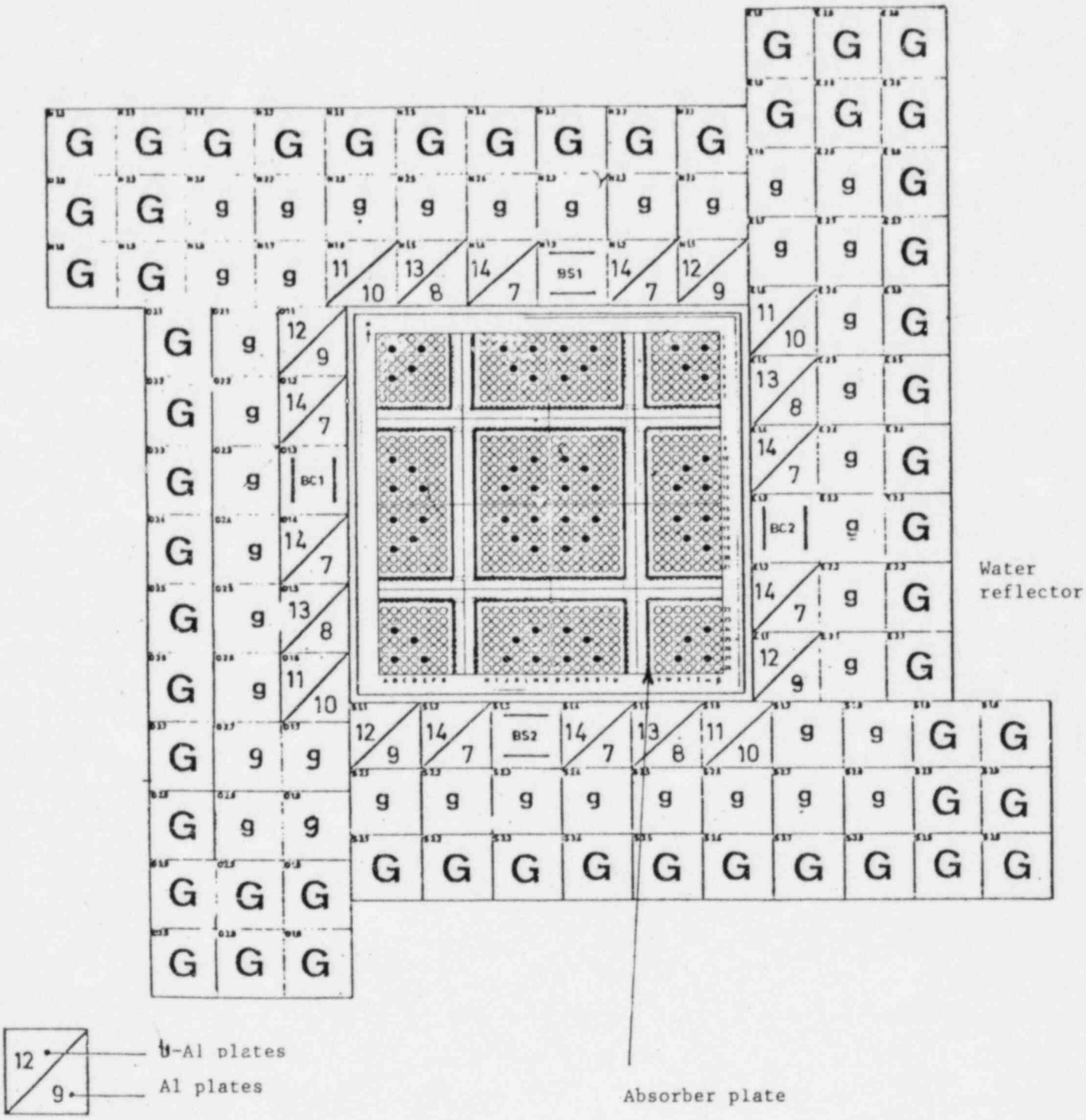

Figure 2

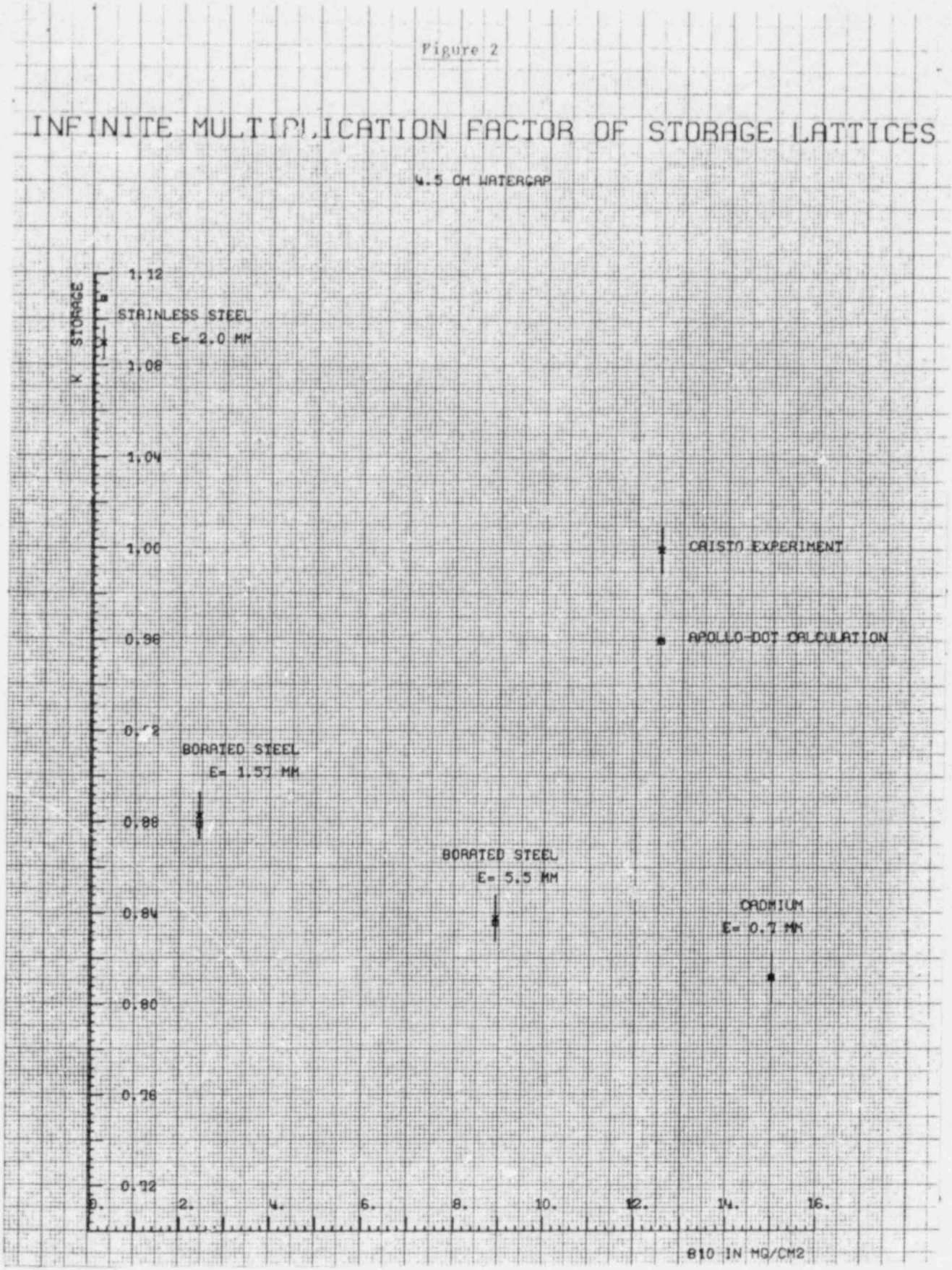
INFINITE MULTIPLICATION FACTOR OF STORAGE LATTICES
4.5 CM WATERGAP
K STORAGE
1.12
1.08
1.04
1.00
0.96
0.92
0.88
0.84
0.80
0.76
0.72
STAINLESS STEEL
E= 2.0 MM
BORATED STEEL
E= 1.57 MM
BORATED STEEL
E= 5.5 MM
CADMIUM
E= 0.7 MM
CRISTO EXPERIMENT
APOLLO-DOT CALCULATION
0.
2.
4.
6.
8.
10.
12.
14.
16.
B10 IN MG/CM2

Figure 3

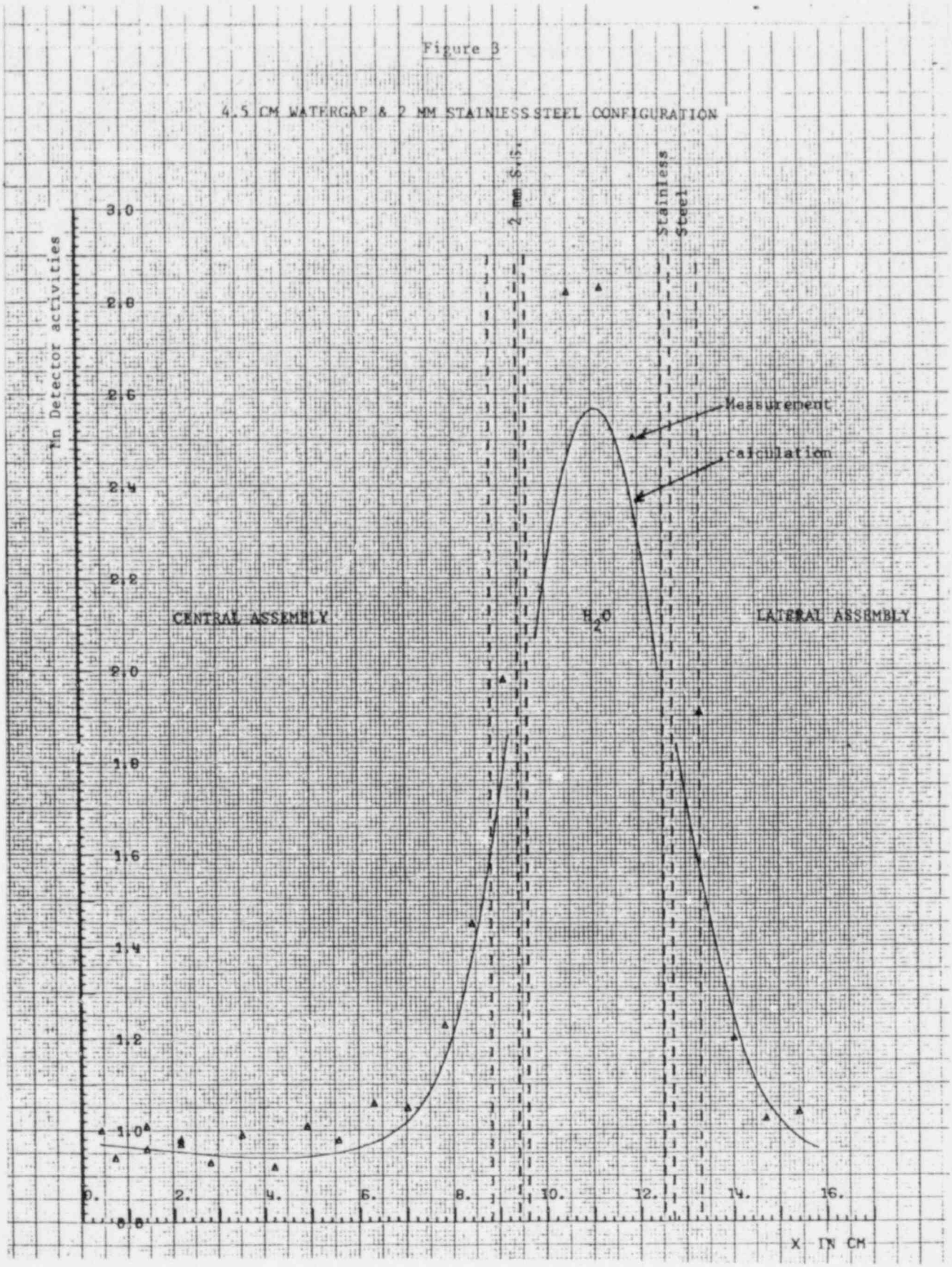
4.5 CM WATERGAP & 2 MM STAINLESS STEEL CONFIGURATION
In Detector activities
3.0
2.8
2.6
2.4
2.2
2.0
1.8
1.6
1.4
1.2
1.0
0.8
2 mm S.S.
Stainless Steel
Measurement
calculation
CENTRAL ASSEMBLY
H_2O
LATERAL ASSEMBLY
0.
2.
4.
6.
8.
10.
12.
14.
16.
X IN CM

ASSESSMENT OF THE COBRA-TF SUBCHANNEL CODE

J. M. Kelly, R. J. Kohrt, M. J. Thurgood
Battelle
Pacific Northwest Laboratory
Richland, Washington

ABSTRACT

The COBRA-TF computer program is being developed to predict the coupled thermal-hydraulic/rod deformation response of a LWR core to both design basis accidents and anticipated transients. COBRA-TF provides a two-fluid, three-field (liquid, entrained-liquid, vapor-gas mixture), three-dimensional representation of two-phase flow. This requires the solution of a nine equation model (4 mass, 2 energy, and 3 momentum) and the specification of numerous constitutive relations for closure of the system. To qualify these models, an extensive assessment effort is planned. Data comparisons with the FRIGG forced flow boiling tests, General Electric 9-rod mixing tests, and the Bennett post-CHF heat transfer tests are presented. The ability to predict axial void profiles in subcooled and bulk boiling, dryout and dispersed flow heat transfer in tubes, and single-phase turbulent mixing was demonstrated. Although the capability to compute lateral void drift exists, the current two-phase mixing model needs improvement.

INTRODUCTION

The COBRA-TF (Coolant Boiling in Rod Arrays-Two Fluid) computer program is being developed at the Pacific Northwest Laboratory by the U.S.-N.R.C to provide a best-estimate LWR hot bundle analysis capability. In particular, this program has two main objectives:

- develop a hot bundle/hot channel code to predict coupled thermal-hydraulic/rod deformation behavior, and
- incorporate and assess flow blockage heat transfer models for the reflood phase of a LOCA (loss of coolant accident).

The code development program designed to meet these objectives is discussed below, followed by a brief code description and a sampling of code assessment results.

Figure 1 illustrates the hot bundle analysis concept. First, a simulation of the primary system response to a designated transient would be performed with one of the best-estimate two-fluid system codes (e.g., COBRA/TRAC[1], TRAC-PF1[2], RELAP-5[3]). From this calculation, which employs a somewhat coarse noding of the core region, the transient boundary conditions (upper and lower plenums) would be defined. Using these boundary conditions several hot bundle transients employing a much finer mesh in the core region, may be run varying such parameters as local peaking factors. Local subchannel fluid conditions and rod temperatures will be calculated by COBRA-TF and fuel rod analysis performed by FRAP-T6[4]. An active link will permit the feedback of

the current fuel rod state (material properties, gap conductance and clad ballooning) from FRAP-T6 to the rod temperature and hydrodynamic solution algorithms of COBRA-TF, and vice-versa. This procedure will provide a hot bundle analysis capability for coupled thermal-hydraulic/rod deformation calculations.

Concurrent with this effort, a joint project with the FLECHT-SEASET program[5] has been initiated. This cooperative effort between Westinghouse and Battelle will produce a version of COBRA-TF capable of addressing Appendix K concerns about reflood heat transfer with flow blockages. As outlined in Figure 2, this program has three distinct phases:

- assess the ability of COBRA-TF to predict reflood heat transfer in an unblocked rod bundle (FLECHT-SEASET 21 rod-unblocked),
- incorporate flow blockage models and assess reflood heat transfer in blocked bundles (FLECHT-SEASET 21 rod-blocked), and
- perform quantitative assessment of flow blockage heat transfer capability (with a fixed version of COBRA-TF) for the FLECHT-SEASET 163 rod bundle (blockage islands with bypass).

To accomplish these objectives, the following tasks are in progress:

- Radiation model development - thermal radiation to fluid and structure,
- Turbulence model development - single phase mixing and void drift formulation,
- COBRA/FRAP linkage,
- Conduction model enhancement - addition of azimuthal conduction and sleeve blockage model,
- Flow blockage heat transfer models, and
- Developmental assessment.

Developmental assessment, an invaluable asset to a code development program, has as its objectives the qualification of the individual models/correlations present in the code and an assessment of their combined performance. An extensive assessment effort is planned as part of the COBRA-TF development. Some preliminary results of this effort are presented below, following a description of the code.

CODE DESCRIPTION

COBRA-TF provides a two-fluid, three-field representation of the two-phase flow. Each field is treated in either a three-dimensional cartesian coordinate system or a subchannel formulation. The three fields are comprised of a continuous vapor-noncondensible gas mixture, continuous liquid and

entrained liquid droplet field. The inclusion of the droplet field is essential to mechanistic modeling of two-phase phenomena having both a liquid film on surfaces within the flow field and liquid drops dispersed in the vapor phase. Countercurrent flow limiting, top and bottom reflood, and film dryout CHF are examples of such phenomena.

This treatment results in a set of nine equations. Four mass conservation equations are required for the vapor, continuous liquid, entrained liquid and noncondensible gas mixture. In vector form they are respectively:

$$\frac{\partial}{\partial t}\alpha_v\rho_v + \nabla \cdot (\alpha_v\rho_v\vec{U}_v) = \Gamma''' + \nabla \cdot \vec{\tau}_v^T$$

$$\frac{\partial}{\partial t}\alpha_\ell\rho_\ell + \nabla \cdot (\alpha_\ell\rho_\ell\vec{U}_\ell) = -\Gamma_\ell''' - S''' + \nabla \cdot \vec{\tau}_\ell^T$$

$$\frac{\partial}{\partial t}\alpha_e\rho_\ell + \nabla \cdot (\alpha_e\rho_\ell\vec{U}_e) = -\Gamma_e''' + S'''$$

$$\frac{\partial}{\partial t}\alpha_g\rho_g + \nabla \cdot (\alpha_g\rho_g\vec{U}_v) = \Gamma_{mg}''' + \nabla \cdot \vec{\tau}_g^T$$

Rate of change of mass	+	Rate of mass gain by convection	=	Rate of mass gain by interfacial transfer or chemical reaction	+	Rate of mass gain by entrainment	+	Rate of mass efflux due to void drift

Two energy conservation equations, the liquid and entrained liquid are assumed to interact at a rate sufficient to nearly maintain equilibrium, are specified for the vapor-gas mixture and the combined liquid fields:

$$\frac{\partial}{\partial t}(\alpha_v\rho_{vg}h_{vg}) + \nabla \cdot (\alpha_v\rho_{vg}h_{vg}\vec{U}_v) = \Gamma''' h_g + q_{iv} + Q_{vg}''' - \nabla \cdot (\alpha_v\underline{q}_{vg}^T)$$

$$\frac{\partial}{\partial t}(\alpha_\ell + \alpha_e)\rho_\ell h_\ell + \nabla \cdot (\alpha_\ell\rho_\ell h_\ell\vec{U}_\ell) + \nabla \cdot (\alpha_e\rho_\ell h_\ell\vec{U}_e) = -\Gamma'''h_f + q_{i\ell} + Q_L''' - \nabla \cdot (\alpha\, q_\ell^T)_\ell$$

Time rate of Change	+	Convection	=	Energy Transport Due to Phase Change	+	Interfacial Heat Transfer

+ Wall Heat Flux	- Turbulent Heat Flux

Three momentum equations are solved in COBRA-TF, allowing the liquid and entrained liquid fields to flow with different velocities relative to the vapor phase. They are:

$$\frac{\partial}{\partial t}(\alpha_v \rho_{vg} \vec{U}_v) + \nabla \cdot (\alpha_v \rho_{vg} \vec{U}_v \vec{U}_v) = -\alpha_v \Delta P + \alpha_v \rho_{vg} \vec{g} - \vec{\tau}_{wv}''' - \vec{\tau}_{I_{\ell v}}''' \vec{\tau}_{I_{ev}}''' + (\Gamma''' \vec{U}) + \nabla \cdot (\alpha_v \underline{\underline{T}}_{vg}^T)$$

$$\frac{\partial}{\partial t}(\alpha_\ell \rho_\ell \vec{U}_\ell) + \nabla \cdot (\alpha_\ell \rho_\ell \vec{U}_\ell \vec{U}_\ell) = -\alpha_\ell \Delta P + \alpha_\ell \rho_\ell \vec{g} - \vec{\tau}_{w\ell}''' + \vec{\tau}_{I_{\ell v}}''' (\Gamma_\ell''' \vec{U}) - (S''' \vec{U}) + \nabla \cdot (\alpha_\ell \underline{\underline{T}}_\ell^T)$$

$$\frac{\partial}{\partial t}(\alpha_e \rho_\ell \vec{U}_e) + \nabla \cdot (\alpha_e \rho_\ell \vec{U}_e \vec{U}_e) = -\alpha_e \nabla P + \alpha_e \rho_\ell \vec{g} + \vec{\tau}_{I_{ev}}''' - (\Gamma_e''' \vec{U}) + (S''' \vec{U})$$

Rate of change of momentum	+	Rate of momentum change by convection	=	Pressure gradient	+	Gravity force	+	Wall shear

+ Interfacial drag between vapor and continuous liquid

+ Interfacial drag between vapor and drops

+ Interfacial momentum exchange

+ Momentum exchange due to entrainment

+ Momentum exchange due to turbulence

In addition, a gas mixture transport equation (for each noncondensible gas present) and a droplet interfacial area concentration transport equation are solved. To complete this set of equations, numerous constitutive relations (e.g., flow regime selection, interfacial friction, subcooled boiling, wall heat flux, etc.) are necessary. To qualify these relations, their interaction with each other and with the conservation equations, a developmental assessment effort has begun.

DEVELOPMENTAL ASSESSMENT

Presented below are COBRA-TF data comparisons with the FRIGG forced flow boiling tests, GE-9 rod mixing tests, and Bennett post-CHF heat transfer. These tests represent only a small portion of the proposed assessment test matrix (not yet finalized), but should illustrate some of the code's capabilities.

FRIGG Boiling Test

Simulation of the FRIGG[6] forced flow boiling tests was done to assess the ability of COBRA-TF to predict axial void fraction distribution. Axial void distribution is most directly affected by the flow regime selection logic, interfacial friction, and subcooled boiling model. One test, with near saturated inlet conditions (#313018), was simulated to isolate the effects of subcooled boiling from interfacial friction.

The test section consisted of a uniformly heated 36-rod cluster with a 4.4 m heated length and a 13.8 mm outside diameter. For these tests, a constant inlet flow and temperature were specified. A gamma ray attentuation device measured both regional and bundle average void fractions at seven axial locations.

A one-dimensional model of the FRIGG test section was employed in this simulation. Twelve axial nodes (Δx = 0.367 m) represented the heated length with fixed mass flow and enthalpy at the inlet and pressure (50 bar) at the outlet. Comparisons are made with the measured profiles of bundle average void fraction. Table 1 presents a summary of the test conditions.

Three tests were simulated (#313016, 313018, and 313020) and the data comparisons are presented in Figures 3 through 5. In test #313018, Figure 3, the inlet conditions approached saturation so that subcooled boiling was relatively unimportant. Thus the agreement between calculated and measured void distribution indicates proper calculation of the flow regime (from single-phase liquid to annular) and interfacial drag forces.[1]

Both tests #313016 and 313020, Figures 4 and 5, had significant regions of subcooled boiling, 2.9 and 2.1 m respectively. In this region, the vapor generation rate is determined by the interaction of nucleate boiling at the wall and condensation in the subcooled liquid core. Consequently, the resultant void fraction is as much a function of the subcooled boiling model as the interfacial drag forces. The good agreement shown in Figures 4 and 5 indicate that the subcooled boiling model[7] combined with the subcooled interfacial heat transfer, flow regime map and interfacial shear models accurately predict the void fraction in a boiling channel. More simulations and other test sections need to be analyzed to quantify the code's error band, but these tests were predicted with a maximum error less than 5%.

General Electric Nine-Rod Tests

Simulation of the GE-9 rod tests[8] were performed to assess the single-phase and two-phase turbulent mixing models. Single-phase turbulent mixing is calculated using the traditional intersubchannel mixing coefficient approach.[9] Where for the ith subchannel:

$$W'_{ij} = \beta \cdot s_{ij} \cdot \overline{G}_{ij}$$

$$v \cdot q''_i = \sum_{k=1}^{NK} W'_{ij} \cdot (h_j - h_i) \cdot \Delta x$$

and,

NK - number of gaps connected to subchannel i.

A similar term appears in the axial momentum equations, but no terms appear in the mass equations since W' represents a fluctuating crossflow with no net mass transfer.

The two-phase mixing model adds the effect of lateral "void drift", which contains a mass transport term, to the fluctuating crossflow. A simple formulation, based on the work of Lahey[10] and Kelly[11] is employed.

$$\left(\frac{\varepsilon}{\ell}\right)_{ij} = W'_{ij}/(s_{ij} \cdot (\langle\bar{\rho}_i\rangle - \langle\bar{\rho}_j\rangle))$$

and,

$$(G_v^T)_{ij} = \left(\frac{\varepsilon}{\ell}\right)_{ij} [((\alpha\rho_v)_i - (\alpha\rho_v)_j) - ((\alpha\rho_v)_i - (\alpha\rho_v)_j)_{EQ}]$$

Where, the equilibrium void distribution is approximated by,

$$((\alpha\rho_v)_i - (\alpha\rho)_j)_{EQ} = \frac{(G_i - G_j)\ (\alpha_i + \alpha_j)}{\overline{G_{ij}}}$$

Terms accounting for the momentum and energy transfer associated with the this mass transfer are added to the conservation equations.

The test section consisted of a nine rod bundle (3x3) with a uniform heated length of 6 ft and development length of 4 ft. A rod diameter of 0.570 in. and a pitch to diameter ratio of 1.295 were employed. Rod position was maintained by 1/8 in. diameter steel pins located every 12 in. in the axial direction (the last set 10 in. upstream of the measurement station). Both subchannel mass fluxes and qualities were isokinetically sampled at the exit plane.

Figure 6 shows the 1/4 symmetry section (one corner, two-edge, and one central subchannel) model employed. Ten axial levels (Δx = 12 in.), constant flow and enthalpy at the inlet and pressure at the outlet (1000 psia) were used. the spacer pins were modeled as loss coefficients calculated by the method of reference 12 and adjusted to yield the correct total single-phase pressure drop.

For these preliminary data comparison, a constant value of the mixing parameter, β=0.01, was selected. The test conditions are listed in Table 2, single-phase results in Table 3, and two-phase results in Table 4.

Overall, a good comparison with the measured mass fluxes for the single-phase tests (see Table 3) was achieved with a constant value of the mixing parameter (β=0.01). However, it appears that this good agreement is due more

to a careful specification of the loss coefficients for the spacer pins than a correct modeling of the turbulent mixing. The importance of the diversion crossflow due to the loss cofficients was illustrated in a debug run where no losses were input for the pins. For this case, the mixing coefficient was increased by an order of magnitude before a reasonable data comparison was seen.

The results of the two-phase mixing tests (see Table 4) indicate an improvement over the calculations without mixing. Also, the trend for vapor to "drift" from the low mass flux corner subchannel to the higher mass flux regions is shown. However, for the higher void fraction cases (tests 2G2 and 2E3) the mixing is severly underpredicted and the central subchannel vapor flowrate is decreased. These deficiencies illustrate the need to enhance the mixing coefficient as a function of void fraction and develop more sophisticated equilibrium void distribution models.

Bennett Post-CHF Tests

COBRA-TF simulations of the Bennett tests[13] were done to assess the code's ability to predict the dryout point and heat transfer to dispersed flow beyond the dryout point. The dryout point is defined as the axial location where the liquid is totally evaporated/entrained (see Figure 7), and a rapid increase in rod surface temperature occurs.

Film dryout is mechanistically predicted by COBRA-TF through the solution of the conservation equations for the continuous liquid film. The constitutive relations for entrainment and de-entrainment in annular flow are given in reference (1). Dispersed flow heat transfer is calculated as a two-step procedure, where the heat is first transferred to superheated vapor and the interfacial heat transfer between the vapor and drops controls the vapor superheat. Although the local vapor temperatures were not measured in these tests and each individual model (convective heat transfer coefficient, interfacial heat transfer) cannot be assessed, the combined performance can be evaluated by comparisons with the wall surface temperature.

The test section consisted of a 0.497 in. I.D., 0.625 in. O.D., Nimonic alloy tube with a heated length of 19 ft. The outlet pressure was 1000 psia and the inlet flow and enthalpy and applied power were held constant at preselected values until a steady-state temperature profile was reached. COBRA-TF employed a one-channel model with axial mesh spacing of 12 in. for these tests.

A total of 37 different Bennett tests were simulated. Table 5 presents the test conditions and the results of the dryout tests for nine different mass fluxes. The error in the prediction of the dryout point is compared to that calculated using the Biasi[14] CHF correlation, which was developed for high pressure film dryout - CHF in tubes. While the average error for the two techniques is similar, the mechanistic treatment of COBRA-TF results in a reduced maximum error.

The entrainment rate is important in determining dryout of a liquid film. COBRA-TF uses separate models for entrainment and de-entrainment that result in a net entrainment rate. Figure 8 shows the effect of entrainment on film dryout in test no. 5373. The entrained liquid fraction increases rapidly at 6 to 8 ft from the bottom of the heated length indicating a large positive entrainment rate. The entrainment rate decreases gradually as the entrained liquid becomes a large fraction of the total liquid mass from 8 to 12 ft. From 13 ft to the dryout point at 16 ft continuous liquid has become a small fraction of the total liquid mass flow. The de-entrainment rate is larger than the entrainment rate and liquid droplets are deposited on the liquid film. Net de-entrainment near the dryout point of the annular film is typical of all the Bennett tests simulated.

The COBRA-TF calculation of CHF is compared with Biasi correlation and the Bennett test measurements as a function of equilibrium quality at the dryout point in Figures 9 through 12. In each figure, measured data, COBRA-TF calculations, and a continuous line representing the Biasi correlation are plotted for a series of tests at a single mass flux. If a trend can be established, the Biasi correlation is superior at high mass flux, low quality dryout and the COBRA-TF mechanistic model better for low mass flux, high quality dryout.

Axial wall temperature profiles for three of the tests listed in Table 5 are shown in Figures 13 through 15. Each figure shows the COBRA-TF calculation a solid line and the temperatures recorded by the thermocouples as open circles. The tests (#5359, 5313, and 5379) are presented in order of decreasing vapor superheat. Test #5359, a low mass flux test, exhibits the presence of considerable vapor superheat by the wall temperature increasing with axial distance after the dryout point. Tests with little or no superheat (#5313 and 5379) exhibit a decreasing temperature profile in the dispersed flow region as the vapor generation enhances the steam convective heat transfer coefficient.

Generally, COBRA-TF tends to underpredict the wall temperature, especially for low to moderate mass fluxes. This behavior is probably due to an overprediction in the interfacial heat transfer due to the entrained drops entering the interfacial area concentration transport equation with the incorrect drop size. Overall, however, the predictions are quite good.

SUMMARY

The COBRA-TF computer program is being developed at the Pacific Northwest Laboratory to provide a best estimate hot bundle analysis capability. Developmental assessment has already begun, concurrent with the code development efforts. Significant capability in predicting basic two-phase flow and heat transfer phenomena has been demonstrated. However, a thorough assessment will be conducted to fully assess the models in the code.

Specific areas for improvement, noted in this paper, are the two-phase mixing model and interfacial heat transfer in dispersed flow film boiling.

NOMENCLATURE

$\bar{G}$ - subcooled average mass flux

$\vec{G}^T$ - mass flux due to lateral void drift

$\vec{J}$ - gravitational acceleration

h - enthalpy

ℓ - effective mixing length

P - pressure

Q''' - wall heat transfer/volume

q_i - interfacial heat transfer

q^T - turbulent heat flux

S''' - volumetric entrainment rate

s - gap width

T^T - momentum exchange due to turbulence

t - time

$\vec{U}$ - vector velocity

W' - fluctuating crossflow

Δx - axial mesh spacing

α - phasic volume fraction

β - nondimensional mixing parameter

ε - eddy diffusivity

ρ - density

Γ''' - vapor generation rate

$\vec{\tau}_w$ - wall shear stress

$\vec{\tau}_I$ - interfacial shear stress

Subscripts

i - suchannel i

e - entrained liquid

g - noncondensible gas

ℓ - liquid

v - vapor

REFERENCES

1. Thurgood, M. J., K. R. Crowell, and J. M. Kelly, "COBRA/TRAC Manual, Volume 1: COBRA-TF Equations and Constitutive Relations," PNL-4220, Battelle-Pacific Northwest Laboratory, Richland, Washington, to be published 1982.

2. Liles, D. R. et al., "TRAC-PD-2: An Advanced Best-Estimate Computer Program for Pressurized Water Reactor Loss-of-Coolant Accident Analysis," NUREG/CR-2054, April 1981.

3. Ransom, V. H. et al., "RELAP5/MOD1 Code Manual," NUREG/CR-1826, September 1981.

4. Siefken, L. J. et al., "FRAP-T6: A Computer Code for the Transient Analysis of Oxide Fuel Rods," NUREG/CR-2148, May 1981.

5. Conway, C. E. et al., "PWR FLECHT Separate Effects and System Effects Test (SEASET) Program Plan," NRC/EPRI/Westinghouse-1, December 1977.

6. Nylund, O. et al., "Hydrodynamic and Heat Transfer Measurements on a Full Scale Simulated 36-Rod Marviken Fuel Element with Uniform Heat Flux Distribution," ASEA and AB Atomenergi Report FRIGG-2, R4-447/RTL-1007, 1968.

7. Stewart, C. W., et al., "Improvements to the COBRA-TF (EPRI) Computer Code for Steam Generator Analysis," NP-1509, September 1980.

8. Lahey, R. T., et al., "Mass Flux and Enthalpy Distribution in a Rod Bundle for Single and Two-Phase Flow Conditions," ASME 70-WA/HT-8, December 1970.

9. Rowe, D. S., "Crossflow Mixing Between Parallel Flow Channels During Boiling," BNWL-371, Pt. 1, March 1967.

10. Lahey, R. T. and F. J. Moody, The Thermal Hydraulics of a BWR, ANS Monograph, (1975).

11. Kelly, J. E. and M. S. Kazimi, "Development of the Two-Fluid Multidimensional Code THERMIT for LWR Analysis," AIChE Symposium Series #199, Vol. 76, 1980.

12. Lahey, R. T., B. S. Shiralkar, and D. W. Radcliffe, "Suchannel and Pressure Drop Measurements in a Nine-Rod Bundle for Diabatic and Adiabatic ConditionsM," GEAP-13049, (1970).

13. Bennett, A. W. et. al., "Heat Transfer to Steam-Water Mixtures Flowing in Uniformly Heated Tubes in Which the Critical Heat Flux Has Been Exceeded," AERE-R-5373, (1967).

14. Biasi, L., et al. 1967. "Studies on Burnout, Part 3." Energia Nucleare, Vol. 14, No. 9, 530-536.

TABLE 1. FRIGG: Forced Convection Boiling Test Conditions

TEST	SUBCOOLING (°C)	POWER (kW/ft)	MASS FLUX (kg/m².s)	EXIT QUALITY
313016	19.3	5.63	1208	4.4%
313020	22.4	8.54	1159	9.6%
313018	3.7	8.50	1124	15.6%

TABLE 2. Summary of GE-9 Rod Test Conditions

Test No.	$G/10^6$ (lb/ft^2-hr)	Power (kw)	Subcooling (Btu/lb)	Exit Quality
1C	0.990	0	504.6	-
1D	1.510	0	504.6	-
1E	1.970	0	504.6	-
2E1	1.080	1064	142.9	0.035
2E3	1.060	1064	29.1	0.215
2G2	1.080	1596	189.8	0.090

TABLE 3. GE-9 Rod Single-Phase Data Comparisons

Test 1C	G_{corner}	G_{edge}	G_{center}
Data	.701	.939	1.150
COBRA-TF (no mixing)	.682	.932	1.144
COBRA-TF (β=0.01)	.748	.941	1.120
Test 1D	G_{corner}	G_{edge}	G_{center}
Data	1.095	1.441	1.690
COBRA-TF (no mixing)	1.046	1.427	1.737
COBRA-TF (β=0.01)	1.159	1.441	1.690
Test 1E	G_{corner}	G_{edge}	G_{center}
Data	1.620	1.910	2.190
COBRA-TF (no mixing)	1.377	1.864	2.258
COBRA-TF (β-0.01)	1.523	1.884	2.197

TABLE 4. GE-9 Rod Two-Phase Data Comparisons

Test 2E1	Corner		Edge		Center	
	G	X	G	X	G	X
Data	.950	.004	1.102	.026	1.162	.051
COBRA-TF (no mixing)	.616	.118	1.108	.028	1.169	.041
COBRA-TF (β=0.01)	.814	.005	1.083	.034	1.146	.042

Test 2E3	Corner		Edge		Center	
	G	X	G	X	G	X
Data	.965	.160	1.081	.185	1.126	.249
COBRA-TF (no mixing)	.616	.301	1.072	.191	1.157	.223
COBRA-TF (β=0.01)	.722	.239	1.003	.323	1.245	.201

Test 2G2	Corner		Edge		Center	
	G	X	G	X	G	X
Data	1.000	.020	1.111	.068	1.130	.110
COBRA-TF (no mixing)	.516	.231	1.154	.064	1.126	.100
COBRA-TF (β=0.01)	.841	.110	1.094	.078	1.116	.096

TABLE 5. Summary of Bennett Test Conditions and Results of Dryout Point Calculations

TEST	MASS FLUX (MLB/HR-FT²)	HEAT FLUX (MBTU/HR-FT²)	DRYOUT LOCATION (IN)	ERROR (ΔZ) BIASI	ERROR (ΔZ) COBRA-TF
5359	0.29	0.173	140	-20	- 8
5336	0.49	0.260	140	-44	- 8
5273	0.75	0.292	140	- 8	+26
5250	1.00	0.290	164	+ 4	+16
5294	1.44	0.348	164	+ 4	+16
5313	1.87	0.381	170	+10	+10
5310	1.88	0.358	185	+19	+ 7
5379	2.80	0.542	140	- 8	+16
5397	3.82	0.584	164	-24	+ 4
			AVG ERROR =	15.7	12.3
			MAX ERROR =	44	26

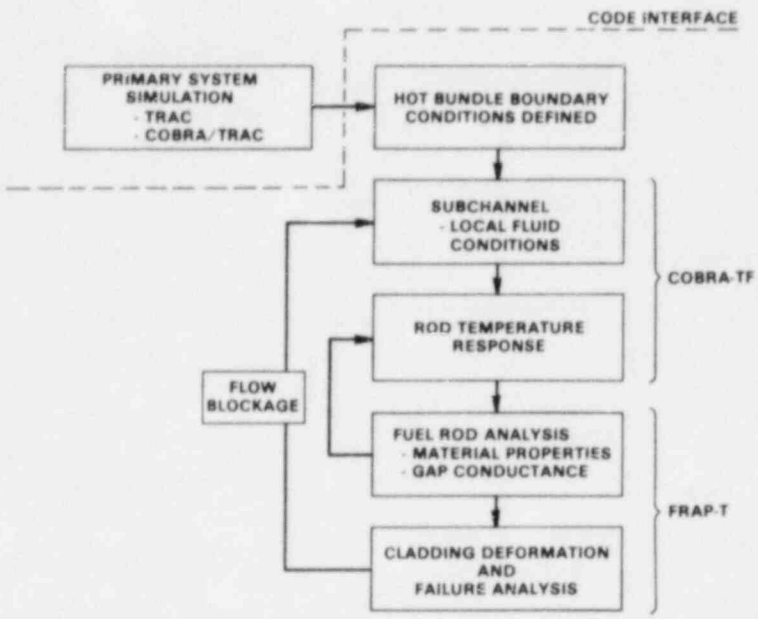

FIGURE 1. Hot Bundle Analysis Concept

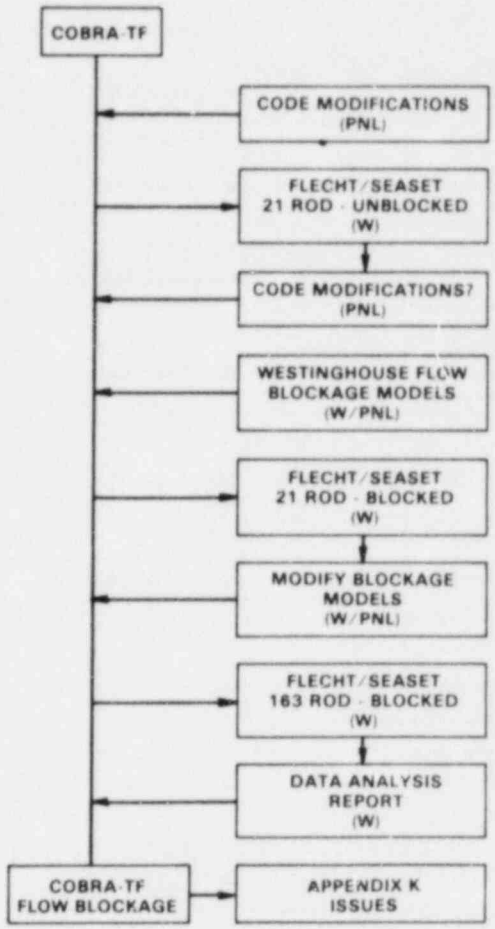

FIGURE 2. Schematic of Westinghouse/ Battelle Flow Blockage Program

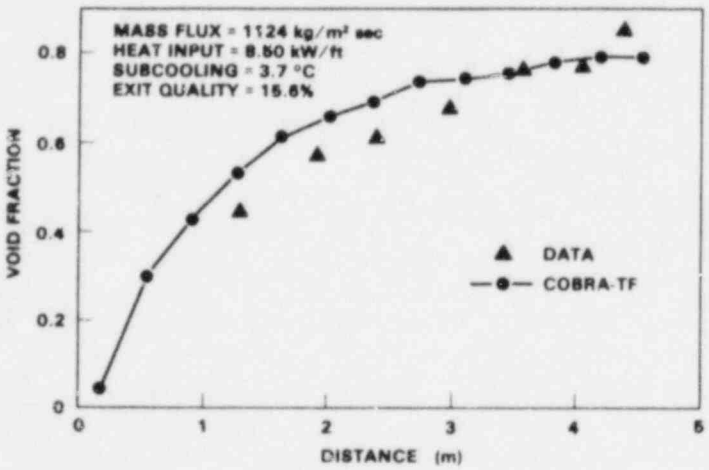

FIGURE 3. Axial Void Distribution for FRIGG Test #313018

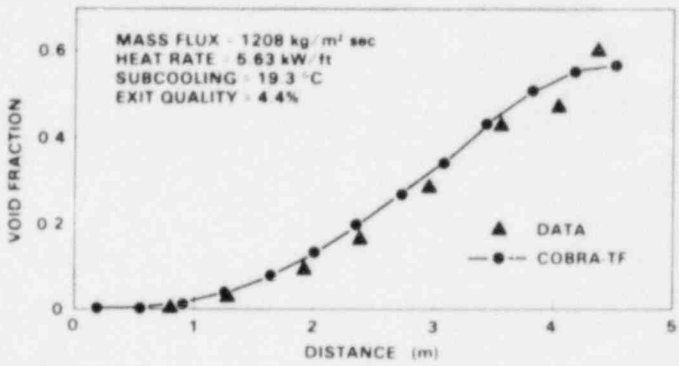

FIGURE 4. Axial Void Distribution for FRIGG Test #313016

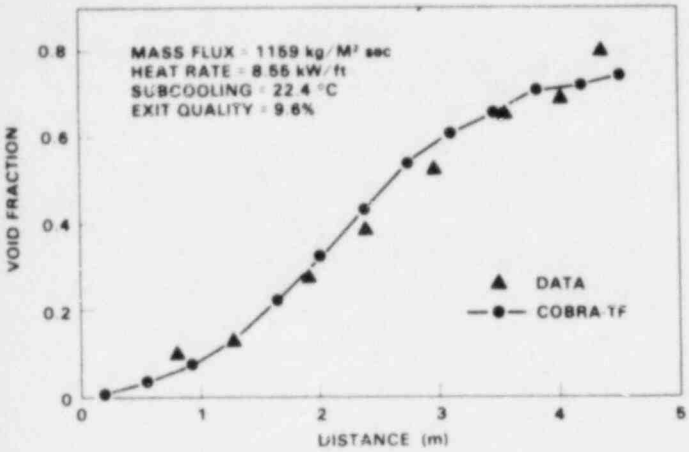

FIGURE 5. Axial Void Distribution for FRIGG Test #31320

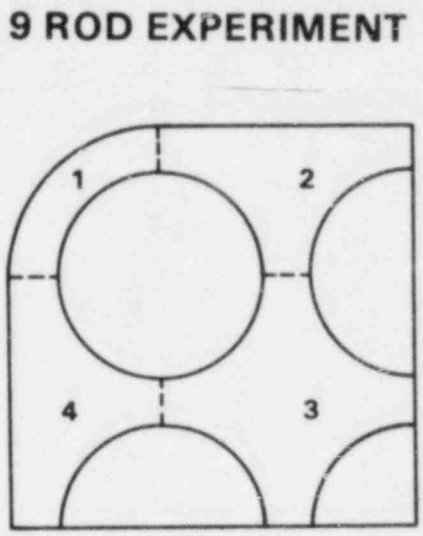

FIGURE 6. Quarter Section of Symmetry for the GE-9 Rod Tests

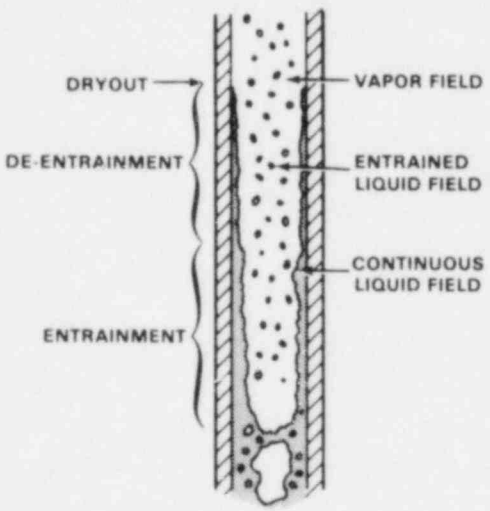

FIGURE 7. Schematic of Annular Flow in the Bennett Tests

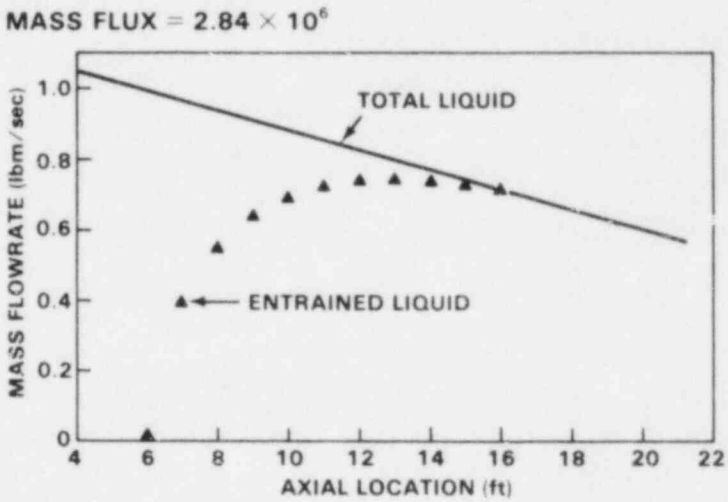

FIGURE 8. Entrained Liquid vs. Total Liquid Flowrate in Bennett Test #5373

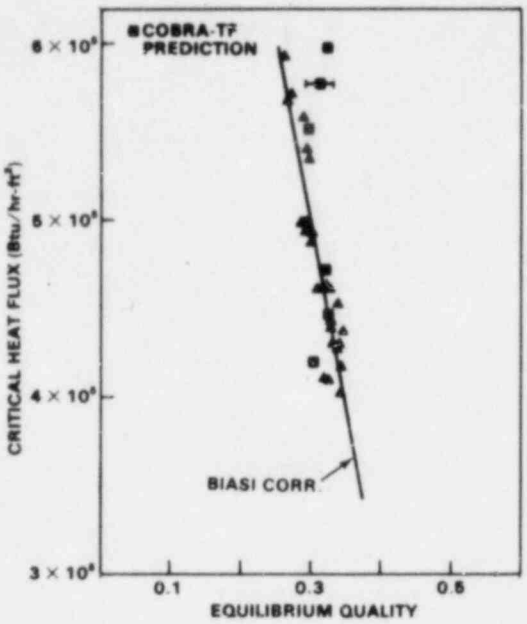

FIGURE 9. Bennett Test Critical Heat Flux vs. Equilibrium Quality at Mass Flux = 2.84×10^6 lb/hr-ft^2

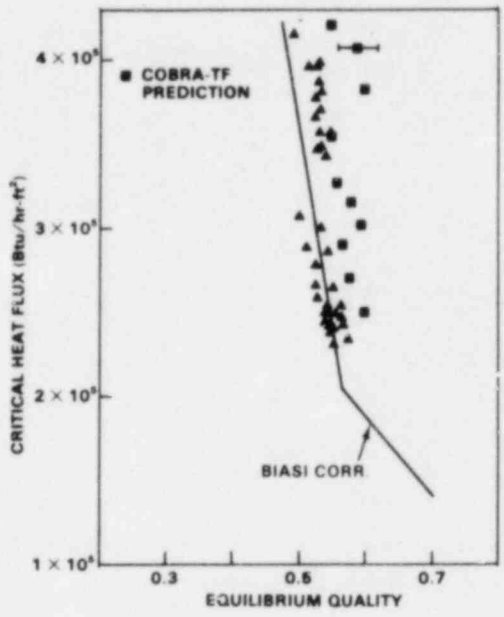

FIGURE 10. Bennett Test Critical Heat Flux vs. Equilibrium Quality at Mass Flux = 1.0×10^6 lb/hr-ft^2

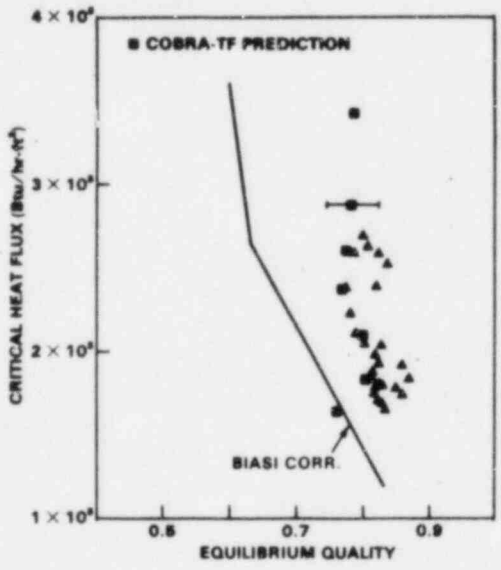

FIGURE 11. Bennett Test Critical Heat Flux vs. Equilibrium Quality at Mass Flux = 0.49×10^6 lb/hr-ft^2

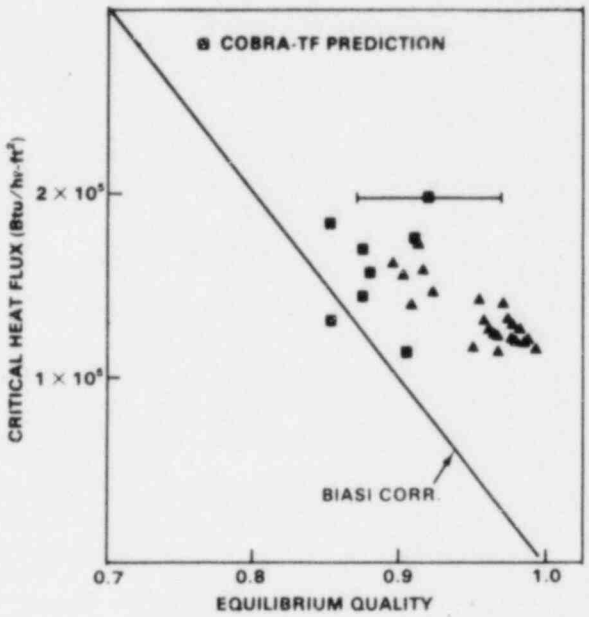

FIGURE 12. Bennett Test Critical Heat Flux vs. Equilibrium Quality at Mass Flux = 0.29×10^6 lb/hr-ft^2

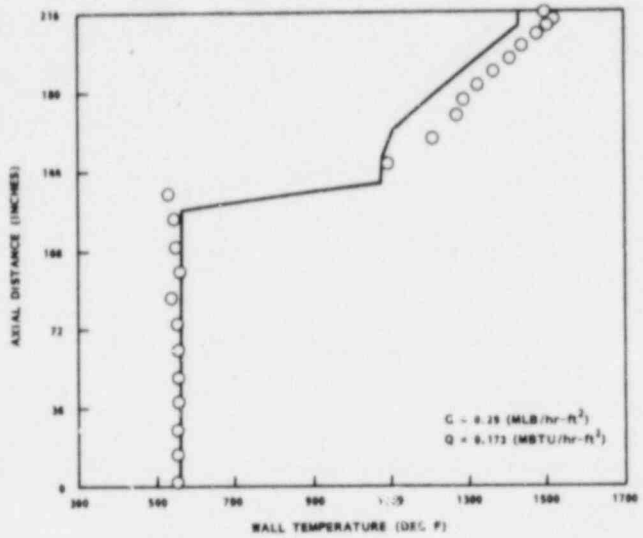

FIGURE 13. Bennett Test 5359 Axial Wall Temperature Profile

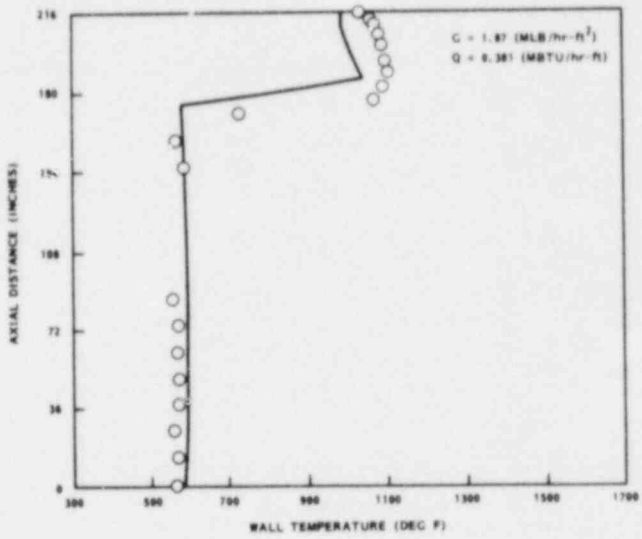

FIGURE 14. Bennett Test 5313 Axial Wall Temperature Profile

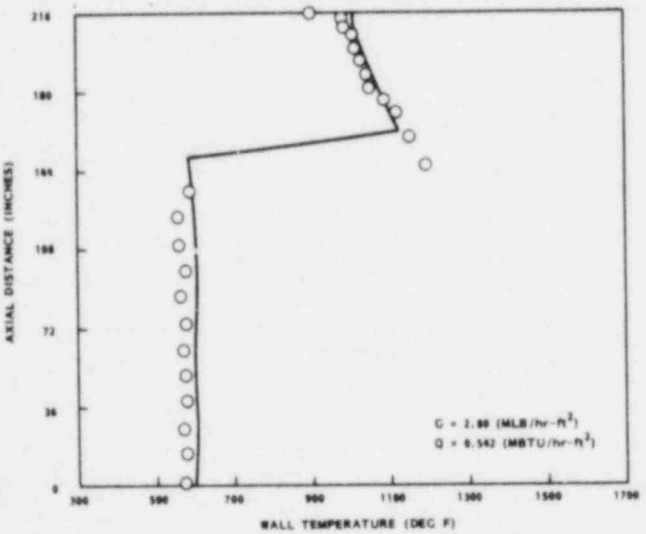

FIGURE 15. Bennett Test 5379 Axial Wall Temperature Profile

INDEPENDENT ASSESSMENT OF THE TRAC-PD2 CODE

F. ODAR

U. S. Nuclear Regulatory Commission

ABSTRACT

An independent assessment of the TRAC-PD2 code has been completed. The assessment was performed in three ways. The first was a quantitative assessment where the uncertainties in calculating selected key parameters were determined. The second was an assessment through separate effects and basic tests where the capabilities of the code to predict basic two phase flow phenomena were addressed. The third was a qualitative assessment where overall predictive capability of the code was assessed. The assessment work indicates that TRAC-PD2 code can predict peak clad temperatures in a large break LOCA within accuracy limits of ± 80K (2 standard deviations).

INTRODUCTION

The TRAC-PD2 code, Reference 1, is an advanced best estimate thermal hydraulics system code developed at Los Alamos National Laboratory primarily for calculations of large break LOCA's in pressurized water reactors (PWR's). The assessment effort has been undertaken at three different National Laboratories - Brookhaven (BNL), Los Alamos (LANL), and Idaho National Engineering Laboratories (INEL), and concentrated on the capability of the code to predict large break LOCA's.

The TRAC-PD2 code has the following important capabilities:

1. Multi-dimensional Modeling

A full three dimensional (r,θ,z) flow is modeled in the reactor vessel. However, flow within loop components is treated one dimensionally. Capability for three dimensional calculations permits the code to calculate the 3-D penetration of the liquid through the downcomer during the emergency core coolant injection. This capability was assessed using Battelle Columbus and Renesselaer Polytechnic Institute (RPI) tests.

2. Nonhomogeneous, Nonequilibrium Modeling

The code contains a six-equation two-fluid thermal hydraulics model for the vessel component and a five-equation drift-flux model for the loop components. This formulation permits nonhomogeneous and nonequilibrium modeling. The interactions between the phases are simulated using a flow-regime dependent constitutive equation package. The assessment of some of the constitutive relationships will be discussed in this paper.

3. Comprehensive Heat Transfer Modeling

The code contains a two-dimensional (r-z) treatment of fuel rod heat conduction with moving fine-mesh rezoning to calculate reflood quench fronts. Assessment of this capability was performed using data from several reflood tests.

QUANTITATIVE ASSESSMENT OF TRAC-PD2 FOR A LARGE BREAK LOCA

Tests from LOFT, Semiscale, LOBI, PKL, FLECHT SEASET and CCTF were used for quantitative assessment. Fifteen different integral system tests were considered. Tests simulated blowdown, reflood as well as full LOCA scenarios. Table I presents the test matrix identifying the test, type of test and the laboratory performing the calculation.

To perform the quantitative assessment a set of key variables is first selected. Next, experimental values are compared with these calculated variables and attempts are made to make statements on the accuracy (or uncertainty) of the predictions. Clearly the selected key variables cannot provide a complete understanding of the predictive capability of the code and, therefore, the quantitative assessment is supported by an assessment through basic and separate effects tests as well as a qualitative assessment. The following key variables are considered in this paper:

1. Global Peak Clad Temperature, T_{CL}
2. Time for Global Peak Clad Temperature, t_{CL}
3. Time for CHF at the hot spot, t_{CHF}
4. Time for quench at the hot spot, t_{Q}
5. Time for accumulator injection, t_{ACC}

Most of these parameters have been identified and discussed in Reference 2. The cladding of the fuel rod is the first barrier against the fission product release and the clad temperature limit of 2200°F is one of the parameters used in licensing. The other key variables are used to determine the best estimate nature (or quality) of the code predictions. Time for Global Peak Clad temperature is important to determine if the same phenomenon in the code and the test is responsible for the occurrence of peak clad temperature. If experiments indicate that the peak clad temperatures occurred during the blowdown, does the code also indicate the same? If the code indicates that the peak temperature occurs during the reflood, clearly the prediction is inadequate. On the other hand, if the code predicts the correct peak clad temperature but the time for its

TABLE I

LARGE BREAK LOCA TESTS USED
TO ASSESS TRAC-PD2

TEST	TYPE OF TEST	CALCULATIONS PERFORMED BY
L2-2	BWDN, REFLOOD, 25 MW_T	LANL
L2-3 (P1A)	BWDN, REFLOOD, 36 MW_T	LANL
S-02-8, MOD1	BWDN, NO ECC	LANL
S-06-3, MOD1	BWDN, REFLOOD	LANL
S-04-5, MOD1	BWDN, REFLOOD, 1.60 MW_T	INEL
S-04-6, MOD1	BWDN, REFLOOD, FOUR UNPOWERED RODS, 1.44, MW_T	INEL
S-28-1, MOD1	BWDN, REFLOOD, 1.60 MW_T, 60 S.G. TUBES RUPTURE	INEL
S-07-4 (MOD 3)	REFLOOD	INEL
FLECHT SEASET 31504	REFLOOD	LANL
FLECHT 4831	REFLOOD	LANL
PKL K9	REFLOOD	LANL
LOBI A1-04 (P1A)	BWDN, NO ECC	LANL
CCTF #14	REFLOOD	LANL
CCTF #39	REFLOOD	LANL
PKL K5	REFLOOD	INEL

TABLE II

COMPARISON OF PEAK CLAD TEMPERATURES (K)

TEST	CALCULATED $(T_{CL})_C$	MEASURED $(T_{CL})_M$	DIFFERENCE $(T_{CL})_C - (T_{CL})_M$
S-02-8	1128	1130	- 2
S-06-3	987	1070	-83
L 2-2	793	789	+ 4
L 2-3 (P1A)	950	890	+60
S-04-6	850	920	-70
S-04-5	950	980	-30
S-28-1	945	950	- 5
S-07-4	785	820	-35
FLECHT-SEA 31504	1375	1423	-48
FLECHT 4831	1204	1243	-39
PKL K9	954	947	- 7
PKL K5	982	975	+ 7
LOBI A1-04 (P1A)	383	417	-34
CCTF C1-5, #14	1080	1039	+41
CCTF C1-20, #39	1215	1225	-10
			-251

* $\bar{X}$ = -16.7K

STANDARD DEVIATION, s = 38K 2s=76K ≈ 80K

occurrence is at great variance with the test data, one must then question the accuracy of predictions of core inlet flow rate, amount of entrainment, steam cooling, film boiling heat transfer, water fallback (top-down quench) from upper plenum, etc.

Time for Critical Heat Flux (CHF) depends on the blowdown and flow reversal in the core. After the occurrence of CHF, the primary parameters affecting the peak clad temperatures will also include the uncertainties in the fuel gap conductance, fuel conductivity and stored energy. These fuel parameters combined with that describing thermal and hydraulic phenomenon such as flow reversal will determine the peak value of clad temperature and its timing.

Time for quench at the hot spot is important to understand the accuracy of the reflood process. Time for accumulator injection permits us to pass a judgment on the accuracy of the pressure predictions. It is also important in replenishing the lost inventory from the system.

As stated, the TRAC-PD2 code has a 3-D vessel analysis capability. However, even in a 3-D nodalization, a node in the core represents a volume with many fuel rods and the code calculates the average parameters in that node. The use of too-fine nodalization in system calculations is prohibitive because of the cost of computations. One procedure is to use a subchannel code to calculate the temperature in the hot rod. The calculations presented in this paper do not contain the subchannel analysis and the peak clad temperatures refer to an average peak clad temperature in a node. In order to have a consistent comparison, the measurements refer to an average peak clad temperature judged from experimental data which may have several thermocouples for the corresponding volume and location. The average temperature, which is the accepted measured value, involves some judgment in data reduction. For example, it does not contain readings from thermocouples which have failed or which are affected by boundaries not modeled in the code. An example of the latter condition is a node containing unpowered rods. In the averaging process, the thermocouple readings in the proximity of unpowered rods are not taken into account.

Tables II through VI present comparisons of the measured and calculated key variables. Figures 1 and 2 are the scatter plots illustrating differences of calculated and measured peak clad temperatures and timing for the rod quench. The following conclusions are reached from these comparisons:

TRAC-PD2 predicts:

1. Slightly lower (about 16K) peak clad temperatures. The uncertainty of calculations (2 standard deviations) is $\pm$ 80K.

2. Time for peak clad temperatures that occur during blowdown is predicted accurately. This is not the case for tests dealing with reflood.

3. Time for the hot spot quench with uncertainty of ± 125s.

4. Accurately the time for CHF.

5. Accurately the onset of accumulator injection.

Figures 1 and 2 show the differences between predictions and measurements for different test facilities in different scales. There is no clearly supportable trend for uncertainties as the scale varies. A slight upward trend in Figure 1 is due to the two points at large test facilities. More calculations using large test facilities are needed to ascertain if this trend exists. If the trend exists, the predictions in a full scale Pressurized Water Reactor (PWR) will be slightly conservative, i.e., a slightly higher peak clad temperature will be predicted than would actually occur. It is planned to perform a few more assessment calculations using large test facilities. It is expected that additions of these runs will not change the uncertainties in Tables II through VI.

ASSESSMENT OF TRAC-PD2 FOR A LARGE BREAK LOCA THROUGH SEPARATE EFFECTS AND BASIC TESTS

This assessment is needed to explain the reasons for some of the differences in key variables calculated above and also to understand the basic capability of the code to predict the physical phenomena occurring during a large break LOCA. The following phenomena and associated tests are considered in this assessment:

1. Critical Flow - Marviken Tests

2. Emergency Core Cooling (ECC) Bypass and Penetration - Battelle-Columbus Laboratory (BCL) Bypass Tests

3. Counter-Current Flow Limitation (CCFL) and Entrainment - University of Houston Tests

4. Reflood - Flecht Seaset Tests

5. Multi-D Calculational Capability - RPI Tests

TABLE III

COMPARISONS OF MEASURED AND CALCULATED TIMES FOR FOR PEAK CLAD TEMERATURES, T_{CL} (s)

TEST	CALCULATED $(T_{CL})_C$	MEASURED $(T_{CL})_M$	DIFFERENCE $(T_{CL})_C - (T_{CL})_M$
S-02-8	48	48	0
S-06-3	71	71	0
L 2-2	5.5	5.5	0
L 2-3 (P1A)	39	6	33
S-04-6	7	8	-1
S-04-5	8	10	-2
S-07-4	7	11	-4
S-28-1	8.5	10	-1.5
PKL K9	32	33	-10
PKL K5	100	100	0
FLECHT SEA, 31504	79	105	-26
FLECHT 4831	40	33	7
LOBI A1-04	2	2	0
CCTF C1-4 #14	130	140	-10
CCTF C1-4 #39	80	110	-30

TABLE IV

COMPARISON OF MEASURED AND CALCULATED TIMES FOR QUENCH OF HOT SPOT, T_Q (s)

TEST	CALCULATED $(T_Q)_C$	MEASURED $(T_Q)_M$	DIFFERENCE $(T_Q)_C - (T_Q)_M$
S-06-3	148	176	-28
L 2-2	52	40	+12
S-04-6	115	190	-75
S-04-5	155	290	-135
S-07-4	60	92	-32
FLECHT SEASET 31504	365	305	+60
FLECHT 4831	340	275	+65
PKL K9	290	265	+25
PKL K5	250	250	0
LUBI A1-04	4	5	-1
CCTF (C1-5) #14	480	390	+90
CCTF (C1-5) #39	590	560	+30
			+11

$\bar{X}$ = .9s

PRACTICALLY NO BIAS

STANDARD DEVIATION: s = 62.7s

2s = 125s

TABLE V

COMPARISON OF MEASURED AND CALCULATED

TIMES FOR CHF AT THE HOT SPOT, T_{CHF}(s)

TEST	CALCULATED $(T_{CHF})_C$	MEASURED $(T_{CHF})_M$	DIFFERENCE $(T_{CHF})_C - (T_{CHF})_M$
S-02-8	1.6	.5	1.1
S-06-3	3	3	0
L 2-2	1	1	0
L 2-3 (P1A)	0	1.5	-1.5
S-04-6	1	3	-2
S-04-5	1	3	-2
LOBI A1-04	1	1	0
S-28-1	1	2.5	-1.5
S-28-10	2	2.5	- .5
			-6.4

$\bar{X}$ = -.7s

STANDARD DEVIATION: s = .99s

2s = 2s

TABLE VI

COMPARISON OF MEASURED AND CALCULATED TIMES

FOR ACCUMULATOR INJECTION, T_{ACC} (s)

TEST	CALCULATED $(T_{ACC})_C$	MEASURED $(T_{ACC})_M$	DIFFERENCE $(T_{ACC})_C - (T_{ACC})_M$
S-04-5 (BROKEN)	3	3.5	- .5
(UNBROKEN)	16	16.5	- .5
S-04-6 (BROKEN)	4	2	+2
(UNBROKEN)	14	17	-3
S-28-10 (BROKEN)	1	2	-1
(UNBROKEN)	13	16	-3
S-28-1 (BROKEN)	3	1	+2
(UNBROKEN)	13	17	-3
L 2-2	19	16.2	+2.8
S-06-3	15	19	-4
			-8.2

$\bar{X}$ = -.82s

STANDARD DEVIATION: s = 2.4s

2s = 5s

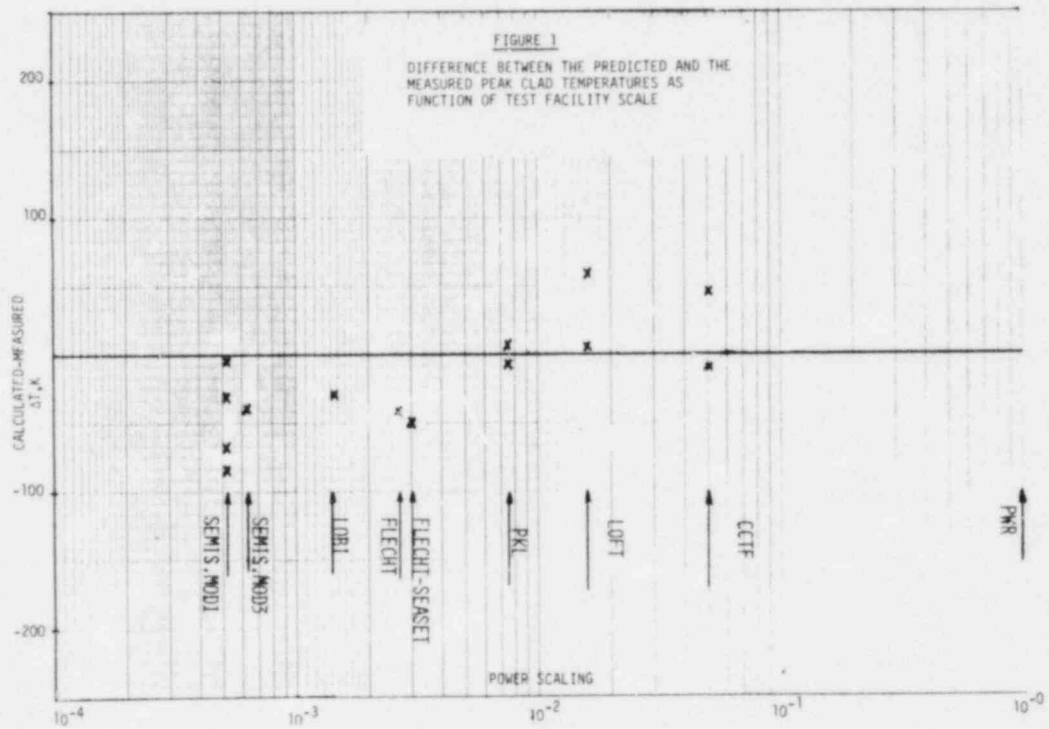

FIGURE 1

DIFFERENCE BETWEEN THE PREDICTED AND THE MEASURED PEAK CLAD TEMPERATURES AS FUNCTION OF TEST FACILITY SCALE

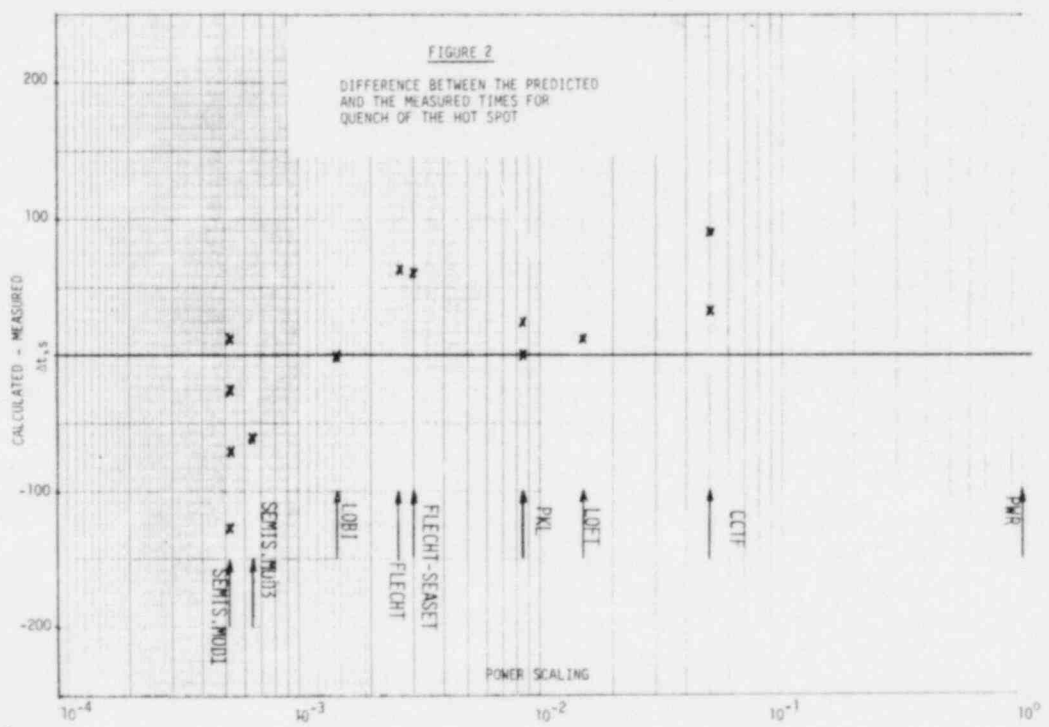

FIGURE 2

DIFFERENCE BETWEEN THE PREDICTED AND THE MEASURED TIMES FOR QUENCH OF THE HOT SPOT

Critical Flow

Five different Marviken tests have been used to assess this capability. The initial pressures and subcooling ranged from 4-5 MPa and 0-50K respectively. The L/D ratio for the nozzle varied from 0.3 to 3.7 and the nozzle diameters varied from 0.2 to 0.5m. Figures 3 and 4 present a sample of comparisons performed at LANL. The following conclusions can be reached:

1. Break flow rates are underpredicted by almost 25% for subcooled conditions. Predictions for the saturated blowdown are good. They are within the experimental data uncertainty.

2. Pressures and temperatures are predicted within 100 kPa (≈1 atm) and 10K respectively except within the first 5s. The predictions within the first 5s are worse because the code does not model delayed nucleation.

3. There are many uncertainties in the initial state of the tests. Temperature distribution was nonuniform. The effects of these uncertainties on predictions are not quantified.

ECC Bypass and Penetration

Four different steady state and two different transient Battelle-Columbus tests have been used to assess the capability of the code to perform multi-dimensional calculations to predict ECC bypass and penetration. Figures 5 and 6 present comparison between code calculations performed at BNL and test data for two steady state cases. The abscissa is the dimensionless ECC water penetration flow rate and the ordinate is the dimensionless steam flow rate. The following conclusions are reached from this study:

1. The code predicted the penetration of ECC water accurately for the case of very low subcooled ECC water. For the case of high subcooled ECC water, the code predicted excessive penetration. The code calculates excessive condensation.

2. The results depend on nodalization. When a node boundary crosses the hot leg, it effectively blocks some part of the flow in the azimuthal direction. In the calculations above, the nodalization was selected such that the flow was only partially (50%) blocked. Further nodalization studies are underway to provide guidance to users.

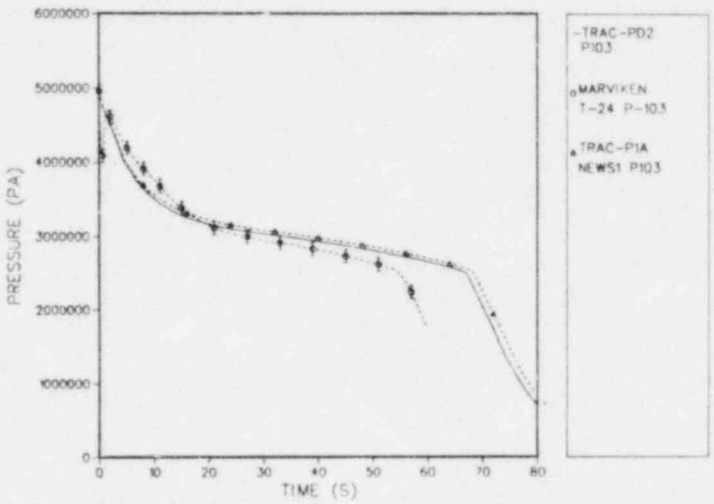

FIG. 3 COMPARISON OF PREDICTED AND MEASURED PRESSURES AT THE TOP OF VESSEL (MARVIKEN TEST NO. 24)

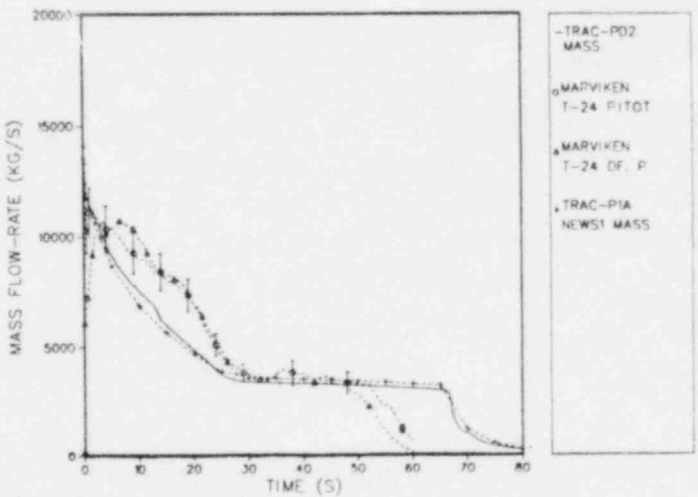

FIG. 4 COMPARISON OF PREDICTED AND MEASURED BREAK FLOW RATES (MARVIKEN TEST NO. 24)

Figure 7 presents comparison between code calculations and test data for transient test 29302 where both steam flow rate and temperature of the hot wall were ramped down. The upper figure shows a comparison of how the water level in the lower plenum changed during the tests and three different code predictions using different nodalizations. Although calculations without modeling of the hot legs give a good agreement with data, they are clearly in error. The other two cases describe calculations with no blockage and 98% blockage of azimuthal flow areas in nodes where hot legs are located. The flow blockage represents the presence of a hot leg. The lower figure illustrates the measured and calculated lower plenum pressures for the same cases. The following conclusions are reached from this study:

1. The code calculates excessively high lower plenum pressures during the early part of the transient. The reason is that TRAC-PD2 has a lumped parameter heat slab model where excessively high wall temperatures and heat transfer to the liquid are calculated. A later version of the code, TRAC-PF1, contains distributed parameter heat slab model where temperature calculations should be more accurate.

2. The results are sensitive to nodalizations which provide different amounts of blockage to the flow. Sensitivity studies are underway to provide guidance to users.

CCFL and Entrainment

University of Houston flooding tests were used in order to assess the capability of TRAC-PD2 to predict CCFL and entrainment. Code calculations were performed at BNL.

Figure 8 shows the comparison between the predictions and test data. The following conclusions can be made:

1. TRAC-PD2 predicts the inception of entrainment and cocurrent liquid film flow at lower air flow rate than the experiment indicates.

2. TRAC-PD2 predicts excessive amount of entrainment compared to data. Judging from the trends of data and calculations a new entrainment model in the TRAC code may be needed. This may involve two liquid fields, one for the liquid film and the other for the droplets since they move at different velocities. Improvement in the entrainment model would improve predictions of clad temperatures along the rod ahead of the quench front and also rod quench time. Using the present model which predicts excessive entrainment, would lead to prediction of cooler rod temperatures.

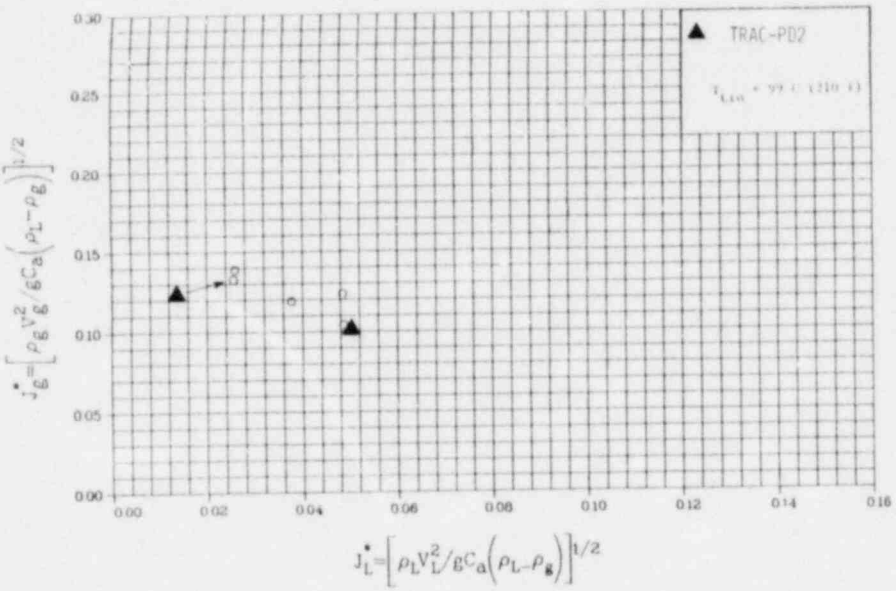

FIG. 5 COMPARISON OF PREDICTED AND MEASURED STEAM AND WATER PENETRATION FLOW RATES (BATTELLE COLUMBUS LABORATORY, TEST 26715-26719)

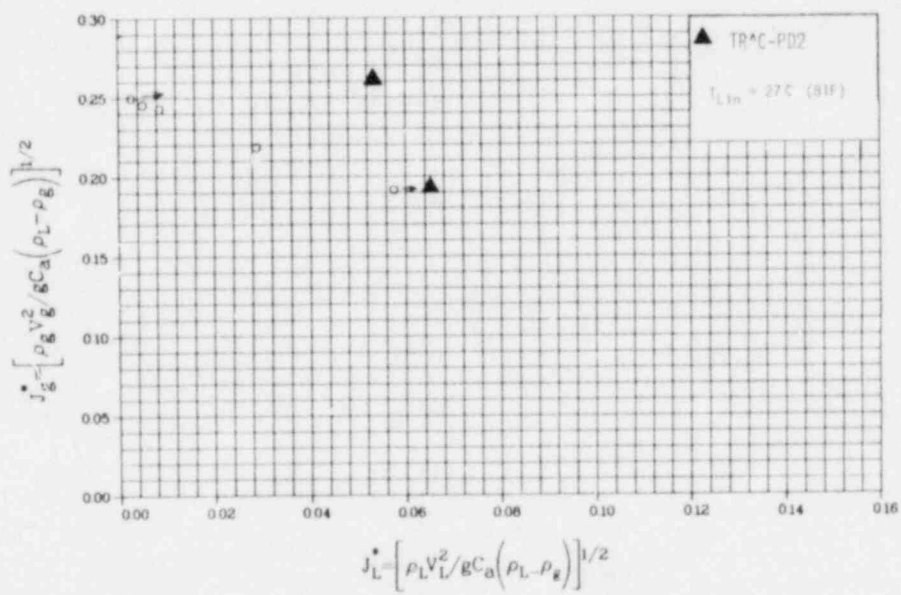

FIG. 6 COMPARISON OF PREDICTED AND MEASURED STEAM AND WATER PENETRATION FLOW RATES
(BATTELLE COLUMBUS LABORATORY TEST NO. 26502-26507)

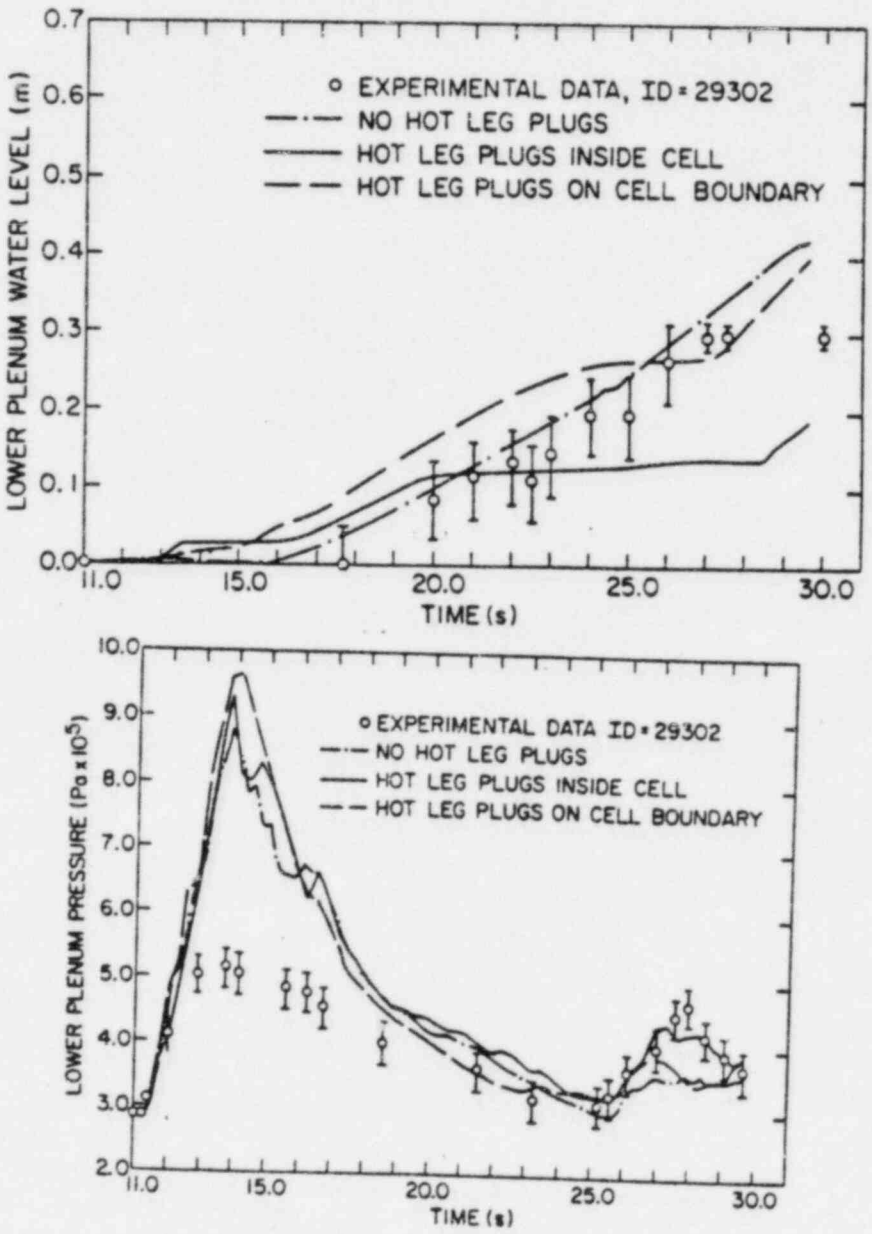

Fig. 7 Comparison Between the Measured and Calculated Values of Lower Plenum Water Level and Pressure

(Battelle Columbus Laboratory Test No. 29302)

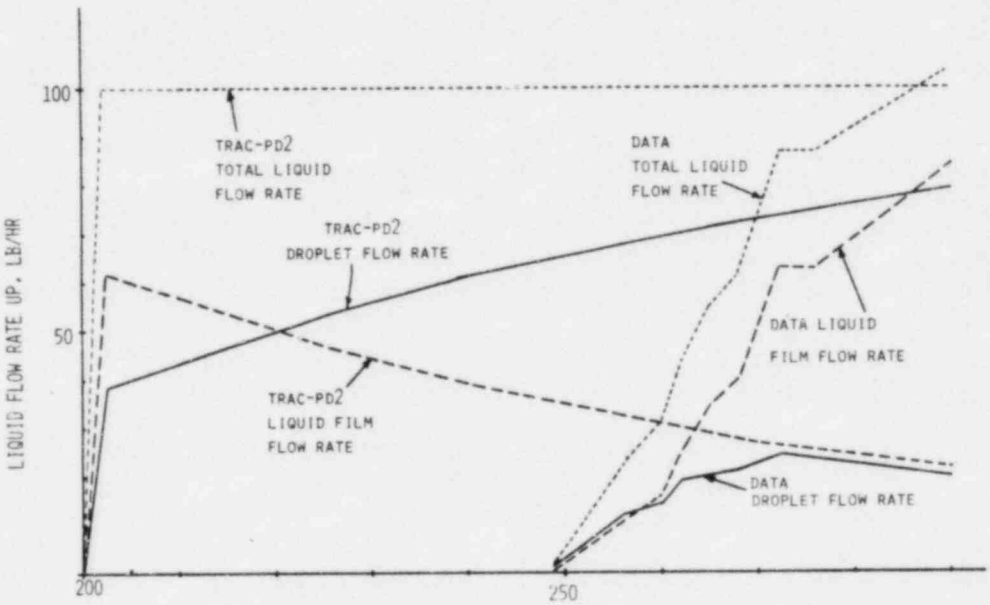

FIG. 8 COMPARISON OF CALCULATED AND MEASURED DROPLET AND LIQUID FILM FLOW RATES (UNIVERSITY OF HOUSTON TEST)

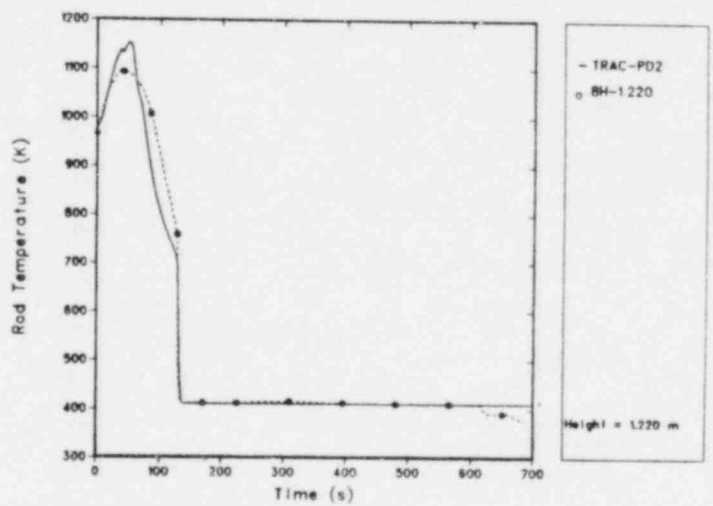

FIG. 9 FLECHT-SEASET 31504, BOTTOM ELEVATION

Reflood

TRAC-PD2 code has a mechanistic model for treating the quench front propagation. Fine nodalization is used in the quench vicinity to calculate accurately the heat conduction in (r,z) cylindrical coordinates. Capability of the code to predict reflood has been tested using many tests. These tests have been identified in Table I.

One of the important tests in the matrix is that from the FLECHT-SEASET facility. This FLECHT-SEASET test is a forced reflood test and thus does not contain the type of uncertainties encountered in gravity reflood tests such as performed at the PKL test facility. The flow rate into the core is a measured input quantity and does not contain uncertainties in calculation of the flow rate. Figures 9 through 11 compare predicted and measured rod temperatures for FLECHT-SEASET Test # 31504 at different elevations. The calculations have been performed by LANL.

The predictions of rod temperatures as well as the quench times at low elevations are very good. At high elevations, after the maximum temperature occurs, cooldown of the rods is overpredicted which is consistent with calculations of excessive entrainment.

Multi-D Calculations

Multi-D calculational capability is required to accurately calculate ECC bypass and penetration and detailed thermal hydraulics phenomena in the core. In order to directly assess how well the code can calculate multi-D hydraulic phenomenon, RPI tests were considered. The RPI tests are conducted using a two-dimensional test section with air and water.

Figures 12 and 13 compare the TRAC-PD2 predictions with the test data from RPI at different elevations. Calculations have been performed by BNL. Comparison illustrates that TRAC-PD2 predicted multi-D effects reasonably well. At the bottom and top elevations predictions and measurements of vapor fractions are in good agreement. At middle elevations the agreement between the test data and predictions is poor. Dispersion of vapor fraction in TRAC-PD2 predictions is too high. A turbulent mixing model may improve predictions. Figure 14 shows TRAC-PD2 predictions of gas and liquid velocities. It shows a similar circulation pattern as observed in experiments; phases go up in the middle and then come down at the edges. Although qualitatively predictions are good, more tests are needed to ascertain the code capability of accounting for multi-D effects.

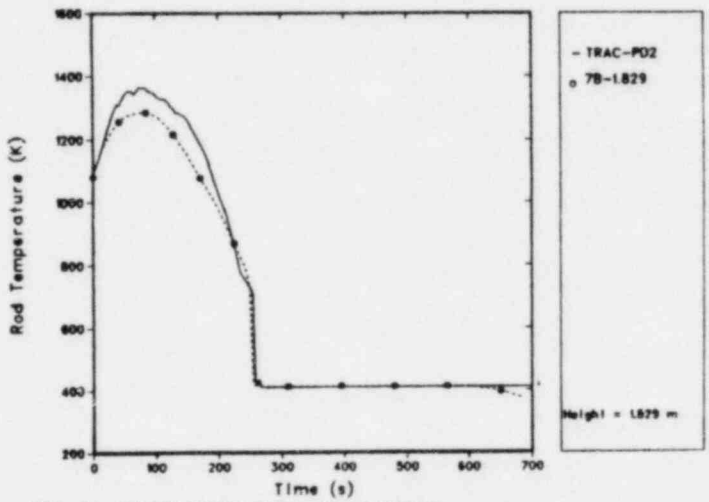

FIG. 10 FLECHT-SEASET 31504, MID-ELEVATION

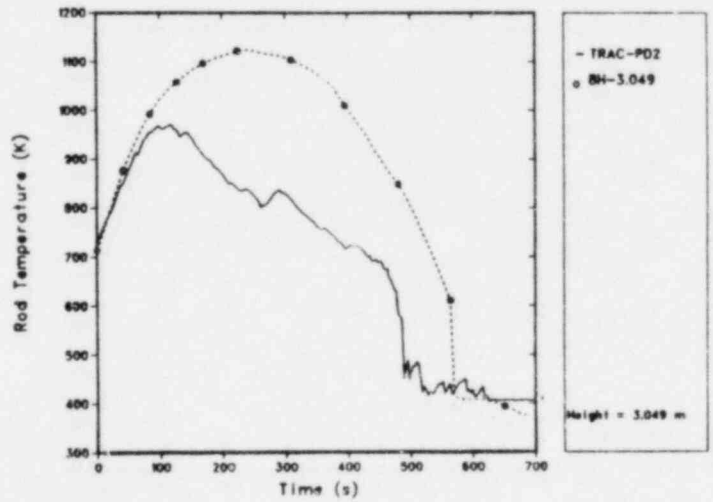

FIG. 11 FLECHT-SEASET 31504, TOP ELEVATION

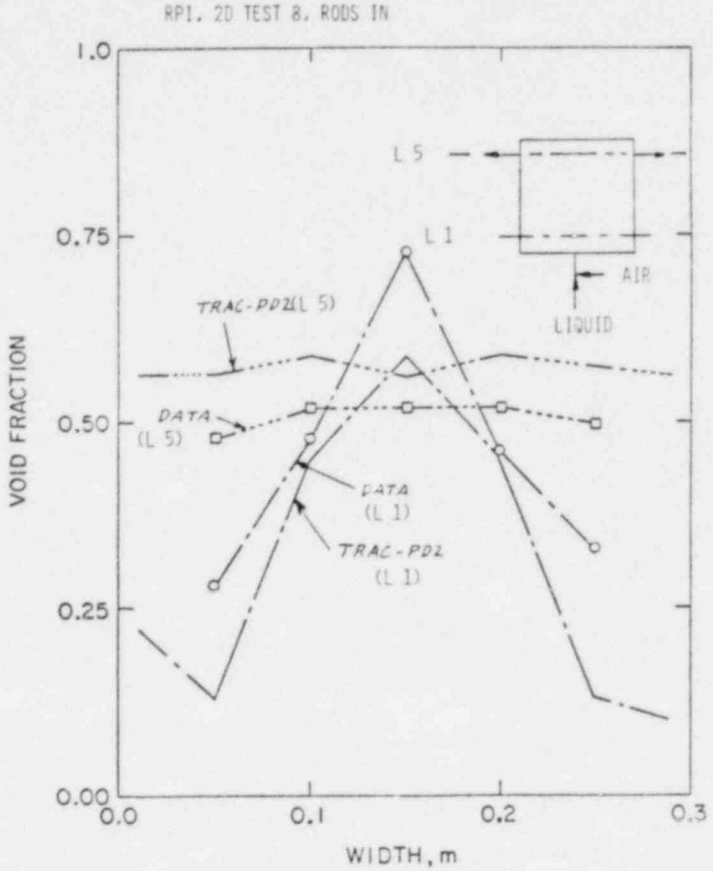

FIG. 12 COMPARISON OF CALCULATED AND MEASURED VOID FRACTIONS (RPI TEST NO. 8)

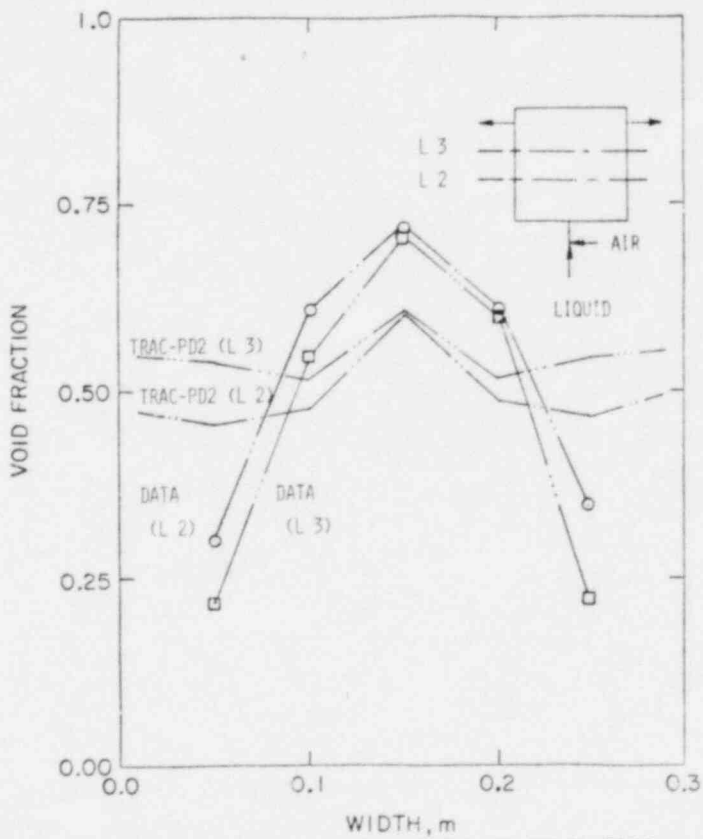

FIG. 13 COMPARISON OF CALCULATED AND MEASURED VOID FRACTIONS (RPI TEST NO. 8)

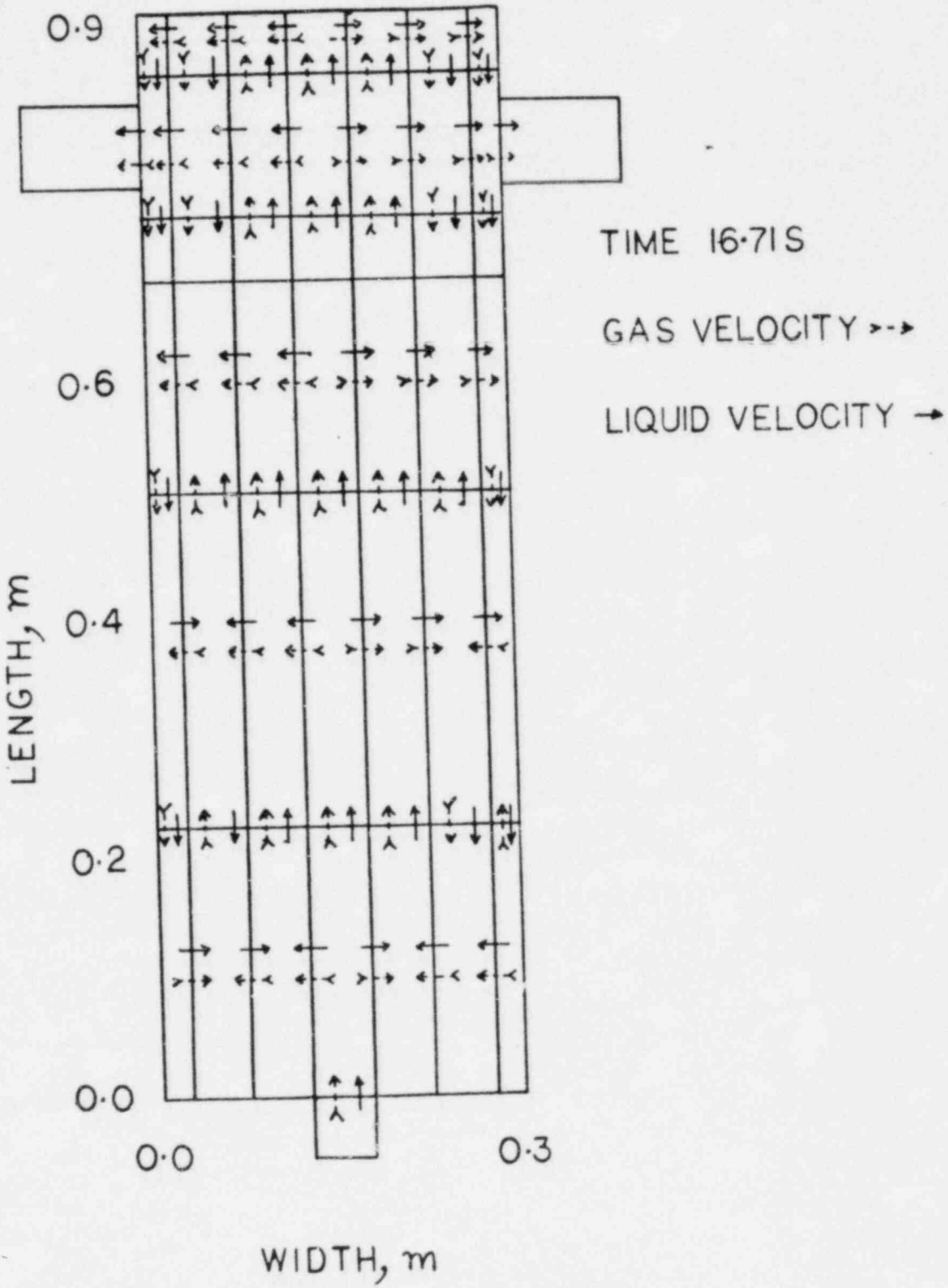

FIG. 14 CALCULATED FLOW PATTERNS (RPI TEST NO. 8)

For tests with high void fractions the code calculated severe oscillations and a stable solution was not reached. It is necessary to improve the numerics in this area.

QUALITATIVE ASSESSMENT FROM INTEGRAL TESTS

Figures 15 through 18 compare predicted and measured clad temperatures for the LOFT test L2-2. Figure 16 shows the clad temperatures at the hot spot in the center bundle (Bundle 5). The predicted initial dryout, peak clad temperature and subsequent rewet are in agreement with the test data. Many subsequent dryouts and rewets have the same trends and the final quench is predicted reasonably well.

Figure 17 shows the clad temperatures above the hot spot. Here, the prediction of peak clad temperature is below that measured. Although the LOFT tests are integral tests, and there may be many other parameters affecting peak clad temperatures, the calculations of lower temperature is consistent with calculation of excessive entrainment. One of the two thermocouples does not show any rise indicating that TRAC-PD2 nodalization is too coarse. However, the cost of computations using fine nodalizations would be prohibitive and not necessary for qualitative assessment.

Figure 15 shows the comparison of the clad temperatures at the bottom elevation. TRAC-PD2 does not predict the peak value but follows the trend. Again finer nodalization to predict 3-D effects may be necessary (two out of four thermocouples show rise in temperature while the other two do not).

Clad temperatures in peripheral assemblies were also well predicted. Figure 18 is a sample comparison of clad temperatures signature and thermocouple traces.

It is clear that there are many multi-dimensional effects in the core. However, the coarse nodalization (192 nodes in the vessel) does not permit very detailed calculation for each bundle. The present nodalization of LOFT is considered satisfactory to obtain a reasonable accuracy in predicting overall 3-D phenomena and overall trends.

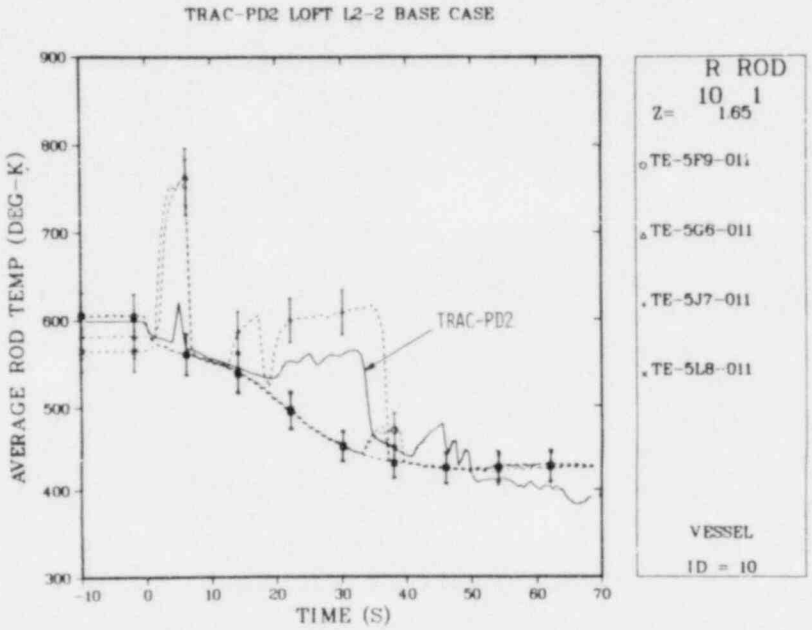

FIGURE 15: COMPARISON OF CALCULATED AND MEASURED CLAD TEMPERATURES
CENTER BUNDLE, LOW ELEVATION

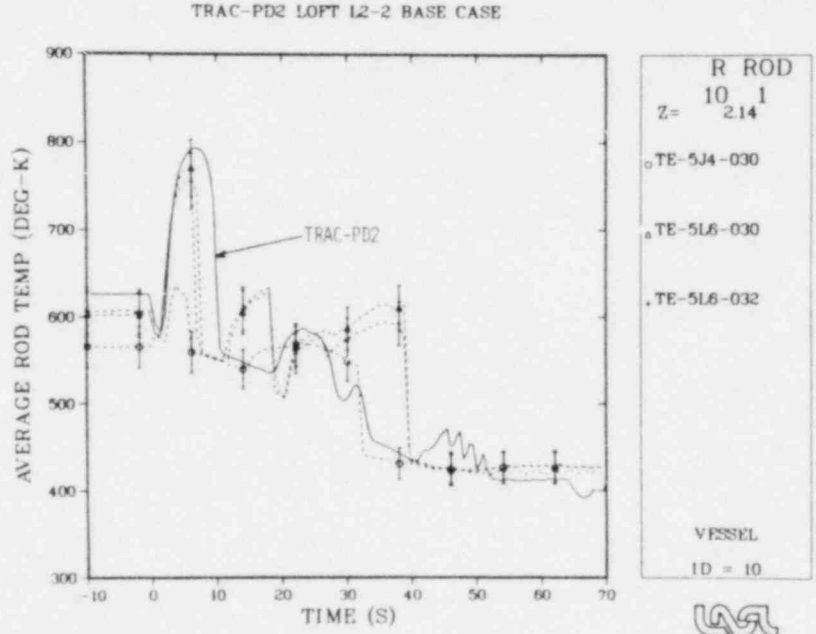

FIGURE 16: COMPARISON OF CALCULATED AND MEASURED CLAD TEMPERATURES
CENTER BUNDLE, MID ELEVATION, HOT SPOT

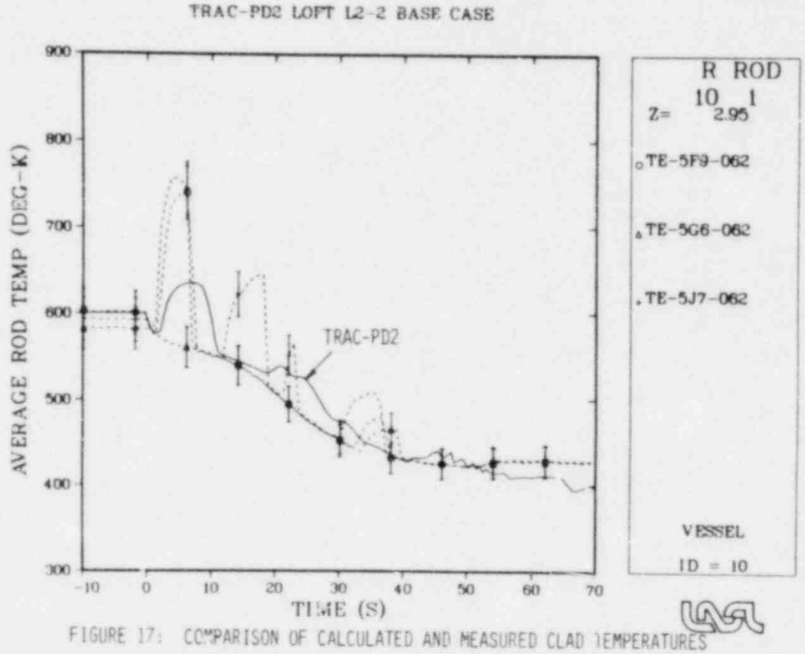

FIGURE 17: COMPARISON OF CALCULATED AND MEASURED CLAD TEMPERATURES CENTER BUNDLE, TOP ELEVATION

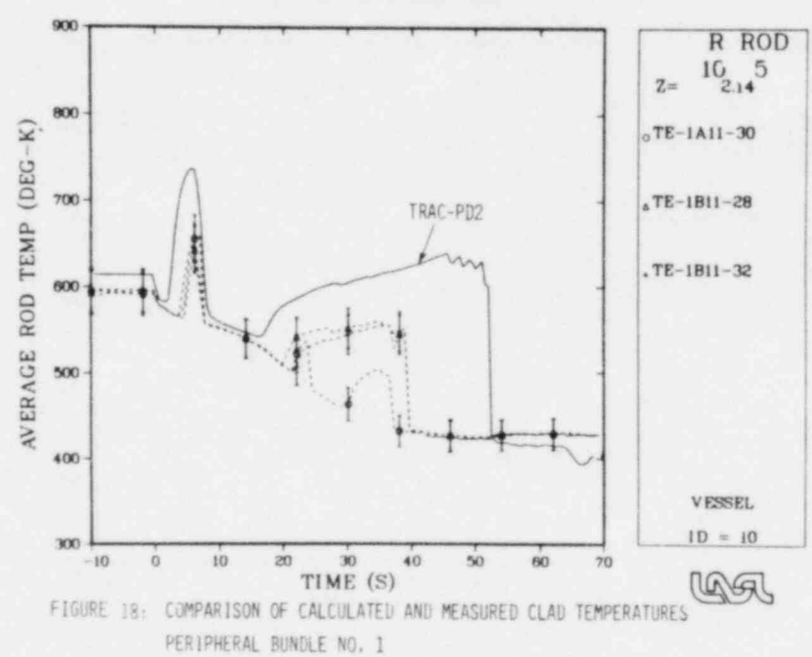

FIGURE 18: COMPARISON OF CALCULATED AND MEASURED CLAD TEMPERATURES PERIPHERAL BUNDLE NO. 1

CONCLUSION

An assessment of TRAC-PD2 for use in analyzing a large break LOCA is complete. The accuracy of predictions of peak clad temperatures is about ± 80K. Other uncertainties in prediction of other key variables are presented in Tables III through VI. In general, the predictions are good.

A few more runs from large test facilities will be added to the assessment matrix to ascertain if there is a slight upward trend in the average value of differences between the calculated and the predicted peak clad temperatures as the facility scale increases. If there is a trend, the predictions in a full scale PWR will be slightly conservative; i.e., a slightly higher temperature will be predicted than the data would indicate. It is expected that addition of these runs will not change the uncertainties in Tables III through VI.

Assessments from basic and separate effects tests, as well as qualitative assessment, provide an enhancement in our understanding of capabilities of the code in simulating various phenomena. This understanding provides a basis for further improvements in the code. Future versions of the code will include some of these suggested improvements. This should reduce the uncertainties found in the quantitative assessment.

REFERENCES

1. TRAC-PD2, An Advanced Best-Estimate Computer Program for Pressurized Water Reactor Loss of Coolant Accident Analysis, NUREG/CR-2054, LA-8709-MS, April 1981.

2. Plans for Assessment of Best Estimate LWR Systems Codes, S. Fabic and P. Andersen, NUREG-0676, July 1981.

REFLOOD CODE VERIFICATION FOR SAFETY ANALYSIS

J. Chiou, L. E. Hochreiter, S. R. Rod, M. Y. Young

Nuclear Technology Division
Westinghouse Nuclear Energy Systems
P.O. Box 355, Pittsburgh, PA 15230

ABSTRACT

The BART code is a Westinghouse PWR reflood safety analysis tool which can be used to address emergency core cooling effectiveness during reflood. The formulation used in BART utilized mechanistic models to describe the two-phase flow and heat transfer, axial conduction, clad rewetting, fuel clad swelling and radiation heat transfer to drops and vapor in the flow. Since the models are mechanistic, the Westinghouse approach has been to utilize separate effects experiments, which can test particular aspects of the BART formulation for verifying the different models in the code.

This paper will describe the BART code verification results with different reflood heat transfer experiments, in particular the Battelle Northwest/USNRC NRU clad ballooning and reflood experiments. These particular experiments will test the BART codes capabilities of distinguishing the difference between an electrical fuel rod simulator and a nuclear fuel rod, as well as the clad swelling behavior of a ballooning fuel rod.

INTRODUCTION

Analytical models and computer codes must be sufficiently verified against experimental data or by independent calculational methods before they are approved for reactor safety analysis. Different techniques exist for code verification. One approach is to compare the entire calculation scheme to prototypical data to show that the model gives a conservative prediction. Another approach is to isolate particular models in the scheme and compare only those models against experimental data. A third method is to perform code-to-code verification with an existing verified code which has more mechanistic models. The more sophisticated code in this case is considered the "experiment".

The preferred method of code verification is to isolate models and compare them individually with prototypical independent experiments or calculations in which all boundary conditions are accurately known. Once the key models are compared separately in this manner, the comprehensive model should than be tested against data from an independent source in which all relevant processes are acting concurrently. As safety analysis has become more refined, the main concern is no longer whether the model yields a conservative estimate of reactor safety performance, but whether the model accurately predicts the true reactor behavior.

For the past several years, Westinghouse has been developing a best estimate one-dimensional PWR reflood analysis computer code which is physically based; the BART code (1) (2) (Best estimate Analysis of Reflood Transient). The BART

code has undergone substantial verification with electrically heated bundle reflood tests as well as more recent NRU (3) (4) (5) nuclear bundle reflood experiments. As reported in reference (2), BART used the low flooding rate cosine FLECHT data (6) for preliminary model verification and used the FLECHT skew power profile (7) and Semiscale data (8) for final validation.

The NRU experiment series offered an opportunity to extend the validation of the BART reflood model because it was one of the few (if not the only) nuclear powered reflood experiments with prototypical dimensions and accurate thermal-hydraulic boundary conditions. This paper will discuss the development of some particular BART models and how they were verified using NRU data.

BART MODEL DESCRIPTIONS

The development of BART took place in several steps. First, from an extensive literature review, the phenomena which were generally felt to be of primary importance during reflood were identified. Second, an attempt was made to derive models for these phenomena from first principles. Simplifying assumptions and empirical correlation were used only when lack of data or a severe hindrance to code efficiency required them. Third, each model was separately checked with data and modified as necessary. Finally, the models were assembled and the resulting reflood model was compared with additional data.

Additional underlying goals in this development were to minimize the number of adjustable parameters, to make the necessary parameters basic physical quantities rather than derived ones, and to require that they be varied in a consistent manner among all component models. A final requirement, essential for any computer code intended for reactor safety analysis, was that adjustable parameters remain fixed when comparing predictions with different experiments.

The primary areas of development for BART are listed here and brief descriptions of the relevant models follow:

1. Two-phase flow behavior during reflood.
2. Quench front propagation along fuel rods.
3. Heat transfer in dispersed flow.
4. Clad swelling and rupture.

1) TWO-PHASE FLOW BEHAVIOR DURING REFLOOD

Physical models had to be capable of following in detail the mechanical and thermal behavior of each phase in all the flow regimes expected during reflood. The dispersed phase was given special attention, since it is the regime in which peak clad temperatures are reached. Accordingly, a drift flux formulation was used for flow regimes near and at the quench front, and a two-fluid formulation was employed for the dispersed regime. The basic equation set used was:

a) a volume flux equation:

$$\frac{\partial j}{\partial z} + \alpha \frac{\partial}{\partial t} \ln \rho_v + j_v \frac{\partial}{\partial z} \ln \rho_v = \Gamma \left(\frac{1}{\rho_v} - \frac{1}{\rho_\ell} \right) \qquad (1)$$

b) a mixture continuity equation:

$$\frac{\partial \rho_s}{\partial t} + \frac{\partial}{\partial z}(G) = 0 \qquad (2)$$

c) a vapor energy equation:

$$\rho_v \left[\alpha \frac{\partial H_v}{\partial t} + j_v \frac{\partial H_v}{\partial z}\right] = q''' - q'''_{boil}\left[1 + \frac{H_v - H_{vsat}}{H_{\ell v}}\right] \qquad (3)$$

d) an equation of state:

$$\rho_v = \rho_v (H,P) \qquad (4)$$

where:

j	= volumetric flux
j_v	= vapor volumetric flux
ρ_v	= vapor density, ρ_l = liquid density
Γ	= volumetric rate of vapor generation
ρ_s	= mixture density
G	= mixture mass flux

The relative velocity, u_r, is determined from drift flux correlations or, in the case of dispersed flow, is calculated from a local vapor-droplet force balance.

Simplifying assumptions were:

1) One dimensional equations
2) Fluid properties are independent of small variations in pressure

2) QUENCH FRONT PROPAGATION

An accounting of the effect of heater rod or fuel rod properties on quench front propagation, and a mechanistic description of the rod to fluid heat transfer at and near the quench front were two main goals in this area. The model of quench front heat release establishes an array of isotherms which migrate along the rod as the quench front propagates as shown in Figure 1. The isotherm model accounts for both radial temperature gradients within the rod and the severe axial gradient about the quench front. The isotherm temperatures are input values and can be chosen to provide any desired degree of detail at the quench front.

The model considers radial conduction in the rod and axial conduction along the rod, which is of the same magnitude as boiling heat transfer to the liquid. The axial conduction leads to additional preheating of the liquid before it reaches the actual quench front. A nominal heat flux profile is shown in Figure 1.

A boiling curve based on the assumption of hydrodynamically controlled heat flux at the quench front was used to locate appropriate heat transfer regimes and the accompanying heat transfer coefficients. The regimes near the quench front include single phase forced convection, nucleate boiling, transition

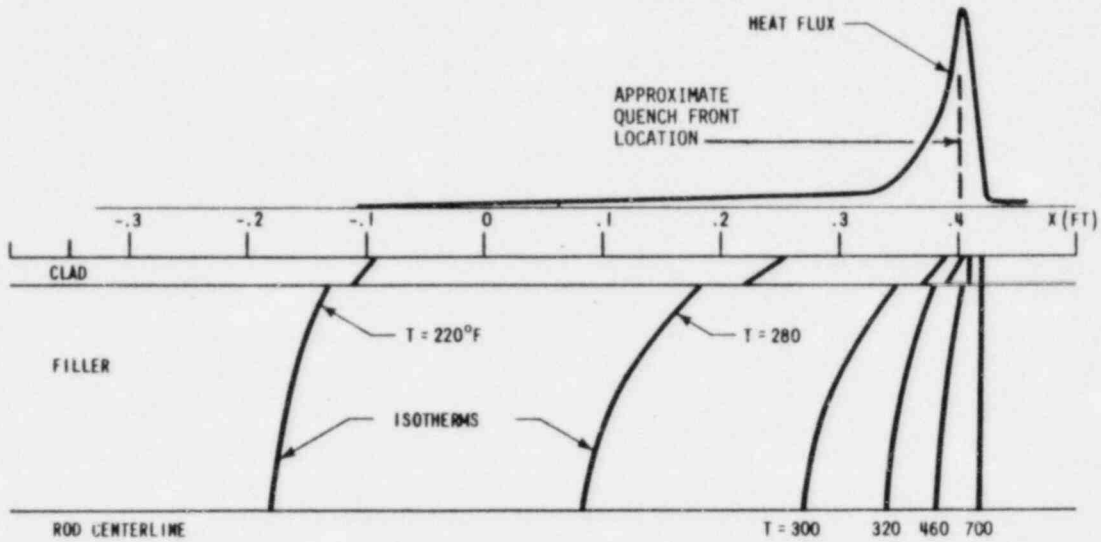

FIGURE 1. THE BART QUENCH FRONT HEAT RELEASE MODEL

boiling and film boiling. Closely spaced isotherms allow very fine detail in locating boiling zones in the region immediately around the quench front, which is typically very narrow, while sacrificing little in computer running time.

3) HEAT TRANSFER IN DISPERSED FLOW

There are four possible mechanisms for heat transfer from the rod surface to the fluid in dispersed flow:

a) Forced convection to vapor
b) Radiation to fluid
c) Radiation to other rods
d) Droplet contact

A careful analysis was made of the forced convection and radiation components of the heat transfer in the FLECHT Cosine and Skewed tests (6) (7). From that analysis, the following conclusions were drawn:

a) Radiation accounted for roughly twenty percent of the total heat flux from the heater rods at upper elevations. The three components of radiation were found to be of the same order of magnitude.

b) The remaining heat flux, attributed to forced convection from the rod surface to the vapor, was significantly higher than could be accounted for by standard correlations such as Dittus - Boelter.

It was concluded in the FLECHT analysis that the physical mechanism providing the most consistent explanation for the excess heat transfer was the level of turbulence within the vapor. Given the same local Reynolds number, turbulent diffusion of heat was more effective during two phase flow in the FLECHT bundle than would be the case in single phase flow in a tube.

In addition to force convection, radiation from the rod to the fluid is calculated using the Sun and Gonzalez model (9). Rod-to-rod radiation is presently ignored, although it is recognized that this component may become important at upper elevations of the rod bundle.

Drop contact heat transfer was ignored in the FLECHT analysis because the droplet contact yielded large amounts of saturated vapor, overwhelming the mechanism of heat transfer from rod to vapor. The high vapor temperatures measured in the FLECHT experiments are inconsistent with the droplet contact model.

4) CLAD SWELLING AND RUPTURE

In the dispersed droplet regime with highly superheated steam the fuel rod cladding has the maximum potential for swelling and rupture. The BART clad swelling model, calculates local clad diametral strain and possible burst in each timestep of the main BART program. The swelling calculations consider fuel rod gap and core channel pressures, thermal expansion of the fuel and clad, elastic and plastic strain of the clad, interference of adjacent rods at large strain and the effects of support grids at certain locations along the rods.

The swelling model provides updated values of several parameters related to fuel rod, core subchannel, fluid flow and heat transfer properties. These updated parameters include rod gap pressure; gap heat transfer coefficient; clad inner and outer diameters; subchannel flow area, heated perimeter and hydraulic diameter; and "whole core" flow area, heated perimeter and hydraulic diameter. The "whole core" takes into account all rods, subchannels and flow bypass paths in the system under consideration. Details of the BART swell model will be considered next.

The initial (cold fill) gap pressure is an input parameter. The model re-initializes gap pressure to correspond to the rod temperature profile at the start of the transient. For the reinitialization and at each timestep during the transient a new value of gap pressure P_{gap}, is calculated from an adaptation of the ideal gas law.

Thermal expansion of the fuel and clad and clad elastic strain are calculated with standard, theoretically based formulas for these effects. In the cases of plastic deformation and burst, however, three empirical models are employed. These models were first developed for the LOCTA Loss-of-Coolant Transient Analysis code (10) and are adapted for BART essentially unchanged.

a) Clad Swelling Prior to Burst

Hardy (11) performed a series of tests in which rods with constant internal pressure were ramped to a series of temperatures at various constant ramp rates. The pressures reported by Hardy were converted to hoop stresses by the formula:

$$\sigma_{hoop} = \Delta PRESSURE_{(across\ clad)} \ / \ 2 \cdot CLAD\ THICKNESS \qquad (5)$$

and the strain at a given temperature and ramp rate were correlated as functions of the derived hoop stress.

b) Clad Burst

The clad is assumed to burst if clad temperature exceeds a criterion "burst temperature". Burst temperature is calculated as a function solely of gap pressure (i.e. hoop stress) based on correlation of the Westinghouse single rod burst test data (12). A best estimate correlation for this data was constructed to be independent of all temporal effects (e.g. rate of temperature rise).

c) Local Hoop Strain After Burst

The localized diametral swelling which occurs rapidly at the time of burst is computed from a correlation of single rod burst test data of Westinghouse (12) and of others.

BART VERIFICATION STUDIES USING THE NRU EXPERIMENTS

The NRU test program is a U.S. NRC fuel behavior research program which is technically directed by Battelle Northwest Laboratories at the Atomic energy of Canada Limited test facility at Chalk River. The NRU reactor is utilized at Chalk river as a fission source for a 12-foot long (3.66 M) 32 rod bundle which is constructed of typical production grade UO_2 fuel and cladding. The NRU test loop serves as a pressure boundary between the reactor and the test bundle. However, the two are coupled by the neutron flux field in the reactor. A cross-section of the test bundle is shown in Figure 2 along with a list of the NRU test rod array dimensions. The test bundle can consist of up to 32 fuel rods (a 6x6 with the corner rods missing). The rod bundle is enclosed in a split, thin wall test section shroud which can be easily disassembled under water for access to the test bundle.

The test bundle instrumentation consisted of shroud wall thermocouples, steam probes which were hung from the grids, thermocouples brazed onto the outside of the fuel rods (at lower elevations) and thermocouples which were placed in grooves in the pellets or welded to the inside of the clad. Self-powered neutron detectors (SPND) measured the axial power shape as well as the flux tilt across the bundle when the test bundle was preconditioned at NRU operating conditions.

The NRU test bundle would be preconditioned at typical NRU reactor operating conditions to crack the fuel pellets such that the fuel was more representative of an operating LWR. After preconditioning, the piping was changed such that steam flow could be forced through the test bundle. The steam flow was high enough such that representative decay heats could be established in the test bundle. The heat losses from the test bundle were estimated to be approximately six percent from the steady state steam flow tests. This was also confirmed by hand calculations using the measured shroud wall temperatures.

Selected adiabatic heat-up tests were also performed to verify the axial power shape and power level. Reflood tests were conducted with programmed or preset flooding rates as well as computer controlled flooding rate tests which were conducted in the second thermal-hydraulic test series.

Cladding Material Specification	=	Zircaloy-4
Cladding Outside Diameter (OD)	=	0.963 cm (0.379 in.)
Cladding Inside Diameter (ID)	=	0.841 cm (0.331 in.)
Pitch (rod to rod)	=	1.275 cm (0.502 in.)
Fuel Pellet Diameter	=	0.826 cm (0.325 in.)
Fuel Pellet Length	=	0.953 cm(0.375 in.)
Active Fueled Length	=	365.76 cm (144 in.)
Total Shroud Length	=	423.1 cm (170.125 in.)
Helium Pressurization	=	3.2 MPa (465 psia)

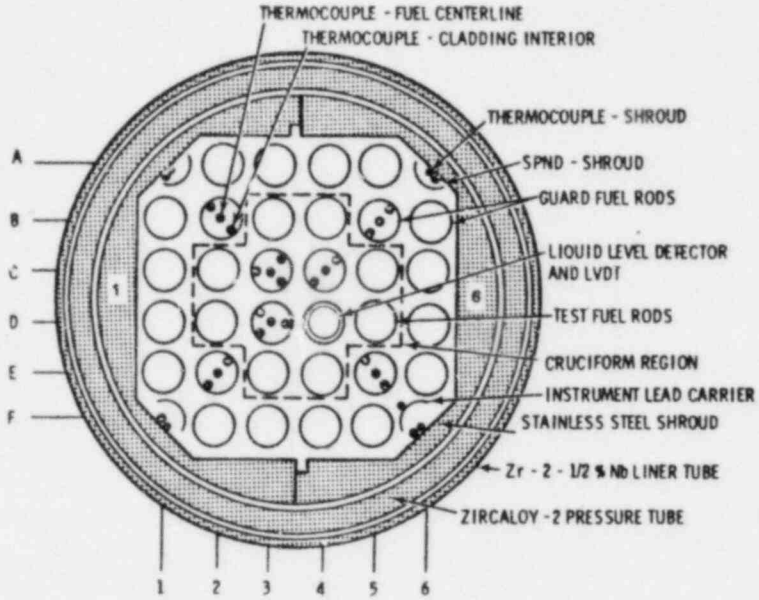

FIGURE 2. CROSS SECTION OF NRU TEST ASSEMBLY

The BART code modelled different NRU tests to allow examination of the code prediction for thermal-hydraulic behavior as well as for materials behavior (i.e. fuel rod swelling). The first NRU test to be modelled was the thermal hydraulic test with unpressurized fuel rods, a test which was nearly the same as a previously conducted FLECHT-SEASET (2) electrically heated reflood experiment. The objective of this anaylsis was to determine if the BART axial conduction quench model could effectively distinguish between a boron-nitride filled heater rod simulator and a PWR nuclear fuel rod. The quench front for the NRU test, the comparable FLECHT-SEASET test and the calculated BART code results for each are shown in Figure 3. As the figure indicates, the BART quench front model, which accounts for axial conduction in the clad and pellet, gives good results when compared to the two sets of data.

A more through examination of the NRU test results as compared to the BART code predictions indicated that the measured heat transfer and rod temperature at the upper elevations were significantly better than the BART predictions (see Figure 4). Several reasons for the BART over-prediction of the NRU rod temperatures at the higher elevations were identified, but they did not result from a deficiency of the basic BART model, but rather from the small size of the test bundle used in the NRU experiments.

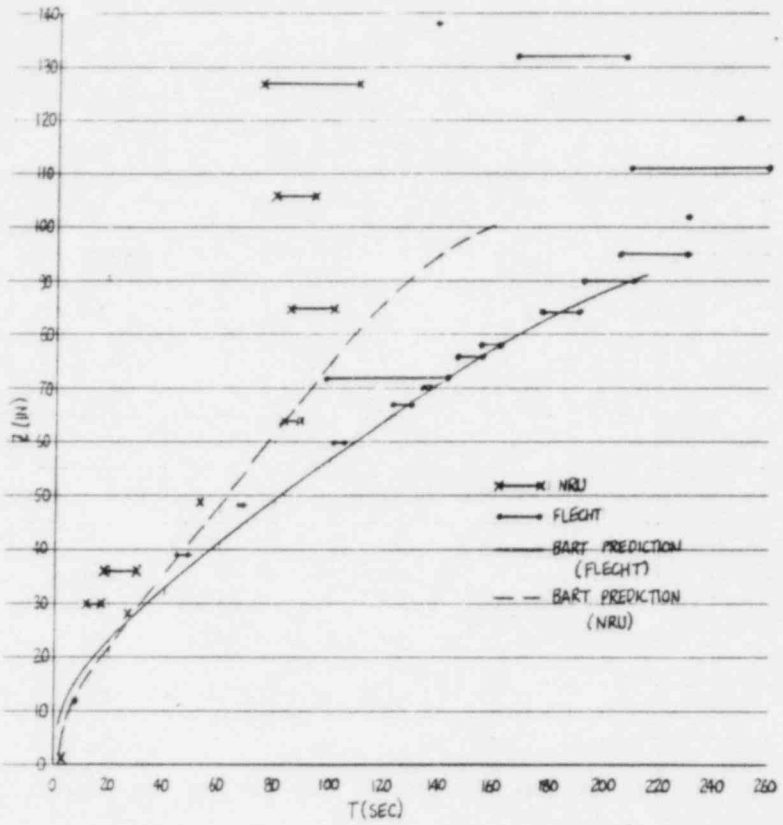

FIGURE 3. BART QUENCH FRONT MOVEMENT PREDICTIONS FOR COMPARABLE FLECHT (#31302) AND NRU (#123) TESTS

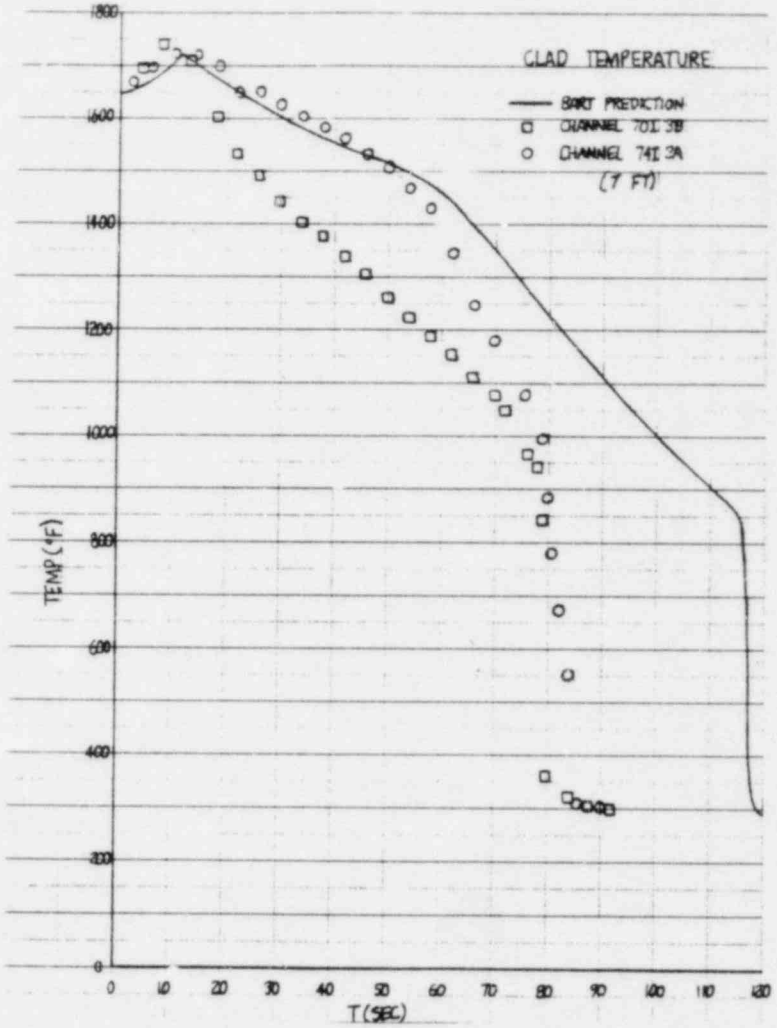

FIGURE 4. BART CLAD TEMPERATURE PREDICTION FOR NRU TEST 123, 7 FOOT ELEVATION

Examinations of the tests results indicated that the thin wall unheated shroud quenched early in the transient. The resulting wetted surface area provided an additional heat sink at the upper elevations of the test bundles. Additional heat transfer by radiation to the quenched and convective heat transfer from the liquid film on the shroud to the superheated vapor resulted in improved upper elevation fuel rod heat transfer.

In addition to the quenched housing, the NRU experiment also had excess flow area relative to a typical PWR fuel assembly. The increased flow area would result in the smaller enthalpy rise for the experiment than for the BART prediction. A portion of the excess flow area was blocked by instrument lines, so that a 10 percent excess flow area was accounted for in BART.

The increased radiation to the wetted shroud was calculated using a cross-string rod-to-rod radiation model which grouped the rods into different zones(13). The resulting radiation heat transfer effect, which was small for the center rod in the NRU bnundle, was added to the total rod heat transfer coefficient when the rod temperature history was calculated. The total heat flux to the shroud was used to define and effective radiation heat transfer coefficient as:

$$h_{\substack{\text{rod to}\\ \text{shroud}}} = q''_{\substack{\text{rod to}\\ \text{shroud}}} / (T_v - T_{shroud}) \qquad (6)$$

Where $T_{shroud} = T_{sat}$ when the shroud quenched.

The quenched shroud also would act as a vapor desuperheater and saturated steam source for the upper elevations of the bundle. The test data indicated that once the shroud quenched, it would stay quenched for the duration of the test. Therefore, the liquid film on the shroud was replenished either from the falling film coming from liquid separation in the NRU upper plenum, or from droplet deposition from the entrained reflood water. The heat transfer from the liquid film to the superheated steam by vapor convection was calculated as:

$$q''_{conv} = h_c (T_v - T_{sat}) \qquad (7)$$

Where the h_c is the convective heat transfer coefficient used in the BART code logic. Values for heat transfer coefficients for falling liquid films were obtained from the NORCOOL(14) and were found to be nearly the same as the BART calculated values of h_c (typically ~20 BTU/hr - ft^2 - °F based on T_{vapor}). Both the radiation to the quench shroud and the convective heat transfer to the shroud would increase the degree of vapor generation as:

$$q'''_{boil} = \frac{(h_{\substack{\text{rod-to-}\\ \text{shroud}}} + h_c) \cdot (T_v - T_{sat}) A_{wall}}{A_{flow} \cdot \Delta z} \qquad (8)$$

The resulting mass increase of saturated vapor per unit volume would then become:

$$\dot{m}_{vap\ shroud} = \frac{q'''_{boil\ shroud}}{h_{fg}} = \Gamma_{shroud} \qquad (9)$$

BART assumes that the the saturated steam generated at the shroud liquid film interface mixes perfectly with the existing superheated vapor equally in each subchannel. The resulting addition of saturated steam would improve the heat transfer at elevations above the shroud quench front location.

It was found that applying the locally calculated BART convective heat transfer coefficient value was not sufficient to make the resulting upper elevation rod temperature agree with the data. A multiplier of four (4) had to be applied to the BART calculated value of h_c to obtain proper agreement. Increasing the value of h_c beyond the BART value was felt to be justified by the following two reasons.

The up-draft steam velocities were sufficiently high to generate waves on the liquid film such that the effective liquid surface area was larger (V_v values were typically 25 - 40 ft/sec.). Increasing the liquid/vapor surface area has the same effect as increasing the vapor-film heat transfer coefficient, h_c. The wave generation effect has been observed in countercurrent annular flows.

In addition to the wettable shroud, the grids which are used to space the fuel rods can also quench (wet) also act as a vapor desuperheater. A hand calculation of single grid indicates that the wetted surface area is 114.4 square inches. If this area is converted to an equivalent shroud length, one wet grid has the same surface area as 10.2 inches of the shroud. The axial grid spacing is approximately 20 inches. If we consider the grids to wet or quench at the same times as the shroud, it would have the same effect as increasing the local heat transfer between the vapor and liquid film (h_c) by a factor of approximately 1.5. Note that this is a rough approximation.

In addition to modeling more exactly the true geometry of the test, BART input conditions included the measured axial flux shape, flooding rate, inlet temperature, pressure, initial temperature of rods and housing, and the total power from steam cooling tests. Heat losses from the housing for the steam cooling tests were also accounted for to obtain the proper power. Examples of the BART calculations using the housing-radiation and convection models (accounting for the excess flow area) are shown in Figures 5 to 8. The BART rod quench front calculation agrees well with the rod quench front data. Good agreement is also obtained for the elevations shown, though clad temperature is still somewhat high at later time.

The second test to be modelled was a stepped flooding rate test which was designed to hold the fuel rod temperatures at a constant temperature in the ballooning window of ~850°C. In order to do this, a stepped (decreasing) flooding rate was used to retard the rod quench front to place only one axial segment of the rod in this temperature range for as long a time as was possible. A special series of thermal-hydraulic experiments, without ballooning,

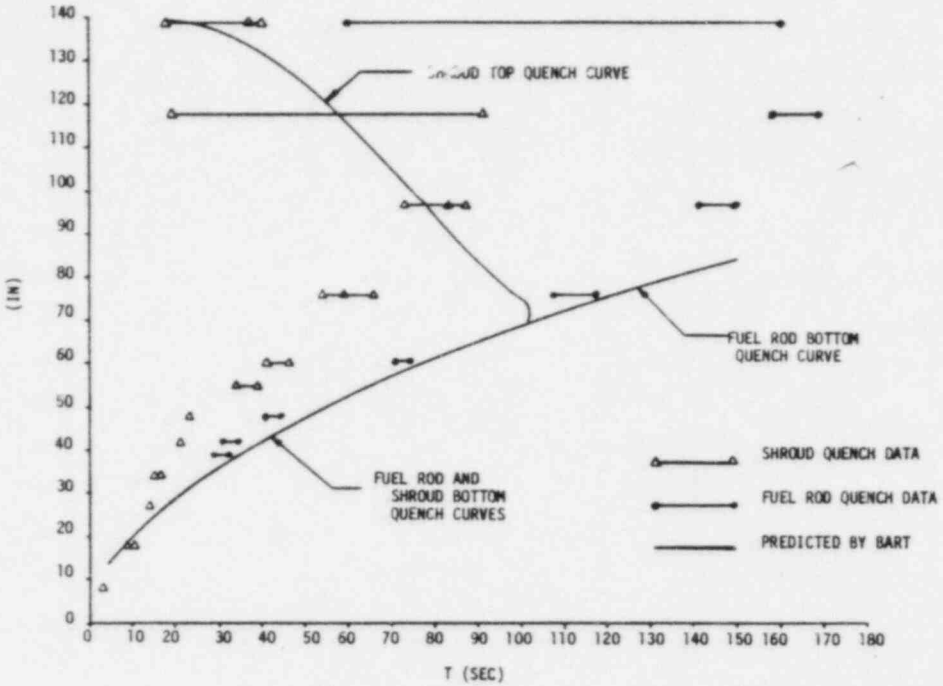

FIGURE 5. BART QUENCH FRONT MOVEMENT PREDICTION FOR NRU TEST 110

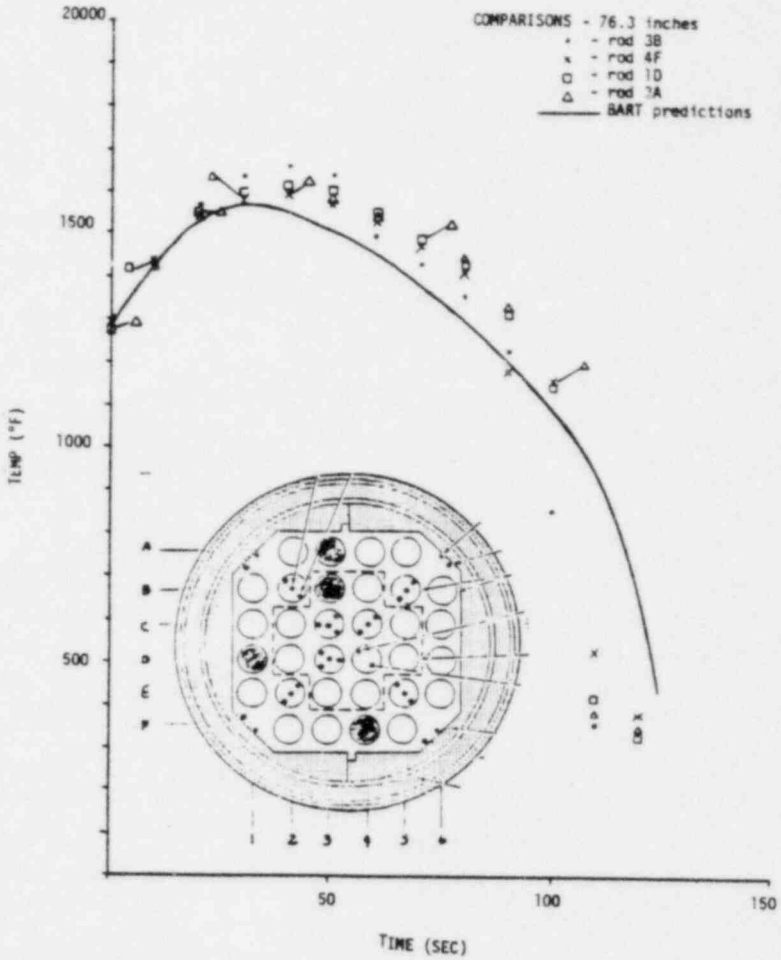

FIGURE 6. BART CLAD TEMPERATURE PREDICTION FOR NRU 110, 76.3 INCH ELEVATION

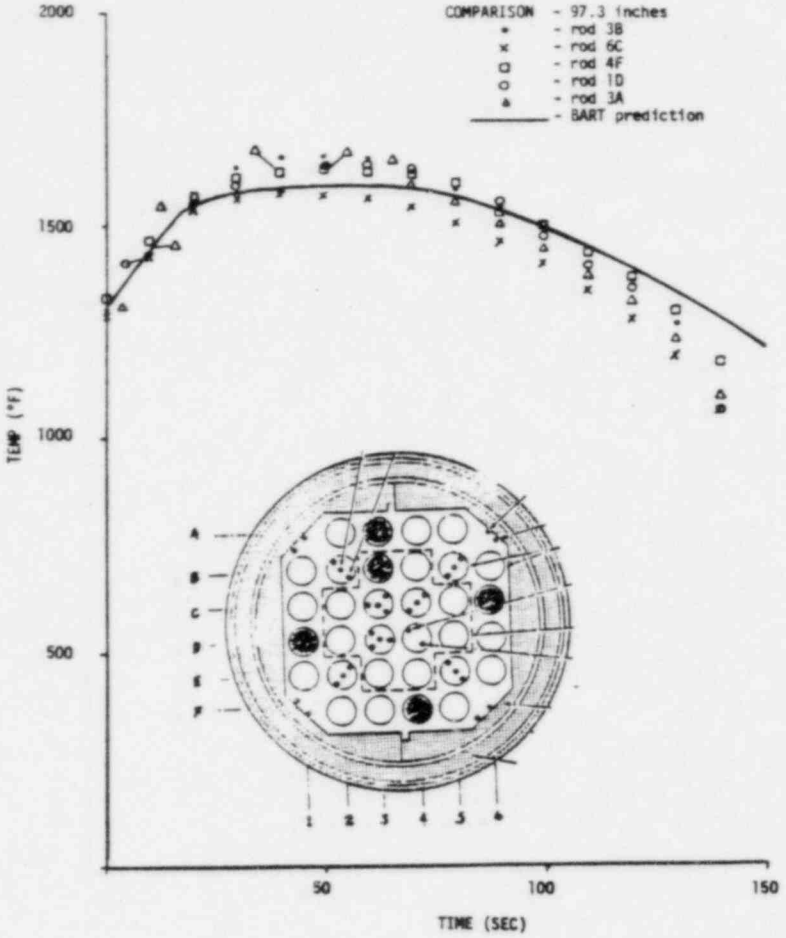

FIGURE 7. BART CLAD TEMPERATURE PREDICTION FOR NRU TEST 110, 97.3 INCH ELEVATION

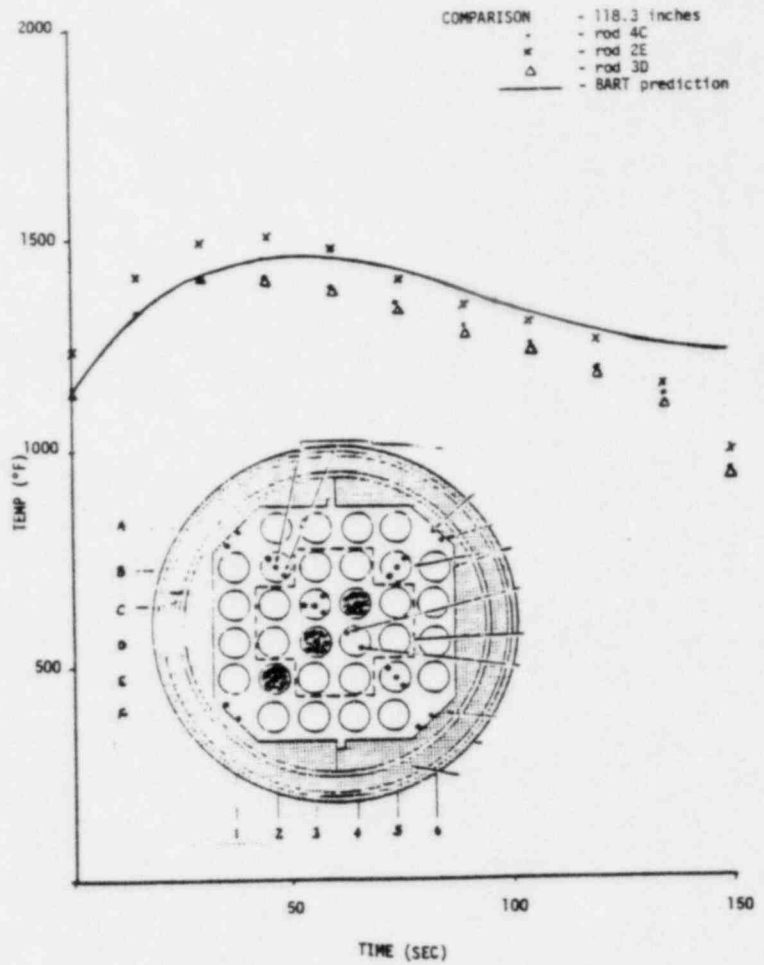

FIGURE 8. BART CLAD TEMPERATURE PREDICTION FOR NRU TEST 110, 118.3 INCH ELEVATION

were conducted to determine the proper reflood range. The as-measured axial power shape and flooding rate transient were used in the BART calculations. The resulting BART quench front is given in Figure 9, and the calculated fuel rod temperatures are shown in Figures 10 to 12. For this particular test, the low flooding rate stalled the quench front. The thermal hydraulic conditions in the heat bundle went from a forced reflooding condition to a boil-off condition in which no liquid entrainment occured. In this case, the rod height above the quench front would be cooled only by the steam flow generated below the quench front. For the constant power NRU tests, the steam flow was not sufficient to cool the upper elevations of the rods, resulting in higher rod temperatures at these locations.

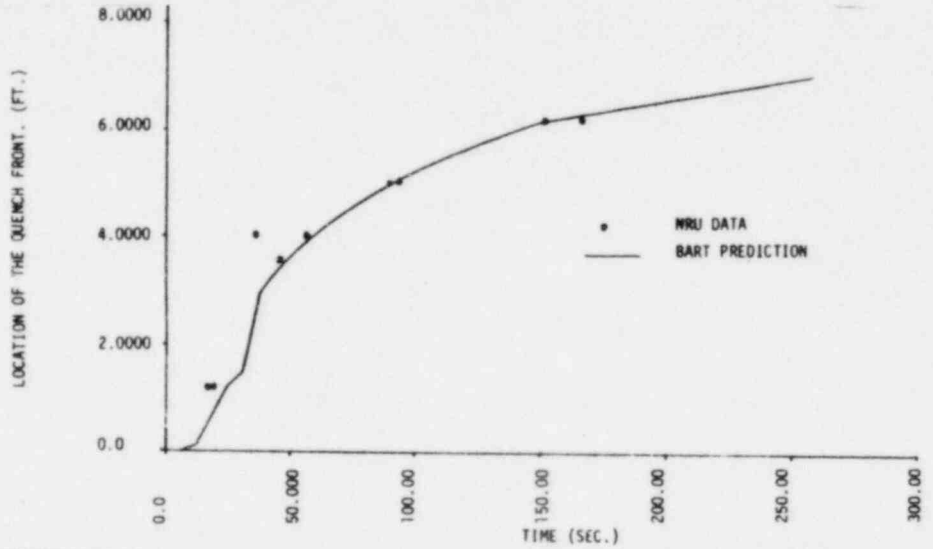

FIGURE 9. BART POST TEST QUENCH FRONT MOVEMENT PREDICTION FOR NRU TEST 2-212

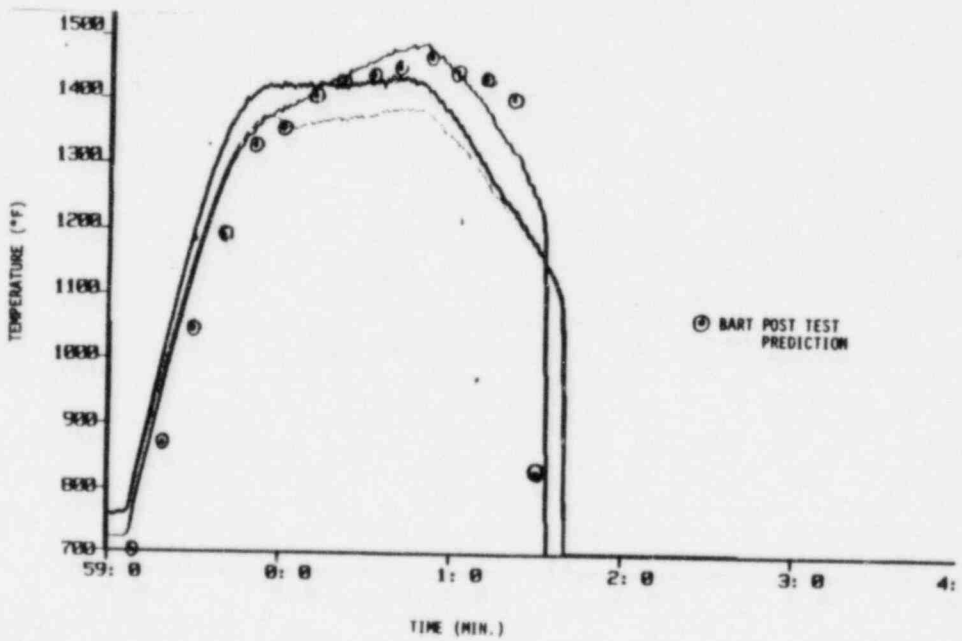

FIGURE 10. BART POST TEST CLAD TEMPERATURE PREDICTION FOR NRU TEST 2-212, 6 FOOT ELEVATION

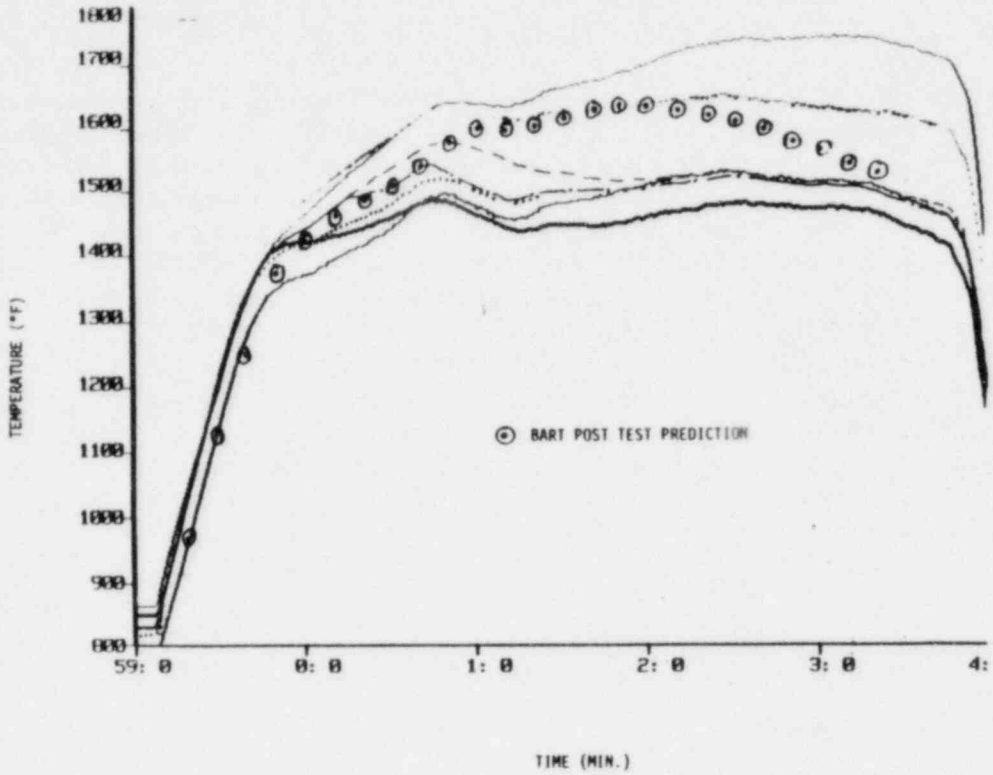

FIGURE 11. BART POST TEST TEMPERATURE PREDICTION FOR NRU TEST 2-212, 8 FOOT ELEVATION

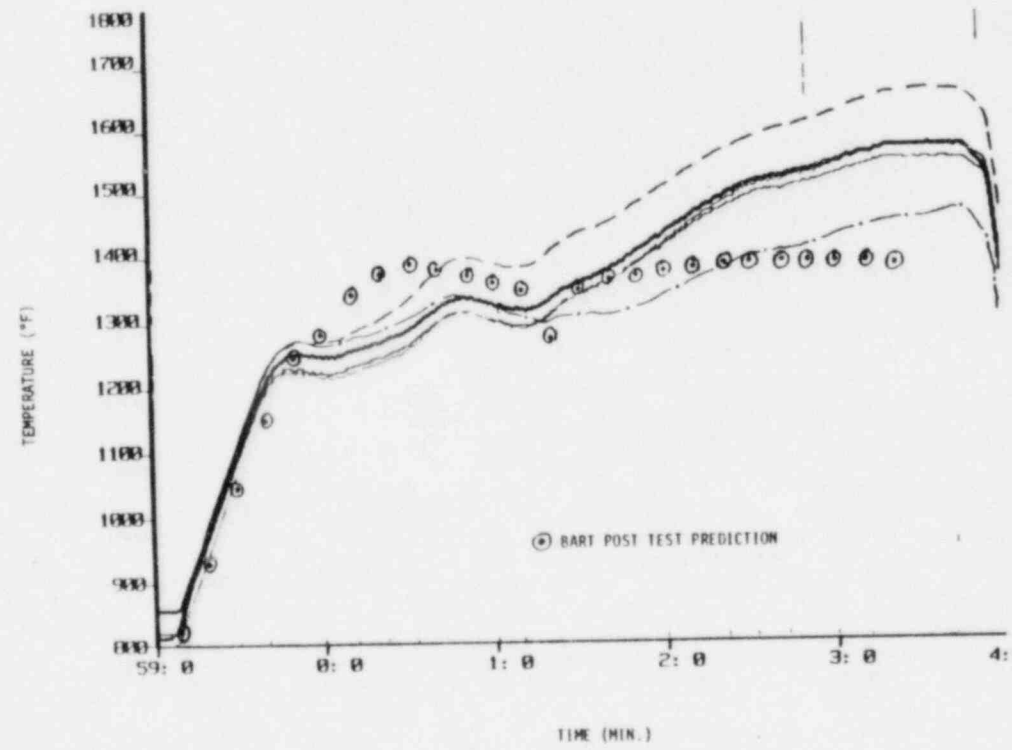

FIGURE 12. BART POST TEST TEMPERATURE PREDICTION FOR NRU TEST 2-212, 10 FOOT ELEVATION

The third type of NRU test used to validate a BART model was the materials test in which the inner 11 NRU fuel rods were pressurized and allowed to swell and burst during the heatup period of reflood. The BART swelling subroutine was used to model the pressurized rods in BART for this particular NRU materials test (MT-1). The first swelling calculation did not account for the mechanical constraint of the grids which would prevent significant strain at grid planes. Without the physical grid restraint the resulting strain distribution predicted by the swell program is shown as the dashed line in Figure 13. However, if the mechanical restraining of the grid is accounted for in the swelling model, a significant improvement in the calculated rod strain profile results, shown as the dotted line in Figure 13. It is apparent that physical processes such as grid support (and possible localized heat transfer enhancement due to grids) must be modelled to obtain accurate strain profiles.

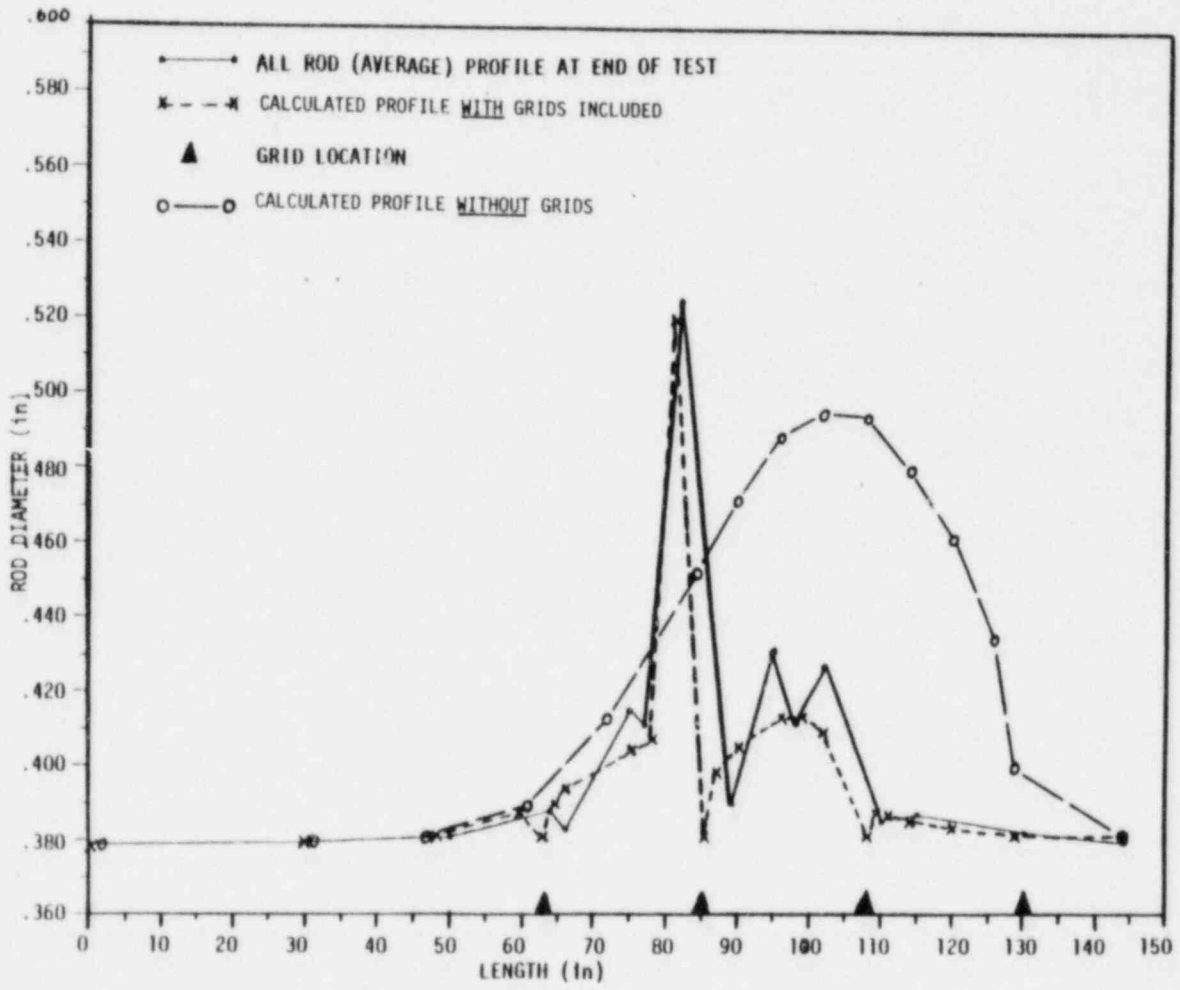

FIGURE 13. COMPARISON OF BART CLAD SWELLING MODEL PREDICTIONS (WITH AND WITHOUT GRIDS) AND NRU TEST MT-1

CONCLUSION

The analytical models developed for the BART reflood code have been verified against several independent sets of electrically heated reflood experiments. The nuclear powered NRU reflood experiments offered a unique opportunity to verify the BART quench model and clad swelling models. However, the NRU test facility is a small scale representation of a PWR fuel assembly and nontypicalities exist between the NRU testing and a PWR. With a mechanistic model such as BART, or other codes, the nontypicalities of a small scale experiment can be modelled and accounted for when making comparisons to code predictions. Models which are more empirical do not have this additional flexibility and hence become more difficult to validate.

This paper outlines the first element of model verification; the separate validation of the component models. The final verification will be accomplished by comparing the assembled comprehensive code to experiments which effectively exercise all subsidiary models in the code concurrently.

REFERENCES

1.) Collier, G., Gurcak, A. W., Kabadi, J., Lin, J. C., Porching, T. A., Spencer, A. C., and Young, M. Y., "BART-A1; A Computer Code for Best Estimate Reflood Analysis", WCAP-9561, Westinghouse Electric Corporation, January, 1980.

2.) Spencer, A. C. and Young, M. Y., "A Mechanistic Model for the Best Estimate Analysis of Reflood Transients (The BART Code)", 19th National Heat Transfer Conference (ASME), Orlando, Florida, July 1980.

3.) Mohr, C. L., Hesson, G. M., Russcher, G. E., Marshall, R. K., King, L. L., Wilding, N. J., Rausch, W. N., and W. D. Bennett, "Prototypic Thermal-Hydraulic Experiments in NRU to Simulate Loss-of-Coolant-Accidents" NUREG/CR-1882 (PNL-3681), January 1981.

4.) Russcher, G. E., Cannon, L. W., Goodman, R. L., Hesson, G. M., King, L. L., McDuffie, P. N., Marshall, R. K., Neally, C., Pelzer, J. P., and C. L. Mohr. "Experimental Operations Plan for a Loss of Coolant Accident Simulation in the National Research Universal Reactor", NUREG-CR-1735/PNL - 3551, April 1981.

5.) Russcher, G. E., Marshall, R. K., Hesson, G. M., Wilding, N. J., Rausch, W. N., King, L. L., Wilson, C. L., Parchen, L. J., Webb, B. J., Bennett, W. D., and C. L. Mohr, "LOCA Simulation in the NRU Reactor-Materials Test-1". NUREG/CR-2152 (PNL-3835), Vol. 1, August 1981.

6.) Rosal, E. R., Hochreiter, L. E., McGuire, M. F. and Krepinevich M. C., "FLECHT Low Flooding Rate Cosine Test Series Data Report", WCAP-8651, Westinghouse Electric Corporation, 1975.

7.) Lilly, G. P., Yeh, H. C., Dodge, C. E. and Wong, S., "PWR FLECHT Skewed Profile Low Flooding Rate Test Series Evaluation Report", WCAP-9183, Westinghouse Electric Corporation, 1977.

8.) Crapo, H. S. et. al., "Experiment Data Report for Semiscale Mod-1 Tests S-03-1 through S-03-4, ANCR-NUREG-1306 (1976).

9.) Sun, K., Gonzalez, J. M., and Tien, C. L., "Calculation of Combined Radiation and Convection Heat Transfer in Rod Bundles under Emergency Cooling Conditions", ASME-AICHE, 15th National H. T. Conference August, 1975.

10.) Bordelon, F. M., et al, "LOCTA-IV Program: Loss-of-Coolant Transient Analysis", WCAP-8301, Westinghouse Electric Corporation, June 1974.

11.) Hardy, D. G., "High Temperature Expansion and Rupture Behavior of Zircaloy Tubing", National Topical Meeting on Water Reactor Safety, Salt Lake City, Utah, March 1973.

12.) Roll, J. B., "Performance of Zircaloy Clad Fuel Rods During a Simulated Loss-of Coolant Accident - Single Rod Tests", WCAP-7805, Westinghouse Electric Corporation December, 1971.

13.) Yao, S. C., Hochreiter, L. E. and Dodge, C. E., "A Simple Method for Calculating Radiative Heat Transfer in Rod Bundles With Droplet and Vapor as Absorbing Media", ASME J. of Heat Transfer Vol. 101, page 736, November 1979.

14.) Andersen, J. G. M., Anderson, P. S., Olsen, A. and J. Miettinen, "NORCOOL, A Model for Analysis of a BWR Under LOCA Conditions", Research Establish Riso, NORHAV - D - 29, October 1976.

PROPAGATION OF REWETTING FRONT DURING BOTTOM REFLOOD -- AN ANALYSIS

Kevin D. Kimball
EDS Nuclear, Inc.
Norcross, GA 30092

and

Ramandra P. Roy
Department of Mechanical & Energy Systems Engineering
Arizona State University
Tempe, AZ 85287

ABSTRACT

A transient, two-dimensional model of the bottom reflood rewetting problem in an annular geometry is presented along with its analytical solution. Multi-region heat transfer is considered, and no a priori assumption (constant or not) is made in regard to the rewetting velocity. A finite length cylindrical geometry is treated. A mode of variation of the rewetting temperature with coolant inlet velocity is proposed. The method of finite integral transform is used in the solution. Predictions of rewetting velocity are compared with a few experimental data for Zircalloy-2 available in literature.

INTRODUCTION

Understanding of the physical mechanisms instrumental in the rewetting of hot, dry surfaces (defined as, when the liquid coolant reestablishes contact with the surface locally) via bottom reflood and their correct mathematical representation have been the subject of several studies, both experimental and theoretical, in recent years. The subject is of considerable importance in our ability to correctly predict the temperature behavior of lightwater nuclear reactor fuel rods during the core reflood phase following a loss-of-coolant accident.

The fuel rod clad rewetting problem is basically a transient, two-dimensional (axial, radial) heat conduction problem coupled to the thermal-hydraulics of the coolant. Theoretical studies reported in literature include the early one-dimensional simplified model solutions of Semeria and Martinet [1] and Yamanouchi [2], followed by several improved one-dimensional model solutions, eg. of Sun, et al. [3] and Chambré and Elias [4], and a few two-dimensional model solutions, eg., of Duffey and Porthouse [5], Yeh [6], and Bonakdar and McAssey [7]. Detailed numerical studies incorporating models of both clad heat conduction and coolant thermal-hydraulics include works by Arrieta and Yadigaroglu [8], and Spencer and Young [9]. In the aforementioned analytical solutions ([1-6]), the simplifying assumptions of constant rewetting front velocity and invariance of the rod (clad) temperature distribution in a coordinate system moving with the rewetting front have typically been made.

Treatment of the rewetting temperature has varied from a priori specification of a fixed value (eg. the critical heat flux temperature) to equating it to the calculated temperature value at the 'sputtering region' front. With the exception of a few numerical studies (eg. [8]), the treatment of precursory cooling downstream of the rewetting front has not been adequate.

In this paper, we present a transient, two-dimensional multi-heat transfer region model of the clad bottom-reflood rewetting problem and its analytical solution with the following improved features:

(i) no a priori assumption is made in regard to the rewetting velocity;

(ii) a finite length cylindrical clad geometry is considered, and the transient temperature distribution throughout the clad calculated in a fixed (laboratory) frame of reference;

(iii) a mode of variation of the rewetting temperature with the coolant inlet velocity magnitude is proposed;

(iv) the relative importance (depending on the coolant inlet velocity) of the inverted annular film boiling (IAFB) region in the precursory cooling of the clad is considered;

(v) the method of finite integral transform (cosine transform in the axial direction, Hankel transform in the radial direction) is used in the solution.

Four heat transfer (clad to coolant) regions based on a generalized boiling curve are considered:

I. forced convective heat transfer to single phase liquid;

II. nucleate boiling (for simplification, the transition boiling region has been included in this region[§]);

III. inverted annular film boiling; and

IV. forced convective heat transfer to steam with entrained droplets.

Other than establishment, on the basis of inlet water mass flux and local subcooling, of these heat transfer regions and the corresponding heat transfer coefficients, detailed fluid-mechanic calculations have not been performed in this work. Bulk fluid (liquid and two-phase mixture) temperature variation along the flow channel have been calculated from heat balance considerations.

[§]This simplification can be removed at the expense of increased computation.

MODEL AND ANALYSIS

Figure 1 shows the 'unit cell' configuration analyzed. The finite length cylindrical shell represents the clad, with the fuel replaced in the present work by an imposed heat flux (of any specified axial shape and time dependence) at the clad inner surface. Volumetric heat generation (of any specified axial- and time-dependence) in the clad is permitted. The axial ends of the clad are

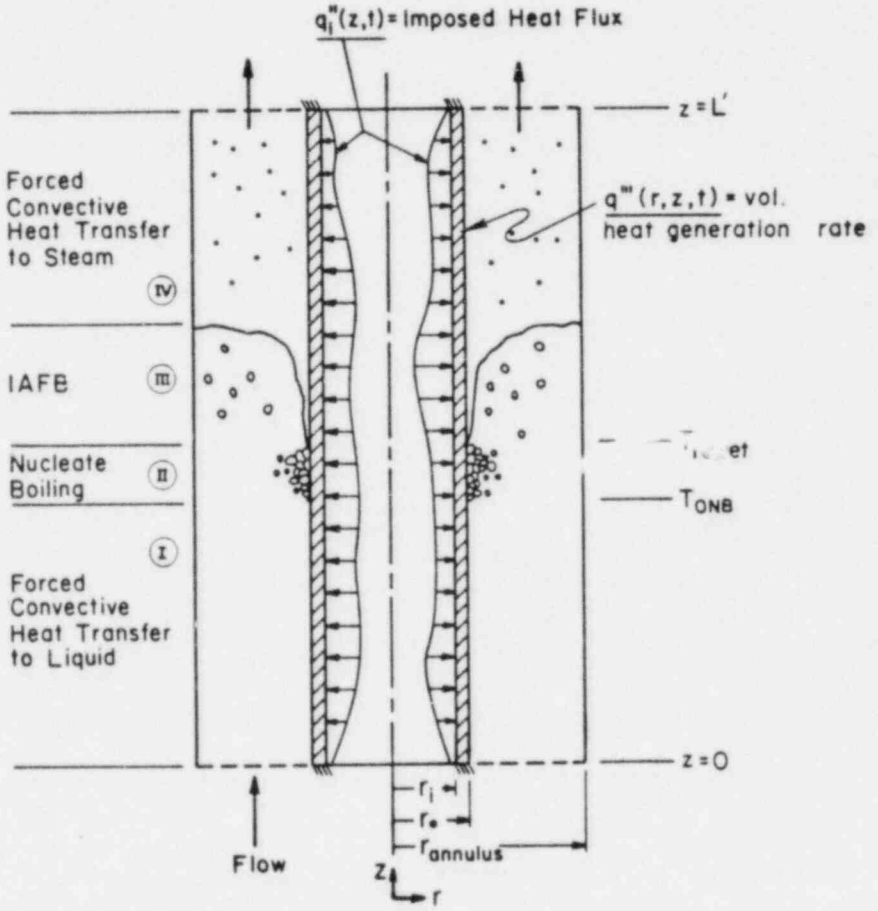

Figure 1. The 'unit cell' configuration analyzed

considered insulated. The coolant flows upward in the surrounding annulus. Azimuthal symmetry and constant clad material properties are assumed. In addition to the clad inner surface heat flux and the clad volumetric heat generation rate, the following inputs are provided:

coolant inlet mass flow rate and temperature,
system pressure (assumed uniform), and
initial clad temperature distribution.

The governing heat conduction equation for the clad, in a non-dimensional form, is:

$$\frac{\partial\theta}{\partial t}(R,Z,t) = \frac{D_h^2}{(r_o-r_i)^2}\left[\frac{1}{R}\frac{\partial}{\partial R}\left(R\frac{\partial\theta}{\partial R}\right)\right] + \frac{\partial^2\theta}{\partial Z^2} + \frac{D_h^2}{kT_{sat}}q''' \quad (R,Z,t) \qquad (1)$$

in the region $\left\{\begin{array}{l} t \geq 0 \ , \\ R_i \leq R \leq R_o \ , \\ 0 \leq Z \leq L \end{array}\right\}$

The boundary conditions are,

Axial

$$\text{at } Z = 0,\ R_i \leq R \leq R_o \ ; \quad \frac{\partial\theta}{\partial Z} = 0 \qquad (2)$$

$$\text{at } Z = L,\ R_i \leq R \leq R_o \ ; \quad \frac{\partial\theta}{\partial Z} = 0 \qquad (3)$$

Radial

$$\text{at } R = R_i,\ 0 \leq Z \leq L \ ; \quad \frac{\partial\theta}{\partial R} = -\frac{q_i''(z,t)[r_o-r_i]}{kT_{sat}} \qquad (4)$$

$$\text{at } R = R_o,\ Z_{j-1}(t) \leq Z \leq Z_j(t) \ ; \quad \frac{\partial\theta}{\partial R} + Bi_j\theta = 0 \qquad (5a,b,c,d)$$

where j = I, II, III, IV (Fig. 1).

(also, for region I, $Z_{I-1} = 0$;

for region IV, $Z_{IV} = L$)

The initial condition is:

$$\theta(R,Z,0) = \theta_o(R,Z) \qquad (6)$$

First, a finite Fourier cosine transform with respect to Z is applied to Eq. (1). This is to be performed heat transfer region by heat transfer region. Let us consider the heat transfer region j bounded axially at a time instant t_m by $Z_{j-1}(t_m)$ and $Z_j(t_m)$.† The transformed non-dimensional temperature in this region is defined as:

†We note that this is a quasi-static analysis in the sense that the physical situation is frozen at $t = t_m$ while we calculate for the condition at a later time ($t = t_{m+1}$).

$$\bar{\theta}_j(R,n,t_m) = \int_{Z_{j-1}(t_m)}^{Z_j(t_m)} \theta(R,Z,t_m) \cos n\pi \left[\frac{Z - Z_{j-1}(t_m)}{Z_j(t_m) - Z_{j-1}(t_m)} \right] dZ \qquad (7)$$

The inversion theorem is:

$$\theta_j(R,Z,t_m) = \frac{\bar{\theta}_j(R,n=0,t_m)}{[Z_j(t_m) - Z_{j-1}(t_m)]}$$

$$+ \frac{2}{[Z_j(t_m) - Z_{j-1}(t_m)]} \sum_{n=1}^{\infty} \bar{\theta}_j(R,n,t_m) \cos n\pi \left[\frac{Z - Z_{j-1}(t_m)}{Z_j(t_m) - Z_{j-1}(t_m)} \right] \qquad (8)$$

Let the temperature values and slopes at the region j axial boundaries be:

$$\theta_j(R,Z_{j-1}(t_m),t_m) = c_{1j}(R) \qquad (9a)$$

$$\left.\frac{\partial \theta_j}{\partial Z}\right|_{Z_{j-1}(t_m)} = c_{2j}(R) \qquad (9b)$$

and

$$\theta_j(R,Z_j(t_m),t_m) = d_{1j}(R) \qquad (10a)$$

$$\left.\frac{\partial \theta_j}{\partial Z}\right|_{Z_j(t_m)} = d_{2j}(R) \qquad (10b)$$

The finite Fourier cosine transformed form of Eq. (1), at time t_m and in heat transfer region j, with boundary values substituted from Eqs. (9) and (10), is:

$$\frac{\partial \bar{\theta}_j}{\partial t}(R,n,t) = \frac{D_h^2}{(r_o - r_i)^2} \left[\frac{1}{R} \frac{\partial}{\partial R} \left(R \frac{\partial \bar{\theta}_j}{\partial R} \right) \right] + (-1)^n d_{2j}(R) - c_{2j}(R)$$

$$- \left[\frac{n\pi}{Z_j(t_m) - Z_{j-1}(t_m)} \right]^2 \bar{\theta}_j + \overline{q'''}(R,n,t) \qquad (11)$$

Next, a finite Hankel transform [10] with respect to the radial coordinate R is performed on Eq. (11). We define the double-transformed non-dimensional temperature in region j at time t_m as:

$$\bar{\bar{\theta}}_j(\lambda_{j,\ell},n,t_m) = \int_{R_i}^{R_o} \bar{\theta}_j(R,n,t_m)\, B_o(\lambda_{j,\ell}R)R\, dR \tag{12}$$

where

$$B_o(\lambda_{j,\ell}R) = J_1(\lambda_{j,\ell}R_i)Y_o(\lambda_{j,\ell}R) - Y_1(\lambda_{j,\ell}R_i)J_0(\lambda_{j,\ell}R) \tag{12a}$$

$\lambda_{j,\ell}$ being the radial eigenvalues.

The inversion theorem is [11]:

$$\bar{\theta}_j(R,n,t_m) = \sum_{\ell=1}^{\infty} \frac{\bar{\bar{\theta}}_j(\lambda_{j,\ell},n,t_m)}{N_{j,\ell}} B_o(\lambda_{j,\ell}R) \tag{13}$$

where $N_{j,\ell}$, the normalization factor =

$$\frac{2}{\pi^2}\left\{\frac{[-J_1(\lambda_{j,\ell}R_i)]^2[Bi_j + \lambda_{j,\ell}]^2 - [-\lambda_{j,\ell}J_1(\lambda_{j,\ell}R_o) + Bi_jJ_0(\lambda_{j,\ell}R_o)]^2}{\lambda_{j,\ell}^2[-\lambda_{j,\ell}J_1(\lambda_{j,\ell}R_o) + Bi_jJ_0(\lambda_{j,\ell}R_o)]^2}\right\} \tag{13a}$$

The double-transformed form of Eq. (1), at time t_m and in heat transfer region j, is:

$$\frac{d\bar{\bar{\theta}}_j}{dt}(\lambda_{j,\ell},n,t) = \left[\frac{D_h^2}{(r_o-r_i)^2}\lambda_{j,\ell}^2 + \left(\frac{n\pi}{Z_j(t_m) - Z_{j-1}(t_m)}\right)^2\right]\bar{\bar{\theta}}_j + \frac{2D_h^2}{\pi(r_o-r_i)^2\lambda_{j,\ell}}\bar{Q}_j + [(-1)^n\,\tilde{d}_{2j,\ell} - \tilde{c}_{2j,\ell}] - \frac{D_h^2}{kT_{sat}}\,\bar{\bar{q}}'''\,(\lambda_{j,\ell},n,t) \tag{14}$$

where

$$\bar{Q}_j = \frac{\bar{q}_j''(r_o-r_i)}{kT_{sat}} \tag{14a}$$

Here, $\tilde{c}_{2j,\ell}$ and $\tilde{d}_{2j,\ell}$ are the finite Hankel transforms of c_{2j} and d_{2j}, respectively.

Equation (14), a first-order inhomogeneous ordinary differential equation in time, can be easily solved for $\tilde{\bar{\theta}}_j(\lambda_{j,\ell},n,t_{m+1})$:

$$\tilde{\bar{\theta}}_j(\lambda_{j,\ell},n,t_{m+1}) = \frac{\left[\frac{2D_h^2}{\pi(r_o-r_i)^2}\cdot\frac{\bar{Q}_j}{\lambda_{j,\ell}} + (-1)^n\,\tilde{d}_{2j,\ell} - \tilde{c}_{2j,\ell} + \frac{D_h^2}{kT_{sat}}\,\tilde{\bar{q}}'''\right]}{\left[\frac{D_h^2\lambda_{j,\ell}^2}{(r_o-r_i)^2} + \left(\frac{n\pi}{Z_j(t_m) - Z_{j-1}(t_m)}\right)^2\right]}$$

$$\cdot\left[1 - \exp\left\{-\left[\left(\frac{D_h\lambda_{j,\ell}}{r_o-r_i}\right)^2 + \left(\frac{n\pi}{Z_j(t_m) - Z_{j-1}(t_m)}\right)^2\right]\cdot(t_{m+1} - t_m)\right\}\right]$$

$$+\,\tilde{\bar{\theta}}_j(\lambda_{j,\ell},n,t_m)\exp\left\{-\left[\left(\frac{D_h\lambda_{j,\ell}}{r_o-r_i}\right)^2 + \left(\frac{\pi}{Z_j(t_m) - Z_{j-1}(t_m)}\right)^2\right]\cdot(t_{m+1} - t_m)\right\} \tag{15}$$

The actual temperature distribution $\theta_j(R,Z,t_{m+1})$ can now be obtained by double-inverse transform using Eqs. (8) and (13). Information on convergence of the series is given in the section on computational results.

Note that the clad temperature field is solved separately for each heat transfer region. Thus, since four heat transfer regions are being accounted for, four regional temperature fields will be calculated. We need to match temperatures and temperature gradients (heat fluxes) at the interfaces between the successive heat transfer regions at time $t = t_{m+1}$ so that a global temperature distribution can be constructed from the piecewise continuous (axially) distribution obtained originally. Now, at each axial location (eg. at $Z = Z_I$) where finite discontinuity in the temperature distribution exists (the discontinuity can be different at different radial locations), the value can be taken to be equal to the average of the upstream limit and the downstream limit values. For example, at $Z = Z_I$, the value would be

$$\frac{1}{2}\left[\theta(R,Z_I^-,t_{m+1}) + \theta(R,Z_I^+,t_{m+1})\right] \tag{16}$$

We note again that the temperature gradients must also be matched.

With this in mind, a straight line interpolation between temperature values at two points, one slightly upstream and one slightly downstream of the interface, was performed at each clad radial location of interest for each regional interface with the exception of the IAFB-Nucleate Boiling one.† At the

†Since rewetting occurs here, a sharp temperature variation can be expected.

IAFB-Nucleate Boiling interface, a more accurate interpolation using a polynomial fit [12] spanning five local points (two upstream and two downstream points, plus an interface value based on Eq. (16)) is used.

VARIOUS CORRELATIONS AND INPUT PARAMETERS

Correlations for Temperatures at Heat Transfer Regional Interfaces

Referring to Fig. 1, two transitional temperatures, viz., the clad surface temperature for onset of nucleate boiling (T_{ONB}) and the clad surface temperature for rewetting (T_{rewet}) are required for our model. A correlation proposed by Sato and Matsumura [13] has been used for T_{ONB}.

The dependence of T_{rewet} on the coolant inlet mass flow rate is strong. A detailed review of all reported experimental studies [14] indicate that T_{rewet} approaches the critical heat flux temperature (T_{CHF}) at very low inlet mass fluxes (velocity less than 15 cm/s), whereas it approaches the minimum film boiling temperature (T_{MFB}) at high inlet mass fluxes (velocity higher than 35 cm/s). We propose the following expression for T_{rewet} as a function of the coolant inlet velocity, u_{in}:

$$T_{rewet} = \left(\frac{T_{CHF} + T_{MFB}}{2}\right) + \left(\frac{T_{MFB} - T_{CHF}}{2}\right) \cdot \tanh\,[f(u_{in})] \qquad (17)$$

where $f(u_{in})$ is an appropriate function of coolant inlet velocity. Equation (17) must permit asymptotic approach to T_{CHF} at very low u_{in} and to T_{MFB} at high u_{in}. Designating the value of u_{in} = 45.72 cm/s (18 inches/s) to be a high coolant inlet velocity, $f(u_{in})$ can be found to be of the form

$$\left(\frac{4\ u_{in}}{22.86} - 4.00\right), \quad \text{where } u_{in} \text{ is in cm/s.} \qquad (17a)$$

Although this approach is somewhat arbitrary, it does yield a realistic dependence of T_{rewet} on the inlet coolant velocity (Fig. 2). We now need to provide proper correlations for T_{CHF} and T_{MFB}. The T_{CHF} correlation adopted is [14]:

$$T_{CHF} = -\,1.1446\ p^2 + 22.751\ p + 112.1 + 3.9 \qquad (18)$$

where p is pressure in bar, and T_{CHF} is in °C. The data used in developing this correlation pertains to stainless steel clad material and a pressure range of 1-8 bars.

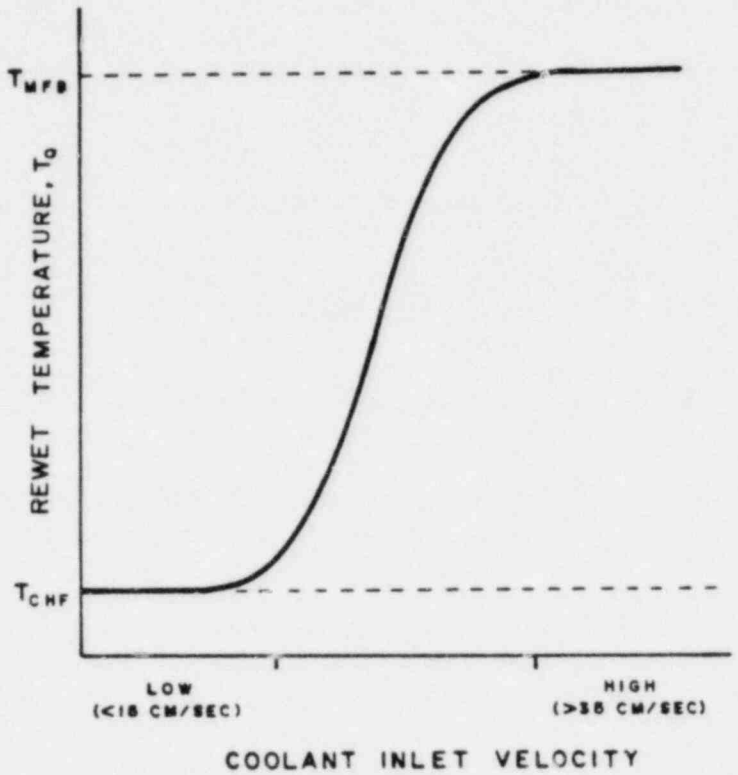

Figure 2. Proposed variation of rewetting temperature with coolant inlet velocity

The T_{MFB} correlation adopted is [14]:

$$T_{MFB} = T_{sat} + (10 + \ell n\ q')(8.49 + 2.8\ \ell n\ p)u^{0.029} \cdot (0.00309\ T_{peak} + 0.452) \qquad (19)$$

where q' = linear heat generation rate (kW/m),

p = pressure (bar),

u = coolant velocity (m/s),

and T_{peak} = peak cladding temperature (°C).

This correlation was obtained [14] by a least squares fit of data from FLECHT tests [15,16]. The applicability of this correlation extends over the following range of conditions:

pressure: 1.38 - 4.14 bars

peak temperature: 350 - 1200°C

water velocity: 0.007 - 0.033 m/s

linear heat generation rate: 0.5 - 40 kW/m

Correlations for Heat Transfer Coefficients

For the single phase liquid region, the Dittus-Boelter correlation and the Collier correlation [17] were used for Reynolds no. > 2000, and ≤ 2000, respectively.

For the nucleate boiling region, a modified version of the Chen correlation as suggested by Collier [17] was used for both subcooled and saturated nucleate boiling regions.

For the IAFB region, rather than using the Bromley correlation for film boiling (which is known to underpredict the heat transfer coefficient considerably in some situations, eg. at high subcooling), a numerically averaged value from the experimental data reported by Chan and Yadigaroglu [18] was used. For example, at u_{in} = 16.5 cm/s and ΔT_{sub} = 26°C, $\bar{h}_{IAFB}$ was calculated to be approximately 261 $W/m^2°K$.

For forced convection to steam with entrained liquid droplets, a correlation proposed by Heineman [19,20] was used.

Precursory Cooling Region

The influence of the precursory cooling region on rewetting is an important consideration. In our model, this region may be dominated by the IAFB region. The length of the IAFB region determines the extent of this dominance. Now, the IAFB region length is essentially determined by the height of the liquid (or, liquid plus entrained vapor) column associated with this region (Fig. 1). A simple linear proportionality relation between this column height and the coolant inlet velocity has been adopted in the present work[§], with an upper bound of 1 meter on the column length (Fig. 3).[†]

The remainder of the precursory cooling region is comprised of steam flow with entrained water droplets (Fig. 1).

[§]This can very well be a nonlinear relation (eg. a quadratic, if based on velocity head considerations). Experimental studies are needed here.

[†]The upper bound of 1 meter is based on visual observations reported from U.C. Berkeley reflood experiments.

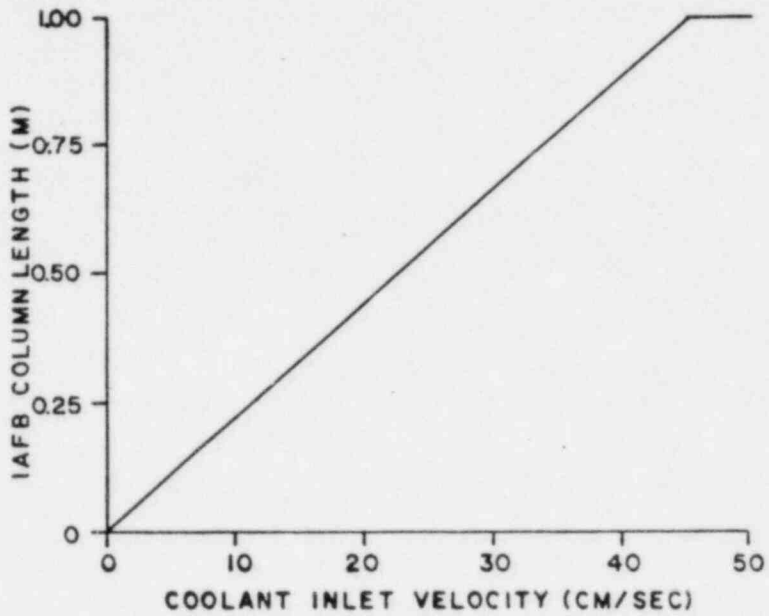

Figure 3. Proposed relation between IAFB column length and coolant inlet velocity

COMPUTATIONAL RESULTS

In order to evaluate the rewetting model and the analysis technique, an annular clad-flow channel configuration similar to that used in an experimental study by Piggot and Duffey [21] has been analyzed for various combinations of inlet coolant flow velocity and clad inner surface heat flux. Table 1 gives the pertinent channel dimensions and the clad physical properties.

Table 1

Physical properties of clad material, and unit cell dimensions

Clad material	Zircalloy-2
density	6500 kg/m^3
specific heat	350 J/kg°C
thermal conductivity	21 W/m°C
Inner radius of clad (r_i)	4.72 mm
Outer radius of clad (r_o)	5.35 mm
Clad length (L')	0.5 m
Outer radius of unit cell ($r_{annulus}$)	13.0 mm

It should be noted that our clad representation does not exactly match the test piece used by Piggot and Duffey [21], since a heating element embedded in a filler material was used as the heat source in the experiments whereas we specify an imposed heat flux at the clad inner surface.

The following describes the physical situation of our test problem briefly. The clad is at a specified initial temperature, with a specified heat flux imposed at the inner surface. The annular flow channel is filled with saturated steam at 1 atm. The initial clad temperature distribution is well above the rewetting temperature throughout. Subcooled water at a specified inlet mass flow rate is provided at the channel bottom. The water attempts to enter the channel in the IAFB mode. Two factors are important at this stage: the ascension rate of the IAFB column which controls the rate of coolant entry, and the appropriate maximum height of this column (Fig. 3). Recall that clad rewetting (quenching) occurs at the IAFB/Nucleate Boiling region interface. We impose a criterion now that the IAFB column is to reach its maximum height at the same time instant at which the lower end of the clad rewets.† This necessitates a trial-and-error solution for the ascension rate.

Once rewetting has occurred at the channel bottom, the nucleate boiling region has begun to be established. Eventually, this region will be bound by the T_{rewet} location at its upper end and the T_{ONB} location at its lower end.

Prior to presenting the computational results, a comment regarding the convergence of the series in Eqs. (8) and (13) is necessary. Generally, one term (involving the first eigenvalue/eigenfunction) was sufficient for Eq. (13), the inverse radial transform. For the inverse axial transform, Eq. (8), convergence was usually obtained with thirty three terms.

Figure 4 shows the calculated clad outer surface axial temperature profile at a time thirty seconds after the coolant first enters the channel for the following case:

Initial clad temperature = 700°C
Clad volumetric heat generation rate = 0
Heat flux at clad inner surface = 4 kW/m^2
Pressure = 1 atm
Coolant inlet velocity = 10.16 cm/s
Coolant inlet temperature = 15°C

The four heat transfer regions are also pointed out in this figure.

Figure 5 shows the clad outer surface axial temperature profile at various times for essentially the same situation as in the previous case (Fig. 4) except that the coolant inlet velocity has been increased to 17.78 cm/s. One can readily see that rapid cooling occurs upon the arrival of the rewetting front.

---

†Otherwise, there would be a pause in coolant entry, which probably is unrealistic.

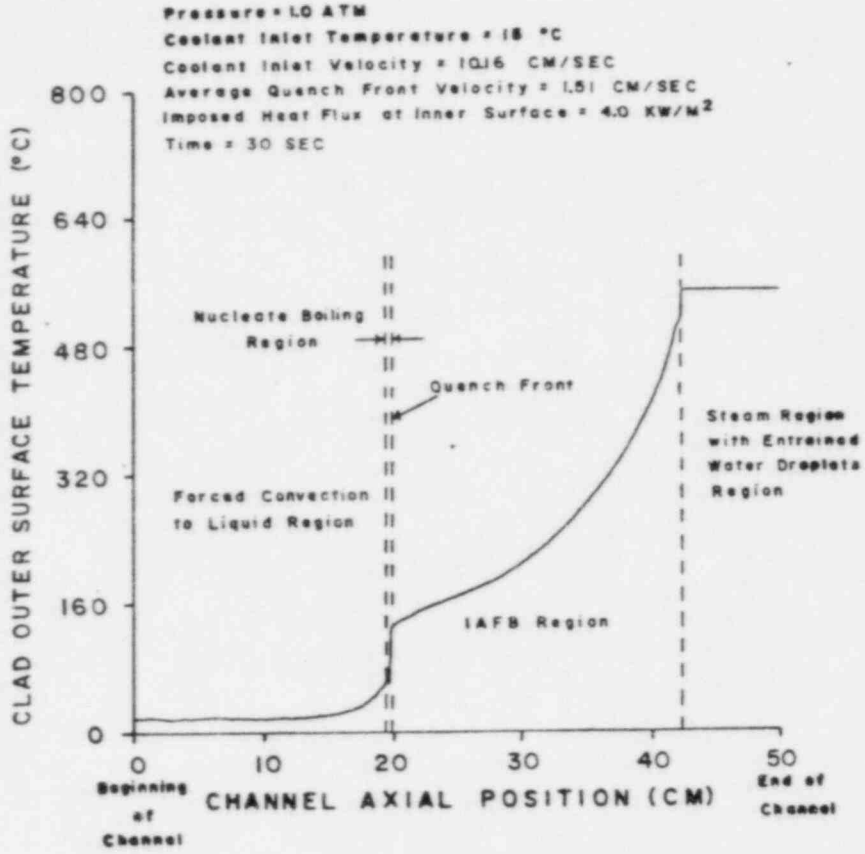

Figure 4. Clad outer surface axial temperature profile at t = 30 s

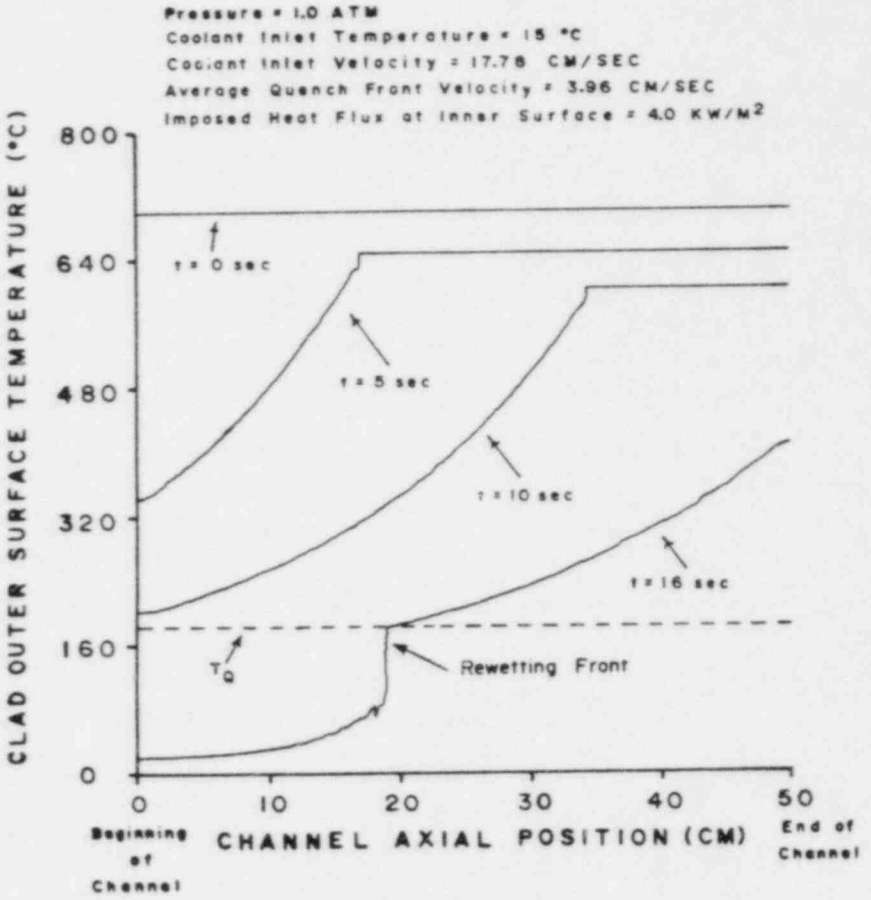

Figure 5. Clad outer surface axial temperature profiles at various times

Figure 6 shows a plot of the rewetting front velocity vs. channel axial position for the following two cases:

Initial clad temperature = 700°C
Clad volumetric heat generation rate = 0
Heat flux at clad inner surface = { (i) 4 kW/m^2 (same case as Fig. 4)
{ (ii) 0 kW/m^2
Pressure = 1 atm
Coolant inlet velocity = 10.16 cm/s
Coolant inlet temperature = 15°C

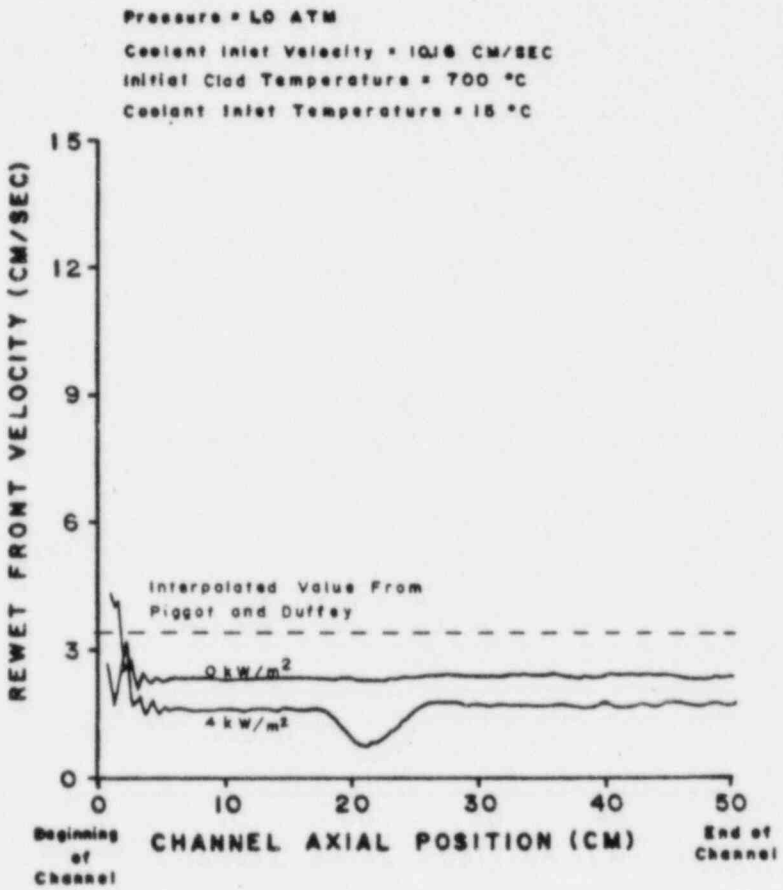

Figure 6. Rewetting front velocity along the channel

The rewetting front velocity is seen to be approximately constant, except for a dip at approximately 20 cm for 4 kW/m^2 case. This reflects the fact that the IAFB column ascension rate value used during the last iteration of the trial-and-error solution mentioned earlier in the text is still slightly high causing the coolant inflow to pause for a short time. A few additional iterations on the IAFB column ascension rate will remove this dip. As can be seen, no dip appears in the 0 kW/m^2 case. The dotted line shown in Fig. 6 is the value of the rewetting front velocity corresponding to this coolant inlet velocity extrapolated from the data of Piggot and Duffey [21]. Our predictions appear to be somewhat conservative. The trend of decreasing rewetting front velocity with increase in surface heat flux is correct.

Figure 7 shows the calculated rewetting front velocity for the following three cases:

Initial clad temperature = 700°C
Clad volumetric heat generation rate = 0
Heat flux at clad inner surface = { (i) 0 kW/m^2; (ii) 4 kW/m^2; (iii) 60 kW/m^2
Pressure = 1 atm
Coolant inlet velocity = 17.78 cm/s
Coolant inlet temperature = 15°C

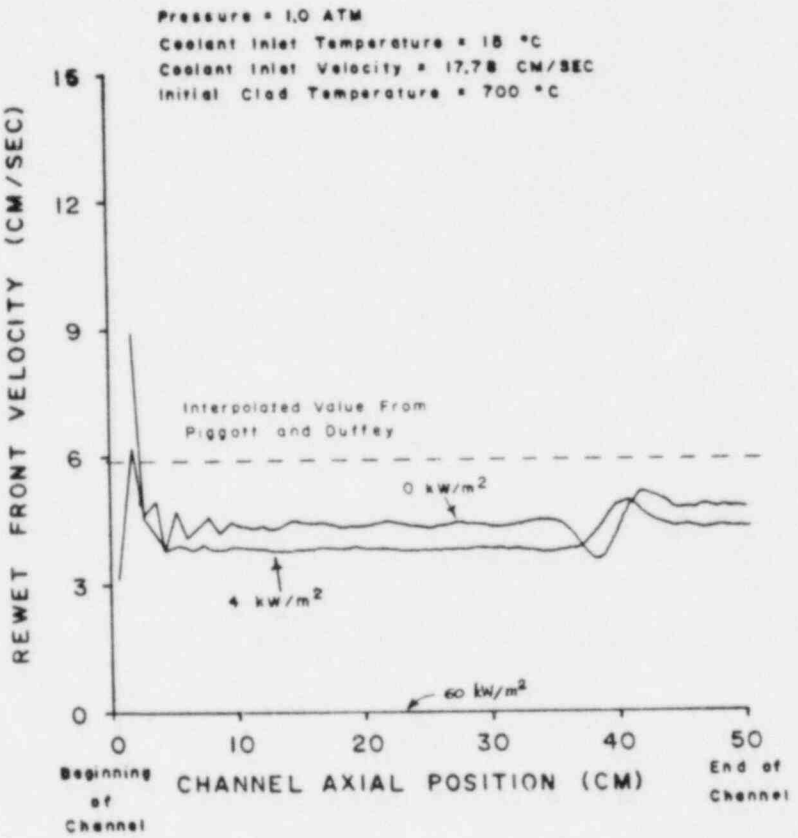

Figure 7. Rewetting front velocity along the channel

As expected, the rewetting front is unable to enter the channel for case (iii). Once again, the dotted line is the rewetting front velocity value for this coolant inlet velocity extrapolated from the data of Piggot and Duffey [21].

Figure 8 shows the calculated rewetting front velocity for three different coolant inlet velocities: (i) 10.16 cm/s, (ii) 17.78 cm/s and (iii) 30.48 cm/s with:

Initial clad temperature = 700°C
Clad volumetric heat generation rate = 0_2
Heat flux at clad inner surface = 4 kW/m^2
Pressure = 1 atm
Coolant inlet temperature = 15°C

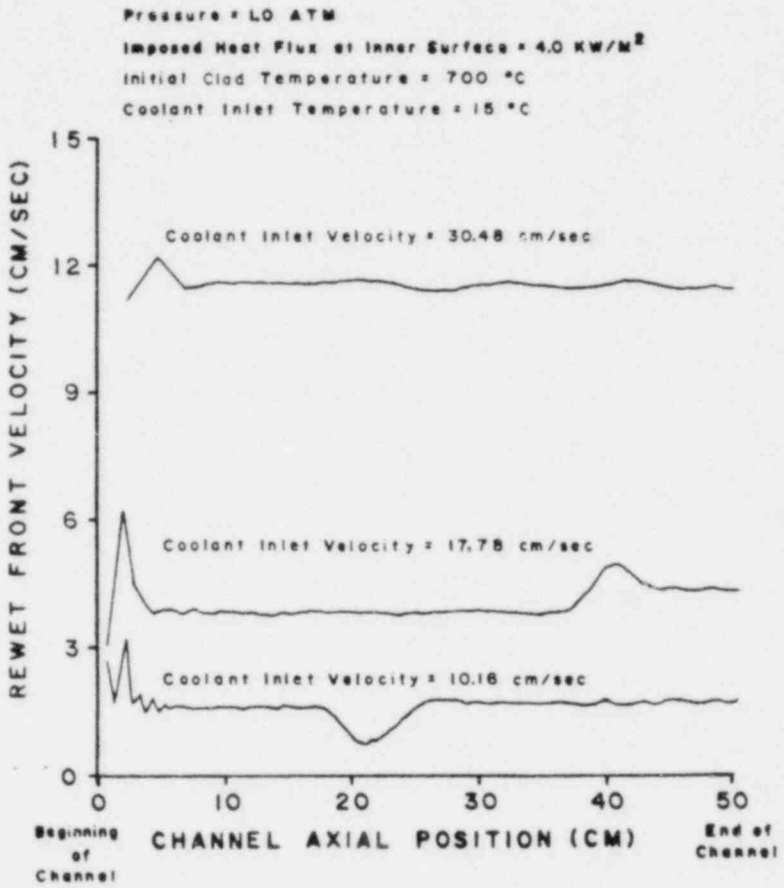

Figure 8. Rewetting front velocity at various coolant inlet velocities

The trend of increasing rewetting front velocity with increasing coolant inlet velocity is as expected.

DISCUSSION

In summary, an improved method for analysis of rewetting front propagation along a hot, dry cylindrical shell (clad) of finite length in an annular flow channel, with imposed inner surface heat flux and volumetric heat generation rate, has been developed and tested successfully. Computational results obtained support the contention of several experimenters that the rewetting front velocity is approximately constant along the channel. Results obtained demonstrate correct trends with variation of parameters such as surface heat flux and coolant inlet velocity.

To help in the development of physically realistic models such as the one proposed here, additional experimental studies of several phenomena are needed. Experiments aimed at providing better understanding of the inverted annular film boiling region over a wide range of coolant inlet mass flux are necessary. Experimental measurements of actual rewetting temperature as a function of coolant inlet mass flux should also be carried out.

NOMENCLATURE

Bi_j	Biot no. for region j, $\triangleq \frac{h_j(r_o-r_i)}{k}$
D_h	hydraulic diameter of flow channel, $\triangleq 2(r_{annulus} - r_o)$
h	heat transfer coefficient
k	thermal conductivity of clad material
L'	clad length
L	non-dimensional clad length, $\triangleq L'/D_h$
q''_i	heat flux at clad inner surface
q'''	volumetric heat generation rate
R	non-dimensional radial coordinate, $\triangleq \frac{r}{(r_o-r_i)}$
r_i, R_i	clad inner radius, non-dimensional inner radius
r_o, R_o	clad outer radius, non-dimensional outer radius
$r_{annulus}$	outer radius of unit cell
t'	time
t	non-dimensional time, $\triangleq \frac{t'\alpha}{D_h^2}$
T	temperature
Z	non-dimensional axial coordinate, $\triangleq \frac{z}{D_h}$
α	thermal diffusivity of clad material
θ	non-dimensional temperature, $\triangleq \frac{T(r,z,t') - T_f(z)}{T_{sat}}$

Subscripts

f	refers to coolant
j	refers to heat transfer region
ℓ	refers to ℓ^{th} radial eigenvalue

REFERENCES

1. R. Semeria and B. Martinet, "Calculation Spots on a Heating Wall; Temperature Distribution and Resorption," Proc. Inst. Mech. Eng., 180, 192 (1966).

2. A. Yamanouchi, "Effect of Core Spray Cooling in Transient State after Loss-of-Coolant Accident," J. of Nucl. Sci. and Tech., 5, 547 (1968).

3. K.H. Sun, G.E. Dix, and C.L. Tien, "Cooling of a Very Hot Vertical Surface by a Falling Liquid Film," J. of Heat Transfer, 96, 126 (1974).

4. P. Chambré and E. Elias, "Rewetting Model Using a Generalized Boiling Curve," EPRI Report No. NP-571 (1977).

5. R.B. Duffey and D.T.C. Porthouse, "The Physics of Rewetting in Water Reactor Emergency Core Cooling," Nucl. Eng. and Des., 25, 379 (1973).

6. H.C. Yeh, "An Analysis of Rewetting of a Nuclear Fuel Rod in Water Reactor Emergency Core Cooling," Nucl. Eng. and Des., 34, 317 (1975).

7. H. Bonakdar and E.V. McAssey, Jr., "A Method for Determining Rewetting Velocity under Generalized Boiling Conditions," ASME Paper No. 80-WA/HT-40 (1980).

8. L. Arrieta and G. Yadigaroglu, "Analytical Model for Bottom Reflooding Heat Transfer in Light Water Reactors (the UCFLOOD Code)," EPRI Report No. NP-756 (1978).

9. A.C. Spencer and M.Y. Young, "A Mechanistic Model for the Best Estimate Analysis of Reflood Transients (the BART Code)," 19th National Heat Transfer Conf., Orlando, Florida (1980).

10. I.H. Sneddon, "The Use of Integral Transforms," McGraw-Hill (1972).

11. G. Cinelli, "An Extension of the Finite Hankel Transform and Applications," Int. J. of Eng. Sci., Vol. 3, pp. 539-559 (1965).

12. H. Akima, "A Method of Interpolation and Smooth Curve Fitting Based on Local Procedures," J. Comput. Machinery, 17, 589 (1970).

13. T. Sato and H. Matsumura, "On the Conditions of Incipient Subcooled Boiling with Forced Convection," Bulletin JSME, Vol. 7-26, pp. 392-398 (1964).

14. A.D. Siegel, "Rewetting Temperature During Top and Bottom Reflood," M.S. Thesis, University of Illinois (1979).

15. E.R. Rosal, L.E. Hochreiter, M.F. McGuire, and M.C. Krepinevich, "FLECHT Low Flooding Rate Cosine Test Series Data Report," WCAP-8651, Westinghouse Electric Corporation, PA (1975).

16. E.R. Rosal, C.E. Conway, and M.C. Krepinevich, "FLECHT Low Flooding Rate Test Series Data Report," WCAP-9108, Westinghouse Electric Corporation, PA (1977).

17. J.G. Collier, "Convective Boiling and Condensation," McGraw-Hill Book Co., New York (1972).

18. K.C. Chan and G. Yadigaroglu, "Calculations of Film Boiling Heat Transfer Above the Quench Front During Reflooding," 19th National Heat Transfer Conf., Orlando, Florida (1980).

19. J.B. Heineman, "An Experimental Investigation of Heat Transfer to Superheated Steam in Round and Rectangular Channels," ANL-6213 (1960).

20. L.S. Tong, "Heat Transfer Mechanisms in Nucleate and Film Boiling," Nuclear Eng. and Des., Vol. 21, pp. 1-25 (1972).

21. B.D.G. Piggot and R.B. Duffey," The Quenching of Irradiated Fuel Pins," Nuclear Eng. and Des., Vol. 32, pp. 182-190 (1975).

TRAC ANALYSIS OF THE EFFECT OF INCREASED ECC SUBCOOLING ON THE REFLOOD TRANSIENT IN THE SLAB CORE TEST FACILITY*

Suzanne T. Smith
Energy Division
Los Alamos National Laboratory
Los Alamos, New Mexico

ABSTRACT

A blind posttest calculation of Slab Core Test Facility (SCTF) Run 510, the high-subcooling test, was completed with TRAC-PD2/MOD1 using initial conditions provided by the Japan Atomic Energy Research Institute (JAERI), but without knowledge of the actual test results. There is good comparison between the calculation and the data for rod temperatures, turnaround times, core differential pressures, and mass inventories, and reasonable comparison for absolute pressures, upper plenum pool formation, and fluid temperatures and mass accumulation in the steam-water separator. Comparison of this calculation with the calculation of the base case test (Run 507) shows that the qualitative behavior during reflood is calculated correctly for both cases. In addition, from this comparison the following conclusions can be drawn: for the high-subcooling case, the peak rod temperature was lower, calculated quench times were earlier, there was more entrainment and liquid carryover from the core to the upper plenum, and the liquid mass accumulation in both the core and the upper plenum was greater.

*Work performed under the auspices of the United States Nuclear Regulatory Commission.

I. INTRODUCTION

The TRAC[1] computer code was used to analyze two Slab Core Test Facility (SCTF) subcooling effects tests performed in 1981, at the Japan Atomic Energy Research Institute (JAERI) in Tokai, Japan. These calculations were performed knowing actual initial and boundary conditions but with no foreknowledge of the results.

In general, this calculation was in good agreement with the test data with regard to overall trends as well as to specific items of comparison. When this calculation is compared with the calculation of the base case test (Run 507), several conclusions can be drawn: in the high-subcooling test, the peak rod temperature was lower, the calculated quench times were earlier, there was more liquid entrainment and carryover from the core, and the liquid accumulation in both the core and the upper plenum was greater. The calculational model is reasonably accurate, and the TRAC code has produced good results.

A. The 2D/3D Program

The SCTF is part of the 2D/3D Program, a multinational program to assess best-estimate thermal-hydraulic computer codes such as TRAC, and to obtain data and develop improved correlations for the analysis of loss-of-coolant accidents (LOCAs) in pressurized water reactors (PWRs) during the end-of-blowdown, refill, and reflood phases by means of experiments in large test facilities in Japan and Germany. The United States, with funding from the U. S. Nuclear Regulatory Commission, is providing analytical support for these test facilities.

B. The Test Facility

The SCTF is composed of the pressure vessel, primary coolant system, and emergency core cooling (ECC) system. The pressure vessel contains the slab core, downcomer, upper and lower plena, core baffle region, and upper head. The facility is full-scale in the axial direction and half-scale in width. The slab core consists of eight bundles of electrically-heated rods in a 16 x 16 matrix. These eight bundles are arranged in a row numbered from the innermost bundle (1) representing the core center to the outermost bundle (8) on the downcomer side. There are blockage sleeves near the core midplane in Bundles 3 and 4 to simulate fuel rod ballooning; these represent 56 % coplanar blockages.

The primary coolant system comprises an intact loop, a broken loop with controllable valves simulating the breaks, a steam-water separator, and two containment tanks.

ECC water can be injected into the intact cold leg or directly into the plena. For the tests discussed in this report, the accumulator (ACC) and low-pressure coolant injection (LPCI) system are connected to the pressure vessel at the bottom of the lower plenum on the downcomer side. For these tests, the ACC and LPCI systems were operational, but the cold-leg and upper-plenum ECC systems were not; the ACC and LPCI systems provided forced injection directly into the lower plenum. Figure 1 shows a sketch of the SCTF.

C. Test Description

The forced-flooding tests discussed herein are Runs 507[2,3] and 510.[4] These were discussed in detail in two unpublished informal reports by the author: "TRAC Analysis of the SCTF Base Case Test, Run 507" (Los Alamos 2D/3D Program Technical Note LA-2D/3D-TN-81-23, October, 1981), and "TRAC Analysis of the SCTF High-Subcooling Test, Run 510" (Los Alamos 2D/3D Program Technical Note LA-2D/3D-TN-81-24, December 1981). Run 507, the base case test, was the first of the main test series for this new facility; Run 510 was considered the

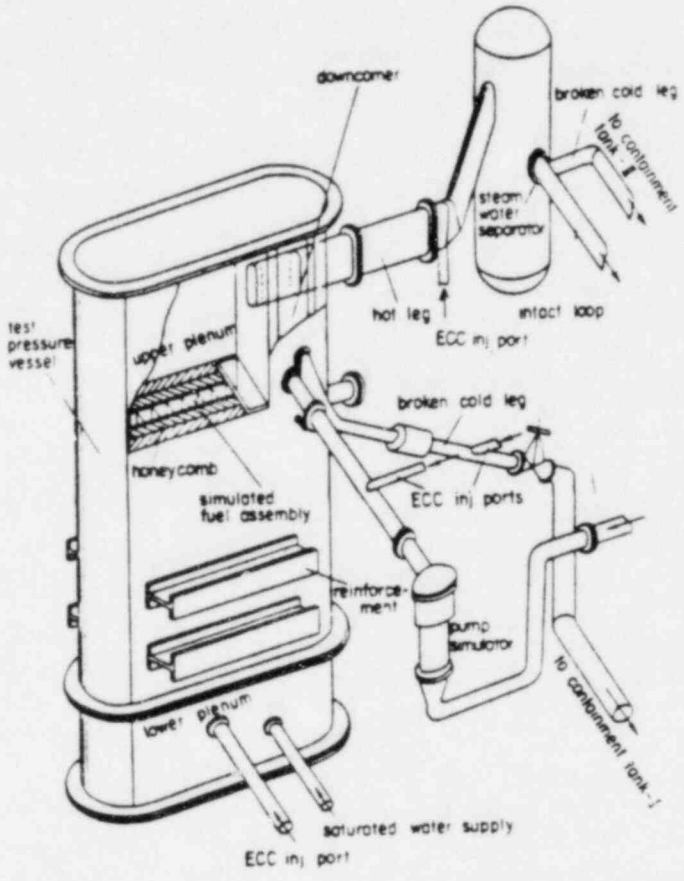

Fig. 1. Pictorial representation of the SCTF.

high-subcooling test. For all these tests, the downcomer was blocked at the bottom, allowing flow only in the core and bypass regions. The initial system pressures were 2.0 bars. The initial vapor and structure temperatures were the saturation temperature at the given system pressure. An initial temperature profile was specified for the rods. The initial power for these tests was about 7 MW. The axial distribution of the power was a chopped cosine, with the radial ratios of bundle power specified as:

Bundles 1 and 2	0.940
Bundles 3 and 4	1.0
Bundles 5 and 6	0.953
Bundles 7 and 8	0.863 .

Initially, the lower plenum was half full; this water was at saturation for Run 507, but was subcooled by about 25 K for Run 510.

Operation of these tests began by heating the rods electrically until a specified maximum cladding temperature (926 K) was reached (t = 0 s). After a 2 s delay, a 20 kg/s ACC flow was initiated and held constant until 17 s, when a 10 kg/s LPCI flow was actuated and held constant for the remainder of the test. For Run 507, the ACC water was subcooled by about 30 K and the LPCI water was about at saturation; for Run 510, the ACC water was subcooled by about 50 K and the LPCI water was subcooled by about 35 K. At 6 s, the power began to decrease according to the American Nuclear Society standard decay curve.

D. The Computational Model

The TRAC computational model developed at Los Alamos, reported in an informal report by the author, "Revision of the TRAC Calculational Model for the Slab Core Test Facility" (Los Alamos 2D/3D Program Technical Note LA-2D/3D-TN-81-17, October, 1981), used a two-dimensional VESSEL component for the pressure vessel (154 cells) and a three-dimensional VESSEL component for the steam-water separator (8 cells). One-dimensional components comprising 51 computational cells were used for the rest of the primary system. There was a total of 213 computational cells in the TRAC model. Figure 2 shows schematic diagrams of the pressure vessel and primary system.

E. TRAC Code Description

The analysis tool used for these calculations is the Transient Reactor Analysis Code (TRAC),[1] which has been developed at Los Alamos to provide an advanced best-estimate predictive capability for the analysis of postulated accidents in light water reactors. TRAC provides this analysis capability for light water reactors and for a wide variety of thermal-hydraulic experimental facilities. It features a three-dimensional treatment of the pressure vessel and associated internals; two-phase nonequilibrium hydrodynamics models; flow-regime-dependent constitutive equation treatment; reflood tracking

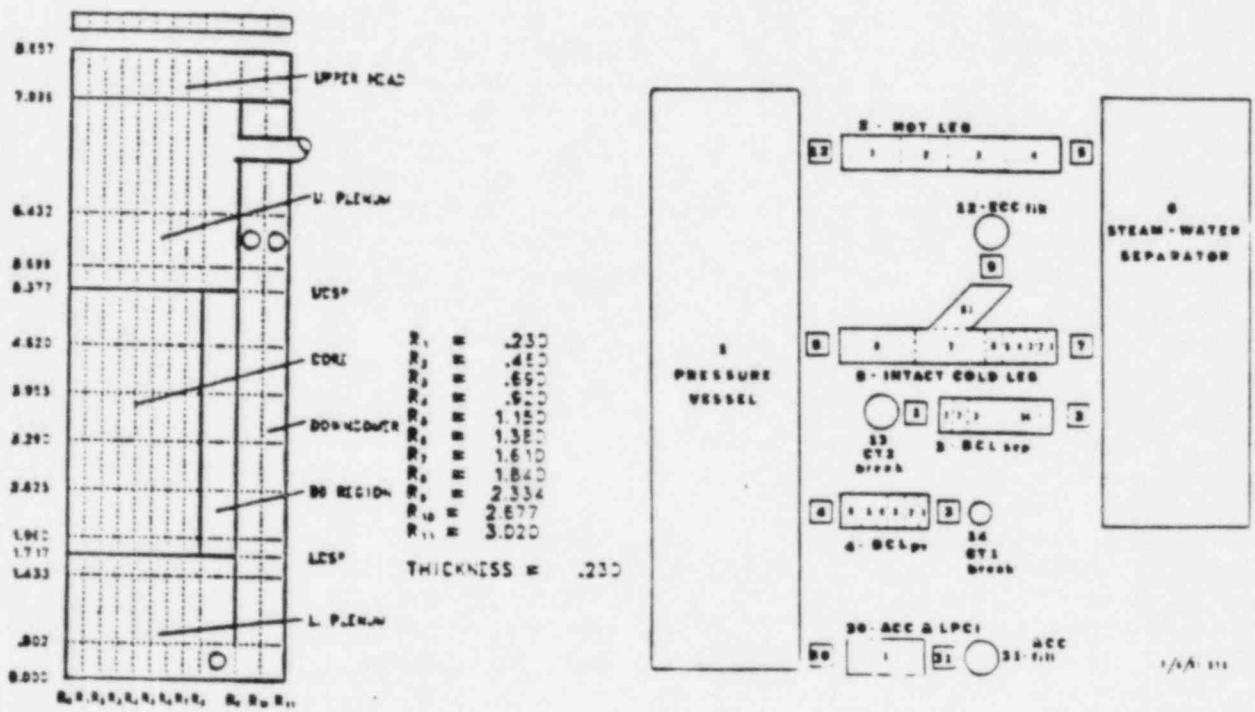

Fig. 1. Schematics of the SCTF pressure vessel and primary system.

capability for both bottom flood and falling film quench fronts; and consistent treatment of entire accident sequences, including the generation of consistent initial conditions.

TRAC-PD2/MOD1 (version 26.2 with updates) was the code version used for these calculations.

II. RESULTS OF THE CALCULATION

This section is subdivided into two parts. First, the calculated results and the experimental data for the base case (Run 507) and the high-subcooling case (Run 510) will be compared and discussed; and, second, a comparison of the calculations of the two tests will be discussed.

A. Comparison of the Test Data with the Calculated Results

The calculated core differential pressures agreed reasonably well with the data, as shown in Fig. 3. For these tests, the calculation underpredicted the differential pressure in the bottom half of the core, but agreed fairly well with the data for the top half of the core. The calculation and the data were in closer agreement for the differential pressures for the full height of the core, particularly later in the transient, although there was a tendency toward underprediction in the earlier portion of the transient. The data for the core lower half may be a bit too high; the differential pressure measurement indicates that the water level is nearly 2 m, and the distance between the two ΔP cells is about 1.97 m. This would indicate that there is no boiling taking place at all in the lower regions of the core after quench in the experiment, an unlikely event. Because of this, the calculated water level of about 1.8 m in the lower half of the core does not seem unreasonable at all.

Comparison of the experimental and calculated rod temperatures is given for several thermocouple elevations in Bundle 4 in Fig. 4. This rod is in the high-powered assembly, having a power of about 930 kW. The quench times and temperatures at corresponding thermocouple locations in all the bundles are almost identical for both the experiments and the calculations at lower core elevations where the cooling results from the direct contact of the flooding water with the rods. In the upper core regions where cooling comes about from steam flow with liquid droplet entrainment and from liquid fallback into the core from the upper plenum, the calculations consistently lead the data in quench times. The maximum temperatures reached at the lower core elevations agree within a few degrees for both the calculations and the data, but at higher core elevations the spread increases to about 50 K. Neither the calculations nor these forced-flood experiments seemed to be affected in quench times and temperatures by the 56% blockages at the midplane in Bundles 3 and 4.

The code slightly underpredicts the hot leg mass flow rate but predicts fairly accurately the two cold leg mass flow rates. This indicates that the correct amount of liquid is not calculated for the entrainment and the carryover from the vessel through the hot leg, but that the steam generation and its flow out of the cold legs is correct. The agreement between the calculation and the experiment in most other parameters was good for both tests.

B. Comparison of This Calculation with the Base Case Calculation

For most of the figures in this section, the base case is shown with a solid line, and the high-subcooling case is shown with a dashed line; the curves are identified on the plot in cases where this is not true.

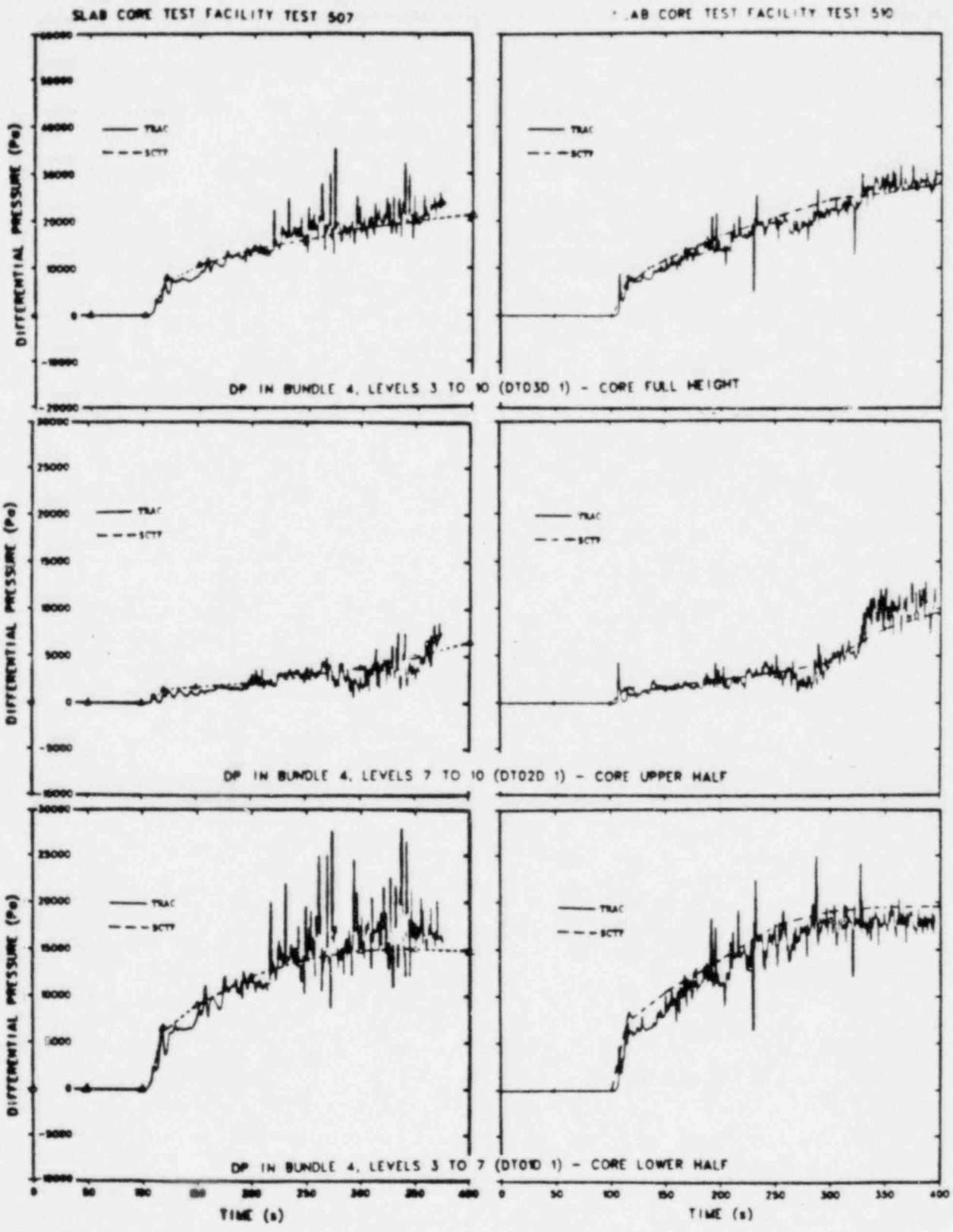

Fig. 3. Comparison of core differential pressures.

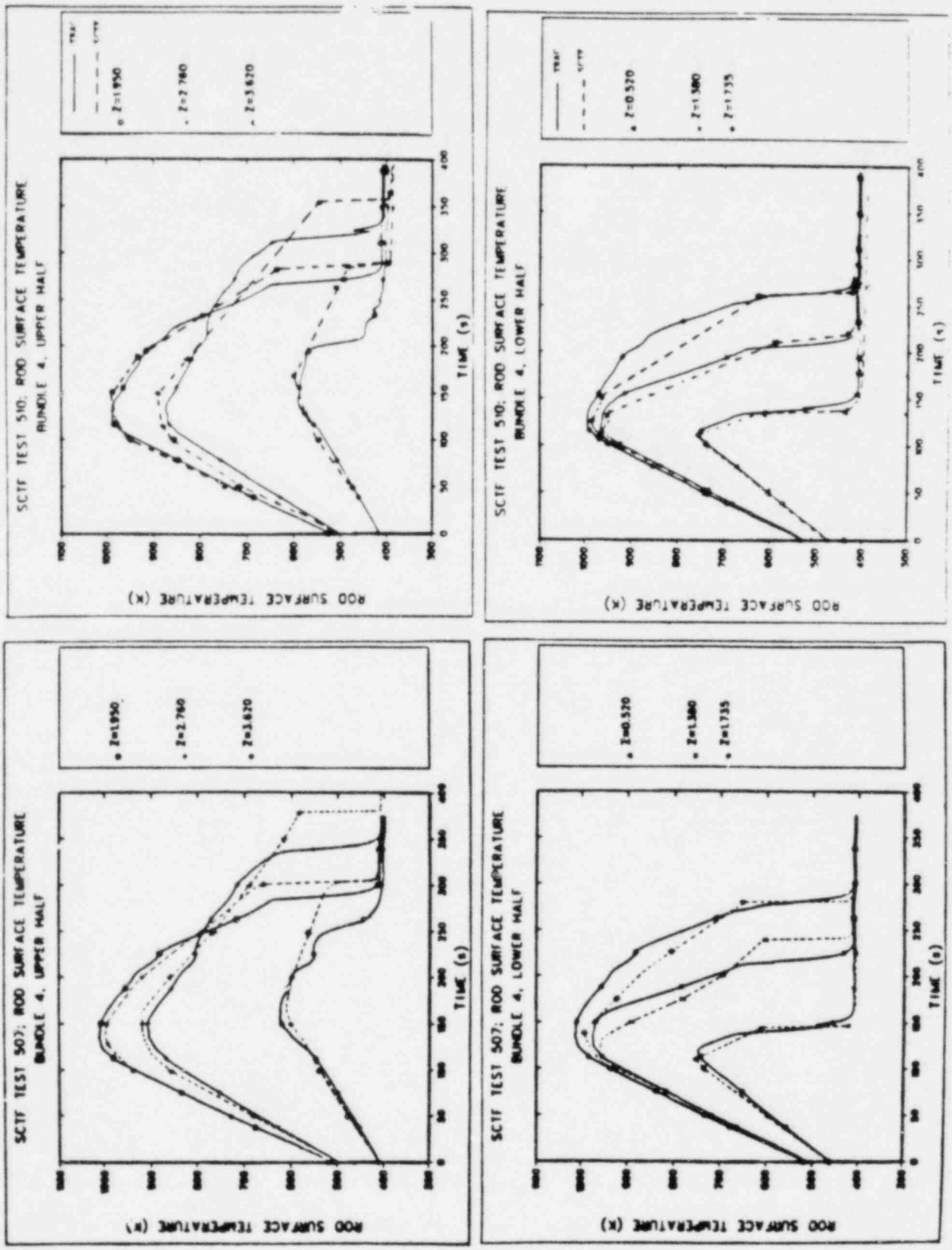

Fig. 4. Comparison of rod surface temperatures.

A comparison of the containment pressure for these two tests is shown in Fig. 5; Fig. 6 compares their ECC mass flow rates. Later reference will be made to the lower containment pressure in Run 510 and to Run 510's higher ECC mass flow. The ECC subcooling and average subcooling in the lower plenum are compared for these two runs in Figs. 7 and 8, respectively.

One noticeable difference between the calculations of Run 510 and Run 507, illustrated in Fig. 9, is that the rods quench earlier in the high-subcooling case than in the base case, particularly above midplane. In the higher regions, the time difference can be as large as 35 - 40 s in both the experiment and the calculation, whereas in the lower regions the difference is smaller, more on the order of 5 - 10 s. This is an effect directly attributable to the high subcooling, in part because the liquid mass in the core is consistently higher throughout the transient for Run 510, and in part because this case has a consistently larger total core outlet liquid mass flow, implying a higher rate of entrainment that results in greater precooling.

The total core inlet liquid mass flow, compared in Fig. 10, the core liquid mass, compared in Fig. 11, and pressure vessel liquid mass, compared in Fig. 12, are greater for Run 510; this is a result of the slightly higher ECC mass flow rate for this test.

The water level in the core was about the same in the two calculations; however, in the experiment the ultimate water level in the base case was less than in the high-subcooling case, as pointed out in the previous section. The calculational result probably comes about from the way in which TRAC approximates the bubbles resulting from the boiling when the code is calculating

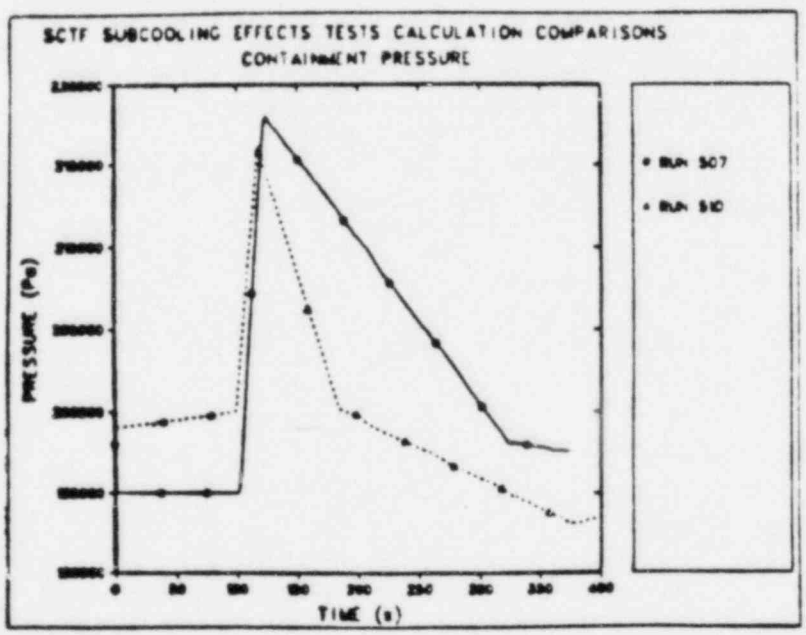

Fig. 5. Comparison of the containment pressure for Runs 507 and 510.

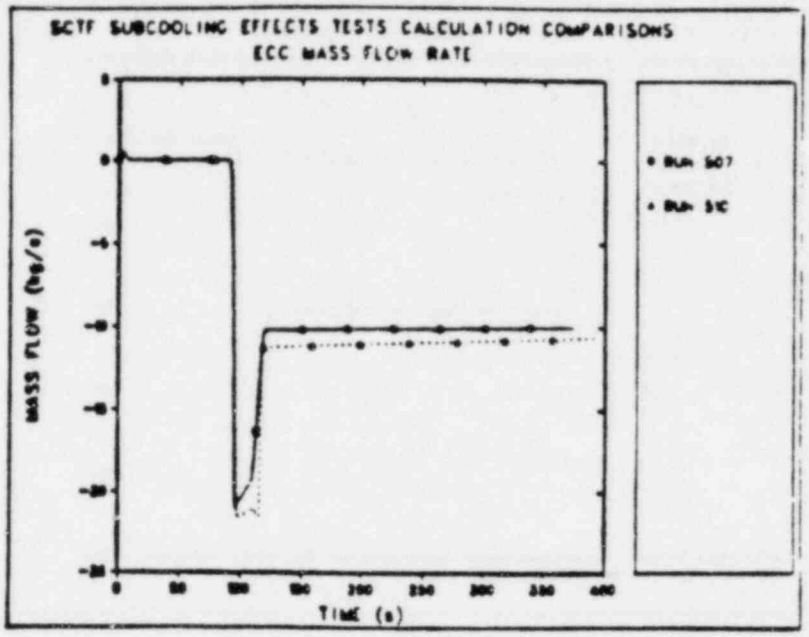

Fig. 6. Comparison of the ECC mass flow rates for Runs 507 and 510.

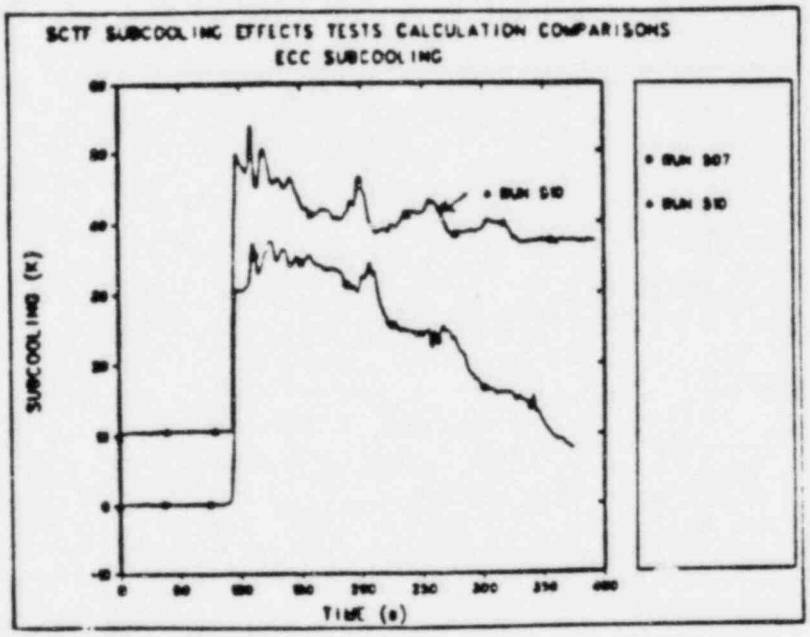

Fig. 7. Comparison of the ECC subcooling for Runs 507 and 510.

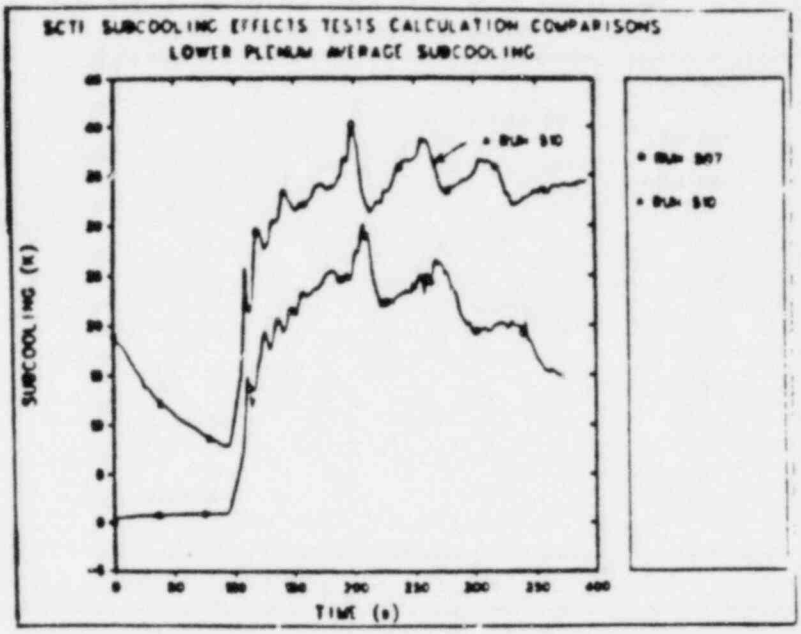

Fig. 8. Comparison of the lower plenum average subcooling for Runs 507 and 510.

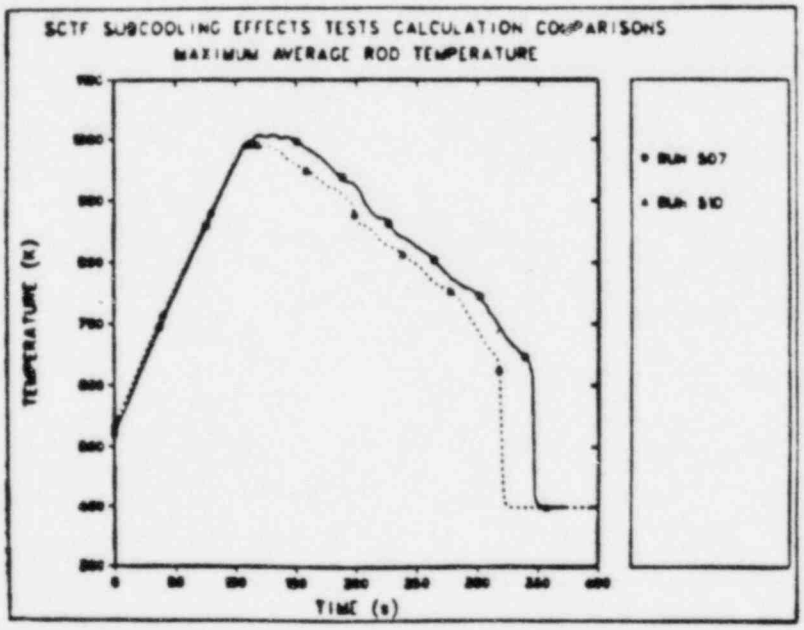

Fig. 9. Comparison of maximum average rod temperatures for Runs 507 and 510.

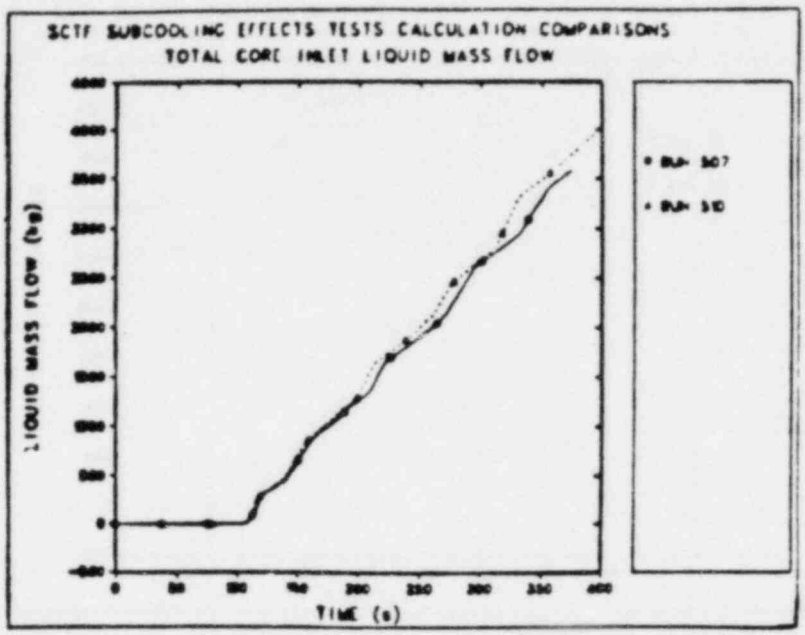

Fig. 10. Comparison of total core inlet mass flow for Runs 507 and 510.

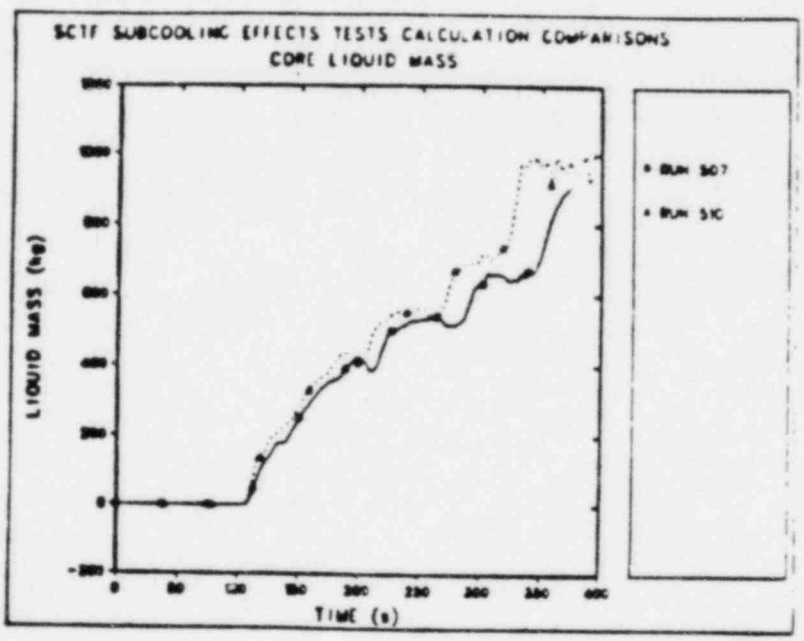

Fig. 11. Comparison of core liquid mass for Runs 507 and 510.

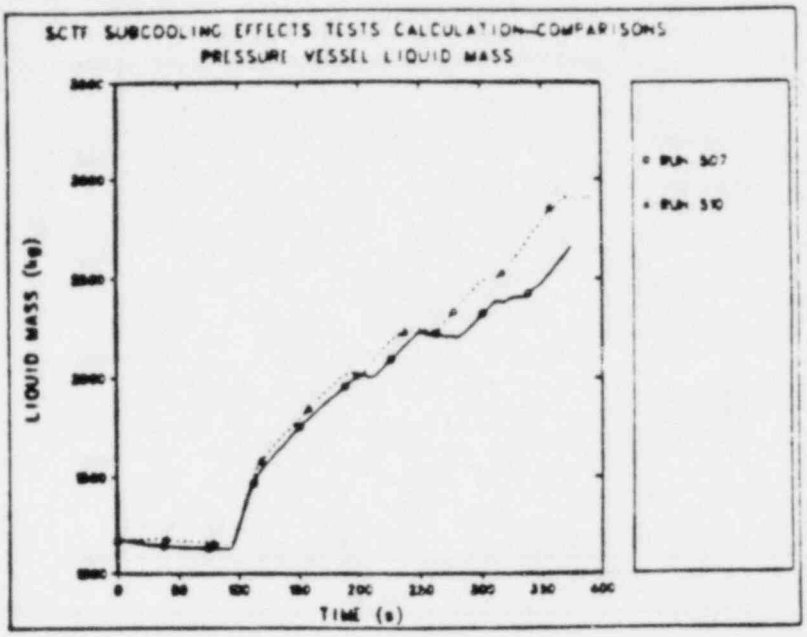

Fig. 12. Comparison of pressure vessel liquid mass for Runs 507 and 510.

collapsed water levels, and the experimental result probably arises from the initial bias of the instruments.

The higher subcooling resulted in subcooled water in the bottom two levels of the core, whereas in the base case the lower plenum liquid remained subcooled, but as soon as this liquid passed into the core, it heated up to saturation. The higher subcooling resulted in more entrainment and more effluent from the core, as shown in Fig. 13; hence, more liquid passed through the hot leg into the separator, as illustrated by the carryover fraction and the separator liquid mass shown in Figs. 14 and 15, respectively. This is in part also attributable to the slightly higher system pressure in Run 510, as the system pressure effects study demonstrated earlier.[3]

Another look at Fig. 14 also shows the greater amount of liquid fallback into the core from the upper plenum in Run 510. The calculation of Run 507 shows a small amount of liquid entering the core at just past 300 s; the calculation of Run 510, however, shows nearly 100 kg of liquid draining back into the core starting at about 325 s.

III. CONCLUSIONS

The comparison between the calculated results and the data from SCTF Run 510 is very good, particularly for rod temperatures, turnaround times, core differential pressures, mass inventories, and fluid temperatures.

Comparison of this calculation with the base case test (Run 507) shows that the qualitative behavior during reflood is calculated correctly for both cases. The high subcooling had its greatest effect upon quench times when compared with the base case. There was a slight difference in the core differential pressures

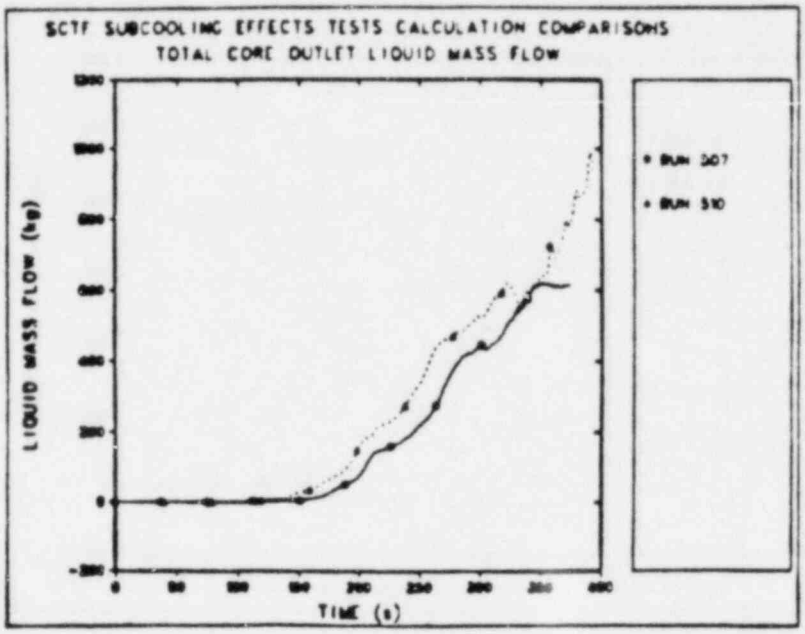

Fig. 13. Comparison of total core outlet liquid flow for Runs 507 and 510.

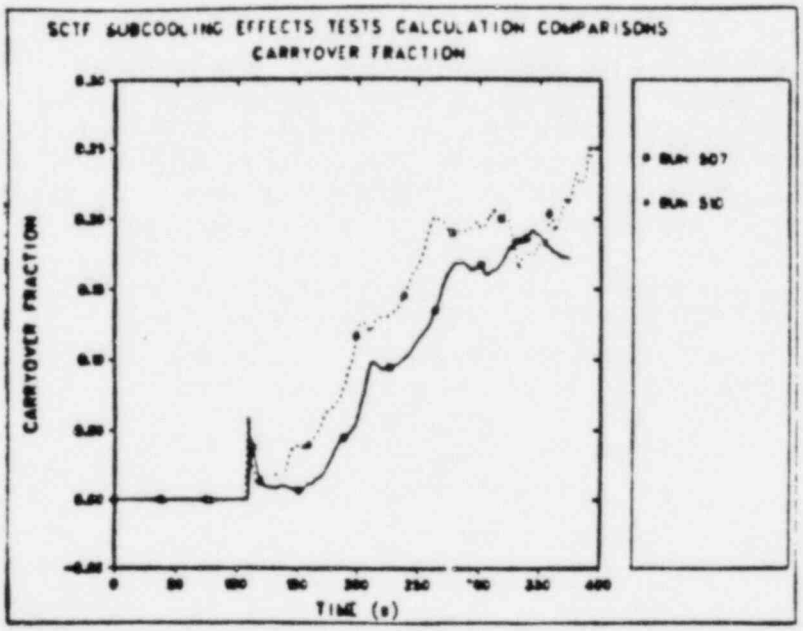

Fig. 14. Comparison of the carryover fraction for Runs 507 and 510.

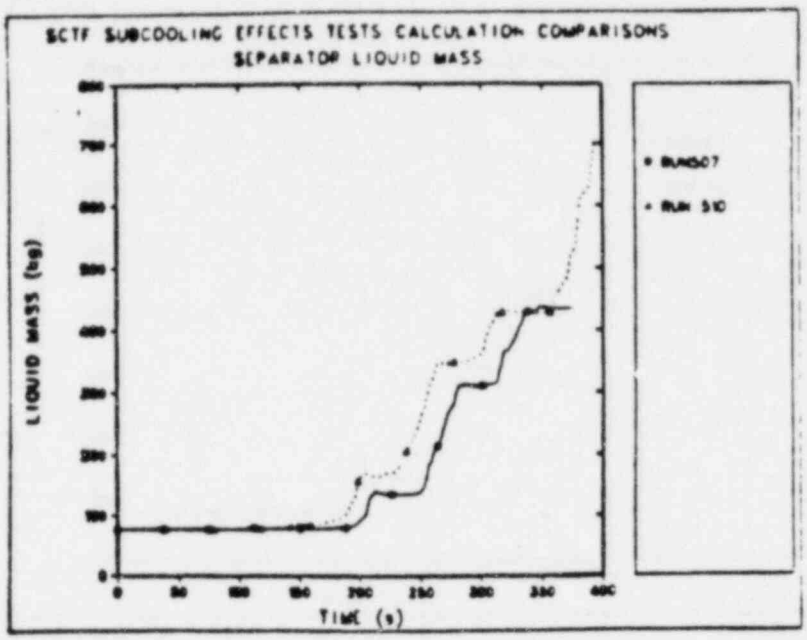

Fig. 15. Comparison of the separator liquid mass for Runs 507 and 510.

when comparing the two runs; the high-subcooling case had more water in the bottom half of the core than did the base case. Also, there was more liquid fallback into the core in the high-subcooling case. Most other parameters behaved in roughly the same way in both Run 510 and Run 507.

In addition, from the comparison of the high-subcooling test with the base-case test, the following conclusions can be drawn: for the high-subcooling case, the peak rod temperature was lower, calculated quench times were earlier, there was more entrainment from and liquid carryover from the core to the upper plenum, and the liquid mass accumulation in both the core and the upper plenum was greater. These are directly attributable to the higher subcooling throughout the system.

From the comparison of the calculation of Run 510 with the experimental data, one concludes that the calculational model and TRAC-PD2/MOD1 can predict well the system responses arising from parametric variations in subcooling conditions.

REFERENCES

1. "TRAC-PD2: An Advanced Best-Estimate Computer Program for Pressurized Water Reactor Loss-of-Coolant Accident Analysis," Los Alamos National Laboratory report LA-8709-MS (May 1981).

2. K. Hirano, private communication.

3. Y. Sudo, "Analysis of TRAC and SCTF Results for System Pressure Effects Tests Under Forced Flooding (Runs 506, 507, and 508)," Los Alamos National Laboratory Report LA-9258-MS (March 1982).

4. K. Hirano, private communication.

POSTTEST TRAC-PD2/MOD1 PREDICTIONS FOR FLECHT SEASET TEST 31504*

Clay P. Booker
Safety Code Development
Energy Division
Los Alamos National Laboratory
Los Alamos, NM 87545

ABSTRACT

The Transient Reactor Analysis Code (TRAC) being developed at the Los Alamos National Laboratory under the sponsorship of the Reactor Safety Research Division of the US Nuclear Regulatory Commission is an advanced, best-estimate systems code to analyze light-water-reactor accidents. TRAC-PD2/MOD1 is a publicly released version of TRAC that is used primarily to analyze large-break loss-of-coolant accidents in pressurized-water reactors (PWRs). TRAC-PD2 can calculate, among other things, reflood phenomena.

In this paper we compare TRAC posttest predictions with test 31504 reflood data from the Full-Length Emergency Core Heat Transfer (FLECHT) System Effects and Separate Effects Tests (SEASET) facility. A false top-down quench is predicted near the top of the core and the subcooling is underpredicted at the bottom of the core. However, the overall TRAC predictions are good, especially near the center of the core.

INTRODUCTION

In this report we assess the capability of the Transient Reactor Analysis Code, TRAC [1], to make accurate posttest predictions for the Full-Length Emergency Core Heat Transfer (FLECHT) System Effects and Separate Effects Tests (SEASET) run 31504. This experiment was an unblocked bundle, low-flooding rate, forced reflood test. We include a description of the TRAC model for the FLECHT SEASET facility, pertinent TRAC predictions, comparisons between the TRAC predictions and the test data, and a concise analysis of our results.

TEST DESCRIPTION

The FLECHT SEASET facility was designed to provide heat-transfer and simulated primary-system performance data for a typical pressurized-water reactor (PWR) during reflood. The facility basically consists of a low-mass test vessel, a water supply, associated piping, a rod bundle, and instrumentation [2]. The rod bundle includes electrically heated rods with a 3.66-m heated section. The rods, identical in size, are arranged such that they duplicate the lattice of a Westinghouse 17 × 17 nuclear fuel assembly.

*Work performed under the auspices of the US Nuclear Regulatory Commission.

In test 31504, the bundle was unblocked and consisted of 161 rods, 2 of which were unpowered. It was a forced reflood test with a nominal 2.46-cm/s reflood rate. The initial and boundary conditions are described more completely in the next section.

TRAC MODEL

Some important TRAC features are two-phase nonequilibrium hydrodynamics, flow-regime-dependent constitutive equations, a two-fluid hydrodynamics model of the VESSEL component, a reflood tracking capability for both bottom reflood and falling quench fronts, and a multidimensional model of the VESSEL.

TRAC-PD2/MOD1 (version 27.0), a publicly released PWR version, corrects several coding errors but does not add any model changes to a previously released version, TRAC-PD2 (version 26.0).

Figure 1 shows the TRAC model for the FLECHT SEASET facility. The FILL and BREAK components simulate the test boundary conditions. The two PIPE components represent some of the major system piping. The two-dimensional option for the VESSEL component models the low-mass test vessel; because there is no radial power gradient and the bundle length-to-diameter ratio is large, we assume that one-dimensional flow is appropriate. The VESSEL has 18 levels and levels 3-17 are heated. Lumped-parameter heat slabs in levels 3-17 simulate the heat capacity of the low-mass housing. The TRAC code references elevations within the VESSEL with respect to the VESSEL bottom, as shown in the right half of Fig. 1; however, the available experimental data reference elevations with respect to the location where heating begins, as shown in the left half of Fig. 1. For convenience, we have referenced these TRAC predictions and analyses from the elevation where heating begins.

Figures 2-4 show some of the initial conditions for test 31504. In each of these figures, unconnected triangular symbols represent the experimental data; the solid curve represents the least-squares fit of the TRAC calculations to the experimental data. The TRAC data points (circular symbols) in Fig. 2 represent the initial heat-slab temperatures at the VESSEL cell centers. The TRAC clad temperatures in Fig. 3 are specified at the cell edges. The initial TRAC vapor temperatures in Fig. 4 are specified at the cell centers. Figure 5 shows the injection velocity for the FILL component; the FILL supplies water at a constant 326.5 K. The TRAC power decay curve closely corresponds with that of the data. The BREAK component maintains a constant 0.27745-MPa backpressure.

RESULTS

Figures 6-12 show average-rod temperature as a function of time at selected elevations above the location where heating begins both for the TRAC predictions and for the FLECHT SEASET data. To the right of the plot is a rectangular legend box that contains pertinent plot information. The information in the upper portion of the box indicates that a solid curve represents the TRAC prediction (TRAC-PD2 designates version TRAC-PD2/MOD1) whereas a curve constructed of circles or triangles represents the FLECHT SEASET data. An instrument designation identifies the FLECHT SEASET data; for example, the instrument designation 9G-0.305 in Fig. 6 specifies that

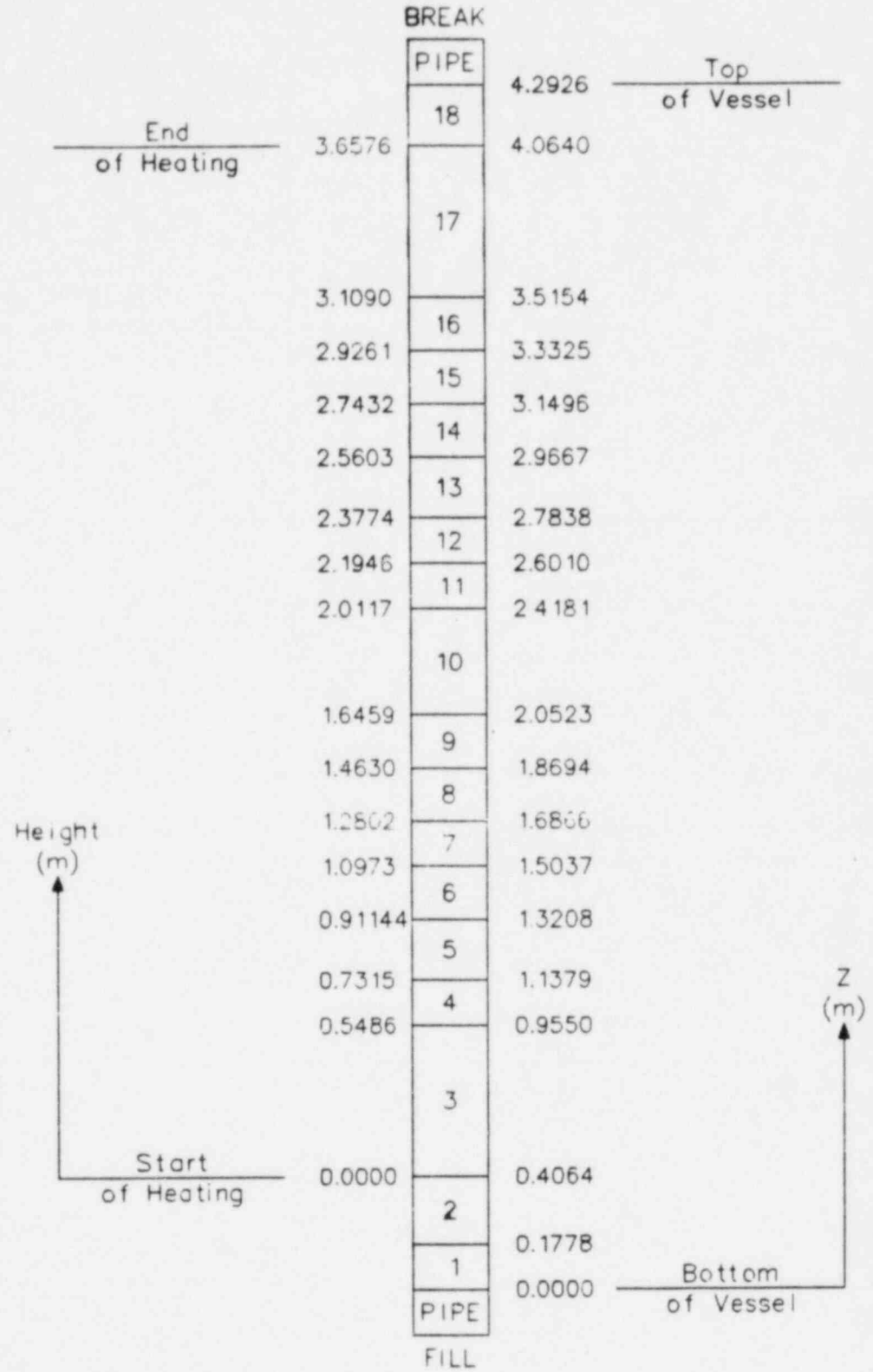

FIGURE 1 : TRAC MODEL OF THE FLECHT SEASET FACILITY

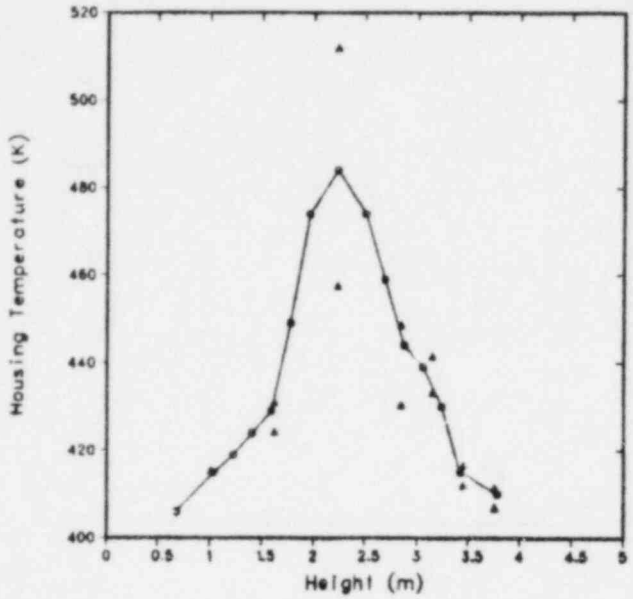

FIGURE 2 : INITIAL HOUSING-TEMPERATURE DISTRIBUTION

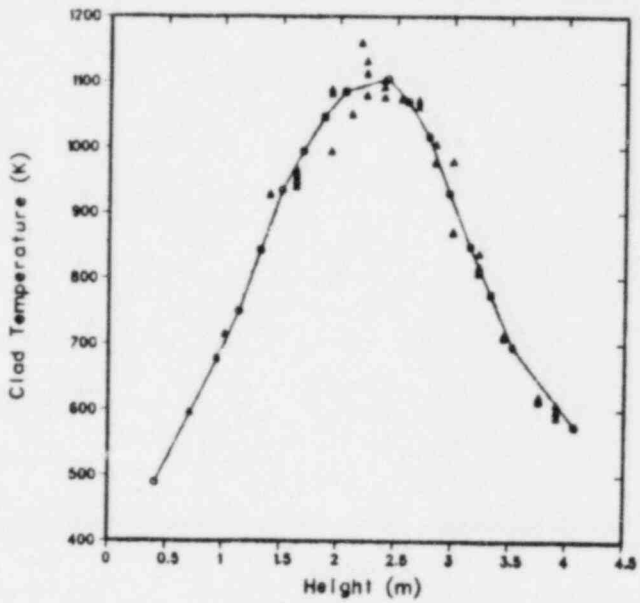

FIGURE 3 : INITIAL AVERAGE-ROD-TEMPERATURE DISTRIBUTION

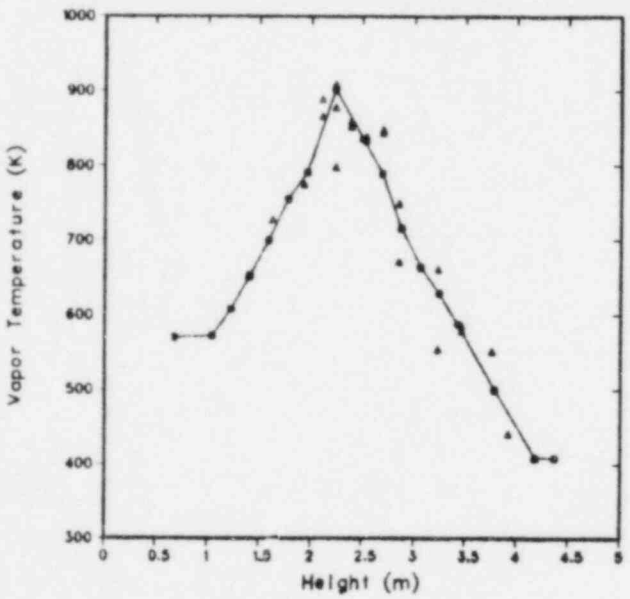

FIGURE 4 : INITIAL VAPOR-TEMPERATURE DISTRIBUTION

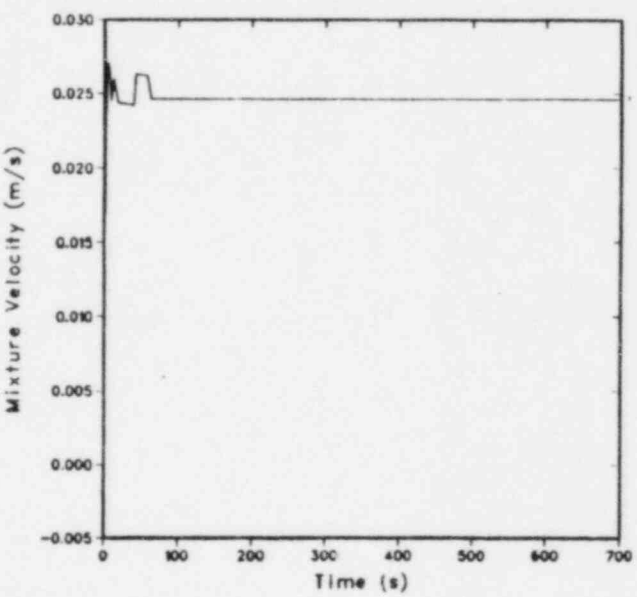

FIGURE 5 : FILL INJECTION VELOCITY

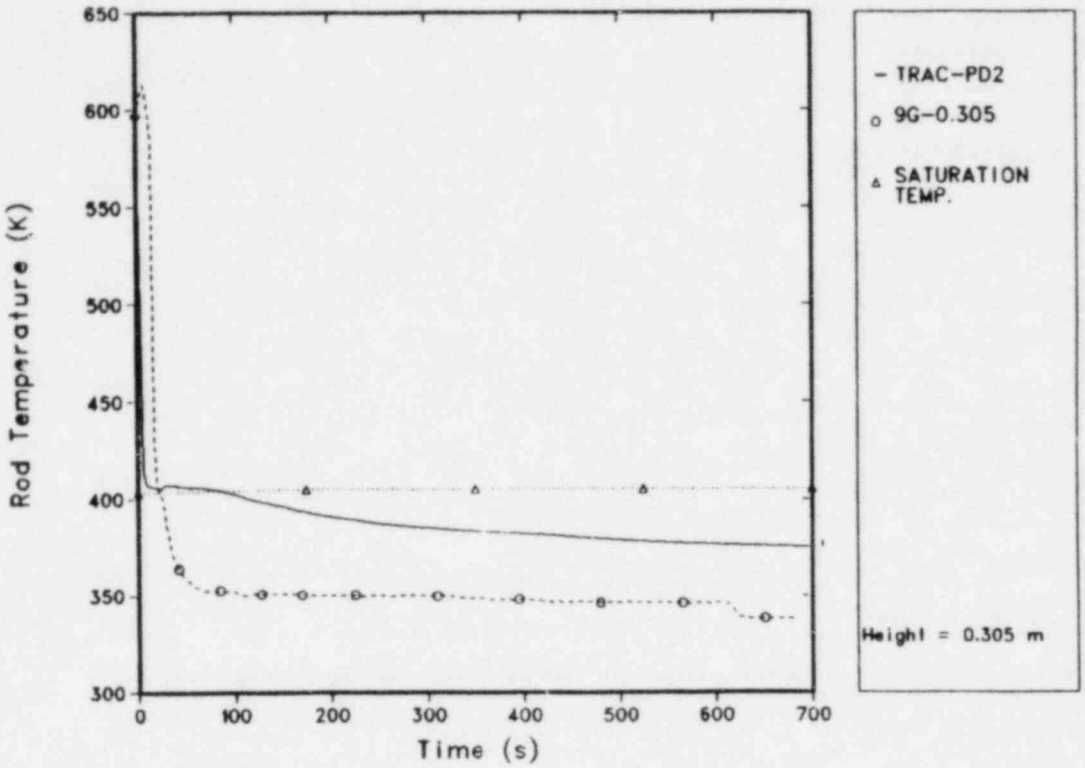

FIGURE 6: AVERAGE-ROD TEMPERATURE AT 0.305-m ELEVATION

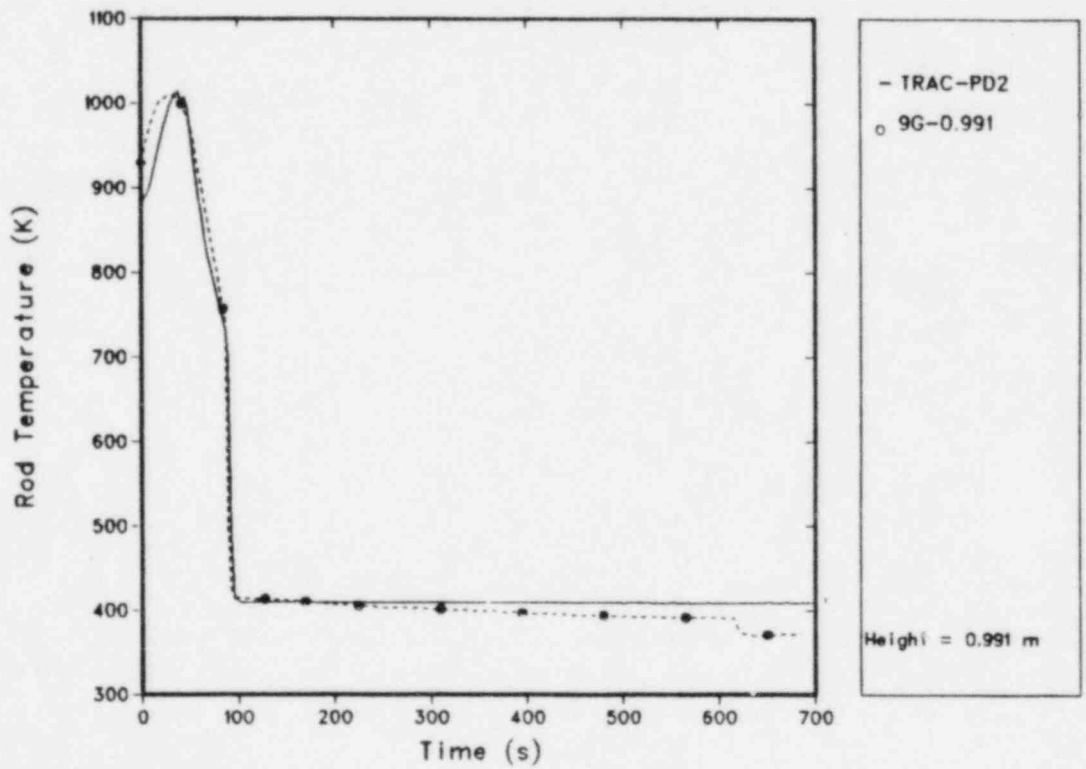

FIGURE 7 : AVERAGE-ROD TEMPERATURE AT 0.9991-m ELEVATION

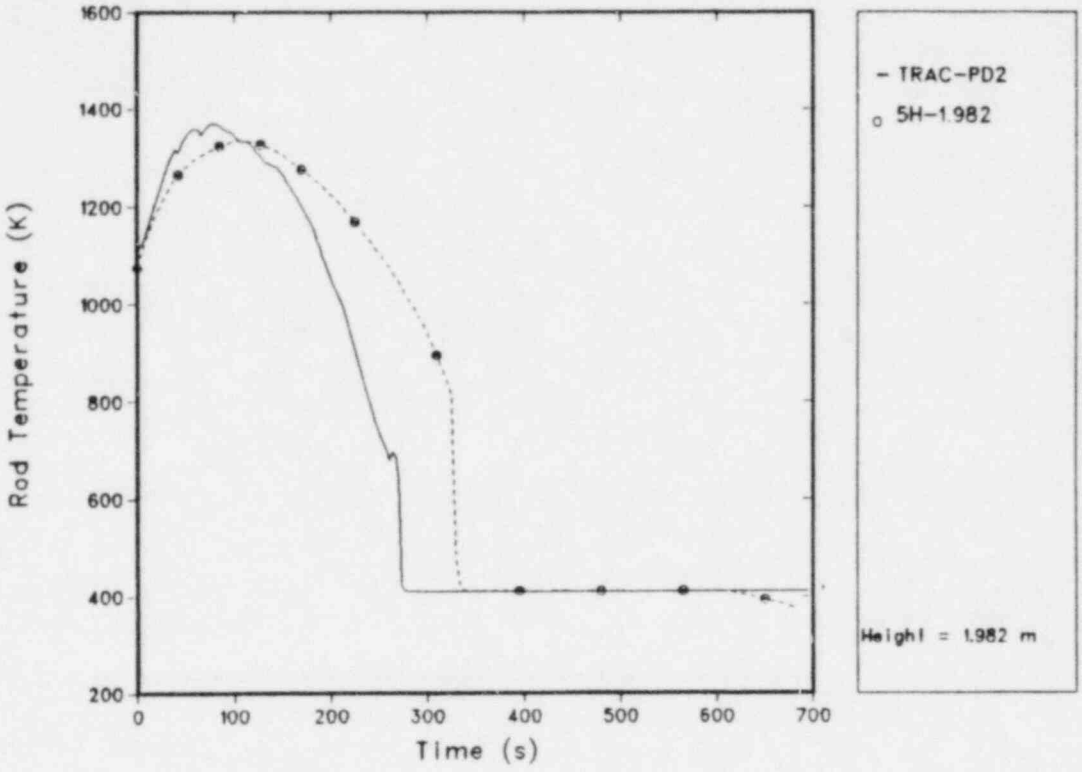

FIGURE 8 : AVERAGE-ROD TEMPERATURE AT 1.982-m ELEVATION

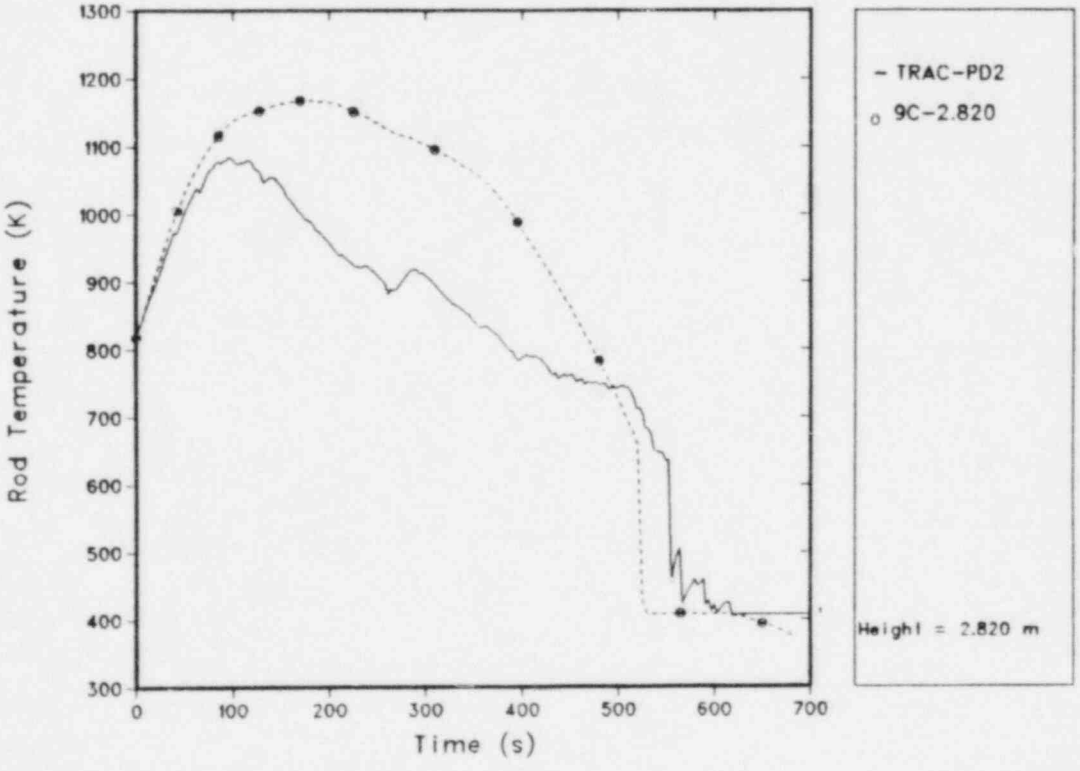

FIGURE 9 : AVERAGE-ROD TEMPERATURE AT 2.820-m ELEVATION

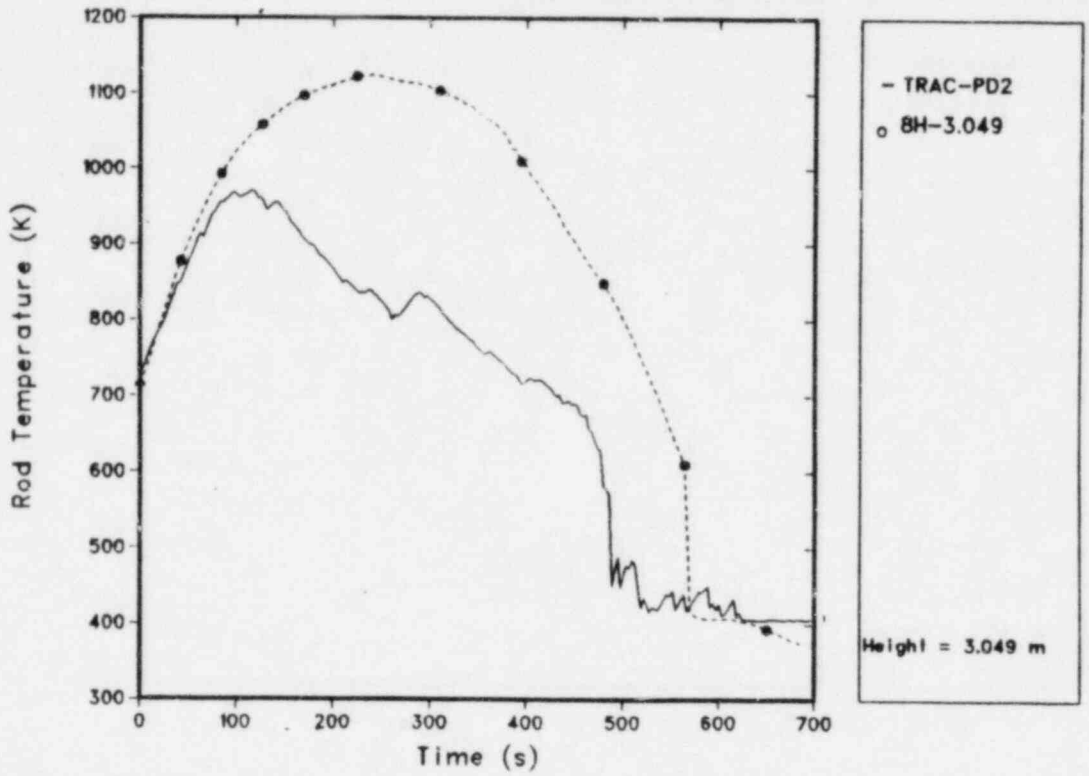

FIGURE 10 : AVERAGE-ROD TEMPERATURE AT 3.049-m ELEVATION

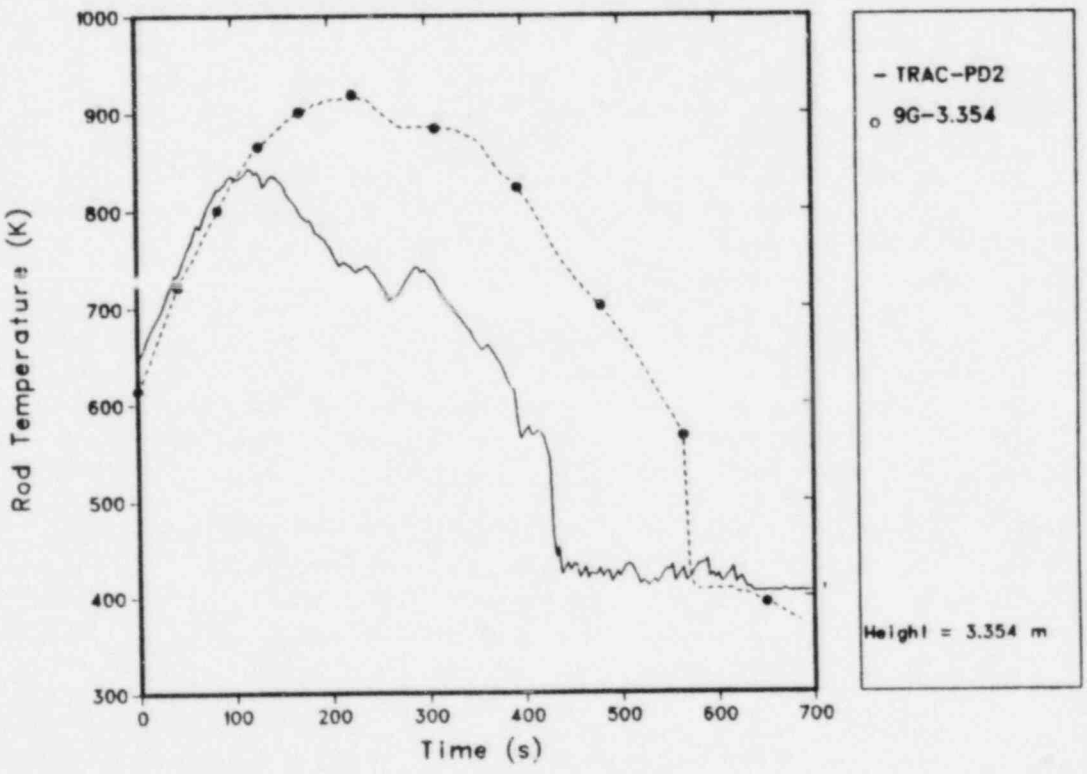

FIGURE 11 : AVERAGE-ROD TEMPERATURE AT 3.354-m ELEVATION

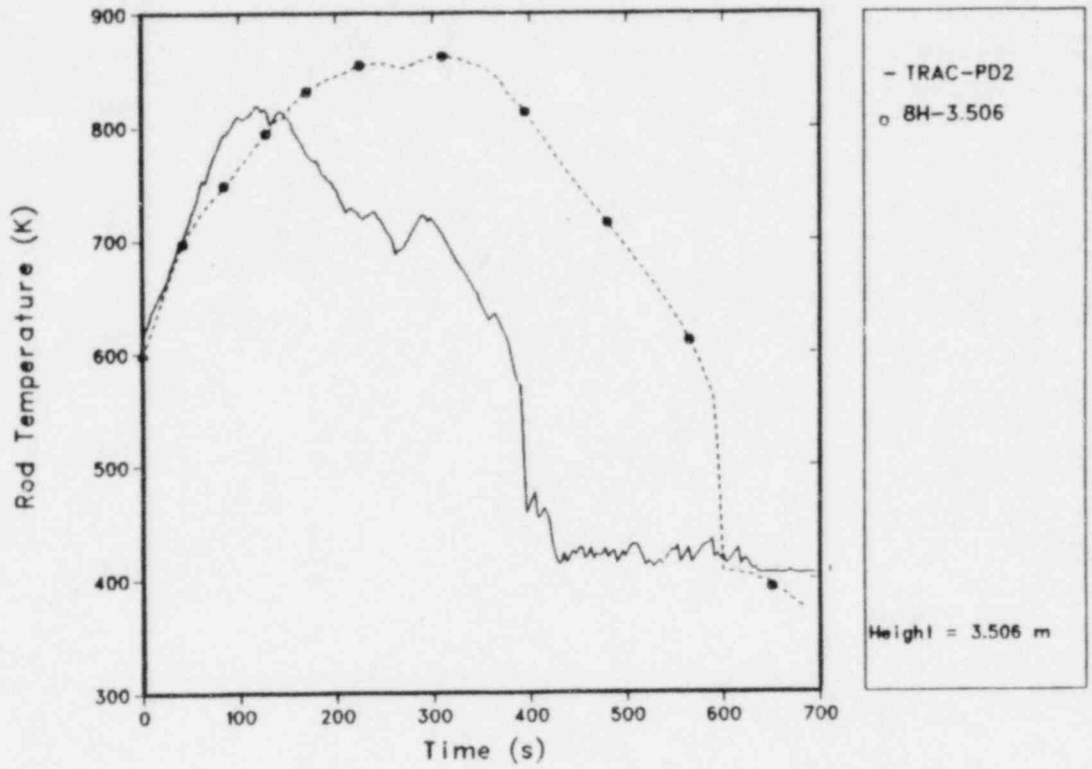

FIGURE 12 : AVERAGE-ROD TEMPERATURE AT 3.506-m ELEVATION

9G is a horizontal location in the rod bundle and that 0.305 is the axial elevation of the instrument in meters above the bottom of the heated length. Data error bars are contained within the symbol. The radial location within the rod, just inside the clad, is the same both for the TRAC prediction and for the FLECHT SEASET data. In Fig. 6, a dotted curve with triangular symbols represents the water saturation temperature for the corresponding TRAC cell. The information at the bottom of the legend box gives the axial elevation above the bottom of the heated length for the TRAC prediction.

Figure 13 shows elevation vs quench time both for the TRAC average-rod prediction (solid curve with circular symbols) and the FLECHT SEASET data (triangular symbols). The FLECHT SEASET quench times [2] were calculated by the Westinghouse Quench Program staff. The TRAC predictions for quench time are based on the rod temperature curves and we assume that the quench occurs when the slope of the TRAC curve approaches vertical.

For most of the calculation, TRAC does a good job of predicting the clad temperature of the rods. For the lower half of the heated zone, the TRAC predictions for quench time, quench temperature, turnaround time, and peak temperature are typically within experimental scatter; Figure 13 clearly shows this for quench time. In the next one-quarter of the heated zone, TRAC begins to predict an early quench (Fig. 13). Also, the calculated turnaround time is early and the calculated peak temperature starts to deviate below the data. In the top one-quarter of the heated zone, TRAC predicts a top-down quench that the data do not indicate; Figure 13 most clearly shows this trend. Moreover,

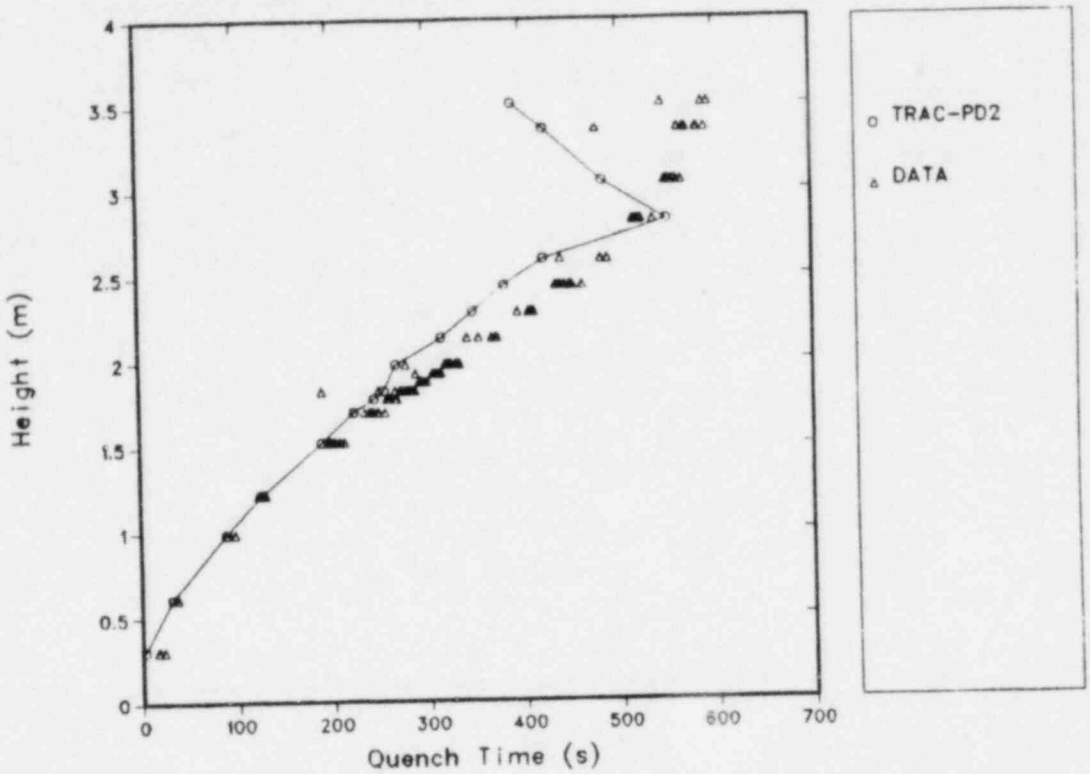

FIGURE 13 : ELEVATION VS QUENCH TIME

in the upper one-quarter, the peak-temperature prediction is low and the TRAC turnaround time is early. Apparently, the top-down cooling and the low peak-temperature prediction are caused by an overpredicted entrainment in the TRAC-PD2/MOD1 code. Increasing the TRAC value for the droplet Weber number from 4 to 16, resulting in a very large drop size, does not reduce the problem significantly even though the increasing Weber number should tend to decrease entrainment. Another code change that appears to affect entrainment more is the correction of the TRAC-PD2/MOD1 interfacial shear calculation |3, 4|. Figures 14 and 15 show the effect of this correction; these figures have an additional curve for the corrected TRAC-PD2/MOD1, represented by a dotted line with triangular symbols and labeled CORRECTED TRAC-PD2. Clearly, these changes are insufficient to correct the top-down quench behavior or the underpredicted peak clad temperatures in the upper part of the heated zone. The FLECHT SEASET rod bundle contains eight grid spacers |2|, which will serve to de-entrain liquid and reduce droplet size; however, TRAC does not model the grid spacers.

An unexplained phenomenon occurs in the bottom 0.610 m of the heated zone. As Fig. 6 shows, the saturation temperature in the data immediately drops well below the experimental saturation temperature when quench occurs--about 50 K lower at 0.305 m. On the other hand, the TRAC prediction drops to saturation when quench occurs and then slowly drops below. Increasing the TRAC heat-transfer coefficient by 30% increases the TRAC predicted subcooling but the temperature still does not fall as fast nor as far as that in the data. This difference remains unexplained. boiling but this possibility was not explored.

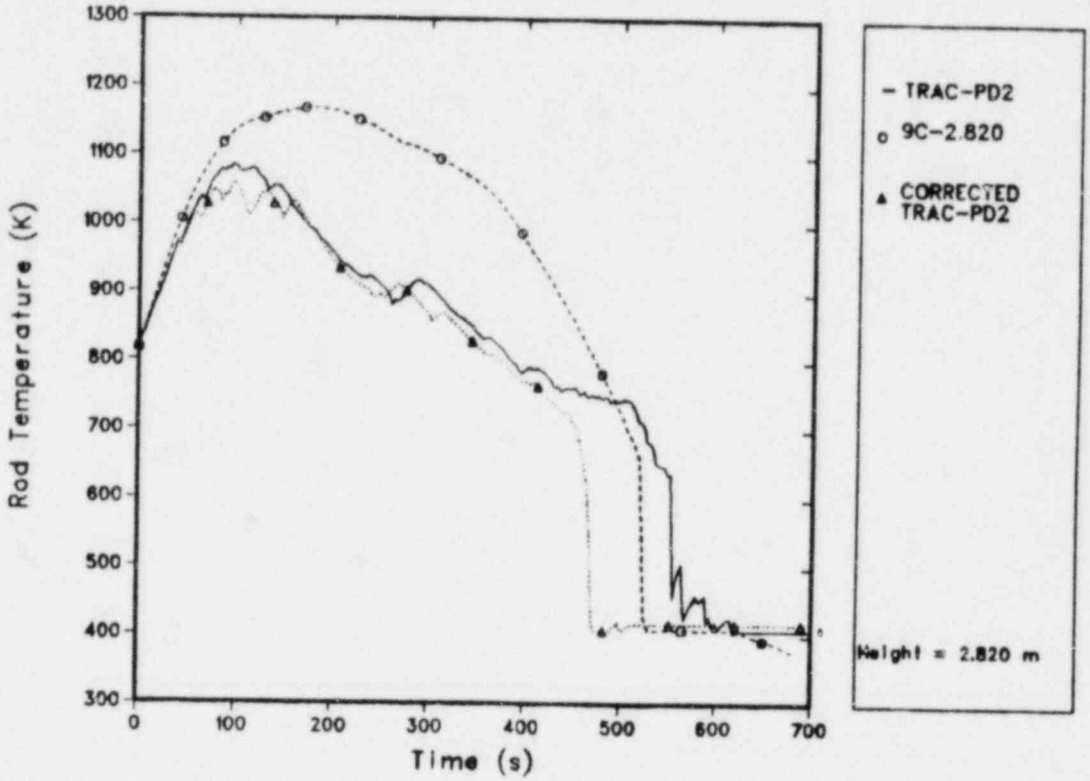

FIGURE 14 : COMPARISON BETWEEN TRAC-PD2/MOD1 CORRECTED AND UNCORRECTED CALCULATIONS FOR ROD TEMPERATURE VS TIME AT 2.820-m ELEVATION

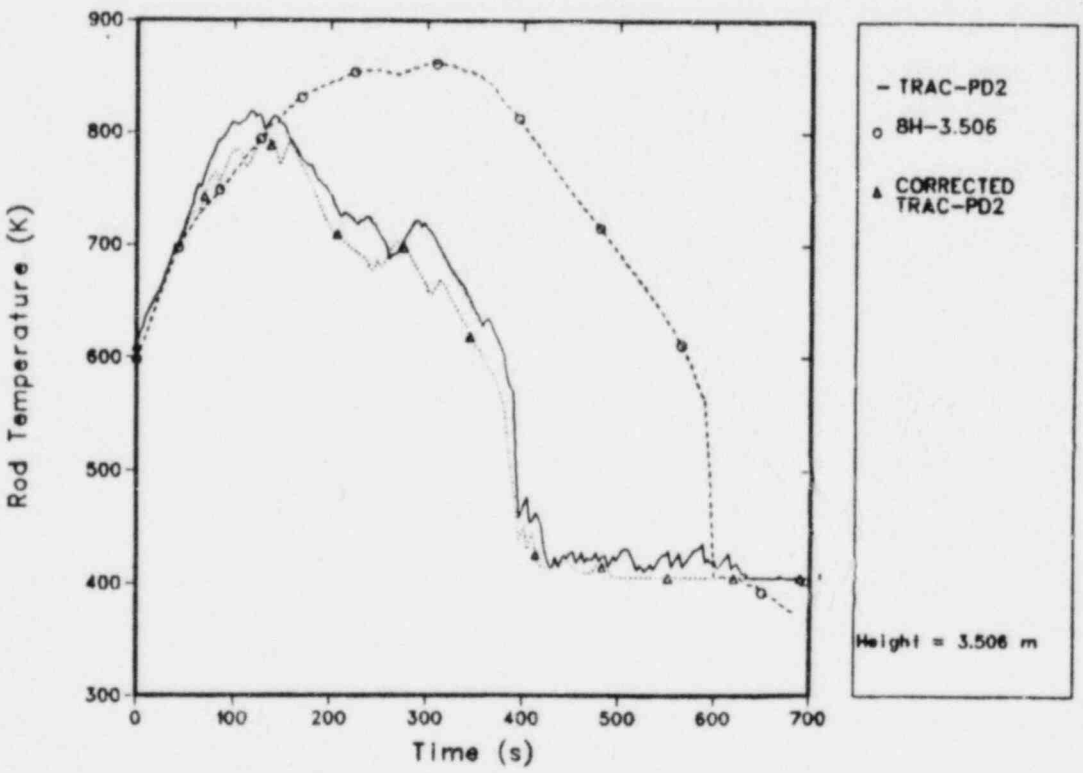

FIGURE 15 : COMPARISON BETWEEN TRAC-PD2/MOD1 CORRECTED AND UNCORRECTED CALCULATIONS FOR ROD TEMPERATURE VS TIME AT 3.506-m ELEVATION

To the author's knowledge, only one other TRAC prediction for test 31504 has been made--by L. Neymotin at Brookhaven National Laboratory [3]. His model differs significantly from the Los Alamos TRAC model. His heat slabs are more than twice as hot initially and have about four times more surface area per unit mass. Further, the upper half of his vessel component is more finely noded; the lower half is more coarsely noded. Based on the three plots in Ref. 3, his TRAC predictions for the bottom half of the core are only marginally closer to the data and his TRAC predictions for the upper half of the core are no better than those presented in this paper.

CONCLUSIONS

Overall, TRAC has predicted well the behavior of FLECHT SEASET run 31504. TRAC's major shortcomings are its tendencies to predict an unrealistic top-down quench at the top of the heated zone because of excessive entrainment and to predict excessive cooling in general above the core midplane. The discrepancies between the calculated cladding temperature and the data in the bottom section of the core after quench require a more detailed analysis before a satisfactory explanation can be given; such an analysis was beyond the scope of this task.

REFERENCES

1. "TRAC-PD2, An Advanced Best-Estimate Computer Program for Pressurized Water Reactor Loss-of-Coolant Accident Analysis," Los Alamos National Laboratory report LA-8709-MS [NUREG/CR-2054] (April 1981).

2. M. J. Loftus, L. E. Hochreiter, C. E. Conway, C. E. Dodge, A. Tong, E. R. Rosal, M. M. Valkovic, and S. Wong, "PWR FLECHT SEASET Unblocked Bundle, Forced and Gravity Reflood Task Data Report," Westinghouse report WCAP-9699 [NUREG/CR-1532, EPRI NP-1459] (June 1980).

3. L. Neymotin, "FLECHT SEASET Forced Reflood Tests," Brookhaven National Laboratory Quarterly Progress Report, Section 7.1.5 (April-June 1981).

4. P. Saha, "BNL Corrections to TRAC-PD2 (Version 26.0)," (internal control number), Brookhaven National Laboratory memorandum to Fuat Odar, Nuclear Regulatory Commission (August 20, 1981).

VERIFICATION OF THE THREE-DIMENSIONAL ANALYSIS CAPABILITY OF THE TRAC ACCIDENT ANALYSIS CODE*

by

F. Motley

Energy Division
Los Alamos National Laboratory

ABSTRACT

The Transient Reactor Analysis Code (TRAC) being developed at Los Alamos National Laboratory provides a best-estimate prediction of the response of light water reactors or test facilities to postulated accident sequences. One of the features of the code is the ability to analyze the vessel and its heated core in three dimensions. The code is being used to analyze the results of tests in a large-scale reflood test facility built in Japan, known as the Cylindrical Core Test Facility (CCTF). Two test runs have been analyzed that are useful for verification of the three-dimensional analysis capability of the TRAC code. One test began with an initial temperature skew across the heated core. The second test had a large radial power skew between the central and peripheral assemblies. The good agreement between the calculation and the experiment for both of these experiments demonstrates the three-dimensional analysis capability of the TRAC code.

I. BACKGROUND AND OBJECTIVE

The realistic analysis of the response of a pressurized water reactor (PWR) to a postulated accident is most important in assuring the public safety. Most current reactor designs have been based upon the predictions of accident analysis codes that were developed to provide a "conservative" or most limiting prediction of fluid conditions or rod temperatures. In this manner it was thought that the public safety would be assured, but in many cases it is not clear what assumptions are required to produce a "conservative" result. Also the accident analysis codes used for licensing of PWR's consider only the axial behavior within the vessel (one-dimensional analysis). By modeling the most limiting portion (highest power) of the core,

*Work performed under auspices of United States Nuclear Regulatory Commission.

again, it was believed that the code predictions would be "conservative". Another deficiency of most of the accident analysis codes is their inability to follow the accident through its entire course. The codes were specialized so that one code was used for blowdown; then a second code was used for refill; and finally, a third code was used for reflood.

In order to overcome many of these shortcomings, the Los Alamos National Laboratory is developing a best-estimate systems code for analyzing PWR accidents known as the Transient Reactor Analysis Code (TRAC).[1] The code has two-phase nonequilibrium hydrodynamics models, flow-regime-dependent constitutive equation treatment, and reflood tracking capability for both bottom flood and falling film quench fronts. The entire accident sequence can be followed by the code, beginning with steady-state normal operating conditions and then proceeding through the blowdown, refill, and reflood phases of the accident. A full three-dimensional flow calculation can be done within the reactor vessel. This allows an accurate calculation of the complex multidimensional flow patterns inside the reactor vessel that determine the core behavior during the accident. Being a best-estimate code allows TRAC to help identify excessively conservative or non-conservative assumptions currently mandated for reactor accident design.

The verification of the TRAC code has been accomplished by comparison of code predictions to many different experiments investigating different aspects of the postulated accident sequence. The most extensive model of a PWR is the Cylindrical Core Test Facility (CCTF),[2,3] which was constructed by the Japan Atomic Energy Research Institute (JAERI) as part of a tri-lateral agreement among the United States (US), Germany (FRG), and Japan, named the 2D/3D Project. The test facility is a 1/20 scale model of a 1000 MW PWR. It can simulate the end of blowdown and the refill and reflood phases of a postulated accident. The core of this test facility is large enough to investigate multidimensional effects. This paper compares the TRAC-PD2/MOD1 predicted results to the experiment for two tests. The two tests selected were characterized by accentuated multidimensional core effects.

II. DESCRIPTION OF CCTF FACILITY AND TRAC MODEL

The facility is a model of a four-loop PWR. The experimental core consists of 1824 electrically heated rods contained in a vessel that models the downcomer, lower plenum, and upper plenum. There are three intact loops and a fourth loop with a cold-leg break. Each loop contains an active steam generator and a pump simulator. The facility is full height and scaled in volume by the ratio of the number of heated rods (1824/39372), roughly a 1/20 factor.

The TRAC input model attempts to reproduce all the pertinent details of the facility's geometry. The overall CCTF facility model is shown in Fig. 1. Only one of the intact loops is shown because all the intact loops are modeled identically. All the hot legs (connecting the upper plenum and the steam generator) are identical. A steam generator for each loop is modeled with the lower portion of the secondary having several short levels to allow modeling of the stratification of the secondary-side water that has been observed in the experimental data. The secondary sides of the steam generator are isolated. The remainder of the intact loop piping (connecting the steam generator to the downcomer) is modeled, including the loop seal, pump simulator, and emergency core coolant (ECC) injection. The pump simulator has an orifice to represent the resistance of an impeller. This orifice is modeled in TRAC as additional friction. The ECC injection enters through the

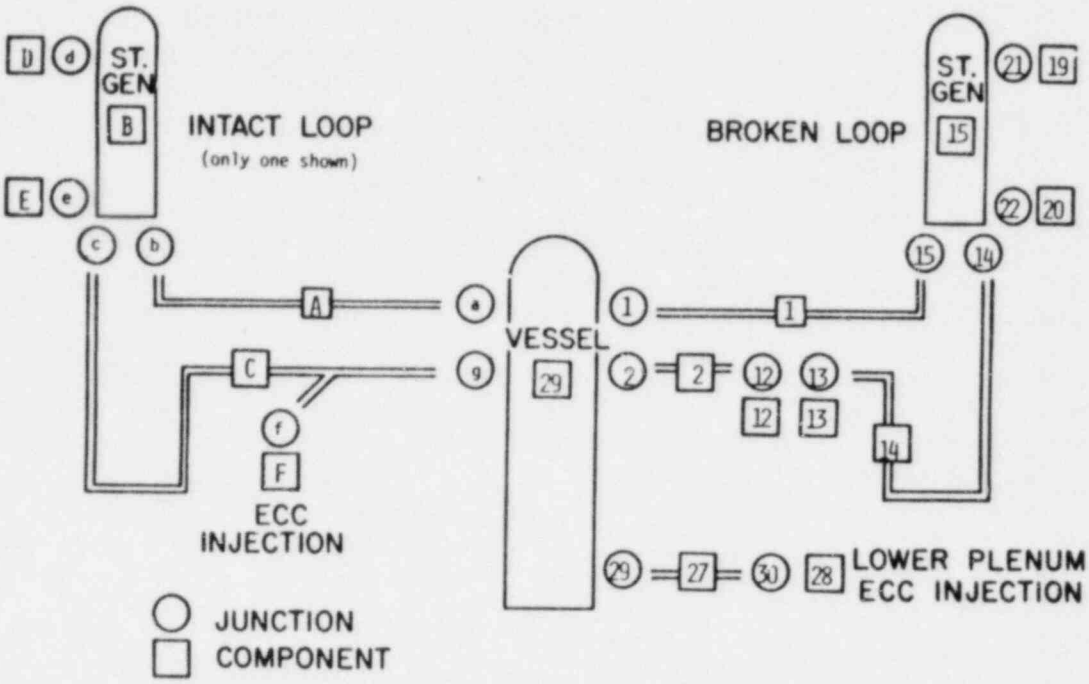

Fig. 1. Schematic of Cylindrical Core Test Facility.

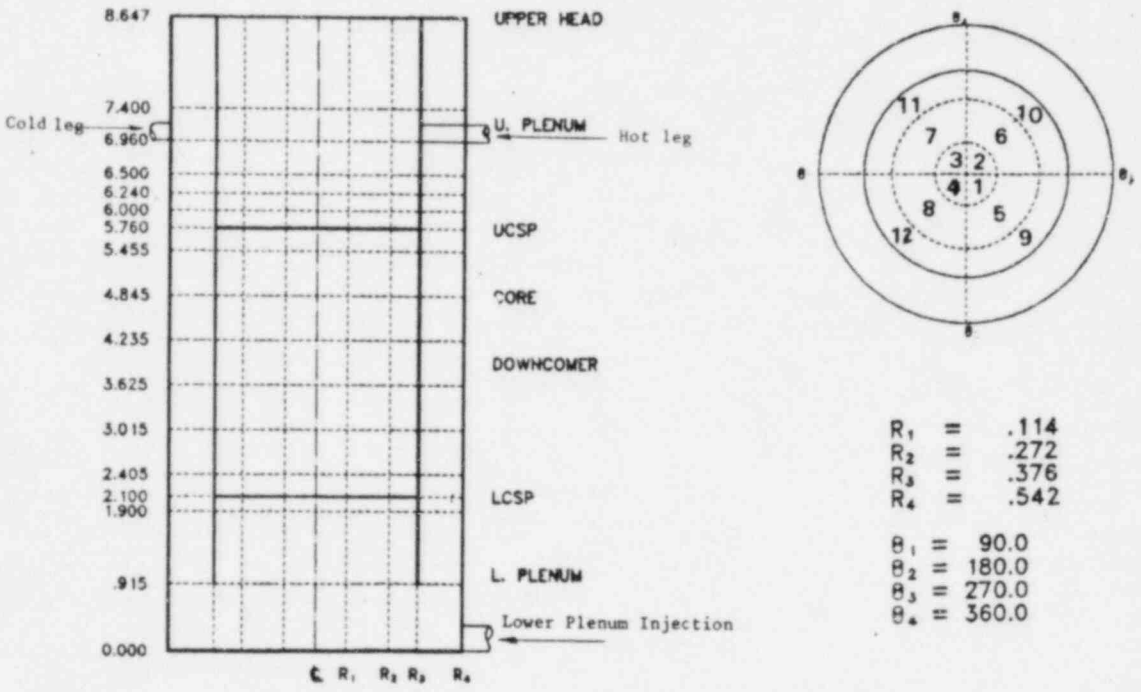

Fig. 2. TRAC noding for the CCTF vessel.

secondary-side branch of a tee just after the pump simulator. In the TRAC model ECC liquid is supplied to this pipe in the same manner as the experimental facility, and is discussed further in the boundary conditions section.

The broken-loop model is identical to the intact-loop model from the steam generator to one cell after the pump simulator. There is no ECC injection in this loop and instead of connecting to the downcomer, the end of the component is connected to a pressure boundary condition similar to that provided by the containment tank in the facility. The other portion of the broken loop is modeled by a pipe extending from the vessel to the same boundary condition as the other end of the broken cold leg. The initial ECC water delivery in the experiment is to the lower plenum. The boundary conditions at this location will be discussed in a later section.

The overall vessel noding is shown in Fig. 2. The inner three rings represent the core. The inner radial ring (cells 1 through 4) corresponds to the inner power zone. The remaining power zones each correspond to a single TRAC cell. The outer-most radial ring in the TRAC noding corresponds to the downcomer and the barrel-baffle region. The flow area and volume fractions have been input to account for the complete isolation of the barrel-baffle region so that the downcomer flow area and volume are modeled properly.

The vessel is divided axially into sixteen levels. The downcomer extends from the top of the first level to the top of the vessel. The lower plenum is contained in the bottom three levels. The elevation of the top of the first level was set equal to the beginning of the downcomer and the position of the lower spacer plate. This also is the approximate elevation of the initial water level at the beginning of an experiment. The top of the second level corresponds to the position where the flow area changes as the heater rod diameters increase to their nominal dimensions. The lower core support plate (LCSP) elevation and the beginning of the heated core is at the top of the third level.

The heated core extends from elevation 2.1 m to 5.76 m. It is divided axially into seven segments. The volume fractions and flow areas at each of the elevations are equal to those of the rod matrix. Extra friction was included in each of the five central core elevations to model the spacer grids, which are used to hold the rods in place.

The next level above the core (6.00 m) corresponds to the elevation between the end of the heater rods and the tie plate. There is an unobstructed flow area at this location followed by the flow area reduction of the tie plate and upper core support plate (UCSP) at the next elevation (6.24 m). These two short levels model the upper internals more accurately, allowing the code to predict upper plenum de-entrainment and location dependent fall-back that have been observed in the experiment.

The remaining vessel levels were chosen in order to maintain the proper elevation of the loop connections. The top of the fourteenth level corresponds to the bottom of the loop pipes, which allows proper modeling of the downcomer height. The loops are connected at the fifteenth level, with the cold leg connection into the outer downcomer ring and the hot leg connection into the upper plenum at the third radial ring. One loop is connected to each azimuthal section. Because there is a composite of different upper plenum hardware in each of the upper plenum cells, averaged flow areas and volume fractions are used. The lower plenum injection connection is at the outer ring of the first level.

All stored energy associated with the pressure vessel walls, core barrel assembly, upper and lower plenum internals, and non-heated rods in the core region has been modeled. These vessel heat sources were modeled with an optional slab heat transfer model, which allows distributed temperature nodes in the walls for improved heat transfer predictions over the standard lumped-parameter model in TRAC-PD2. The initial wall temperatures were input with a flat profile and no variation in the radial direction.

As discussed previously, the heated core model contains seven axial hydrodynamic levels; on each level there are twelve nodes, which divide the core in the same manner as the CCTF heating zones. The chopped-cosine axial power profile of the heater rod is modeled with a peak to average value of 1.49. The radial power profile of the test with the initial temperature skew was 1.15 in the inner ring, 1.08 in the intermediate ring, and 0.89 in the outer ring. The second test was more radially skewed, with 1.30 for the innner ring, 1.09 for the intermediate ring and 0.84 for the outer ring. All the rods are modeled with identical material properties and six radial nodes.

III. INITIAL AND BOUNDARY CONDITIONS

The TRAC calculation was performed in a manner very similar to the actual execution of the test. Starting from an initial condition, there was a constant power heatup period. When some of the rod locations attained a predetermined temperature, ECC injection was initiated into the lower plenum from an accumulator and continued until shortly after water began to penetrate the core. A power decay was initiated at the beginning of core recovery (BOCREC). The ECC injection was switched from the lower plenum to the cold legs, and then switched from accumulator injection to a low-pressure coolant injection (LPCI) equivalent flow rate shortly after BOCREC. This lower ECC injection flow continued until all the rods were quenched. The skewed temperature test had an initial core temperature distribution which was skewed up to 350 K along a core diagonal, hot rods in the lower half to cold rods in the upper half in Fig. 2. This distribution was obtained by selectively pulsing the power to the various heater regions prior to the start of the test.

IV. COMPARISON OF EXPERIMENTAL RESULTS AND TRAC CALCULATIONS

The comparison is divided into two parts, one for each of the two tests. The experimental data is shown as a dashed line on each of the figures and the TRAC results as a solid line.

A. Radical Power Skew Test (C1-19 Run 38)

The TRAC calculated results show that as the ECC begins flowing at 92 s, the lower plenum fills and then the downcomer fills rapidly during the period of accumulator flow and remains full (Fig. 3) during the test. The core liquid mass (Fig. 4) shows oscillations (+100 kg) as the water first begins to enter the core. These oscillations persist until 180 s, when the bottom two levels of the core fill and remain full of liquid. These oscillations are also evident in the downcomer mass (Fig. 3), thus indicating core-to-downcomer manometer oscillations. After these oscillations end at 180 s the core continues to fill gradually.

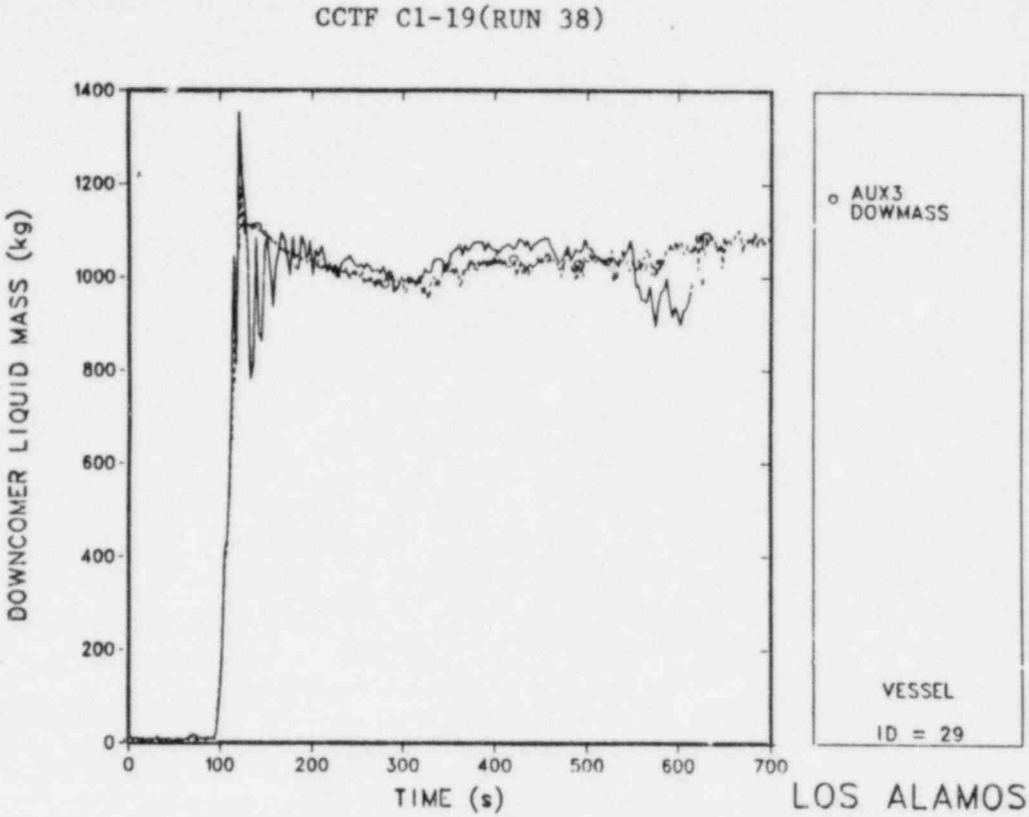

Fig. 3. Downcomer liquid mass.

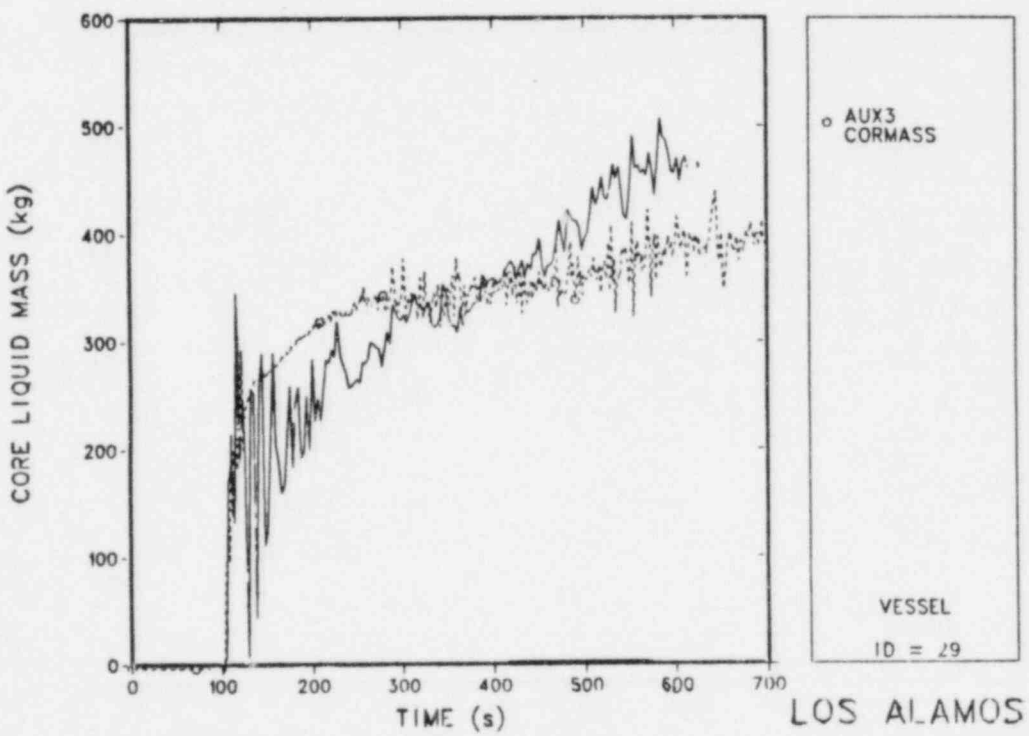

Fig. 4. Core liquid mass.

The mass in the downcomer and core during the experiment can be approximated by converting the signals from the level transducers into mass equivalents, assuming that the liquid is saturated. The experimental values are shown as dashed lines on Figs. 3 and 4. There is good agreement between the experiment and the calculation in the downcomer, except for the oscillations just after the initial filling. The core liquid mass plot shows that the experiment had oscillations for about 15 s during the initial core filling, but these damped out and the core continued to fill until 300 s.

The calculated and measured absolute pressures at the top of the vessel are compared in Fig. 5. The deficiency of core water in the calculation until 300 s resulted in the underprediction of the pressure during this period, indicating that the core cooling and liquid vaporization were underpredicted in the calculation.

In this paper, two rods were chosen to present the five elevations of measured heater rod temperatures: an average rod in the central high power heating zone (Fig. 6) and an average rod in the peripheral low power heating zone (Fig. 7). During the period of rod heatup and lower plenum filling, the calculated rod temperatures show good agreement with the data at all elevations. This confirms that the material properties and the input core power were correct. The oscillatory period following the first arrival of water into the core is noticeable in the calculated temperatures at the core midplane and above. In most cases there is a slight delay in heatup, with the upper elevations of the lower-powered peripheral-zone rods showing a short cooling period. The bottom thermocouple elevation quenched simultaneously at all core locations immediately after water first entered the core. Close inspection of the data shows that, at the next thermocouple elevation, the

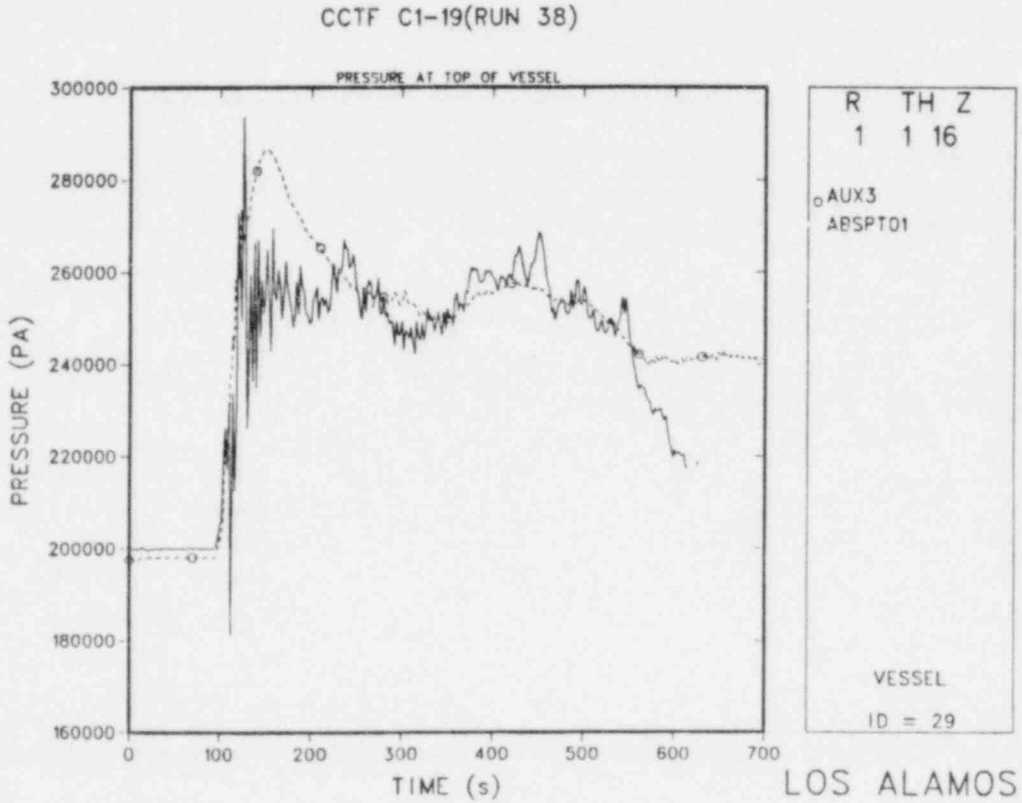

Fig. 5. Pressure at top of vessel

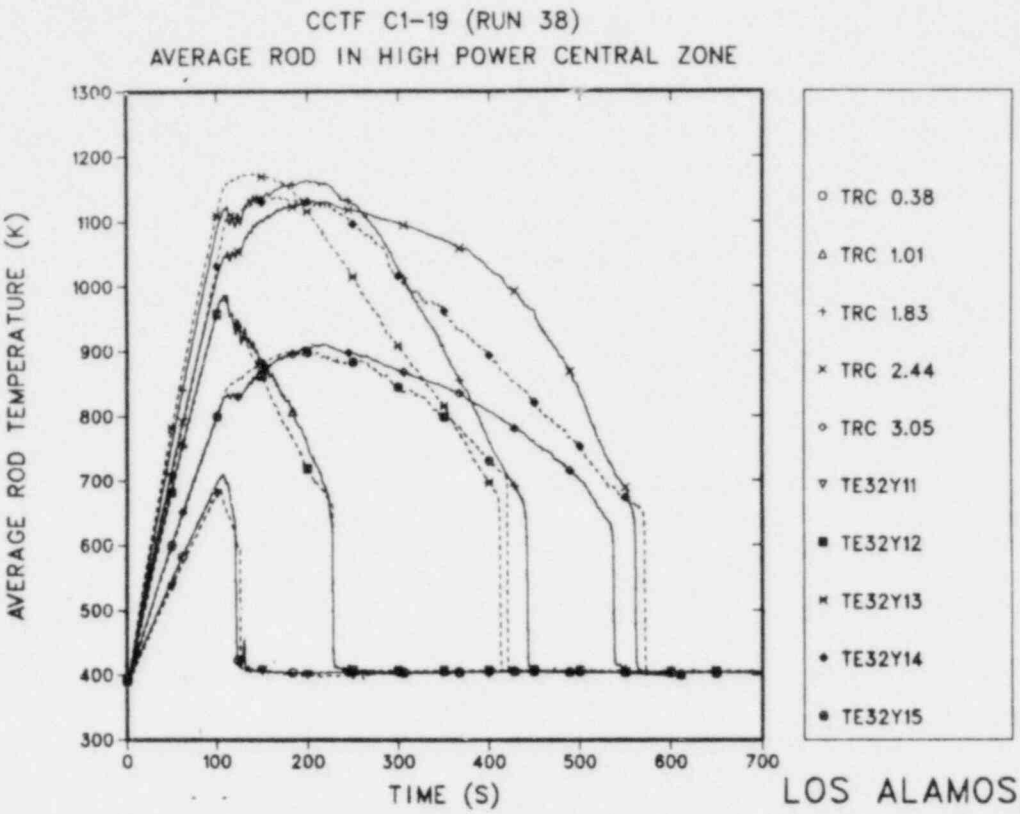

Fig. 6. High power central zone rod temperature.

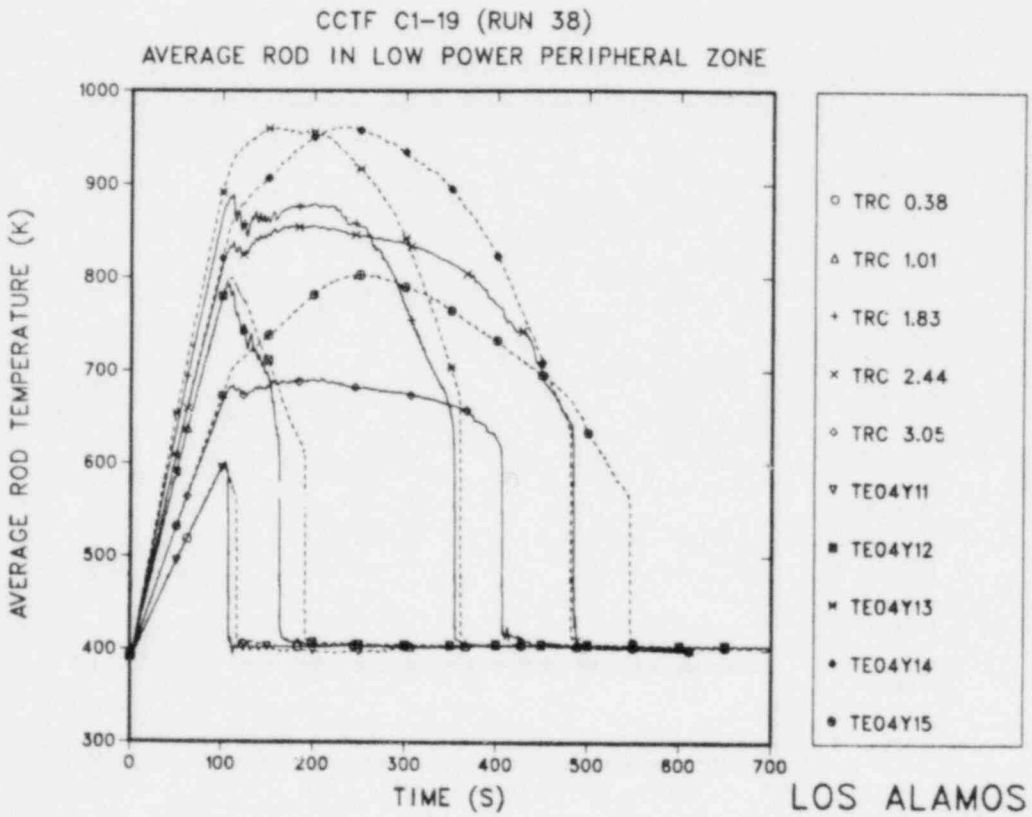

Fig. 7. Low power peripheral zone rod temperature.

peripheral rods quenched first and the inner rods quenched last. The calculated results agree very closely with the data in the inner two regions, but the calculated quench occured slightly early in the peripheral heating zone.

The data and the calculation indicate that the temperature turnaround time is the same for all rods at each elevation, but the calculation shows a slightly later turnaround of the midplane temperature. This is caused by the reduced vessel mass during this period, as discussed previously. Comparisons of the turnaround temperatures show reasonable agreement between the experiment and the calculation, except in the peripheral heating zone where the rod temperatures did not recover from the the excessive cooling during the oscillation period. The quench temperatures and times also show good agreement between the calculation and the experiment, except for the top elevation. The generally good agreement between measured and calculated quench times is shown in Fig. 8, which compares the quench envelopes of several bundles. The calculation accurately predicts the multidimensional radial behavior of the quenching. It can be seen that at the core midplane the average rods in the outer bundles are calculated to quench 74 s earlier than average rods in the central bundles. The experimental data shows that the maximum difference in quench times at the midplane locations is 100 s.

The response of the loop may be judged by considering the pump orifice as a flow meter. The calculated differential pressure across the pump simulator (Figs. 9 and 10) is in good agreement with the measured experimental value, indicating that the calculated loop flows are correct. The oscillatory period from 120 to 180 s is evident, as is the deficient cooling period at 200 s. The calculation reproduces the measured two-and-one-half times larger flow in the broken loop, compared to the intact loops.

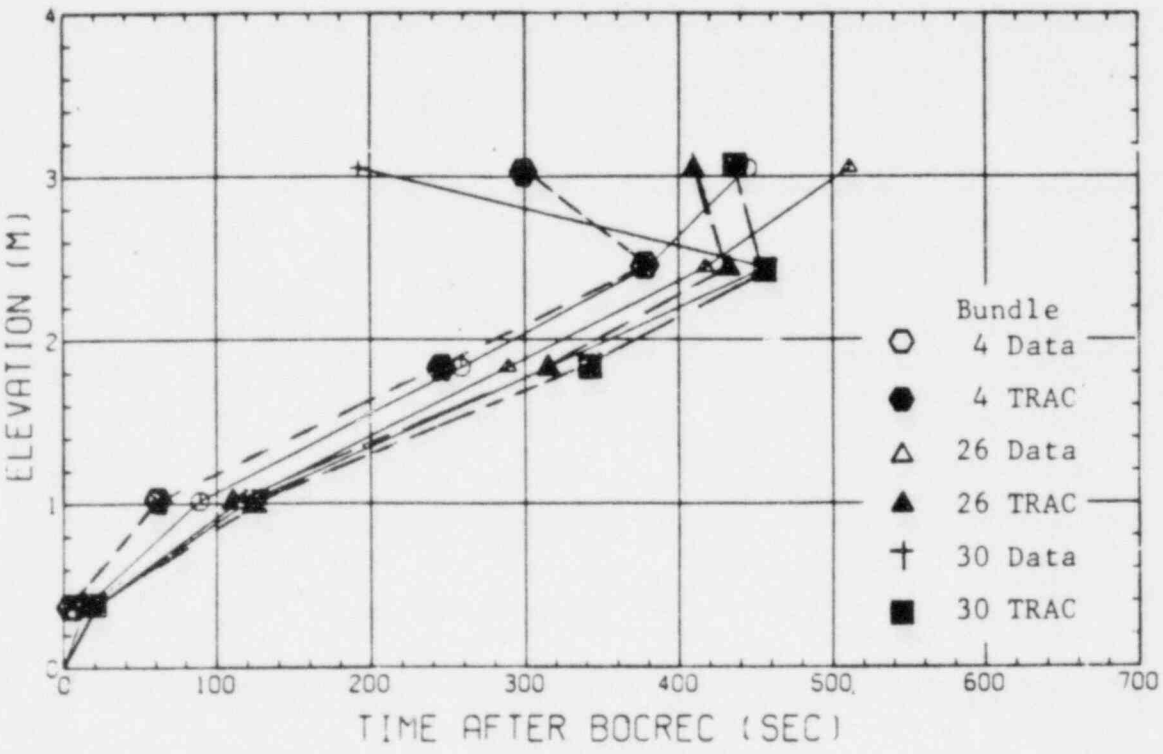

Fig. 8. Quench envelopes (CCTF Run 38).

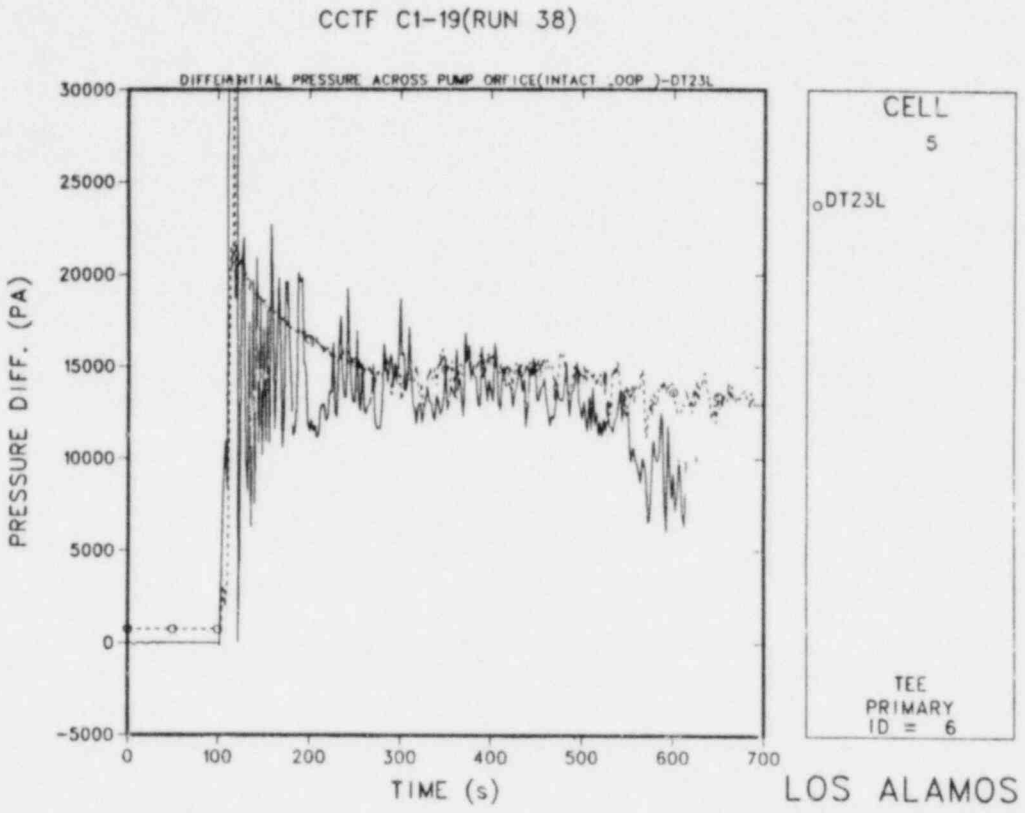

Fig. 9. Intact loop pump orifice differential pressure.

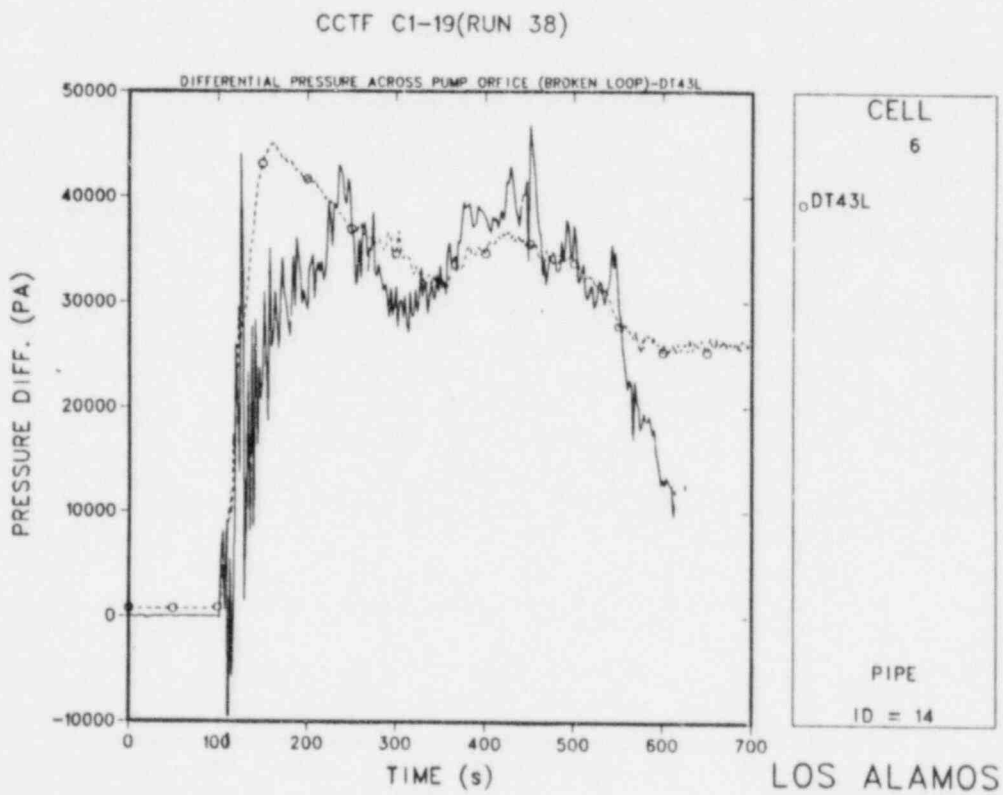

Fig. 10. Broken loop pump orifice differential pressure.

B. Temperature Skew Test (C1-20 Run 39)

The TRAC calculation for this test[4] was completed without any prior knowledge of the test results. The lower plenum and the downcomer fill rapidly during accumulator flow into the lower plenum. The downcomer continues to fill during accumulator flow into the cold legs. The calculation fills the downcomer more rapidly than the experiment (Fig. 11). There was not any liquid accumulation calculated in the cold legs, but in the experiment there was evidence of water in the pump simulator until 70 s. The calculated downcomer mass shows an oscillation period between 30 s and 80 s. With the exception of filling the downcomer somewhat early, there is good agreement between the experiment and the calculation. The core liquid mass (Fig. 12) also shows good agreement between the experiment and the calculation.

The measured and calculated temperature responses of the rods in two opposite core segments along the temperature skew direction are shown in Figs. 13 and 14. Inspection of the figures shows that, prior to water entering the core, the rods heatup at a similar rate, maintaining the initial temperature skew. There is a discrepancy between the measured and calculated initial temperature because the calculated temperature represents the average of several rods in the modeling segment. In the lower portion of the rod (0.38 m and 1.01 m) there is an earlier quench of the cold side of the core, but the temperature response of the midplane and above elevations is similar on both the hot and cold sides of the core. The hotter rod temperatures do not increase after core flooding begins, whereas the cooler rods continue to heat up. The peak clad temperatures are only 100 K different (whereas the initial temperatures were 350 K different). The quench times are identical for both sides of the core at the midplane and above (Fig. 15). The calculation reproduced these results accurately, except for a short period just as the core flooded when the calculation had oscillations of fluid between the core and the downcomer. These oscillations caused excessive cooling, which is especially noticeable on the cooler upper portions of the rods. Quench times are predicted well. The calculated pressures and loop flows were accurately predicted by the TRAC calculation and the comparisons are similar to those shown previously (Figs. 5, 9, and 10).

V. CONCLUSIONS

The TRAC calculation of the CCTF Skewed Radial Power Test (Run 38) agrees very well with the experimental data. The data and the calculation indicate that the bottom of all the rods quenched simultaneously across the core, that the remaining elevations quenched in the outer low power regions first, and then quenching proceeded toward the high power center region. At the core midplane, the difference in quench times was over 100 s. This behavior was expected because of the large radial power gradient (1.3/0.84) between the inner and outer core regions.

The TRAC calculation of the CCTF Skewed Temperature Profile Test (Run 39) also agrees very well with the experimental data. The data and the calculation indicate that there is more rapid quenching of the bottom of the rods on the cold side of the core than on the hot side. At the midplane and higher elevations there is very little difference in response between the rods on the hot and cold sides of the core. There was some delay in the turnaround time of the rods on the cold side, equalizing the peak clad temperatures. The

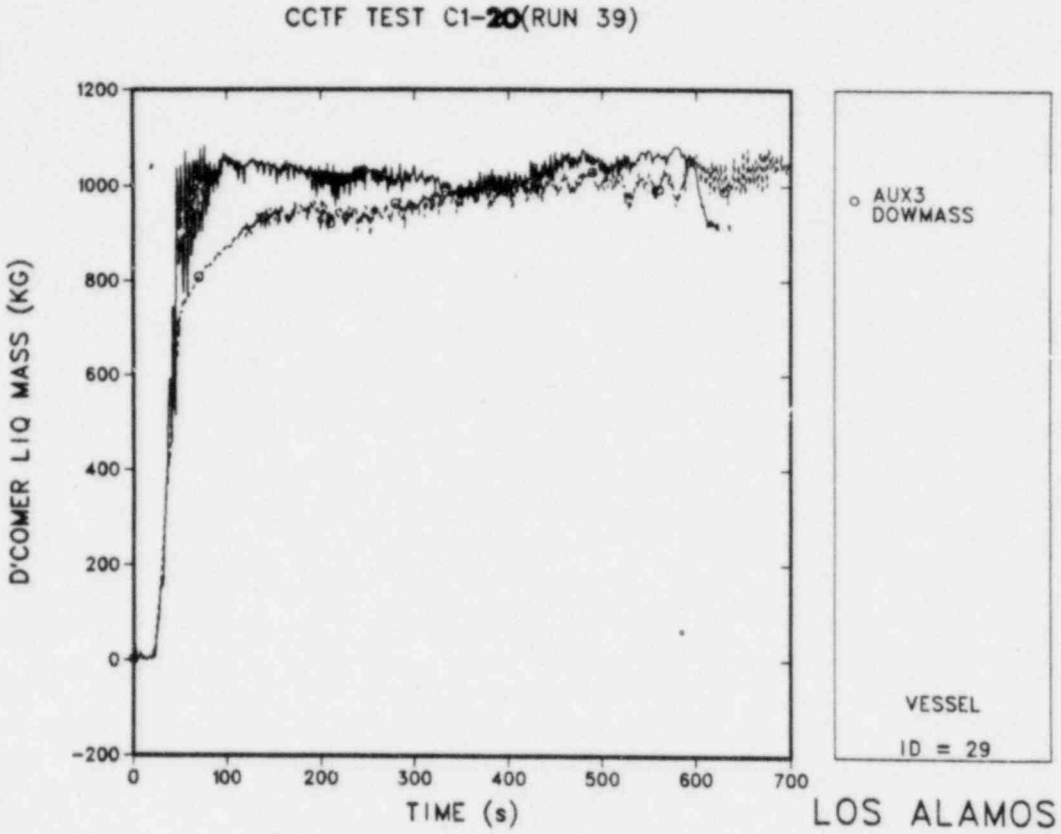

Fig. 11. Downcomer mass.

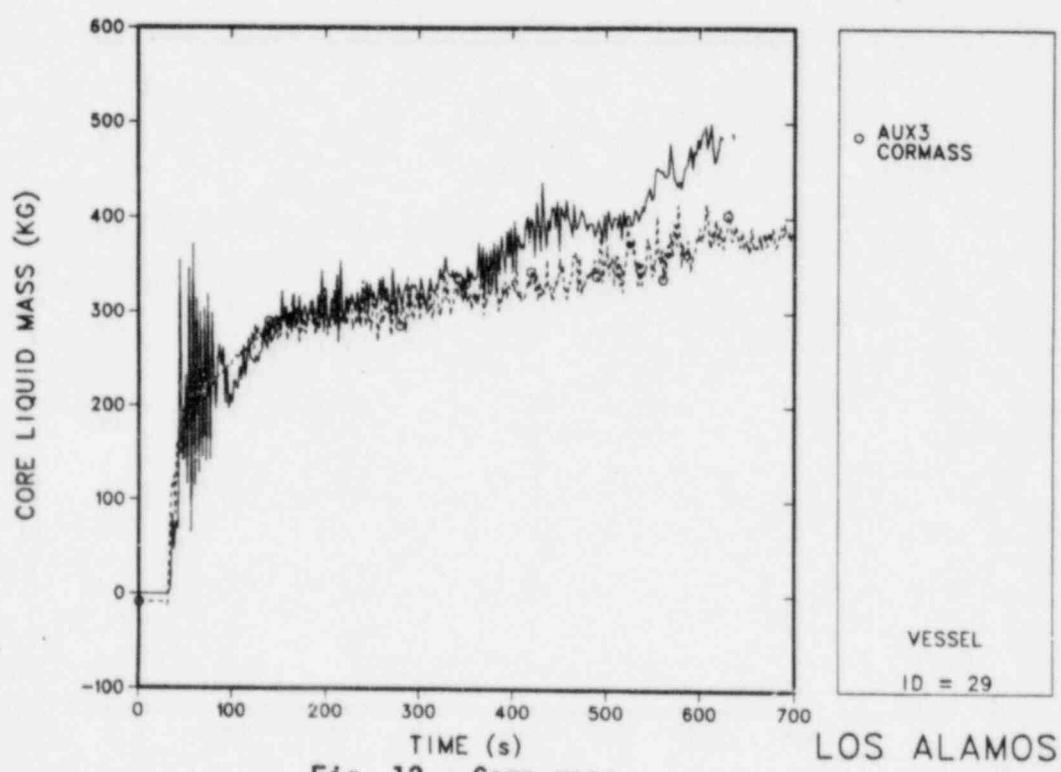

Fig. 12. Core mass.

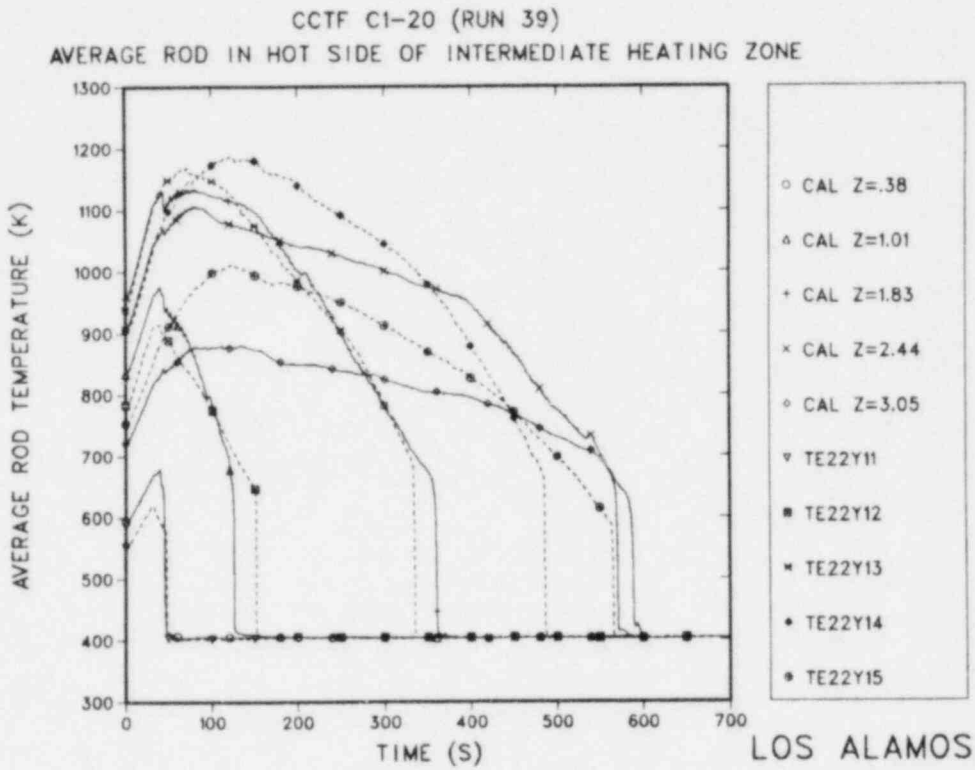

Fig. 13. Hot-side rod temperature.

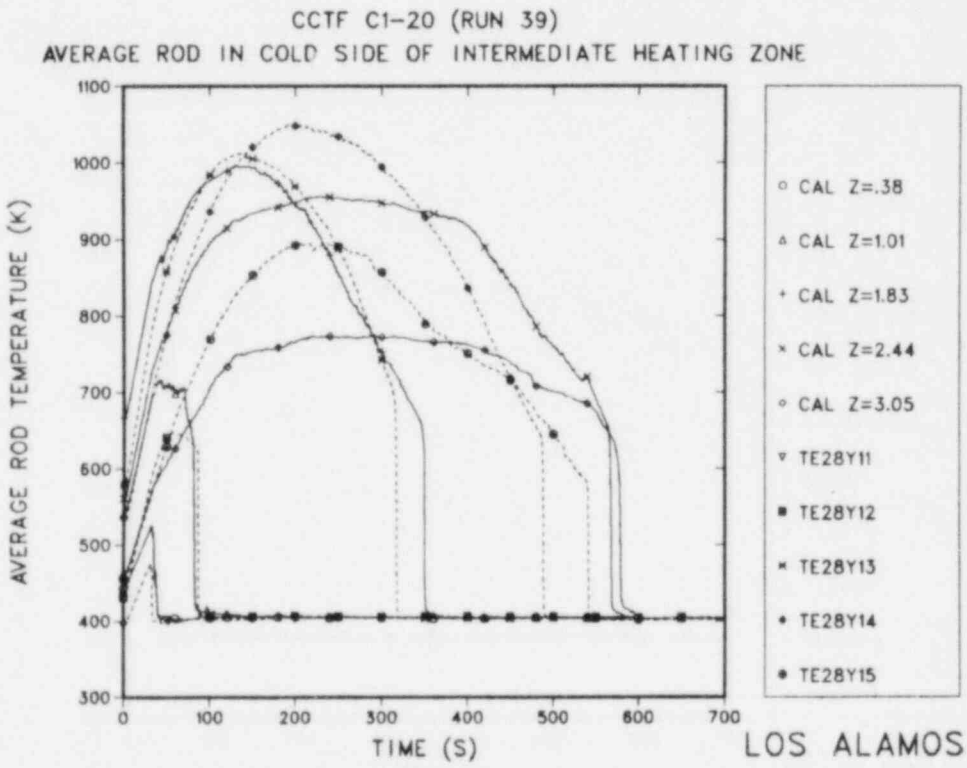

Fig. 14. Cold-side rod temperature.

explanation for this behavior is that the water level is the same on both sides of the core. In the lower part of the core the water level determines quenching. In the upper part of the core the quenching is determined by steam flow and entrainment. On the hotter side of the core the steam flow is increased because of the greater heat input due to the higher initial rod temperature.

The three-dimensional analysis capability of the thermal-hydraulic models of the TRAC code has been further verified by the good agreement between the data and code prediction.

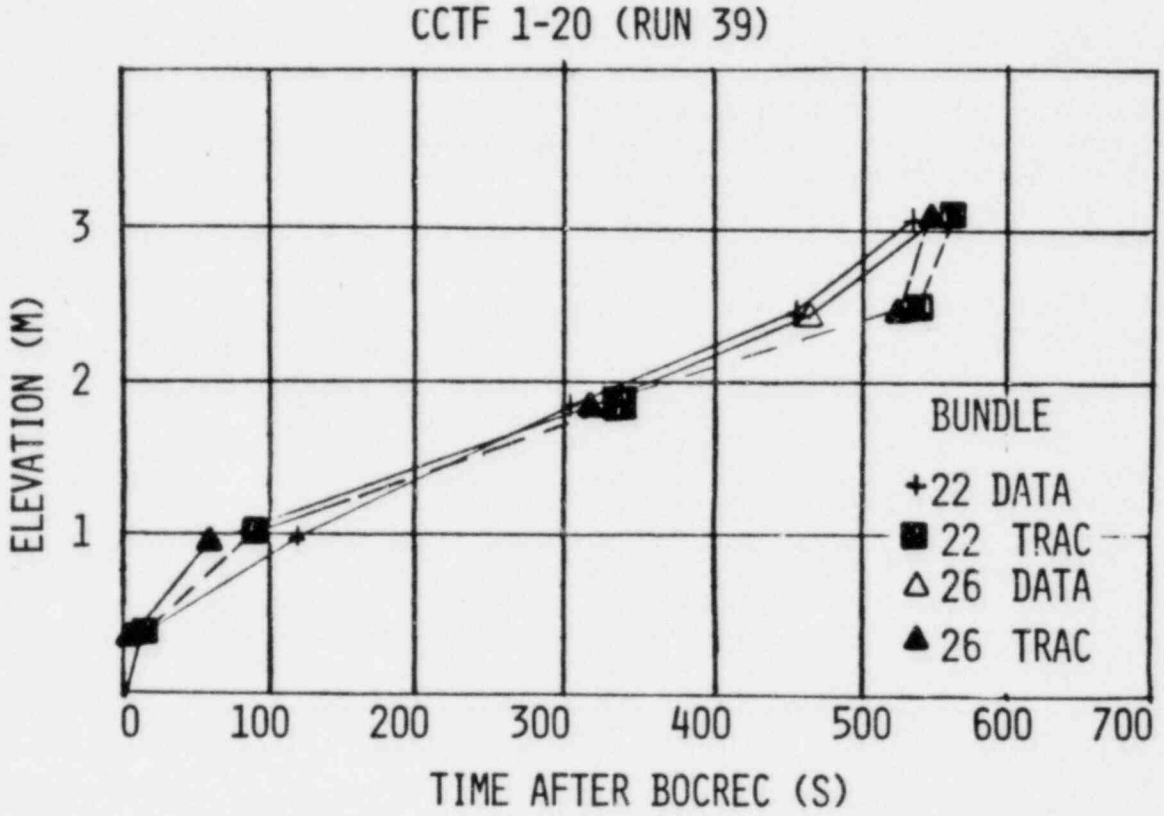

Fig. 15. Quench envelopes.

REFERENCES

1. "TRAC-PD2: An Advanced Best-Estimate Computer Program for Pressurized Water Reactor Loss-of-Coolant Accident Analysis," Los Alamos National Laboratory report LA-8709-MS (May 1981).

2. K. Hirano, personal communication.

3. K. Hirano, personal communication.

4. F. Motley, "The Effect of a Skewed Initial Temperature Distribution on the Reflood Transient," ANS Transactions, 39, 568-569 (November 1981).

SIMULATION OF SMALL-BREAK LOCA TESTS WITH NOTRUMP

Naugab Lee
Nuclear Technology Division
Westinghouse Electric Corporation
P. O. Box 355
Pittsburgh, PA 15230

ABSTRACT

Westinghouse has developed a small-break LOCA analysis model using the NOTRUMP code. This is a general purpose, one-dimensional code for thermal-hydraulic analyses. The core model of the code was utilized to simulate the small-break LOCA tests conducted at Oak Ridge National Laboratory (ORNL).

The simulation showed that the core model was properly working in calculating the mixture and collapsed liquid level during uncovering tests in the test bundle. These two parameters are important in the analysis of small-break LOCA consequences. The reflooding behavior at high pressures was also adequately simulated, including the expected initial decrease of mixture level at the start of reflooding due mainly to the sudden increase of system pressure.

This favorable comparison of the simulation results with the test data indicates that the core model of the NOTRUMP code provides a good model for the thermal-hydraulic behavior in the core during small-break LOCA transients.

INTRODUCTION

It is very important to know the mixture level in a pressurized water reactor (PWR) core during a small-break, loss-of-coolant accident (LOCA) to properly assess the fuel integrity. The void fraction below the mixture level is also important because it affects the reflooding flow rate during the accident and the flow rate is mainly controlled by the hydrostatic head difference between the downcomer and core zone. Therefore, any thermal-hydraulic code for analyzing reactor transients during a small-break LOCA must be able to calculate the mixture level and void fraction in the core adequately.

Westinghouse developed the NOTRUMP code (1) to analyze small-break LOCA transients of PWR's. NOTRUMP is a general one-dimensional network code. The fluid and metal volume of a problem are modeled by control volume (nodes) which are interconnected by links of fluid flow and heat transfer. Flow links connect two fluid nodes and heat links connect

fluid nodes and metal nodes. Then integral forms of the conservation equation in the nodes and links control the transients. Flow slip in two-phase flow is handled by using drift flux models or bubble rise models. The code has a flexible noding capability to analyze complicated thermal-hydraulic transients. "Boundary nodes" and "critical links" of the code provide a flexible way of imposing boundary conditions. In addition to the general thermal-hydraulic calculations, this code has an improved flow regime calculation for two-phase flows and it can handle a horizontal countercurrent flow. This feature is very useful in hot leg flow calculations during a reflux mode operation.

The purpose of this paper is to present the results of verification efforts of the NOTRUMP core model for application to small break LOCA transients. The test data of the small-break LOCA tests conducted at ORNL (2,3) were used.

NOTRUMP CORE MODEL

The core model of NOTRUMP is basically comprised of two parts:

1. A heat transfer model from fuel rods to fluid, including fuel model (core node).

2. A fluid flow model using fluid nodes and flow links.

The fuel rod model determines the radial temperature profile in a fuel rod and the heat flux at the rod surface using the inputs of thermal properties of fuel and cladding, rod geometries, and heat generation rate. The heat generation in the cladding due to metal-water reaction is also calculated with no limitation of steam availability. The effects of fuel gap pressure and expansion of fuel and cladding are also accounted for.

Heat transfer coefficients from rod to coolant are calculated from a set of correlations based on the rod temperature and coolant flow conditions of flow rate, fluid temperature, flow quality, and flow regime. A steam cooling correlation with radiation effect is used to calculate heat flux from the rod to the steam space above the mixture level.

The fluid flow part of the model is handled by using NOTRUMP fluid nodes and flow links with a bubble rise model to account for the steam separation from the mixture. The fluid nodes, which represent the fluid volumes in the core, are connected to the core nodes so that the rod heat flux is introduced into the fluid nodes.

One feature of NOTRUMP is its capability of stacking vertically connected fluid nodes. This capability allows the tracking of a single mixture level in the set of fluid nodes instead of tracking the mixture level in each of the connected fluid nodes. This eliminates the unrealistic "sandwich" problem of vapor and two-phase mixture in vertically connected fluid nodes.

ORNL SMALL-BREAK TRANSIENT TESTS

A series of small-break transient tests has been conducted at the Thermal Hydraulic Test Facilities (THTF) of ORNL. These tests included the bundle steady-state uncovering test (2), and the reflood test (3). The uncovering test was conducted in two series. The first series of the uncover tests and the reflood tests were used for verification work due to the availability of the official test data to the public at the time of this work.

The details of the test facility and procedure are presented in references (2) and (3). A brief explanation of the tests is provided here to help readers understand the simulation of the tests by NOTRUMP presented in this paper. The THTF is a high-pressure, thermal-hydraulic loop designed for use in transient heat transfer studies. The test bundle characteristics are shown in Table 1. The electrically heated rods used in the test bundle had stainless steel cladding and were filled with boron nitride and Inconel heating elements.

TABLE 1

Bundle Characteristics

Rod Array	8 x 8 on a square lattice
Rod Array Pitch	0.501 in.
Rod Diameter	0.374 in.
Heated Length of Rod	12 ft
Axial Power Profile	flat
Radial Power Distribution	uniform
Number of Heated Rods	60
Number of Unheated Rods	4

Both cladding and fluid temperatures were measured. The cladding temperature measurements were used to determine the mixture level in the test bundle and an overall differential pressure cell was used to measure the collapsed liquid level.

The uncovering test was started by boiling off water from the bundle which was originally filled with water. The inlet flow rates and power level were set so that a steady-state condition was reached during which a part of the test bundle was uncovered. Measurements were made at this steady-state condition. The high-pressure reflood test starts from the steady-state, partially uncovered bundle by opening the inlet flooding valve. Then the test section flow rate, system pressure, and inlet fluid temperature go through transients according to the THTF loop response.

SIMULATION

The core model of NOTRUMP is modeled for nuclear fuel rods. Therefore, a simple and straightforward modification was made to handle the electrically heated rods.

The ORNL tests were simulated by representing the heated section of the test bundle one-dimensionally with 12 one-foot-long core nodes and fluid nodes. Therefore, radial variation in the bundle was not considered. The bottom node of the heated section was connected to a boundary node by a critical flow link to impose the inlet flow rate boundary condition. The top node of the heated section was connected to one additional fluid node which worked as an upper plenum of the test bundle and this upper plenum was connected to a boundary node which is used to control the system pressure. This scheme is shown in Figure 1.

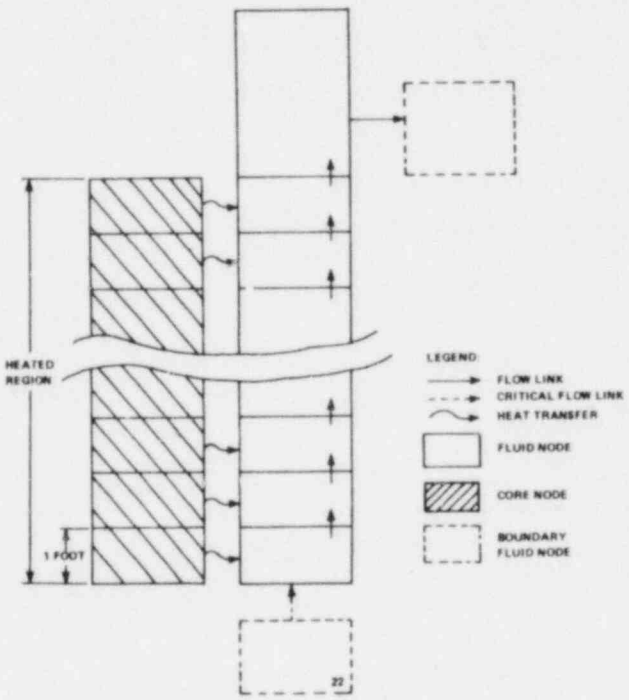

Figure 1. Schematic of Simulation

Four tests were selected for this simulation effort to cover a wide range of operational conditions of system pressure, flow rates, heat generation, and subcooling of inlet fluid. The boundary conditions for the uncovering tests are constants and can be obtained directly from the operating conditions as shown in Table 2. During these tests heat was lost to the environment and housing wall bundles during operation; therefore, these heat losses must be accounted for in the power generation rate. Anklam (4) estimated the heat losses as shown in Table 2. As will be shown in the discussion section, the calculated heat losses are good estimates.

TABLE 2

Operating Conditions of the Uncovering Tests

Test	Pressure (psia)	Mass Flux (lb/ft^2-sec)	Inlet Temp. (^oF)	Power (kw/ft)	Heat Loss (%)
3.02.10C	419	3.0	381	0.36	5.1
3.02.10E	617	3.6	408	0.41	1.2
3.02.10F	1018	2.1	464	0.27	22
3.02.10H	387	3.4	375	0.42	6.1

The high pressure reflood tests are transient processes and the reflood rate, inlet fluid temperature, and pressure are the results of the overall loop response in addition to the test bundle response. The purpose of this study is to calculate the bundle response only. Therefore, the transients of flooding rates, inlet fluid temperature, and system pressure were taken as boundary conditions of the test. These conditions are presented in Table 3.

The initial conditions for the uncovering simulation was a water-filled system which was slowly boiled off to uncover the heater bundle just as the test was conducted. The reflood test was started from the partially uncovered test bundle by imposing the boundary conditions shown in Table 3.

RESULTS AND DISCUSSION

It was mentioned that the test bundle lost heat to the environment and the estimated heat losses shown in Table 1 were used in the simulations. Therefore, it is important to see whether those estimated heat loss factors are reasonable. These check calculations were made using a simple one-dimensional heat and mass balance over the bundle.

Figure 2 shows a schematic relation of the fluid flows during an uncovering test. The mass and energy balance over the mixture zone can be written as:

$$\dot{M}_{in} - \dot{M}_{out} = 0 \qquad (1)$$

$$\dot{M}_{out} h_{out} - \dot{M}_{in} h_{in} = \int_0^{Z_m} \dot{q}\, dz \qquad (2)$$

The combination of Equations (1) and (2) gives

$$\dot{M}_{in} (h_{out} - h_{in}) = \int_0^{Z} \dot{q}\, dz \qquad (3)$$

TABLE 3

Boundary Conditions of Reflood Tests

Test	3.02.10C (power 0.36 kw/ft)								
Time (sec)	0.0	5.0	6.0	7.5	10.0	11.5	13.0	16.0	18.0
Flow Rate (gpm)	1.7	1.7	11.0	25.0	24	22	21	14.0	11.0
Pressure (psia)	415	415	418	425	440	465	495	705	745
Coolant Inlet Temp. (^{o}F)	375	375	125	225	330	350	370	370	370

Test	3.02.10E (power 0.41 kw/ft)							
Time (sec)	0.0	7.5	8.5	10	12.5	15	18	20.5
Flow Rate (gpm)	2.05	2.05	18	25	22	20	13	10
Pressure (psia)	620	620	622	635	665	735	935	995
Coolant Inlet Temp. (^{o}F)	400	400	180	310	375	395	400	400

Test	3.02.10F (power 0.27 kw/ft)							
Time (sec)	0	4	5	7	42	52	70	90
Flow Rate (gpm)	1.16	1.16	2.85	2.78	2.72	2.72	2.72	2.72
Pressure (psia)	1018	1018	1018	1023	1023	1027	1027	1017
Coolant Inlet Temp. (^{o}F)	466	466	466	468	475	475	473	472

Test	3.02.10H (power 0.42 kw/ft)						
Time (sec)	0	6.0	7.0	15.0	22.0	30	47.0
Flow Rate (gpm)	1.75	1.75	4.0	5.5	5.3	5.2	5.1
Pressure (psia)	346	346	347	358	377	417	515
Coolant Inlet Temp. (^{o}F)	368	368	220	250	319	360	368

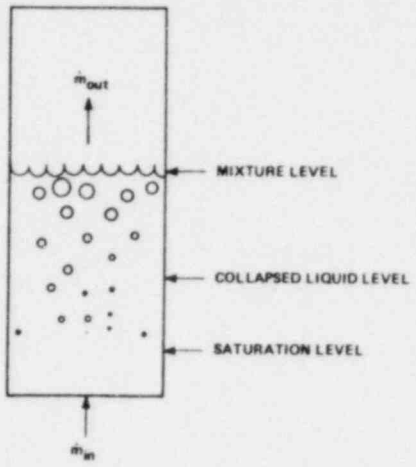

Figure 2. Schematic Relation in Test Bundle During Uncovery Test

Since the axial power distribution is flat in the test and all generated heat is transferred to fluid below the mixture level (Z_m), Eq. (3) can be rewritten as

$$Z_m = \frac{\dot{M}_{in}\,(h_{out} - h_{in})}{\dot{q}_{gen}} \qquad (4)$$

The parameters, $\dot{M}_{in}$ and h_{in} are known for the test and the enthalpy of the exiting steam can be taken as the enthalpy of the saturated steam as shown by Lee et al. (5). The heat input is calculated from the nominal operating power and the heat loss factors shown in Table 2. Equation (4) was used to calculate the mixture level shown in Table 4. The calculated mixture levels are slightly higher than those of the test data (see Table 5) which is expected due to neglection of the axial heat conduction at the mixture and steam interface. If this heat conduction at the interface is considered, it is believed the heat loss factors are reasonably good.

The reported data of mixture and collapsed liquid level of the uncovering tests were presented as the distance from the saturation level (Z_{sat}) in the bundle where the subcooled inlet liquid is heated to the saturation temperature. The saturation level was calculated using a similar mass and energy balance as above.

The result is expressed as

$$Z_{sat} = \frac{\dot{M}_{in}[(h_l)_{sat} - h_{in}]}{\dot{q}_{gen}} \qquad (5)$$

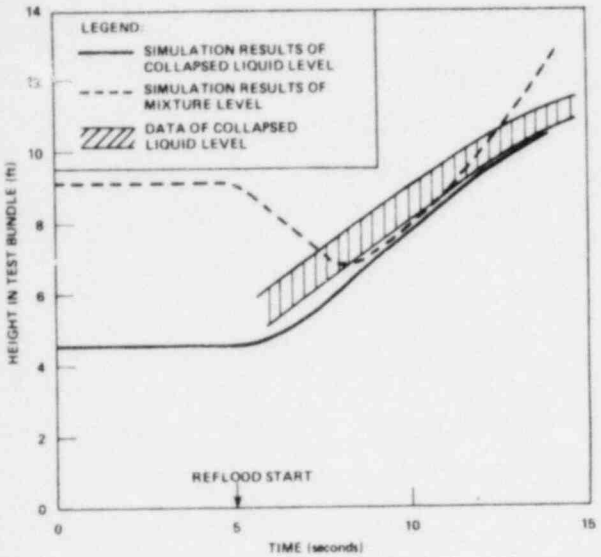

Figure 3.
Simulation Results of Reflood Test C

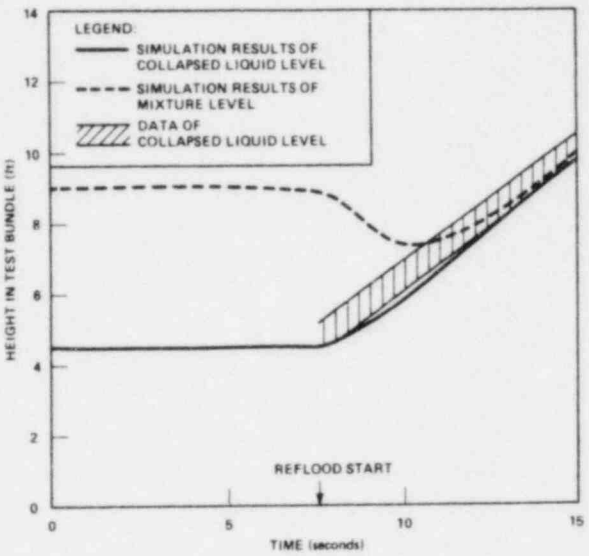

Figure 4.
Simulation Results of Reflood Test E

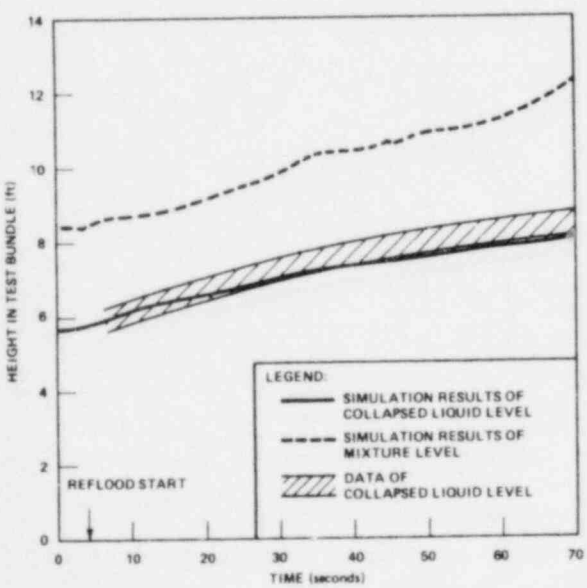

Figure 5.
Simulation Results of Reflood Test F

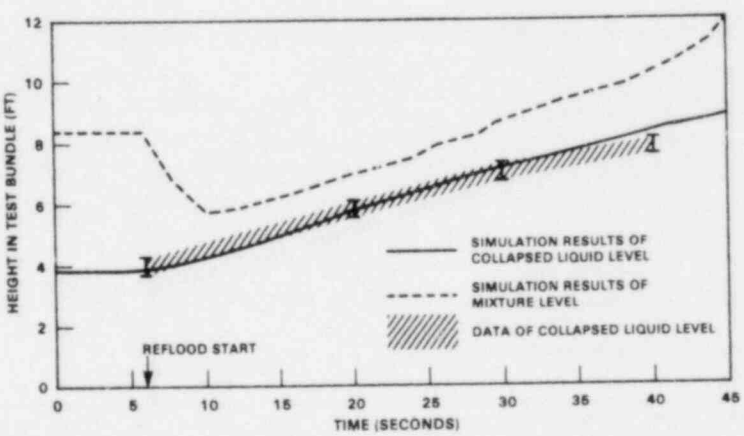

Figure 6.
Simulation Results of Reflood Test H

The calculated saturation levels are also presented in Table 4.

TABLE 4

Calculated Saturation and Mixture Level by Equations (4) and (5)

Test	Saturation Level (ft)	Mixture Level (ft)
C	0.65	9.27
E	1.02	8.81
F	0.79	8.81
H	0.65	8.67

Table 5 presents the simulation results of the uncovering test compared with the test data. As discussed, the mixture level and collapsed liquid level are the most important parameters of these tests. It can be observed that the simulation results are in good agreement with the test data within the estimated uncertainties.

The simulation results of the reflooding tests are presented in Figures 3 through 6. These figures show the calculated mixture level and collapsed liquid level transients. The collapsed liquid level data bands are also presented in the figures. Again the simulation results are in good agreement with the data. Also it is noted that the slopes of simulated collapsed liquid level transients are in good agreement with the data which indicates good simulation of the rate of water accumulation in the bundle.

TABLE 5

Results of Uncovering Test Simulation

Test	Mixture Level (ft)		Collapsed Liquid Level (ft)	
	Simulation	Data	Simulation	Data
C	8.55	8.63±0.49	3.96	4.30±0.33
E	7.98	8.01±0.49	3.54	4.30±0.36
F	7.68	7.58±0.49	4.96	5.81±0.36
H	7.86	7.28±0.49	3.42	3.41±0.33

One interesting phenomenon observed from the result of the simulations is the decrease of mixture level during the initial period of fast transient operations of reflood tests. This decrease is expected due to the pressure rise and the introduction of cold water into the test bundle. The NOTRUMP capability of predicting this behavior shows that the code is capable of calculating complicated thermal-hydraulic behavior. Note that the quench front in the bundle does not follow the mixture level

immediately during this initial period due to the time required to heat up the uncovered cladding. This fact can be observed in Figure 7. There is a time lag between the mixture level and the quench front from 6 to about 14 seconds for this case.

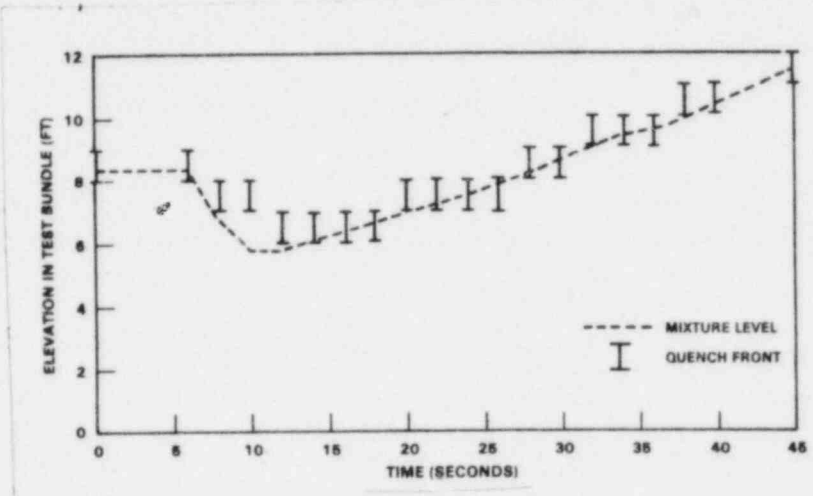

Figure 7.

Comparison Between Quench Front and Mixture Level for Reflood Test H

CONCLUSIONS

It is demonstrated that the NOTRUMP core model can calculate thermal hydraulic behaviors observed in the small-break LOCA transient tests. Also, the code was able to predict the initial mixture level decrease at the start of the reflood tests. This effect is expected due to the sharp increase in pressure and the introduction of highly subcooled water into the heater bundle.

Therefore, it is believed the the NOTRUMP core model is able to handle very well the flow transients in the core which follow a small break LOCA of a PWR.

NOMENCLATURES

h_m = enthalpy of bundle inlet fluid

$(h_l)_{sat}$ = enthalpy of saturate liquid

h_{out} = enthalpy of steam leaving the mixture in the bundle

$\dot{M}_{in}$ = inlet flow rate

$\dot{M}_{out}$ = outlet flow rate

$\dot{q}$ = heat input rate to the fluid in bundle

$\dot{q}_{gen}$ = heat generation rate in the heater rods

Z_m = mixture level

Z_{sat} = saturation level

Z = elevation

REFERENCES

(1) Meyer, P. E. and Frick, G. K., "NOTRUMP: A Nodal Transient Steam Generator and General Network Code", WCAP 9237, Westinghouse Electric Corporation, February (1978).

(2) Anklam, T. M., "ORNL Small Break LOCA Heat Transfer Test Series I: Two-Phase Mixture Level Swell Results", NUREG/CR-2115, August (1981).

(3) Anklam, T. M., "ORNL Small Break LOCA Heat Transfer Test Series I: High Pressure Reflood Analysis", NUREG/CR-2114, August (1981).

(4) Anklam, T. M., "ORNL Small Break LOCA Heat Transfer Test Series I: Rod Bundle Heat Transfer Analysis", NUREG/CR-2052, August (1981).

(5) Lee, N., et al., "Heat Transfer Mechanism During Rod Bundle Reflooding", presented at the 3rd CSNI Specialist Meeting, Pasadena, California, March 23-25, (1981).

CROSS SECTION NEEDS: DETERMINATION AND STATUS*

C. R. Weisbin, D. Gilai,** G. deSaussure, and R. T. Santoro
Oak Ridge National Laboratory
Oak Ridge, Tennessee 37830

ABSTRACT

This paper summarizes the highlights and conclusions of a recent review[1] by the authors entitled "Meeting Cross Section Requirements for Nuclear Energy Design." The purpose of that paper was to provide a status report of some perceived current requirements in cross-section data for nuclear energy programs.

INTRODUCTION

It is generally accepted that the uncertainties in the prediction of reactor properties will result in excessive design margins and, as a result, costs. There are, however, only a few good published studies that demonstrate the consequences of uncertainties in nuclear data. Significant complexity is introduced in such studies when factors such as feedback of operating data, design flexibility in accommodating errors, calibration of prototypic experiments, methods and modeling uncertainties, etc., are included in a systematic way. The work of Greebler et al.,[2] for fast reactors was completed ten years ago and an update of this work is very much needed. The investigations of Becker and Harris[3] for thermal reactors show there are potentially substantial impacts of nuclear data uncertainties on the light water fuel cycle. Critical review of such important conclusions by vendor and utility organizations would be most useful. Some work has also been carried out to assess the impacts of cross-section uncertainties on fusion reactor design,[4,5] but this work is still in its early stages.

The cross section data, and the uncertainties in these data, have changed dramatically since the early 1970's and the necessary updating must be completed and made available. High accuracy measurements often require several years of planning, data collecting, and analyses. Also, the needs of nuclear energy programs change and as data requirements are met, new problems identify different and new data needs. An attempt is made here to update the nuclear data requirements and to summarize the state of the data as of 1981 for the current generation of reactors.

DESIGN PARAMETERS AND TARGET ACCURACIES: A CRUCIAL BUT SOMEWHAT AMBIGUOUS FORCE

Target accuracies and achievable accuracies for light water reactor parameters are proprietary so that published figures must be regarded as mere guidelines. Furthermore, as pointed out by Crowther et al.,[6] "the accuracy target is a moving one. The standards for predictive accuracy have progressively become tighter as reactor performance has been improved and constraints have been sharpened." For fast reactors, figures from different sources are not always

*Research supported by the U.S. Department of Energy under Contract W-7405-eng-26 with the Union Carbide Corporation.
**Ben-Gurion University of the Negev, P.O. Box 653, Beer-Sheva, ISRAEL

consistent illustrating that target accuracies reflect subjective judgement in the compromise between design conservatism and cost, and that there are different standards by which to estimate achieved accuracies. For instance adjusted data may meet some requirements but some would prefer the prediction of safety parameters[7] to be based only on differential data with integral measurements playing a confirmatory role.

Target and achievable accuracies compiled from the literature are presented in Tables 2.2 through 2.10 of Ref. 1. These apply to thermal and fast reactors, shielding, fuel handling and fusion reactors. As an example, McFarlane[8] tabulates uncertainties and design targets for demonstration sized LMFBR's in the Federal Republic of Germany as well as in the United States. The status of uncertainties in 1972 as well as the present status for SNR-300 and CRBR is described. Table 1 is reproduced below indicating that current LMFBR designs appear close to meeting their targets. However, the targets were set in the early 1970's and based on the capabilities at that time. A revision of target accuracies is probably desirable.

Table 1. Uncertainties in Demonstration Reactor Design Parameters

	Uncertainty,[a] %					
	Status				Target[e]	
Parameter	FRG[b] (1972)	USA (1972)[c]	SNR-300[d] (1978)	CRBR (1980)	FRG[b]	USA[c]
k_{eff}	1.1	1.6	0.4	0.7	0.9	0.6
peak/average power	2.7	12	2.5	~4.7[f]	2-3	3
Control rod worth	6	15	4-10	5	6	3
Doppler coefficient	6-12	15	--	10[g]	6-12	10
Sodium void reactivity	12-18	~50	15	20	9	17

[a] 1 σ level, where σ is the standard deviation of a normal distribution.
[b] Federal Republic of Germany, see Ref. 9.
[c] See Ref. 10.
[d] See Ref. 11.
[e] As of 1972 as defined in Refs. 9 and 10.
[f] Includes many engineering uncertainties; only about 2% comes from ability to calculate power distribution in the criticals. Also just for peak power--may be correlated to average.
[g] Mainly from SEFOR experiments.

In comparing goals and achieved accuracies across countries one must be particularly careful, since arbitrary multiples of the uncertainties are chosen in order to add what is thought to be a proper amount of conservatism.

McFarlane[8] notes that CRBR typically uses 1 σ for design margins and 3 σ for safety margins, while the German program typically uses 1.7 σ, corresponding to 90% probability.

Another picture of an LMFBR Program is obtained from the paper of Hammer,[12] where uncertainties on design parameters are compared to target accuracies for commercial fast power plants. In this case, target accuracies are considerably more stringent than those stated in Table 1 for demonstration plants. Target accuracies for shielding calculations are often related to specific design issues and hence strongly dependent on a particular design. Approximations in methods and modeling rather than uncertainties in basic nuclear data may dominate shielding analysis.[13] In general, there is a desire to reproduce prototypic shielding design experiments to within 10-20% while deep penetration dose rates are desired to within factors of 2-3.

The nuclear data requirements for the magnetic fusion energy program were delineated by Head[14] at the IAEA Advisory Group Meeting on Nuclear Data for Fusion Technology in December 1973. Detailed discussions on the specific data needs and target accuracies for fusion reactor design,[15] nuclear heating,[16] activation,[17] radiation damage,[18] shielding,[19] and hybrid reactor studies[20] were also presented at this meeting. More recent reviews summarizing the changes and modifications to these data requirements have been published by Haight,[21] Browne and Lisowski,[22] and Bhat and Abdou.[23] More precise data are required for analyzing the nuclear performance of the blanket and superconducting magnets than the other components of the reactor and reactor building. The tritium recovery and nuclear heating rates in the blanket must be accurately determined since these strongly impact the economics of the reactor. While the data accuracies for the shield can be less than those for the blanket, accurate prediction of the radiation leaking through the shield and incident on the cryogenic magnets (particularly in tokamak reactors) is necessary for estimating nuclear responses.

APPROACH TOWARD DETERMINATION OF MEASURED AND EVALUATED DIFFERENTIAL CROSS SECTION DATA

Measurements of differential cross section data are closely interrelated. The interpretation, evaluation, and representation of experimental results is intimately interwoven with the development of nuclear models. These models are based on studies of systematic trends which necessitate an extensive data base. Nuclear models are necessary for those cross sections which cannot be measured directly. In other cases, cross sections are best evaluated by combining the results of direct measurements with nuclear model calculations. Measurements and nuclear theory are interwoven also at a much more fundamental level; indeed the results of most direct measurements are usually interpreted, fitted, and represented with some parametrization based on nuclear models, such as the Wigner Eisenbud reaction theory,[25] etc. Even at the level of data reduction, continuous use is made of nuclear theory to compute corrections to the measurements (due to changes in efficiency of detectors, multiple scattering, angular distributions) and to interpolate and extrapolate the data. Similarly throughout the evaluation process the results of nuclear theory are used as tools to check the internal consistency of the data base. The use of these "tools" in evaluating data for the interaction of neutrons with light elements has been described in a recent paper of L. Stewart.[28] Because of the interrelationship of different types of differential cross section data

(e.g., the role of measurement standards) and of experimental data and nuclear models, it is often desirable to improve a broad data base rather than address measurements only to narrow specific requirements.

Experimental uncertainties are dominated by systematic errors which are not necessarily reduced by repeated measurements. The reduction of uncertainties requires new experimental techniques or improved methods of data reduction, interpretation or evaluation. Indeed, since differential cross section measurements of high accuracy can take many years, there are those who suggest that specific reactor problems should be addressed through the use of appropriate integral measurements while differential cross sections are developed to treat unforeseen problems and those problems which cannot currently be satisfactorily addressed with integral measurements. This view is balanced by those who believe that nuclear data programs should support the needs of reactor design and minimize the role of integral experiments to a confirmatory mode. Both of these views manifest themselves in the latest U.S. compilation of requests for nuclear data,[24] which is now under review by the Cross Section Evaluation Working Group. It seems obvious that a better definition of need would be facilitated by the existence of high quality uncertainty files for nuclear data. Current information on uncertainties in the ENDF/B file is very incomplete and often unreliable; improvement of the quantity and quality of this data should be a major goal of ENDF/B-VI.

INFERRED NEEDS FROM ANALYSIS OF INTEGRAL EXPERIMENTS

The adequacy of the Evaluated Nuclear Data File is tested, for several applications, against results of benchmark integral experiments.[29] These benchmarks currently test only a limited domain of important nuclear data (e.g., there is a need for fast reactor burnup benchmarks, high temperature experiments, etc.) and the quality of the experimental uncertainties of these benchmarks is very uneven. The discrepancies between calculated and measured integral quantities may point to data problems, but could also be due to methods or modeling approximations or to errors in the integral benchmark measurement. Only for the light water reactor TRX series was there any attempt by CSEWG to formally estimate methods and data uncertainties separately. Much more effort in this area is sorely needed in order to derive specific recommendations from the data testing process.

Important differences encountered in data testing still persist in several areas. Needs are suggested in the areas of both differential and integral measurements. For example:

1. In Fast Benchmarks:

   a. The ^{238}U capture to ^{239}Pu (or ^{235}U) fission ratio is overpredicted in large dilute assemblies (by ~3-6% relative to ^{25}f and 4-8% relative to ^{49}f). This discrepancy is most sensitive to the $^{238}U(n,\gamma)$ cross section in the range 10-100 keV. This is a longstanding discrepancy. The ENDF/B-V ^{238}U evaluators have stated emphatically that the differential measurements do not support the adjustment required to remove the observed overprediction.

   b. The central fissile worth is overpredicted (calculation/experiment values are in the range of 1.1-1.2 for ^{239}Pu and ^{235}U worths) in the softer spectrum LMFBR assemblies. The interpretation of this discrepancy is not clear.

c. The ^{238}U to ^{235}U fission ratios in small fast assemblies is not predicted correctly (underprediction in JEZEBEL by 8-10%, overprediction in GODIVA by 2-4%). The discrepancy is usually interpreted as pointing to an inadequate evaluation of the neutron-induced neutron emission spectra in fissile materials.

2. In Thermal Benchmarks:

a. Although $^{25}\delta$ in the TRX assemblies hardly changed in going from ENDF/B-IV to ENDF/B-V, and the comparison with integral experiments remains good, it should be noted that the ENDF/B-V ^{235}U fission resonance integral is 282 b (above 0.5 eV), while the best integral results is 275 ± 5b. Taking into account that stated uncertainties of the integral measurements may be smaller than those of differential capture measurements, a re-evaluation of ^{235}U fission and capture appears worthwhile.

b. For Pu-H_2O assemblies, calculated k_{eff} using ENDF/B-V averages 1.011. The overall picture is unchanged from Version IV. The large scatter of k_{eff} (2.7%) shows no convincing trends and is attributed to uncertainties of plutonium content. This scatter makes it difficult to draw any detailed conclusions about data inadequacies. In any case, sensitivities are sufficiently small that it is hard to explain the high k_{eff} on the basis of obvious data deficiencies. Thus, despite a good deal of work and the analysis of more benchmarks, the picture is about the same as it was at the time of the ENDF/B-IV data report. There remains a need for several highly accurate benchmark critical experiments to be performed. In addition, careful studies should be made to identify the source of the high k_{eff} values.

3. Shielding Benchmarks

a. Data testing suggests inadequate (8-20% difference) total cross sections of C, Ni, Cr, in the 1-10 MeV region and poor agreement for capture gamma-ray production data for Cl and Cr below 6 and 4.5 MeV respectively.

b. Additional benchmark candidates exist, including measurements in concrete and air. Only recently has a major series of fusion shielding integral experiments been documented as CSEWG benchmarks, and efforts are currently under way to test the performance of ENDF/B-V relative to these measurements.

c. Pulsed sphere studies indicate that problems (15-30% discrepancies) remain in the analysis of spectra from 14-MeV neutron-induced reactions in Mg, Ca, Ti, V, Cr, Ni, Cu, Nb, and W. Calculated fast-neutron gamma-ray production for S, K, and Cu should be substantially increased if experimental results of benchmarks SB3 are valid.

d. Many materials available from ENDF/B-V have no photon-production data. Among them are ^{3}He, ^{11}B, Zr, Cd, ^{152}Eu, ^{154}Eu, the Gd isotopes, ^{197}Au, ^{233}Pa, ^{233}U, ^{234}U, ^{236}U, ^{237}Np, and ^{238}Pu. These represent areas in which data are needed.

4. Fission-Product and Actinide Benchmarks

a. The data for which the calculation/experiment ratio deviates significantly from unity (relative to crudely estimated uncertainties) is for neutron capture in ^{108}Pd, ^{109}Ag, ^{134}Xe, ^{137}Cs, ^{142}Ce, ^{146}Nd, ^{148}Nd, ^{150}Nd, ^{152}Sm, ^{144}Nd, ^{145}Nd, ^{149}Sm, $^{151}\varepsilon\xi$, ^{154}Eu, ^{242}Pu, ^{241}Am, and ^{243}Am.

b. In general, experimental gamma decay energies at short cooling times (<100 sec) are low at low energies (<0.8 MeV) and high at high energies (>1.6 MeV) in comparison to calculated energies.

c. In general, experimental beta decay energies are high at all cooling times for low energies (<1.4 MeV) and low for high energies (>1.8 Mev).

5. Dosimetry Benchmarks

a. Discrepancies are defined here to exist when the calculation/experiment ratio deviates from unity by more than 10%. The reactions include Al(n,p), Mn(n,2n), $^{47}Ti(n,p)$, $^{48}Ti(n,p)$, $^{58}Ni(n,2n)$, $^{63}Cu(n,\alpha)$ $^{126}I(n,2n)$, $^{232}Th(n,\gamma)$, ^{6}Li(n, tot He), ^{10}B(n, tot He), $^{58}Fe(n,\gamma)$ and $^{237}Np(n,f)$.

b. There is not CSEWG experimental dosimetry data for $^{23}Na,(n,\gamma)$, $^{65}Cu(n,2n)$, or $^{60}Ni(n,p)$. High energy threshold reactions [i.e., $^{58}Ni(n,2n)$] should be dropped or a suitable spectrum adopted. Other reactions [e.g., $^{93}Nb(n,n')$, $^{103}Rh(n,n')$, $^{199}Hg(n,n')$] are in demand and should be considered for future libraries. Uncertainties should be developed which quantitatively characterize the spectrum of all fields used in CSEWG dosimetry testing.

6. Fusion Applications

a. Total cross section and photon-production data with accuracies between ±10-15% in the energy range below a few MeV to ~50 MeV are required to meet shielding needs for both test facilities and reactors. Data for radiation damage and dosimetry studies are required with accuracies of ±10-40% over this same energy region (see 2.b). The $^{7}Li(n,n',\alpha)t$ cross section must also be reevaluated to resolve problems of tritium breeding.

SUMMARY RECOMMENDATIONS

Many needs were identified in the section on Inferred Needs from Analysis of Integral Experiments, and these are by no means exhaustive. As noted previously, benchmarks test only a limited domain of important data and perceived discrepancies cannot always point clearly to the specific data in need of improvement. From the material in the previous section, other review papers, and the data request lists, we highlight a few proposed measurements and/or evaluations for particular consideration.

These include:

1. The ^{235}U fission cross section (a standard) requested to 1% accuracy up to at least 14 MeV (an energy where absolute measurements have been performed with neutrons from the D-T reaction).

2. The value of ν (S.F.) for ^{252}Cf requested to 0.25% accuracy. (The recent measurement of R. R. Spencer, when finalized, might satisfy this request.)

3. The cross sections of the fertile and fissile nuclei in the resonance region (below 20 keV).

4. The cross sections of the fissile and fertile nuclei below 1 eV.

5. The spectra of secondary neutrons emitted from scattering and fission in ^{235}U, ^{238}U, and ^{239}Pu.

6. Reevaluation of the $^{7}Li(n,n',\alpha)t$ reaction.

In addition there is a consensus of measurers, evaluators, and designers that data covariance files need to be improved. We also perceive a need for a more extensive documentation of the process by which design requirements and results of data testing lead to specific requests for measurements and evaluation. Some of these measurements/evaluations are already being addressed.

REFERENCES

1. C. R. Weisbin, D. Gilai, G. deSaussure, and R. .. Santoro, "Meeting Cross Section Requirements for Nuclear Energy Design," ORNL/TM-8220 (May 1982), accepted for publication in Annals of Nuclear Energy.

2. P. Greebler, et al., "Implications of Nuclear Data Uncertainties in Reactor Design," 2nd International Conference on Nuclear Data for Reactors, Helsinki, CN-26/102 (June 1970).

3. M. Becker and D. R. Harris, "Sensitivity of Nuclear Fuel Cycle Cost to Uncertainties in Nuclear Data," EPRI NP-1632 (1980).

4. S. A. W. Gerstl, D. J. Dudziak and D. W. Muir, "The Application of Sensitivity Analysis to Nuclear Data Assessment," Proceedings of Specialists Meeting on Sensitivity Studies and Shielding Benchmarks, Paris, France (October 7-9, 1975).

5. R. G. Alsmiller, J. Barish, C. R. Weisbin, "Uncertainties in Calculated Heating and Radiation Damage in the Toroidal Field Coil of a Tokamak Experimental Power Reactor Due to Neutron Cross Section Errors," Nucl. Tech., Volume 34 (August 1977).

6. R. L. Crowther, et al., "Feedback of Reactor Operating Data to Nuclear Methods Development," Advances in Reactor Physics, CONF-780401 (April 1978).

7. J. Rowlands, BNL-NCS-51363, I, 23 (1981).

8. H. McFarlane, "The Use of Critical Experiments in CRBR Design: Status and Historical Perspective," ANL-80-119 (November 1980).

9. H. Kusters, "Progress in Fast Reactor Physics in the Federal Republic of Germany," KFK-1632 (August 1973).

10. P. Greebler and B. A. Hutchins, "Significance of Integral Parameters in Design and Performance of Fast Breeder Reactors," New Developments in Reactor Physics and Shielding, CONF-720901, pp. 928-939.

11. F. Helm, "Summary of Results for the SNEAK-9 Series of Critical Experiments and Conclusions for the Accuracy of Predicted Physics Parameters of the SNR-300," KFK-2586 (August 1978).

12. P. Hammer, "Nuclear Data Needs for Plutonium Breeders," Nuclear Cross Sections for Technology, NBS Special Publication 594, p.6 (October 1979).

13. J. Butler, "Nuclear Data for Reactor Shielding," Neutron Physics and Nuclear Data, Proceedings of International Conference, p.28, Harwell, England (September 1978).

14. C. R. Head, "Nuclear Data Requirements of the Magnetic Fusion Power Program of the United States of America," Proceedings of the Advisory Group Meeting on Nuclear Data for Fusion Reactor Technology organized by IAEA, Vienna, IAEA-TECDOC-223, p.1 (1979).

15 G. Constantine, "Nuclear Data Requirements for Fusion Reactor Design, Neutronics Design, Blanket Neutronics and Tritium Breeding," Proceedings of the Advisory Group Meeting on Nuclear Data for Fusion Reactor Technology organized by IAEA, Vienna IAEA-TECDOC-223, p.11 (1979).

16. Y. Seki, "Review of Nuclear Heating in Fusion Reactors," Proceedings of the Advisory Group Meeting on Nuclear Data for Fusion Reactor Technology organized by IAEA, Vienna, IAEA, IAEA-TECDOC-223, p.31 (1979).

17. O. N. Jarvis, "Nuclear Data Requirements for Transmutation and Activation of Reactor Wall and Structural Materials," Proceedings of the Advisory Group Meeting on Nuclear Data for Fusion Reactor Technology organized by IAEA, Vienna, IAEA-TECDOC-223, p.47 (1979).

18. S. M. Qaim, "Nuclear Data Needs for Radiation Damage Studies Relevant to Fusion Reactor Technology," Proceedings of the Advisory Group Meeting on Nuclear Data for Fusion Reactor Technology organized by IAEA, Vienna, IAEA-TECDOC-223, p.75 (1979).

19. M. A. Abdou, "Nuclear Data Requirements for Fusion Reactor Shielding," Proceedings of the Advisory Group Meeting on Nuclear Data for Fusion Reactor of the Advisory Gorup Meeting on Nuclear Data for Fusion Reactor Technology organized by IAEA, Vienna, IAEA-TECDOC-223, p.91 (1979).

20. D. V. Markovskii and G. E. Shatalov, "Neutron Data for Hybrid Reactor Calculations," Proceedings of the Advisory Group Meeting on Nuclear Data for Fusion Reactor Technology organized by IAEA, Vienna, IAEA-TECDOC-223, p.111 (1979).

21. R. C. Haight, "Neutron Cross Sections for Fusion," Proceedings of the International Conference on Nuclear Data for Technology, NBS Spec. Pub. 594, Knoxville, TN, pp. 228-238 (October 1979).

22. J. C. Browne and P. W. Lisowski, "Status of High Energy Neutron Cross Sections," BNL-NCS-51245, p.215 (1980).

23. M. R. Bhat and M. A. Abdou, "Nuclear Data Requirements for Fusion Reactor Nucleonics," Proc. of the Fourth Topical Meeting on the Technology of Controlled Nuclear Fusion, King of Prussia, PA. (October 14-17, 1980).

24. Compilation of Requests for Nuclear Data, BNL-NCS-51354 (March 1981).

25. E. P. Wigner and L. Eisenbud, "Higher Angular Momenta and Long Range Interaction in Resonance Reaction," Phys. Rev. 72, p.29 (1947).

26. H. Fesbach, C. E. Porter and V. F. Weisskopf, "Model for Nuclear Reactions with Neutrons," Phys. Rev. 96, p.448 (1954).

27. D. G. Madland, "Prompt Fission Neutron Spectra and $\bar{\nu}_p$," Proceedings of the Conference on Nuclear Data Evaluation Methods and Procedures held at BNL September 22-25, 1980, INDC(USA)-85, p.861 (1981).

28. L. Stewart, "Methods Used in Evaluating Data for the Interaction of Neutrons with Light Elements," Proceedings of the Conference on Nuclear Evaluation Methods and Procedures held at BNL September 22-25, 1980, INDC(USA)-85 (1981).

29. C. R. Weisbin, R. D. McKnight, J. D. Hardy, Jr., R. W. Roussin, R. E. Schenter and B. Magurno, "Benchmark Testing of ENDF/B-V," (to be published in 1982).

Verification of Nuclear Cross Section Processing Codes

by

Dermott E. Cullen, Nuclear Data Section, IAEA, Vienna
Willem L. Zijp, Stichting Energieonderzoek Centrum Nederland (ECN), Petten
Robert E. MacFarlane, Los Alamos National Laboratory.

Summary of an Invited Paper which will be presented at the 1982 Kiamesha Lake Topical Meeting of the American Nuclear Society.

Abstract

Introduction

The International Atomic Energy Agency (IAEA) has begun a project for the intercomparison of neutron cross section processing codes in order to verify their ability to reproduce numerical results. In this report this reproducibility aspect is referred to as the "processing accuracy" of a code. This paper will discuss: the scope of this project, the most prominent areas and sources of disagreement between processing codes and the current status of this project toward improving the reliability of the output from processing codes.

The cross section processing code is merely a link between evaluated data on the one hand and transport or adjustment codes on the other hand. This fact has been used in order to simplify the verification task; specifically, the IAEA project attempts to assure that for a given input of evaluated data and physical assumptions, the output of the cross section processor is accurate. This project does not address the "evaluation accuracy" of the evaluated data (which are used as input to the processor), nor the "model accuracy" of the transport or adjustment code (which uses the output of the processor).

The objectives of this project are: (1.) to test the accuracy of processing codes, (2.) to understand and eliminate the sources of discrepancies, (3.) to arrive at the point where we have a number of cross section processing codes which can be used as "black boxes", without worry, to accurately process cross section data, for use in a variety of applications. As will be pointed out below, at the present time, we are far from the point of achieving these objectives.

Background

In 1981 a report was published (1) on a comparison (performed in 1980) between the 620 group (SAND-II structure (2)) group averaged cross sections derived from the ENDF/B-V Dosimetry Library (3) at Brookhaven and those derived at ECN Petten, Netherlands. Of the twenty-five

materials in the ENDF/B-V Dosimetry Library large differences were found in fourteen reactions. In individual reactions, in specific groups, differences were found of up to a factor of twenty (not twenty per-cent, a factor of twenty). Fig. 1 illustrates the ratio of the 620 group ^{237}Np fission cross sections calculated at Brookhaven to those calculated at Petten (1). Unfortunately this study (1) could not address the question of which of these two sets of data is correct.

In order to determine which of these two sets is correct the IAEA obtained additional multigroup data sets from a number of laboratories in the United States and Europe. Comparison of data sets generated at eight different laboratories showed general agreement and confirmed that the cross sections generated at Brookhaven were incorrect. In none of these eight sets were differences seen that were anywhere near those found in the Brookhaven/Petten comparison. However, in no case did any two of the data sets agree for all reactions in all groups to within 6%. This was a very surprising result, since generally these data sets were purported to be accurate to within a small fraction of one per-cent.

Problem Areas

The results of this comparison indicate large differences in the cross sections generated by various codes, primarily in the resolved and unresolved resonance regions. These differences will affect both the self-shielding and Doppler broadening properties of the cross sections. Similarly, recently Perez (4) has shown an inconsistency in the methods normally used to calculate group averaged cross sections in the unresolved resonance region. By calculating self-shielded cross sections in the resolved resonance region first directly from the resolved data and then by treating the data as unresolved and using the equivalent average level widths and spacings Perez found differences in excess of 30%. In addition, Perkins (5) has recently investigated the numerical stability of the methods used to generate group-to-group transfer matrices and has found that if extreme care is not used severe round-off problems can occur.

A more subtle problem area is the effect of these inconsistencies on the many relatively new applications that we are seeing which use the uncertainties quoted for the evaluated data in order either to assign confidence limits to calculational results or to improve our knowledge of spectra or cross sections (6) (e.g. unfolding procedures (7)). The results of these calculations can be very sensitive to the uncertainties assigned to the cross sections used. If the cross section processor introduces an error which is large compared to the error assigned to the evaluated data (as occurred in the comparison described herein) the results obtained using the processed cross sections and only the uncertainties assigned to the evaluated data, without folding in the errors introduced by the cross section processor, are of questionable validity.

Step by Step Verification

Attempting to eliminate this multitude of sins from processing codes in one fell swoop is too ambitious an undertaking and one that would be

almost bound to fail. Therefore the IAEA has decided to begin a step-by-step verification project in an attempt to address first the most glaring areas of disagreement, using the simplest possible test cases. Then more subtle areas of disagreement will be addressed, using progressively more complex test cases.

Following the step-by-step philosophy the area of largest disagreement that we see is in the calculation of cross sections in the resolved and unresolved regions. The simplest way to investigate this problem would be to compare the energy dependent point cross section values generated by a variety of processing codes. However, this information is not available from all processing codes. The next best, simple comparison is constant (flat-weighted), cold, unshielded cross sections using a fine group structure.

Results to Date

The experience gained in comparing 620 group cross sections generated from the ENDF/B-V Dosimetry library has led to recognizing the problems with several existing processing codes. These codes have now either been improved or abandoned. A direct result of these comparisons was the distribution by Brookhaven of a new version of the ENDF/B-V Dosimetry library in the 620 group, SAND-II structure. Fig. 2 illustrates the ratio of the 620 group ^{237}Np fission cross sections from the new version of the ENDF/B-V Dosimetry library as distributed by Brookhaven, to those calculated at Petten (7). Comparison of figs. 1 and 2 easily illustrates the improvements that have been achieved. These results indicate that we now have data which may be used as a standard for benchmark comparisons.

First Round

For the first round of comparisons the IAEA is asking all those interested in participating in this exercise to use the same evaluated data: ENDF/B-V Dosimetry Library (mod. 1), to calculate flat weighted, 0 Kelvin, unshielded cross sections using the SAND-II 620 group structure. Those who use energy-dependent cross sections (e.g. continuous energy Monte Carlo calculations) will be asked to send energy-dependent cross sections and the IAEA will convert them to multigroup form for comparison. Anyone who uses cross sections is encouraged to participate in this study.

Comparison will be simplified if the cross sections are sent in the ENDF/B format (each reaction as a section of file 3 using the histogram interpolation law) (3). However, any well documented, computer readable format is acceptable for this comparison.

The results of the comparison will be reported back to the participants. If there are any differences participants will be asked to investigate and eliminate the sources of these differences and to then re-submit their results. At the end of each round of tests the IAEA will publish the list of participants who have obtained agreement with the benchmark standard.

Subsequent rounds of testing will introduce the complications of: spectrum weighting, Doppler broadening and self-shielding. However, these complications will be introduced in a step-by-step manner so that when we see differences we can isolate the cause of the difference, which will simplify the task of remedying the problem.

Conclusions

The IAEA has begun a project which is intended to use a step-by-step approach to verifying the accuracy of cross section processing codes. Anyone who is presently using a cross section processing code is encouraged to participate in this project. To date this project has been successful in detecting and correcting problems with several cross section processing codes and in particular has directly led to improvements in the ENDF/B-V Dosimetry Library as distributed in 620 groups (3).

References

[1] ZIJP, W.L., et al., "Comparison of two fine group cross section libraries resulting from the ENDF/B-V dosimetry file", Report ECN-97, Netherlands Energy Research Foundation, ECN, Petten, August (1981).

[2] SIMONS, R.L., and MCELROY, W.N., Evaluated reference cross section library, BNWL-1312 (1970), Richland.

[3] GARBER, D., et al., Data Formats and procedures for the evaluated nuclear data file, ENDF, BNL-NCS-50496 (ENDF-102) (1975). Brookhaven.

[4] PEREZ, R.B., et al., Trans. Amer. Nuc. Soc., TANSAO 39, pp. 883 (1981).

[5] PERKINS, S.T., Multigroup Transfer Matrices for Charged Particle and Neutron Induced Reactions", UCRL-86106 and UCRL-86782 (1981), Livermore.

[6] PEREY, G.F., Least Squares Dosimetry Unfolding, The programme STAY'SL, ORNL/TM-6062, ENDF-254 (1977), Oak Ridge.

[7] ZIJP, W.L., NOLTHENIUS, H.J., "Comparison of four neutron spectrum unfolding codes", Contribution to Rottger, H. (editor), Proc. ASTM-EURATOM Symposium on Reactor Dosimetry, Report EUR 6813, Vol. II, p. 787 (CEC-JRC, Petten, 1980).

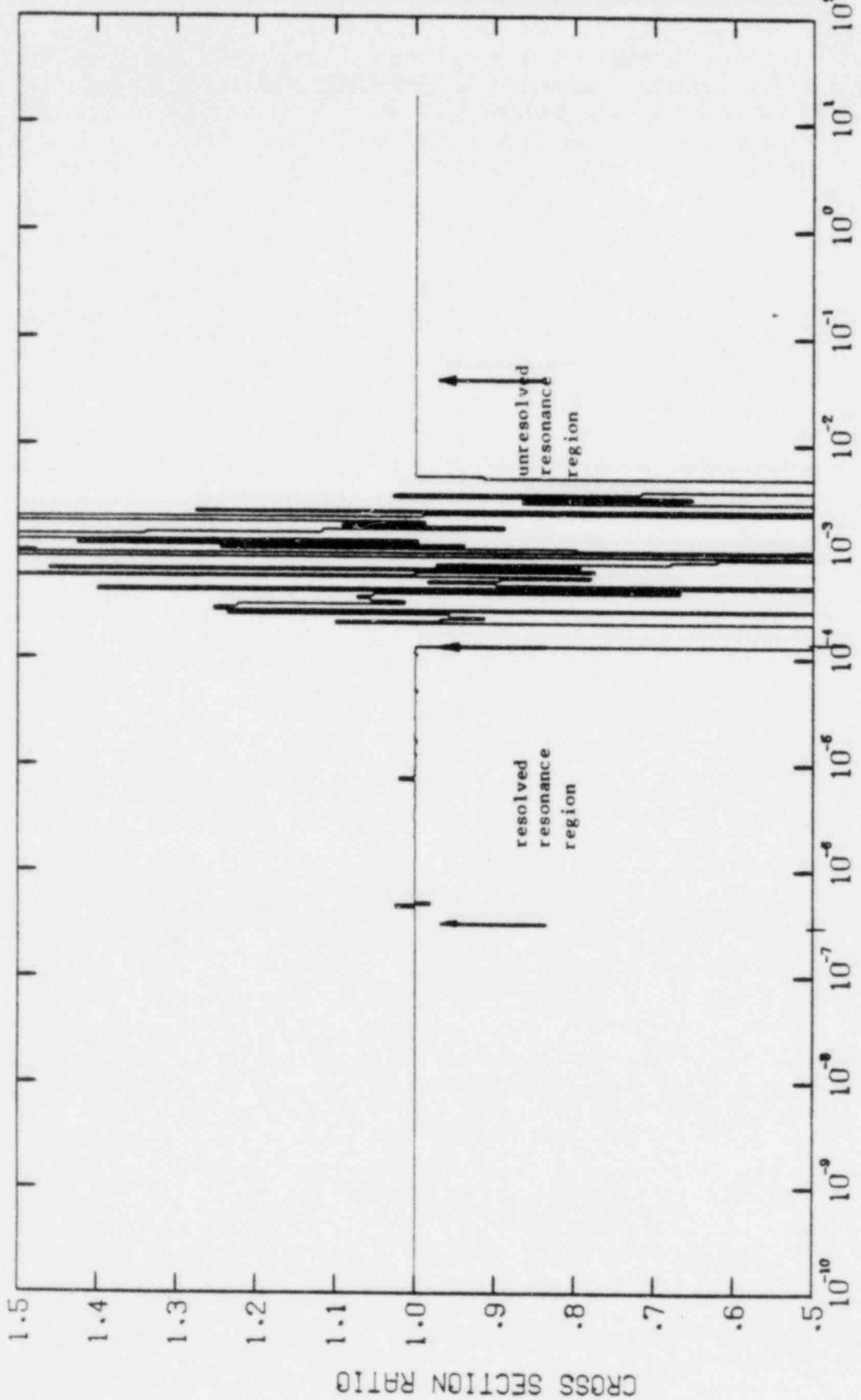

Fig. 1: CROSS SECTION RATIO FOR THE REACTION NP237(N,F)F.P.

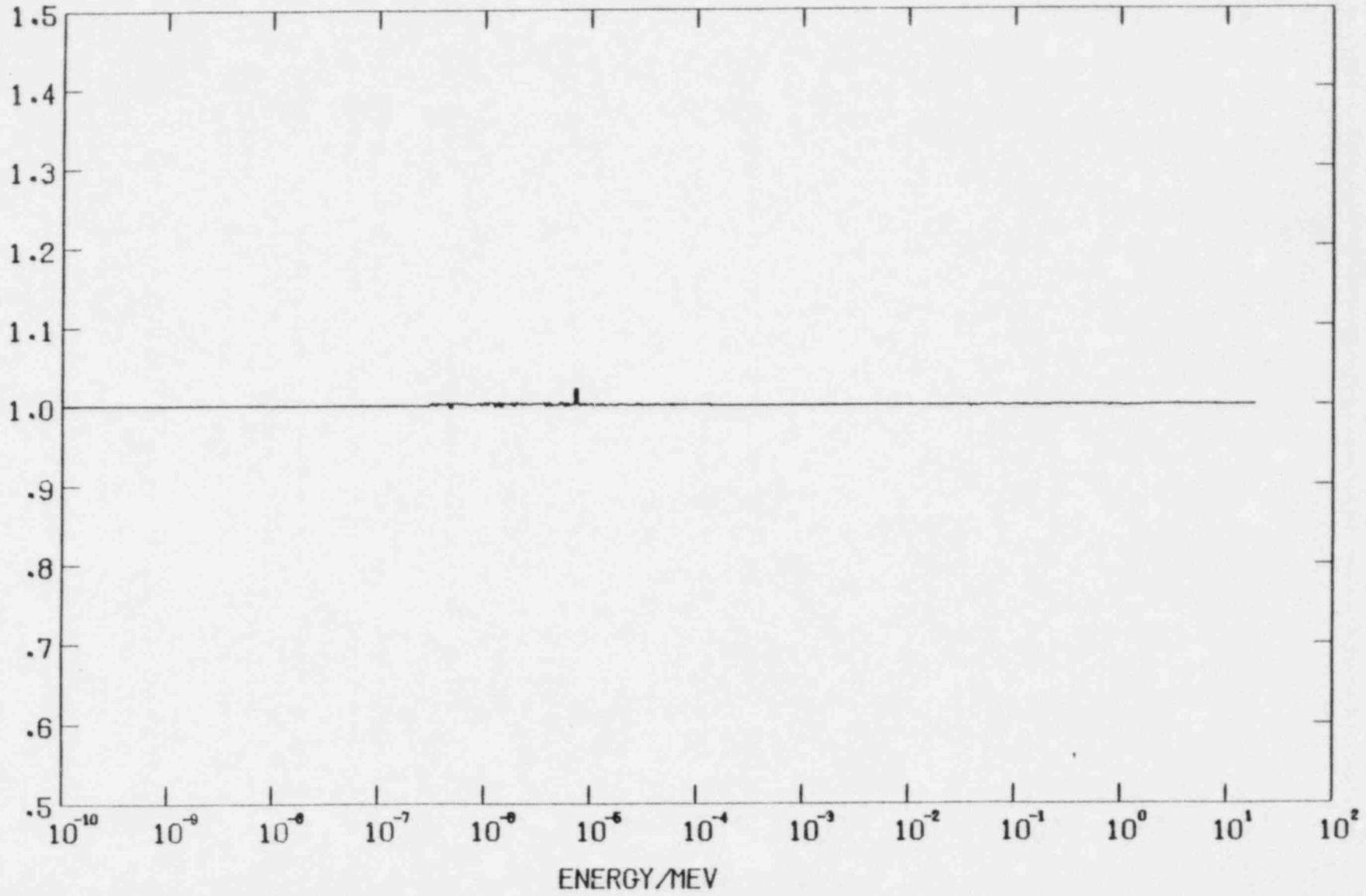

Fig. 2: CROSS SECTION RATIO FOR THE REACTION NP237(N.F)F.P. (BNL/ENTOSAN)

^{238}U SELF-INDICATION RATIO MEASUREMENT IN THE RESONANCE REGION

J. T. Yang
Institute of Nuclear Research
Taiwan, Republic of China

J. L. Munoz-Cobos
Universidad Politecnica de Valencia
Spain

G. de Saussure, R. B. Perez, and J. H. Todd
Oak Ridge National Laboratory
Oak Ridge, Tennessee 37830

INTRODUCTION

An accurate representation of the ^{238}U cross-section structures in the resonance region is required to compute the resonance self-shielded effective cross sections used in the calculation of thermal[1] and fast-reactor[2] performance parameters.

Several authors have demonstrated the usefulness of self-indication[3,4] and average transmission measurements[5,6] to investigate the resonance structure of the ^{238}U cross sections. Byoun et al.[4] at RPI have analyzed self-indication ratio and average-transmission measurements at several temperatures to obtain stochastic parameters above 1 keV. A similar analysis on thick transmission data was done by Vankov et al.[5]

Sowerby[7] noted that the stochastic parameters proposed by Byoun et al.[4] and by Vankov et al.[5] are not in good agreement with each other nor with data evaluated from other sources.

Sowerby[7] and others[8] have recommended that evaluations should be made consistent not only with high-resolution transmission, capture and scattering data but also with average transmission and self-indication measurements for several sample thicknesses. Such comparisons test not only the individual resonance parameters but also several model assumptions used in the representation, such as the cross-section formalism, the representation of the contribution of truncated levels, and small levels not observed in transmission.[9]

This paper compares measured self-indication ratios with calculations based on ENDF/B-V,[10,11] in the resolved energy range from 100 eV to 4 keV. In that energy range the ENDF/B-V evaluation is chiefly based on high resolution transmission measurements.[11] The immediate purpose of the comparison presented is <u>not</u> to generate a new set of improved resonance parameters but to provide an additional test of the adequacy of the ENDF/B-V representation for the calculation of resonance self-shielding.

EXPERIMENT

The Oak Ridge Electron Linear Accelerator (ORELA)[12] was utilized as the pulsed source of neutrons for the time-of-flight measurements. A 0.0031 atom/barn ^{238}U disk was placed on a 40-m flight path from the neutron source. Neutron capture events in this sample were detected by observing the capture gamma rays with four C_6F_6 liquid scintillators surrounding the sample.[13]

Five high-purity ^{238}U transmission samples (0.0038, 0.0124, 0.0341, 0.0528, and 0.1146 atom/barn) were sequenced in and out of the neutron beam by a computer controlled sample changer located 20 m from the neutron source. The incident neutron-beam intensity was monitored by a fast-neutron counter located near the neutron source.[14]

The measured self-indication ratio averaged over the energy interval ΔE was taken to be:

$$\langle SIR \rangle^{M}_{\Delta E} = \frac{m_o}{m_s} \frac{\sum_i (C_{si} - B_{si})}{\sum_i (C_{oi} - B_{oi})} \tag{1}$$

where the summations are taken over the time-of-flight channels, i, included in the energy interval ΔE. The first subscripts, s and o, refer to measurements with the self-indication sample in and out of the beam, respectively. Where m represents the number of monitor counts proportional to the incident neutron beams, C_i and B_i represent the capture detector counts and the estimated background in channel i. The backgrounds were determined from the count rate between resonances at low energy where the resonances are well resolved, and from the count-rate under black resonances obtained from a set of auxiliary measurements with filters of Na, Al, and V.

The computed self-indication ratio was obtained as

$$\langle SIR \rangle^{c}_{\Delta E} = \frac{\sum_i \phi_i \exp(-n_s \sigma_{ti})(1 - e^{-n_c \sigma_{ti}}) \frac{\sigma_{ci}}{\sigma_{ti}} ms_i \Delta E_i}{\sum_i \phi_i (1 - e^{-n_c \sigma_{ti}}) \frac{\sigma_{ci}}{\sigma_{ti}} ms_i \Delta E_i} \tag{2}$$

where again the summations are taken over the time-of-flight channels included in the energy interval ΔE. The thickness (atom/barn) of the self-shielding and capture samples, is represented by n_s and n_c, respectively. The Doppler-broadened capture and total cross sections corresponding to the energy of channel i, is represented by σ_{ci} and σ_{ti}. An energy-dependent multiple-scattering correction, ms_i, was estimated by the Monte Carlo technique. The cross sections in Eq. (2) were obtained from ENDF/B-V. The incident neutron spectrum ϕ_i in Eq. (2) was taken proportional to $E_i^{-0.81}$ in accordance with several measurements of the energy dependence of the Linac neutron spectrum in the resonance region.[15]

The self-indication ratio measurements were averaged over the same 0.1 lethargy-groups used by Byoun et al.[4] The statistical errors were from 2 to 4% above 1 keV and 10 to 15% near 100 eV. The systematic errors considered were (1) the uncertainty in the self-indication sample thicknesses, (2) the uncertainty in the monitor normalizations (the ratio m_o/m_s in Eq. (1), (3) the uncertainty in the multiple scattering correction, (4) the approximation in replacing integrations with sums over channels in Eq. (2), and (5) the uncertainty in the background level. By far the most important uncertainty, particularly for thick self-indication samples, is the uncertainty in the background level. For the .052 atom/barn self-indication sample, for instance, a 1% uncertainty in background level results in an 8% uncertainty in the self-indication ratio above 1 keV.

RESULTS AND CONCLUSIONS

Examples of the results are given in Figs. 1 and 2 which show comparisons of the present measurements, the data of Byoun et al.,[4] and the calculation based on ENDF/B-V for four energy groups. The errors shown in the present data include the statistical and systematic errors combined by root-mean squares. The systematic uncertainties on the RPI data were not available at the present time. Within the rather large systematic errors, the present results are consistent with the calculations based on ENDF/B-V and with the RPI measurements. Unfortunately the small signal- to-background ratio for strongly self-shielded conditions results in rather large uncertainties and, hence, does not represent a very stringent test on the adequacy of ENDF/B-V for strongly self-shielded situations.

ACKNOWLEDGMENTS

The authors are indebted to R. Q. Wright for providing the ENDF/B-V cross sections in the required format and to E. H. Kobisk for providing the high-purity ^{238}U transmission samples. Special thanks are due to R. C. Block for communicating the results and part of the Ph.D dissertation of T. Y. Byoun.

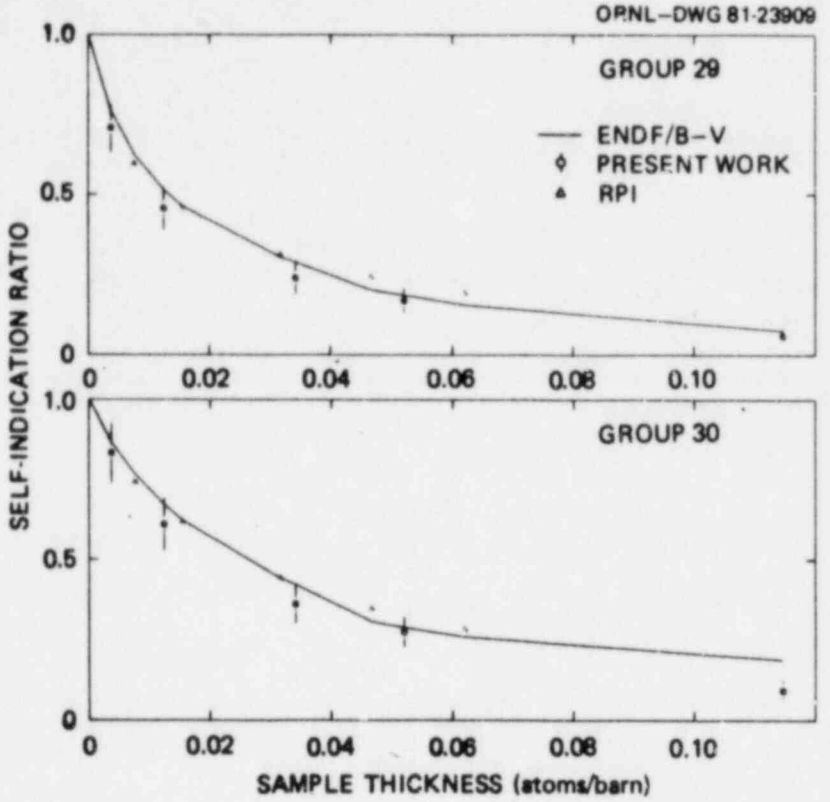

Figure 1. Comparison of the present self-indication ratio measurement with the data of Byoun et al. (Ref. 4) and the calculation based on ENDF/B-V for the neutron energy group 29 (2503 keV $\leq$ E $\leq$ 2767 eV) and group 30 (2767 eV $\leq$ E $\leq$ 3058 eV) as a function of sample thickness.

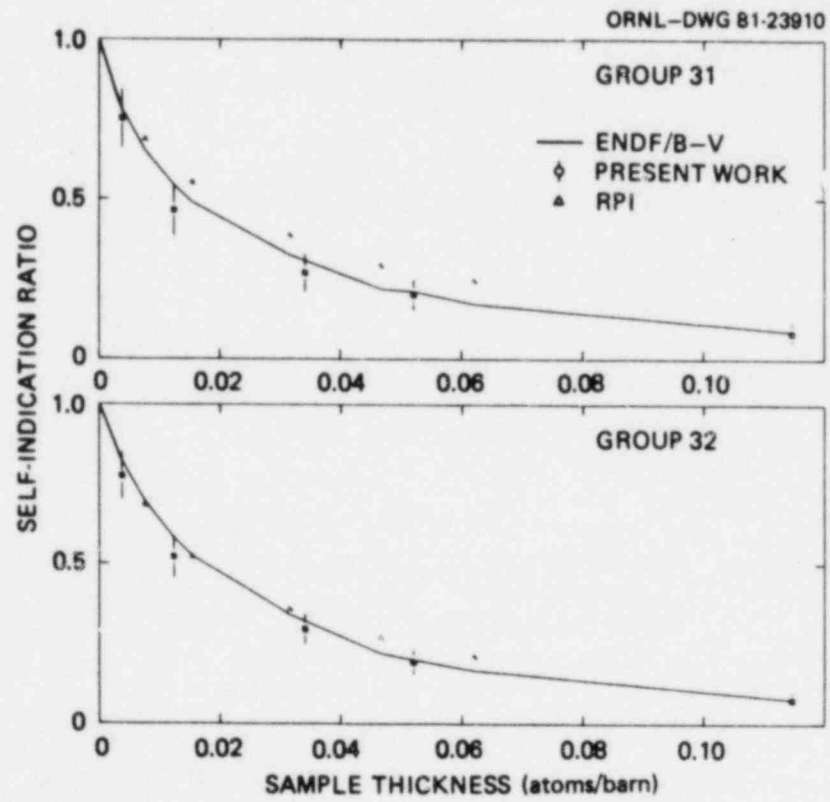

Figure 2. Comparison of the present self-indication ratio measurement with the data of Byoun et al. (Ref. 4) and the calculation based on ENDF/B-V for the neutron energy group 31 (3058 eV $\leq$ E $\leq$ 3380 eV) and group 32 (3380 eV $\leq$ E $\leq$ 3736 eV) as a function of sample thickness.

REFERENCES

1. O. Ozer, "Nuclear Data for LWR Applications," p. 1 NBS Special Publication 549 (1980).

2. M. Salvatores et al., "Resonance Parameter Data Uncertainties Effects on Integral Characteristics of Fast Reactors," in IAEA Consultants Meeting on Uranium and Plutonium Resonance Parameters, Paper 51, INDC(NDS)-129/GJ (1981).

3. R. C. Block et al., "^{238}U Resonance Self-Indication Capture Measurements and Analysis," EPRI-NP-996 (1979).

4. T. Y. Byoun, Experimental Investigation of the Resonance Self-Shielding and Doppler Effect in Uranium and Tantalum, unpublished Ph.D Thesis RPI (1973); and T. Y. Byoun, R. C. Block, and T. Semler, New Developments in Reactor Physics and Shielding, Vol. II, CONF-720901 p. 1115 (1972).

5. A. A. Vankov et al., Nuclear Data for Reactors, Vol. I, p. 559, IAEA, Vienna (1970).

6. T. J. Haste and M. G. Sowerby, "A Study of the Temperature Dependence of the Neutron Transmission of Uranium Dioxide," J. Phys. 12, 1203 (1979).

7. M. G. Sowerby, "Some Comments on the Evaluation of Unresolved Resonance Parameters of U-238," p. 183 in Resonance Parameters of Fertile Nuclei and ^{239}Pu, NEANDC(E), Saclay, May 1974.

8. G. de Saussure and R. B. Perez, "Representation of the Neutron Cross Sections of Several Fertile and Fissile Nuclei in the Resonance Regions," Nucl. Sci. Eng. 61, 496 (1976).

9. G. de Saussure, D. K. Olsen, R. B. Perez, "The ENDF/B-IV Representation of the Uranium-238 Total Neutron Cross Section in the Resolved Resonance Energy Region," Nucl. Sci. Eng. 61, 496 (1976).

10. E. M. Pennington et al., ENDF/B-V file for ^{238}U (MAT-1398); ENDF/B-V dosimetry file for ^{238}U (MAT-6398) (1979).

11. G. de Saussure et al., "Evaluation of the ^{238}U Neutron Cross-Sections for Incident Neutron Energies up to 4 keV," Progress in Nucl. Energy, Vol. 3, p. 87 (1979).

12. F. C. Maienschein, "Neutron Cross Section Measurements of Reactor Interest with the Oak Ridge Electron Linear Accelerator (ORELA)," Energia Nuclear 79, 533 (1972).

13. R. L. Macklin and B. J. Allen, "Fast Neutron Capture Cross Section Facility," Nucl. Instr. Meth. Vol. 91, p. 565 (1971).

14. J. H. Todd, Instrumentation and Control Division Annu. Prog. Rep. September 1, 1970, ORNL-4620, Oak Ridge National Laboratory, Oak Ridge, Tenn., p. 76.

15. R. B. Perez et al., "Measurement of the ^{232}Th(n,f) Subthreshold and Near-Subthreshold Cross Section," to be published.

FISSION CROSS SECTION MEASUREMENTS OF ^{244}Cm, ^{246}Cm AND ^{248}Cm+

Carlos R.S. Stopa, Harry T. Maguire, Jr.*
Donald R. Harris, Robert C. Block
Gaerttner Linac Laboratory
Rensselaer Polytechnic Institute
Troy, New York USA

and

Rudolf E. Slovacek
Knolls Atomic Power Laboratory
Niskayuna, New York USA

and

John W.T. Dabbs
Oak Ridge National Laboratory
Oak Ridge, Tennessee USA

and

Rodney J. Dougan, Richard W. Hoff, Ronald W. Lougheed
Lawrence Livermore National Laboratory
Livermore, California USA

ABSTRACT

The fission cross sections of ^{244}Cm, ^{246}Cm and ^{248}Cm have been measured from 0.1 to 80,000 eV using the Rensselaer Polytechnic Institute LINAC as a pulsed neutron source and the RINS spectrometer. Results were normalized to the ^{235}U ENDF/B-V broad-bin-averaged fission cross section. Fission widths were determined for the resolved low-energy resonances.

INTRODUCTION

The even isotopes of curium have large spontaneous fission decay rates, requiring a large neutron intensity to measure the fission cross section in the presence of a strong spontaneous fission background. The Rensselaer Intense Neutron Spectrometer (RINS) coupled to the Rensselaer Polytechnic Institute Gaerttner Laboratory electron LINAC |1|, produces a very intense neutron flux of broad resolution in the 0.1 to 80,000 eV energy range, and this system has been used to measure the fission cross sections of ^{244}Cm, ^{246}Cm and ^{248}Cm. Results of earlier measurements have been reported |2,3| for ^{246}Cm and ^{248}Cm. The fission cross sections reported in this paper were

+ Research supported by U.S. Department of Energy

* Now at Westinghouse Electric Corporation, Pittsburgh, PA

obtained from a simultaneous measurement of all three isotopes of curium and ^{235}U, and these results were normalized to the broad-bin-averaged ENDF/B-V ^{235}U fission cross section [4].

EXPERIMENTAL METHOD

The RINS system is described in detail in reference 1, and only a few features pertinent to this experiment will be presented here. Following the method developed for RINS by Bicknell et al.[5], the measurement was made with a gaseous fission ionization chamber located inside the lead spectrometer. Hemispherical electrodes [6] and fast electronics designed and constructed at Oak Ridge National Laboratory were used for this measurement. A photograph of the inside of the five-sample chamber is shown in Fig. 1. Five pairs of hemispherical electrodes are mounted inside of a common gas-filled aluminum envelope (not shown in this figure). Each fissile sample was deposited on a ≈4-mm-diameter spot on the inner electrode of each pair, and all five pairs of electrodes were operated at a bias of 500 V. The chamber was filled with 3 atm (absolute) of pure methane.

The cylindrical chamber was surrounded by machined lead pieces to approximate a square cross section of slightly less than 10 cm on a side, and the lead-plus-chamber assembly was placed inside a 10-cm-square port inside the 75-ton lead assembly. The LINAC was operated at a repetition rate of 100 pps with ≈0.7 kW of power on the photo-neutron target. The measurements consisted of sequences of one-hour runs recorded on magnetic tape. A total of 16 hours of fission data and 24 hours of background (machine off) data were taken in the following sequence: two hours of fission data, 16 hours of background, 14 hours of fission data, 8 hours of background.

For the measurements reported in this paper, and in the direction from top-to-bottom in Fig. 1, the samples inside this chamber were ^{248}Cm, ^{244}Cm, ^{235}U + ^{252}Cf, ^{246}Cm and ^{252}Cf. The ^{235}U + ^{252}Cf sample had a small admixture of ^{252}Cf added to highly-enriched ^{235}U; this enabled the fission detection efficiency for this sample to be measured from the ^{252}Cf spontaneous fission. The ^{252}Cf sample (on the bottom) was used to monitor electronic effects which might occur from the intense gamma flash caused by the electrons striking the photoneutron target. The masses and isotopic compositions of the curium samples are listed in Table 1; both number of atoms and mass fractions are tabulated. The ^{235}U + ^{252}Cf sample was composed of 37.5±2.5 μg of 99.7 a/o ^{235}U and 2.2×10^{-12} g of ^{252}Cf. A 2.0×10^{-9} g deposit of ^{252}Cf was contained in the (lower) ^{252}Cf sample.

The fission detection efficiency was 0.93±0.02, 0.97±0.02, 0.98±0.02 and 0.96±0.02 respectively, for the ^{248}Cm, ^{246}Cm, ^{244}Cm and ^{235}U + ^{252}Cf samples. These efficiencies were determined by measuring the spontaneous fission counting rate vs. integral discriminator setting and extrapolating the plateau in the observed pulse-height distribution to zero discriminator setting. The quoted errors are mainly due to the uncertainty in the extrapolation. Since the ^{235}U + ^{252}Cf sample only has spontaneous fission from the ^{252}Cf, it was assumed that the ^{235}U efficiency is the same as the ^{252}Cf efficiency.

DATA REDUCTION

The fission cross section for sample "x" in the slowing-down-time channel "i" is given by:

$$\sigma_{x,i} = \frac{(C-B)_{x,i}}{F\, N_x\, \eta_x\, \phi_i\, \Delta E_i} \qquad (1)$$

where F is the flux normalization factor which is the same for all five samples inside the fission chamber; $(C-B)_{x,i}$ is the net fission counts for sample x in channel i, corrected for dead time losses and spontaneous fission background; N_x is the number of x atoms in the sample; ϕ_i is the un-normalized neutron flux per unit energy at channel i and ΔE_i is the neutron energy span of channel i. The value of the neutron flux is the same reported previously [1], i.e., $\phi = 1.2 \times 10^4\ P E^{-0.775} cm^{-2} s^{-1} eV^{-1}$ above 20 eV and $\phi = 8.0 \times 10^3\ P\ E^{-0.638} cm^{-2} s^{-1} eV^{-1}$ from 1 to 20 eV, where P is the electron beam power on the target (in W) and E is the neutron energy (in eV). Below 1 eV this flux relation is not accurate but it was utilized in this paper.

The normalization factor F is determined from the RINS ^{235}U fission data and the broad-bin-averaged fission cross section determined by Bhat [4] from the ENDF/B-V evaluated data. There are 14 energy groups in the Bhat data between 1 and 50 keV, and F was determined for each of these groups as:

$$F_g = \frac{1}{N_U\, \eta_U} \frac{\left[\sum_j \frac{(C-B)_{U,j}}{\phi_j}\right]_g}{\sigma_g^V\, \Delta E_g} \qquad (2)$$

where σ_g^V is the Bhat fission cross section in group g, ΔE_g is the energy span of the group and the sum over j of the measured data corresponds to the energy region of group g. The final value of F is the arithmetic average of 14 F_g's obtained from Eq. (2).

RESULTS

The fission cross sections for the samples enriched in the three Cm isotopes are listed in Table 2 and plotted in Fig. 2. No corrections have been applied as yet for the non-principal isotopes in each sample. The error in Table 2 (between the parentheses) include the uncertainties in the number of atoms, the efficiency, the normalization factor and the counting statistical error. We observe fully or partially resolved resonances below ~100 eV. At higher energies the RINS resolution can no longer resolve individual resonances so that any structure must be interpreted in terms of a local strength or cluster of resonances. The results are described for each isotope as follows:

^{244}Cm

For this sample the ratio of the neutron-induced fission to the spontaneous fission counting rate (the 'signal-to-background' ratio) was about 5:1 in the 6 to 50 eV region and $\gtrsim$10:1 in the higher energy region. Compared to the other samples, the ^{244}Cm sample had the smallest spontaneous fission (SF) background ($\sim$20 SF/s), and thus had the largest signal-to-background ratio.

The data in this energy range of 10^{-4} to 80 keV were obtained with 840 slowing-down-time channels. Consistent with the RINS resolution, the time data were grouped into macrochannels (preserving the relevant structure) resulting in a total of 155 energy bins (Table 2 and Fig. 2).

Parameters for the resolved resonances at 7.67, 16.2, 22.8 and 35 eV were calculated by integrating the experimental area under the resonance peak and using the relation:

$$A_f = \frac{\pi}{2} \sigma_o \Gamma_f = \sum_f \sigma_{f,m} \Delta E_m \qquad (3)$$

where A_f is the area (in units of b-eV) under the σ_f vs E curve, $\sigma_{f,m}$ is the experimental fission cross section in macrochannel m, ΔE_m is the energy span of the time macrochannel, σ_o is the peak cross section (in b) given by:

$$\sigma_o = \frac{2.6 \times 10^6 \; g \; \Gamma_n}{E_o \; \Gamma} \quad , \qquad (4)$$

where E_o is the resonance energy (in eV), and Γ_n, Γ and Γ_f are respectively the neutron width, the total width and the fission width. Since it is assumed that only s-wave neutrons are responsible for the interaction with the even target nucleus, the statistical weight factor g is equal to 1.

The errors reported in Table 2 for the fission areas A_f are mainly due to the counting statistical error and the uncertainty in determining the background fission cross section. The area of the resonances at 16.2, 22.8 and 35 eV were determined as follows: we integrated the areas under the low-energy half of the 16.2-eV and under the upper-energy half of the 35-eV resonances; from these half areas and from the total area under the 3 resonances we obtained the area for each resonance as listed in Table 3.

The Γ_f values for the 35.0- and 22.8-eV resonances, viz. 2.9 ± 0.6 and 3 ± 1 meV, can be compared with those earlier reported by Moore and Keyworth [7], 2.5 ± 0.07 and 3.7 ± 0.3 meV, respectively. The present data are the first to be reported for the 16.2- and 7.67-eV resonances since earlier fission experiments [7] did not extend below $\gtrsim$20 eV.

^{246}Cm

For this sample, the signal-to-background ratio was approximately 2:1 in the 4-to 15.3-eV region and 10:1 in the 200-to 1000-eV region. As discussed for the ^{244}Cm data, the same procedure of grouping was utilized (with different time macrochannels) reducing the data from 840 to 183 energy bins (see Table 2 and Fig. 2).

The resonance appearing at 1.2 eV (Fig. 2) was not reported in earlier studies of ^{246}Cm. Based on our measurements of the other even isotopes present in the ^{246}Cm samples (see Table 1), this resonance could not be assigned to either ^{244}Cm or ^{248}Cm; from the results of Browne |10| we see that the ^{245}Cm does not have resonances at the observed energy. A possible candidate would be the ^{247}Cm for which there are no data in this energy region. Therefore, we tentatively assigned the 1.2-eV resonance to the ^{246}Cm, although the possibility that it may be ^{247}Cm must be considered. An estimate of its Γ_f value was obtained from average values of Γ_n and Γ_γ for ^{246}Cm.

For ^{246}Cm, resonance parameters have been reported from neutron transmission measurements by Belanova et al. |8| and Benjamin et al. |9|. We have determined the fission width Γ_f for the 4.3-, 15.3- and 158.5-eV resonances based on both sets of parameters, as shown in columns 5 and 8 of Table 3. Our Γ_f results for the 4.3- and 15.3-eV resonances are in agreement with the results we reported previously |3|. The resonances at 84.4 and 91.8 eV are not resolved in this measurement (see Fig. 2), but they have a combined fission area of A_f=14.5±2.5 b-eV, which compares well with the value of 15.1±0.6 b-eV reported by Moore and Keyworth |7|. For the 158.5-eV resonance, our result of A_f=12±4 b-eV and Γ_f=1.0±0.5 meV agrees within the quited errors with the A_f=8.2±0.8 b-eV and Γ_f=0.73±0.11 meV reported in reference 7.

^{248}Cm

This sample had the largest SF background (∿355 SF/s). The signal-to-background ratio was 1.5:1 in the 7- to 80 eV energy range and ∿8:1 at 100 eV. The grouping into time macrochannels was the same for ^{244}Cm, resulting in 155 energy bins (see Table 2 and Fig. 2).

The only resonance clearly resolved in Fig. 2 is at 7.3 eV. The resonances at 26.8 and 35 eV appear as a broad peak and the large peak near 80 eV has many unresolved resonances contributing to the high-energy side. The fission area under the combined 26.8- and 35-eV resonances is 7.5±0.5 b-eV. Moore and Keyworth |7| reported an area of 5.1±0.5 b-eV for the 26.8 eV resonance; from this value and from our total area we calculate A_f=2.4±0.6 b-eV for 35-eV resonance. Thus we obtain a Γ_f value for the 35-eV resonance. The A_f value for the 75.6-eV resonance was calculated by doubling the low-energy half-area of the resonance. Moore and Keyworth obtained 162.0±10.0 b-eV which is in good agreement with our value of 160±20 b-eV. The results for the 7.3-eV resonance is in agreement with our earlier measurement |2|.

INTERPRETATION OF GROSS STRUCTURE IN THE FISSION CROSS SECTION

The RINS spectrometer cannot resolve individual curium resonances above ∿200 eV. In Fig. 2 we observe several peaks in the ^{244}Cm and ^{246}Cm curves between ∿200 eV and several keV, and we suspect that these are probably unresolved clusters of strongly fissioning resonances. For ^{248}Cm we observe a broad peak or plateau near 10 keV. In addition, the ^{244}Cm and ^{246}Cm fission cross sections decrease smoothly with energy and with about the same slope above a few keV, whereas the ^{248}Cm cross section decreases more slowly with energy and is strongly affected by the peak near 10 keV.

The ^{244}Cm and ^{246}Cm data in the 0.2-to-few-keV region are suggestive of intermediate structure. However, it is interesting to note that based on the theoretical calculations of Howard and Möller [11] the neutron binding energy is higher than the outer barrier (which is ∿1MeV lower than the inner barrier) and therefore, one does not expect to see strong intermediate structure effects in the fission cross section. In the ^{248}Cm fission cross section, the peak or plateau at ∿10 keV could also result from clusters of resonances unresolved by the RINS resolution which may be the result of intermediate structure.

CONCLUSIONS

We have measured the fission cross sections of ^{244}Cm, ^{246}Cm, and ^{248}Cm, in the range of 10^{-4} to 80,000 eV. Those results are the first to be reported below ∿20 eV. Fission areas and widths were obtained for the resolved low-energy resonances.

ACKNOWLEDGEMENTS

The authors wish to thank E. Vanterpool, H. Fisher and B. Alam for the many helpful discussions about the RINS resolution function. We also acknowledge Dr. R.C. Little from the Los Alamos National Laboratory for providing us with his results of the Monte Carlo modeling of the RINS resolution function. One of us (C.R.S. Stopa) wishes to thank the Brasilian "Comissão Nacional de Energia Nuclear" and the "Centro Técnico Aeroespacial" for their financial support.

REFERENCES

1. R.E. Slovacek, D.S. Cramer, E.B. Bean, J.R. Valentine, R.W. Hockenbury, and R.C. Block, Nucl. Sci. Eng., 62, 445 (1977).

2. H.T. Maguire, Jr., C. Stopa, D.R. Harris, R.C. Block, R.E. Slovacek, R.W. Hoff, and J.W.T. Dabbs, Trans. Am. Nucl. Soc., 38, 648 (1981).

3. R.C. Block, H.T. Maguire, Jr., C. Stopa, D.R. Harris, R.E. Slovacek, R.W. Hoff, R.W. Lougheed, and J.W.T. Dabbs, Trans. Am. Nucl. Soc., 39, 876 (1981).

4. M.R. Bhat, "Evaluation of ^{235}U Neutron Cross Section and Gamma Ray Production Data for ENDF/B-V," March 1980, BNL-NCS-51184 (ENDF-248).

5. P.A. Bicknell, R.C. Block, G. Krycuk, and Y. Nakagome, Nucl. Instrum. Methods, 178, 221 (1980).

6. J.W.T. Dabbs, N.W. Hill, C.E. Bemis, and B. Raman, "Nuclear Cross Sections and Technology," NBS Spec. Publ. 425, Vol. 1, p. 81, National Bureau of Standards (1975).

7. M.S. Moore and G.A. Keyworth, Phys. Rev. C3, 1656 (1971).

8. T.S. Belanova, et al., "Proc. of the IVth USSR Conf. on Neutron Phys.," Kiev, USSR, Vol. 2, p. 260 (1977).

9. R.W. Benjamin, C.E. Ahfeld, J.A. Harvey, and N.W. Hill, Nucl. Sci. Eng. 55, 440 (1974).

10. Browne, J., Nucl. Sci. Eng. 65, 166 (1978).

11. W.M. Howard, P. Möller, At. Data & Nucl. Data Tables, 25, 219 (1980).

Table 1. Curium Sample Composition

No. of Atoms (in units of 10^{16})

SAMPLE	MASS(μg)	^{243}Cm	^{244}Cm	^{245}Cm	^{246}Cm	^{247}Cm	^{248}Cm
^{244}Cm	5.21±.16	.00111	1.279	.0014	.00342	.000098	
^{246}Cm	17.04±.85		.1199	.00455	4.031	.00348	.003384
^{248}Cm	31.16±1.6		.000162	.00234	.233	.001169	7.330

Mass Fraction (%)

^{244}Cm		.0861	99.53	.1094	.2682	7.69(-3)	
^{246}Cm			2.86	.109	96.87	.084	.082
^{248}Cm			.00211	.0306	3.06	.0154	96.89

Table 2. FISSION CROSS SECTION (ERROR)
(BARN)

NEUTRON ENERGY(eV)	Cm-244	Cm-246	Cm-248
.136E+00	1.107(0.273)	0.468(0.131)	0.086(0.193)
.215E+00	0.303(0.273)	0.512(0.219)	0.002(0.326)
.250E+00	0.392(0.393)	0.488(0.192)	0.038(0.286)
.295E+00	0.580(0.343)	0.116(0.163)	-0.053(0.248)
.353E+00	0.383(0.293)	0.165(0.141)	0.303(0.214)
.429E+00	0.635(0.250)	0.498(0.124)	0.329(0.181)
.534E+00	0.105(0.203)	0.192(0.099)	-0.028(0.148)
.682E+00	0.126(0.164)	0.419(0.085)	0.302(0.122)
.808E+00		0.370(0.142)	
.868E+00		0.693(0.142)	
.901E+00	0.299(0.131)		0.212(0.095)
.935E+00		0.736(0.136)	
.101E+01		0.780(0.130)	
.110E+01		0.915(0.128)	
.119E+01		0.963(0.124)	
.125E+01	0.166(0.098)		0.254(0.073)
.130E+01		0.790(0.110)	
.143E+01		0.745(0.103)	
.157E+01		0.481(0.087)	
.174E+01		0.466(0.081)	
.183E+01	0.306(0.072)		0.157(0.052)
.194E+01		0.423(0.073)	
.217E+01		0.501(0.071)	
.233E+01		0.433(0.120)	
.240E+01		0.254(0.112)	
.248E+01		0.562(0.119)	
.256E+01		0.415(0.111)	
.264E+01		0.705(0.119)	
.273E+01		0.649(0.114)	
.282E+01		0.860(0.121)	
.291E+01		0.731(0.113)	
.296E+01	0.234(0.048)		0.098(0.034)
.301E+01		0.559(0.103)	
.312E+01		0.786(0.110)	
.323E+01		0.925(0.115)	
.335E+01		1.192(0.126)	
.347E+01		1.344(0.133)	
.360E+01		1.803(0.157)	
.374E+01		2.150(0.177)	
.389E+01		2.259(0.183)	
.404E+01	0.516(0.156)	2.388(0.190)	0.235(0.107)
.421E+01	0.605(0.154)	2.429(0.191)	0.227(0.103)
.438E+01	0.463(0.145)	2.528(0.196)	0.391(0.103)
.457E+01	0.278(0.135)	2.127(0.169)	0.256(0.097)
.477E+01	0.487(0.136)	1.940(0.156)	-0.084(0.090)
.498E+01	0.534(0.134)	1.541(0.130)	0.302(0.091)
.521E+01	0.681(0.134)	1.333(0.116)	0.230(0.086)

FISSION CROSS SECTION (ERROR)
(BARN)

NEUTRON ENERGY(eV)	Cm-244	Cm-246	Cm-248
.545E+01	0.876(0.137)	0.933(0.091)	0.416(0.088)
.571E+01	1.390(0.154)	0.942(0.090)	0.334(0.082)
.599E+01	2.074(0.182)	0.896(0.086)	0.438(0.082)
.629E+01	3.070(0.228)	0.685(0.073)	0.604(0.085)
.661E+01	4.287(0.289)	0.743(0.074)	0.793(0.091)
.696E+01	4.714(0.309)	0.774(0.075)	0.664(0.083)
.733E+01	5.088(0.327)	0.644(0.066)	0.770(0.085)
.774E+01	4.902(0.315)	0.641(0.065)	0.494(0.072)
.818E+01	3.998(0.264)	0.548(0.058)	0.477(0.068)
.866E+01	2.945(0.205)	0.552(0.057)	0.333(0.060)
.919E+01	2.098(0.159)	0.542(0.055)	0.180(0.054)
.976E+01	1.473(0.125)	0.399(0.046)	0.140(0.050)
.104E+02	0.961(0.098)	0.401(0.045)	0.097(0.047)
.111E+02	0.860(0.090)	0.333(0.040)	0.106(0.045)
.118E+02	0.845(0.087)	0.329(0.039)	0.070(0.042)
.127E+02	1.080(0.095)	0.424(0.042)	0.183(0.042)
.136E+02	1.704(0.124)	0.519(0.047)	0.111(0.038)
.147E+02	2.655(0.172)	0.595(0.050)	0.100(0.035)
.159E+02	3.180(0.199)	0.507(0.044)	0.011(0.032)
.172E+02	3.199(0.198)	0.484(0.042)	0.125(0.032)
.187E+02	2.989(0.185)	0.365(0.034)	0.094(0.029)
.204E+02	3.026(0.186)	0.342(0.032)	0.232(0.032)
.223E+02	2.975(0.182)	0.277(0.027)	0.425(0.040)
.245E+02	2.379(0.148)	0.295(0.027)	0.654(0.052)
.271E+02	1.914(0.121)	0.240(0.024)	0.658(0.052)
.301E+02	2.342(0.143)	0.238(0.023)	0.482(0.040)
.323E+02	2.751(0.196)	0.201(0.033)	0.375(0.048)
.332E+02	2.554(0.185)	0.202(0.032)	0.321(0.045)
.342E+02	2.714(0.193)	0.287(0.036)	0.356(0.046)
.352E+02	2.362(0.172)	0.233(0.033)	0.280(0.042)
.362E+02	2.411(0.174)	0.187(0.030)	0.165(0.038)
.373E+02	1.731(0.136)	0.208(0.031)	0.162(0.037)
.385E+02	1.735(0.135)	0.254(0.033)	0.199(0.037)
.397E+02	1.462(0.119)	0.231(0.031)	0.203(0.037)
.409E+02	1.276(0.108)	0.202(0.029)	0.129(0.034)
.422E+02	1.047(0.095)	0.158(0.027)	0.182(0.035)
.436E+02	1.038(0.094)	0.196(0.028)	0.195(0.035)
.451E+02	0.959(0.089)	0.238(0.030)	0.127(0.032)
.466E+02	0.811(0.080)	0.217(0.028)	0.177(0.033)
.482E+02	0.796(0.078)	0.207(0.027)	0.174(0.032)
.499E+02	0.752(0.075)	0.197(0.026)	0.221(0.033)
.517E+02	0.861(0.080)	0.151(0.024)	0.300(0.036)
.536E+02	0.695(0.070)	0.180(0.025)	0.488(0.045)
.555E+02	0.598(0.064)	0.238(0.028)	0.817(0.065)
.576E+02	0.631(0.065)	0.174(0.024)	1.255(0.094)
.599E+02	0.671(0.066)	0.231(0.026)	2.001(0.144)
.622E+02	0.623(0.063)	0.254(0.027)	2.952(0.209)
.647E+02	0.609(0.061)	0.329(0.032)	3.973(0.279)

FISSION CROSS SECTION (ERROR)
(BARN)

NEUTRON ENERGY(eV)	Cm-244	Cm-246	Cm-248
.673E+02	0.683(0.064)	0.349(0.033)	4.983(0.348)
.701E+02	0.671(0.063)	0.435(0.038)	5.666(0.395)
.731E+02	0.844(0.071)	0.495(0.041)	6.171(0.430)
.763E+02	0.901(0.074)	0.634(0.050)	5.809(0.405)
.797E+02	1.017(0.079)	0.669(0.052)	5.131(0.358)
.833E+02	0.933(0.074)	0.728(0.056)	4.465(0.312)
.872E+02	0.959(0.075)	0.609(0.048)	3.432(0.240)
.913E+02	0.953(0.074)	0.557(0.044)	2.710(0.191)
.958E+02	0.987(0.075)	0.483(0.039)	2.179(0.154)
.101E+03	0.817(0.065)	0.406(0.034)	1.680(0.120)
.106E+03	0.687(0.057)	0.288(0.026)	1.305(0.094)
.111E+03	0.683(0.056)	0.286(0.025)	1.096(0.079)
.117E+03	0.651(0.054)	0.251(0.023)	0.893(0.066)
.124E+03	0.701(0.056)	0.253(0.023)	0.808(0.060)
.131E+03	0.673(0.053)	0.293(0.025)	0.714(0.053)
.139E+03	0.633(0.050)	0.330(0.027)	0.615(0.046)
.147E+03	0.574(0.052)	0.349(0.028)	0.576(0.043)
.156E+03	0.615(0.048)	0.331(0.027)	0.511(0.039)
.166E+03	0.679(0.051)	0.315(0.026)	0.493(0.038)
.177E+03	0.794(0.057)	0.243(0.021)	0.468(0.036)
.190E+03	0.765(0.054)	0.231(0.020)	0.507(0.038)
.203E+03	0.777(0.055)	0.219(0.019)	0.497(0.037)
.218E+03	0.792(0.055)	0.230(0.019)	0.491(0.037)
.235E+03	0.586(0.043)	0.219(0.018)	0.452(0.034)
.254E+03	0.523(0.039)	0.256(0.020)	0.419(0.031)
.275E+03	0.468(0.035)	0.275(0.021)	0.319(0.025)
.299E+03	0.468(0.035)	0.316(0.024)	0.298(0.023)
.326E+03	0.493(0.036)	0.333(0.025)	0.251(0.020)
.357E+03	0.567(0.039)	0.358(0.026)	0.216(0.017)
.393E+03	0.582(0.039)	0.283(0.021)	0.185(0.015)
.434E+03	0.559(0.038)	0.241(0.018)	0.174(0.014)
.482E+03	0.492(0.033)	0.174(0.014)	0.155(0.013)
.539E+03	0.438(0.030)	0.154(0.012)	0.140(0.011)
.606E+03	0.422(0.029)	0.166(0.013)	0.124(0.010)
.665E+03	0.421(0.032)	0.184(0.015)	0.128(0.012)
.709E+03	0.471(0.035)	0.197(0.016)	0.107(0.010)
.758E+03	0.472(0.034)	0.201(0.016)	0.114(0.010)
.812E+03	0.495(0.035)	0.224(0.017)	0.104(0.010)
.872E+03	0.418(0.030)	0.213(0.017)	0.104(0.009)
.939E+03	0.375(0.028)	0.204(0.016)	0.099(0.009)
.101E+04	0.346(0.026)	0.170(0.013)	0.092(0.008)
.110E+04	0.280(0.022)	0.147(0.012)	0.088(0.008)
.119E+04	0.287(0.022)	0.137(0.011)	0.078(0.007)
.130E+04	0.239(0.019)	0.120(0.010)	0.075(0.007)
.143E+04	0.229(0.018)	0.106(0.009)	0.068(0.006)
.157E+04	0.240(0.018)	0.116(0.009)	0.065(0.006)
.173E+04	0.264(0.019)	0.102(0.008)	0.062(0.006)
.193E+04	0.232(0.017)	0.095(0.008)	0.063(0.006)

FISSION CROSS SECTION (ERROR)
(BARN)

NEUTRON ENERGY(eV)	Cm-244	Cm-246	Cm-248
.215E+04	0.197(0.015)	0.093(0.007)	0.065(0.006)
.242E+04	0.178(0.013)	0.089(0.007)	0.058(0.005)
.274E+04	0.166(0.012)	0.097(0.008)	0.061(0.005)
.314E+04	0.166(0.012)	0.093(0.007)	0.058(0.005)
.362E+04	0.155(0.011)	0.089(0.007)	0.052(0.004)
.422E+04	0.148(0.011)	0.082(0.006)	0.055(0.004)
.499E+04	0.131(0.008)	0.071(0.005)	0.059(0.004)
.557E+04	0.152(0.014)	0.069(0.007)	0.056(0.005)
.584E+04	0.131(0.013)	0.069(0.006)	0.058(0.006)
.612E+04	0.108(0.011)	0.068(0.006)	0.059(0.005)
.643E+04	0.117(0.012)	0.064(0.006)	0.055(0.005)
.676E+04	0.131(0.013)	0.067(0.006)	0.056(0.005)
.712E+04	0.142(0.013)	0.068(0.006)	0.061(0.005)
.750E+04	0.135(0.012)	0.058(0.005)	0.061(0.005)
.792E+04	0.103(0.010)	0.065(0.006)	0.059(0.005)
.837E+04	0.123(0.011)	0.056(0.005)	0.055(0.005)
.886E+04	0.105(0.010)	0.062(0.006)	0.055(0.005)
.940E+04	0.120(0.011)	0.056(0.005)	0.063(0.005)
.998E+04	0.105(0.010)	0.056(0.005)	0.058(0.005)
.106E+05	0.110(0.010)	0.059(0.005)	0.055(0.005)
.113E+05	0.112(0.010)	0.051(0.005)	0.061(0.005)
.121E+05	0.110(0.010)	0.049(0.004)	0.054(0.005)
.130E+05	0.104(0.009)	0.053(0.005)	0.052(0.004)
.139E+05	0.085(0.008)	0.049(0.004)	0.050(0.004)
.150E+05	0.104(0.009)	0.044(0.004)	0.050(0.004)
.162E+05	0.095(0.008)	0.046(0.004)	0.052(0.004)
.176E+05	0.105(0.009)	0.043(0.004)	0.055(0.004)
.191E+05	0.083(0.007)	0.042(0.004)	0.051(0.004)
.208E+05	0.083(0.007)	0.045(0.004)	0.049(0.004)
.228E+05	0.077(0.007)	0.042(0.004)	0.052(0.004)
.251E+05	0.079(0.006)	0.039(0.003)	0.047(0.004)
.277E+05	0.074(0.006)	0.039(0.003)	0.045(0.003)
.308E+05	0.069(0.006)	0.037(0.003)	0.042(0.003)
.344E+05	0.067(0.005)	0.039(0.003)	0.043(0.003)
.387E+05	0.063(0.005)	0.036(0.003)	0.039(0.003)
.438E+05	0.064(0.005)	0.033(0.003)	0.037(0.003)
.501E+05	0.054(0.004)	0.032(0.003)	0.037(0.003)
.577E+05	0.053(0.004)	0.030(0.002)	0.033(0.002)
.673E+05	0.043(0.003)	0.030(0.002)	0.032(0.002)
.795E+05	0.041(0.003)	0.029(0.002)	0.028(0.002)

Table 3. Curium Resonance Parameters

		Belanova et al.[8]		RPI	Benjamin et al.[9]		RPI
^{244}Cm							
E_o(eV)	A_f(b-eV)	Γ_n(meV)	Γ(meV)	Γ_f(meV)	Γ_n(meV)	Γ_γ(meV)	Γ_f(meV)
7.67	14.9±.8	10.4±.4	44±3	.2 ±.01			
16.2	18±3	1.9±.3	37±5	1.4±.4			
22.8	12±4	.84±.1	36±10	3 ± 1			
35.0	43±4	4.5±.3	35±5	2.9±.6			
^{246}Cm							
1.2*	.4±.1				.43**	31**	.01
4.3	4.1±.5	.34±.01	27±2	.34±.05	.31±.02	31±6	.44±.1
15.3	1.6±.3	.52±.01	28±3	.32±.07	.55±.12	31	.35±.11
158.5	12±4				26.5±8.8	31	1.0±.5
^{248}Cm							
7.25	2.2±.3	1.9±.04	36±3	.07±.01	1.78±.05	23.3 1.0	.06±.01
26.8							
35.0	2.4±.6+	9.5±2.0	38±5	.08±.03	11.72±.47	30.2±2.7	.07±.02
75.6	160±20				96.83±4.36	26	3.9±.5

*Tentatively Assigned to ^{246}Cm

**Average Values for 15.3- and 158.5-eV resonances

+Deduced from Moore & Keyworth [7]

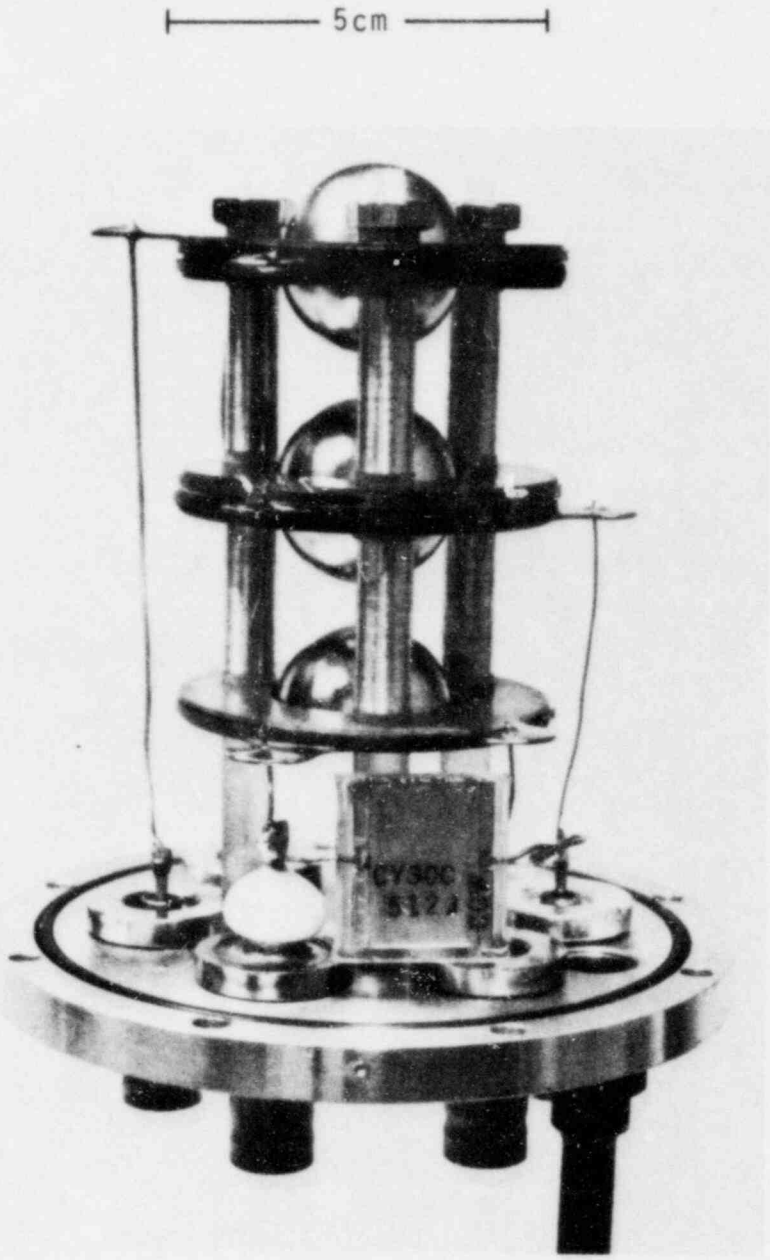

Figure 1. Photograph of the inside of the five-sample fission chamber

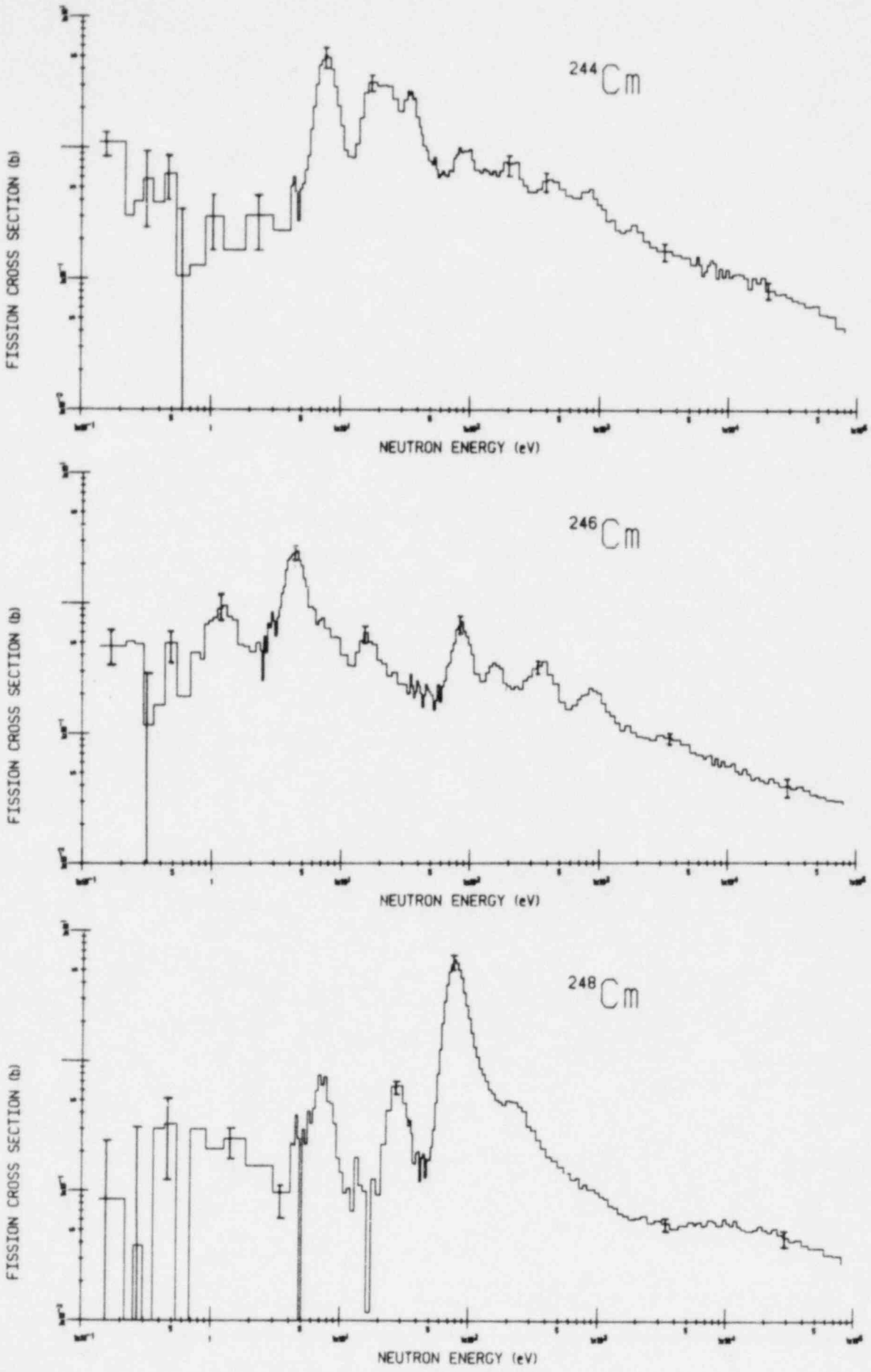

Figure 2. Fission cross section vs. neutron energy for the curium isotopes

FAST INTEGRAL CROSS SECTIONS FOR ^{241}Am AND ^{243}Am*

R. A. Anderl, N. C. Schroeder, Y. D. Harker
EG&G Idaho Inc.
Idaho National Engineering Laboratory
Idaho Falls, Idaho 83415

ABSTRACT

This paper reports on integral capture and fission cross-section experiments for ^{241}Am and ^{243}Am in the fast neutron field of the Coupled Fast Reactivity Measurements Facility (CFRMF). The integral cross sections were derived from measurements of the $^{241}Am(n,f)$, $^{241}Am(n,\gamma)$ ^{242g}Am, $^{243}Am(n,f)$ and $^{243}Am(n,\gamma)$ ^{244g}Am integral reaction rates using gamma-spectrometric and isotope-dilution alpha-spectrometric (IDAS) techniques. Integral cross sections in barns obtained from this work are as follows: 0.450 ± 6.2% for $^{241}Am(n,f)$, 1.22 ± 3.5% for $^{241}Am(n,\gamma)$ ^{242g}Am, 0.353 ± 6.1% for $^{243}Am(n,f)$ and 0.0976 ± 4.8% for $^{243}Am(n,\gamma)$ ^{244g}Am. Conventional integral-testing analyses, based on ratios of calculated-to-measured spectrum-averaged cross sections, and least-squares-adjustment analyses were made to assess the consistency of these integral data with the corresponding cross sections on ENDF/B-V. The results of these studies are also reported here.

1. INTRODUCTION

In recent years, considerable attention has focused on the adequacy of the neutron cross-section data for higher mass actinides including ^{241}Am, ^{243}Am, ^{242}Cm and ^{244}Cm[1]. Because these nuclides are produced in substantial quantities in high-burnup fast reactor cores, they impact fuel cycle optimization and waste management for fast reactors. The americium isotopes have sizable neutron capture cross sections in fast reactor spectra and, as such, are poisons. They also have significant cross sections for fission above 2 MeV neutron energy and they therefore contribute to the neutron source term for the reactor. The curium isotopes, which are produced via neutron capture in the americium isotopes followed by β^- decay, both undergo spontaneous fission and, therefore, they impact reactor shutdown and startup operations. From a fuel-handling and waste-management perspective, all four nuclides are relatively long lived, they are intense alpha and gamma emitters and, in the case of ^{242}Cm and ^{244}Cm, they are intense neutron sources.

An accurate prediction of the buildup and burnup of these nuclides depends explicitly on accurate specifications of the respective neutron cross sections, especially for ^{241}Am and ^{243}Am. The ENDF/B-V evaluation of the capture and fission cross sections for these nuclides relied heavily on theoretical calculations, especially in the intermediate and fast neutron energy regions for the capture cross sections[2]. At the time of this evaluation[2], there was a very limited integral data base to test the evaluated cross sections in the intermediate and fast neutron energy regions. The present paper is concerned with improving the fast reactor integral data base for these nuclides.

* Work supported by the US Department of Energy under DOE contract No. DE-AC07-76ID01570.

The primary purpose of this paper is two fold: (1) to report measurements of the integral capture and fission cross sections for ^{241}Am and ^{243}Am in the fast neutron field of the Coupled Fast Reactivity Measurements Facility (CFRMF)[3] and (2) to assess the consistency of these integral data with the evaluated cross sections on ENDF/B-V. The results reported here update the preliminary values reported earlier[4]. Pertinent experimental details are addressed in Section 2. This includes a description of the CFRMF irradiation experiments and the determination of integral capture and fission reaction rates by means of gamma-spectrometric and isotope-dilution alpha-spectrometric (IDAS) techniques. Section 3 presents detailed results concerning the application of the measured integral data in both integral-test and least-squares-adjustment analyses for the ENDF/B-V cross sections. We conclude this paper in Section 4 with an assessment of the principal results of the cross-section data-testing analyses and we point out those areas for future work. Complete documentation of the measurement phase of this work is found in Reference 5.

2. EXPERIMENTAL DETAILS AND RESULTS

2.1 Irradiation Experiments

The irradiation facility for these experiments was the CFRMF[3,6] which is located at the Idaho National Engineering Laboratory (INEL). The CFRMF is a zoned-core critical assembly with a fast neutron spectrum zone in the center of an enriched ^{235}U, water moderated thermal driver. Approximately 95% of the neutrons in the central spectrum are between 4 keV and 4 MeV and the median and mean neutron energies are 370 keV and 1760 keV, respectively. The central neutron spectrum is a Cross-Section Evaluation Working Group (CSEWG) benchmark field for testing dosimetry, fission-product and actinide cross sections for ENDF/B-V. An update of the CFRMF central neutron spectrum characterization has been reported recently[7].

Source material for these experiments was obtained as americium oxide powder from Oak Ridge National Laboratory from lot number BP75-38D for ^{241}Am and lot number Am-1-91 for ^{243}Am. The ^{241}Am sample material was isotopically enriched to 100% in ^{241}Am and had no measurable ^{242}Cm impurity. The ^{243}Am material was isotopically enriched to 99.99% ^{243}Am with 0.01% ^{241}Am and < 1 ppm ^{244}Cm. Samples with masses ranging from 0.25 mg to 1.25 mg were sealed in thin walled quartz ampoules for irradiation in the CFRMF.

Five ampoules containing ^{241}Am and two ampoules containing ^{243}Am were irradiated at different times at the core midplane of the CFRMF. The reactor was operated at a power level of 100 kW which produces a neutron flux level of $\sim 8.7 \times 10^{11}$ n/cm^2-s at the sample location. Power level monitoring for the irradiations was done by means of the activation of gold monitors which accompanied each irradiation package.

2.2 Measurement Techniques

Post-irradiation measurements for the samples employed a combination of gamma-spectrometric[8,9] and isotope-dilution alpha-spectrometric techniques[10,11]. The gamma spectrometric approach was used for the measurements of the $^{197}Au(n,\gamma)$ ^{198}Au activation rate, the fission rates of ^{241}Am and ^{243}Am based

on prominent lines (328, 487, 537, 815 and 1596) in the β^- decay of ^{140}Ba and of ^{140}La, and the $^{243}Am(n,\gamma)$ ^{244g}Am capture rate based on the 744-keV and 898-keV lines for ^{244g}Am. Isotope-dilution alpha-spectrometry was used for mass assaying the contents of each ^{241}Am and ^{243}Am ampoule and for the measurement of the ^{242}Cm contents in the irradiated ^{241}Am samples.

Gamma measurements were made with three calibrated Ge(Li) spectrometers, each with a large coaxial Ge(Li) detector. Standard gamma-ray counting techniques[8,9] were followed for the CFRMF activation experiments. Equation 1 was used for the determination of the reaction rates RR from the gamma-ray data.

$$RR = \frac{A}{b \cdot \varepsilon} \cdot \frac{1}{N} \cdot \frac{1}{Y} \cdot D \cdot \frac{1}{\delta_1 \cdot \delta_2 \cdot \delta_3 \cdot \delta_4 \cdot \delta_5} \qquad (1)$$

The symbols in equation 1 are defined as follows: A is the measured peak area, b is the gamma-ray branching ratio, ε is the detector efficiency, N is the number of atoms for the isotope of interest in the sample, Y is the fission yield, D is the irradiation/decay/count time history factor, and the δ_i are corrections for gamma-ray self-absorption (1), gamma-ray attenuation in an external absorber (2), random summing and live timer effects (3), neutron resonance self-shielding (4) and coincidence summing (5).

Decay data used in the analysis of the gamma-spectrometric measurements were taken from the following sources: Reference 8, half lives for ^{140}Ba, ^{140}La and ^{198}Au and emission probability for ^{198}Au 411 line; Reference 12, emission probabilities for ^{140}Ba and ^{140}La gammas; Reference 13, half lives and emission probabilities for ^{239}Np and ^{244g}Am; and Reference 14, half lives for ^{241}Am and ^{243}Am. A mass 140 cumulative fission yield of 5.5% with a 5% uncertainty was used in all fission-rate determinations[15].

The technique of isotope-dilution alpha-spectrometry is based on the following:[10,11]

(1) mixing a mass aliquot, $\hat{M}$, of a precalibrated spike solution (concentration N_y for isotope y) with a mass aliquot, $\bar{M}$, of the solution with unknown concentration for isotope x;

(2) electroplating sources of the spike solution, the unspiked sample solution and the spiked sample solution;

(3) using alpha spectrometer measurements to determine the relative atom concentrations of the isotopes in the three solutions: R_{xy}, the x to y atom ratio in the spike solution; $u\bar{R}_{yx}$, the y to x atom ratio in the unspiked sample solution; and $\bar{R}_{xy}$, the x to y atom ratio in the spiked sample solution;

(4) computing the concentration, $\bar{N}_x$, of the isotope of interest in the unknown solution using equation 2.

$$\bar{N}_x = \frac{(\bar{R}_{xy} - \hat{R}_{xy}) \cdot \hat{N}_y \cdot \hat{M}}{\bar{M}\,(1 - \bar{R}_{xy} \cdot u\bar{R}_{yx})} \qquad (2)$$

Isotope-dilution alpha-spectrometry was used to determine the ^{241}Am and ^{243}Am masses in each irradiated ampoule and to determine the ^{242}Cm content in three of the irradiated ^{241}Am samples. Spike solutions of ^{243}Am and ^{241}Am were used for the ^{241}Am and ^{243}Am mass assays, respectively. A ^{244}Cm spike solution was used in the analysis for the ^{242}Cm content. The procedures for the determination of the ^{242}Cm in the irradiated ^{241}Am samples required a chemical separation of the curium fraction from the americium fraction prior to alpha spectrum measurements. The ion exchange methods of Smith and Hoffman[16] were used for this purpose. Generally the separation procedure reduced the amount of ^{241}Am relative to ^{242}Cm in the sources by better than 1000.

The integral reaction rate, $\phi\sigma$, for $^{241}Am(n,\gamma)\ ^{242g}Am$ was derived from the results of the IDAS determination of the ^{241}Am and ^{242}Cm atom concentrations in each applicable irradiated sample by equation 3.

$$\phi\sigma = \frac{\lambda'}{f} \cdot \frac{N'(\tau_s)}{N_1^o} \cdot \left\{ \frac{\lambda}{\lambda-\lambda'}(1-e^{-\lambda' t})e^{-\lambda'\tau_s} - \frac{\lambda'}{\lambda-\lambda'}(1-e^{-\lambda t})e^{-\lambda\tau_s} \right\}^{-1} \quad (3)$$

In equation 3 the symbols are defined as follows: λ and λ' are decay constants for ^{242g}Am and ^{242}Cm, respectively; f is the β^- branching fraction for ^{242g}Am; t is the irradiation time; τ_s is the time from end of irradiation to start of Cm/Am chemical separation; $^sN'(\tau_s)$ is the ^{242}Cm atom concentration at time τ_s; and N_1^o is the ^{241}Am atom concentration. The nuclear data required for the IDAS analyses were taken from Reference 14.

2.3 Measured Integral Reaction Rates

Two irradiation experiments were carried out to determine the integral fission reaction rate for ^{241}Am. Gamma-ray spectra were measured for each encapsulated specimen (~250 ug) for decay times ranging from one day to 17 days after the end of the irradiation. A cadmium absorber with a thickness of~ 0.5 mm was placed between the ^{241}Am source and the detector to reduce the intensity of the 59.0-keV line and, therefore, dead time problems. Integral fission reaction rates, corresponding to each prominent line in the ^{140}Ba-^{140}La decay, were obtained for each irradiated sample by the radiometric method described in Section 2.2. Average reaction-rate values for each irradiation were obtained by combining the values corresponding to each gamma line. These average integral fission rates and the corresponding gold monitor capture rates are listed in Table 1 for each irradiation.

Three irradiation experiments were carried out to determine the $^{241}Am(n,\gamma)\ ^{244g}Am$ capture rate based on measurements of ^{242}Cm production relative to ^{241}Am sample content. Approximately one mg samples were used in each experiment. After a decay period following each irradiation to allow for grow in of the ^{242}Cm, each ampoule was opened and the contents were assayed for their ^{241}Am and ^{242}Cm atom concentrations by using IDAS as outlined in Section 2.2. Equation 3 was used to derive the "measured" integral reaction rate from the IDAS results. Integral rates for each irradiation experiment are listed in Table 1.

Table 1. Summary of Measured Integral Reaction Rate (RR) Data, Derived Neutron Fluxes and Integral Cross Sections for ^{241}Am and ^{243}Am Irradiated in CFRMF at 100 kW

Experiment Type	Measured or Derived Quantity[a]	Irradiation 1	Irradiation 2	Irradiation 3
^{241}Am Fission	RR- $^{197}Au(n,\gamma)$	3.341×10^{-13}(1.6,0.5)[b]	3.427×10^{-13}(1.6,0.5)	---
	RR- $^{241}Am(n,f)$	3.975×10^{-13}(5.9,3.1,1.3)	4.011×10^{-13}(5.9,3.1,1.2)	---
	Neutron Flux	8.87×10^{11}(3.1,2.7)	8.86×10^{11}(3.1,2.7)	---
	Fission Cross Section	0.448(6.7,3.5)	0.453(6.7,3.5)	---
^{242}Cm Production	RR- $^{197}Au(n,\gamma)$	3.470×10^{-13}(1.6,0.5)	3.435×10^{-13}(1.6,0.5)	3.471×10^{-13}(1.6,0.5)
	RR- $^{241}Am(n,\gamma)^{242g}Am$	1.078×10^{-12}(2.7,2.1)	1.096×10^{-12}(3.4,2.9)	1.098×10^{-12}(2.4,1.6)
	Neutron Flux	8.97×10^{11}(3.1,2.7)	8.88×10^{11}(3.1,2.7)	8.98×10^{11}(3.1,2.7)
	Capture Cross Section	1.20(4.1,2.6)	1.23(4.6,3.3)	1.22(3.9,2.3)
^{243}Am Fission and Capture	RR- $^{197}Au(n,\gamma)$	3.380×10^{-13}(1.6,0.5)	3.363×10^{-13}(1.6,0.5)	---
	RR- $^{243}Am(n,f)$	3.08×10^{-13}(5.6,2.5,1.3)	3.07×10^{-13}(5.5,2.4,1.2)	---
	RR- $^{243}Am(n,\gamma)^{244g}Am$	8.25×10^{-14}(4.1,3.5)	8.75×10^{-14}(3.7,3.3)	---
	Neutron Flux	8.74×10^{11}(3.1,2.7)	8.70×10^{11}(3.1,2.7)	---
	Fission Cross Section	0.352(6.4,3.0)	0.353(6.3,2.9)	---
	Capture Cross Section	0.0944(5.1,3.8)	0.101(4.8,3.7)	---

a. Units of Integral Reaction Rate (RR), neutron flux and integral cross section are reactions per second per nucleus, neutrons per cm^2-sec and barns, respectively.

b. First value in parenthesis is total error estimate. Second and third values are reduced errors which do not include uncertainty contributions which are fully correlated from irradiation to irradiation. See text for details.

Two irradiations of approximately 1.25 mg samples of ^{243}Am were made for the purpose of measuring the integral fission and capture reaction rates. The integral fission rate is based on the gamma spectrometric method for measuring the emission rates of the prominent lines in ^{140}Ba-^{140}La. The capture rate to 10.1 h ^{244g}Am is also based on the same method for measuring the emission rates of the 744.1-keV and 898.2-keV gamma rays in the β^- decay of ^{244g}Am. Measurements of the gamma intensities of the activation and fission products were made relative to prominent gammas from ^{239}Np. Because ^{239}Np, the alpha decay daughter of ^{243}Am, was in secular equilibrium with the parent ^{243}Am activity, this approach bypassed the need for a direct ^{243}Am mass determination. Consequently, only relative peak areas, efficiency factors branching ratios and attenuation factors were required for the analyses. However, the analyses relative to ^{239}Np agreed well with subsequent absolute analyses which used the IDAS determined ^{243}Am masses.

Gamma-ray spectra for the ^{243}Am fission experiment were measured on a single Ge(Li) spectrometer system with a source-to-detector distance of 10 cm and with an external absorber packet of ~ 0.5 mm Cd and ~5 mm Pb placed between the sample and the detector. The absorbers were required to reduce the intensity of the low energy photons from ^{243}Am and ^{239}Np relative to the fission-product gammas. Corrections for gamma-ray attenuation through the absorber packet were determined by transmission experiments with ^{152}Eu and ^{154}Eu sources. Average integral fission rates, obtained by combining the values corresponding to each gamma line in the ^{140}Ba-^{140}La decay, and the corresponding gold monitor capture rates are listed in Table 1 for each irradiation.

Gamma-ray spectra for the ^{243}Am capture experiment were measured on two different Ge(Li) spectrometers with source-to-detector distances of ~ 60 cm and with no external absorbers. Integral capture rates, corresponding to the two ^{244g}Am lines, were obtained by the radiometric method described in Section 2.2. Average capture rate values, obtained by combining the values for each gamma line, are listed in Table 1 for each irradiation.

In Table 1, the values in parenthesis show a partial breakdown of the uncertainty contributions for the measured integral data. All values are tabulated as percent errors. The first value given is the total estimated error and second and third values are reduced errors. That is, they do not include all identified error contributions. For the ^{197}Au(n,γ) integral measurements, the first error value is the quadrature sum of the following: statistical error, and errors associated with each foil mass, the detector efficiency and the branching ratio for the 411-keV line. The second error value represents the statistical component only.

Three values are given for the errors in each measured ^{241}Am fission rate. The first value, the total error, is the quadrature sum of error contributions from the following: fission yield (5%), detector efficiency (~ 1.5%), sample mass (~ 2.4%) and the standard deviation resulting from averaging together the integral rates computed for each ^{140}Ba-^{140}La gamma line. The fission yield uncertainty was removed from the total error to give the second value in parenthesis. The third value represents the standard deviation resulting from the averaging process.

Two error values are given for the ^{241}Am(n,γ) ^{242g}Am integral data. The total estimated error, which is given first, includes the uncertainty in the β^-

branching ratio for ^{242g}Am and statistical and systematic errors associated with the IDAS determination of the ^{242}Cm and ^{241}Am atom concentrations in each sample. The branching ratio uncertainty is not included in the second error value.

Three error values are given for the ^{243}Am fission rates. The computation of the total error included the following uncertainties: the uncertainty in the branching ratio for the 334-keV line in ^{239}Np; a relative efficiency factor uncertainty of 1%, a 1% uncertainty in the relative attenuation factor, a 5% fission yield uncertainty and the standard deviation resulting from combining individual reaction rate determinations for each ^{140}Ba-^{140}La line. The second error value represents the total error without the fission yield uncertainty contribution. The third error value is the standard deviation resulting from the averaging process.

3. CROSS-SECTION DATA TESTING

3.1 Integral Tests

Integral test analyses included the following: (1) determination of the neutron flux for each irradiation, (2) derivation of spectrum-averaged cross sections from the measured reaction-rate data, (3) computation of spectrum-averaged cross sections for these reactions using multigroup representations of the evaluated cross sections and the CFRMF spectrum, and (4) comparison of the "measured" and calculated spectrum-averaged cross section and a consistency assessment of the integral test.

The neutron flux for each irradiation experiment was determined by correlating the reaction rates measured for the gold power level monitors at 100 kW operation with reaction rates for gold power level monitors used in the Interlaboratory Reaction Rate Program (ILRR)[17] for 6 kW operation[18]. An independent flux determination had been made for the 6 kW operation based on a flux transfer using measured fission rates for ^{239}Pu in the CFRMF and in the National Bureau of Standards (NBS) ^{252}Cf standard field[6,8]. Neutron fluxes for the present americium irradiation experiments are given in Table 1. Two values are given for the error in the neutron fluxes. The second value is the error in the neutron flux for the reference 6 kW power level. The first error is the quadrature sum of the reference level error and errors in using the gold power level monitor data to scale the neutron flux to 100 kW operation.

Integral cross sections for each of the americium capture and fission reactions were derived by dividing the measured integral reaction-rate values in Table 1 by the appropriate neutron fluxes. The results are given in Table 1. Two error values are listed for each derived integral cross section. The first error is the total estimated error in the derived quantities. For ^{241}Am and ^{243}Am fission, the second error quoted does not include the 5% yield error and the 2.7% error in the reference flux level. The second error given for each ^{241}Am(n,γ)^{242g}Am cross-section value does not include the 1.7% uncertainty in the β^- branching fraction for ^{242g}Am and the 2.7% reference flux level error. Errors which are not included in the second error for each ^{243}Am capture integral cross section value, are a 1.4% uncertainty in the branching ratio for the 277-keV line in ^{239}Np, a 1.5% detector efficiency error and the 2.7% reference flux uncertainty. The results from the different irradiation experiments were combined to give the following integral cross

sections in barns: 0.450 ± 6.2% for $^{241}Am(n,f)$, 1.22 ± 3.5% for $^{241}Am(n,\gamma)$ ^{242g}Am, 0.353 ± 6.1% for $^{243}Am(n,f)$ and 0.0976 ± 4.8% for $^{243}Am(n,\gamma)$ ^{244g}Am. Total capture cross sections for ^{241}Am and ^{243}Am were derived from the partial cross sections by utilizing isomer ratio information reported by Mann and Schenter[19]. Assuming ratios for ground state branching relative to total neutron capture of 0.787 for $^{241}Am(n,\gamma)$ and 0.109 for $^{243}Am(n,\gamma)$, total integral capture cross sections in barns are 1.55 ± 3.5% for ^{241}Am and 0.895 ± 4.8% for ^{243}Am.

Integral cross sections were computed using 620-group representations of the CFRMF central spectrum and of the evaluated cross sections on ENDF/B-V. The spectrum corresponds to that used for testing the dosimeter cross sections on ENDF/B-V[20]. A comparison of these calculated integral cross sections to the "measured" integral cross sections gives the following C/M ratios: 1.17 ± 9% for $^{241}Am(n,f)$, 0.71 ± 4% for $^{241}Am(n,\gamma)$, 1.19 ± 9% for $^{243}Am(n,f)$ and 0.65 ± 5% for $^{243}Am(n,\gamma)$. The uncertainty computed for each C/M ratio is the quadrature sum of the error in the measured quantity and the error in the calculated integral cross section due to spectrum uncertainties only. The spectrum uncertainty contribution was obtained by using a flux spectrum covariance matrix which was generated in a sensitivity and uncertainty analysis for the CFRMF[21].

3.2 Least-Squares-Adjustment Analysis

Least-squares-adjustment analyses were made with the FERRET code[22,23]. The adjustment analysis was made in a 53-group energy structure and it included the following input data: (1) 23 dosimeter integral reaction rates[7], (2) six integral reaction rates for capture and fission in ^{242}Pu, ^{241}Am, ^{243}Am, (3) CFRMF spectrum and associated covariance matrix, (4) cross sections processed with CFRMF spectrum weighting from ENDF/B-V for all reactions, and (4) covariance matrices for all reactions. The measured integral data were assumed to have zero correlation in the analyses. Covariance matrices for the dosimeter reactions were a mixture of matrices generated from the ENDF/B-V covariance files with the PUFF-2 code[24] and matrices generated by F. Schmittroth to improve upon the ENDF/B-V prescriptions . Twenty-one dosimeter covariances were from the Schmittroth library. Covariance matrices for the actinide reactions were generated in two ways: (1) PUFF-2 processing of the error files in ENDF/B-V and (2) using a gaussian-type parametric form[22] to describe the short-range correlations between the group wise uncertainties as obtained from ENDF/B-V and adding an additional normalization uncertainty in the unresolved and smooth energy ranges. The second approach to generating covariance matrices for the actinide reactions was emphasized in this study because of the limitations of the error files on ENDF/B-V (no error files for ^{243}Am, missing error and correlation information for some energy regions for ^{241}Am and ^{242}Pu, block-type correlation specifications). The ^{241}Am uncertainty information on ENDF/B-V was used for ^{243}Am, however, the normalization component was doubled from 15% for ^{241}Am to 30% for ^{243}Am.

Preliminary results of the least-squares-analysis using the parametric covariance prescription for ^{241}Am and ^{243}Am are illustrated in Figures 1-4. The upper part of each figure shows a direct comparison of the 53-group cross sections over the neutron energy ranges in which the CFRMF spectrum is sensitive. The bottom part of each figure shows the ratio of the

adjusted-to-unadjusted cross sections for the analysis. The input cross-section uncertainties are indicated by the upper and lower bounds. The adjusted uncertainties are illustrated by vertical lines through the group mid-energy points. These figures indicate the energy range and the magnitude of the adjustments required to achieve consistency between the measured integral data and the evaluated cross sections. It should be noted that within the constraints of the input uncertainties and correlations, the cross-section adjustments were of sufficient magnitude to reduce the discrepancies between the measured and calculated integral cross sections to 1.7% or better.

5. CONCLUDING REMARKS

In this paper we have reported on integral capture and fission reaction-rate measurements for ^{241}Am and ^{243}Am irradiated in the fast neutron field of the CFRMF. A comparison of spectrum-averaged cross sections derived from the measured reaction rates to integral cross sections calculated with ENDF/B-V cross-section data indicate significant discrepancies between the integral measurements and the evaluated cross sections. Possible sources of the discrepancies include the following: (1) the evaluated cross sections on ENDF/B-V, (2) the ^{140}Ba cumulative fission yield used in the determination of the fission rates, (3) the neutron capture branching fractions to the ground states of ^{242}Am and ^{244}Am, and (4) the spectrum characterization. We do not suspect the spectrum characterization to be the source of the inconsistencies for several reasons: (1) an extensive measurement and calculational effort[3,6,7] to characterize the spectrum has been made and (2) a least-squares-adjustment analysis with dosimeter integral data only indicates a high degree of consistency between a broad range of dosimeter reactions and the spectrum[7]. However, the fission yield and neutron-capture branching fraction data used are based on calculation only. Experimental verification of these data are required.

The impact of these integral data on the evaluated cross sections was assessed by means of a least-squares-adjustment analysis with the FERRET code[22]. As shown in Figures 1-4, the least-squares-adjustment analysis indicates that to achieve consistency between the measured integral data and the evaluated cross sections, the following cross-section adjustments are required: ^{241}Am(n,f), ~ 10% down (0.2 MeV to 17 MeV); ^{241}Am(n,γ), ~ 30% up (0.1 keV to 17 MeV); ^{243}Am(n,f), ~ 13% down (0.2 MeV to 17 MeV) and ^{243}Am(n,γ), ~44% up (0.1 keV to 17 MeV). The FERRET analysis points to the need for re-evaluating the ENDF/B-V fast capture and fission cross sections for these nuclides and for refining in a substantial way the associated covariance information on ENDF/B.

REFERENCES

1. R. E. Chrien, Editor, Proceedings of the Specialists' Meeting on Nuclear Data of Plutonium and Americium Isotopes For Reactor Applications, Brookhaven National Laboratory, November 20-21, 1978, USDOE Report BNL 50991, BNL (May 1979).

2. F. M. Mann and R. E. Schenter, "HEDL Evaluation of Actinide Cross Sections for ENDF/B-V," US DOE Report HEDL-TME 77-54, HEDL (1977).

3. J W Rogers, D. A. Millsap and Y. D. Harker, Nucl. Tech. 25, 330 (1975).

4. Y. D. Harker, R. A. Anderl, E. H. Turk, and N. C. Schroeder, "Integral Measurements for Higher Actinides in CFRMF," in Proc. International Conference on Nuclear Cross Sections for Technology, Knoxville, Tennessee, October 22-26, 1979, NBS Special Publication 594, 548 (September, 1980).

5. R. A. Anderl, N. C. Schroeder, "Integral Capture and Fission Cross Sections for ^{241}Am and ^{243}Am in the CFRMF," US DOE report EGG-PHYS-5691, INEL, to be published.

6. J W Rogers, D. A. Millsap and Y. D. Harker, "The Coupled Fast Reactivity Measurements Facility (CFRMF)," in Proc. of IAEA Consultants Meeting on Integral Cross-Section Measurements for Reactor Dosimetry, IAEA, Vienna, Austria, November 15-19, 1976, IAEA-208, Vol. II, 117 (1976).

7. R. A. Anderl, Y. D. Harker, D. A. Millsap, J W Rogers and J. M. Ryskamp, "CFRMF Spectrum Update and Application to Dosimeter Cross-Section Data Testing," in the Proc. for the Fourth ASTM-EURATOM Symposium on Reactor Dosimetry, National Bureau of Standards, March 22-26, 1982.

8. R. C. Greenwood, et. al., "Radiometric Reaction-Rate Measurements in CFRMF and BIG-10," in Proc. Second ASTM-EURATOM Symposium on Reactor Dosimetry, Palo Alto (1977), NUREG/CP-004, Vol. 3, 1207 (1978).

9. R. J. Gehrke, R. G. Helmer, and R. C. Greenwood, Nucl. Inst. Meth. 147, 405 (1977).

10. M. V. Ramaniah, et. al., Nucl. Tech. 49, 121 (1980).

11. J. D. Baker and L. D. McIsaac, "Isotope Dilution Analysis of Picogram Quantities of Pu, Am and Cm in Nuclear Fuel Processing Plant Streams," US DOE Report ICP-1094, INEL (1976).

12. K. Debertin, U. Schotzig and K. F. Waltz, Nucl. Sci. Eng. 64, 784 (1977).

13. R. L. Bunting, INEL, private communication (1980).

14. C. M. Lederer and V. S. Shirley, editors, Table of Isotopes Seventh Edition, John Wiley and Sons, Inc. (1978).

15. H. L. Smith and D. C. Hoffman, J. Inorganic and Nucl. Chem. 3, 243 (1956).

16. M. E. Meek and B. F. Rider, "Compilation of Fission-Product Yields, Vallecitos Nuclear Center," NEDO-12154-2 (January, 1977).

17. W. N. McElroy and L. S. Kellogg, Nucl. Tech. 25, 180 (1975).

18. Y. D. Harker, J W Rogers and D. A. Millsap, "Fission-Product and Reactor Dosimetry Studies at Coupled Fast Reactivity Measurements Facility," US DOE Report TREE-1259, Idaho National Engineering Laboratory (1978).

19. F. M. Mann and R. E. Schenter, Nucl. Sci. Eng. 63, 242 (1977).

20. R. A. Anderl, D. A. Millsap, J W Rogers, and Y. D. Harker, "INEL Integral Data-Testing Report for ENDF/B-V Dosimeter Cross Sections," US DOE Report EGG-PHYS-5608, INEL (October, 1981).

21. J. M. Ryskamp, et. al., Nucl. Tech. 57, 20 (1982).

22. F. Schmittroth, "FERRET Data Analysis Code," HEDL-TME-79-40, Hanford Engineering Development Laboratory (1979).

23. F. Schmittroth, Nucl. Sci. Eng. 72, 19 (1979).

24. "PUFF2 Determination of Multigroup Covariance Matrices from ENDF/B-V Uncertainty Files," RSIC Computer Code Collection, PSR-157 (1980).

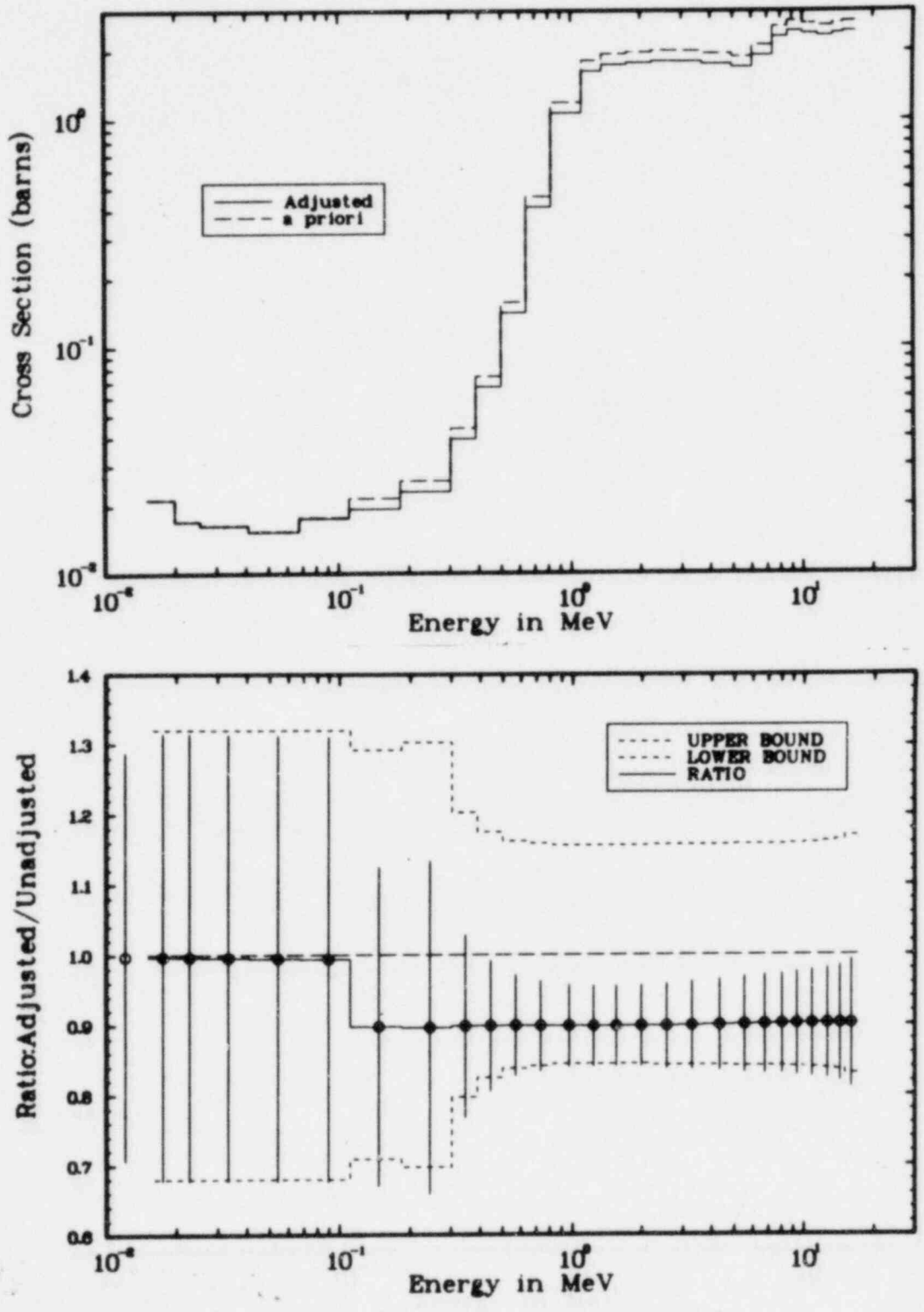

Figure 1. Comparison of adjusted and unadjusted cross sections for $^{241}Am(n,f)$. In the lower half of the figure, input cross-section uncertainties are indicated by upper and lower bounds and adjusted uncertainties are indicated by vertical lines through the group mid-energy points.

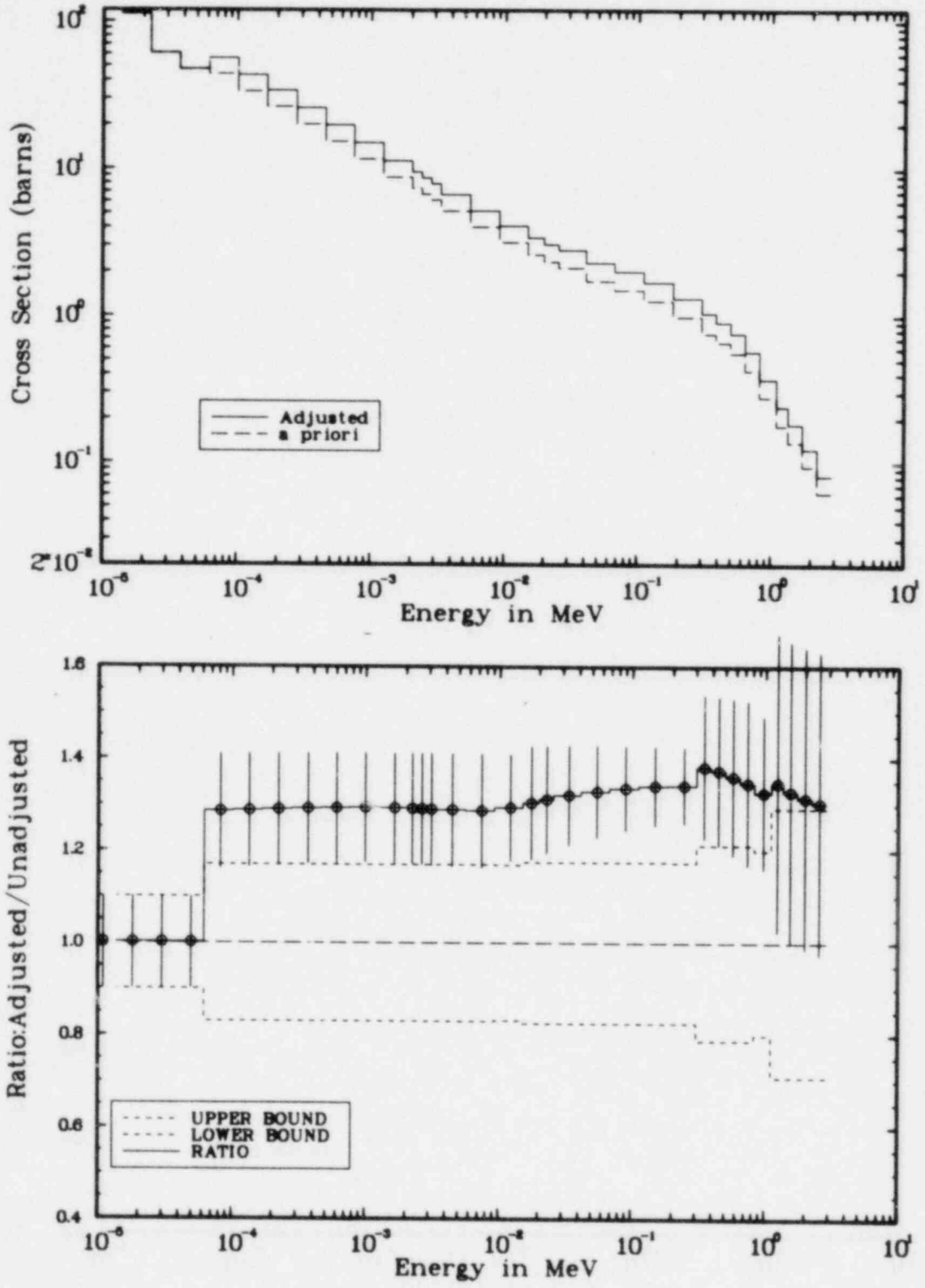

Figure 2. Comparison of adjusted and unadjusted cross sections for $^{241}Am(n,\gamma)$. In the lower half of the figure, input cross-section uncertainties are indicated by upper and lower bounds and adjusted uncertainties are indicated by vertical lines through the group mid-energy points.

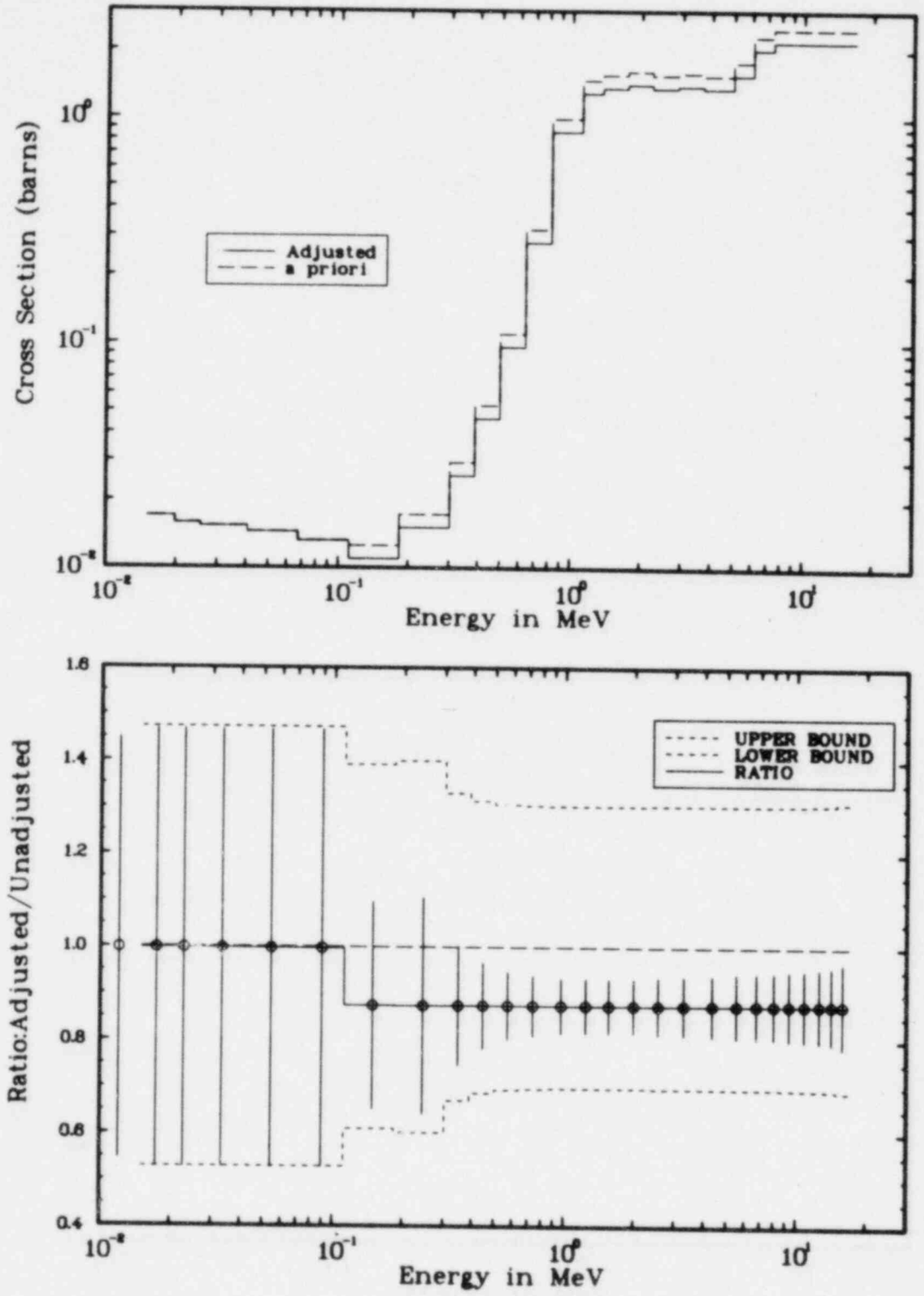

Figure 3. Comparison of adjusted and unadjusted cross sections for $^{243}Am(n,f)$. In the lower half of the figure, input cross-section uncertainties are indicated by upper and lower bounds and adjusted uncertainties are indicated by vertical lines through the group mid-energy points.

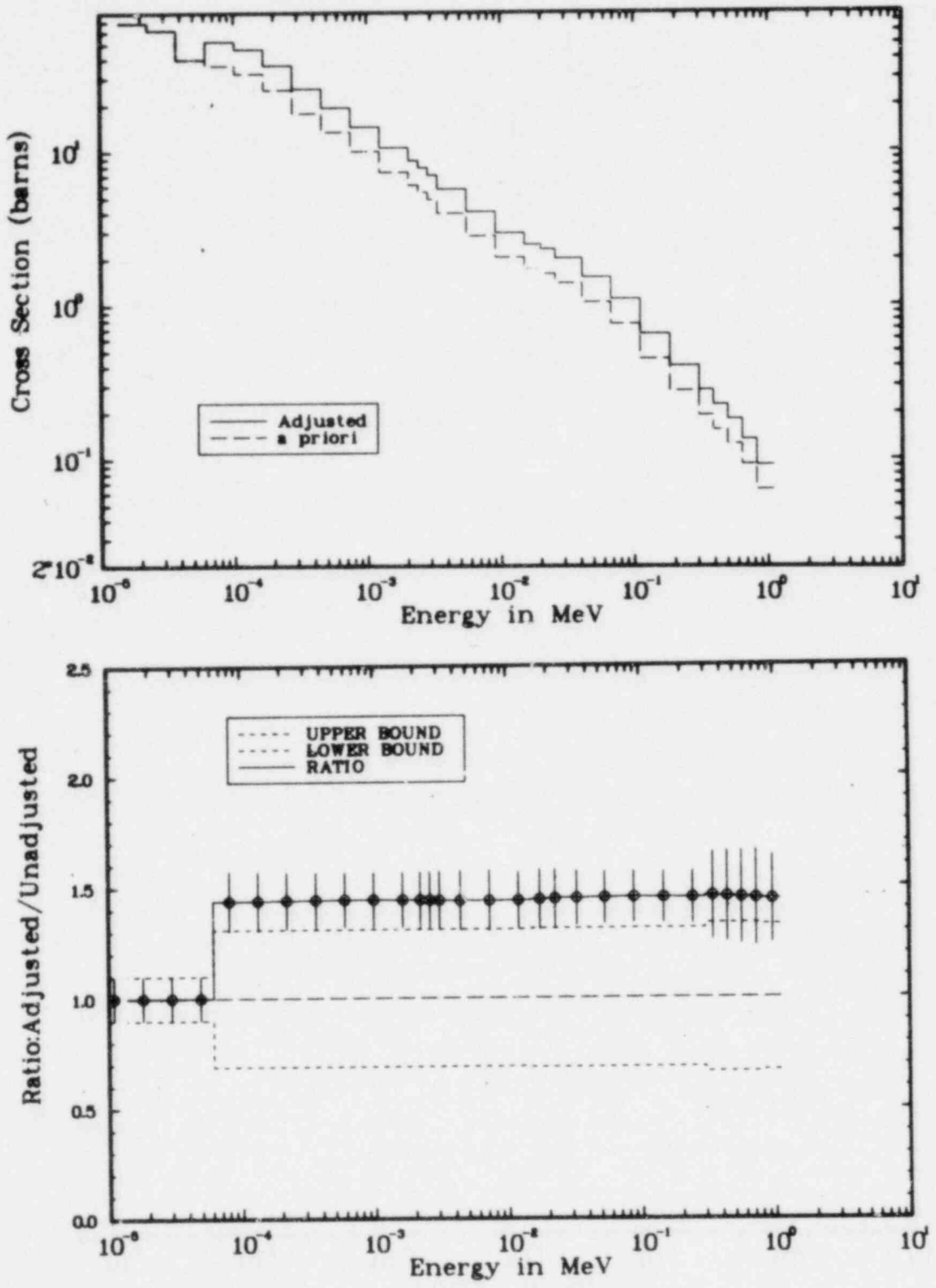

Figure 4. Comparison of adjusted and unadjusted cross sections for $^{243}Am(n,\gamma)$. In the lower half of the figure, input cross-section uncertainties are indicated by upper and lower bounds and adjusted uncertainties are indicated by vertical lines through the group mid-energy points.

SENSITIVITIES AND UNCERTAINTIES OF A LARGE LMFBR USING ADJUSTED CROSS-SECTION LIBRARY ORACLE-1*

J. H. Marable, D. G. Cacuci, C. R. Weisbin and J. R. White†
D. Biswas‡ and J. M. Kallfelz**
C. L. Cowan and R. Protsik††

ABSTRACT

Integral experiment data have been combined with the VITAMIN-E cross-section library to create the adjusted library ORACLE-1. This adjusted library has been applied to the sensitivity and uncertainty analysis of a large LMFBR. Four responses namely, K_{eff}, breeding ratio, peak power density ratio, and sodium void reactivity, have been analyzed. A comparison of the results for K_{eff}, in particular, with previously reported results is presented. The uncertainty in K_{eff} due to nuclear data uncertainties is reduced from 3% (unadjusted data) to 0.4% by use of the adjusted library.

I. INTRODUCTION

The joint work reported here is a continuation of a cooperative effort between General Electric Company, Georgia Institute of Technology, and Oak Ridge National Laboratory, with the main goal of investigating sensitivities and uncertainties associated with calculated values of key performance parameters in fast reactors. Earlier work was reported in Refs. 1 through 4. Related effort has been concentrated on developing a least-squares adjusted cross section and covariance library, ORACLE-1, for application to fast reactor design. A preliminary version of this library was described in Ref. 5. A final version of this library, i.e., ORACLE-I, has now been completed. This library is based on the a priori 174-group VITAMIN-E cross section library,[6] a priori covariances derived from ENDF/B-V[7] and other sources, and twenty-seven benchmark integral experiments. This adjusted library consists of not only adjusted cross sections in 174-group structure but also includes adjusted cross section covariances in 26-group structure.

ORACLE-I cross sections and covariances have been used in conjunction with the VENTURE,[8] DEPTH-CHARGE,[9] and FORSS[10] code systems to perform a sensitivity and uncertainty analysis of key parameters for an R-Z model of a large heterogeneous fast reactor core. This model was also used in Ref. 4 to perform a sensitivity and uncertainty analysis of K_{eff}, breeding ratio (with and without the so-called "K-reset"[2] mechanism), and power density ratio. The cross

*Research sponsored by Union Carbide Corporation under contract W-7405-eng-26 with the U.S. Department of Eenrgy.
†Oak Ridge National Laboratory, Oak Ridge, Tennessee 37830
‡Singer Company, Link Simulation Systems Division, 11800 Tech Rd. Silver Spring, MD 20904
**Georgia Institute of Technology, Atlanta, Georgia 30332
††General Electric Company, Sunnyvale, California 94086

sections and covariances used in Ref. 4, though, were based on ENDF/B-IV data. In the meanwhile, a new set of sensitivities for these parameters has been derived by using ENDF/B-V and ORACLE-I cross sections, and, in particular, considerable effort has been devoted to investigations[11-13] of sensitivities of extrema of functions, such as the peak power density. In addition, sodium-void reactivity sensitivities have also been calculated and investigated.

Comprehensive reporting of all of the above mentioned results is beyond the scope of this paper. Instead, after briefly describing, in Sec. II, the design and typical configuration of the large LMFBR, we present in Sec. III the major characteristics of the adjusted cross section library ORACLE-I. Section IV discusses the basic model and methods used to determine sensitivities and uncertainties. Section V presents selected sensitivity results and standard deviations for K_{eff}, and highlights the importance of the adjustment procedure by presenting a comparative analysis of the new, ORACLE-I based, results, and ENDF/B-IV-based results that have previously been reported.[2-4] Finally, Sec. VI summarizes and concludes this work.

II. REACTOR DESCRIPTION

The key design parameters for a large heterogeneous LMFBR of the 1000 MWe class were specified as part of a DOE-sponsored project. The design objectives and criteria for this project emphasized the following:

1. High reliability,
2. Near term design features (components that can be developed within five years),
3. Sufficiently low sodium-void worth to preclude hypothetical core disruptive accidents from consideration as design-basis accidents,
4. Breeding of fissile fuel at a rate equivalent to a compound system doubling time of twenty years or less, and
5. Allowances for the future accomodation of advanced fuels.

On the basis of the above objectives, the reference design was chosen to be a 2540 MW_{th}, mixed plutonium uranium oxide, heterogeneous reactor with three driver fuel zones and three inner blanket zones. The core layout for the reference system is shown in Fig. 1, and the principal core design and performance parameters are summarized in Table I. All design calculations discussed in this section were carried out in linked r-z and x-y triangular mesh geometry using the two-dimensional-diffusion theory code SN2D[14] and the fuel management and burnup code FUMBLE,[15] and cross sections based on ENDF/B-V data.

The fuel pin diameter for the LMFBR design was selected on the basis of earlier sensitivity studies to give near-optimum breeding and economic performance for the heterogeneous core. The core layout as shown in Fig. 1 was specified to minimize the peak radial power throughout the operating cycle based upon a single fissile enrichment for the supplied fuel in all driver fuel regions. The twelve burnup control rods in the outer driver fuel zone are also utlized to shape the radial power profile during reactor operations.

Reactor shutdown is accomplished by each of two independent control systems. The primary control system consists of 21 natural carbide rods, including 12 rods in the outer control ring for burnup reactivity adjustments. The secondary control system consists of 9 enriched boron carbide rods which are distributed in the inner and middle control rings.

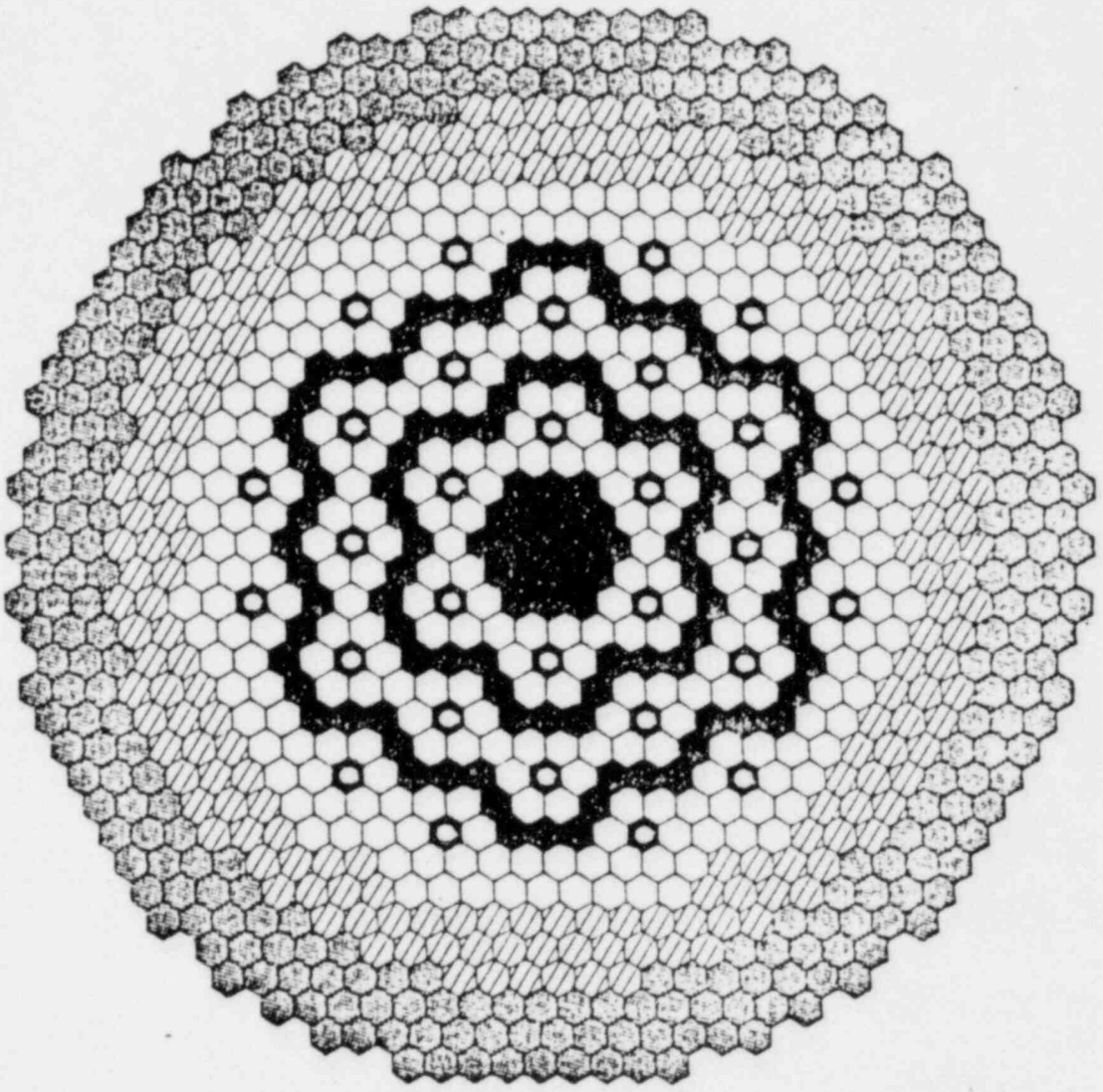

Fig. 1. Core layout for the reference design

TABLE I

General Design Parameters & Calculated
Performance Parameters for a
LMFBR Heterogeneous Core

Design Parameters	
Core Height (cm)	101.6
Core Effective Outer Radius (cm)	166.8
Axial Blanket Thickness (cm)	35.6
Radial Blanket Thickness (cm)	34.2
Number of Assemblies	
Driver Fuel	300
Inner Blanket	115
Radial Blanket	204
Control	30
Assembly Pitch (cm)	15.06
Pin Diameter (cm) - Driver Fuel/Blankets	0.6985/1.118
Clad Thickness (cm) - Driver Fuel/Blankets	0.03683/0.03556
Smeared Fuel Density (%TD) - Driver Fuel/Blankets	86.5/93.3
Refueling Interval (Days)	365
Fuel and Internal Blanket Residence Time (Days)	730
Capacity Factor (%)	80
Performance Parameters	
Total Power (MW_{th})	2540
Loaded Fissile Enrichment (% - Atoms of U-235 + Pu239 + Pu241/Total Atoms of Fuel)	17.7
Average Breeding Ratio	1.35
Doubling Time, CSDT (years)	17
Average Discharge Driver Burnup (MWD/MT)	58,600

III. DESCRIPTION OF ORACLE-I

ORACLE-I is an adjusted cross-section and covariance library derived from the VITAMIN-E[6] 174-group cross-section library and based on covariance data from ENDF/B-V and other evaluations. Data from the twenty-nine benchmark integral experiments reported in Ref. 5 were selected for incorporation into this adjusted library. Calculated-response correctors were applied as described in Refs. 2 and 16.

The use of all twenty-nine integral experiments led to a statistically unacceptable value of 5.3 for chi-square per degree of freedom. This unacceptable result was found to be due to (1) several inconsistent correlations, (2) low values for the uncertainties of ^{239}Pu inelastic and ^{235}U inelastic cross sections, and (3) one grossly discrepant integral experiment - ZPR-3/48 ^{28}c/^{25}f. The inconsistent correlations were eliminated, the ^{235}U and ^{239}Pu inelastic uncertainties were increased to more reasonable values,[17] and the discrepant experiment was dropped along with one other benchmark. This latter benchmark, JEZEBEL ^{49}f/^{25}f, did not have a discrepant value for C/E but the correlations with other benchmarks did not appear entirely consistent.

ORACLE-I is the result of the adjustment based on this revised data which led to a chi-square of 1.15 per degree of freedom. The revised covariance data upon which ORACLE-I is based is shown in Fig. 2. Recalculation of the integral experiments using the adjusted library agreed well with the predictions of the linear least-squares adjustment procedure indicating that nonlinear effects were negligible. Using the same codes as for the initial calculations with VITAMIN-E, the results calculated with adjusted library ORACLE-I gave substantial overall improvement in the C/E ratios - even for JEZEBEL ^{49}f/^{25}f, which was not included in the adjustment.

IV. MODEL AND METHODS

The reactor model used for sensitivity studies is characteristic of the middle of equilibrium cycle (MOEC) conditions. It is an R-Z model, as shown in Fig. 3, and the composition of its principal regions are given in Table II. This model will henceforth be called the "basic model." Control is virtually all withdrawn; only the outer control bank is inserted slightly to achieve criticality for the nuclear data set[4] obtained by collapsing the ENDF/B-IV-based 171 group cross section library VITAMIN-C[18] to 32 groups using fluxes from a 1-D, cylindrical XSDRN-PM[19] transport calculation (S_4P_1) of the reactor.

The ORACLE-I adjusted cross-section library discussed in the foregoing Sec. III, the diffusion theory-based VENTURE[8] code, and the DEPTH-CHARGE[9] sensitivity code were used to determine group-dependent sensitivities $(\partial I/I)/(\partial\sigma_i/\sigma_i)$, where I denotes an integral parameter. Four integral parameters were considered, namely K_{eff}, the breeding ratio (BR), the ratio of peak power density to total power (PD), and the sodium-void reactivity. Note that the power density ratio PD is directly related to the linear power in the reactor.

These integral parameters can be expressed mathematically as ratios of linear functionals of the flux densities. Therefore, as in previous sensitivity studies,[1-4] the sensitivities of K_{eff} and BR are calculated by using the

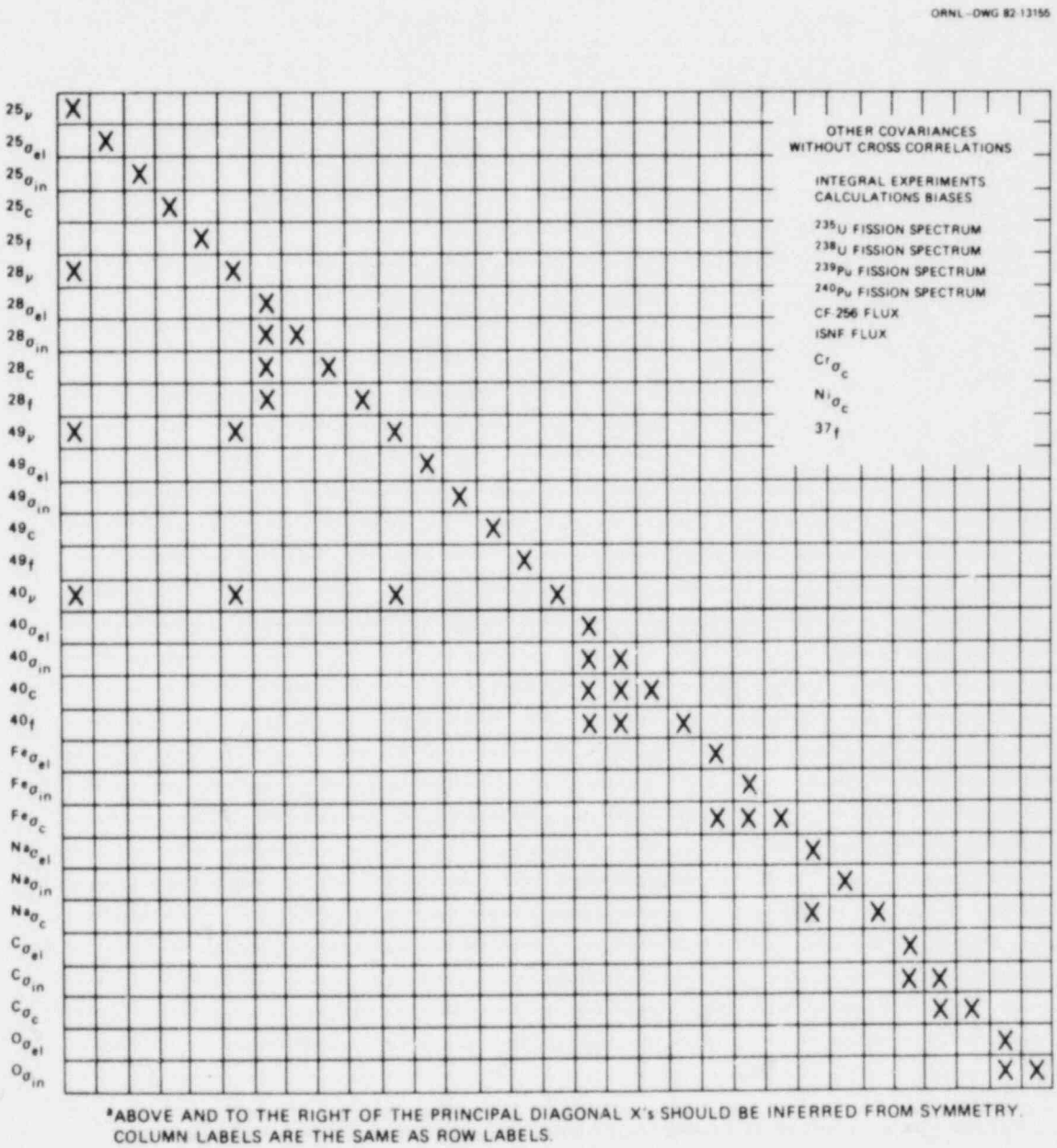

[a]ABOVE AND TO THE RIGHT OF THE PRINCIPAL DIAGONAL X's SHOULD BE INFERRED FROM SYMMETRY. COLUMN LABELS ARE THE SAME AS ROW LABELS.

Fig. 2. Covariance Data for Adjusted Library ORACLE-1[a]

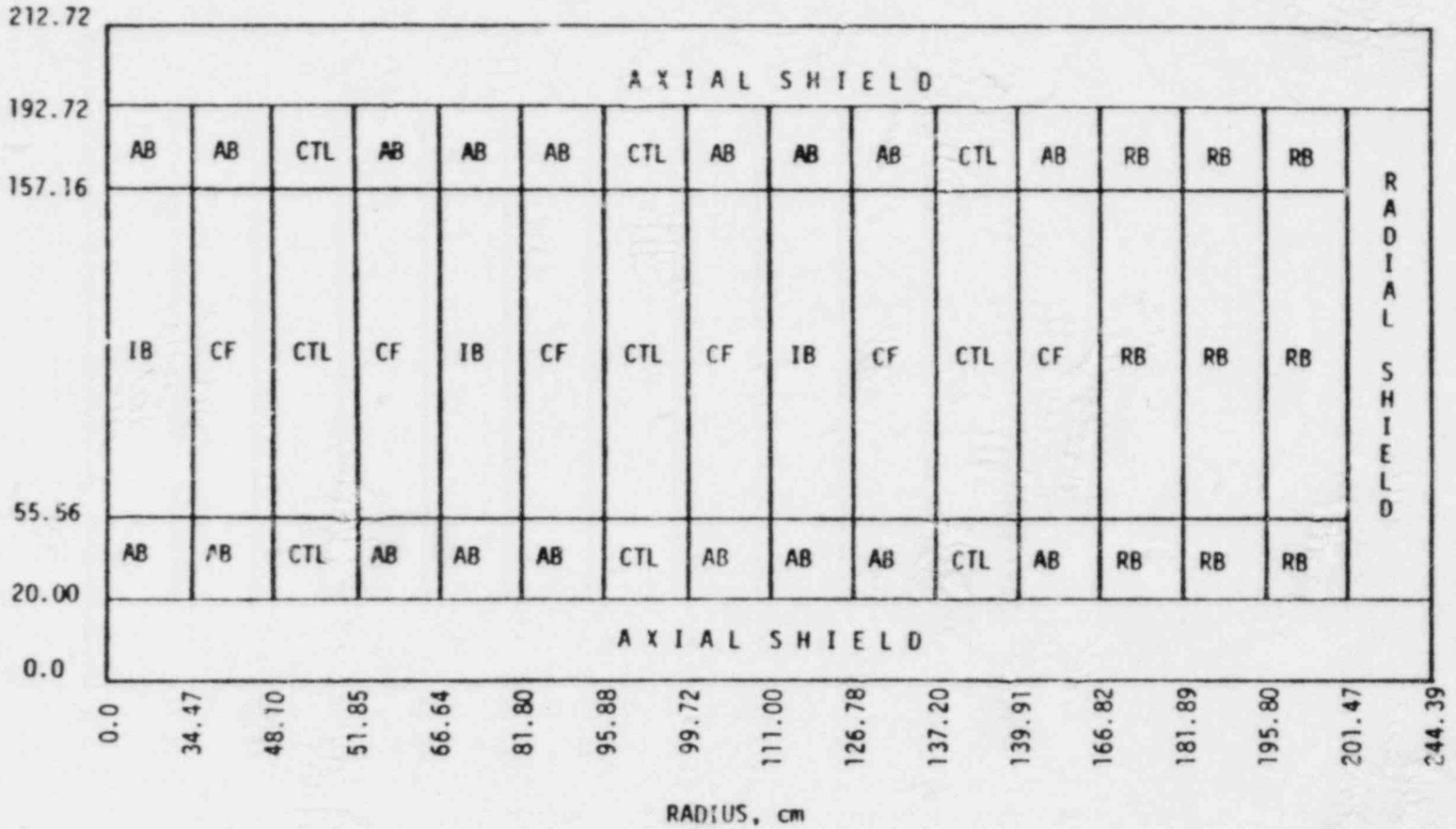

Fig. 3. Region Map of a Typical Heterogeneous Core
(Not to Scale)

Table II. Approximate Nuclide Densities, Principal Constituents of Reactor Model, Fig. 3 (10^{21} atoms/cc)[a]

Nuclide	CF	IB	AB over CF	AB over IB	RB	Prim. CTL Out	Second. CTL Out	Prim. CTL IN	Second. CTL In
U^{238}	6.75	12.4	9.58	12.6	12.6				
Pu^{239}	1.33	2.4-1	5.1-2	7.5-2	1.0-1			Nuclides for CTL In only	
Pu^{240}	4.4-1	7.8-3	4.1-4	7.2-4	2.0-3			B10:13.3	11.7
Pu^{241}	1.8-1	1-9-4						B11: 2.3	2.0
Pu^{242}	5.4-2							C: 7.2	6.4
U^{235}	1.2-2	2.1-2	1.8-2	2.4-2	2.3-2				
FP PAIRS	2.6-1	5.4-2	5.4-3	6.3-3	1.3-2				
O	18.1	25.4	As CF	As IB	As IB				
Na	8.2	6.1	"	"	"	20.8	19.6	8.3	8.9
Fe	11.9	9.6	"	"	"	3.7	6.7	17.8	18.4
Cr	2.4	2.0	"	"	"	7.5-1	1.4	3.6	3.7
Ni	2.8	2.2	"	"	"	8.7-1	1.6	4.2	4.3

[a] CF, IB, AB, RB and CTL signify driver, internal blanket, axial blanket, radial blanket, and control zones, respectively.

(customary) generalized adjoint functions Γ^*. For sensitivity values involving the criticality constraint, the so-called "K-reset" procedure has been performed by altering the driver zone "plutonium enrichment," i.e., (total Pu)/(total heavy metal). The power density ratio at a point $\vec{r}_p$ is defined as[4]

$$PD(\vec{r}_p) = \frac{a_1}{a_2} = \frac{\sum_j \Sigma_{1j}(\vec{r}_p)\ \phi_j(\vec{r}_p)}{\int_{\text{reactor}} \sum_j \Sigma_{2j}(\vec{r})\ \phi_j(\vec{r})\ d\vec{r}} \quad . \tag{1}$$

Considering only fission energy and assuming localized energy deposit, the quantities Σ_{1j} have the form:

$$\Sigma_{1j}(\vec{r}) = \sum_k p^k\ \Sigma^k{}_{f,j}(\vec{r}) \quad , \tag{2}$$

where p^k is the total energy release per fission in the k-th isotope. Thus, the fixed source in the equation for $\vec{\Gamma}^*$ for $PD(\vec{r}_p)$ has the form:

$$S^*_j(\vec{r}) = \Sigma_{1j}(\vec{r})/a_1 - \Sigma_{2j}(\vec{r})/a_2 \quad , \tag{3}$$

where Σ_{1j} is zero for $\vec{r} \neq \vec{r}_p$. The capability to generate the adjoint functions Γ^* for the source S^* given in Eq. (3) has been implemented in VENTURE.[8] The Γ^* and ϕ files generated by VENTURE were then input into the DEPTH-CHARGE[9] code to calculate the respective sensitivities.

It is not necessary to use "generalized" adjoint calculations to determine sodium-void sensitivity coefficients SC(Na-void). Instead, these coefficients can be determined from the difference

$$SC(\text{Na-void}) = \frac{1}{R}\left[-\frac{1}{K_1}\ SC_1 + \frac{1}{K_2}\ SC_2\right], \tag{4}$$

where R is the sodium-void reactivity, K_1 and K_2 denote K_{eff} for the base-case and voided-case, respectively, and SC_1 and SC_2 are sensitivities obtained from two "normal" perturbation theory calculations corresponding to K_1 and K_2, respectively.

Performance parameter uncertainties arising from nuclear data uncertainties are obtained by using the expression

$$VAR\ (I) = \sum_{i,j} \frac{\partial I}{\partial \sigma_i}\ \frac{\partial I}{\partial \sigma_j}\ COV\ (\sigma_i, \sigma_j) \quad , \tag{5}$$

where VAR(I) is the variance of integral parameter I, and $\partial I/\partial\sigma$ and $COV(\sigma_i,\sigma_j)$ denote sensitivities and covariances of various cross sections, respectively. To obtain a reliable estimate of the standard deviation

$SD(I) = [VAR(I)]^{1/2}$, Eq. (5) should include all data that significantly impact I. Note also that the covariance of two integral parameters I_1 and I_2 is given by

$$COV(I_1, I_2) = \sum_{i,j} \frac{\partial I_1}{\partial \sigma_i} \frac{\partial I_2}{\partial \sigma_j} COV(\sigma_i, \sigma_j) , \quad (6)$$

while the correlation $COR(I_1, I_2)$ between I_1 and I_2 is expressed as

$$COR(I_1,I_2) = COV(I_1,I_2)/[SD(I_1)\ SD(I_2)] . \quad (7)$$

For the results reported in the next section, the sensitivities and covariances $COV(\sigma_1,\sigma_2)$ used in Eqs. (5) and (6) are based on the ORACLE-I adjusted cross section library. Note that, for all reported sensitivities, the partial reaction cross sections were taken to be the independent variables, and the transport and total cross sections were treated as dependent variables. Thus for the diffusion theory calculations, a perturbation in a partial cross section had an associated perturbation in the transport cross section. For consistency the same convention must be used for the covariance data $COV(\sigma_i,\sigma_j)$ in Eq. (6).

V. DISCUSSION OF SELECTED RESULTS FOR K_{eff}

Table III presents selected total (energy-integrated) relative sensitivities of K_{eff} to $\bar{\nu}$, and to capture and fission cross sections. In addition to the results based on ORACLE-I, this table also shows, for comparison, sensitivites (from Ref. 4) for the same heterogeneous LMFBR but obtained by using ENDF/B-IV data, and ENDF/B-IV based sensitivities (from Ref. 2) from the homogeneous LCCEWG-LMFBR.[20] These results indicate that the largest sensitivities are for heavy metals, and the largest of them are for the same reactions and have roughly the same values in all three cases. In particular, for the heterogeneous LMFBR, the sensitivities based on ORACLE-I are within about 15% of those based on ENDF/B-IV unadjusted data. Note that, in all cases, the sensitivities of K_{eff} to $\bar{\nu}$ sum to unity.

Standard deviations for K_{eff} are obtained by using Eq. (5), and the resulting values are presented in Table IV. The value of 0.4% shown in this table has been obtained by using ORACLE-I based nuclear data sensitivities and covariances. For the sake of comparison, Table IV also presents previously reported[2,4] standard deviations for K_{eff}. Thus, the value of 3.2% was obtained[4] for the same LDP-type reactor model, but by using unadjusted ENDF/B-IV data and sensitivities for the reactions indicated in Fig. 4. The marked difference between this "unadjusted" value and the "adjusted" value of 0.4% is largely due to the effect of including results of integral experiments. Note that contributions due to thermal-hydraulic and other engineering design uncertainties have not been included for the heterogeneous LMFBR model.

Also shown in Table IV are the previously reported[2] standard deviations for K_{eff} for the homogeneous LCCEWG-LMFBR reactor.[20] The value of 3.1% was obtained by using sensitivities and covariances, based on ENDF/B-IV data, for the reactions indicated in Fig. 5; of course, methods and modeling biases,[2] and integral experiment results were omitted in this case. When the respective biases and integral experiment results were included, the adjustment reduced the standard deviation from 3.1% to 0.5%. Note that, although only

TABLE III

Selected Total Relative Sensitivities (x100) for K_{eff}

Nuclide	Reaction	Heterogeneous LMFBR ORACLE-I	K_{eff} Sensitivities Heterogeneous LMFBR ENDF/B-IV[a]	Homogeneous LCCEWG-LMFBR ENDF/B-IV[b]
^{235}U	$\bar{\nu}$	1.0	0.9	1.3
	σ_f	0.7	0.7	0.9
	σ_c	- 0.1	- 0.1	- 0.1
238U	ν	13.0	12.4	13.6
	σ_f	7.8	7.7	8.3
	σ_c	-22.0	-21.9	-23.3
^{239}Pu	ν	69.0	69.1	62.3
	σ_f	49.0	50.1	45.3
	σ_c	-22.0	-21.9	-23.3
^{240}Pu	ν	5.2	5.1	5.4
	σ_f	3.5	3.5	3.8
	σ_c	- 1.7	- 1.5	- 1.8
^{241}Pu	ν	12.0	12.0	16.3
	σ_f	8.5	8.8	12.0
	σ_c	- 0.6	- 0.6	- 0.8
^{242}Pu	ν	0.4	0.5	1.2
	σ_f	0.3	0.3	0.8
	σ_c	- 0.2	- 0.2	- 0.5

[a]See also Ref. 4.
[b]See also Ref. 2.

TABLE IV

Standard Deviations for K_{eff}

Heterogeneous LMFBR		LCCEWG-LMFBR[b]	
ORACLE-I	ENDF/B-IV[a]	Unadjusted	Adjusted
0.4%	3.2%	3.1%	0.5%

[a]See also Ref. 4.
[b]See also Ref. 2.

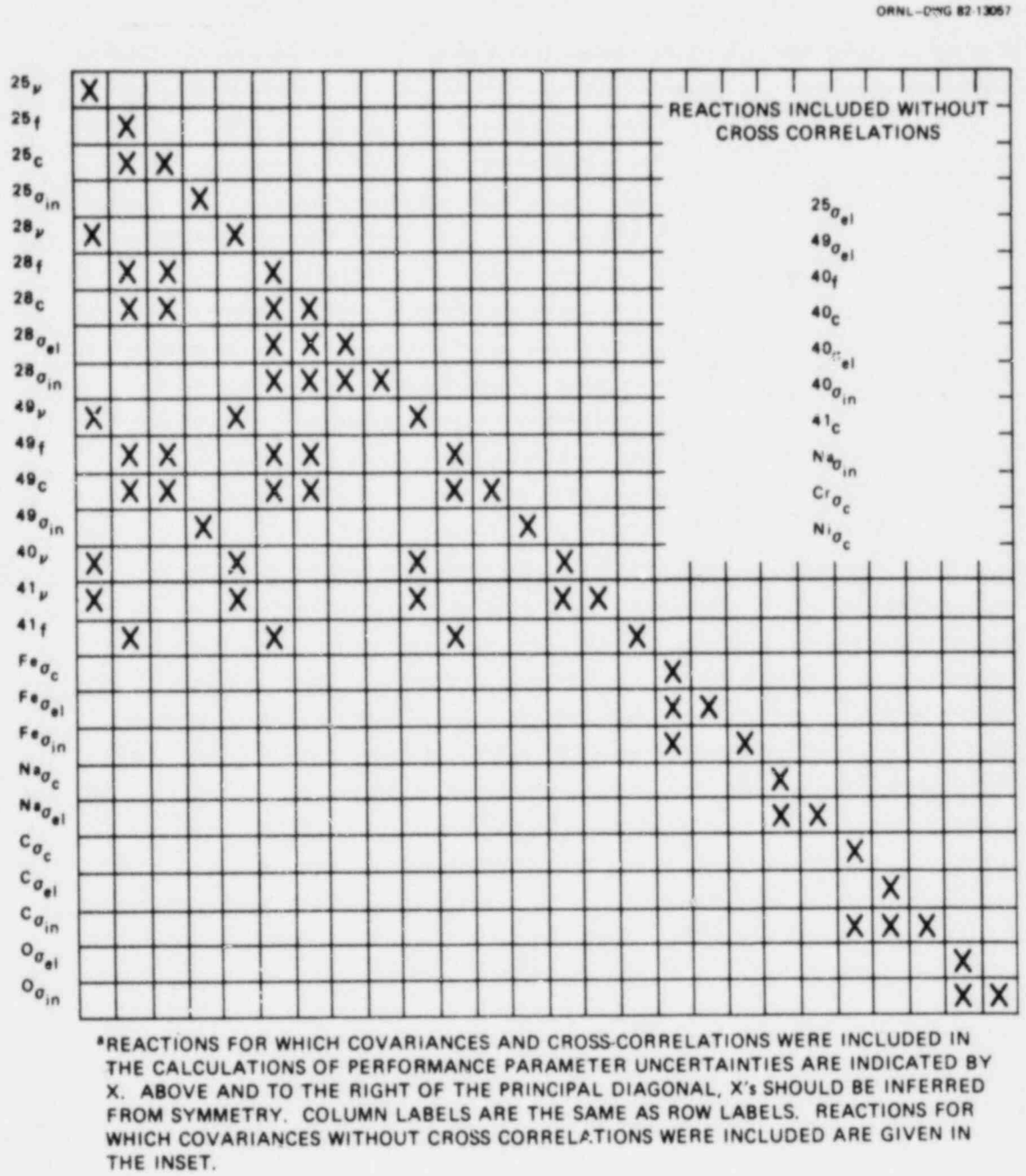

[a]REACTIONS FOR WHICH COVARIANCES AND CROSS-CORRELATIONS WERE INCLUDED IN THE CALCULATIONS OF PERFORMANCE PARAMETER UNCERTAINTIES ARE INDICATED BY X. ABOVE AND TO THE RIGHT OF THE PRINCIPAL DIAGONAL, X's SHOULD BE INFERRED FROM SYMMETRY. COLUMN LABELS ARE THE SAME AS ROW LABELS. REACTIONS FOR WHICH COVARIANCES WITHOUT CROSS CORRELATIONS WERE INCLUDED ARE GIVEN IN THE INSET.

Fig. 4. Unadjusted covariance data for large heterogeneous LMFBR reactors.[a]

ORNL–DWG 82-13058

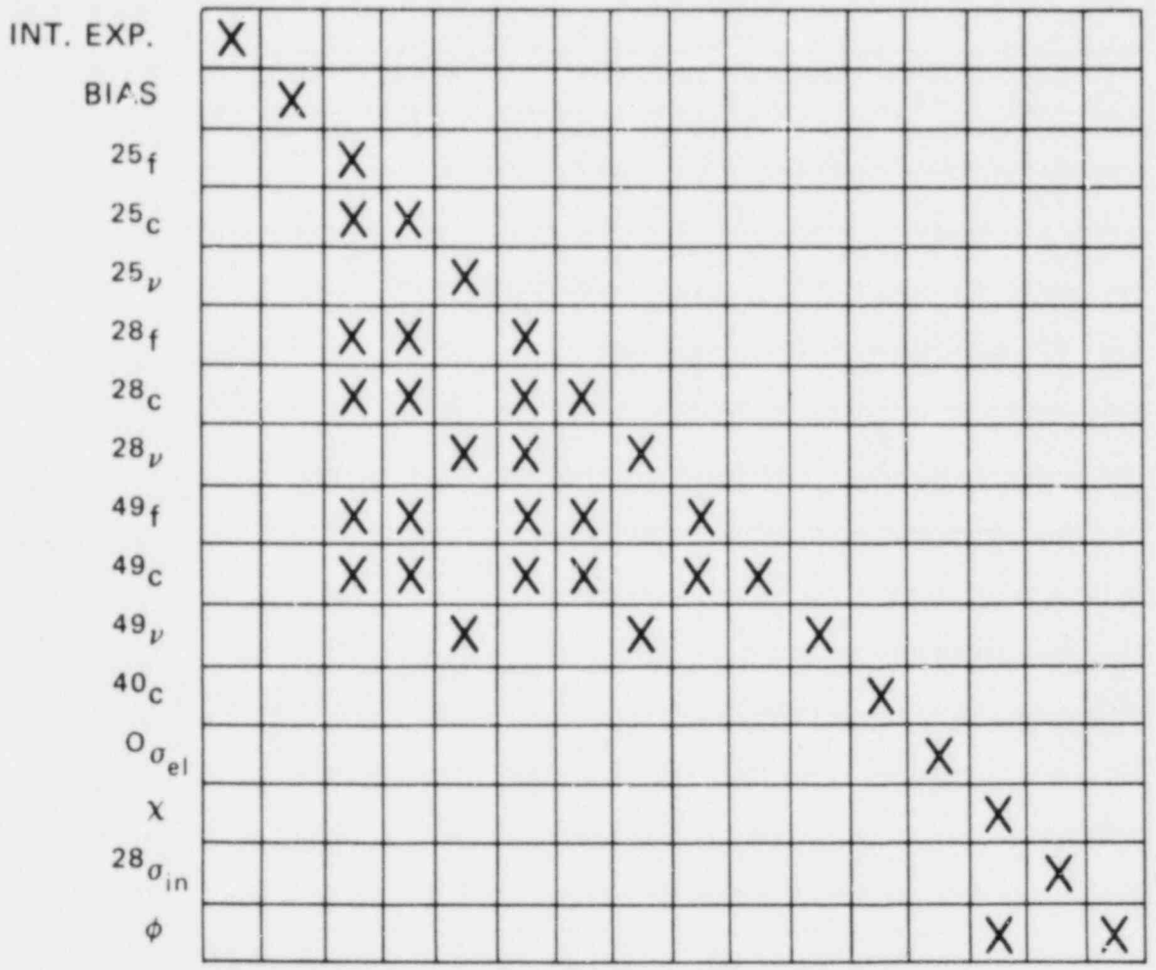

[a]REACTIONS FOR WHICH COVARIANCES AND CROSS-CORRELATIONS WERE INCLUDED IN THE CALCULATIONS OF PERFORMANCE PARAMETER UNCERTAINTIES ARE INDICATED BY X. ABOVE AND TO THE RIGHT OF THE PRINCIPAL DIAGONAL, X's SHOULD BE INFERRED FROM SYMMETRY. COLUMN LABELS ARE THE SAME AS ROW LABELS. REACTIONS FOR WHICH COVARIANCES WITHOUT CROSS CORRELATIONS WERE INCLUDED ARE GIVEN IN THE INSET.

Fig. 5. Covariance data for the LCCEWG-LMFBR reactor[a]

thirteen benchmark integral experiments (i.e., ZPR-6/7 K_{eff}, $^{28}f/^{49}f$, $^{28}f/^{49}f$, $^{28}c/^{49}f$; ZPR-6/6A K_{eff}, $^{28}f/^{25}f$, $^{28}c/^{25}f$; and ISNF $^{49}f/^{25}f$, $^{28}f/^{25}f$) were included in the adjustment procedure[2] for the LCCEWG-LMFBR, the reduction in the SD(K_{eff}) from 3.1% to 0.5% is quite close to the corresponding reduction from 3.2% to 0.4% obtained for the heterogeneous LMFBR when using ORACLE-1. This indicates that inclusion of these thirteen integral experiments results in the adjustment procedure is responsible for the bulk of the resulting reduction in the standard deviation of K_{eff} for large fast reactors.

VI. SUMMARY AND CONCLUSIONS

In summary, the adjusted cross section and covariance library ORACLE-I has been developed based on the VITAMIN-E 174-group cross section library and on associated covariances. With a chi-square per degree of freedom of 1.15, integral experiment data from twenty fast reactor benchmarks and seven standard neutron-field benchmarks were incorporated using a least-squares adjustment procedure.

This adjusted library was applied to a sensitivity and uncertainty analysis of a large heterogeneous LMFBR. Responses included in this analysis were K_{eff}, breeding ratio, peak power density, and the sodium-void reactivity. The calculation of sensitivities of peak power density, which is an extremum, required special considerations which have been explored.

A comparison of the uncertainty results for K_{eff} with previous analyses shows that the inclusion of the 27 benchmarks via the least-squares adjusted library reduces the uncertainty in K_{eff} to 0.4%. This again stresses the need for inclusion of integral experiments in design calculations.

REFERENCES

1. J. M. Kallfelz, M. L. Williams, D. Lal, and G. F. Flanagan, "Sensitivity Studies of the Breeding Ratio for the Clinch River Breeder Reactor," in J. M. Kallfelz and R. A. Karam, eds.; Advanced Reactors; Physics, Design, and Economics, Pergamon Press, Oxford and New York (1980).
2. J. H. Marable, C. R. Weisbin, and G. de Saussure, Nucl. Sci. Eng. 75, 30 (1980).
3. J. H. Marable and C. R. Weisbin, "Uncertainties in the Breeding Ratio of a Large LMFBR," in E. G. Silver, ed., Advances in Reactor Physics, CONF-780401, U.S. Dept. of Energy, p. 231 (1978).
4. J. M. Kallfelz, D. Biswas, C. L. Cowan, J. H. Marable, M. L. Williams, C. R. Weisbin, J. D. Drischler, T. B. Fowler, and J. R. White, "Design and Sensitivity Analysis of a CDS-Type LMFBR Heterogeneous Core," Proceedings of the ANS Topical Meeting, 1980 Advances in Reactor Physics and Shielding, p. 467, September 14-19, 1980.
5. Y. Yeivin, J. H. Marable, C. R. Weisbin, and J. J. Wagschal, "ORACLE: An Adjusted Cross Section and Covariance Library for Fast Reactor Analysis," Proceedings of the ANS Topical Meeting, 1980 Advances in Reactor Physics and Shielding, p. 705, September 14-19, 1980.
6. J. Barhen, D. G. Cacuci, W. E. Ford, III, R. W. Roussin, J. J. Wagschal, C. R. Weisbin, J. E. White, and R. Q. Wright, "VITAMIN-E: A Multipurpose ENDF/B-V Coupled Neutron-Gamma Cross-Section Library," American Physical Society International Conference on Nuclear Cross Sections and Technology, Knoxville, Tennessee, October 22-26, 1979.

7. R. Kinsey, "ENDF/B Summary Documentation," Brookhaven National Laboratory, BNL-NCS-17541, (ENDF-201)(July 1979).
8. D. R. Vondy, T. B. Fowler, and G. W. Cunningham, "VENTURE," ORNL-5062/R1, Oak Ridge National Laboratory (1977).
9. J. R. White, "The Development, Implementation, and Verification of Multicycle Depletion Perturbation Theory for Reactor Burnup Analysis," ORNL/TM-7305, Oak Ridge National Laboratory (1980).
10. J. Lucius et al., "A User's Manual for the FORSS Sensitivity and Uncertainty Analysis Code System," ORNL-5316, ENDF-291, Oak Ridge National Laboratory (1980).
11. D. G. Cacuci, J. Math. Phys., 22, 2803 (1981).
12. V. A. Perone, J. M. Kallfelz, and L. A. Belbiidia, Nucl. Sci. Eng., 79, 326 (1981).
13. D. G. Cacuci, P. J. Maudlin, and C. V. Parks, "Applications of Differential Sensitivity Theory for Extrenum-Type Responses," ORNL/TM-7717, Oak Ridge National Laboratory (1982).
14. R. Protsik, General Electric-Sunnyvale, Private Coumunication (1971).
15. C. L. Cowan and C. S. Russell, "FUMBLE-II," GEAP-14138, General Electric-Sunnyvale (1976).
16. C. R. Weisbin et al., "Sensitivity and Uncertainty Analysis of Reactor Performance Parameters," in Advances in Nuclear Science and Technology, J. Lewins and M. Becker, Editors, Plenum Publishing Corp., N.Y., Vol. 14 (1982).
17. L. Weston, Oak Ridge National Laboratory, private communication (1981).
18. "VITAMIN-C," RSIC Report DLC-41/VITAMIN C, Oak Ridge National Laboratory (1978).
19. N. M. Greene et al., "AMPX," ORNL/TM-3706, Oak Ridge National Laboratory (1976).
20. E. Kujawski and H. S. Bailey, Nucl. Sci. Eng., 64, 90 (1977).

FAST REACTOR DATA TESTING OF ENDF/B-V AT ORNL

R. Q. Wright, W. E. Ford, III, J. L. Lucius, C. C. Webster
Computer Sciences at Oak Ridge National Laboratory
Union Carbide Corporation, Nuclear Division

J. H. Marable
Engineering Physics Division
Oak Ridge National Laboratory

ABSTRACT

Data from the ENDF/B-V processed multigroup cross-section libraries VITAMIN-E and FORSS-V were used in the calculation of twelve CSEWG fast reactor benchmarks. Results obtained include the eigenvalues, central reaction rate ratios, and central reactivity worths. Conclusions and recommendations based on the trends in these results are given. Finally, the ORNL results are compared with those obtained by other data testers.

INTRODUCTION

The Cross Section Evaluation Working Group (CSEWG) is coordinating a program to assess the adequacy of ENDF/B-V cross sections for both fast- and thermal-reactor design applications.[1] A secondary goal is to evaluate cross-section processing codes, cross-section libraries, and radiation-transport codes. Fast reactor data testing (FRDT) goals are accomplished, in part, by comparison of calculated results with documented performance parameters of CSEWG fast reactor benchmarks[2-4] and with results obtained by other data testers. The purpose of this paper is to describe the results of FRDT at the Oak Ridge National Laboratory (ORNL).

Data from two ENDF/B-V processed multigroup cross-section libraries, VITAMIN-E and FORSS-V, were used in the benchmark calculations. VITAMIN-E is an evolving 174-neutron, 38-gamma group library applicable to fusion reactor neutronics, fast reactor core and

shield analysis, weapons analyses, and LWR shielding and dosimetry problems.[a,5,6] FORSS-V is an undocumented ORNL 100-neutron-group library for FRDT per se. Neutron data in the libraries were processed with MINX.[7] Resonance self-shielding calculations for the benchmarks were made with BONAMI-2;[8,9] one-dimensional transport calculations were made with either XSDRNPM[8,9] or ANISN.[10] Bias factors accounting for modeling approximations were obtained from Refs. 2-4.

The benchmarks studied in the FRDT program are identified in Table 1. The benchmark set includes five Pu-fueled and seven U-fueled assemblies which have a wide variety of fuel and reflector compositions. GODIVA and JEZEBEL are bare metal spheres; the others are reflected. For the reflected assemblies, the fuel fertile to fissile ratio varies from about 1:13 for FLATTOP-25 to 9:1 for BIG TEN. The reflectors generally contain large amounts of ^{238}U with the exception of ZPR-3/56B which has a Ni reflector.

The twelve benchmarks also cover a wide range in spectral hardness. GODIVA and JEZEBEL have very hard spectra, ZPR-6/6A and ZPR-6/7 are soft spectrum benchmarks, and BIG TEN is an intermediate case. The ZPR-6/7 and BIG TEN central neutron flux spectra are compared in Fig. 1. For ZPR-6/7, shown as the solid line, the flux peaks at about 150 keV and there is a relatively large low-energy component. The BIG TEN flux peaks at ~400 kev and the low-energy component is much smaller. The hardest spectra benchmarks, e.g., GODIVA and JEZEBEL, have spectra which peak at about 1 MeV and the low-energy component is essentially zero. Clearly the various benchmarks are sensitive to cross sections in different energy ranges as a function of spectral hardness.

The materials needed for fast reactor data testing are shown in Table 2. ENDF/B-V data were used except for gallium which was not available in ENDF/B-V at the time the calculations were performed. Gallium, which is needed for the JEZEBEL benchmark, was processed from data in the Lawrence Livermore cross-section library.[11,12] Some materials, e.g., ^{242}Pu and ^{241}Am, appear in the benchmarks with very small concentrations. ^{10}B does not appear in any benchmark but is needed for central reactivity worths.

ORNL CALCULATIONAL RESULTS, OBSERVATIONS, AND RECOMMENDATIONS

ORNL eigenvalue results for the benchmarks are given in Table 3. These results were obtained using the one-dimensional benchmark models and correction factors given in the CSEWG specifications.[2-4]

---

[a] VITAMIN-E is sponsored by the Department of Energy (DOE) Division of Reactor Research and Technology (DRRT) and Office of Fusion Energy (OFE), the Defense Nuclear Agency (DNA), and the Electric Power Research Institute (EPRI).

JEZEBEL, GODIVA, FLATTOP-25, BIG TEN, ZPR-9/31, ZPR-6/6A, and ZPR-6/7 were calculated with VITAMIN-E cross sections; ZPR-3/6F, ZPR-3/12, ZPR-3/11, ZPR-3/48, and ZPR-3/56B were calculated with FORSS-V data.

The benchmarks are ordered in Table 3 according to decreasing spectral hardness with three hard spectra, four intermediate spectra, and five soft spectra assemblies. The measured F28/F25 ratio,[b] given in Column 2 of the table is an indication of spectral hardness. The following observations and recommendations are derived from Table 3.

1. The average ORNL eigenvalue for the Pu-fueled benchmarks is 1.0051 and for the U-fueled benchmarks it is 1.0037; the average for the 12 benchmarks is 1.0042. Thus, there is essentially no bias between the Pu- and U-fueled benchmarks when all 12 benchmarks are used as the reference set. When we consider only the two pairs, JEZEBEL:GODIVA and ZPR-6/7:6/6A, there is a bias of 0.8% between the Pu-fueled and U-fueled benchmarks.

2. The ZPR-6/6A eigenvalue is quite low relative to the other benchmarks; this may indicate a need to re-examine the benchmark specifications and correction factors.

3. K-eff for FLATTOP-25 is 0.8% higher than the GODIVA value. The core composition of these two benchmarks is essentially the same; the differences are the core radius and the fact that GODIVA is unreflected while FLATTOP-25 has a reflector. The eigenvalue difference may indicate that the leakage from GODIVA is overpredicted.

4. K-eff of ZPR-9/31 is 0.7% higher than k-eff of ZPR-6/7; this difference may be due to spectral differences and should be investigated. Recall that ZPR-6/7 has plutonium oxide fuel and ZPR-9/31 is a carbide assembly.

The ORNL C/E (calculated/experimental) values for selected central reaction-rate ratios are given in Table 4. The ZPR-9/31 ratios (with the exception of C28/F49) are considered unreliable and have been omitted. The following conclusions and recommendations are suggested based on the results in Table 4:

1. The JEZEBEL F28/F25 C/E is ~8% low and the calculated leakage spectrum is too soft relative to the measured spectrum. These two results may justify a harder fission spectrum.

---

[b] Symbolically, the ^{238}U fission to ^{235}U fission reaction-rate ratio is denoted herein as F28/F25. Likewise, F49 denotes ^{239}Pu fission and C28 denotes ^{238}capture.

2. For GODIVA, FLATTOP-25, and the four intermediate spectra benchmarks, the F28/F25 C/E values are well above unity; the average is 1.06 for the six benchmarks. Since the F28/F25 ratio is very sensitive to the spectrum, the extent to which this bias is due to spectral determining factors should be investigated. The GODIVA, FLATTOP-25, and BIG TEN experimental values have been carefully measured and the uncertainties in the measured values (1σ) are about 1.1% for each of the three benchmarks. The ZPR-3 series has bigger uncertainties, the largest being for ZPR-3/12 which is 4.2%. Since the six benchmarks are all U-fueled, a softer ^{235}U fission spectrum would improve the agreement between calculation and experiment. Changes to the ^{235}U and ^{238}U inelastic scattering cross sections could also help reduce this discrepancy.

3. With the exception of ZPR-3/48, the F28/F25 C/E's are less than one for the soft spectra Pu-fueled benchmarks. The uncertainty in the ZPR-3/48 measured value is 5% so that a C/E of 1.064 is acceptable.

4. The F49/F25 C/E values vary from about 4% low to 4% high with an average value of 0.998.

5. There is a trend for C28/F25 C/E to increase for the softer spectra assemblies.

6. For ZPR-9/31 and ZPR-6/7 the central reaction-rate ratios are measured relative to F49. This is the reason that C28/F49 is given for only these two benchmarks. The C28/F49 C/E for ZPR-6/7 is overpredicted by 5%.

Central reactivity worths have been obtained for ZPR-6/7, GODIVA, and JEZEBEL. The results are given in Table 5 as C/E ratios. With the exception of GODIVA ^{10}B (C/E = 0.82) and JEZEBEL ^{238}U (0.88), the GODIVA and JEZEBEL C/E's are close to unity. For ZPR-6/7, the ^{239}Pu worth is overpredicted by 16% and the ^{235}U worth by 11%.

COMPARISON OF LANL, ANL, AND ORNL RESULTS

The twelve benchmarks analyzed in this study have also been calculated by R. Kidman at Los Alamos.[13] A comparison of the ORNL k-eff's with those obtained at LANL is given in Table 6; the percent differences are also given. With the single exception of ZPR-3/6F, the overall agreement is very good, generally within 0.25%. There is a trend for the LANL values to be slightly higher for the hard spectra benchmarks and slightly lower for the soft spectra benchmarks. We consider the level of agreement to be quite acceptable and have not investigated these differences.

Five of the benchmarks in Table 6 have been calculated by E. M. Pennington at ANL;[14] these results are given in Table 7, along with the LANL and ORNL results (from Table 6). The ORNL and ANL values are in good agreement for JEZEBEL, GODIVA and ZPR-9/31 but for ZPR-6/6A and ZPR-6/7 the ANL values are about 0.5% lower than the ORNL values.

In the case of ZPR-6/7, a study was done to investigate possible causes of the rather large ANL-ORNL k-eff difference. Earlier ORNL studies by Marable, Lucius, and Weisbin had shown that the eigenvalue was very sensitive to the processed ENDF/B-IV Fe(n,γ), ^{238}U(n,γ), and ^{239}Pu(n,f) cross sections.[15,c] Cross sections for the three reactions were obtained in a 28-group structure from Pennington. Corresponding data were prepared from the ORNL self-shielded ZPR-6/7 cross sections. It was noted that there were large differences between the ANL and ORNL cross sections for Fe(n,γ) in some groups. In particular, Group 20 (748-1234 eV), which contains the 1.15 keV Fe p-wave resonance, was observed to be the most important group. This observation was based on the magnitude of the sensitivity of ZPR-6/7 k-eff to the iron capture cross-section in this group (see Fig. 7, p. 20 of Ref. 15) and the cross-section difference, defined as (ANL-ORNL)/ORNL. The difference was found to be 24%. Groups 8-12 (41-498 keV) had differences of 14 to 30% but had lower sensitivity coefficients.

The SENTINEL code, written at ORNL, can be used to predict the change in a given response, e.g., k-eff, resulting from a given cross-section change.[16-17] The input to SENTINEL consists of the cross-section differences and sensitivity coefficients. Using the ORNL-ANL Fe(n,γ) cross-section differences and the Fe(n,γ) sensitivity coefficients in SENTINEL gave a predicted change in the ORNL-calculated ZPR-6/7 k-eff of -0.24%. (An ORNL recalculation of ZPR-6/7 using the ANL Fe(n,γ) cross sections gave a change of -0.22% in k-eff which is in excellent agreement with the SENTINEL result.) SENTINEL runs for ^{238}U (n,γ) and ^{239}Pu(n,γ) predicted an additional 0.08% decrease in k-eff which, when added to the predicted 0.24% decrease for Fe(n,γ), results in a decrease of 0.32% for the ORNL eigenvalue, giving a value of 0.9978. (See Table 7.) Ignoring the effect of the denominator in determining the cross-section percent difference, it can be argued that the SENTINEL results predict a 0.32% increase in the ANL eigenvalue, which results in a value of 0.9978. The ORNL vis-a-vis ANL cross-section difference is assumed to be due to the self-shielding treatment. The cause of the difference is being investigated.

---

[c] Sensitivity coefficients for CSEWG benchmarks are available in an undocumented ORNL in-house library which resulted from the work reported in Ref. 15.

Table 8 gives a comparison of ANL, LANL, and ORNL C/E values for selected central reaction rate ratios. The values in Table 8 are in good agreement with differences of $\leq$ 1.0%, the largest differences being for the C28/F25 and C28/F49 ratios.

A comparison of the central reactivity worths calculated by ANL, LANL, and ORNL for GODIVA, JEZEBEL, and ZPR-6/7 is given in Table 9. The GODIVA worths are in good agreement with a spread of approximately 2%. For JEZEBEL the ORNL values are a few percent lower than the ANL and LANL results. In the case of ZPR-6/7 there is a fairly large spread in the ^{238}U and ^{10}B worths with the ORNL worths about midway between the ANL and LANL values.

CONCLUSIONS

Results of fast reactor benchmark testing of ENDF/B-V data by the various laboratories is being documented by CSEWG.[18] Generally, the ORNL results are in good agreement with those of other data testers. One of the highest priorities for future work is a review of the existing CSEWG benchmarks, with specific emphasis on the flux spectra.

Table 1. CSEWG Benchmarks Studied in the ORNL Fast-Reactor Data Testing Program

Benchmark	Characteristics
	Pu-Fueled Benchmarks
JEZEBEL	Bare metal sphere, ~95% ^{239}Pu.
ZPR-3/48	Carbide Assembly, U:Pu approximately 4:1, ^{238}U blanket.
ZPR-3/56B	Mixed oxide fuel, Ni reflector.
ZPR-6/7	Plutonium oxide fuel, U:Pu approximately 6:1, ^{238}U blanket.
ZPR-9/31	Carbide assembly, U:Pu approximately 6:1, uranium carbide blanket, stainless steel reflector.
	U-Fueled Benchmarks
GODIVA	Bare metal sphere, ~93% ^{235}U.
FLATTOP-25	93% ^{235}U sphere with a thick natural uranium reflector.
ZPR-3/6F	~1:1 fertile to fissile, ^{238}U reflector.
ZPR-3/11	7:1 fertile to fissile uranium metal with ^{238}U reflector.
ZPR-3/12	4:1 uranium-graphite, ^{238}U blanket.
ZPR-6/6A	Uranium oxide fuel 5:1 fertile to fissile, ^{238}U blanket.
BIG TEN	Uranium-metal core, averaging 10 wt % ^{235}U, reflected by depleted-uranium metal.

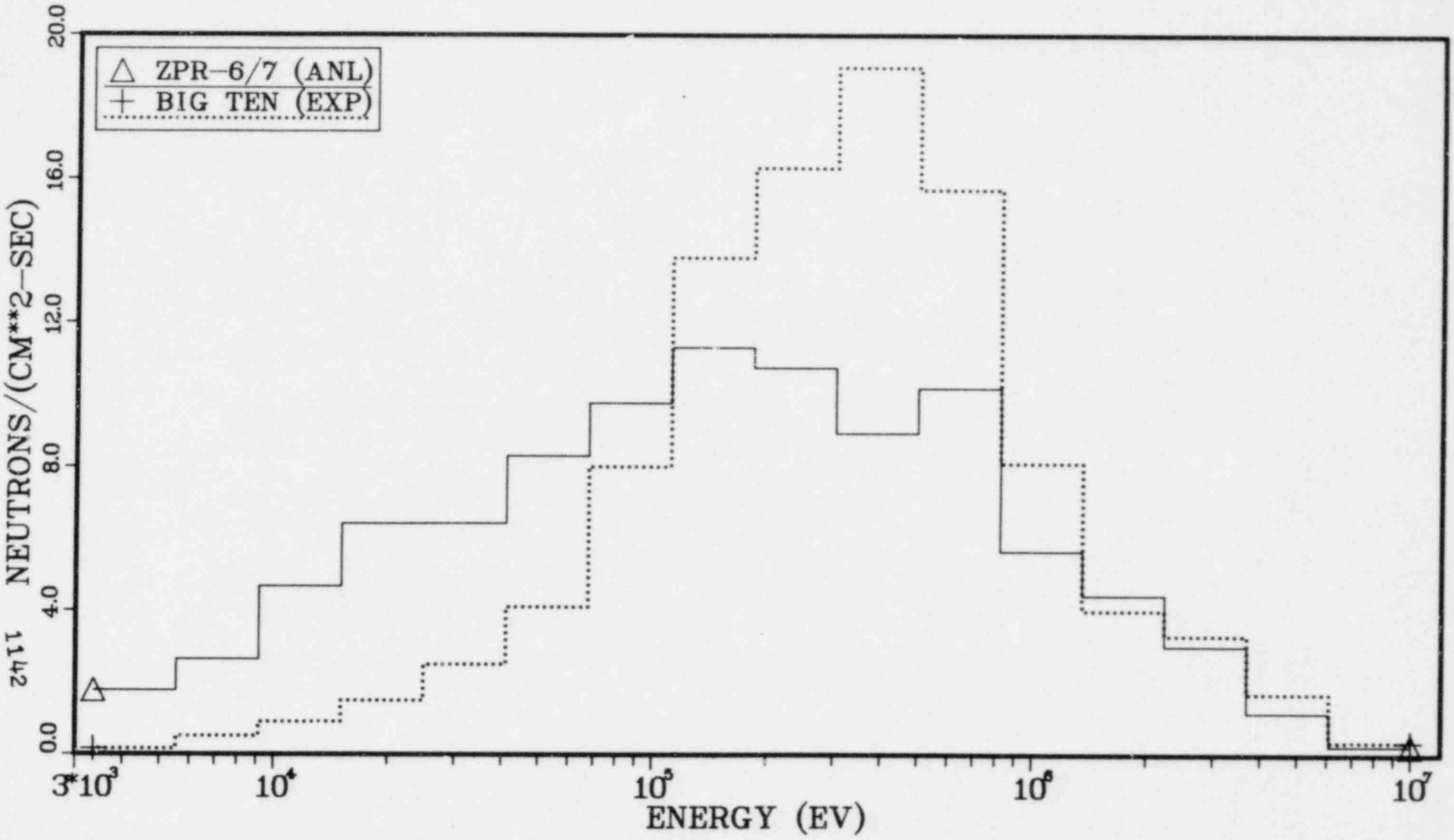

Fig. 1. CENTRAL NEUTRON FLUX SPECTRA

Table 2. Materials Needed for Fast Reactor Data Testing

Material	MAT[a]	Authors	Lab
B-10	1305	G. Hale, L. Stewart, P. Young	LANL
C-12	1306	C. Fu, F. Perey	ORNL
O-16	1276	P. Young, D. Foster, Jr., G. Hale	LANL
Na-23	1311	D. Larson	ORNL
Al-27	1313	P. Young, D. Foster, Jr.	LANL
Si	1314	Larson, Perey, Drake, Young	ORNL
Cr	1324	A. Prince, T. Burrows	BNL
Mn-55	1325	S. Mughabghab	BNL
Fe	1326	C. Fu, F. Perey	ORNL
Ni	1328	M. Divadeenan	BNL
Mo	1321	Howerton, Schmittnoth, Schenter	LLL,HEDL
Ga	b		
U-234	1394	Divadeenan, Mann, Drake, Reich	BNL,HEDL
U-235	1395	M. Bhat	BNL
U-238	1398	E. Pennington, A. Smith, W. Poenitz	ANL
Pu-238	1338	Mann, Schenter, Atter, Dunford	HEDL,AI
Pu-239	1399	E. Kujawaski, L. Stewart	GE,LANL
Pu-240	1380	L. Weston	ORNL
Pu-241	1381	L. Weston, R. Wright, R. Howerton	ORNL
Pu-242	1342	Mann, Benjamin, Madland, Howerton	HEDL,SRL
Am-241	1361	Mann, Schenter, Weston	HEDL,ORNL

[a] ENDF/B-V evalutations unless otherwise noted.

[b] Ga evaluation from ENDL library (Lawrence Livermore National Laboratory).[11,12]

Table 3. FRDT Eigenvalues Based on ENDF/B-V[a,c]

Benchmark	Measured F28/F25[b]	k-eff
Hard Spectrum:		
JEZEBEL	0.2137	1.0043
GODIVA	0.1647	0.9967
FLATTOP-25	0.1488	1.0046
Intermediate Spectrum:		
ZPR-3/6F	0.078	1.0061
ZPR-3/12	0.047	1.0044
ZPR-3/11	0.038	1.0121
BIG TEN	0.0373	1.0102
Soft Spectrum:		
ZPR-3/48	0.0321	1.0089
ZPR-3/56B	0.0308	1.0056
ZPR-9/31	0.02896	1.0066
ZPR-6/6A	0.02388	0.9915
ZPR-6/7	0.02261	1.0000

[a] Pu-fueled benchmarks include JEZEBEL, ZPR-3/48, ZPR-3/56B, ZPR-9/31, and ZPR-6/7; the others are U-fueled (benchmarks are ordered according to spectral hardness).

[b] The measured ^{238}U fission to ^{235}U fission central reaction-rate ratio is an indication of spectral hardness; the breakpoint between hard and intermediate is 0.1, and between intermediate and soft 0.035.

[c] ORNL results are from VITAMIN-E data with the exception of ZPR-3/6F, ZPR-3/12, ZPR-3/11, ZPR-3/48, and ZPR-3/56B which are from FORSS-V.

Table 4. ORNL C/E Values for Central Reaction Rate Ratios Based on ENDF/B-V[a,b]

Benchmark[c]	F28/F25 C/E	F49/F25 C/E	C28/F25 C/E	C28/F49 C/E
Hard Spectrum:				
JEZEBEL	0.917	0.973	NC[d]	
GODIVA	1.039	0.996	NC	
FLATTOP-25	1.039	1.002	NC	
Intermediate Spectrum:				
ZPR-3/6F	1.035	1.038	0.930	
ZPR-3/12	1.093	1.013	0.970	
ZPR-3/11	1.089	1.003	0.954	
BIG TEN	1.070	1.005	0.972	
Soft Spectrum:				
ZPR-3/48	1.064	NC	0.976	
ZPR-3/56B	0.989	0.961	NC	
ZPR-9/31[e]				1.036
ZPR-6/6A	0.987	NC	1.031	
ZPR-6/7	0.961	0.992	1.041	1.050

[a]Results are from VITAMIN-E data with the exception of ZPR-3/6F, ZPR-3/12, ZPR-3/11, ZPR-3/48, and ZPR-3/56B which are from FORSS-V. Symbolically, the ^{238}U fission to ^{235}U fission reaction-rate ratio is denoted herein as F28/F25. Likewise, F49 denotes ^{239}Pu fission and C28 denotes ^{238}U capture.

[b]The uncertainties in the experimental values (1σ) range from 1 to 5%. The C/E values must be interpreted relative to the uncertainty in the measured value.

[c]Pu-fueled benchmarks include JEZEBEL, ZPR-3/48, ZPR-3/56B, ZPR-9/31, and ZPR-6/7; the others are U-fueled (benchmarks are ordered according to spectral hardness).

[d]NC means not calculated because experimental value was not available.

[e]The ZPR-9/31 F49/F25 experimental value is presently not considered to be reliable; the C/E values (other than C28/F49) should receive no consideration and have been omitted.

Table 5. ORNL Central Reactivity Worths (C/E) Based on ENDF/B-V

Material	JEZEBEL	GODIVA	ZPR-6/7
^{240}Pu	0.95	1.04	
^{239}Pu	0.96	0.99	1.16
^{235}U	0.97	0.97	1.11
^{238}U	0.88	0.99	1.00
^{10}B	0.94	0.82	1.05
Mo			1.38
Na			1.24
Fe			1.25
Cr			1.60
Ni			1.22

Table 6. Comparison of LANL and ORNL Values of k-eff

Benchmark	LANL	ORNL	$\Delta\%$[a]
Hard Spectrum:			
JEZEBEL	1.0058	1.0043	0.15
GODIVA	0.9981	0.9967	0.14
FLATTOP-25	1.0067	1.0046	0.21
Intermediate Spectrum:			
ZPR-3/6F	1.0101	1.0061	0.40
ZPR-3/12	1.0061	1.0044	0.17
ZPR-3/11	1.0121	1.0121	0.0
BIG TEN	1.0101	1.0102	0.0
Soft Spectrum:			
ZPR-3/48	1.0066	1.0089	-0.23
ZPR-3/56B	1.0051	1.0056	-0.05
ZPR-9/31	1.0083	1.0066	0.17
ZPR-6/6A	0.9897	0.9915	-0.18
ZPR-6/7	0.9977	1.0000	-0.23

[a] $\Delta\% \equiv \frac{\text{LANL-ORNL}}{\text{ORNL}} \times 100\%$.

Table 7. Comparison of ANL, LANL, and ORNL Values of k-eff

Benchmark	ANL	LANL	ORNL
JEZEBEL	1.0042	1.0058	1.0043
GODIVA	0.9962	0.9981	0.9967
ZPR-9/31	1.0054	1.0083	1.0066
ZPR-6/6A	0.9862	0.9897	0.9915
ZPR-6/7	0.9946	0.9977	1.0000

Table 8. C/E Values for Central Reaction Rate Ratios Based on ENDF/B-V

Benchmark	ANL	LANL	ORNL
GODIVA			
F28/F25	1.036	1.036	1.039
F49/F25	0.996	0.994	0.996
ZPR-6/6A			
F28/F25	0.991	0.995	0.987
C28/F25	1.038	1.036	1.031
JEZEBEL			
F28/F25	0.920	0.917	0.917
F49/F25	0.974	0.972	0.973
ZPR-6/7			
F28/F25	0.961	0.967	0.961
F49/F25	0.994	0.994	0.992
C28/F25	1.052	1.051	1.041
C28/F49	1.058	1.057	1.050

Table 9. Central Reactivity Worths (C/E) Using ENDF/B-V

Benchmark	ANL	LANL	ORNL
JEZEBEL			
^{240}Pu	0.98		0.95
^{239}Pu	0.99		0.96
^{235}U	1.00	1.02	0.97
^{238}U	0.92	0.94	0.88
^{10}B		1.00	0.94
GODIVA			
^{239}Pu	1.01		0.99
^{235}U	0.99	0.98	0.97
^{238}U	1.01	1.00	0.99
^{10}B		0.83	0.82
ZPR-6/7			
^{239}Pu	1.17	1.17	1.16
^{235}U	1.13	1.12	1.11
^{238}U	0.95	1.04	1.00
^{10}B	1.00	1.12	1.05

REFERENCES

1. R. Kinsey, Ed., "ENDF/B Summary Documentation," BNL-NCS-17541 (ENDF-201), 3rd ed., Brookhaven National Laboratory (1979).

2. "Cross Section Evaluation Working Group Benchmark Specifications," BNL 19302 (ENDF-202) (November 1974).

3. NNDC to Holders of BNL-19302 (ENDF 202), "Cross Section Evaluation Working Group Benchmark Specifications," Brookhaven National Laboratory letter (October 30, 1978).

4. G. E. Hansen and H. C. Paxton to R. J. LaBauve, "Specifications of Los Alamos Fast-Neutron Assemblies in the CSEWG Benchmark Format," Los Alamos Scientific Laboratory letter (October 1979).

5. C. R. Weisbin, et. al., "VITAMIN-E: An ENDF/B-V Multigroup Cross-Section Library for LMFBR Core and Shield, LWR Shield, Dosimetry and Fusion Blanket Technology," ORNL-5505 (February 1979).

6. J. Barhen, D. G. Cacuci, W. E. Ford, III, R. W. Roussin, J. J. Wagschal, C. R. Weisbin, J. R. White, and R. Q. Wright, "VITAMIN-E: A Multipurpose ENDF/B-V Coupled Neutron-Gamma Cross Section Library," NBS Special Publication 594 (September 1980).

7. C. R. Weisbin, P. D. Soran, R. E. MacFarlane, D. R. Harris, R. J. LaBauve, J. S. Hendricks, J. E. White, and R. B. Kidman, "MINX, A Multigroup Interpretation of Nuclear Cross Sections," LA-6486-MS (1976).

8. N. M. Greene, J. L. Lucius, L. M. Petrie, W. E. Ford, III, J. E. White, and R. Q. Wright, "AMPX: A Modular Code System for Generating Coupled Multigroup Neutron-Gamma Libraries from ENDF/B," ORNL-TM-3706 (1976).

9. "AMPX-II Modular Code System for Generating Coupled Multigroup Neutron-Gamma-Ray Cross-Section Libraries from Data in ENDF Format," Radiation Shielding Information Center documentation for PSR-63 (November 1978).

10. W. W. Engle, Jr., "A Users Manual for ANISN A One Dimensional Discrete Ordinates Transport Code With Anisotropic Scattering," Union Carbide Corporation, Nuclear Division Report K-1693 (March 1967).

11. R. J. Howerton, "The Lawrence Livermore Laboratory Evaluated Nuclear Data Library (ENDL) Translated into the ENDF/B Format," UCID-16727 (March 1975).

12. "LENDL Livermore Evaluated Neutron and Secondary Gamma-Ray Production Cross-Section Library in ENDF/B-IV Format," Radiation Shielding Information Center Documentation for DLC-34, Oak Ridge National Laboratory (January 1980).

13. R. B. Kidman, "ENDF/B-V, LIB-V, and the CSEWG Benchmarks," LA-8950-MS, (August 1981).

14. E. M. Pennington, "ENDF/B-V Fast Reactor Data Testing," Argonne National Laboratory FRA-TM-123 (May 1980).

15. J. H. Marable, J. L. Lucius, and C. R. Weisbin, "Compilation of Sensitivity Profiles for Several CSEWG Fast Reactor Benchmarks," ORNL-5262 (ENDF-234) (March 1977).

16. J. L. Lucius, C. R. Weisbin, J. H. Marable, J. D. Drischler, R. Q. Wright, and J. E. White, "A Users Manual for the FORSS Sensitivity and Uncertainty Analysis Code System," ORNL-5316 (ENDF-291) (January 1981).

17. J. H. Marable, J. D. Drischler, and C. R. Weisbin, "SENDIN and SENTINEL: Two Computer Codes to Assess the Effects of Nuclear Data Changes," ORNL/TM-5446 (ENDF-250) (July 1977).

18. R. D. McKnight, "Benchmark Testing of ENDF/B-V Data for Fast Reactors," Included as Chapter 2 of "Benchmark Testing of ENDF/B-V," to be published 1982.

*U.S. GOVERNMENT PRINTING OFFICE : 1982 0-361-297/2341

NRC FORM 335 (11 81)

U.S. NUCLEAR REGULATORY COMMISSION

BIBLIOGRAPHIC DATA SHEET

1. REPORT NUMBER (Assigned by DDC)
NUREG/CP-0034, Vol. 2

4. TITLE AND SUBTITLE (Add Volume No., if appropriate)
Proceedings of the Topical Meeting on Advances in Reactor Physics and Core Thermal Hydraulics

2. (Leave blank)

3. RECIPIENT'S ACCESSION NO.

7. AUTHOR(S)

5. DATE REPORT COMPLETED
MONTH: July YEAR: 1982

9. PERFORMING ORGANIZATION NAME AND MAILING ADDRESS (Include Zip Code)
Proceedings printed by
U.S. Nuclear Regulatory Commission
Washington, DC 20555

DATE REPORT ISSUED
MONTH: August YEAR: 1982

6. (Leave blank)

8. (Leave blank)

12. SPONSORING ORGANIZATION NAME AND MAILING ADDRESS (Include Zip Code)
Northeastern New York Section of the American Nuclear Society
Reactor Physics Division of the American Nuclear Society
Thermal Hydraulics Division of the American Nuclear Society

10. PROJECT/TASK/WORK UNIT NO.

11. FIN NO.

13. TYPE OF REPORT
Proceedings

PERIOD COVERED (Inclusive dates)
Held at Kiamesha Lake, NY
September 22-24, 1982

15. SUPPLEMENTARY NOTES

14. (Leave blank)

16. ABSTRACT (200 words or less)

Technical papers presented at the ANS Topical Meeting on Advances in Reactor Physics and Core Thermal Hydraulics, September 22-24, 1982, at Kiamesha Lake, N.Y. are included in these Proceedings. Reactor physics, core thermal hydraulics, and the interactions between core physics and thermal hydraulics are covered both for thermal reactors and for fast breeders. There are sessions on current challenges in these areas, on measurement and analysis of fast reactor physics parameters, on coupled core physics and thermal-hydraulics analysis, on in-core fuel management, on nodal and homogenization methods in reactor physics, on core thermal hydraulic and nuclear instrumentation, and on validation of fast reactor thermal hydraulic methods. In addition there are sessions on reactor theory, on measurement and analysis of thermal reactor physics parameters, on validation of thermal reactor thermal hydraulics methods, and on development and utilization of differential and integral nuclear data. This report consists of two volumes.

17. KEY WORDS AND DOCUMENT ANALYSIS

17a. DESCRIPTORS

17b. IDENTIFIERS/OPEN-ENDED TERMS

18. AVAILABILITY STATEMENT
Unlimited

19. SECURITY CLASS (This report)
Unclassified

21. NO. OF PAGES

20. SECURITY CLASS (This page)
Unclassified

22. PRICE
$

NRC FORM 335 (11 81)

UNITED STATES
NUCLEAR REGULATORY COMMISSION
WASHINGTON, D.C. 20555

OFFICIAL BUSINESS
PENALTY FOR PRIVATE USE, $300

FOURTH CLASS MAIL
POSTAGE & FEES PAID
USNRC
WASH D C
PERMIT No G67